CHARACTERIZATION OF THE ENGINEERING PROPERTIES OF MEXICO CITY CLAY

by

Sergio Covarrubias Fernández

Licenciado en Ingenieria Civil, Universidad Iberoamericana
México D.F., México
(1991)

Submitted to the
Department of Civil and Environmental Engineering
in partial fulfillment of the requirements for the degree of

Master of Science in Civil and Environmental Engineering

at the

MASSACHUSETTS INSTITUTE OF TECHNOLOGY

January, 1994

Signature of Author:.....
Dept. of Civil and Environmental Engineering, January 14, 1993

Certified by:.....
Dr. John T. Germaine, Thesis Supervisor

Accepted by:.....
Prof. Joseph Sussman
Chairman, Departmental Committee on Graduate Studies

CHARACTERIZATION OF THE ENGINEERING PROPERTIES OF MEXICO CITY CLAY

by

Sergio Covarrubias Fernández

Submitted to the Department of Civil and Environmental Engineering on
January 14, 1994 in partial fulfillment of the requirements
for the degree of Master of Science in Civil and Environmental Engineering

ABSTRACT

Geotechnical studies characterizing the "nature and behavior" of México City Clay have been limited since 1959. In recent years, new techniques have been developed for laboratory testing which enable more reliable characterization of clay properties than possible from the "standard" procedures. In this study, a thorough assessment of the engineering properties of México City Clay at the site of México City's Cathedral is conducted using "state-of-the-art" sampling and automated testing equipment. Additionally, these characteristics of México City Clay are studied in the context of its depositional history and mineralogy, and to evaluate the influence of various sampling methods on sample disturbance.

The sampling program for this investigation consists of drilling three boreholes with three different drilling techniques and obtaining samples with two different samplers. The laboratory program can be divided into two categories; tests for index properties and tests for engineering properties. Tests for index properties include standard geotechnical tests in addition to scanning electron microscopy and X-ray diffraction tests. Tests for engineering properties include: 15 constant rate of strain consolidation tests, 12 SHANSEP K_o-consolidated undrained direct simple shear tests, and 10 SHANSEP K_o-consolidated undrained triaxial compression and extension tests.

Radiography of the sample tubes revealed the heterogeneity of México City Clay. Scanning electron microscopy (SEM) revealed that México City Clay is, largely composed of microfossils (i.e., diatoms, ostracods, siliceous skeletons, etc.) and that the microstructure of the soil changes significantly with depth. Compositional analysis with the SEM revealed that silica and iron are the predominant elements of the soil. X-ray diffraction tests revealed the presence of particles with basic a crystal structure that is consistent with clay minerals. However, the crystal units are not consistently arranged to form a defined clay mineral. Based on SEM results and X-ray diffraction tests, México City Clay is described as soil constitute of (1) basic crystal units that do not have a consistent arrangement to conform a well defined clay mineral, and (2) a considerable amount of amorphous siliceous material (i.e., microfossils).

Based on results from the consolidation phase of all tests, strong correlations were found between water content and the compressibility and flow properties of the soil. Normalized Soil Parameters (NSP) are presented for the three modes of shear tested. It was found that México City Clay has unique NSP and the highest recorded undrained strength ratio for each mode of shearing. Based on the results, recommendations are made for sampling techniques and for drained compressibility-flow properties and undrained strength-deformation properties.

Thesis Supervisor: Dr. John T. Germaine
Title: Principal Research Associate in Civil and Environmental Engineering

ACKNOWLEDGMENTS

I would like to acknowledge the following people and organizations for providing the assistance and support necessary to accomplish this thesis:

Dr. John T. Germaine for his time and advice through many hours of data analysis. It was a pleasure working with someone so friendly and eager to help out his students in any possible way.

Dr. R. T. Martin for his advice and suggestions.

Ana Lukasiak for her hard work performing laboratory tests.

The Consejo Nacional de Ciencia y Tecnologia for the funds to support my studies.

Geotecnologia, S.A. for providing the funds and equipment to obtain the samples for this investigation.

Arq. Sergio Zaldivar Guerra, Director General de Sitios y Monumentos Historicos del Patrimonio Cultural, de la Secretaria de Desarrollo Social, for allowing me to perform this investigation on soil from México City's Cathedral.

Jose and Erna Sanchez for making me feel part of their family and for taking care of me when I needed it the most.

My friends at MIT who helped make the days and nights spent in office and in lab more enjoyable. I would like to give special thanks to Doug Cauble for the days he spent helping me proofread and finish this thesis, for the innumerable rides he gave me, and for great conversations. Finally, I would like to thank Mike Geer and Marika Santagata for always trying to answer many of my questions about soil mechanics.

Debra Berman for being part of the most special memories of my years in Boston. For the many hours she spent teaching me how to run the equipment in the laboratory, for the days she spent finishing this thesis, and most importantly for being my best friend.

Above all, my family for their unconditional love and support in all that I do. The hardest part of being at MIT was not being by your side.

TABLE OF CONTENTS

ABSTRACT 2

ACKNOWLEDGEMENTS 4

TABLE OF CONTENTS 5

LIST OF TABLES 10

LIST OF FIGURES 11

1. INTRODUCTION 19

1.1 BACKGROUND 19

1.2 RATIONALE FOR CHARACTERIZATION OF MEXICO CITY CLAY 20

1.3 RESEARCH OBJECTIVES AND SCOPE 21

1.4 ORGANIZATION OF THE THESIS 22

2. **BACKGROUND** 25

2.1 **HISTORICAL BACKGROUND** 25

2.1.1 General Information on the Valley of México 25

2.1.2 Geology of the Valley of México 25

2.1.3 Zoning of México City 29

2.1.4 Former Studies of México City Clay 30

2.1.5 Subsoil Investigations of México City's Cathedral 31

2.1.6 Stratigraphy at México City's Cathedral 34

2.1.7 Ground Water Conditions and Effective Stress Profile at México City's Cathedral 36

2.2 **TECHNICAL BACKGROUND** 37

2.2.1 Overview 37

2.2.1.1 Sampling 37

2.2.1.2 Laboratory Testing Program and Data Analysis 38

2.2.2 Equipment and Testing Procedure 40
2.2.2.1 Radiography 40
2.2.2.2 Soil Preparation 43
2.2.2.3 Index Tests 43
2.2.2.4 Testing Equipment 44
2.2.2.4.1 MIT Constant Rate of Strain Apparatus 44
2.2.2.4.2 MIT Automated Direct Simple Shear Apparatus 45
2.2.2.4.3 MIT Automated Stress Path Triaxial Apparatus 47
2.2.2.5 Data Acquisition System and Data Reduction 49
3. INDEX PROPERTIES, MICROSTRUCTURE AND MINERALOGY 75
3.1 INTRODUCTION 75
3.2 INDEX PROPERTIES 75
3.2.1 Natural Water Content and Undrained Strength Index Tests 75
3.2.2 Atterberg Limits and Plasticity Chart 77
3.2.3 Grain Size Distribution 81
3.2.4 Specific Gravity, Salt Concentration and pH 81
3.2.5 Void Ratio, Total Unit Weight and Saturation 82
3.3 MICROSTRUCURE AND MINERALOGY 83
3.3.1 Overview 83
3.3.2 Scanning Electron Microscopy, Environmental Scanning Electron Microscopy, and X-ray Diffraction Results 87
3.3.2.1 Introduction 87
3.3.2.2 Sample Preparation 88
3.3.2.3 Results 90
3.3.3 Conclusions and Comments 99

4. EVALUATION OF SAMPLE DISTURBANCE, STRESS HISTORY, AND CONSOLIDATION PROPERTIES 137

4.1 INTRODUCTION 137

4.2 SAMPLING 138

4.2.1 Disturbance Overview 138

4.2.2 Description of Sampling Process Used for this Investigation 142

4.2.3 Sample Disturbance Evaluation and Effects 146

4.3 ONE-DIMENSIONAL COMPRESSION CURVES AND DETERMINATION OF THE PRECONSOLIDATION PRESSURE 148

4.3.1 Typical Compression Curves 148

4.3.2 Comparison of Consolidation Testing Methods 150

4.3.3 Methods for Estimating Preconsolidation Pressure 151

4.3.4 Normalization of Compression Curves 153

4.4 STRESS HISTORY 155

4.4.1 Background 155

4.4.2 Stress History at México City's Cathedral 156

4.5 CONSOLIDATION PROPERTIES 160

4.5.1 Compressibility 160

4.5.1.1 Compression Index and Compression Ratio 160

4.5.1.2 Recompression Index and Recompression Ratio 161

4.5.1.3 Swell Index and Swell Ratio 162

4.5.1.4 Compressibility Correlations 163

4.5.1.5 Secondary Compression Index 165

4.5.2 Flow Properties 168

4.5.2.1 Coefficient of Consolidation 168

4.5.2.2 Coefficient of Permeability 169

4.6 LATERAL STRESS RATIO K_0 172

4.7 CONCLUSIONS 175

4.7.1 Sample Quality 175

4.7.2 The Soil 176

5. RESULTS OF SHANSEP STRENGTH TESTING PROGRAM 223

5.1 INTRODUCTION 223

5.2 SAMPLE DISTURBANCE AND RECONSOLIDATION TECHNIQUES 224

5.3 SHANSEP TECHNIQUE PROOF TESTS 228

5.4 SHANSEP CK_0 UNDRAINED SHEAR STRENGTH TEST PROGRAM 229

5.4.1 Overview 229

5.4.2 General Undrained Shear Behavior 229

5.4.2.1 SHANSEP CK_0UDSS Tests 229

5.4.2.2 SHANSEP CK_0U Triaxial Compression and Extension Tests 231

5.4.3 Undrained Strength Ratio 233

5.4.3.1 SHANSEP CK_0UDSS Tests 233

5.4.3.2 SHANSEP CK_0U Triaxial Compression and Extension Tests 233

5.4.4 Failure Envelope 236

5.4.4.1 SHANSEP CK_0UDSS Tests 236

5.4.4.2 SHANSEP CK_0U Triaxial Compression and Extension Tests 236

5.4.5 Other Parameters 238

5.5 SUMMARY OF SHANSEP RESULTS AND EFFECTS OF ANISOTROPY 239

5.5.1 Normally Consolidated México City Clay 239

5.5.2 Overconsolidated México City Clay 241

6. SUMMARY, CONCLUSIONS AND RECOMMENDATIONS 271

6.1 INTRODUCTION 271

6.2 SUMMARY OF SAMPLING AND TESTING PROGRAM 273

6.3 SUBSURFACE CONDITIONS, INDEX PROPERTIES, MICROSTRUCTURE AND MINERALOGY 274

6.3.1 Subsurface Conditions 274

6.3.2 Index Properties 275

6.3.3 Microstructure and Mineralogy 276

6.4 EVALUATION OF SAMPLE DISTURBANCE, STRESS HISTORY, AND CONSOLIDATION PROPERTIES 277

6.4.1 General Overview 277

6.4.2 Sample Quality 278

6.4.3 Stress History and Compressibility Characteristics 278

6.4.4 Coefficient of Consolidation and Permeability 280

6.4.5 Lateral Stress Ratio K_o 280

6.5 SHANSEP UNDRAINED STRENGTH TESTING PROGRAM 281

6.5.1 General Overview 281

6.5.2 NC Strength-Deformation Properties 281

6.5.3 OC Strength-Deformation Properties 284

7. REFERENCES 287

APPENDIX A Boring and Sample Logs 293

APPENDIX B Summary of Laboratory Results from SEDUE 1990 315

APPENDIX C Microstructure and Mineralogy Results 326

LIST OF TABLES

Table 2.1	Sampling Depths and Distribution of Index and Engineering Tests	51
Table 3.1	Distribution and Summary of Results of Index Tests	102
Table 3.2	Atterberg Limits, Natural Water Contents, Plasticity Indices, and Liquidity Indices from Boring PC28 (from Marsal and Mazari 1959)	105
Table 3.3	Summary of Mineralogy Results Obtained by Peralta (1989)	106
Table 4.1	Summary of Consolidation Results from CRSC Tests	179
Table 4.2	Summary of Consolidation Results from SHANSEP CK_0U DSS Tests	180
Table 4.3	Summary of Consolidation Results from SHANSEP CK_0UC/E Triaxial Tests	181
Table 4.4	Sources of Sample Disturbance in Cohesive Soils (from Jamiolkowski et al. 1985)	182
Table 4.5	Major Types of Thin-Walled Tube Samplers (from Gilbert 1992; after Marcuson and Franklin 1979)	183
Table 4.6	Preconsolidation Pressure Mechanisms (For Horizontal Deposits with Geostatic Stresses) (from Jamiolkowski et al. 1985)	184
Table 5.1	Summary of Shear Results from SHANSEP CK_0UDSS Tests	244
Table 5.2	Summary of Shear Results from SHANSEP CK_0UC/E Triaxial Tests	245

LIST OF FIGURES

Figure 2.1	Map of the Valley of México (from Marsal and Mazari 1959)	52
Figure 2.2	Approximate NE-SW Cross Section from the Tacubaya Hills to Texcoco Lake (from Zeevaert 1949)	53
Figure 2.3	Map of the Superficial Geology of the Valley of México (from Marsal et al 1959)	54
Figure 2.4	Map of the Geological Zoning of México City (from Marsal and Mazari 1959)	55
Figure 2.5	Facade of México City's Cathedral and its Location in Reference to México City's Historical Center (from Tamez et al 1992)	56
Figure 2.6	Location of México City's Cathedral Exploratory Program Performed by TGC Geotecnia, S.A. (from SEDUE 1990)	57
Figure 2.7	Groundwater Elevation Contour Lines based on Observation Wells; obtained by TGC Geotecnia, S.A. as of May 7, 1990 (from Tamez et al 1992)	58
Figure 2.8	Piezometric Condition around SCE-1 (from Tamez et al 1992)	59
Figure 2.9	Schematic Drawing of TGC Geotecnia, S.A. Soft Soil Sampler Design (from Tamez et al 1992)	60
Figure 2.10	Thin Walled Shelby Tube Sampler with Toothed Cutting Shoe (from Tamez et al 1992)	61
Figure 2.11	Schematic Drawing of TGC Geotecnia, S.A. Stiff Soil Sampler Design (from Tamez et al 1992)	62
Figure 2.12	Summary of Laboratory Results of Boring SMC-1, and Net Tip Resistance of the Closest Cone Penetration Test (from Tamez et al 1992)	63
Figure 2.13	Summary of Laboratory Results of Boring SMC-2, and Net Tip Resistance of the Closest Cone Penetration Test (from Tamez et al 1992)	64
Figure 2.14	Stratigraphy Underneath the Main Entrance of México City's Cathedral (from Tamez et al 1992)	65

Figure 2.15	Perimetrical Stratigraphy of México City's Cathedral (from Tamez et al 1992)	66
Figure 2.16	Location of Borings S1, S2, and S3 in reference to the Cathedral and to TGC Geotecnia, S.A. Exploratory Program	67
Figure 2.17	Schematic Drawing of MIT's Radiographing Technique	68
Figure 2.18	Radiograph Results of Sample Tube S3-4	69
Figure 2.19	Radiograph Results of Sample Tube S2-5	70
Figure 2.20	Schematic Drawing of MIT's Constant Rate of Strain Apparatus (modified from Wissa et al. 1971)	71
Figure 2.21	Schematic Drawing of Modified Geonor Direct Simple Shear Apparatus (from Ortega 1992)	72
Figure 2.22	Schematic Drawing of MIT's Automated Stress Path Triaxial Apparatus (from de la Beaumelle 1990)	73
Figure 2.23	Schematic Drawing of MIT's Triaxial Cell (from Hadge 1979)	74
Figure 3.1	Depth vs. Natural Water Content and Average Torvane Strength	107
Figure 3.2	Depth vs. Atterberg limits, Plasticity Index and Liquidity Index	108
Figure 3.3	Liquid Limit vs. Natural Water Content	109
Figure 3.4	Depth vs. Atterberg limits for Borings PC143 & PC28 (from Hiriart & Marsal 1969)	110
Figure 3.5	Plasticity Index vs. Natural Water Content	111
Figure 3.6	Plasticity Chart (A. Casagrande) for Atterberg limits	112
Figure 3.7	Drying Effects on Atterberg limits (from Marsal & Mazari 1959)	113
Figure 3.8	Relative Consistency vs. Natural Water Content (from Marsal & Mazari 1959)	114

Figure 3.9	Effects of Consolidation on Atterberg limits & Relative Consistency (from Marsal & Mazari 1959) (a) Water Content vs. Atterberg Limits (b) Relative Consistency vs. Water Content	115
Figure 3.10	Influence of Carbon on Water Content and Plasticity Index (from Marsal & Mazari 1959) (a) Depth vs. W_n, Total Carbon, and Inorganic Carbon (b) Plasticity Index vs. Organic Carbon	116
Figure 3.11	Depth vs. Specific Gravity	117
Figure 3.12	Depth vs. Salt Concentration and pH	118
Figure 3.13	Depth vs. Unit Weight and Void Ratio	119
Figure 3.14	Depth vs. Initial Saturation	120
Figure 3.15	SEM Pictures of the Surface of Specimen SCS1	121
Figure 3.16	SEM Pictures of the Surface of Specimen SCS2	122
Figure 3.17	SEM Pictures of the Surface of Specimen SCS3	123
Figure 3.18	SEM Pictures of the Surface of Specimen SCS4	124
Figure 3.19	SEM Pictures of the Surface of Specimen SCS5	125
Figure 3.20	SEM Pictures of the Surface of Specimen S6	126
Figure 3.21	SEM Pictures of the Surface of Specimen SJ-K	127
Figure 3.22	SEM Pictures of the Surface of Specimen SH	128
Figure 3.23	SEM Pictures of the Surface of Specimen SK	130
Figure 3.24	ESEM Pictures of the Surface of Specimen S7	131
Figure 3.25	X-Ray Diffraction Pattern of Specimen S5X	133
Figure 3.26	X-Ray Diffraction Pattern of Specimen SHX	134
Figure 3.27	X-Ray Diffraction Pattern of Specimen SKX	135
Figure 3.28	X-Ray Diffraction Pattern of Specimen S6X	136

Figure 4.1	Schematic Drawings of an Acker 3" Fixed Piston Sampler and Shelby Tube Open-Drive Sampler	185
Figure 4.2	Schematic Drawing of La Rochelle et al. (1981) Sampler Design and Use	186
Figure 4.3	Schematic Drawing of a Hollow Stem Continuous Flight Auger	187
Figure 4.4	Radiograph Results of Sample Tube S1-3	188
Figure 4.5	Schematic Drawing of a Modified Fixed Piston Sampler Proposed by Author	189
Figure 4.6	Typical Compression Curves from CRSC Tests (a) Axial Strain vs. σ'_v (b) Void Ratio vs. σ'_v	190
Figure 4.7	Typical Compression Curves from SHANSEP CK_oUDSS Tests (a) Axial Strain vs. σ'_v (b) Void Ratio vs. σ'_v	191
Figure 4.8	Typical Compression Curves from SHANSEP CK_oU Triaxial Tests (a) Axial Strain vs. σ'_v (b) Void Ratio vs. σ'_v	192
Figure 4.9	Strain at the Overburden Stress vs. Effective Overburden Stress	193
Figure 4.10	Consolidation Results - DSS322 (a) Casagrande Construction (b) Strain Energy	194
Figure 4.11	Consolidation Results - TX233 (a) Casagrande Construction (b) Strain Energy	195
Figure 4.12	Casagrande Method vs. Strain Energy Technique from CRSC Tests, CK_oUDSS and CK_oU TX Tests	196
Figure 4.13	Compression Curves from all CRSC Tests (a) Normalized Water Content vs. σ'_v (b) Normalized Water Content vs. Normalized σ'_v	197

Figure 4.14	Compression Curves from all SHANSEP CK_0U DSS Tests (a) Normalized Water Content vs. σ'_v (b) Normalized Water Content vs. Normalized σ'_v	198
Figure 4.15	Compression Curves from all SHANSEP CK_0U Triaxial Tests (a) Normalized Water Content vs. σ'_v (b) Normalized Water Content vs. Normalized σ'_v	199
Figure 4.16	Stress History at México City's Cathedral (a) Depth vs. σ'_p (b) Depth vs. OCR	200
Figure 4.17	(a) Depth vs. Strain at the Overburden Stress (b) Depth vs. Strain at the Preconsolidation Pressure	201 202
Figure 4.18	Depth vs. Virgin Compression Index, Swell Index and Recompression Index for CRSC, and SHANSEP CK_0U DSS and Triaxial Tests	203
Figure 4.19	Depth vs. Virgin Compression Ratio, Swell Ratio and Recompression Ratio for CRSC, and SHANSEP CK_0U DSS and Triaxial Tests	204
Figure 4.20	Unloading Compression Curves (a) CRS87 (b) CRS89	205
Figure 4.21	Compressibility Index Relationships (a) Compression Index vs. Natural Water Content (b) Recompression Index vs. Natural Water Content	206
Figure 4.22	Depth vs. Compressibility Ratios	207
Figure 4.23	Preconsolidation Pressure due to Secondary Compression (from Mesri and Castro 1987)	208
Figure 4.24	CK_0UC Consolidation Results - TX227. Void Ratio vs. Elapsed Test Time	209
Figure 4.25	Consolidation Results - TX227 (a) Hold Stress at σ'_{vm} (b) Hold Stress at σ'_{vc}	
Figure 4.26	Relationship between Secondary Compression Index and Compression Index (NC) and Compression Index	210

Figure 4.27	CRSC Consolidation Results - CRS89 (a) Compression Curve (b) Coefficient of Consolidation (c_v) vs. σ'_{vc}	211
Figure 4.28	Depth vs. NC Coefficient of Consolidation	212
Figure 4.29	Coefficient of Consolidation (NC) vs. Natural Water Content; CRSC Data	213
Figure 4.30	CRSC Consolidation Results - CRS76 (a) Void Ratio vs. Permeability; Loading Data (b) Void Ratio vs. Permeability; Unloading Data	214
Figure 4.31	Depth vs. Permeability at the Initial Void Ratio	215
Figure 4.32	Void Ratio vs. Permeability	216
Figure 4.33	C_k vs. Initial Void Ratio	217
Figure 4.34	Water Content vs. Permeability at the Initial Void Ratio	218
Figure 4.35	Consolidation Results - TX233 (a) Compression Curve (b) K_c vs σ'_{vc}	219
Figure 4.36	Depth vs. NC Lateral Stress Ratio	220
Figure 4.37	$K_c(OC)/K_o(NC)$ vs. Overconsolidation Ratio	221
Figure 4.38	NC Lateral Stress Ratio vs. 1-sinϕ' for Trixial Tests; OCR=1	222
Figure 5.1	Consolidation Procedure for Laboratory CK_oU Testing (from Ladd et al. 1977)	246
Figure 5.2	Consolidation and Shear Results: DSS311, DSS315, DSS317 (a) Compression Curve (b) Normalized Shear Stress vs. Shear Strain	247
Figure 5.3	Normalized Stress Paths for SHANSEP CK_oUDSS Tests at Varying OCR	248
Figure 5.4	SHANSEP CK_oUDSS Tests at Varying OCR (a) Normalized Shear Stress vs. Shear Strain (b) Normalized Pore Pressure vs. Shear Strain	249

Figure 5.5	Normalized Undrained Modulus vs. Shear Strain for SHANSEP CK_0UDSS Tests at Varying OCR	250
Figure 5.6	Normalized Effective Stress Paths for SHANSEP CK_0UC/E Triaxial Tests at Varying OCR	251
Figure 5.7	SHANSEP CK_0UC Triaxial Tests at Varying OCR (a) Normalized Shear Stress vs. Axial Strain (b) Normalized Pore Pressure vs. Axial Strain (c) Friction Angle vs. Axial Strain	252
Figure 5.8	SHANSEP CK_0UE Triaxial Tests at Varying OCR (a) Normalized Shear Stress vs. Axial Strain (b) Normalized Pore Pressure vs. Axial Strain (c) Friction Angle vs. Axial Strain	253
Figure 5.9	Normalized Undrained Modulus vs. Axial Strain for SHANSEP CK_0UC Triaxial Tests at Varying OCR	254
Figure 5.10	Normalized Undrained Modulus vs. Axial Strain for SHANSEP CK_0UE Triaxial Tests at Varying OCR	255
Figure 5.11	Depth vs. NC Undrained Strength Ratio for SHANSEP CK_0UC/E Triaxial Tests and CK_0UDSS Tests	256
Figure 5.12	Undrained Strength Ratio vs. Overconsolidation Ratio for SHANSEP CK_0UDSS Tests	257
Figure 5.13	NC Undrained Strength Ratio vs. Lateral Stress Ratio for SHANSEP CK_0UC/E Triaxial Tests	258
Figure 5.14	NC Undrained Strength Ratio vs. Lateral Stress Ratio for SHANSEP CK_0UC Triaxial Tests; for Various Soils	259
Figure 5.15	Lateral Stress Ratio vs. Pore Pressure Parameter, Strain at Failure, and Peak Friction Angle	260
Figure 5.16	Undrained Strength Ratio vs. Overconsolidation Ratio for SHANSEP CK_0UC/E Triaxial Tests	261
Figure 5.17	"Failure" Envelope at Large Strain for SHANSEP CK_0UDSS Tests	262
Figure 5.18	Effective Stress Failure Envelope at Maximum Obliquity for SHANSEP CK_0UC/E Triaxial Tests	263

Figure 5.19	Effective Stress Failure Envelope at the Peak Shear Stress for SHANSEP CK_0UC/E Triaxial Tests	264
Figure 5.20	Depth vs. Strain at Failure for SHANSEP CK_0UC/E Triaxial Tests and CK_0UDSS Tests at OCR=1	265
Figure 5.21	Strain at Failure vs. Overconsolidation Ratio for SHANSEP CK_0UC/E Triaxial and CK_0UDSS Tests	266
Figure 5.22	Depth vs. Normalized Undrained Modulus for SHANSEP CK_0UC/E Triaxial Tests and CK_0UDSS Tests at OCR=1	267
Figure 5.23	Normalized Undrained Modulus vs. Overconsolidation Ratio for SHANSEP CK_0UC/E Triaxial Tests and CK_0UDSS Tests	268
Figure 5.24	Undrained Strength Ratio versus Plasticity Index for Various Soils (from Ladd 1991)	269
Figure 5.25	Depth vs. SHANSEP Undrained Shear Strength for Different Modes of Shear	270

CHAPTER 1
INTRODUCTION

1.1 BACKGROUND

For all practical purposes the valley of México can be considered a closed basin. The valley has an area of 7160 km^2, its maximum length in the north-south direction is approximately 135 km, and the width at the center of the valley is approximately 76 km (Zeevaert 1949). The valley of México is surrounded by a large number of volcanoes and volcanic deposits from the Middle Tertiary, Pliocene, and Pleistocene eras. The latest filling of the valley occurred during the Pleistocene. The upper section of the fill was deposited in the lakes formed during the late Pleistocene, and consists of a fine grained soil mass with a large quantity of microfossils, layers of fine grained clastic material, sand, and gravel. This portion of the deposit has been traditionally called México City Clay. The thickness of the deposit varies throughout the valley, and in the center of the city has an approximate thickness of 50 m.

México City Clay exhibits rather unusual index and engineering properties. Some of its index properties are:

(a) natural water content ranging between 100 to 600%.

(b) void ratio ranging from 2 to 10, and the density of solids of approximately 2.5.

(c) liquid limit ranging from 100 to 500%, and plastic limit ranging from 20 to 150%.

México City Clay has a high initial stiffness and almost an elastic behavior during recompression. Once the preconsolidation pressure is exceeded, the soil is highly compressible; compression ratios greater than one are common. Additionally, the soil exhibits a low undrained strength, which is due to the low effective consolidation stress of soil, and an unusually high undrained strength ratio. These unusual properties give rise to intricate foundation problems when tall and heavy buildings are designed and erected. In addition to the unusual soil characteristics pumping from the aquifer underlying México

City has increased the effective stress on the soil, which has led to increased rates of regional settlement.

The long history of practical foundation problems has resulted in extensive investigation into the consolidation characteristics of the soils underlying México City. As a result much is understood about the consolidation characteristics. Apparently, the shear strength properties have been less thoroughly studied and it appears that data of shear strength are confined to those from unconfined compression tests and a limited number of isotropically consolidated undrained triaxial tests.

1.2 RATIONALE FOR CHARACTERIZATION OF MEXICO CITY CLAY

The research for this thesis was prompted by the author's belief that there was a need for an encompassing study of México City Clay using state of the art equipment and techniques.

The last thorough study of México City Clay was performed by Marsal and Mazari in 1959. Their work contains data from a large number of exploratory borings from which systematic tests were performed on samples from different locations in the city. Since then, investigations have concentrated on very specific characteristics of the soil's behavior.

Recently at MIT, there have been advances in geotechnical engineering that now enable a more reliable and economical characterization of clay properties than possible from "standard" procedures used in general practice. These advances include new techniques used for in situ testing, and new laboratory testing techniques which allow better measurements of preconsolidation pressure, undrained strength-deformation properties and drained compressibility-flow properties. These new techniques have been extensively evaluated at MIT and have proved successful in practice.

In the late 1980's research on the engineering properties of México City Clay was prompted by the structural deterioration of México City's Cathedral. The deterioration

was caused by increasing differential settlements. The research project, initiated by the Secretaria de Desarrollo Urbano y Ecologia (SEDUE, Ministry of Urban Development and Ecology), included: analyzing the behavior of the soil underlying México City's Cathedral, assessing the effects of this behavior on the Cathedral's structure, and establishing corrective actions to ensure its structural safety. SEDUE contracted TGC Geotecnia, S.A. to perform the investigation. In turn, TGC undertook an exploration and laboratory testing program which employed the state of the art techniques available at the time in México.

The soil exploration program for this thesis was conducted at the site of México City's Cathedral. The study performed by SEDUE, discussed above, was used as a basis of comparison for the results presented herein.

1.3 RESEARCH OBJECTIVES AND SCOPE

The objectives and corresponding scope of the research can be divided into the following two components:

1) *Characterize the engineering properties of México City Clay at México City's Cathedral.*

This objective was accomplished with sophisticated laboratory tests run on undisturbed samples. Special features of this program included:

(a) constant rate of strain consolidation tests to measure the stress history, compressibility, and flow characteristics of the soil;

(b) automated direct simple shear tests, which produce one-dimensional compression curves and shear information

(c) automated triaxial testing, which produce one-dimensional compression curves, and measurements of the coefficient of earth pressure at rest (K_o).

(d) the SHANSEP reconsolidation technique for K_o consolidated-undrained strength testing, which incorporates different modes of failure to assess the anisotropic undrained stress-strain-strength properties of México City Clay.

2) *Understand the general natural characteristics of México City Clay in the context of its depositional history and mineralogy.*

This objective was accomplished by studying the microstructure of the soil with Scanning Electron Microscopy and identifying the mineralogy with compositional analysis and X-ray diffraction tests.

3) *Evaluate the influence of various sampling methods relative to sample disturbance.*

This objective was accomplished by evaluating the results of sophisticated laboratory tests performed on undisturbed samples obtained from three different boreholes. The boreholes were drilled using three drilling techniques while the samples were obtained with two different samplers as follows:

(a) thin walled Shelby tube sampling with a heavy weight drilling mud (γ_t=1.2 t/m^3); and hollow stem augers.

(b) thin walled Shelby tube sampling and hollow stem augers. No drilling fluid was used, and hence, the borehole was dry.

(c) fixed Piston Sampling with a light weight drilling mud, (γ_t<1.1 t/m^3); and hollow stem augers.

1.4 ORGANIZATION OF THE THESIS

Chapter 2 contains background information related to this thesis. The geologic history of the Valley of México and the soils forming its basin are discussed, followed by a summary of prior geotechnical investigations on México City Clay. The summary includes an overview of the study of the foundation of México City's cathedral and the stratigraphy at the site. The rest of the chapter focuses on information specific to this thesis. First is

an overview of the sampling and testing program used to determine index and engineering properties. Second is a description of the equipment and testing procedures.

Chapter 3 discusses the index properties, microstructure and mineralogy of México City Clay at México City's Cathedral. The chapter begins by presenting the index properties. This is followed by an overview of former studies on the microstructure and mineralogy and the results of this investigation.

Chapter 4 discusses two principal topics: sample disturbance and consolidation properties. First a discussion on sample disturbance presents an overview of disturbance and a detailed description of the sampling processes used to obtain sample for this investigation. Second, a discussion on the consolidation properties presents an evaluation of the stress history and consolidation properties of México City Clay at the cathedral site. This discussion also contains an evaluation of sample disturbance and its effects on specific tests. The evaluation includes an estimation of the preconsolidation pressure and resulting stress history profile, determination of compressibility and flow properties, and an estimation of the lateral stress ratio (K_o). The chapter also presents correlations found between the natural water content and the compressibility and flow properties of México City Clay.

Chapter 5 presents and analyzes the results of the SHANSEP K_o consolidated undrained direct simple shear and triaxial testing program. The chapter presents recommendations for Normalized Soil Properties related to undrained shearing.

Chapter 6 summarizes the most important results from the research, presents the correlations found, and the best estimates of Normalized Soil Properties.

Chapter 7 contains the list of references used during this investigation.

Accompanying this thesis is a MIT Department of Civil and Environmental Engineering Research Report Number R94-01. The report contains the numerical and graphical data of all constant rate of strain consolidation (CRSC) tests, K_o consolidated

undrained direct simple shear (CK_oUDSS) tests, and K_o consolidated undrained triaxial compression and extension (CK_oUC/E) tests.

CHAPTER 2
BACKGROUND

2.1. HISTORICAL BACKGROUND

2.1.1 General Information on the Valley of México

For all practical purposes the valley of México can be considered a closed basin, even though the Nochistongo Cut and some tunnels to the northeast of the valley have been constructed for drainage purposes. The valley's geographical limits are: Tepozotlán, Tezontlalplan and the Pachuca hills to the north; the Apan plains and the Sierra Nevada to the east; the Cuauhtzín and Ajusco mountain ranges to the south; and the Sierras of Las Cruces, and Monte Alto to the west. Figure 2.1. shows a map of the valley of México. The valley has an area of 7160 km^2, of which 3080 km^2 are mountainous regions with altitudes of more than 200 m above the valley floor and 2050 km^2 are regions with altitudes between 0 and 50 m above the valley floor. The lowest area of the valley has a mean altitude of 2240 m above sea level (Marsal & Mazari, 1959). The maximum length of the valley in the north-south direction is approximately 135km, and the width at the center of the valley is approximately 76km (Zeevaert 1949).

2.1.2 Geology of the Valley of México

The following section is summarized from Mooser (1956) and from a conversation with Mooser in 1992.

The large number of volcanoes and volcanic deposits that surround the valley of México can be classified in three groups: Middle Tertiary, Pliocene, and Pleistocene. Classification is based on stratigraphic sequence and degree of erosion. It has not been possible to determine precise chronological limits for the different groups due to the lack or shortage of fossils present in the formations.

It is assumed that due to tectonic forces acting from the beginning of the Tertiary, fractures developed in the earth's crust which allowed lavas to flow and create substantial volcanic apparatuses. The Xochitepec range, to the west of Xochimilco and at the foot of the Ajusco, is formed entirely of deposits of the Middle Tertiary group (see Figure 2.1). It has been inferred from the present day smooth relief of Las Cruces range, 1000 m above the valley floor, that volcanic activity decreased towards the end of the Miocene era and was followed by a period of intense erosion.

During the Pliocene, new volcanic activity started north of the valley in the Pachuca region and in the center of the valley in the Guadalupe hills. This activity was characterized by the emission of great masses of acidic, dacitic and rhyolitic lavas. Later in time, sections of the Sierra Nevada and Las Cruces range were covered with lavas from the Iztaccíhuatl and the Ajusco volcanoes (see Figure 2.1). After the Iztaccíhuatl and the Ajusco volcanoes stopped erupting, new volcanic activity appeared in the northern part of the valley. The basaltic andesites of this new activity (Upper Pliocene) cut off the drainage towards the north near Zimapan and Tula (see Figure 2.1).

In the Upper Pliocene a semi-arid climate prevailed. Strong winds and intermittent torrential rains eroded the rough relief resulting in the deposition of alluvial fans formed by andesitic fragments, sands and silts. This formation has been named "Tarango". The Tarango formation, which covers the entire valley, is characterized by the absence of lavas and is therefore placed subsequent to the Pliocene formation with respect to chronological order.

During the Pleistocene a cold damp climate prevailed and ice-caps formed on the Iztaccíhuatl and Popocatépetl volcanoes; also during this period tectonism started the last volcanic cycle. Rain and water from the ice-caps caused the destruction of a large part of the Tarango formation, creating gorges and two main valleys that drain to the south into the Amacuzac river (not in map), outside the limits of the valley. The larger of the two valleys was the westernmost one. This valley started at Pachuca and Zumpango,

continued east around the Sierra de Guadalupe, passed through the area now occupied by México City and Xochimilco, and extended to Cuernavaca. The smaller valley ran along the foot of the Sierra Nevada, crossed Chalco and Amecameca, and reached the Upper Amacuzac basin at Cuautla. The geologic formation that separated the two valleys was created during the Middle Tertiary but is now buried. It is possible to appreciate the geometry of these valleys by observing the location of the alluvial deposits in Figure 2.3.

After this fluvial net was created, the last volcanic cycle started at the northern end of the valley. Deposits created during this cycle are referred to as the Chichinautzin Basaltic Series. Volcanic activity gradually shifted in a southern direction forming the Chiconautla, Chimalhuacán, and El Cerro de la Estrella (see Figure 2.1). Lastly, strong lava effusions from the Chichinautzin (about 2000m in thickness) filled the space between the Las Cruces and the Sierra Nevada ranges. Hence, a closed valley was formed by plugging off the southern drainage. This obstruction caused clastic fluvial deposits to accumulate in gorges, thus smoothing the rough topography created by the erosion of the Tarango formation. On the northern edge of the lava effusions of the Chichinautzin, up to 800m of clastic fluvial deposits accumulated. This formation has received the name of fluvial and alluvial clastic deposits of the Cuaternary. What was once a complicated series of gorges and valleys was transformed into a large plain with shallow lakes.

The Pleistocenic fill of the valley can be divided in two sections; (1) the upper layer which consists of fine grained deposits, and (2) the lower layer one which consists of coarse grained material (sands, gravel, boulders, etc.). The lower layer is characterized by well rounded elements enclosed in a sandy matrix. The lower section of the fill has a high permeability due to the absence of clay and silts in its matrix. The absence of clay and silt distinguishes this layer from the older Tarango formation. Some of the drinking water of México City is obtained from the aquifer formed by the lower section of the pleistocenic fill. The upper section of the fill was deposited during the late Pleistocene, and consists of a fine grained soil mass with a large quantity of microfossils and layers of fine grained

pyroclastic material, sand, and gravel. This portion of the fill has been traditionally called México City Clay. The thickness of this portion of the deposit varies throughout the valley, and in the center of the city it has an approximate thickness of 50m.

The literature offers different classifications and descriptions of the filling process for the upper section of the Pleistocenic fill, but they can be summarized as follows. An important portion of the upper section of the deposit is a product of the transformation and decomposition of very fine pyroclastic material. Accompanying the Chichinautzin lava effusions were explosions of great quantities of steam which formed dense clouds containing very fine volcanic ash and other pyroclastic materials. The material suspended in the clouds was deposited with rain on the waters of the lake. Other fine material that fell on the mountains enclosing the valley was transported by air and rain water into the lake. As the sedimentation process took place, there were climatic cycles which consisted of wet and dry periods that caused changes in the lake's general conditions. During different time periods the physiochemical characteristics and the depth of the lake changed causing depositional differences in the sedimented material. Additionally, there were isolated volcanic explosions that covered the entire lake with coarser grained pyroclastic material. An important characteristic of this section of the fill is the significant presence of microfossils. Apparently, lake conditions were such that they promoted the proliferation of diatoms and other microfossils. Figure 2.2 presents an approximate cross section of the upper section of the pleistocenic fill. The cross section proceeds from the northeast to the southwest from the Tacubaya Hills to Texcoco Lake, and passes close to El Peñon de los Baños.

The last volcanic activities were the Xitli, approximately 2400 years ago and the Popocatépetl eruption in 1920. Figure 2.3 shows the actual superficial geology of the Valley of México.

2.1.3 Zoning of México City

In their work, Marsal and Mazari (1959) divided México City into three zones according to properties of the subsoil in the top 50m, as shown in a plan view in Figure 2.4. Figure 2.2 shows the approximate locations of the three zones for a particular cross section.

The western and southwestern part of the city lies on the skirts of the mountain ranges that enclose the valley. This zone has been denominated "Zona de Lomas" (Zone of Hills) on account of its relative altitude compared to the rest of the valley. This zone is characterized by materials of volcanic origin, consisting of lava flows and silts produced by the erosion of the lava flows, and by their high strength and low compressibility.

The second zone is the transition zone between the western zone of Lomas and the bottom of Texcoco Lake. This zone is characterized by erratic subsoil conditions. In general, superficial organic clays or silts cover a strata of very compressible clay, which is interspersed with seams of compact silty sand or sand. The clay rests over thick layers of sand and gravel.

The Zona de Lago (Lake Zone) corresponds to the central and eastern parts of the city, which were partially built on the Texcoco lake bed. Texcoco Lake is mostly dry due to drainage works undertaken in the valley on different occasions from the colonial period onwards. This zone is characterized by a thick strata of very compressible clay with very high water contents. The stratigraphy within this zone is mostly consistent, although thicknesses in the strata change due to varying degrees of consolidation.

In general, the term "Mexico City Clay" and its unusual characteristics pertain to the clays found in the Lake Zone. The clay analyzed in this thesis was obtained from this zone.

2.1.4 Former Studies of México City Clay

México City Clay has been the topic of numerous studies and it would not be feasible or practical to mention all of them here. Most of these studies concentrate on very specific aspects of México City Clay and there was not enough information to link the studies together. For this reason it was very difficult to compare the findings of this thesis to those presented in the literature.

The most comprehensive and notable study on México City Clay was prepared by Marsal and Mazari in 1959. It contains data from a large number of exploratory borings from which systematic tests were performed on samples from different locations in the city. Data was collected between 1947 and 1959. The study can be classified into three main parts; laboratory work, general subsidence of the city, and behavior of different structures built in the valley of México. This study provided helpful insight while preparing this thesis and is referred to quite often in the text.

The following paragraphs outline the contents of the main references used in the preparation of this thesis. Full bibliographical detail of these references can be found in Chapter 7.

Mesri et.al. (1975)

This paper presents a study on the composition and compressibility of typical samples of México City Clay. The composition study includes scanning electron microscopy, X-ray diffraction, and chemical analysis, as well as measurements of physical properties. Compressibility characteristics were investigated by means of one-dimensional consolidation tests. The primary objective of this study was to analyze the secondary compressibility of México City Clay with special reference to the effects of previous secondary compression and thixotropic hardening. This paper is referenced quite often in Chapters 2 and 4, as it provides a good description of the composition and consolidation behavior of México City Clay.

Lo (1962)

Lo analyzes the shear strength properties and the composition of a block sample of México City Clay. This is the only study found in the literature that presents one-dimensionally consolidated undrained compression (CK_oUC) triaxial tests. The results of Lo's investigation are compared to those obtained in this thesis.

Mooser (1956)

Mooser presents a detailed physical description of the Valley of México and presents the geologic history and nature of the different volcanic series that compose the valley. The geological section of this thesis was summarized from Mooser's work.

Peralta (1989)

This paper describes how the sedimentation conditions and the type of materials that constitute México City Clay determine the soils microstructure and hence, its mechanical behavior. The paper also presents the findings from a detailed compositional analysis.

2.1.5 Subsoil Investigations of México City's Cathedral

According to Tamez et. al. (1992), the cathedral's construction began in 1573 and was finished in 1813. It was constructed over the remains of Aztec temples and constructions destroyed by the Spaniards. Figure 2.5 shows the facade of the cathedral, and a map of its location in reference to México City's Historical Center.

The following section has been summarized from a publication entitled, "Study of the Foundation of the Cathedral of México", published by the Secretaria de Desarrollo Urbano y Ecologia (SEDUE, Ministry of Urban Development and Ecology) in 1990; and from Tamez et. al. (1992), which is a revised and shortened version of SEDUE (1990).

Sometime between 1988 and 1989, SEDUE contracted TGC Geotecnia, S.A. to do the following; analyze the behavior of the subsoil underlying México City's Cathedral,

assess the effects of this behavior on the structure, and establish corrective actions to assure the structural safety of the Cathedral.

In turn, TGC undertook an exploration and laboratory testing program of the subsoil. The exploration program consisted of:

- twenty one electric Cone Penetrometer tests (CPTs, SCE 1 to 21);
- two continuous sampling borings (SMC 1 and 2);
- the installation of eleven piezometric stations (EP 1 to 11); seven located in the vicinity of the cathedral property (EP 1 to 7), and four in the cathedral surroundings (EP 8 to 11);
- the installation of twenty observation wells, (the location of these wells are not well defined in SEDUE (1990));
- and two deeply seated settlement points.

Figure 2.6. shows a plan view of the exploratory program. The laboratory program included tests to establish the index, consolidation (incremental oedometer) and strength properties (Unconsolidated Undrained triaxial tests, UU) of the subsoil.

The CPTs were located as follows; thirteen around the cathedral's perimeter, four inside the cathedral, and four in the surrounding area. An observation well was installed within a few feet of most CPTs. The only information presented in SEDUE (1990) from the CPTs is the net tip resistance. The excess pore pressure was not measured during the tests. The average depth of the CPTs was 40m and six of tests penetrated to nearly 60m.

As shown in Figure 2.6, piezometric stations EP 2 through 7 are located within a few feet of the CPTs. The average depth of the piezometers is 17.5m. Piezometric station EP-1 is composed of several cells, and is located in the vicinity of SCE-1. The cells are installed at a depth of 18.0, 21.2, 26.7, 39.0, 44.0, 50.5 and 53.0 m. The piezometers installed are similar to the Casagrande M206 piezometer. Figure 2.7 shows ground water elevation contour lines, constructed from the observation well readings

obtained by TGC as of May 7, 1990. Figure 2.8 shows the piezometric condition around SCE-1.

The two continuous sampling boreholes were drilled using a Mobil Drill B61 drill rig. Boring SMC-1, located within a few feet of SCE-6, was sampled to a depth of 75 m, and boring SMC-2, located within a few feet of SCE-7, was sampled to a depth of 60 m. Three types of samplers were used. The first type is a sampler developed by TGC which was used in borings SMC-1 and SMC-2. Figure 2.9 shows a schematic drawing of this sampler. A characteristic which distinguishes this sampler from other samplers is that it contains an inner aluminum liner. Samples are contained within this liner, which preserves and protects them after sampling. The samples are taken by simply pushing the sampler into the soil with the hydraulic feed of the drill rig, and then shearing off the samples and lifting them to the surface. The samples are left in the liner and are extruded in the laboratory by pushing the soil out of the liner in 30cm sections. The sampler is primarily used in soft soils.

The second type of sampler which is shown in Figure 2.10, was also used in borings SMC-1 and SMC-2. It is basically a thin walled Shelby tube with a toothed cutting shoe. This sampler was used in soils that yielded high values (peaks) of net tip resistance. The samples are taken by rotating and pushing the sampler into the soil, and then shearing off the samples and lifting them to the surface. The samples are left in the sampling tube and are extruded in the laboratory by pushing the soil out of the liner in 30cm sections.

Figure 2.11 shows the third type of sampler used. This sampler also contains an inner liner. The sampler is used by rotating it into the soil. This sampler was designed for extremely stiff soils ans was only used to sample the "hard layer" of borings SMC-1 and SMC-2 (the hard layer will be defined in Chapter 3).

Drilling mud and standard DCDMA casing was used in both borings. The drilling mud was maintained at a constant Marsh funnel viscosity of forty seconds. A fish tail bit and circulating mud at low pressure were used to clean out the boreholes before sampling.

Figures 2.12 and 2.13 show summaries of the laboratory results of borings SMC-1 and SMC-2. These figures also present the net tip resistance of the penetrometer test located closest to the respective borings. More of TGC's laboratory results will be presented in the following chapters. Appendix B contains most of the laboratory results reported in SEDUE (1990).

It is worth mentioning that the samples obtained for this thesis were taken 15 feet from penetrometer test SCE-6 and boring SMC-1.

2.1.6 Stratigraphy at México City's Cathedral

The following section has been summarized from SEDUE (1990). As mentioned above, TGC performed 21 CPTs. The objective of the tests was to establish the stratigraphy of the subsoil. Figure 2.14 shows the stratigraphy inferred from the three CPTs performed in front of the main entrance of the cathedral. Figure 2.15 shows the perimetrical stratigraphy of the cathedral. The stratigraphy as presented in SEDUE (1990) consists of 6 main substrata, which can be described as follows:

1) Rellenos (Fill)

As the name indicates, this strata is a heterogeneous material that has accumulated over time. It consists primarily of pieces of pavements, previous foundation material, rock fragments, silt size soils, etc. The depth range of the fill around the site ranges from an average of 0.0m and 11.1m. The average thickness of the strata is 11.1±2.2m.

2) Costra Superficial (Superficial Crust)

This layer can be described as a desiccated crust. It contains low compressibility clays overlying overconsolidated silts. The depth of the crust ranges from an average of 11.1m to 13.0m. The average thickness of the strata is 1.9±0.3 m.

3) Serie Arcillosa Superior (Upper Clay Series)

This deposit is composed of seven clay layers, which are separated by "hard" lenses. In SEDUE, (1990) TGC describes three of the hard lenses as volcanic ash and three as desiccated crusts. The net tip resistance profiles in Figures 2.12 and 2.13 clearly show the location of each of the seven clay layers. The peaks in the net tip resistance correspond to the location of the hard lenses, which most likely correspond to a historical event. The average depth range of the deposit is 13.0m to 36.7m; the average thickness is 23.7±1.1m. The soil from this deposit is commonly referred to as México City Clay. The clay is very heterogeneous, and significant changes in color, consistency, touch, appearance, and index and mechanical properties are not uncommon over minimal changes in elevation. All of the samples collected for this investigation were obtained from this substrata.

4) Primera Capa Dura (First Hard Layer)

The first hard layer is composed of a sequence of hard and soft layers. The hard layers are usually sands and gravels and the soft layers silts and clays. This hard layer is commonly used as the bearing strata for buildings with end bearing piles. The average depth range of this deposit is 36.7m to 39.9m. The average thickness of the strata is 3.2±0.4m.

5) Serie Arcillosa Inferior (Lower Clay Series)

This deposit is made of at least three clay layers separated by hard layers. The hard layers are usually sands, silts, and volcanic glass and ash. The depth range of this deposit ranges from an average of 39.9m to 50.5m. The average thickness of the deposit is 10.6±0.4m. It is presumed that the clay of this substrata is of the same nature as that of the upper series. The clay of this substrata has undergone significant deformation due to a consolidation process induced by pumping of the underlying acquifer.

6) Depositos Profundos (Deep Deposits)

These deposits consist mainly of compact sand with scattered clay lenses and are part of alluvial clastic deposits, which were described in Section 2.1.2. This deposit forms a high permeability aquifer. Drinking water for México City is extracted from this aquifer. The extraction of water from the aquifer is the main cause of the subsidence of México City (Carrillo 1969). The initial average depth of this deposit is 50.5±0.7m.

2.1.7 Ground Water Conditions and Effective Stress Profile at México City's Cathedral

In the preparation of this thesis it was assumed that the ground water conditions and effective stress profile presented in SEDUE (1990) prevailed at the time the samples were taken for this study. There are several sources of uncertainty associated with effective stress calculations, i.e. stress increment caused by the building, unit weight of various materials, seasonal variation of the pore pressure, etc. This investigation did not produce sufficient information to clarify all of these uncertainties. Therefore, the effective stress profile used in this thesis was calculated using the results presented in SEDUE (1990), of depth and effective stress, for consolidation tests from boring SMC-1. Unfortunately, neither SEDUE (1990) nor Tamez et. al. (1992) present any information about how the effective stress profile was calculated. Some simple calculations were performed to ensure that the effective stress profile given in SEDUE (1990) is reasonable. The results of these calculations yielded effective stress values very similar to those presented in SEDUE (1990).

SEDUE (1990) report the depth and effective stress on all the consolidation tests performed on samples from boring SMC-1. Also, in SEDUE (1990) the piezometric head and installation depth of the piezometers in piezometric station EP-1 are reported. Additionally, SEDUE reports that the groundwater pressures measured at station EP-1 were used to calculate effective stress profiles throughout the site. Using the depth of the piezometers as boundaries, four linear regressions were performed on the depth and

effective stress data of the consolidation tests. The regression equations were used to back calculate the effective stress profile between piezometer depths. The results of these regressions are expressed in equations 2.1 through 2.4.

Between 7.5 to 18.0 m $\sigma'_V = 1.016 + ((\text{depth} - 7.5) \times 0.01428)$.....(2.1)

Between 18.0 to 21.2 m $\sigma'_V = 1.166 + ((\text{depth} - 18.0) \times 0.03241)$.....(2.2)

Between 21.2 to 26.7 m $\sigma'_V = 1.269 + ((\text{depth} - 21.2) \times 0.05440)$.....(2.3)

Between 26.7 to 39.0 m $\sigma'_V = 1.569 + ((\text{depth} - 26.7) \times 0.13927)$.....(2.4)

2.2 TECHNICAL BACKGROUND

2.2.1 Overview

The Cathedral site was chosen as the location to obtain samples for this thesis for the following reasons: (1) a thorough geotechnical investigation of the subsoil had just been finished by TGC Geotecnia, S.A., in partial fulfillment of the work it had been hired to do by SEDUE, and the results from this investigation were readily available; (2) it was believed that TGC's results would serve as a good basis of comparison because their investigation had implemented the best sampling techniques, transportation, conservation of samples, and laboratory specimen preparation presently available in México.

This thesis can be divided into two main parts: (1) sampling, which consisted of drilling three boreholes using different drilling and sampling techniques; and (2) a laboratory testing program and data analysis.

2.2.1.1 *Sampling*

One of the objectives of this thesis was to ascertain the amount of sampling disturbance caused by different samplers and sampling techniques. The 3 borings were performed using a CME Model 55 drill rig, supplied by Geotecnología, S.A.. In the first (S1) and second (S2) boreholes, thin walled Shelby tubes and hollow stem augers were used. For S1, a heavy weight drilling mud (γ_t=1.2t/m^3) was also used, whereas the mud

was omitted for S2 (the borehole was "dry"). In the third borehole (S3), an Acker Fixed Piston Sampler, a very light weight drilling mud (γ_t<1.1t/m^3), and hollow stem augers were used. Nine samples were retrieved from boring S1 (1 through 9), nine samples from boring S2 (1 through 9), and six samples from boring S3 (1 through 6).

Figure 2.16 shows the location of borings S1, S2, and S3 in reference to the cathedral and TGC's exploratory program. As mentioned earlier, the borings performed for this thesis are within a few of from boring SMC-1. Table 2.1 presents the depth and recovery of each sample. Appendix A contains the boring logs of the boreholes drilled for this thesis as well as a sample log for each of the samples obtained for this thesis.

Of the 24 undisturbed samples, 18 were sent to MIT. The breakdown is the following: three from boring S1 (3, 8 and 9); nine from boring S2 (1 to 9); and six from boring S3 (1 to 6). Chapter 4 will discuss why only 18 of the twenty four samples were sent to MIT.

2.2.1.2 *Laboratory Testing Program and Data Analysis*

The objectives of the laboratory program were to assess sampling disturbance caused by different sampling techniques and to fully characterize the engineering properties of México City clay at México City's Cathedral. The laboratory program can be divided into two categories as follows:

(A) Tests for Index Properties

Profiles for various soil index properties were constructed for this investigation. Index properties measured include natural water content, torvane strength, Atterberg limits, total unit weight, grain size distribution, specific gravity, salt concentration, and pH. In most cases the index tests were performed on trimmings from engineering tests or dedicated sample sections. Table 2.1 contains the distribution of the index tests performed for this study.

B) Tests for Engineering Properties

This portion of the testing program consisted of consolidation and undrained strength tests. The first step was to determine the soil's permeability and the stress history at the site. This was accomplished with constant rate of strain consolidation (CRSC) tests. The soil permeability was needed to calculate the appropriate rate of strain for the CRS consolidation portion of direct simple shear (DSS) and triaxial (TX) tests. The preconsolidation pressure was needed to estimate the maximum vertical consolidation stress for DSS and triaxial tests, which were conducted according to SHANSEP procedures as described by Ladd and Foott (1974). Table 2.1 shows the distribution of engineering tests performed.

B.1) Evaluation of Stress History and Consolidation Properties

The objectives of the consolidation tests were to: assess sample disturbance, develop a well defined preconsolidation profile (σ'_p), and characterize the compressibility and flow properties of the soil. Estimates of the preconsolidation pressure and compressibility came from the results of 15 constant rate of strain consolidation (CRSC) tests, 12 SHANSEP direct simple shear tests (CK_0DSS), and 10 SHANSEP K_0 consolidated triaxial (CK_0TX) tests. The CK_0TX tests also provided information on K_0 as a function of OCR. The CRSC tests also provided information about the coefficient of consolidation and permeability of the soil.

B.2) Undrained Strength Testing

The objective of the strength testing program was to establish the SHANSEP normalized soil parameters of México City Clay, as well as to obtain reliable estimates of the in situ undrained strength. Specimens were sheared in triaxial compression (7 tests), triaxial extension (3 tests), and direct simple shear (12 tests). Both triaxial tests and direct simple shear tests were reconsolidated using the SHANSEP technique.

The SHANSEP reconsolidation technique requires consolidation of the specimen to a vertical stress of 1.5 to 2 times the preconsolidation pressure to ensure that the specimen is truly normally consolidated (Ladd and Foott 1974). For most soils, this stress range is reached at an axial strain of about 10%. The amount of strain during virgin compression loading for México City Clay is so large that it is impossible to consolidate a specimen to the prescribed stress range without exceeding the capabilities of the testing equipment. Specimens of México City Clay reach the preconsolidation pressure between 6 and 9% of axial strain, and might strain an additional 5% with only slight increases in vertical stress.

Initially, three normally consolidated CK_0UDSS SHANSEP tests were performed to evaluate SHANSEP applicability. The three specimens were obtained from a 4.5 inch section of tube S2-3. These tests were performed to establish if changes in consolidation stress (which would incorporate varying amounts of axial deformation), would affect the SHANSEP normalized soil parameters. The tests showed that the normally consolidated normalized soil parameters were not affected by increasing amounts of axial deformation. The results of these three tests can be found in Section 5.3.

Tests were also performed to check for variation in normalized behavior at different elevations. This was accomplished by performing tests at different elevations and comparing the results with the results from the first three tests.

2.2.2 Equipment and Testing Procedure

2.2.2.1 *Radiography*

Sample tubes were X-rayed at the radiography facility of MIT's Geotechnical Laboratory. Based on experienced gained at MIT since 1978, radiography can show the following:

(1) Variations in soil types, especially granular versus cohesive materials;

(2) Macrofabric features resulting from bedding planes, varves, fissures, shear planes, etc;

(3) Presence of "intrusions" such as sand lenses, stones, shells, calcareous nodules, peaty materials, drilling mud, etc;

(4) Voids or cracks due to gas pockets;

(5) Variations in the degree of sample disturbance, ranging from barely detectable curvature adjacent to the sample edges to gross disturbance evidenced by a completely contorted appearance and large voids and cracks (most often occurring at the ends of the tube).

The information provided by radiographs was used to help select the most appropriate and highest quality material for testing.

The procedure described below is for radiographing soil in three inch diameter, three feet long steel tubes. Since the tubes are cylindrical, x-rays that strike the center of the tube must travel through 0.2 inches of steel and 2.8 inches of soil, while those hitting the edges of the tube penetrate much less soil. Therefore, aluminum plates of varying thickness are positioned in back of the tube such that all x-rays will penetrate an approximately equal mass. Lead numbers and letters are placed at one inch intervals along the tube to provide depth reference marks. At MIT, the tubes are x-rayed in 10 inch segments. Each segment is exposed for 5 minutes. The radiation is generated by a Philips MG151-160kv constant potential high voltage generator which excites a metal ceramic focus beryllium x-ray tube. The x-ray machine is operated at a constant voltage of 160kv and a current of 3.4mA. Figure 2.17 presents a schematic drawing of the MIT's Radiographing technique.

The image produced on the radiograph is an integration of all the material along the line from the x-ray source to the film. Changes in darkness depend on the relative absorption capacity of the materials being penetrated (i.e. soil, air, shells, etc.). Some features do not cause a sufficient change in absorption capacity and, hence cannot be seen

on the x-ray photograph, unless the x-ray is taken at the correct orientation. For example, an inclined air crack within the sample will not be seen unless the x-ray path is parallel to the crack orientation. In general, changes in absorption capacity (absorption capacity is generally equated to density) as small as 5% can be observed.

This x-ray procedure was developed for Boston Blue Clay. Radiograph results of this investigation may suggest the following changes to the x-ray procedure when radiographing México City Clay: use of shorter exposition times (three minutes); lower current used to generate the x-rays; and exchanging of the aluminum plates to plates having a density closer to the value of México City Clay.

After analyzing the x-ray results, no evidence of sample disturbance was found in any of the tube samples of boreholes S2 and S3. The radiographs showed very interesting features of the soil. In most of the radiographs, mixing of materials of different densities can be appreciated. Upon opening the tube at the mixing location, no physical evidence was found to suggest changes in density (i.e. changes in color, consistency, touch, appearance, etc.) Other interesting features found in the radiographs were failure planes and hydraulic fractures. Hydraulic fracturing was observed in radiographs of tube samples from borehole S1 where heavy weight drilling mud was used. Figure 4.4 shows a radiograph which demonstrates the effect that hydraulic fracturing has on the soil. Figure 2.18 presents a radiograph of sample tube S3-4. The radiograph shows that the deposit changes from a lower density material at F to a high density material at location "E". The high density material is composed of fine, sand size pyroclastic particles. Below location "D" the soil becomes a mixture of high and low density materials. Figure 2.19 presents a radiograph of sample tube S2-5. The figure clearly shows the heterogeneous nature of the soil by presenting the different density materials present in the soil.

2.2.2.2 *Soil Preparation*

Specimens were prepared for all engineering tests using the following procedure. The tubes were cut above and below the selected specimens to reduce disturbance due to extrusion. The remaining segments of the tube were resealed for later use. Torvane and water contents were taken either above or below the specimen before extrusion. The specimen was extruded from the tube using the following procedure:

a) A fine wire was pushed through the soil along the inside wall of the tube.

b) The wire was used to cut the soil from the inside perimeter of the tube.

c) The soil was gently pushed out of the tube by hand.

The resulting block of soil was trimmed in different manners depending on the specific type of test.

2.2.2.3 *Index Tests*

Atterberg limits, hydrometer tests, and specific gravity tests were performed in accordance with ASTM Standards D4318-84, D422-63, and D854-83, respectively.

Procedure for Salt Concentration and pH

The method used for the determination of soluble salts in a soil specimen is described below. It uses the electrical conductivity of the supernatant liquid to approximate the soluble salts present in the soil pore fluid. For a detailed discussion of this method, suggested by R.T. Martin, the reader is referred to "Methods of Soil Analysis-Part 2," section 62, published by the Am. Soc. of Agron. in cooperation with ASTM.

The soil to be tested is mixed thoroughly on a glass plate. The water content is taken and about 20 gm of the remaining wet soil is added to a preweighed 50 ml centrifuge tube. The tube is capped and weighed. Distilled water is added to make the total water content about 200%. The tube is weighed again. The tube is shaken

intermittently for about 20 to 30 minutes and then placed in an IEC Model HT bench top centrifuge and run at about 5000 rpm for 10-20 minutes.

The pH of the supernatant liquid is measured with a Cole Palmer model 5985-80 Digi-Sense pH meter. It was found that pH measurements were more accurate if the probe was soaked in Methanol for about an hour after the equipment was calibrated. This ensured that no calibration buffers were left on the probe.

The supernatant liquid is decanted from the centrifuge tube into a glass cup. The resistance is measured with a Beckman Instruments Model RC-16B2 AC wheatstone bridge. The resistance of a 0.02N KCl reference solution is also measured. The soluble salt concentration present in the supernatant of the water:soil slurry is determined from a calibration curve, which was determined using prepared solutions of varying degrees of KCl. The salt concentration is then corrected for the water content difference between the conductivity test and the water content of the soil for which the pore fluid salt concentration is desired.

2.2.2.4 *Testing Equipment*

The three principal types of testing equipment used in this study were:

1) The MIT Constant Rate of Strain Apparatus

2) The MIT Automated Direct Simple Shear Apparatus

3) The MIT Automated Stress Path Triaxial Apparatus

2.2.2.4.1 *MIT Constant Rate of Strain Apparatus*

Wissa et. al. (1971) describes the MIT CRS device which is still in use today. Figure 2.20 shows an schematic drawing of this device. The equipment has been modified by removing the inner diaphragm seal to reduce the potential for friction errors. The test is monitored by two pressure transducers, a Direct Current Linear Variable Displacement Transducer (LVDT), and a load cell. The apparatus is enclosed in an insulated, wooden

environmental chamber, which maintains temperature at 30°±0.5°. The general test sequence involves the following steps:

a) Trim the specimen with a trimming shoe into the specimen ring and cut the top and bottom with a wire saw and smooth with a knife. This procedure is designed to minimize disturbance. The initial mass and dimensions of the specimen are measured for subsequent calculations.

b) Assemble the equipment and back pressure saturate the specimen at a constant volume to about 3 or 4 ksc.

c) Consolidate the specimen using a fixed axial displacement rate equal to 0.5 to 1%/hr, depending on the specimen's permeability. Measure the base pore pressure and the vertical load.

d) Unload (rebound) the specimen (generally without allowing dissipation of excess pore pressure) to a small effective stress and allow time for equalization of pressure.

e) Remove specimen and measure final water content and dry weight of solids.

f) Calculate engineering properties based on Linear Theory presented by Wissa et. al. (1971).

2.2.2.4.2 *MIT Automated Direct Simple Shear Apparatus*

The MIT Direct Simple Shear (DSS) apparatus consists of the basic hardware from a Geonor Model 4 DSS device, modified to improve the quality of the test. Two Geonor devices are used in the MIT Geotechnical Laboratory's DSS facility (Geonor 1 and 2).

The modified Geonor device is shown in Figure 2.21. The apparatus features load cells for measuring vertical and horizontal forces, and LVDTs for measuring vertical and horizontal displacements. The full automation of the apparatus allows the DSS specimen to consolidate under constant rate of strain (CRS) loading and to maintain constant

specimen height during shear. Details about the automation of the DSS device can be found in Ortega (1992). Each DSS apparatus is enclosed in an insulated, wooden environmental chamber, which maintains temperature at 30°±0.5°.

The methods of DSS specimen confinement, consolidation, shear, and maintenance of undrained conditions in the MIT-DSS apparatus are similar to those described by Bjerrum and Landva (1965). The test specimen is about 2 cm tall and 35 cm^2 in cross-section. The general test sequence involves the following steps:

a) Trim the specimen with special equipment designed by Geonor and enclose the soil in a wire reinforced rubber membrane. This procedure is designed to minimize disturbance. The initial mass and dimensions of the specimen are measured for subsequent calculations.

b) Consolidate the specimen at a rate of axial deformation of 0.5 to 1%/hr to a predetermined maximum vertical consolidation stress or axial deformation greater than 10%. The maximum stress is held for about 24 hrs to allow for the dissipation of excess pore pressures and secondary consolidation.

c) When appropriate, rebounding the soil to a specified OCR is performed at a rate of axial deformation of 0.5 to 1%/hr. Again, the final consolidation stress is held for about 24 hrs.

d) Undrained shear is performed at a constant rate of 5% of horizontal deformation/hr. Undrained conditions are maintained by computer control of the vertical stress which maintains a constant specimen height. The computer automatically adjusts the stress for the compliance of the apparatus.

e) Calculations consider vertical apparatus compressibility, membrane resistance and shear piston friction.

2.2.2.4.3 *MIT Automated Stress Path Triaxial Apparatus*

Consolidated-Undrained triaxial tests were performed using a new computer controlled system and procedures developed at MIT over the past several years. A schematic diagram of the testing apparatus is shown in Figure 2.22. The diagram shows the five main components of the system: the triaxial cell and pressure control cylinders, the three control motors, the motor control box and the personal computer. Four MIT Automated Triaxial devices weree used in the MIT Geotechnical Laboratory's Triaxial facility (MIT03-MIT06).

The triaxial cells, manufactured by Wykeham Farrance, were modified to feature a low friction rolling diaphragm seal, a fixed top cap geometry, and double drainage. The cell is shown in detail in Figure 2.23. The cell is monitored by a load cell, two pressure transducers and a LVDT for axial deformations.

The triaxial cell is mounted on a Wykeham Farrance load frame which can be moved up or down to cause vertical deformations. Although the load cell and LVDT connected to the piston allow one to conduct tests with either stress or strain control, the tests in this research project were strain controlled.

The pressure controllers consist of two hydraulic cylinders, one containing silicon oil, used for the cell fluid to prevent membrane leakage, and one containing distilled water, used for the pore fluid. A second LVDT is attached to the pore pressure controller to measure volumetric strains in the specimen. Each cell and its respective pressure controllers are enclosed in an insulated, wooden environmental chamber, which maintains temperature at 30°±0.5°.

The following steps outline the general triaxial test procedure:

a) Trim the specimen diametrically using a miter box and a wire saw. Square the specimen ends initially with a wire saw and finally with a straight edge. The final specimen is about 8 cm tall and 10 cm^2 in cross section. The final specimen is weighed and measured for subsequent calculations.

b) Assemble the specimen in the previously saturated triaxial cell, place the piston on the specimen and, if necessary, adjust the specimen so that it is seated properly. Apply vertical filter drains for compression tests and spiral drains for extension tests. Enclose the specimen in two prophylactic membranes and install the Plexiglas cell chamber. Assemble the remaining equipment and apply hydrostatic total stress with the drainage lines closed. Let the specimen sit for about 12 hrs.

c) Record the initial effective stress as the difference between the cell pressure and the pore pressure.

d) Gradually increase the back pressure, while maintaining the initial effective stress, until the pore pressure parameter, B, is greater than 95%.

e) Consolidate the specimen to the desired maximum stress using a constant rate of axial deformation of 0.1 to 0.5%/hr. For SHANSEP tests, the computer control maintains the K_O condition, and the maximum vertical consolidation stress chosen is between 1.5 to 2.0 times the preconsolidation pressure. The maximum stress is maintained for 24 hrs.

f) For overconsolidated SHANSEP tests, rebound the specimen to the desired OCR using a constant rate of axial deformation and computer control to maintain the K_O condition. The final stress is held for about 24 hrs.

g) Close the drainage lines and monitor the change in pore pressure for 30 minutes to confirm that the rate of secondary compression is small and no internal leaks exist.

h) Shear the specimen at a constant rate of axial deformation of 0.5%/hr to failure under the specified condition. Triaxial compression tests are sheared in loading and triaxial extension tests are sheared in unloading.

i) Calculations correct for piston friction, weight of the piston and accessories, membrane and filter paper strength contribution, and sample cross sectional area change.

For details concerning components of the MIT Automated Stress Path Triaxial Apparatus, the control algorithm, testing procedure, and data reduction, the reader is referred to La Beaumelle (1991) and Estabrook (1991). For a thorough explanation of the design of the triaxial system, the reader is referred to Sheahan (1988) and Sheahan et. al. (1990).

2.2.2.5 *Data Acquisition System and Data Reduction*

Transducer outputs from triaxial tests, direct simple shear tests, and constant rate of strain tests are converted from analog to digital readings, and stored in the central data acquisition unit. The tester defines the interval and number of readings collected by the system. The MIT Geotechnical Laboratory's central data acquisition system consists of a Hewlett Packard 3497A Data Acquisition/Control Unit and an IBM PC AT compatible computer. The resolution of this unit is 0.1 mV for LVDTs, and approximately 1μV for the pressure and load transducers. This translates to a resolution of strain to approximately 0.0005%, and pressures to about 0.0001 ksc, which far exceed the sensitivity of the control programs. The system is capable of analog to digital conversion and storage of data at a trigger rate of up to 1 Hz.

Data files created during testing are transferred to 5.25" floppy diskettes and, the transducer output is reduced to engineering units using the appropriate data reduction software. The CRS reduction program corrects for apparatus compressibility. The DSS reduction program corrects for apparatus compressibility, frictional resistance, and horizontal membrane resistance. The triaxial reduction program makes the following four corrections:

a) The calculated area of the specimen is corrected for the change in area geometry that takes place during the consolidation and undrained shear phases of the test. During the consolidation phase of the test, the specimen is assumed to remain cylindrical, during undrained shear in compression, the specimen is assumed to

deform parabolically, and during undrained shear in extension, the specimen is assumed to deform as a right cylinder.

b) A correction is made to account for the increase in axial stress due to the load carried by the filter strips during consolidation and the shear phase of compression tests.

c) A correction is made to account for the increase in axial and radial stress caused by the two thin prophylactic membranes that enclose the specimen.

d) The vertical stress is adjusted to account for the area of the piston and the weight of the piston and the attached accessories.

Each reduction program requires the user to input test specific information, such as initial specimen dimensions, transducers zeroes, and calibration factors. Once the transducer output is reduced to engineering units, it is stored in a results file, which may be imported into commercially available spreadsheet and graphic programs.

Table 2.1 Sampling Depths and Distribution of Index and Engineering Tests

Boring # and Sample #	Bottom depth (m)	Top depth (m)	INDEX TESTS (#)			ENGINEERING TEST NUMBER			
			Atterberg Limits	Specific Gravity	Salt Conc pH	CRSC	SHANSEP CKoU DSS	TC	TE
S2-1	-12.80	-12.00	1	1	1	CRS73		TX226	
S2-2	-13.60	-12.80	1	1	1	CRS74	DSS311 DSS315 DSS317		TX230
S2-3	-14.40	-13.60	1	1	1	CRS75			
S2-4	-24.15	-23.40	1	1	1	CRS79	DSS322	TX227	
S2-5	-24.95	-24.15	2	1	1	CRS82 CRS88		TX201	
S2-6	-25.75	-24.95	1	1	1	CRS84			
S2-7	-28.80	-28.15	1	1	1	CRS83	DSS327 DSS340		
S2-8	-29.60	-28.80	1	1	1			TX221	TX228
S2-9	-35.50	-34.70	1	1	1		DSS342	TX223	
S3-1	-12.45	-12.00	1	1		CRS76 CRS89 CRS90 CRS92	DSS318 DSS320		
S3-2	-13.60	-12.80	1	1	1	CRS77		TX222	
S3-3	-14.40	-13.60	1	1		CRS78	DSS330		
S3-4	-24.45	-23.70	1	1	1	CRS85			
S3-5	-25.10	-24.35	1	1	2			TX225	
S3-6	-25.70	-24.95	1	1	1	CRS80	DSS324 DSS337		TX233
S1-1	-9.30	-8.50							
S1-2	-10.30	-9.50							
S1-3	-24.30	-23.50							
S1-4	-26.05	-25.25							
S1-5	-26.85	-26.05							
S1-6	-27.65	-26.85							
S1-7	-28.45	-27.65							
S1-8	-29.20	-28.40							
S1-9	-29.85	-29.20							

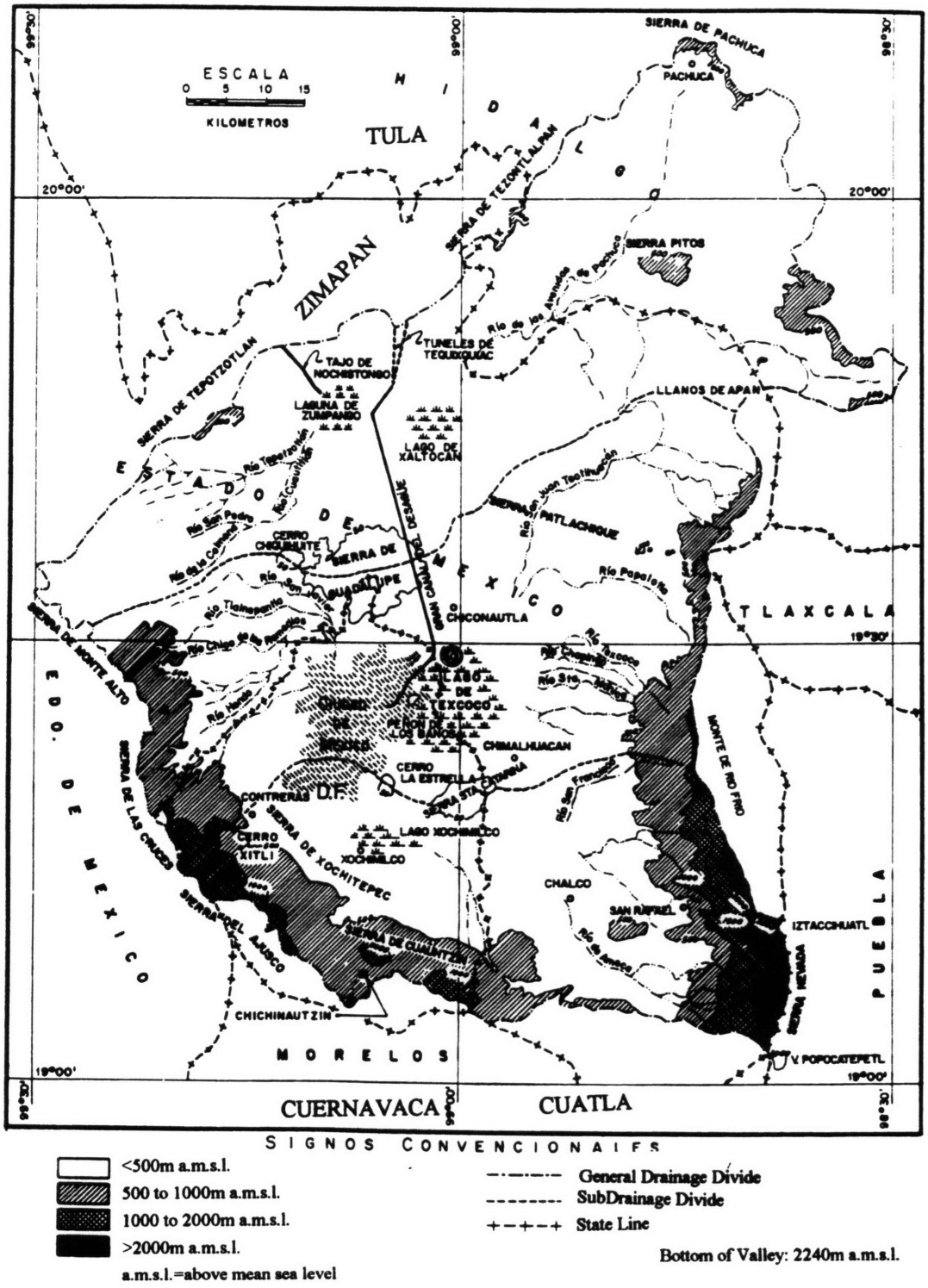

Figure 2.1 Map of the Valley of México
(from Marsal and Mazari 1959)

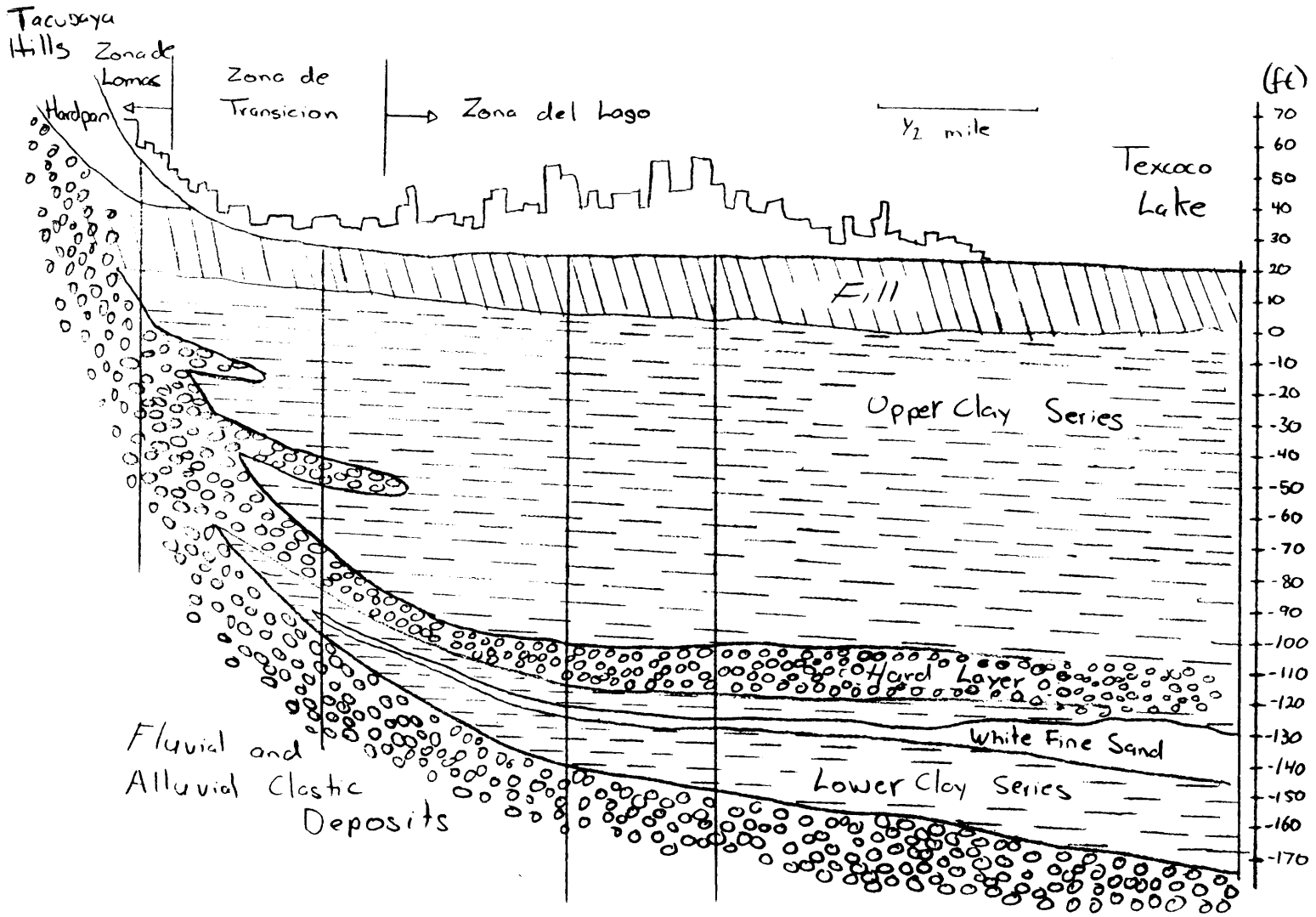

Figure 2.2 Approximate NE–SW Cross Section from the Tacubaya Hills to Texcoco Lake (from Zeevaert 1949)

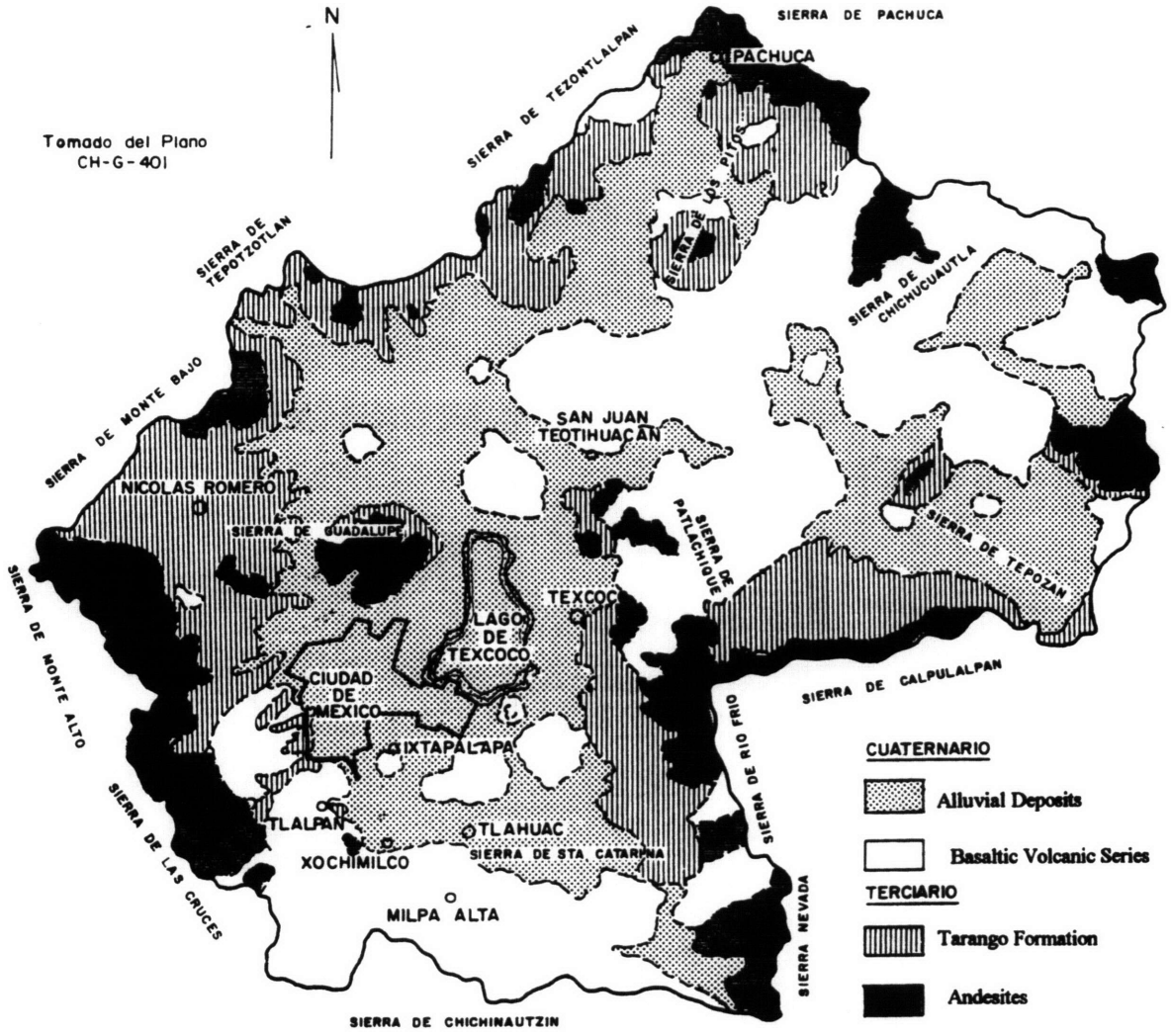

Figure 2.3 Map of the Superficial Geology of the Valley of México (from Marsal et al 1959)

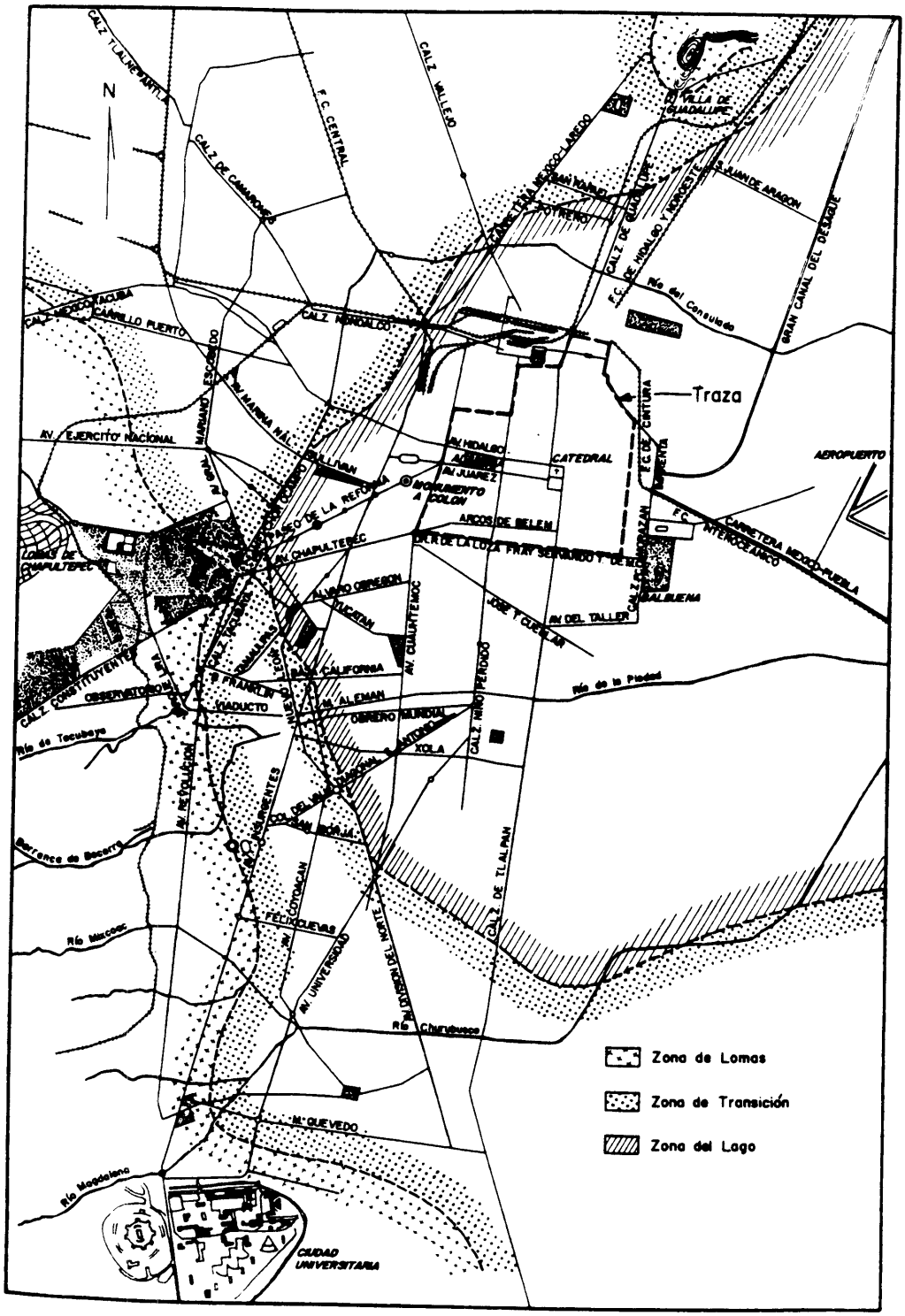

Figure 2.4 Map of the Geological Zoning of México City (from Marsal and Mazari 1959)

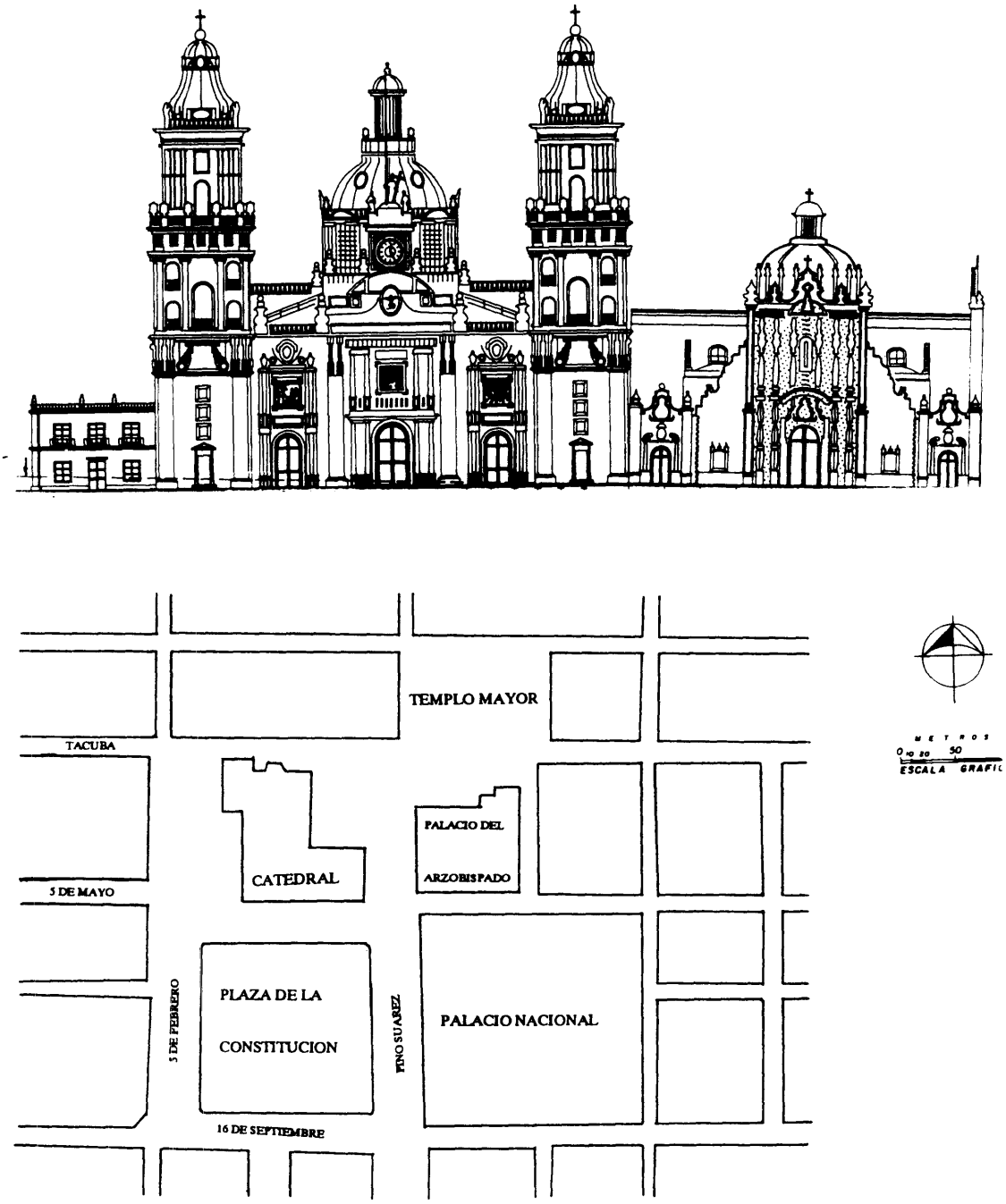

Figure 2.5 Facade of México City's Cathedral and its location in Reference to México City's Historical Center (from Tamez et al 1992)

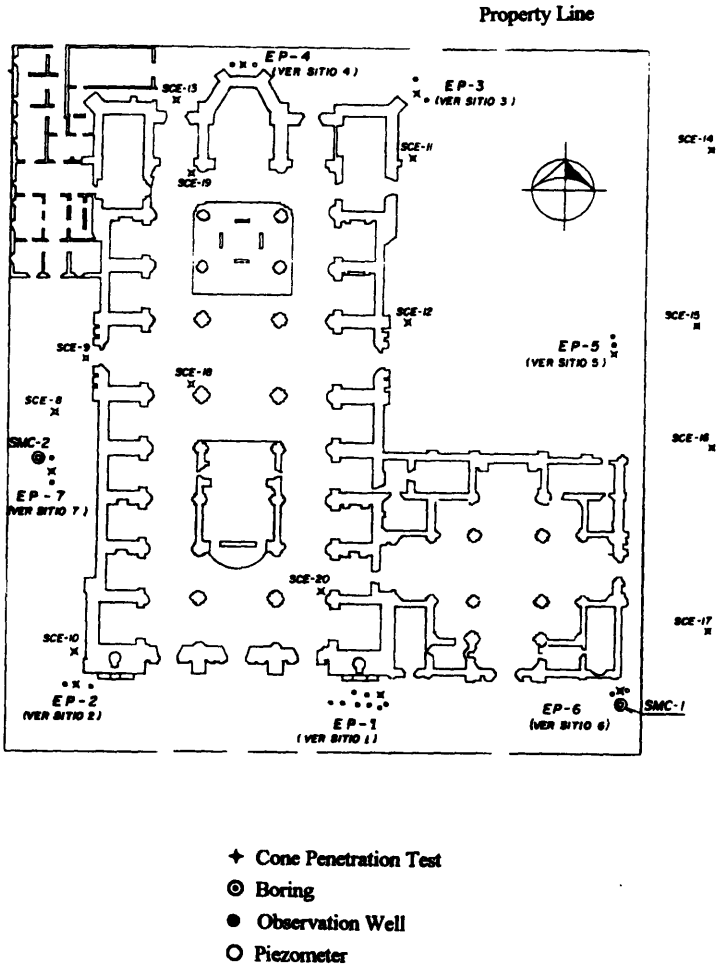

Figure 2.6 Location of México City's Cathedral Exploratory Program Performed by TGC Geotecnia, S.A. (from SEDUE 1990)

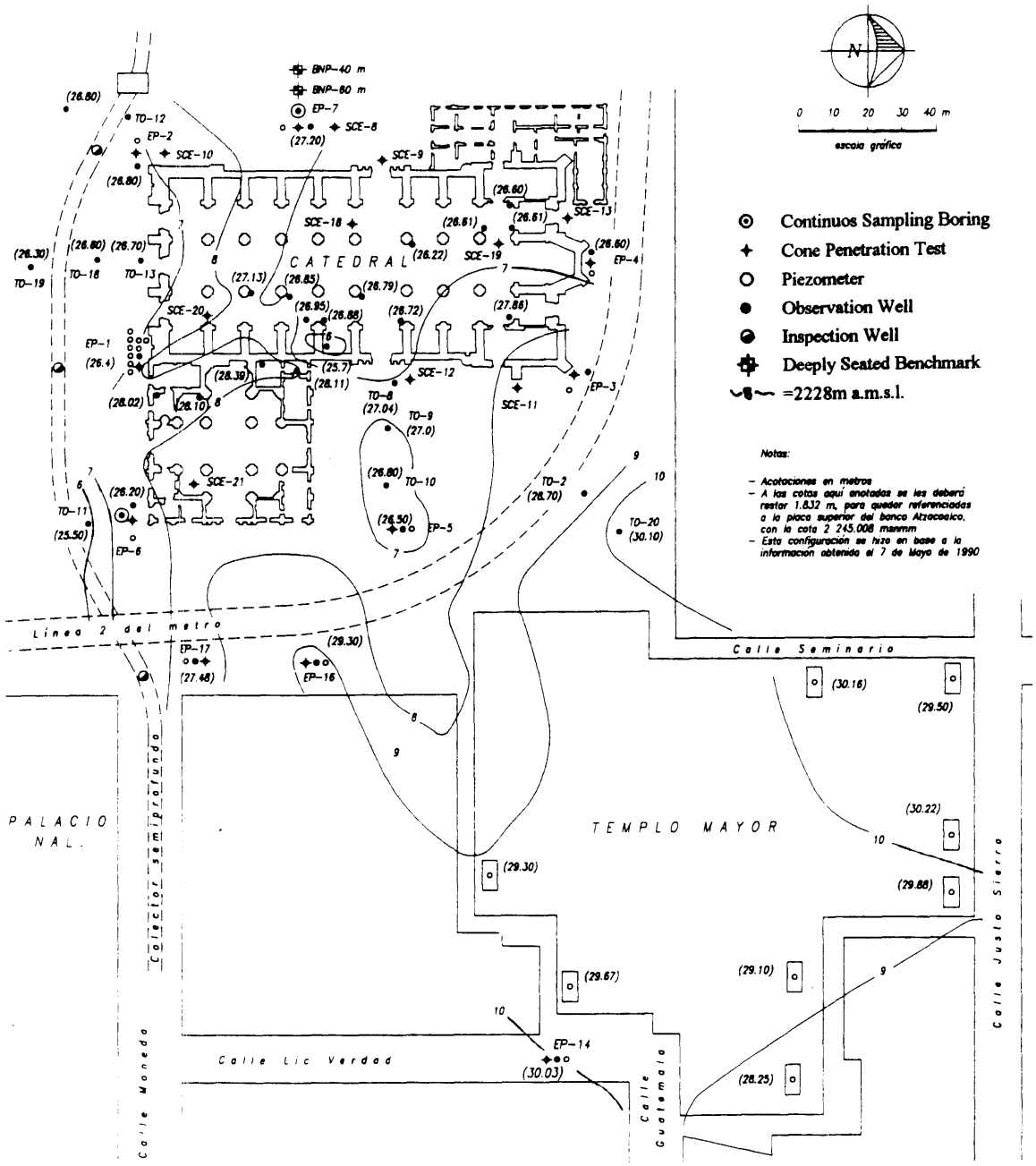

Figure 2.7 Groundwater Elevation Contour Lines based on Observation Wells; obtained by TGC Geotecnia, S.A. as of May 7, 1990 (from Tamez et al 1992)

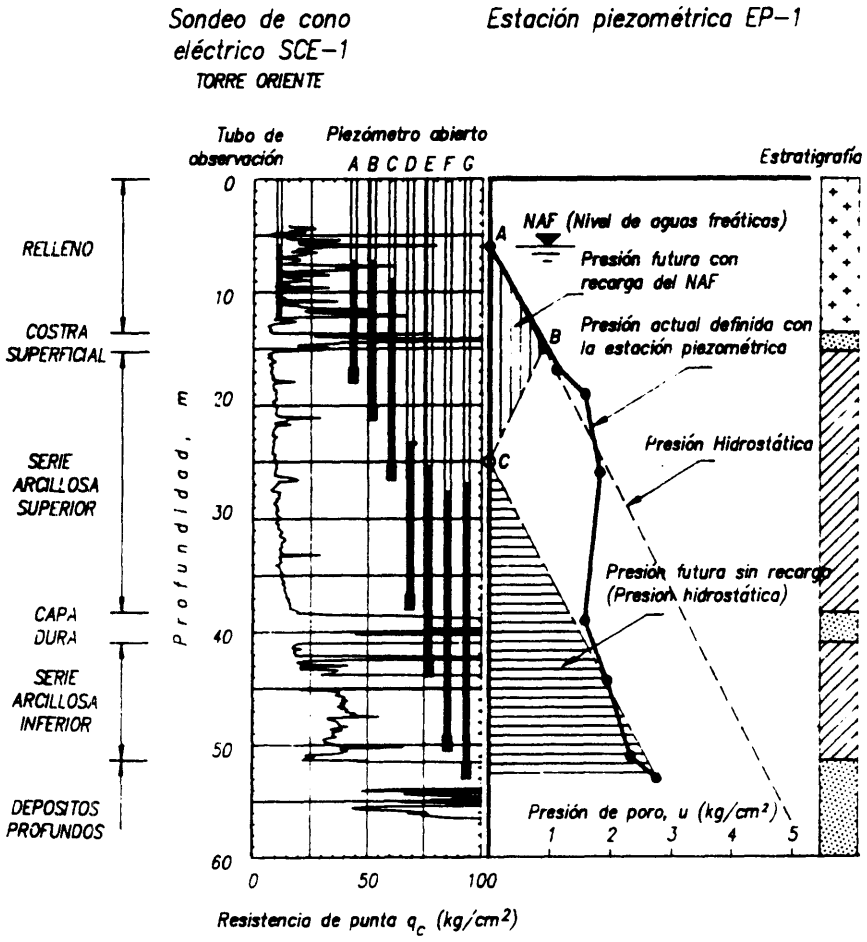

Note: Figure 2.7 and 2.8 are not referenced to the same elevation.

Figure 2.8 Piezometric Condition around SCE-1 (from Tamez et al 1992)

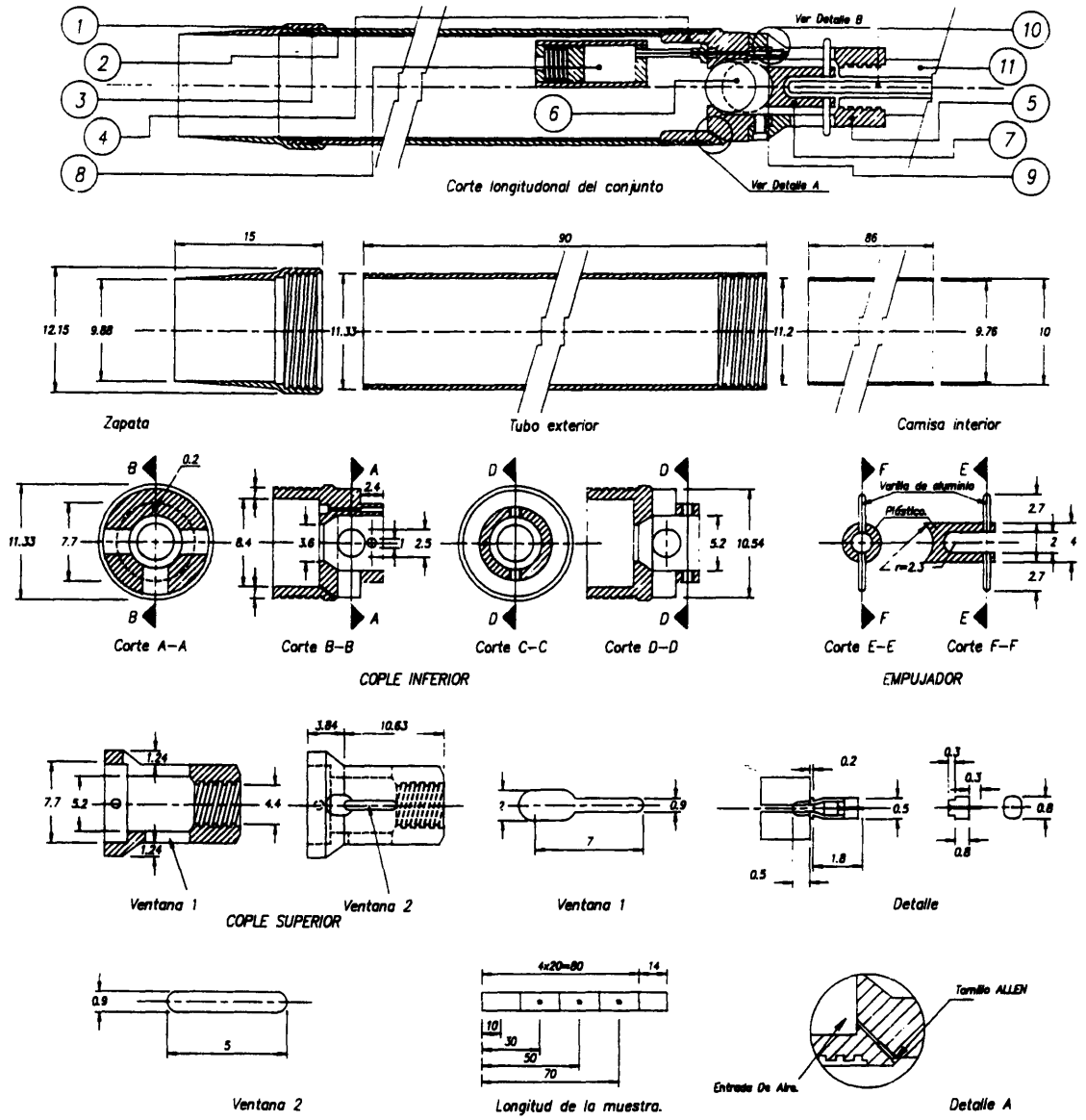

(1) Zapata de acero templado con diámetro interior de 9.88mm
(2) Tubo exterior de acero con cuerdas hembra y macho, tratado al cadmio.
(3) Camisa interior de aluminio anodizado, de 10cm diámetro y 1.2mm de espesor
(4) Cople inferior de acero
(5) Cople superior de acero
(6) Válvula de pie, pelota de hule de 4.4cm de diámetro y 35.8 g de peso
(7) Empujador de plástico delrin, con brazos de aluminio.
(8) Válvula de vacio (Acumulador de aire) con resorte
(9) Pivote neumático.
(10) Varilla de empuje de 1.25cm de diámetro y 100cm de longitud.
(11) Barra BW convencional.

NOTA: Acotaciones en centímetros

Figure 2.9 Schematic Drawing of TGC Geotecnia, S.A. Soft Soil Sampler Design (from Tamez et al 1992)

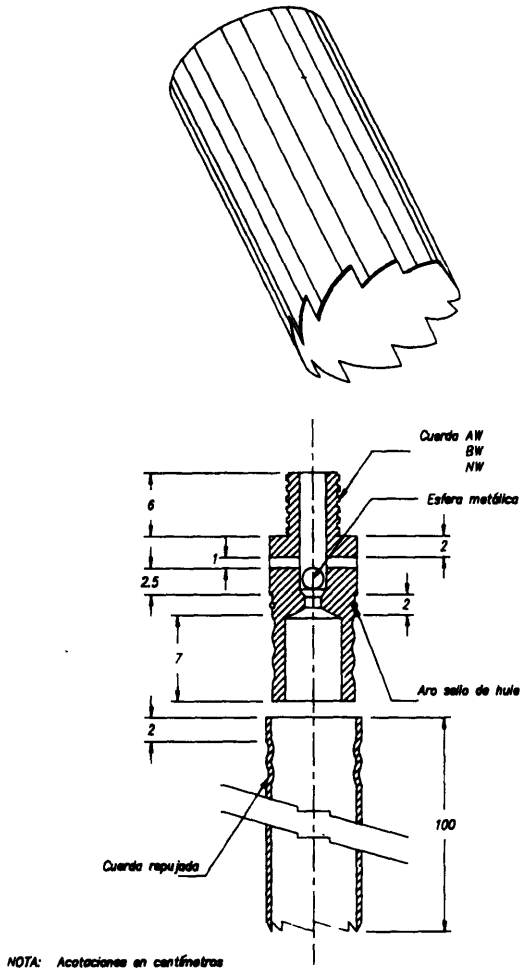

Figure 2.10 Thin Walled Shelby Tube Sampler with Toothed Cutting Shoe (from Tamez et al 1992)

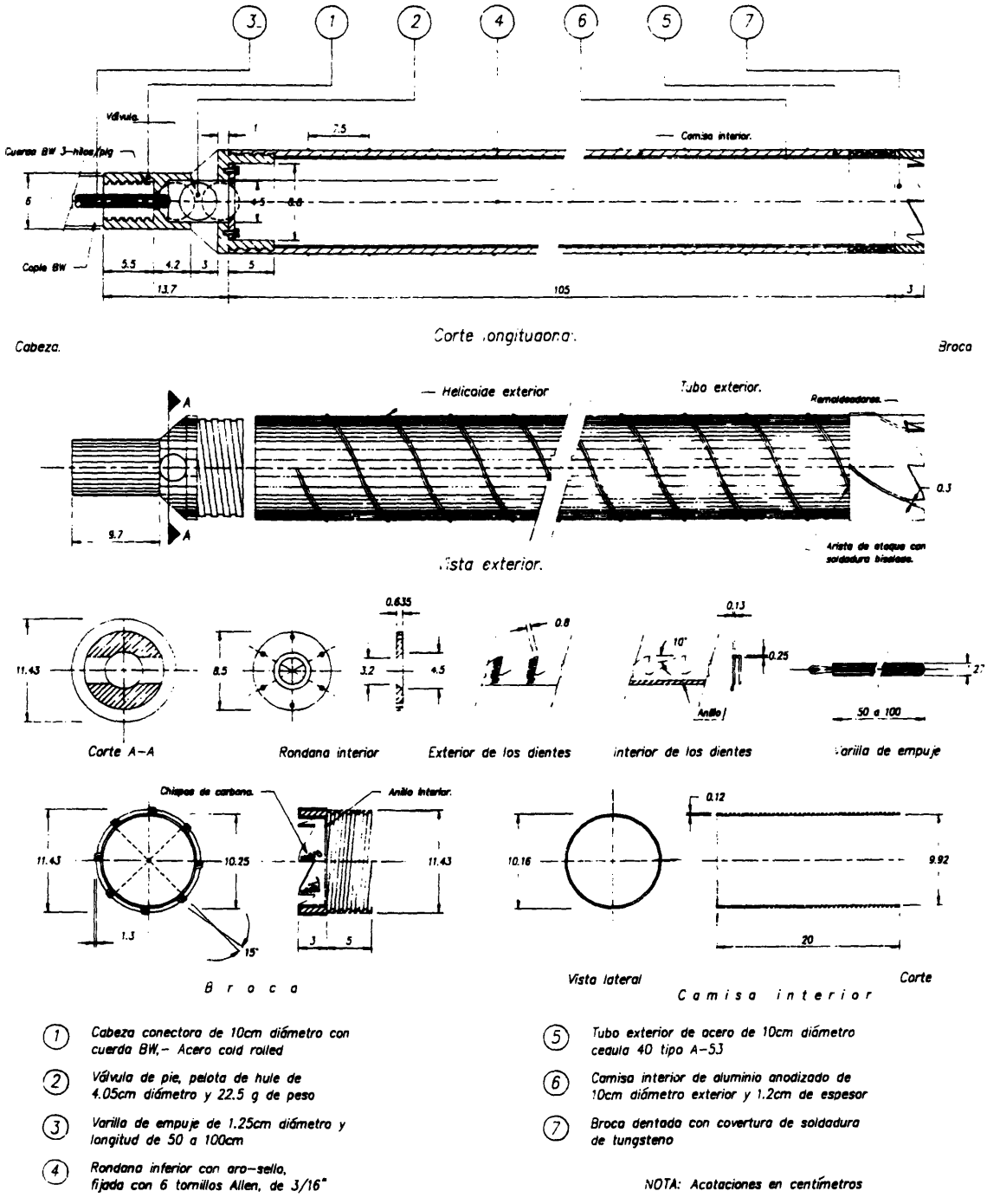

Figure 2.11 Schematic Drawing of TGC Geotecnia, S.A. Stiff Soil Sampler Design (from Tamez et al 1992)

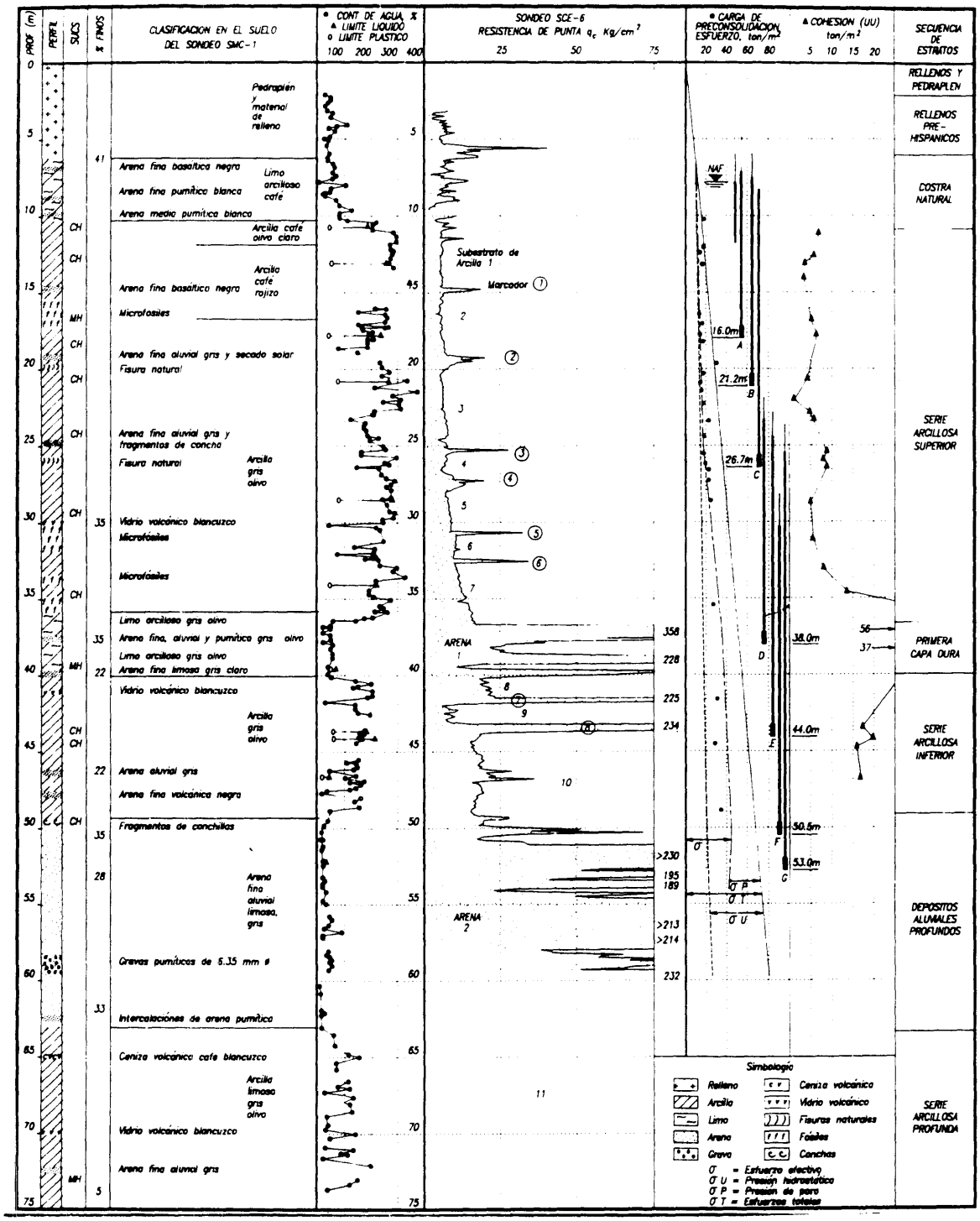

Figure 2.12 Summary of Laboratory Results of Boring SMC-1, and Net Tip Resistance of the Closest Cone Penetration Test (from Tamez et al 1992)

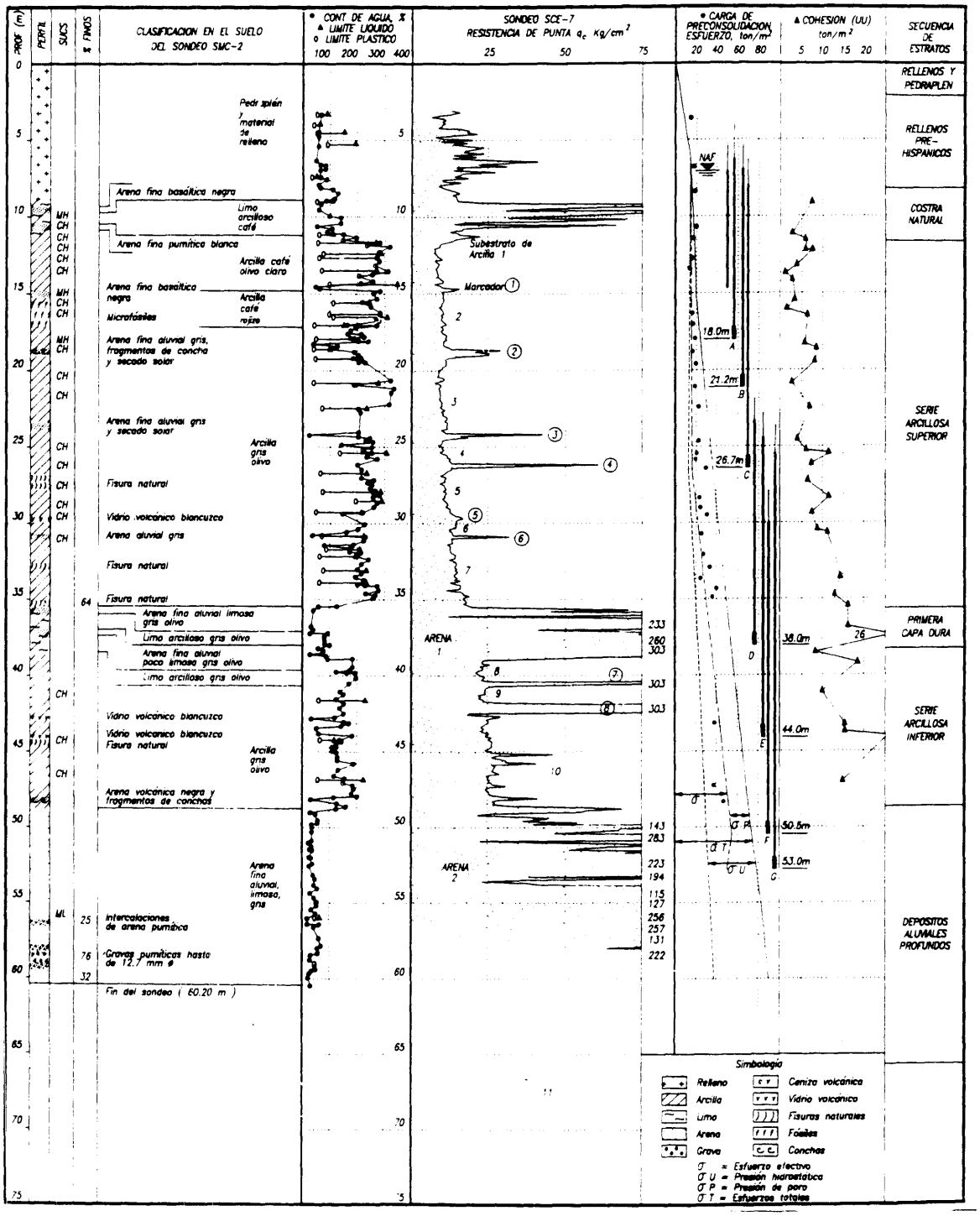

Figure 2.13 Summary of Laboratory Results of Boring SMC -2, and Net Tip Resistance of the Closest Cone Penetration Test (from Tamez et al 1992)

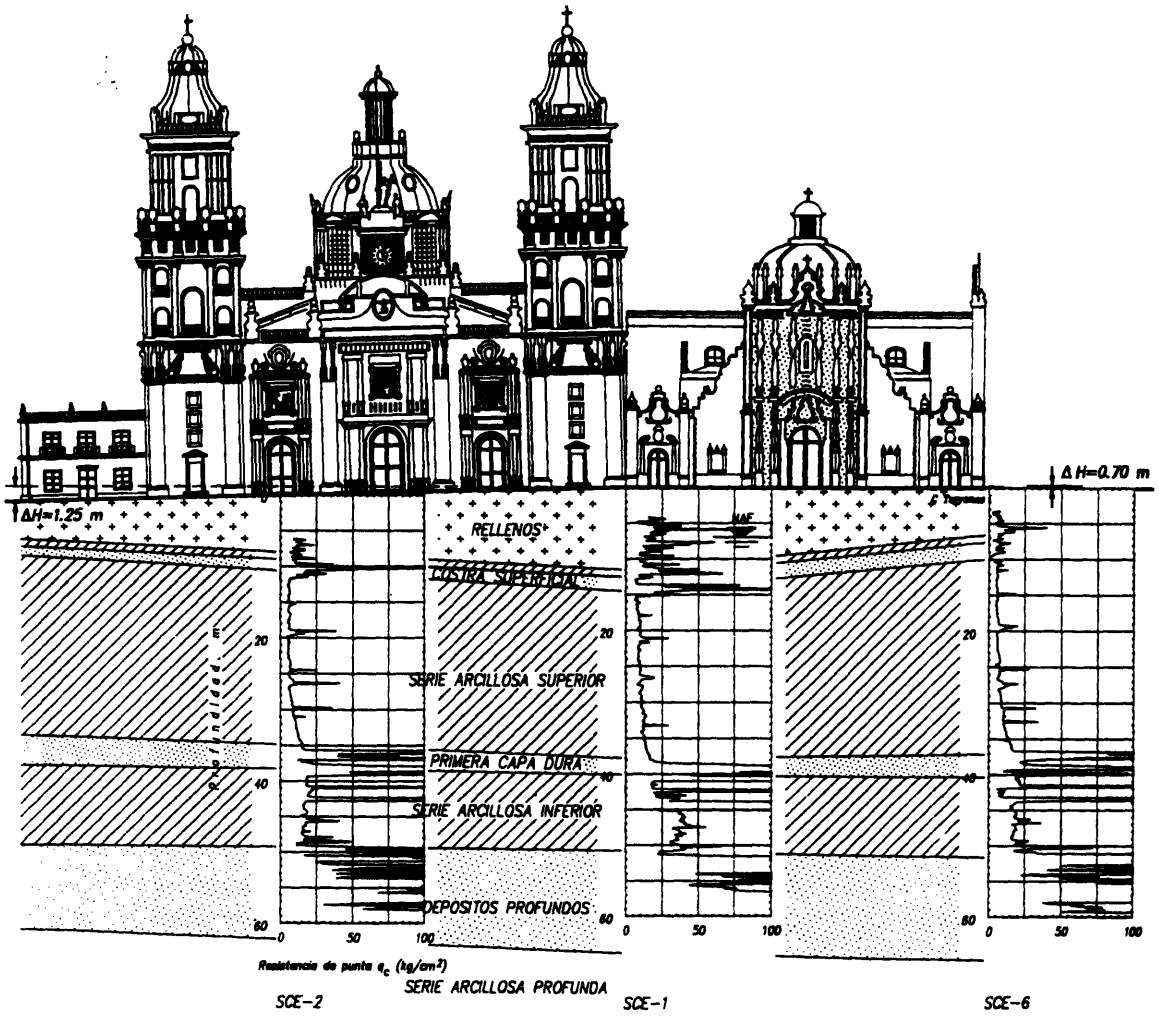

Figure 2.14 Stratigraphy Underneath the Main Entrance of México City's Cathedral (from Tamez et al 1992)

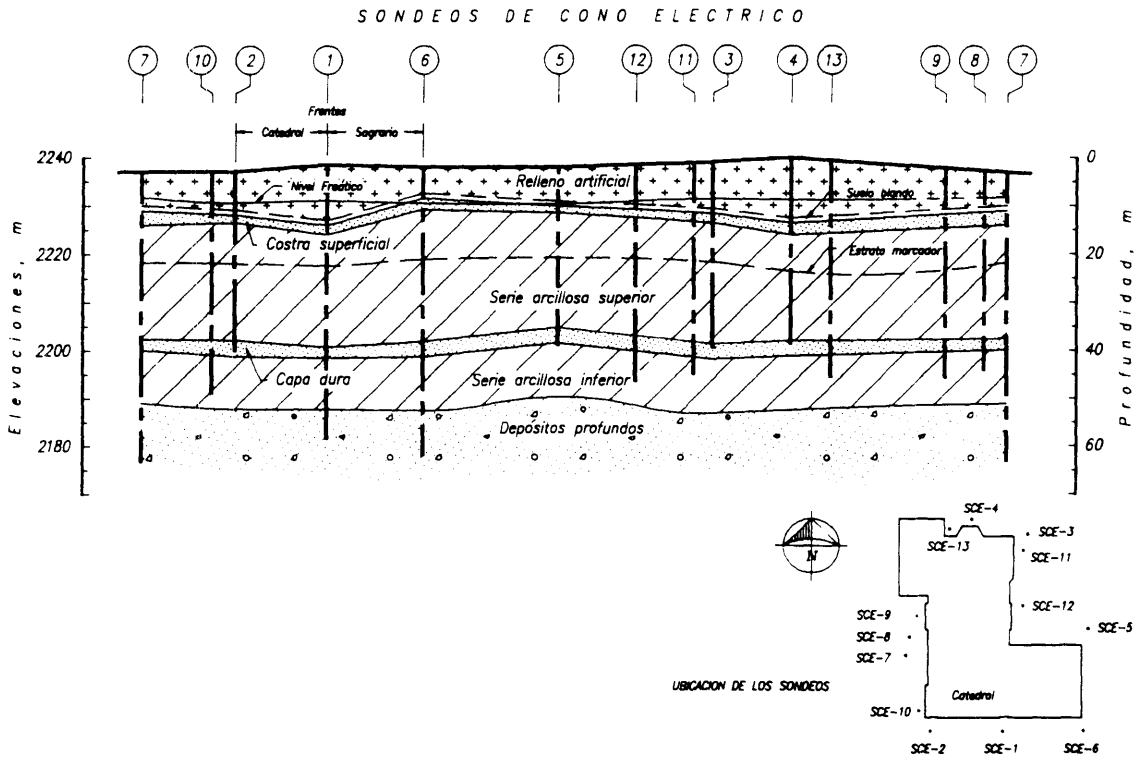

Figure 2.15 Perimetrical Stratigraphy of México City's Cathedral (from Tamez et al 1992)

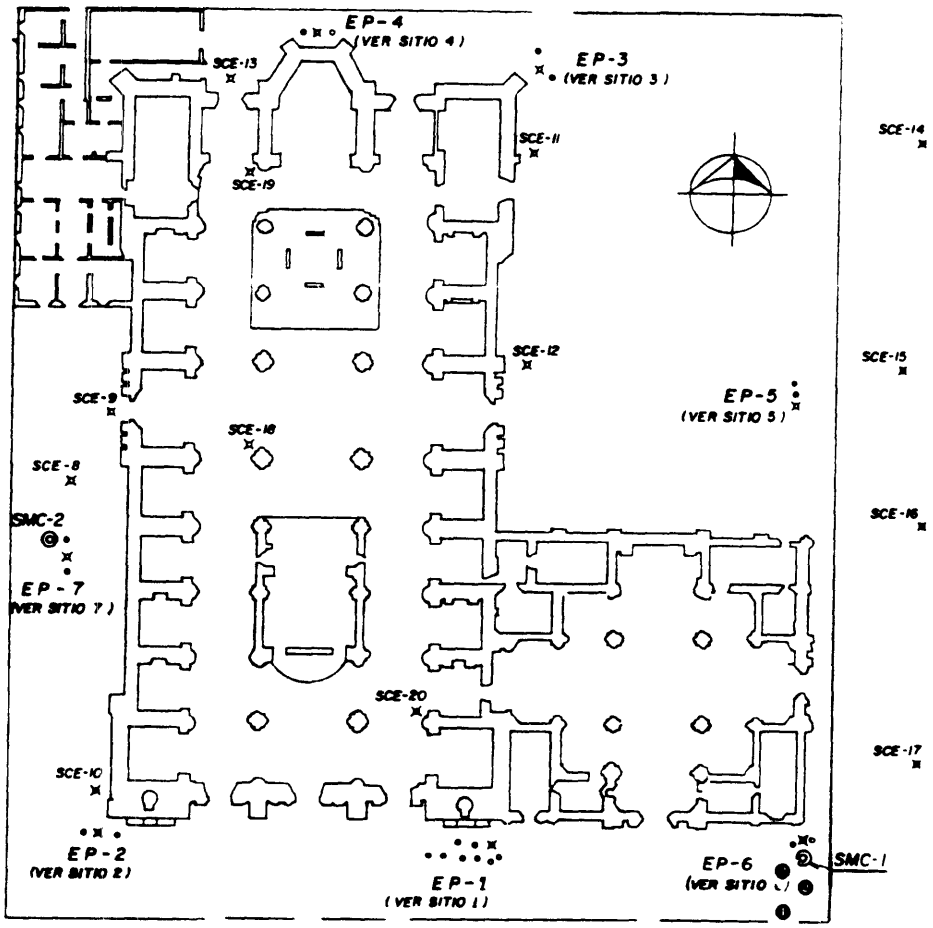

- ✦ Cone Penetration Test
- ⊙ Boring
- ● Observation Well
- ○ Piezometer

- ❶ Boring S1
- ❷ Boring S2
- ❸ Boring S3

Figure 2.16 Location of Borings S1, S2, and S3 in reference to the Cathedral and to TGC Geotecnia, S. A. Exploratory Program

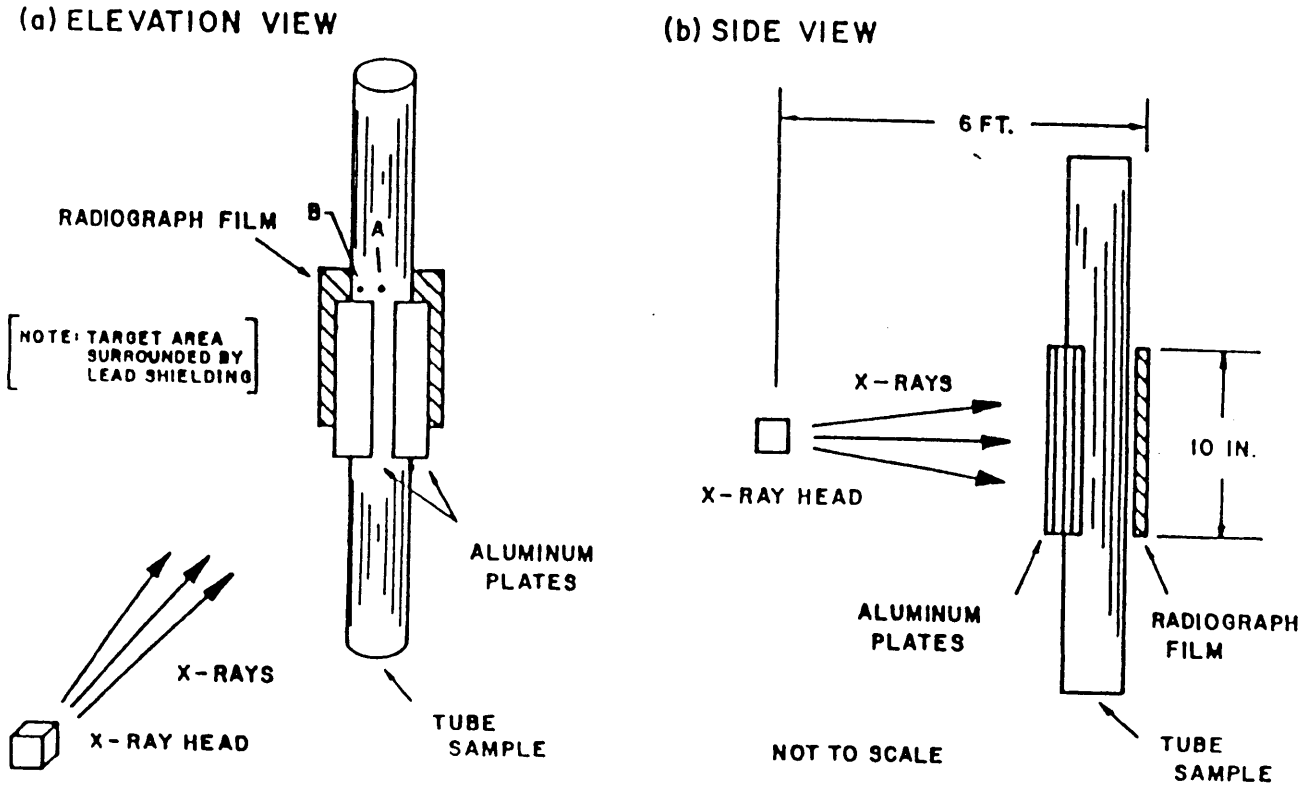

Figure 2.17 Schematic Drawing of MIT's Radiographing Technique

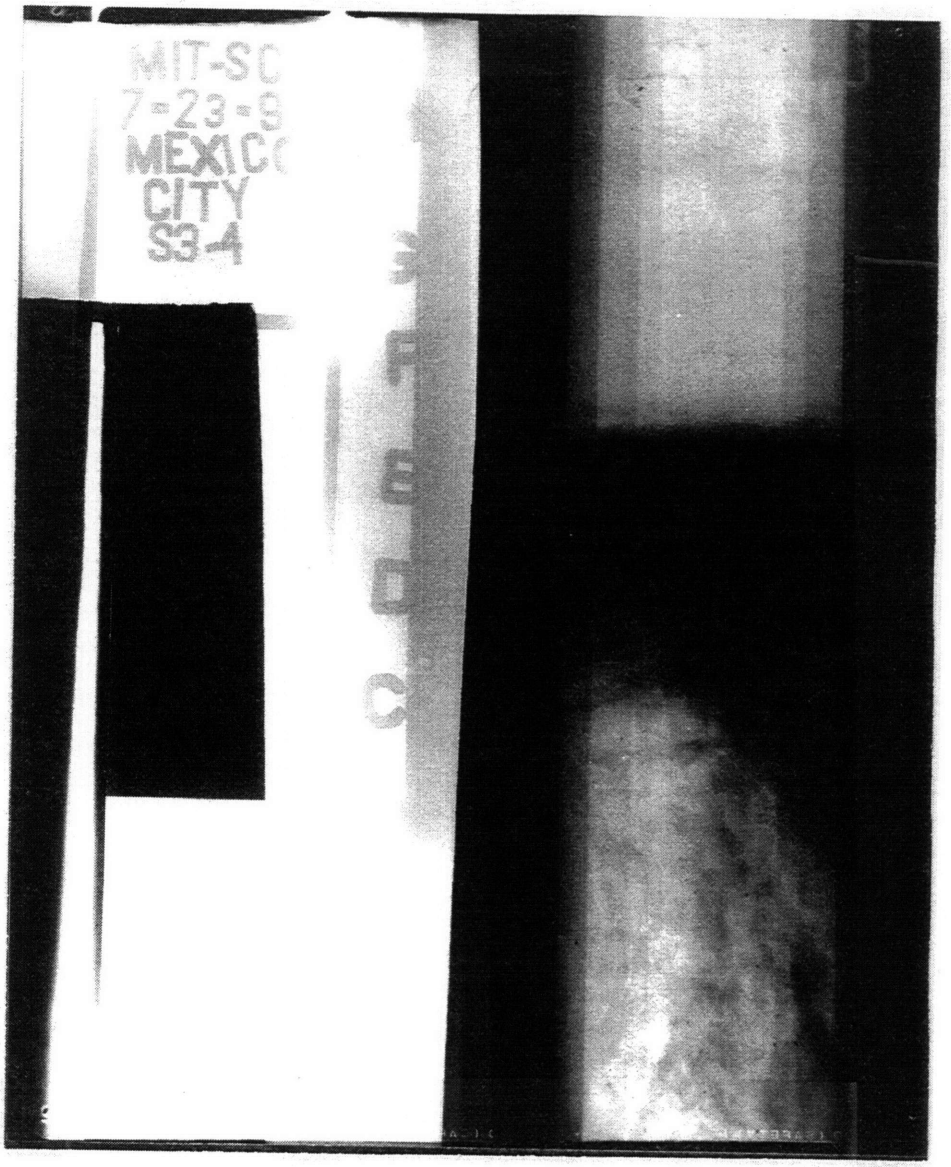

Figure 2.18 Radiograph Results of Sample Tube S3–4

Figure 2.19 Radiograph Results of Sample Tube S2–5

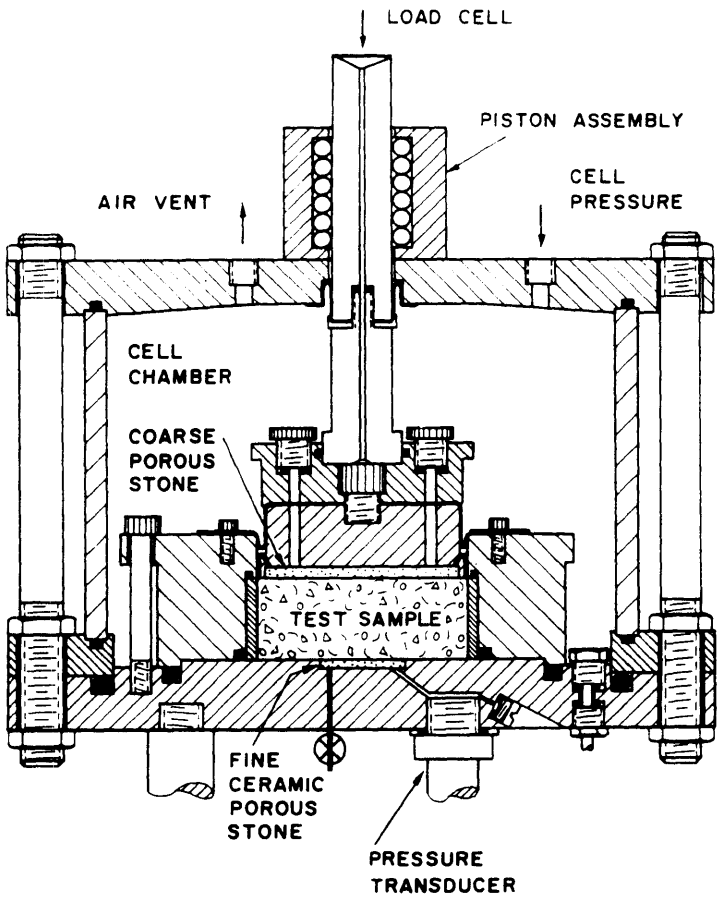

Figure 2.20 Schematic Drawing of MIT's Constant Rate of Strain Apparatus (modified from Wissa et al. 1971)

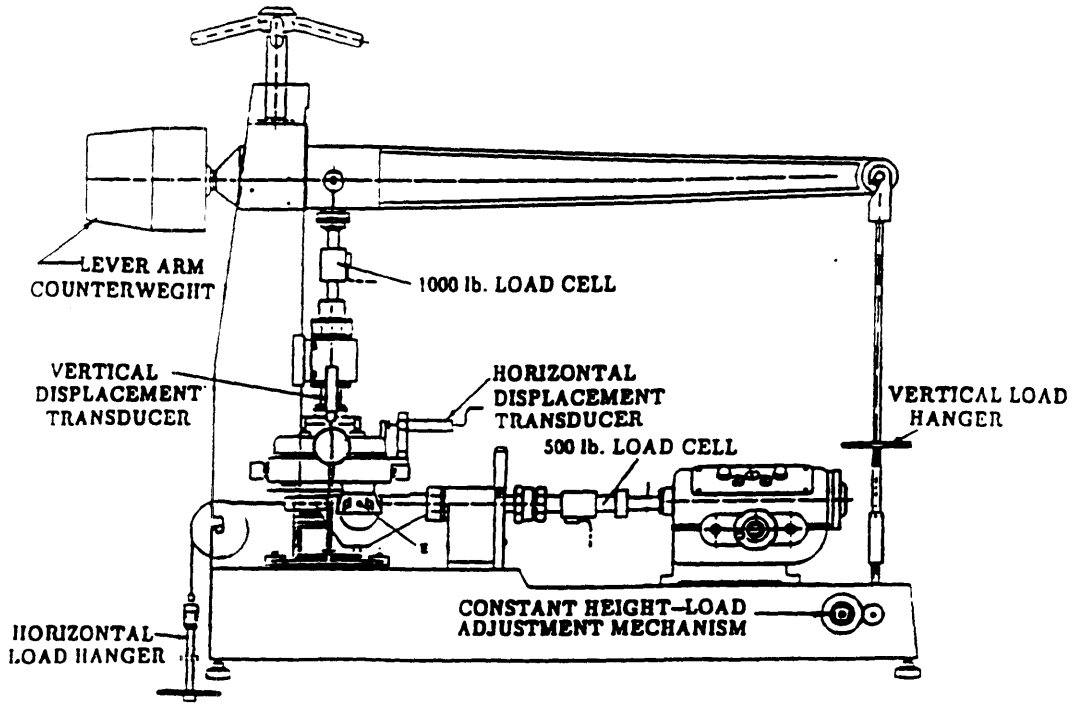

Figure 2.21 Schematic Drawing of Modified Geonor Direct Simple Shear Apparatus (from Ortega 1992)

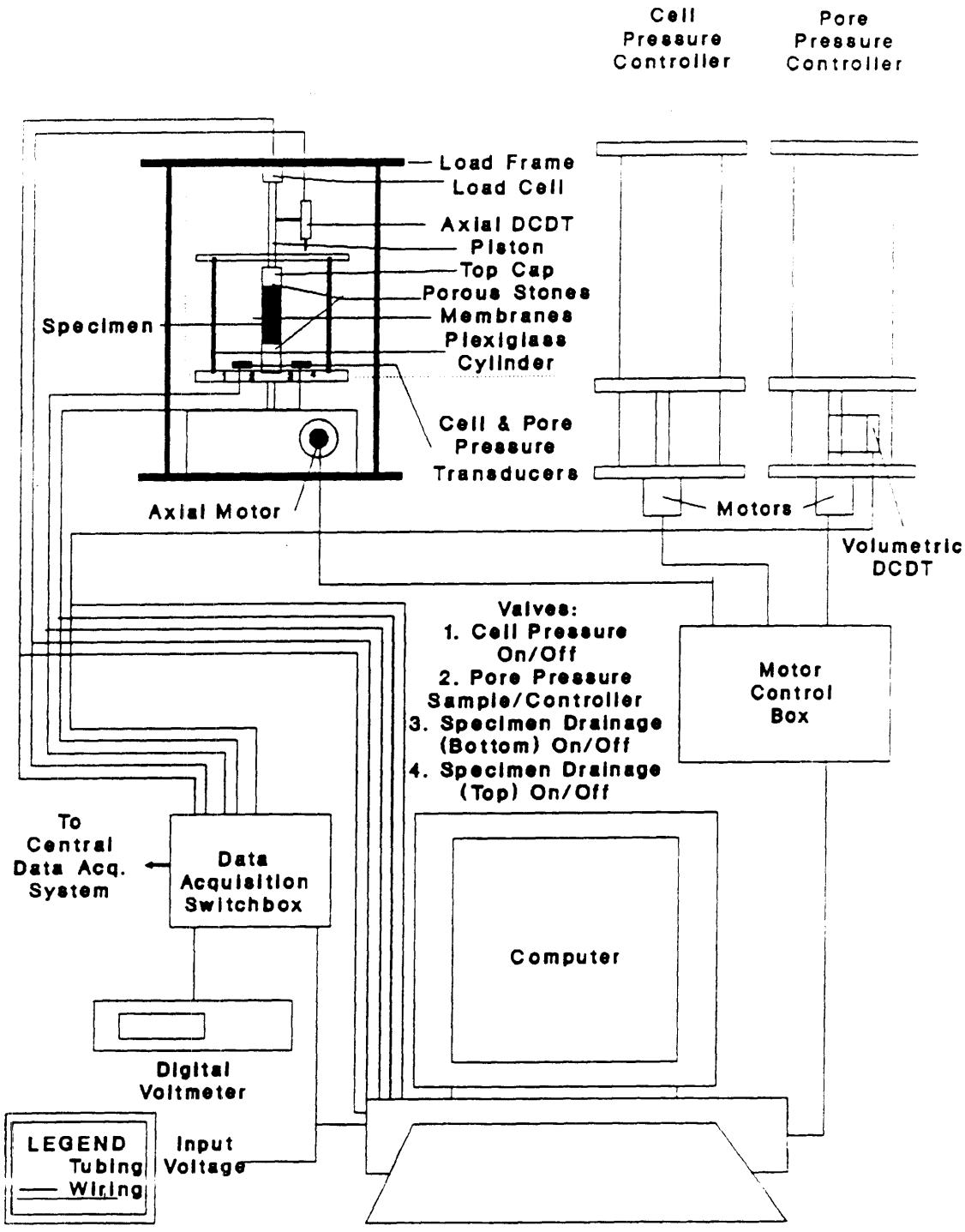

Figure 2.22 Schematic Drawing of MIT's Automated Stress Path Triaxial Apparatus (from de La Beaumelle 1990)

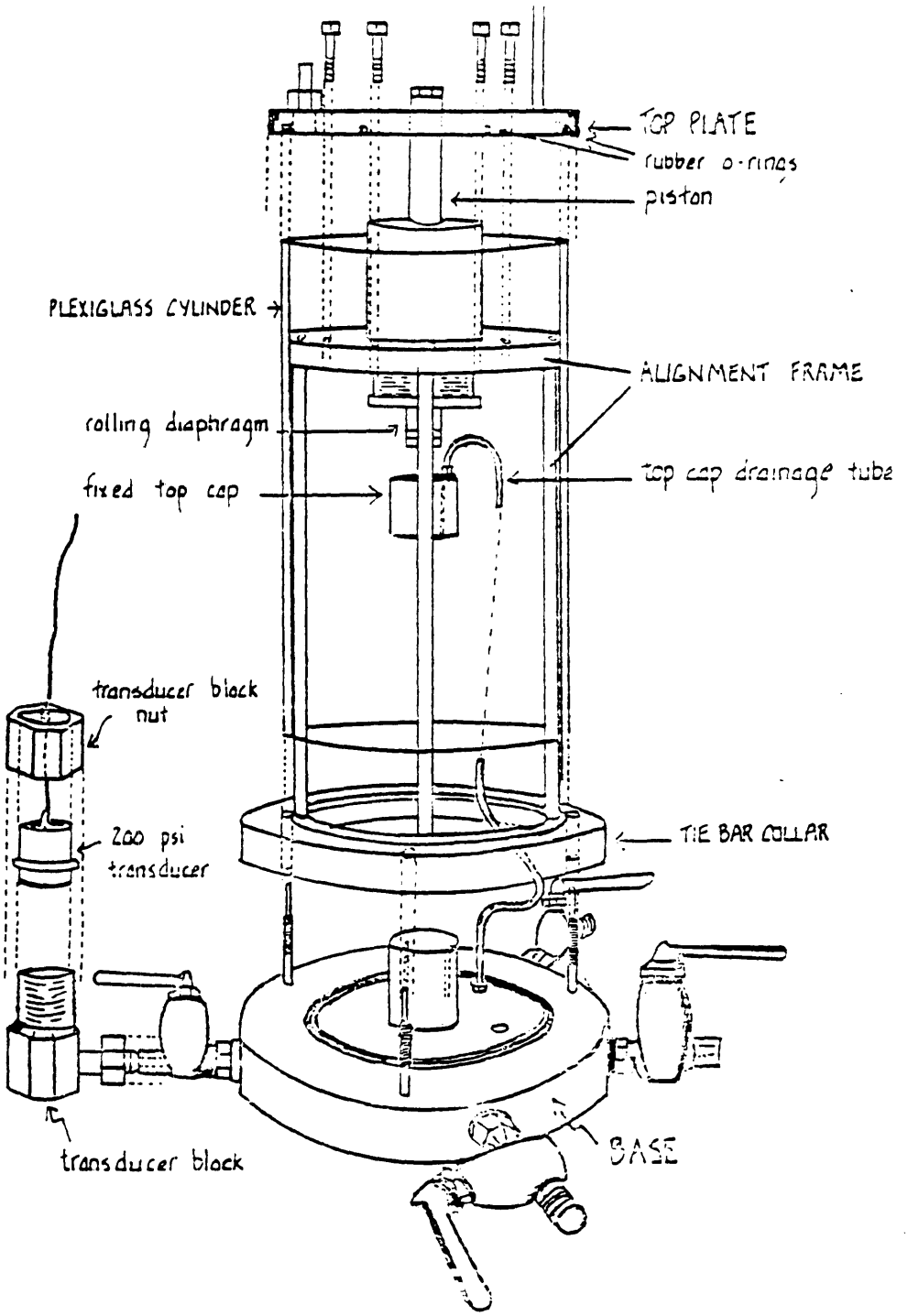

Figure 2.23 Schematic Drawing of MIT's Triaxial Cell (from Hadge 1979)

CHAPTER 3
INDEX PROPERTIES, MICROSTRUCTURE AND MINERALOGY

3.1. INTRODUCTION

The objective of this chapter is to present and discuss the index properties, microstructure, and mineralogy of the clay underlying Mexico City's Cathedral. This chapter also contains a brief overview of previous microstructure and mineralogy investigations.

3.2. INDEX PROPERTIES

Table 3.1 presents a summary of all the index tests performed for this investigation. The following sections will discuss the results of these tests in greater detail.

3.2.1 Natural Water Content and Undrained Strength Index Tests

The water content was measured each time a tube was cut to perform an engineering test or index test. These water contents are listed on the sample logs in Appendix A. Natural water contents were also measured from the trimmings of each engineering test and as part of the procedure for Atterberg limits testing and salt concentration determination. At the end of each engineering test, the water content is calculated for the entire test specimen, based on the initial wet weight of the test specimen and the final weight of solids.

Figure 3.1a presents depth vs. natural water content for the all values calculated throughout this investigation. The water contents calculated at the end of engineering tests are presumed to be more accurate than the water contents measured for index tests or those measured each time a tube was cut, because they consider a larger volume of soil. The data show a fair amount of scatter and no particular trend with depth. The average

natural water content calculated from engineering tests is 247.18% ± 61.11SD. This amount of scatter is typical for México City Clay as was shown in Chapter 2 of Marsal and Mazari (1959). After comparing the water contents from engineering tests, sample trimmings, and fresh cut tube samples, no trend or correlation was found to explain the cause of the variability of the values. This is an indication of true soil heterogeneity. The water contents of borings S2 and S3 are very similar except at a depth of -25m where borehole S2 yielded lower water contents than borehole S3. The average of the average natural water contents for each of the 7 clay substrata reported in SEDUE (1990) is 238.57% ± 23.65SD.

Each time a tube is cut to perform an engineering test, up to 3 torvane tests are performed. Figure 3.1b presents depth vs. the average value of torvane strength measured each time the tube was cut (note: measurements were performed by two different people). The mean torvane strengths ± SD and number of torvane tests performed at each location are listed in Table 3.1.

Based on the data presented in Figure 3.1b, the torvane strength gives a poor indication of the trend of undrained strength with depth. There is a large amount of scatter in the data, which is expected based on the large amount of scatter in the natural water contents. No direct relationship was found between water content and torvane strength. In some cases, fracturing of the soil occurred while inserting the torvane shoe. Fracturing of the soil results in lower torvane strength and was common in most samples below a depth of -15m. Therefore, it is likely that the torvane underestimated the strength of the soil below a depth of -15m. Based on observations from this investigation, the author recommends using the small shoe of the torvane (reading x 2.5) for México City Clay samples that yield torvane strengths higher than 0.4 to 0.5 ksc. Using the small shoe should stop the soil from fracturing and should give more accurate results of strength.

3.2.2 Atterberg Limits and Plasticity Chart

At least one set of Atterberg limits was performed on each undisturbed sample obtained from Boreholes S2 and S3. Based on radiograph results, a section of each sample tube was chosen for index testing. The location and result of each test can be found in Table 3.1.

Figure 3.2 plots depth versus Atterberg limits (plastic limit and liquid limit), natural water content, plasticity index, and liquidity index. For a few tests the natural water content was not measured, therefore the liquidity index could not be calculated. Figure 3.2 also presents the Atterberg limits reported in SEDUE (1990) for Borehole SMC-1.

The data show some scatter in the liquid limit with values ranging from 200% to 450%, but typically around 300% (16 tests; mean 290.7% ± 61.4SD). These values are within the typical range of values presented in the literature. The plastic limit remains fairly constant with the exception of two high values. The average plastic limit is 104.1% ± 32.8SD. The plasticity index data shows a fair amount of scatter with values ranging from 100% to 250%, but typically around 180% (16 tests; average 186.6% ± 47.4SD). These values are within the range of values reported in the literature. The liquidity index values range from 0.5 to 0.9, and the average of 12 determinations is 0.75 ± 0.13SD. These values are also within the range of values reported in the literature.

Figure 3.3 presents a correlation between the natural water content and the liquid limit. The figure includes data from this investigation and data presented in Marsal and Mazari (1959) for boring PC28. Table 3.2 presents the data obtained from boring PC28. Boring PC28 was drilled within the "Lake Zone" (defined in section 2.1.3) and, according to Marsal and Mazari, it is representative of the soil found in the Historical Center of México City. Boring PC28 is located within two kilometers of the Cathedral. A linear regression on the data from this investigation and the data from boring PC28 yielded the following equation:

$$W_{lc} = 27.214 + (W_n \times 1.002) \quad SD=\pm 40.61\% \quad r^2=0.8178 \qquad (2.1)$$

where W_{lc} = corrected liquid limit; and W_n = natural water content. Based on these results, it seems possible to estimate the liquid limit from the natural water content. Due to the limited data set, this equation should only be used for natural water contents below 300%. Figure 3.4 presents depth versus natural water content, liquid limit, and plastic limit for borings PC28 and PC143. Boring PC143 was performed in semi-virgin section (i.e., no heavy loads applied and relatively little pore pressure reduction caused by pumping) of the Lake Zone, and boring PC28 was performed in a section where heavy loads were applied and pore pressure reduction has occurred due to groundwater pumping. As shown in the figure, the water content and the liquid limit maintain a fairly constant ratio with depth, which adds validity to the correlation presented above.

Figure 3.5 presents a correlation between the plasticity index and the natural water content. The figure includes data from this investigation and data from boring PC28. A linear regression on the data yielded the following equation:

$$PI = -10.060 + (W_n \times 0.795) \quad SD=\pm 34.41 \quad r^2=0.7970 \qquad (2.2)$$

where PI = plasticity index. Based on these results, it seems possible to estimate the plasticity from the natural water content. Due to the limited data set, this equation should only be used for natural water contents below 300%.

No strong correlations were found between natural water content and the plastic limit or between the natural water content and the liquidity index. The data from Marsal and Mazari (1959), shown in Figure 3.4 also shows no obvious relationship between the water content and the plastic limit. This is surprising since a correlation between natural water content and plastic limit can be derived mathematically using Equations 2.1 and 2.2.

Figure 3.6 plots the data from this investigation and from boring PC 28 on the Plasticity Chart developed by A. Casagrande. This figure also shows a statistical regression developed by Marsal and Mazari (1959), for the plasticity index with respect to the liquid limit for México City Clay. The regression analysis was based on 7750 determinations and yielded the following equation:

$$PI = 0.84 \times (W_l - 39) \quad (2.3)$$

where W_l = water content at the liquid limit. As shown in Figure 3.6 the data from this investigation plots below Marsal and Mazari's line, and data from boring PC 28 plots much closer to this line. However, the data from this investigation plots within the standard deviation of the regression. Marsal and Mazari suggest that soils which plot below their proposed line might have experienced a decrease in water content from drying. The author does not believe this to be the case for the data from this investigation as distilled water was added to the specimens to be tested immediately after they were extruded from the tubes and then the specimens were stored inside a humid room.

The following equation was derived from Equations 2.1 and 2.2 using simple algebra:

$$PI = 0.8 \times (W_l - 40) \quad (2.4)$$

The strong similarity between Equations 2.3 and 2.4 emphasizes the validity of Equations 2.1 and 2.2.

Marsal and Mazari (1959) studied the effects of gradual drying (evaporation of pore water) of the soil specimen on the measured Atterberg limits. Figure 3.7 presents their results. They concluded that the soil had to undergo substantial drying (below the plastic limit) before any significant effect could be measured.

Figure 3.8, from Marsal and Mazari (1959), plots "Relative Consistency" ($C_r=(W_l-W_n)/PI$) versus natural water content for México City Clay. A negative value of relative consistency indicates a liquidity index greater than one, a positive value indicates a liquidity index less than one, and a zero value equals a liquidity index of one. The plot shows a regression which is based on more than 7000 data points. The following observations can be made from the figure: (1) below a natural water content of 360% the relative consistency is positive (i.e., liquidity index less than one), and (2) above 360% the relative consistency is negative (i.e., liquidity index greater than one). Marsal and Mazari's results suggest that Equation 2.1 should only be valid for natural water contents below

360% (i.e., in the range where the slope of C_r remains approximately constant). Their results also indicate that above a W_n=360% the slope of Equation 2.1 should decrease so that the liquid limit will be greater than the natural water content.

Marsal and Mazari also studied the effects of consolidation on the measured Atterberg limits using two remolded samples. Figure 3.9 presents results from these tests. Figure 3.9a shows water content versus the liquid and plastic limit, and Figure 3.9b plots relative consistency versus water content. For these figures, a decrease in water content indicates an increase in consolidation. The plot show that as a sample consolidates, the plastic limit remains constant, the liquid limit decreases, and C_r increases positively (i.e., liquidity index decreases). The change in liquid limit with consolidation stress suggests a transformation of the soil microstructure.

Figure 3.10a from Marsal and Mazari (1959) presents depth versus natural water content, total carbon, and inorganic carbon for boring PC28. The figure presents the striking similarity between the natural water content and the total carbon (correlation factor = 0.72). Figure 3.10b presents a trend of plasticity index versus organic carbon for boring PC28 (correlation factor = 0.71). Organic carbon is the difference between the total carbon and inorganic carbon. These results suggests that the microstructure of the soil is also a function of the amount of carbon (organic and inorganic) present in the soil.

The results from this investigation showed a correlation between the natural water content and the liquid limit. Marsal and Mazari's work suggested that this correlation is also related to consolidation (i.e., stress state) and the structure of the soil. At this time it is not possible to determine the nature of the relationship among the water content, liquid limit, and "stress". The data becomes especially confusing as it does not show a relationship between water content and stress level (i.e., depth Section 3.2.1). To the authors knowledge the correlations presented in this chapter have never been reported for any other soil.

3.2.3 Grain Size Distribution

Two hydrometer tests were performed, but no results are presented as the tests yielded unreliable results due to flocculation of the soil slurry. The tests were performed in accordance with ASTM guidelines, using sodium hexametaphosphate as a dispersing agent. Marsal and Mazari (1959) report the following, "Tests were run at the beginning by the hydrometer method in order to find out the gradation curves. Materials in suspension were treated with a dispersing agent and mixed in a high speed mixer for 15 minutes. Although different dispersing agents were used, of varying concentration, it was impossible to avoid association of particles; for this reason results are unreliable.". The author refers the reader to ASTM STP 1095, "Effects of Small Concentrations of Soluble Salts on Hydrometer Analysis". This article presents a method to prevent flocculation in hydrometer tests by previously treating the soil sample. This paper also suggests that even though flocculation is not visible, flocculation could be occurring and affecting the test results.

3.2.4 Specific Gravity, Salt Concentration and pH

Fifteen tests were performed to determine the specific gravity of the soil grains. Figure 3.11 plots depth versus specific gravity. There is no particular trend with depth and the scattered data give an average specific gravity of $2.46 \pm .08$SD.

The salt concentration and pH of the clay was determined in most cases at the bottom of each tube. Figure 3.12 presents a plot of depth versus salt concentration and pH. Salt concentrations are expressed as equivalent KCl concentration in grams per liter of pore fluid and grams per kilogram of dry soil. Above an approximate depth of -25m salt concentrations and pH vary significantly, but below -25m they remain fairly constant. The range of values of salt concentration measured are 1 to 6 g/liter of pore fluid or 2.5 to 17 g/kg of soil. The values of pH measured range from 7 to 9. The average salt

concentration below -25m is 1.87±0.4SD g/liter of pore fluid or 4.52±0.96SD g/kg of soil. The average pH below -25m is 7.68±0.35SD.

Below a depth of -25m the value of pore pressures measured at piezometric station EP1 is lower than hydrostatic pressure. The decrease in pore pressure is caused by the pumping of the underlying acquifer (Section 2.1.7). Constant salt concentration and pH, and decreasing pore pressures below -25m together suggest the presence of a permeable layer above -25m that is connected to a water source. This layer allows sufficient flow and head to stop the decrease in pore pressure above -25m and to dilute the pore fluid below a depth of -25m.

No relationships were found between:

- salt concentration and pH
- salt concentration and Atterberg limits
- pH and Atterberg limits

The results of the tests discussed in this section are listed in Table 3.1.

3.2.5 Void Ratio, Total Unit Weight and Saturation

The void ratio and total unit weight of the clay beneath the cathedral were determined from engineering test specimens. Figure 3.13 plots depth versus total unit weight and depth versus void ratio. The scatter in the values of unit weight and void ratio are consistent with the scatter in the natural water content values shown in Figure 3.1. The average unit weight is 1.19g/cc ± 0.05SD and the average void ratio is 6.15 ± 1.52SD. SEDUE (1990) does not report an average unit weight for the deposit, but does report the average void ratio for each of the seven clay substratas. The average of the seven averages 6.27 ± 0.84SD, and there is no trend with depth.

Figure 3.14 plots depth versus initial degree of saturation calculated from engineering tests. The average initial saturation is 98.41% ± 3.46SD.

3.3 MICROSTRUCTURE AND MINERALOGY

3.3.1 Overview

It is well documented in the literature that México City Clay has exceptional engineering properties. A few investigations have been performed to explain these properties through studying the microstructure and mineralogy of the clay. These studies have used techniques such as X-ray diffraction, electronic microscopy, differential thermal analysis, proton spectrography, and chemical analysis. The results from these investigations are sometimes contradictory and inconclusive.

Zeevaert (1949) described México City Clay as an organic silty clay composed of large quantities of fossils (ostracods and very fine diatoms), and volcanic ash and glass particles. He found 40% of the particles to be less than 2μm in size, and 50% of this clay-sized fraction was montmorillonite, the balance being mostly skeletal material and volcanic ash. Zeevaert also reported that México City Clay contains calcium carbonate and 5-10% organic colloids (based on tests performed by Dr. R. E. Grim at Univ. of Illinois). According to Zeevaert (1949) the montmorillonite in México City Clay is high in magnesium content, has a poor crystalline structure, and appears to be "sodium montmorillonite". It seems that, based on Zeevaert's results, several investigators have referred to the mineralogy of México City clay as montmorillonitic or bentonitic (Casagrande and Wilson 1951, Skempton and Northey 1952, Skempton 1953, and Moum and Rosenqvist 1961). Zeevaert does not mention the precise location where he obtained his samples, but he does state that the samples were obtained from the Lake Zone.

Marsal and Mazari (1959) reported a detailed compositional study on a large number of samples obtained from different depths and from different locations within the Lake Zone. Their results indicate that 22% to 63% of the component particles are smaller than 2μm, there is 3% to 21% carbonate content, and 1% to 7% of the soil is organic matter. Their results also indicate that the coarse size fraction of the soil has a high number of diatoms and ostracods. Marsal and Mazari's compositional study used a large

number of techniques to study the mineralogy of the soil but not one method gave conclusive results. Based on the results of two nuclear spectrography tests, the samples could be classified as illites or nontronites. Based on the results of Electronic Microscopy (using a RCA Victor EMC-1 electronic microscope) performed on 154 samples (864 pictures), Marsal and Mazari estimate that 78% to 85% of the samples were montmorillonite, 10% to 18% kalonite, 3% to 5% beidelite, 3% as illite, and 0.6% as hallosite. The results of 18 cation exchange tests suggested the presence of illite. Marsal and Mazari also point out that the results of several X-ray diffraction tests and differential thermal analysis tests were inconclusive. The compositional study was performed between 1950 and 1952. After Dr. Grim published his book on clay mineralogy in 1953, Marsal and Mazari reexamined their results based on Grim's observations. The revised results from electronic microscopy tests are; 54% illite, 13% montmorillonite, 4% kaolinite, 2% dickite, 1% hallosite, 3% nontronite, 3% fossils, and 20% inconclusive. It seems that, based on the new interpretation of the electronic microscopy results and cation exchange results, Marsal and Mazari concluded that the clay content of México City Clay might be classified as illite. However, they point out that their investigation did not yield conclusive results.

Leonards and Girault (1961) reported the results of compositional analyses on samples of México City Clay. Their samples contained about 8% to 10% organic matter and a small amount of calcite. Based on X-ray diffraction and differential thermal analysis tests, the remaining material was identified as amorphous and was classified as allophane. Leonards and Girault concluded that there was no evidence of the presence of any montmorillonite or illite. Their samples were obtained from two handcut blocks at depths of 6.4 and 7.5m. Although they do not give a location for the samples, they are presumably from within the Lake Zone.

Lo (1962) reported that his investigations performed on a sample of México City Clay revealed that the samples consisted mainly of amorphous materials. Some of the

amorphous materials were identified as fragments of diatoms, and the rest were probably silica-alumina gels or altered volcanic material. Lo reports the presence of 10% calcite and suggests that it probably originated from microorganisms (ostracods). Also, electron diffraction tests detected an unknown amount of montmorillonite. The montmorillonite was considered to be of poor crystallinity since X-ray diffraction tests partly failed to detect it. Lo indicates that the content of organic matter is quite high and contributes to the high water content and susceptibility of settlements. Based on a chemical analysis of the pore water, the exchangeable cations of the montmorillonite content were identified as sodium and potassium. Lo obtained his samples from a handcut block sample at a depth of 8m, from an unmentioned location within the Lake Zone.

Girault (1964) reviewed the existing information on the mineralogy of the fine fraction of México City Clay and added additional references to tests performed by Dr. R.T. Martin (MIT) and Dr. J. L. White (Purdue University). Dr. Martin at MIT examined two samples using X-ray diffraction and differential thermal analysis. Based on Martin's X-ray diffraction results, it was concluded that the only crystalline material present was carbonates. Based on Martin's differential thermal analysis results, Girault concluded that the samples did not contain a sufficient amount of montmorillonite or illite to produce a typical curve. Girault, referencing Grim (1962) states that some amorphous materials have some organization of its units and that this organization might be similar to the organization of montmorillonite. Girault mentions that not all clay of volcanic lacustrine origin will be montmorillonite. He cites a clay in Switzerland that transformed to illite, and a clay in New Zealand that transformed to amorphous hallosite. Girault concludes that México City Clay is amorphous and classifies it as allophane.

Mesri et. al. (1975) performed a compositional study of México City Clay that included scanning electron microscopy, X-ray diffraction, and chemical analysis. Mesri et. al. report that their samples consisted of about: 5% to 10% sand-sized concretionary particles or ooliths composed of calcium carbonate; 55% to 65% silt-sized siliceous

diatoms; 20% to 30% clay-sized particles, of which probably 10% were interlayered smectite and the remaining were biogenic or volcanogenic silica; and 5% to 10% organic matter. Mesri et. al. classify their samples of México City Clay as impure diatomites. The samples used in this investigation were undisturbed tube samples obtained at a depth of -15m in a site between Eduardo Molina and Gran Canal. This site is not far from the sampling site used for this thesis.

Peralta (1989) reports that around the year 1980 a study began in México to resolve the discrepancies reported by the various investigators and to definitively establish the mineralogical composition of México City Clay. A continuous sampling borehole was performed using thin walled sampling tube. Samples were collected from ground surface to a depth of -31.5m at a location between Reforma y Juarez (downtown México City; within the Lake Zone). This site is within one kilometer of the cathedral. After close examination of the undisturbed samples, 770 layers were counted based on color changes, texture, inclusions, sand lenses, volcanic ash, etc. (layer thickness $\approx$ 4cm). A total of 163 samples were obtained from the most representative layers. From each sample, electron microscopy specimens and up to 4 X-ray diffraction specimens were prepared.

The mineralogical composition results show that all of the above authors were correct. Peralta points out that there is a significant change in mineralogy with depth, especially for the fine size fraction of the soil. Montmorillonite, illite, and amorphous material were all found at different depths. Gomez Looh (1987) performed and interpreted X-ray diffraction tests to fulfill her thesis requirements for an undergraduate degree in Chemical Engineering. The X-ray diffraction samples were mechanically divided into three size fractions: (1) between 2 and 38 μm; (2) between 0.2 and 2 μm; and (3) between 0.08 and 0.2μm. Table 3.3 presents a summary of the results obtained by Looh (presented by Peralta in 1989). It was concluded that different size fractions of the soil have different mineralogies. The study does not to completely define the mineralogical composition of the clay. It defines the clay as a transforming mix of clayey and non-clayey

materials into stable minerals. The study also found that a great abundance of microfossils are present in the soil. Sixteen types were identified, the majority belonging to the Pennales order. Peralta suggests that it is not possible to compare compositional analyses of México City Clay from various locations unless the samples are taken from the same depth and they have the same particle size fractions.

3.3.2 Scanning Electron Microscopy, Environmental Scanning Electron Microscopy, and X-ray Diffraction Results

3.3.2.1 *Introduction*

To investigate the mineralogy and microstructure of México City Clay, the following tests were performed for this theses: nine samples were viewed using a Cambridge Instrument Stereoscan 240 Scanning Electron Microscope (SEM); one sample was viewed using an Electroscan E3 Environmental Scanning Electron Microscope (ESEM); and four X-ray diffraction tests were performed using a Ragukh RU300 Difractometer. Additionally, compositional analyses were performed on samples while viewing them with the SEM using a Link Analytical AN10000 X-ray Analyzer. The X-ray spectra is created by Electron Energy Loss (EELS), which is a byproduct of scanning electron microscopy. The results of the compositional analyses were interpreted by Link Analytical software ZAF 4/FLS. The interpretation of the analyses regarding mineralogy and microstructure was performed with the help of Dr. R. T. Martin (former MIT Research Associate). Mr. Stephen Rudolph was the technician in charge of operation of the SEM, and Mr. Joseph Adario performed the X-ray diffraction tests at the MIT X-ray Diffraction Laboratory.

An unsuccessful attempt was made to see the surface of a sample utilizing an Atomic Force Microscope (AFM). In order to get any results with the AFM, the specimen should have an extremely flat surface, $\pm$ 5μm. The advantage of this microscope is that it does not work under a high vacuum, therefore the sample can be seen in its

natural state (wet). Additionally, the AFM offers extremely high magnifications and up to nanometer resolutions.

Samples for SEM viewing, ESEM viewing, and X-ray diffraction were prepared from laboratory test specimens and from undisturbed soil obtained from the sampling tubes.

3.3.2.2 *Sample Preparation*

A total of nine specimens were viewed with the SEM. The following table presents basic information about the SEM samples examined:

Specimen Number	Engineering Test	Sample Location	Depth (m)
SCS1	CRS77	S3-2	-13.56
SCS2	CRS75	S2-3	-14.36
SCS3	CRS82	S2-5	-24.76
SCS4	CRS80	S3-6	-25.63
SCS5	TX221	S2-8	-29.51
S6	----	S2-5	-24.77
SJ-K	----	S2-5	-24.46
SH	----	S2-5	-24.52
SK	----	S2-5	-24.44

The location for specimens SCS1 through samples SCS5 were randomly chosen. The location of specimen S6 was chosen in hopes of explaining the high preconsolidation pressure estimated at this location (as discussed in Chapter 4). The location of the rest of the specimens were chosen to interpret the pictures obtained from specimen S6. All specimens were oven dried with the exception of specimen SCS5, which was air dried. During the drying process all specimens experienced a large volume decrease ($\approx$ 40%), resulting in the closing of interparticle spacing. In addition, samples obtained from laboratory test specimens had undergone significant consolidation. Therefore, the interparticle spacing viewed with the SEM is smaller than the actual in situ interparticle

spacing. Once completely dry, the samples were coated with a gold palladium conducting resin in an evaporator.

Specimen S7 was the only specimen viewed with the ESEM. Specimen S7 was obtained at a depth of -28.62m (tube S2-7). The ESEM is a relatively new apparatus that offers the capability of viewing a specimen under a controlled atmosphere (i.e., temperature and pressure). The ESEM operates under a gas ionization principal. Once the electron beam hits the specimen, the specimen releases secondary electrons that ionize the atmosphere of the ESEM chamber. The ionization of the atmosphere produces additional electrons and positive ions. The ESEM is able to reproduce the surface of the specimen by collecting the secondary electrons released by the specimen and the electrons produced by the ionization of the atmosphere. The positive ions produced during ionization of the atmosphere neutralize the charge buildup on the surface of the specimen. Therefore, there is no need to apply a conducting coating to a non conducting sample. Additionally, since a high vacuum is not applied to the chamber of the ESEM, specimens can contain water. Due to the unique characteristics of the ESEM it was possible to view specimen S7 in its undisturbed natural condition.

A total of four specimens were prepared for X-ray diffraction tests. The locations of the X-ray diffraction tests were based on the interpretation of SEM pictures. The samples tested were those which were thought to have the highest probability of containing clay minerals. The following table provides basic information about the specimens tested:

Test Number	Engineering Test	Sample Location	Depth (m)
S5X	TX221	S2-8	-29.51
SHX	---	S2-5	-24.52
SKX	---	S2-5	-24.44
S6X	---	S2-5	-24.77

Test S5X was performed on a random powder specimen. The specimen was obtained by crushing oven-dried soil with a mortar and pestle, and then sieving it through the number 200 sieve. The rest of the tests were performed on oriented specimens. These specimens were prepared in the following way. A 4% soil slurry (4 gm soil: 100 cc water) was prepared in a plastic jar which was placed in an ultrasonic cleaner for 2 hrs to ensure the breakdown of soil particles. After the coarse grained material settled to the bottom, 5cc of the slurry was placed in a small bowl. Three drops of glycerin were added and mixed thoroughly with the slurry, and then the slurry was then placed on a glass substrate to air dry.

3.3.2.3 *Results*

This section begins by presenting the pictures obtained with the SEM as well as the compositional analysis of the soil in each picture. Following these will be the ESEM pictures and the X-ray diffraction results. Appendix C contains the compositional analysis results obtained with the SEM of specimens SCS1 through SCS5. The analysis spectrum is shown for each specimen. All the spectra are plotted on the same vertical scale for easy comparison. For some specimens a printout containing the interpretation of the spectrum is also shown. The appendix also contains the raw data of some X-ray diffraction tests and additional X-ray diffraction patterns.

Scanning Electron Microscopy Results

Figure 3.15 shows SEM pictures of specimen SCS1. Specimen SCS1 is a piece of CRS77, taken after it was oven dried to obtain the final water content. Picture SCS1P1 shows the surface of the sample at 50x magnification. Open channels are visible in the sample, and the general appearance is porous. At higher magnifications (Pictures SCS1 P2 and P3), the porous nature of the soil can be appreciated. Pictures SCS1P2 and SCS1P3 show a diatom and a microfossil respectively, found during examination of the surface. The rest of the surface of the specimen looks like the background of Picture P2

and P3. The compositional analysis of the three pictures revealed silica and iron as the most predominant elements. It also revealed small traces of calcium, potassium, and aluminum, in that order of significance.

Figure 3.16 shows SEM pictures taken of specimen SCS2. Specimen SCS2 was obtained from CRS75. This CRS sample had vertical inclusions of white powdery material that slightly effervesced in the presence of HCl. Specimen SCS2 is composed of this powdery material. Picture SCS2P1 shows the surface of the specimen at 100x magnification. The general appearance of the specimen is porous, but no open channels or voids are visible. At higher magnifications (Pictures SCS2 P2 and P3), the material does not appear to be as porous as specimen SCS1. The compositional analysis of picture P1 revealed silica to be the primary element. Looking closely at pictures SCS2 P2 and P3 one can see a small white dot on each picture. The compositional analysis for these pictures was limited to the area of those dots. Picture P2 revealed that the two most common elements are sulfur and iron. This suggests that the material analyzed is pyrite. The compositional analysis of Picture P3 revealed silica to be the main element. It was surprising that calcium was not the main element present, since the material effervesced in the presence of HCl.

Figure 3.17 presents SEM pictures taken from specimen SCS3. Sample SCS3 is a piece of CRS82 taken after it was oven dried to obtain the final water content. Picture P1 shows the sample at 19.6x magnification. Even at this low magnification open voids and channels are noticeable, and they are larger in size than those found in specimen SCS1. Picture P2 at 401x magnification shows that the soil is primarily composed of the remains of micro-organisms and precipitated material. The structure has big open channels and is generally porous. A fragment of a shell can be seen in the lower mid-left section of the picture. Picture P3 taken at 6,690x magnification shows pyrite cubes (deduced from compositional analysis). The geometry of the cubes and their size suggest that they were formed by crystallization inside the soil structure. Pictures P2 and P3 also show evidence

of diagenesis of the soil, (i.e., a transformation of the structure by the dissolution, transportation, and precipitation of particles). The compositional analysis of the soil in pictures P1 and P2 revealed silica to be the predominant element. The analysis also revealed traces of calcium, iron, potassium, and aluminum, in that order of significance. The compositional analysis and the interpretation of pictures P1 and P2, suggest that the specimen is composed primarily of diatoms, ostracods or shells, and pyrite. Unfortunately, the X-ray analyzers cannot identify light elements, such as carbon, due to their low electron energy levels. Even though the presence of carbon cannot be detected, the presence of calcium and shells strongly suggest the presence of calcium carbonate.

Figure 3.18 presents pictures taken of specimen SCS4. Specimen SCS4 is a piece of CRS80, taken after it was oven dried to obtain the final water content. Picture P1, at low magnification (184x), shows a very porous uniform structure, but no localized channels or voids. Pictures P2 and P3, at higher magnifications, show that the particles are stacked in clumps, therefore giving the appearance of a very porous but uniform structure with flow channels. Additionally, the pictures show that the specimen is primarily composed of very thin elongated particles that appear to be some type of skeletal formation. The compositional analysis for all three pictures revealed silica to be the predominant element of the soil. The analysis also revealed traces of calcium, iron, and potassium in that order of significance.

Figure 3.19 presents pictures taken of specimen SCS5. Specimen SCS5 was taken from a part of a triaxial specimen. After examining the failure surface of the triaxial specimen, it was evident that sliding of the failure surface had occurred during shearing. After the sample was air dried, a piece of the failure surface was broken off to become specimen SCS5. Picture P1, at 42x magnification, shows striations on the surface caused by sliding. Picture P2 is a close-up of this surface, which does not seem to be porous at all. Diatoms are visible, and some are crushed, broken, and bent. Pictures P3 and P4 show close-ups of the surface perpendicular to the failure surface. The specimen appears

to be composed of very thin circular diatoms enclosed in a matrix. The general structure of the sample does not appear to be very porous. After closer inspection of the matrix, it appears to be composed of lumpy granular material. The compositional analysis revealed silica to be the predominant element. The analysis also revealed traces of iron, aluminum, calcium and potassium in that order of significance.

Figure 3.20 presents some of the pictures taken of specimen S6. Specimen S6 was prepared from an oven dried undisturbed piece of sample S2-5. This specimen was examined to help understand the high preconsolidation pressure found at this location. Picture P1 shows the surface of the sample at 60x magnification. Specimen S6 is approximately one centimeter below specimen SCS3. The microstructure appears to be somewhat uniform. Picture P2, a close-up of the center of Picture P1, reveals a dense microstructure with some shell like particles. Compositional analysis of Picture P1 and of the shell like structure in the center of Picture P2 revealed silica to be the predominant element in the specimen, followed next by calcium. Picture P3 shows the surface of the specimen at another location. Picture P3 shows a dense microstructure with small voids and channels. Picture P4, a close-up of the center of the Picture P3, shows that the structure is formed by crystallized material, microfossils, sheet like structures, and pyrite cubes. The compositional analysis of the large flake in the upper right center section of the picture revealed silica and calcium to be the most predominant elements. The compositional analysis of the large particle in the upper left center section of the picture revealed silica and aluminum to be the main elements. Picture P5 shows another close-up of the surface of Picture P3. Picture P5 shows more crystalline and sheet like particles than Picture P4, as well as slightly more voids and channels. Interesting features of Picture P5 include the crystal in the upper right corner, the sheet like particle in the upper left corner and the small crystalline growths below the sheet like particle. Compositional analysis of the large crystal and the sheet like structure revealed silica to be the predominant element. The analysis also revealed traces of aluminum and calcium, in that

order of significance. Picture P6 shows a close-up of the small crystalline growth below the sheet like structure. Compositional analysis revealed calcium to be the predominant element. The pictures indicate that the soil of specimen S6 underwent or is undergoing a diagenesis process that is characterized by the formation of minerals. Therefore, it is likely that some type of clay mineral is part of the microstructure of the specimen. For this reason, a X-ray diffraction test was performed at this location. Inspection of the sample with the SEM did not produce any information to explain the high preconsolidation pressure measured at this location.

In an effort to understand what initiated the diagenesis process of soil in tube sample S2-5 (SEM samples SCS3 and S6) the x-rays of the tube were examined. The x-rays revealed that approximately 25cm above sample SCS3 and S6 there was a small layer of higher density material. Below this layer significant mixing of materials of different densities was evident. Figure 2.18, which shows a radiograph of tube S3-4, presents the same layer. Figure 2.19 shows an x-ray of tube sample S2-5. This figure illustrates an area between the layer of high density material and samples SCS3 and S6, where mixing of materials of different densities is evident. It was decided that it would beneficial to study the material forming the high density layer as well as the material above and below this layer using the SEM and X-ray diffraction equipment.

Figure 3.21 presents pictures of the surface of specimen SJ-K. Specimen SJ-K was obtained from the high density material in tube S2-5. The material was found to be fine, sand-sized pyroclastic material. Picture P1 shows the general appearance of the material, which is very porous. Picture P2 shows a close-up of the large standing particle in the center of the Picture P1. Picture P3 shows a close-up of the large horizontal particle in the right center side of the picture. Pictures P2 and P3 reveal the porous nature of the material. Compositional analyses of Pictures P1, P2 and P3 revealed calcium to be the predominant element of the specimen. The analysis also revealed traces of silica,

magnesium, and aluminum. Pictures P4 and P5 show a diatom and a fossil, respectively, which were found on the surface of one of the particles.

Figure 3.22 presents the pictures obtained from the surface of specimen SH. Specimen SH was prepared from soil obtained one inch below specimen SJ-K. Picture P1 shows the surface of the specimen. The surface appears to be very dense compared to the surface of other samples. Pictures P2, P3 and P4 are progressive close-ups of the soil in the center of Picture P1. The pictures reveal that the surface contains large fragments of ostracods and diatoms. It appears that these fragments are in a matrix composed of a material which is the product of the decomposition of these diatoms and ostracods. The compositional analysis of the surface revealed silica to be the predominant element. The analysis also revealed small traces of calcium, aluminum and magnesium in that order of significance. Picture P1 also shows two apparent seams of a different material. One seam infiltrates through the center of the sample, while the other seam travels through the upper right hand corner of the specimen. Picture P5 shows a close-up of one of the seams. These "lines" are formed by uniformly sized rectangular particles, which are arranged in a consistent manner. Picture P6 shows a close-up of some of the particles which appear to be of a powdery nature. Picture P7 shows a close-up of the connection of the two particles in the lower center of Picture P6. Compositional analysis of the particles revealed silica to be the most predominant element. Picture P8 shows two spheres composed of pyrite cubes found on the surface of one of the particles. It was not possible to determine the nature of the rectangular particles.

Figure 3.23 presents the pictures taken from the surface of specimen SK. Specimen SK was prepared from soil obtained one inch above specimen SJ-K. Pictures P1 through P4 present the surface of the soil at different locations and at different magnifications. Pictures P1 and P2 revealed that the specimen contains a large number of ostracods enclosed in a matrix. Pictures P3 and P4 revealed that the matrix contains a significant number of diatoms. Compositional analysis of all pictures revealed silica to be

the predominant element. The analysis also revealed traces of calcium, aluminum and magnesium. It was surprising that calcium was not a predominant element since a great number of ostracods are present.

Environmental Scanning Electron Microscopy Results

Figure 3.24 presents the ESEM pictures obtained from specimen S7. Ideally, the pictures obtained should show the undisturbed microstructure of the soil (i.e., natural undisturbed wet state). In reality, this might not be the case. If the surface of the specimen contains too much water, the surface detail cannot be appreciated. Therefore, some drying of the specimen is necessary to observe details on the specimen surface. By controlling the temperature and pressure inside the ESEM chamber, it was possible to slowly evaporate some of the water from the surface of the specimen.

Picture P1 presents the surface of the specimen. In comparison to the SEM pictures, the microstructure seems somewhat "tighter". Even though a significant number of microfossils are present, they seem very well enclosed in the soil matrix. Picture P2 presents a close-up of the surface. Initially, some of the diatoms appeared to be plump. As time elapsed and water dried off the surface of the specimen, the same diatoms appeared to be flatter. The change in appearance is probably due to the loss of water. Pictures P3 and P4 present close-ups of the soil matrix. The matrix appears very different compared to how it appears when viewed with the SEM. The difference in appearance is probably caused by the presence of water in the structure. It appears that the matrix is composed of sheet like particles with a high surface area. Picture P5 presents a close-up of some of the sheet like particles, as well as some pyrite cubes. Picture P6 presents a close-up of the corner of one of these particles. There is a possibility that the sheet like particles in Pictures P5 and P6 could be clay minerals. Unfortunately, no analysis was performed to determine the composition of these particles, even though the ESEM does have the capability to do so.

X-ray Diffraction Test Results

The following three paragraphs are summarized from Mitchell (1976).

X-ray diffraction is the most widely used method for identification of fine grained soil minerals and the study of their crystal structure. It is because wave lengths of about 1 A° are of the same order as the spacing of atomic planes in crystalline materials that makes X-rays useful for the analysis of crystal structures. All prominent atomic planes will produce a reflection when properly positioned with respect to the X-ray beam. Since each clay mineral has a different crystal structure it will produce a characteristic set of reflections. The intensities of the different reflections vary according to the density of atomic packing, the uniformity of the packing, the number of layers, and other factors. Therefore, it is possible to identify different clay minerals with X-ray diffraction because each mineral has a particular diffraction pattern. Additionally, the common nonclay minerals occurring in soils are also detectable by X-ray diffraction. The basal planes generally give the most intense reflections of any planes in the crystals because of the close packing of atoms in these planes. The distance between successive units is the basal spacing in the "c" direction, or d_{001}. This dimension is most often used to identify clay minerals. For example illite, kaolintie, and montmorillonite have basal spacings of 7, 10, and 14 A°, respectively.

The clay minerals that are commonly found in soils are layered silicates. The structures of the common layer silicates can be considered in terms of two simple structural sheets. The two basic sheets in clay mineral structures are the silica tetrahedron and the silica octahedral sheets. The different clay mineral groups are characterized by the stacking arrangements of these "sheets" (i.e., units), and the manner in which successive units are held together. For example, a montmorillonite particle consists of units composed of one octahedral sheet and two silica tetrahedron, and a illite particle consists of at least ten units composed of one octahedral sheet and two silica tetrahedron held together by potassium molecules.

Two methods are commonly used to perform X-ray diffraction tests, the powder method and the oriented aggregate method. The oriented aggregate is preferred because basal reflections are intensified and reflections from other planes are minimized.

Figure 3.25 through 3.28 present the X-ray diffraction patterns of Samples S5X, SHX, SKX, and S6X, respectively. As shown in the figures, Samples S5X, S6X, and SHX have very similar shaped X-ray diffraction patterns. The first characteristic of the patterns is the considerable background signal. This implies that the crystal structure is not well developed, i.e., much of the material is amorphus in nature. Generally, the background signal hides the diffraction peaks associated with atomic planes and makes it difficult to select the correct 2θ value for a particular peak. The peaks become small and broad. Most important is the lack of low angle basal plane reflections in all samples (random powder and oriented aggregate). The lack of the basal reflection means that these units are not arranged in a consistent way. Based on this fact, it appears that the soil does not contain any of the typical clay particles. However, secondary reflections consistent with clay minerals are present in all diffraction patterns. Some of these reflections are found at approximate 2θ values of 20, 35, 54, 57, and 61 degrees (i.e., spacings of 4.47, 2.56, 1.70, 1.61, and 1.52A°). Most clay minerals have secondary reflections at approximately the same 2θ values. From this information it appears that the soil contains substantial quantities of particles having a clay type crystal structure. However, it is not possible to identify clays minerals just based on secondary reflections, basal plane reflections are needed.

The X-ray diffraction patterns also reveal the presence of other minerals like feldespar, and carbonates. For example fedlespar reflections are found in all diffraction patterns at 2θ values of 22 and 28°. All diffraction patterns with the exception of SKX present carbonate reflections at 2θ values of 30°.

3.3.3 Conclusions and Comments

The SEM and ESEM pictures show that the specimens of México City Clay studied are, in large part, composed of amorphous siliceous material. This amorphous material is composed of microfossils; mainly diatoms, and siliceous skeletons. The production of diatoms is proportional to the amount of dissolved silica content in the water. Apparently, the large quantities of silica produced by the weathering of volcanic glass initiated a great bloom of diatoms in the lakes that occupied the valley of México.

The following lines are taken from Mesri et. al. (1975). "The water filled diatom particles make up the open framework of México City and are probably responsible for its unusual physical properties. Extreme lightness and elasticity of diatom particles can account for the lightness and elasticity of the undisturbed México City clay. Water filled diatoms are also mostly responsible for the unusually high plastic limit. The extremely high plasticity of México City clay, with its unusually high angle of internal friction, can only be explained by its diatom content."

All of the SEM specimens, with the exception of specimen SCS1, generally contained one type of microfossil. It appears that the type of microfossil present in a sample changes with depth. This might suggest that as the lake conditions changed so did the type of living organisms. Therefore, each layer of microfossils might represent a specific period of geologic time. Peralta (1989) writes that the abundance and type of microfossils present in the soil dictates its behavior. For example, he mentions that soil that appears to be sandy or silty probably has a high ostracod content, and for this reason, the microstructure of this particular type of soil is discontinuous and brittle.

Some SEM pictures suggest that at some locations the soil underwent or is undergoing a diagenesis process. This process might have been originated by groundwater flow. As water flows through the soil, water will dissolve, transport and precipitate particles, therefore changing the microstructure of the soil.

The compositional analysis performed inside the SEM revealed that silica is the predominant element of all the samples examined. The anaylsis also revealed that iron is the second most predominant element. The analysis generally revelaed a ratio of 2:1 between silica and iron. As mentioned in Section 3.3.1, México City Clay is generally classified as montmorillonite or illite. The most common octahedral sheets of clay minerals are gibbsite and brucite. Gibbsite is an aluminum hydroxide and brucite is a magnesium hydroxide. The octahedral sheets of montmorillonite and illite are generally gibbsite. Therefore, a compositional analysis of montmorillonite or illite should show a 2:1 to 3:1 ratio of silica to aluminum. For the samples studied of México City Clay for this investigation, this was not the case. Generally, only small traces of aluminum were found compared to the amount of silica present. The fact that iron was the second most predominant element together with the low amount of aluminum measured might suggest that México City Clay is neither montmorillonite or illite. It might also suggest that the large number of diatoms, which are composed of silica, increases the ratio of silica to aluminum; however this is not likely.

X-ray diffraction results revealed the presence of a crystal structure which is typical of clay minerals (i.e., units of silica tetrahedrons and octahedral sheets). The results also revealed that the arrangement of theses units is not very consistent (i.e., no basal reflection).

The compositional analysis of the specimens and the X-ray diffracttion results together suggest unusual and poorly developed particles.

During this investigation different colored soils were encountered. Some of these colors were; olive green, reddish brown, gray, brownish green, light gray, etc. After the different colored soils were dried, either by air or in the oven, they all turned to a creamy tan to light gray color. The literature does not offer any explanation for this phenomenon, and neither does the author. Another interesting observation is that dried samples of México City Clay do not completely rehydrate upon rewetting. They appear to vitrify.

Finally, this investigation describes México City Clay as a soil composed of (1) basic crystalline units that do not have a consistent arrangement, and (2) a considerable amount of microfossils.

Table 3.1 Distribution and Summary of Results of Index Tests (p.1/3)

BORING # AND SAMPLE #	DEPTH m.	TORVANE Su ksc	TORVANE # of tests	TORVANE S.D.	Wn (%) from eng tests	ATTERBERG LIMITS Wn (%)	ATTERBERG LIMITS Wp (%)	ATTERBERG LIMITS WI (%)	ATTERBERG LIMITS PI (%)	ATTERBERG LIMITS LI	Gs	Salt Conc. (gm/l)	Salt Conc. (gm/kg)	pH
S2-1	-12.52	0.58	3	0.02										
	-12.57				321.16						2.37			
	-12.62	0.48	2	0.03										
	-12.65	0.48	3	0.04			173.39	439.85	266.46			5.73	18.36	9.07
	-12.70	0.48	3	0.04										
	-12.72				277.11									
	-12.75	0.48	3	0.02										
S2-2	-13.37				246.70						2.51			
	-13.42	0.48	3	0.01										
	-13.46				294.49									
	-13.47	0.47	3	0.01			87.17	292.08	204.91			1.74	4.89	8.42
	-13.52	0.41	3	0.06	298.19									
	-13.55	0.43	3	0.02	272.88									
	-13.57				293.27									
S2-3	-14.27	0.57	3	0.02										
	-14.32					213.75	118.96	296.00	177.04	0.54	2.39	5.36	11.47	7.87
	-14.35	0.49	2	0.01										
	-14.37				211.17									
S2-4	-23.95	0.59	2	0.01										
	-24.00				184.90						2.41			
	-24.07	0.58	3	0.02	245.24									
	-24.11				196.98	187.53	76.20	245.96	169.76	0.66				
	-24.12	0.57	3	0.05								2.68	5.02	7.20
S2-5	-24.70	0.48	3	0.06	114.74									
	-24.75	0.55	1	0.00	152.50									
	-24.77					165.65	85.18	181.88	96.70	0.83				
	-24.85				278.09						2.58			
	-24.90	0.48	3	0.04		301.03	97.75	318.18	220.43	0.92		1.77	5.33	7.71
S2-6	-25.60	0.40	2	0.10										
	-25.62	0.41	3	0.06							2.54			
	-25.67	0.44	3	0.03	169.63	177.68	80.51	191.33	110.82	0.88		1.60	2.84	7.61
	-25.70	0.40	3	0.00										
S2-7	-28.60	0.60	2	0.03							2.51			
	-28.65	0.47	3	0.02										
	-28.67				281.52									
	-28.72	0.48	3	0.01	265.60	273.86	90.67	299.98	209.31	0.88		2.20	6.01	7.83
	-28.75	0.40	2	0.05	283.53									

Table 3.1 Distribution and Summary of Results of Index Tests (p.2/3)

BORING # AND SAMPLE #	DEPTH m.	TORVANE Su ksc	TORVANE # of tests	TORVANE S.D.	Wn (%) from eng tests	ATTERBERG LIMITS Wn (%)	Wp (%)	WI (%)	PI (%)	LI	Gs	Salt Conc. (gm/l)	Salt Conc. (gm/kg)	pH
S2-8	-29.35	0.75	3	0.00										
	-29.42				266.51									
	-29.45	0.68	3	0.06										
	-29.51				232.48						2.41			
	-29.55	0.52	3	0.07										
	-29.57					244.30	85.89	303.80	217.91	0.73		2.11	5.14	7.31
S2-9	-35.30	0.91	3	0.03	259.54									
	-35.37				234.95						2.36			
	-35.40	0.63	2	0.00										
	-35.45	0.65	1	0.00	205.21									
	-35.47					208.84	100.91	296.65	195.74	0.55		1.80	3.76	7.34
S3-1	-12.15	0.45	2	0.10							2.46			
	-12.17	0.47	3	0.02	184.06									
	-12.22	0.52	3	0.02	262.53									
	-12.25	0.58	3	0.02										
	-12.27				262.76									
	-12.30	0.68	1		228.84									
	-12.32	0.52	3	0.01	314.82									
	-12.35	0.28	3	0.12										
	-12.37				309.02									
	-12.40	0.41	2	0.01		288.89	96.29	355.63	259.34	0.74				
S3-2	-13.40	0.45	3	0.02										
	-13.45				296.20						2.56			
	-13.50	0.47	3	0.06										
	-13.52	0.38	3	0.04								3.89	9.88	8.63
	-13.56				300.23		68.65	236.66	168.01					
S3-3	-13.79	0.52	3	0.02										
	-14.15	0.56	2	0.01										
	-14.20	0.59	3	0.07										
	-14.22	0.57	3	0.05							2.38			
	-14.27	0.48	3	0.05	294.13									
	-14.30	0.48	3	0.01	288.10									
	-14.32	0.45	2	0.00		278.08	177.58	331.35	153.77	0.65				
	-14.35	0.37	3	0.06										

Table 3.1 Distribution and Summary of Results of Index Tests (p.3/3)

BORING # AND SAMPLE #	DEPTH m.	TORVANE Su ksc	TORVANE # of tests	TORVANE S.D.	Wn (%) from eng tests	ATTERBERG LIMITS Wn (%)	ATTERBERG LIMITS Wp (%)	ATTERBERG LIMITS WI (%)	ATTERBERG LIMITS PI (%)	ATTERBERG LIMITS LI	Gs	Salt Conc. (gm/l)	Salt Conc. (gm/kg)	pH
S3-4	-24.30	0.54	3	0.03										
	-24.32										2.52			
	-24.35	0.46	3	0.08	273.50									
	-24.37	0.47	3	0.07		287.44	83.12	308.26	225.14	0.91		1.56	4.47	8.48
	-24.40	0.35	3	0.03										
S3-5	-24.90	0.53	2	0.03										
	-24.96				277.26						2.55			
	-25.00											1.15	3.04	7.90
	-25.02	0.48	3	0.04			126.66	282.31	155.65					
	-25.04											1.79	4.71	7.72
S3-6	-25.42	0.60	3	0.04										
	-25.50				211.73									
	-25.52	0.57	3	0.02										
	-25.55	0.53	3	0.02							2.35			
	-25.57				287.77									
	-25.60	0.59	2	0.01	274.04									
	-25.62	0.60	3	0.00	236.11									
	-25.65					233.10	116.38	271.87	155.49	0.75		2.09	4.87	7.72

Table 3.2 Atterberg Limits, Natural Water Contents, Plasticity Indices, and Liquidity Indices from Boring PC28 (from Marsal & Mazari 1959)

Depth (%)	Wp (%)	Wn (%)	Wl (%)	Pl (%)	LI
5.0	45.0	75.0	80.0	35.0	0.86
9.0	35.0	65.0	75.0	40.0	0.75
10.0	70.0	265.0	270.0	200.0	0.98
13.0	80.0	290.0	315.0	235.0	0.89
15.0	35.0	110.0	90.0	55.0	1.36
27.0	55.0	210.0	145.0	90.0	1.72
22.7	90.0	340.0	405.0	315.0	0.79
26.0	70.0	210.0	250.0	180.0	0.78
26.1	65.0	140.0	200.0	135.0	0.56
16.0	95.0	405.0	350.0	255.0	1.22

Table 3.3 Summary of Mineralogy Results Obtained by Peralta 1989

TOTAL SAMPLE	SOIL FRACTION $2 < \varnothing < 38$ μm	SOIL FRACTION $.2 < \varnothing < 2$ μm	SOIL FRACTION $.08 < \varnothing < .2$ μm
Clayey material poorly crystalized. Ilite. Calcite. Dolomite. Plagioclase. Quartz. Cristobalite. Hornblend.	Montmorilonite. Mica. Ilite. Kaolinite and/or Clorite and Clayey Kaolinitic material poorly crystalized. Calcite. Dolomite. Plagioclase. Quartz. Cristobalite. Hornblend.	Poorly crystalized montmorillonite. Calcite. Plagioclase. Quartz ???. Cristobalite. Kaolinite and/or Clorite poorly crystalized	Montmorillonite. Probably some Kaolinte and/or clorite poorly crystalized.

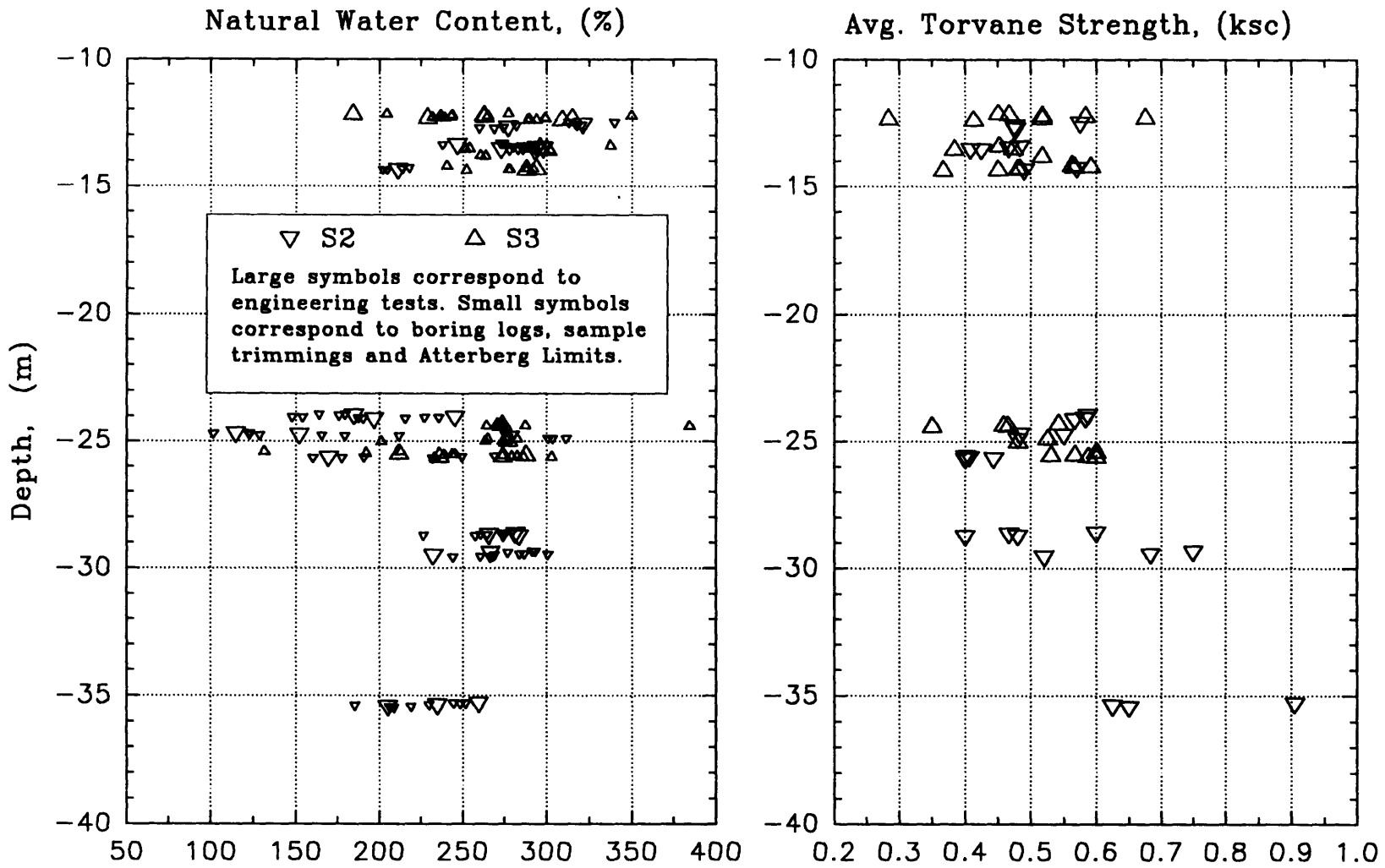

Figure 3.1 Depth vs. Natural Water Content and Average Torvane Strength

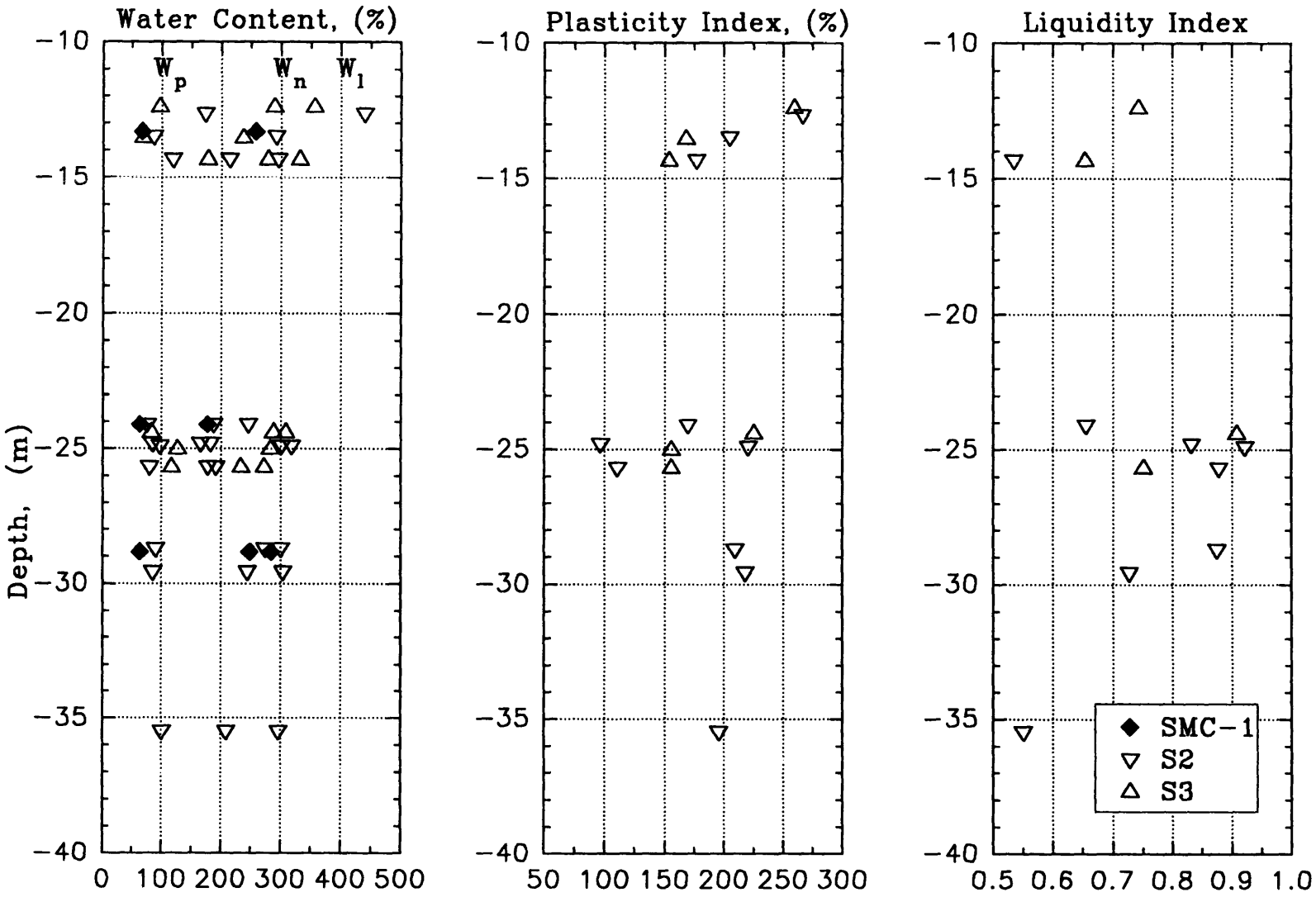

Figure 3.2 Depth vs. Atterberg limits, Plasticity Index and Liquidity Index

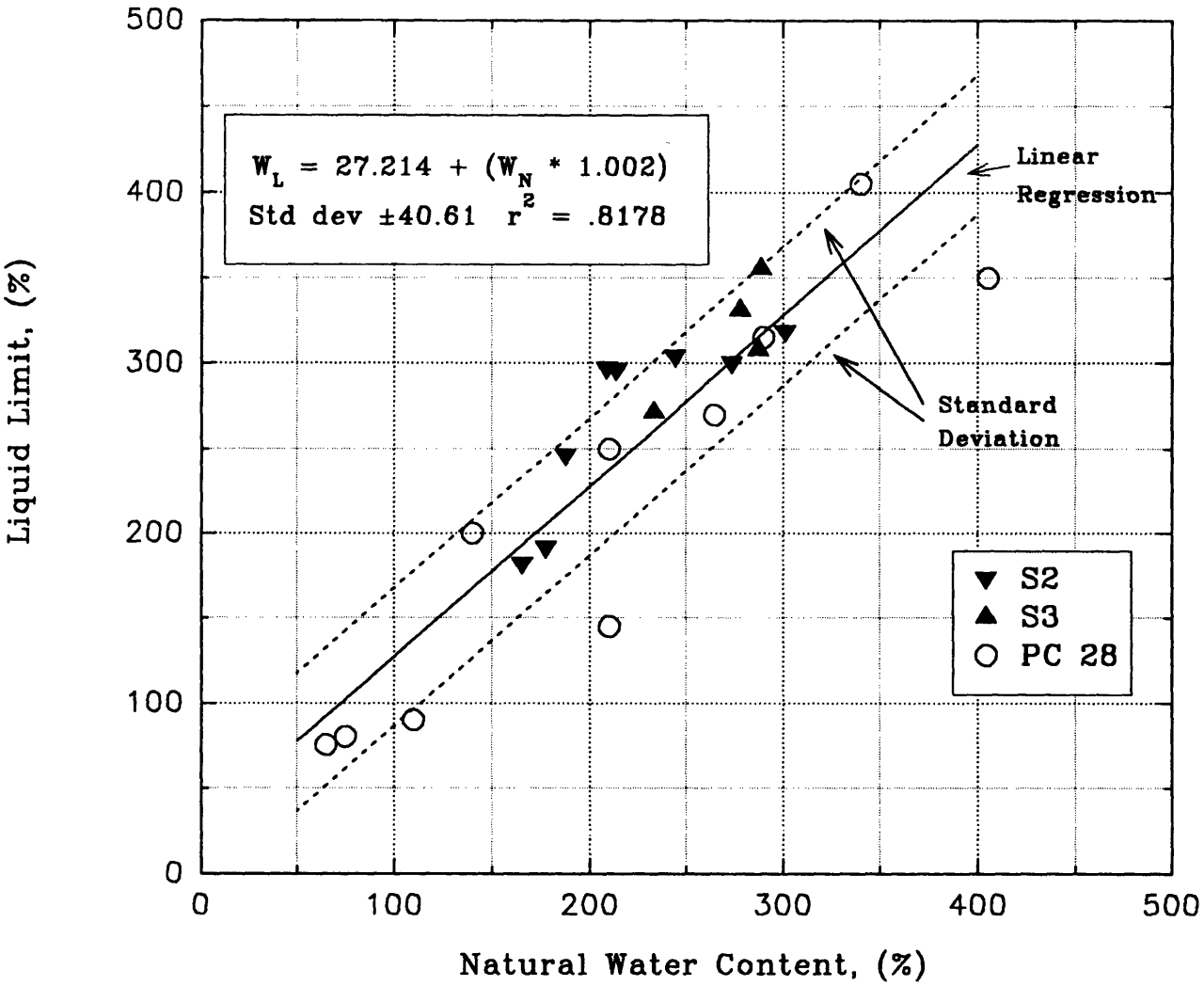

Figure 3.3 Liquid Limit vs. Natural Water Content

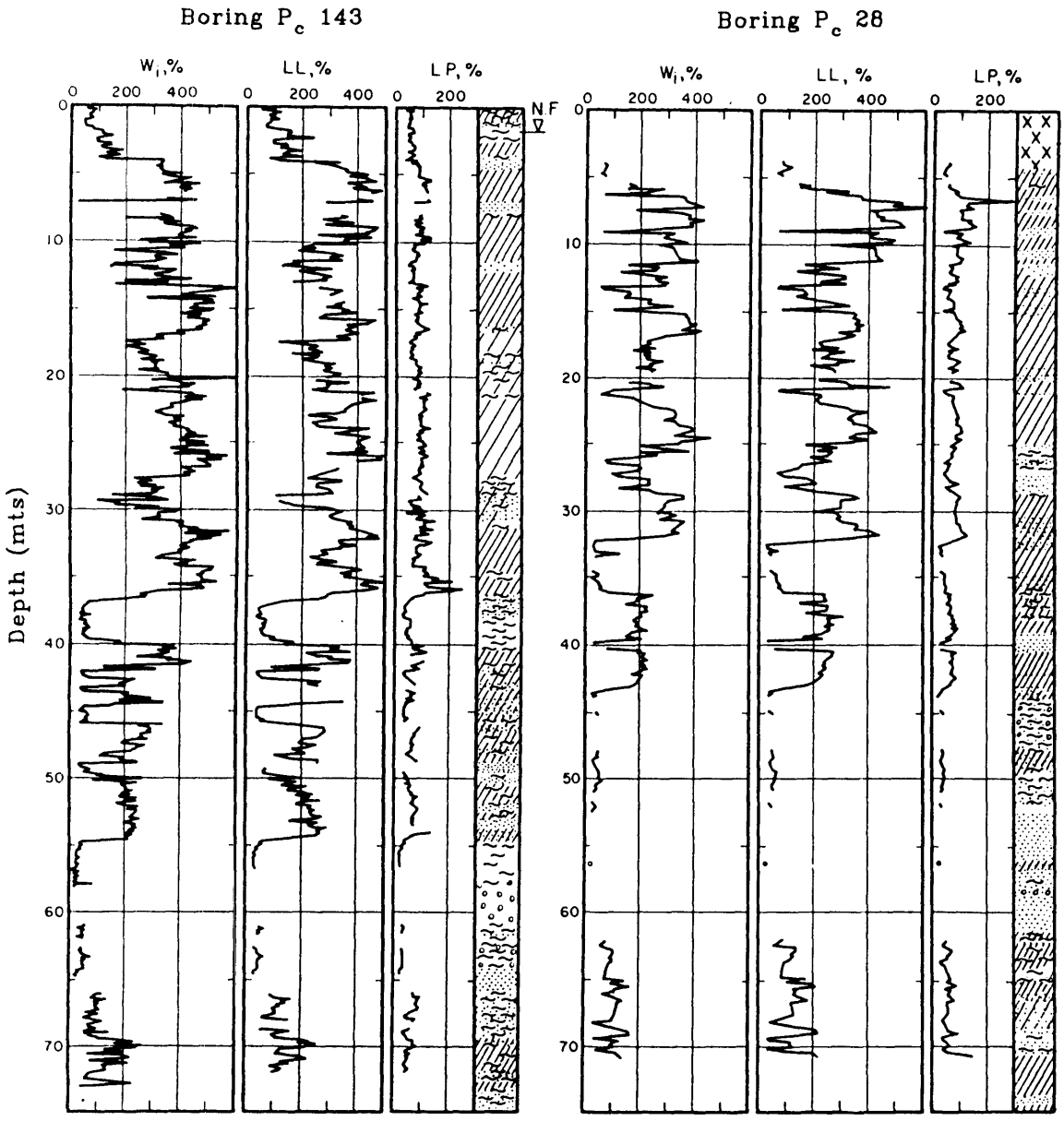

Figure 3.4 Depth vs. Atterberg limits for Borings Pc143 & Pc28 (from Hiriart & Marsal 1969)

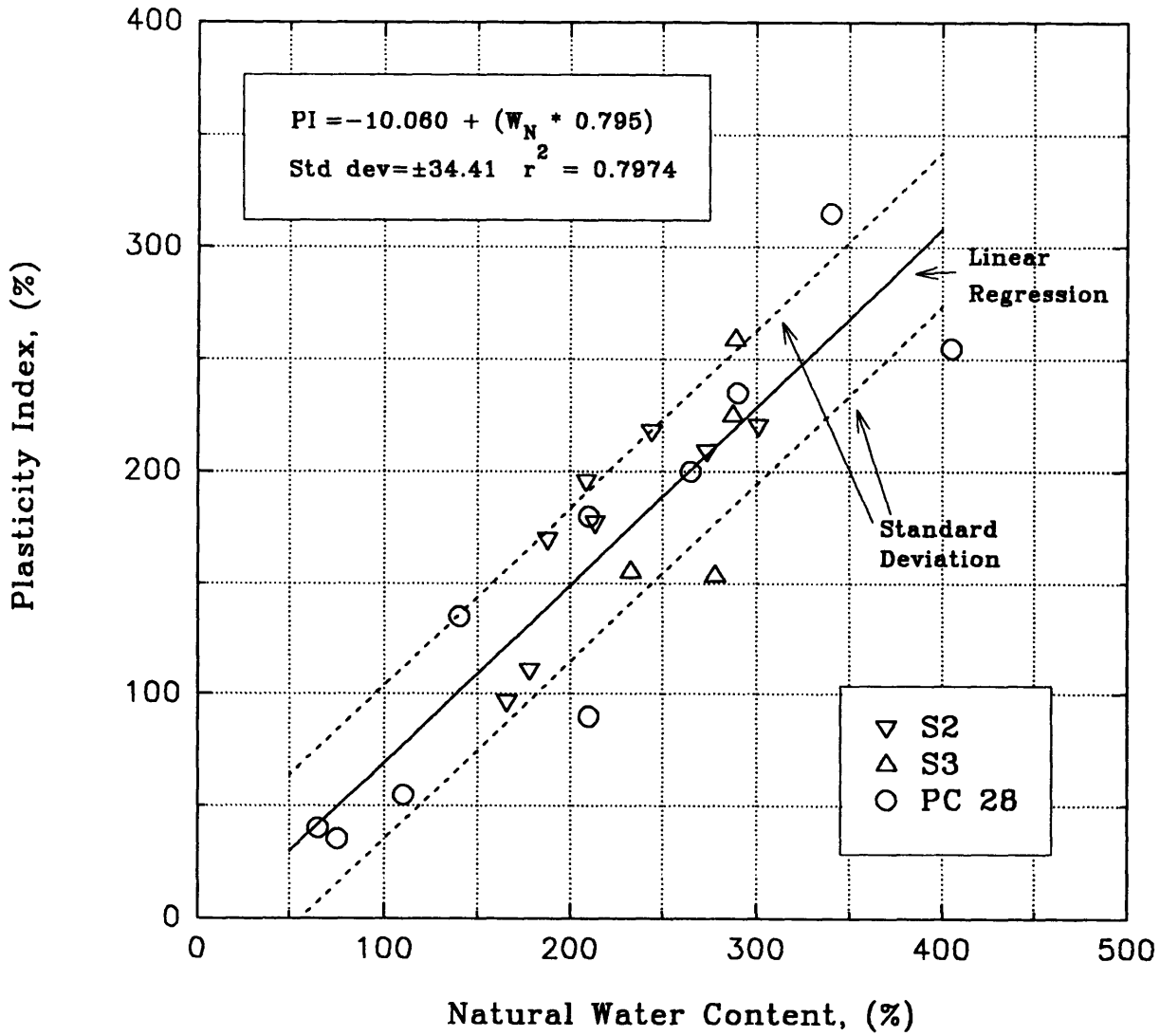

Figure 3.5 Plasticity Index vs. Natural Water Content

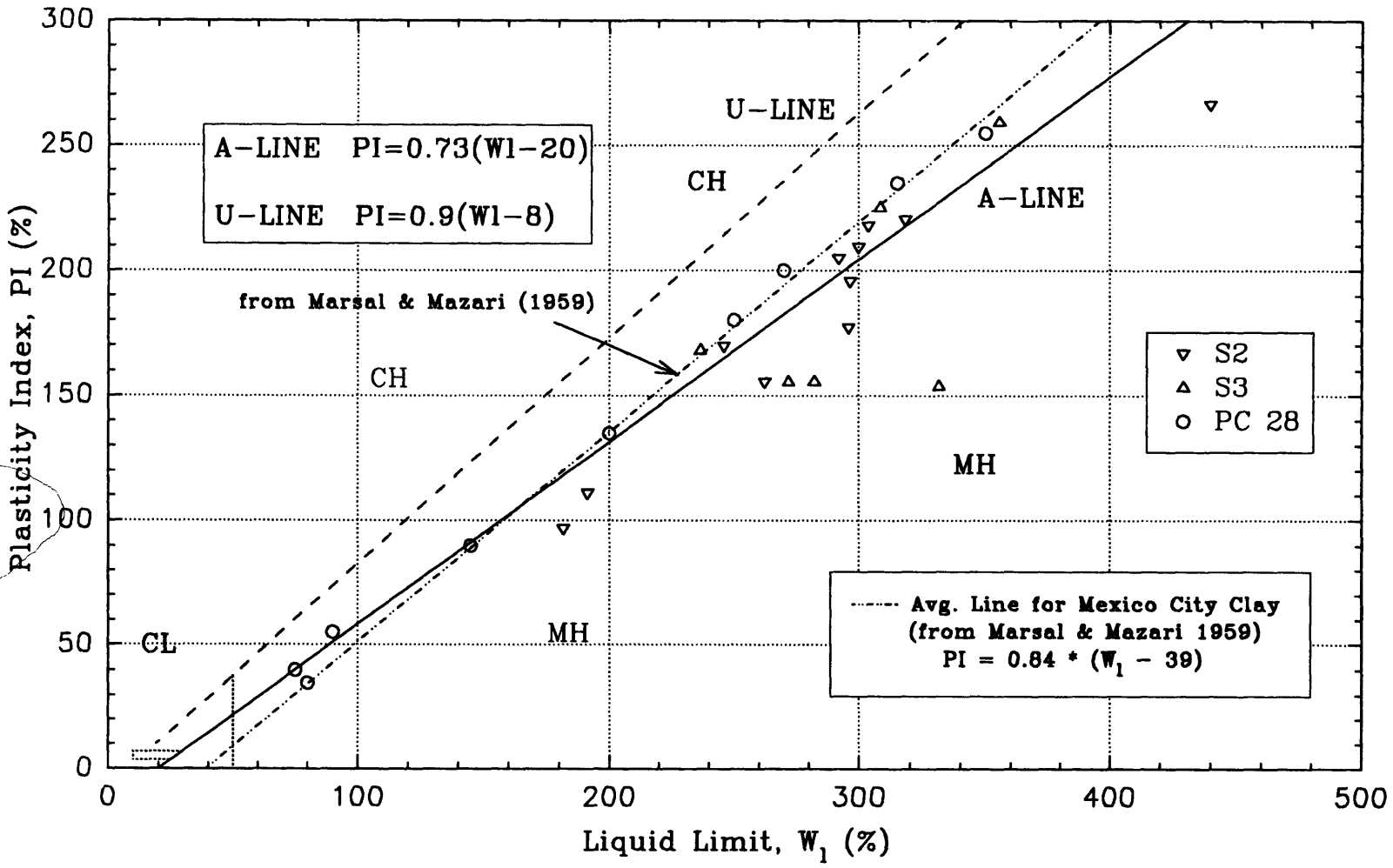

Figure 3.6 Plasticity Chart (A. Casagrande) for Atterberg limits

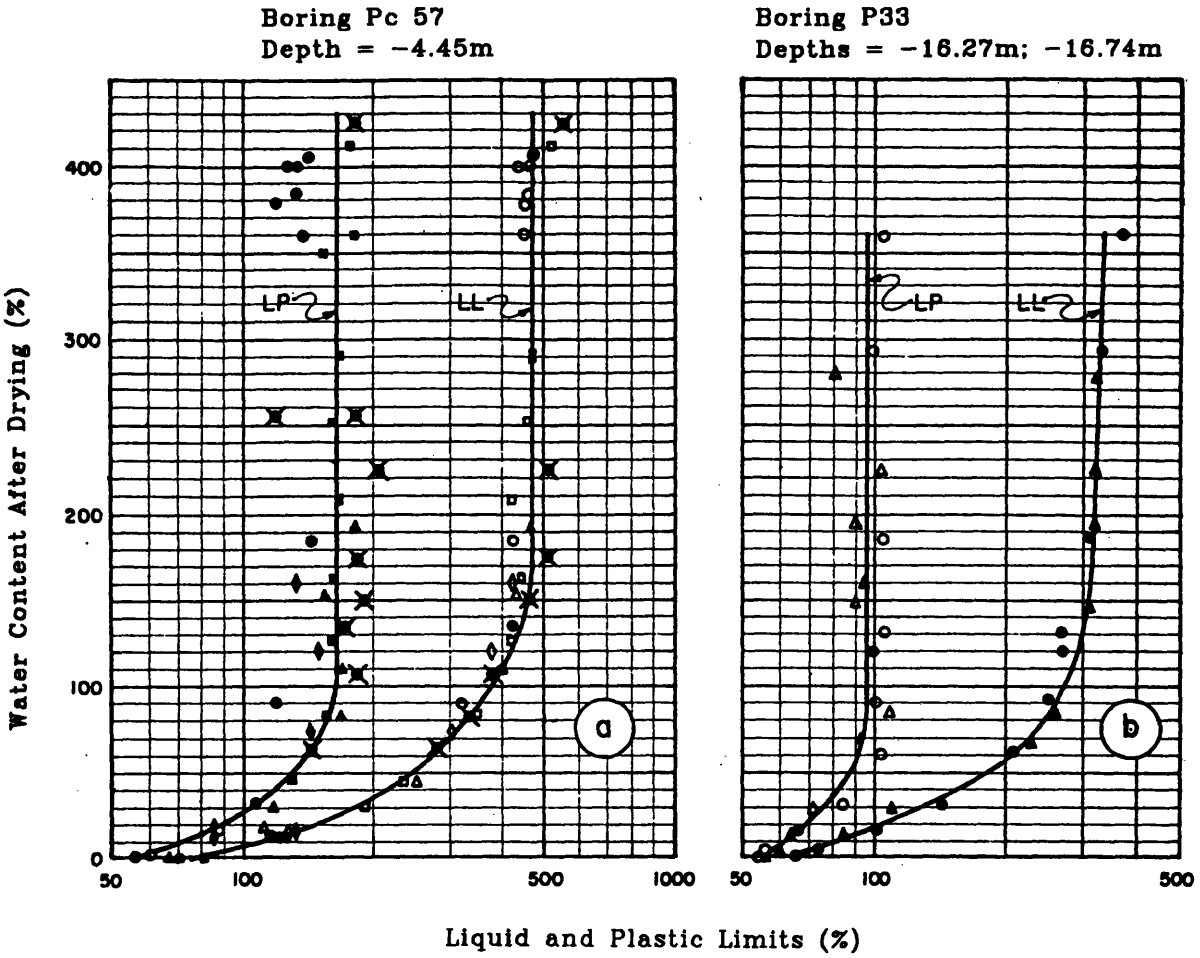

Figure 3.7 Drying Effects on Atterberg limits
(from Marsal & Mazari 1959)

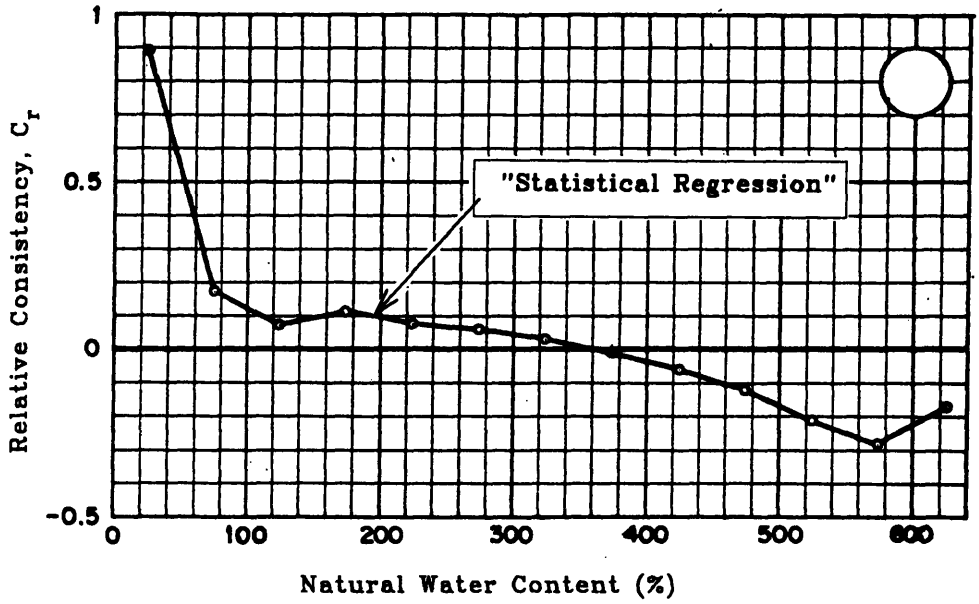

Figure 3.8 Relative Consistency vs. Natural Water Content (from Marsal & Mazari 1959)

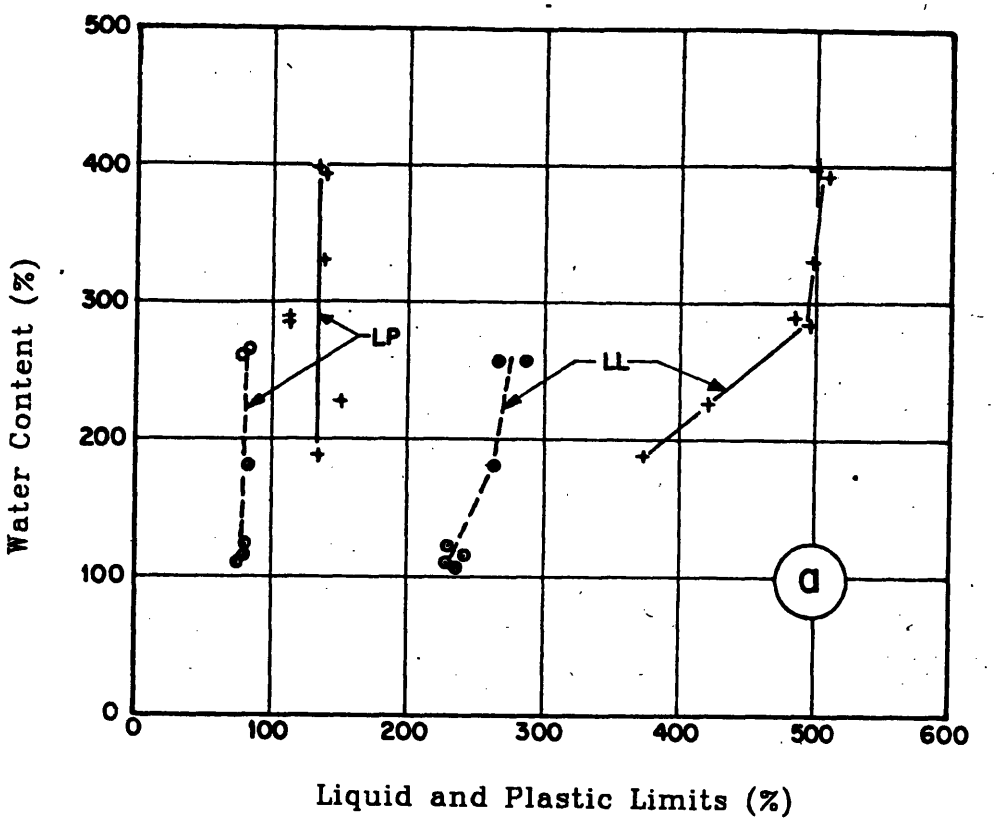

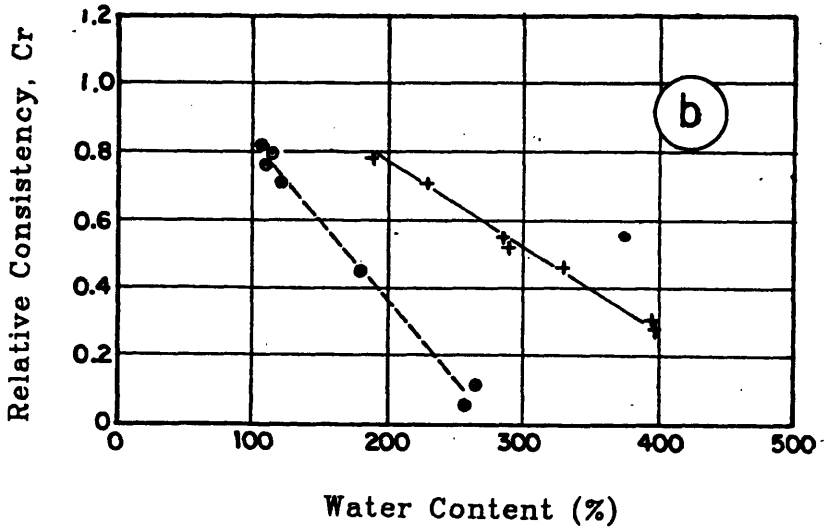

Figure 3.9 Effects of Consolidation on Atterberg limits & Relative Consistency (from Marsal & Mazari 1959)
(a) Water Content vs. Atterberg limits
(b) Relative Consistency vs. Water Content

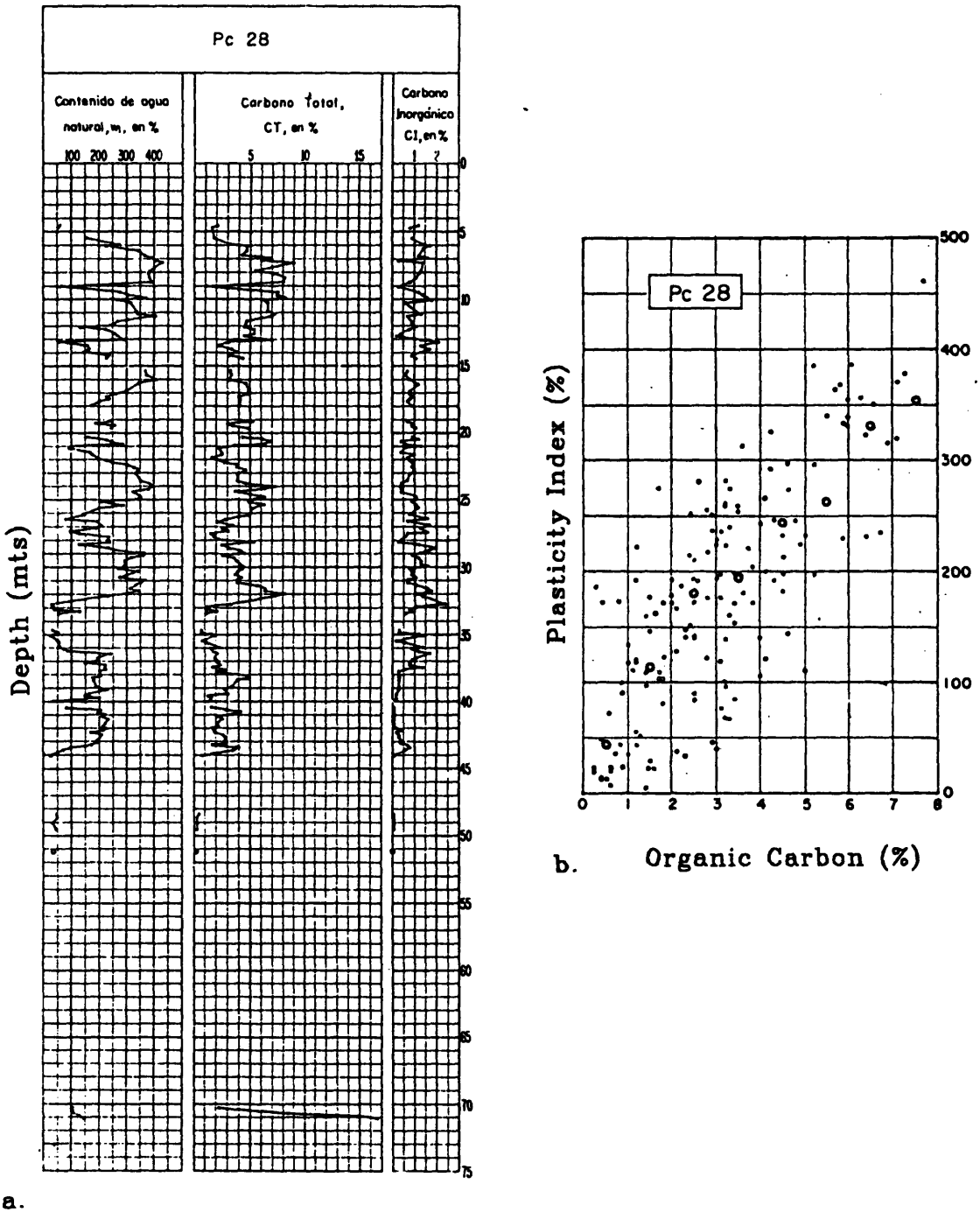

Figure 3.10 Influence of Carbon on Water Content and Plasticity Index (from Marsal & Mazari 1959)
(a) Depth vs. Wn, Total Carbon, and Inorganic Carbon
(b) Plasticity Index vs. Organic Carbon

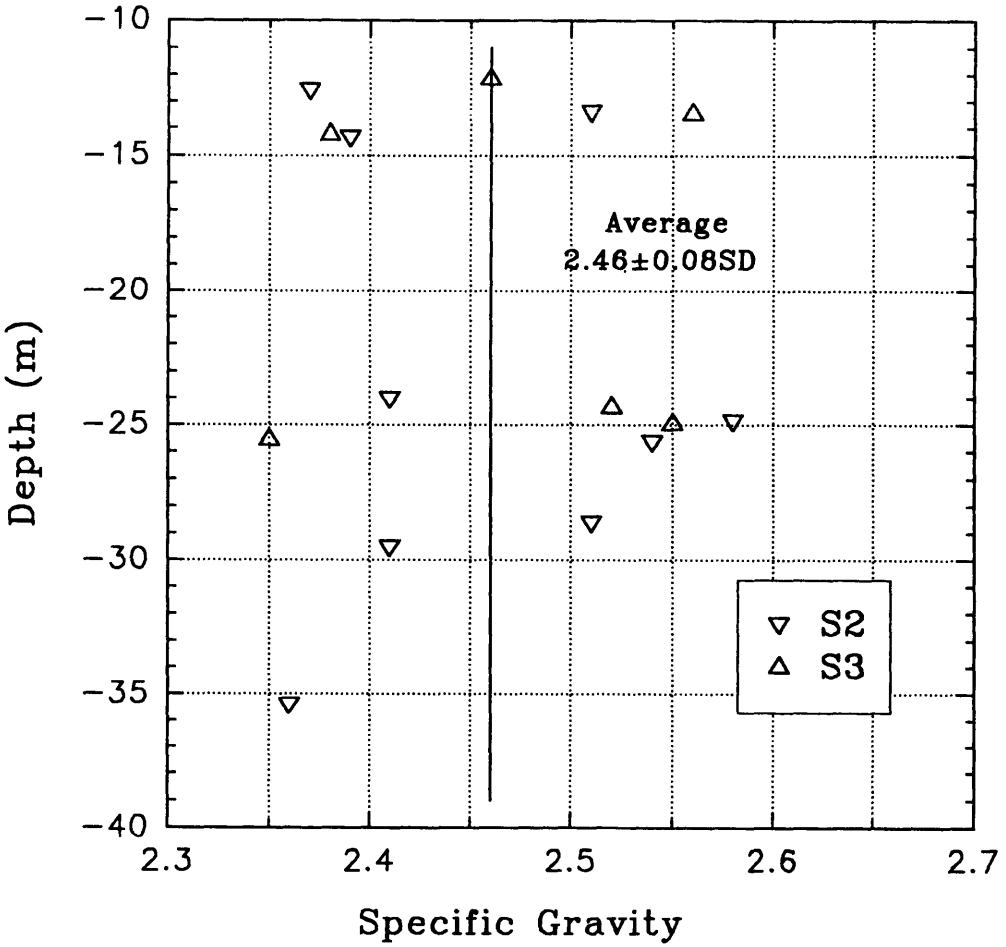

Figure 3.11 Depth vs Specific Gravity

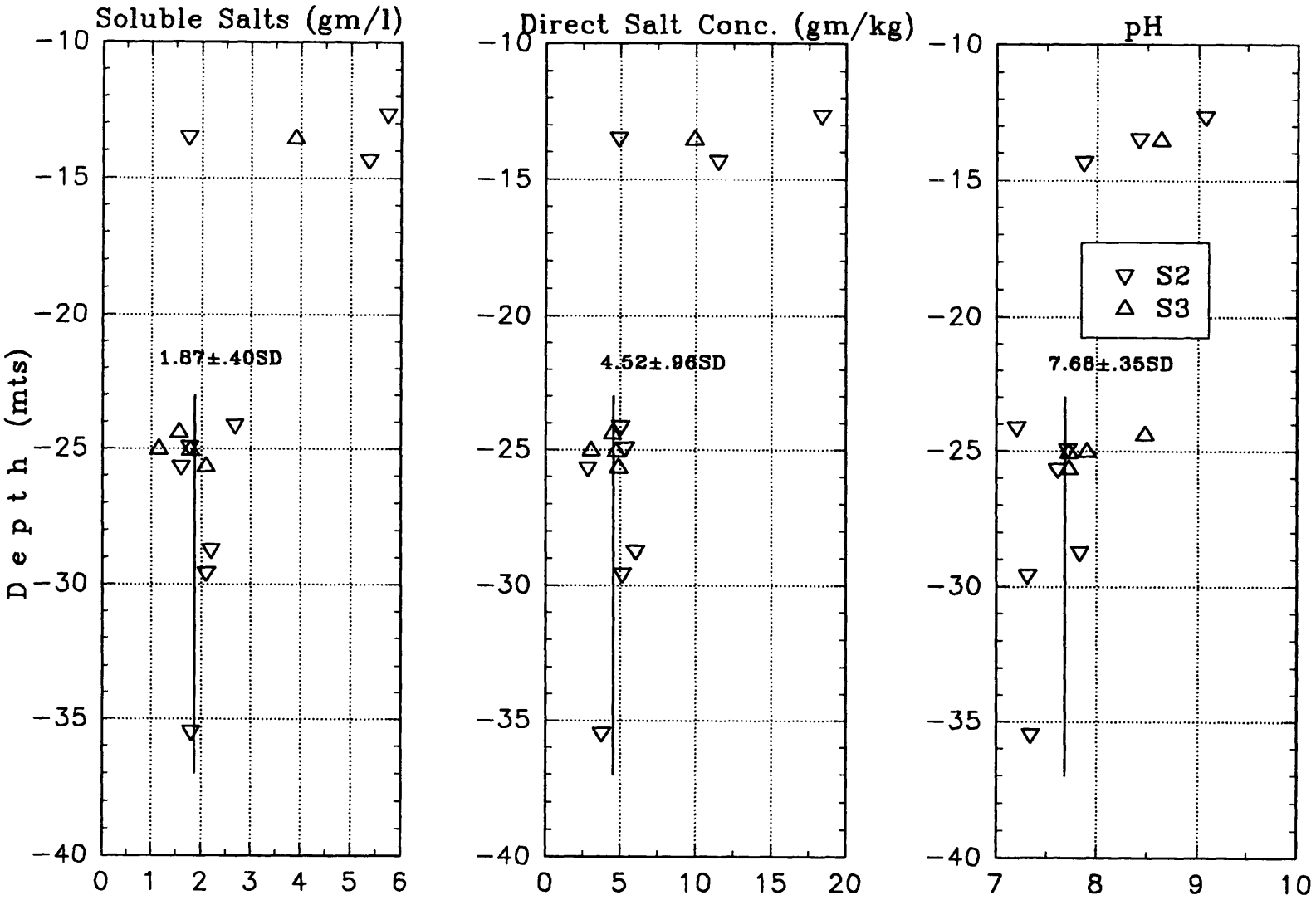

Figure 3.12 Depth vs. Salt Concentration and pH.

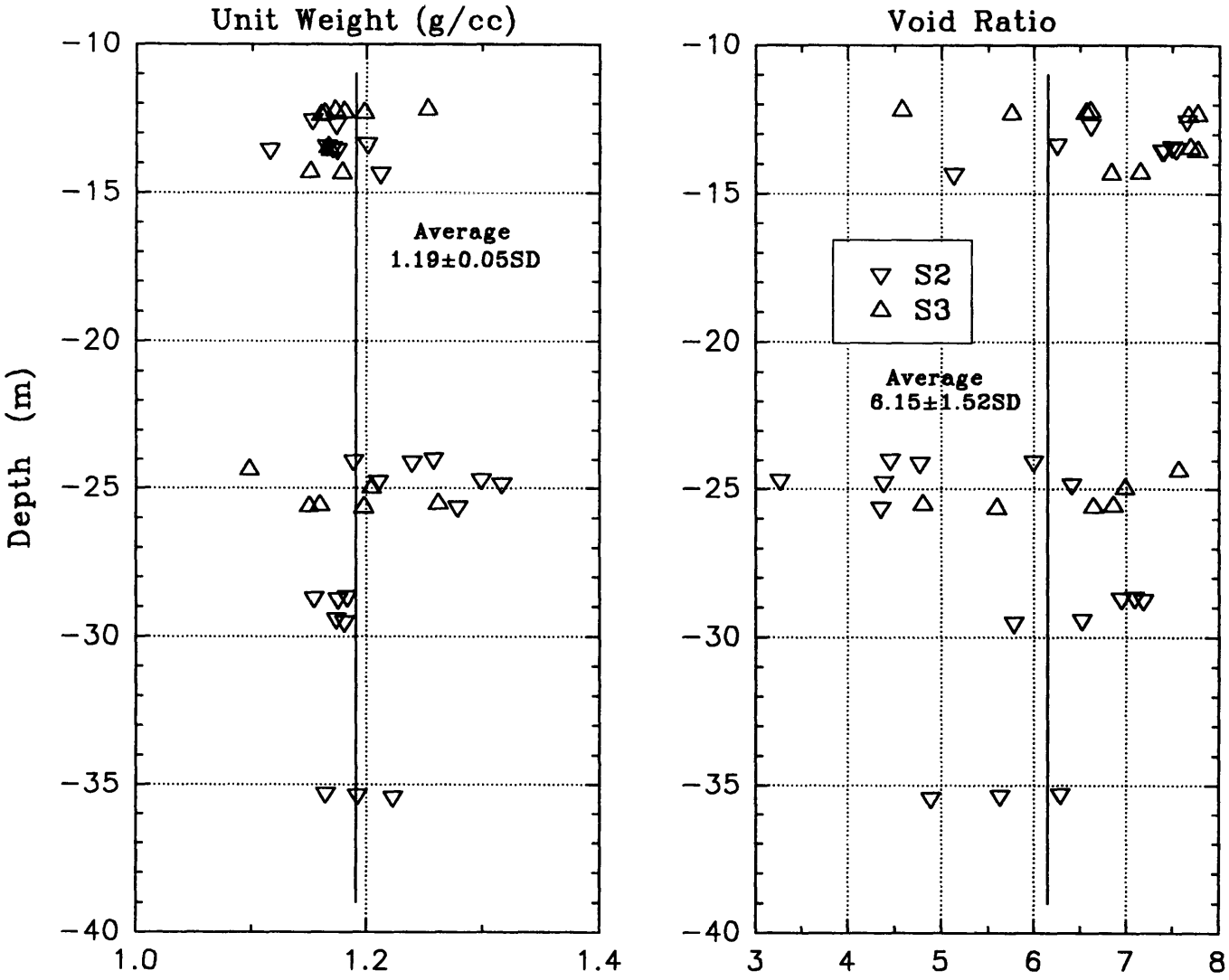

Figure 3.13 Depth vs. Unit Weight and Void Ratio

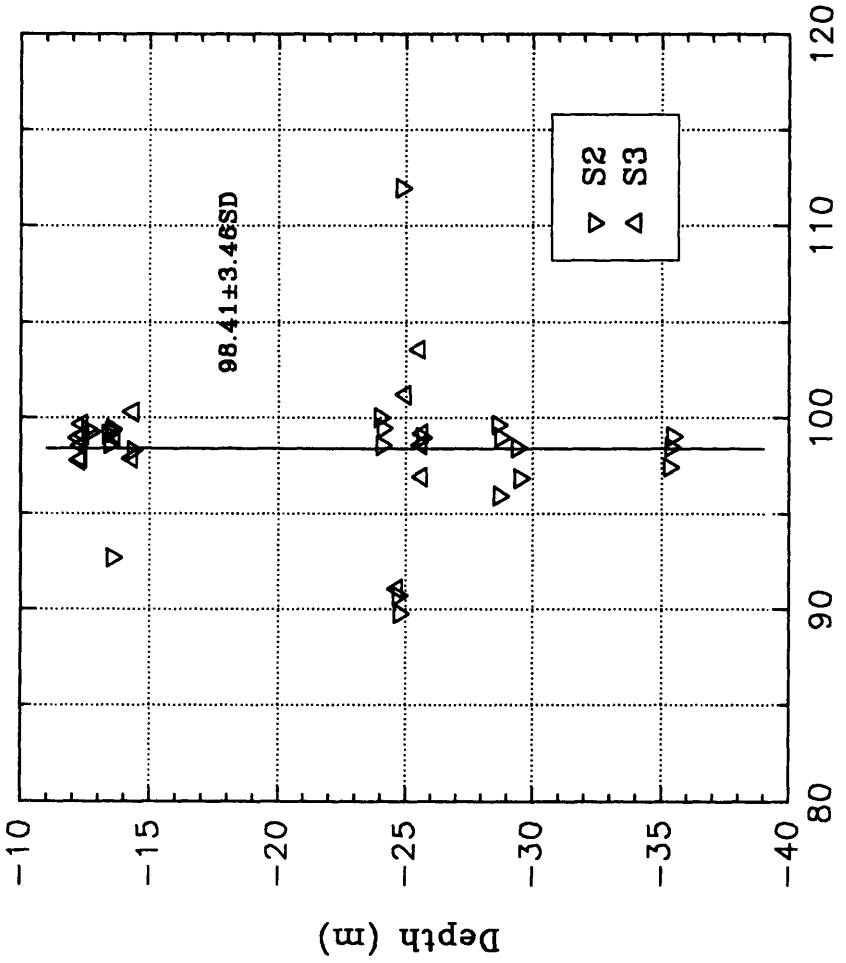

Figure 3.14 Depth vs Initial Saturation

P1.

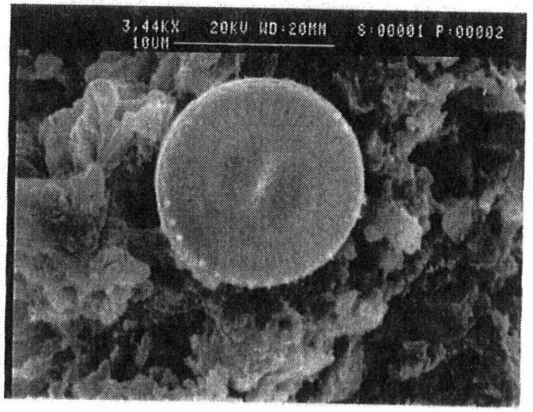

P2.

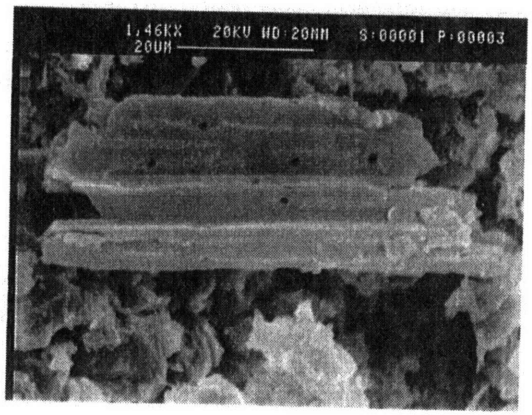

P3.

Figure 3.15 SEM Pictures of the Surface of Specimen SCS1

P1.

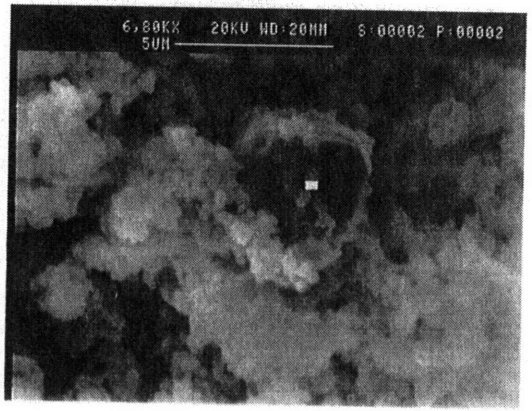

P2.

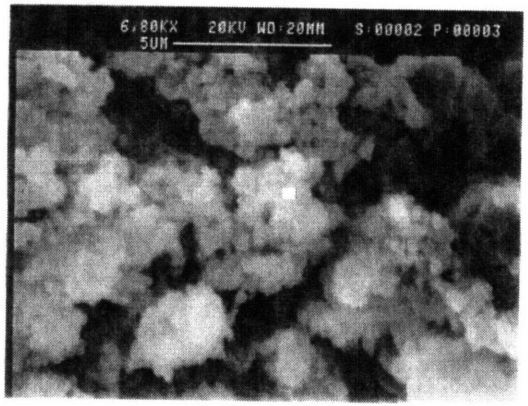

P3.

Figure 3.16 SEM Pictures of the Surface of Specimen SCS2

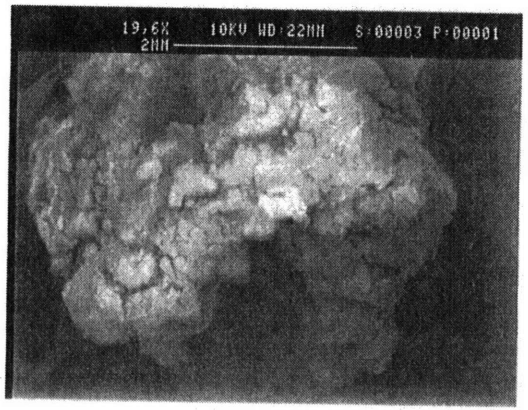

P1.

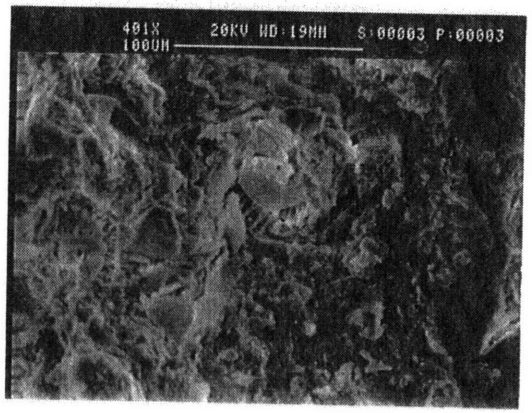

P2.

P3.

Figure 3.17 SEM Pictures of the Surface of Specimen SCS3

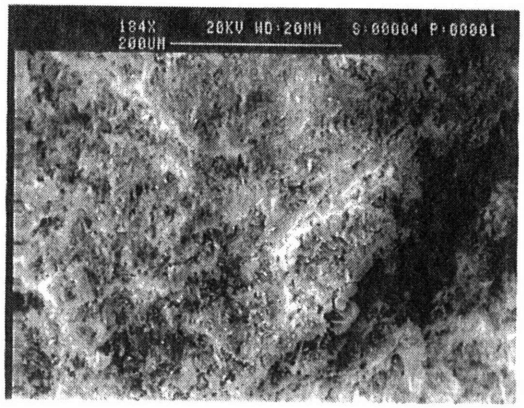

P1.

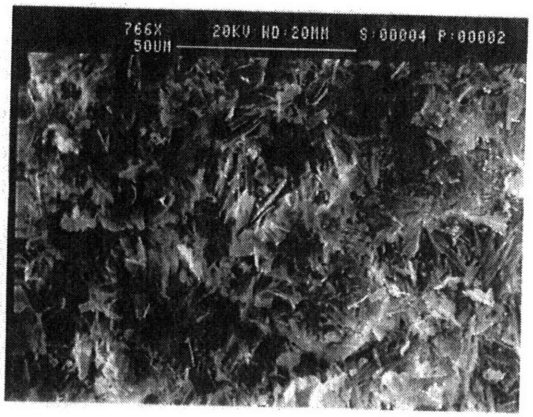

P2.

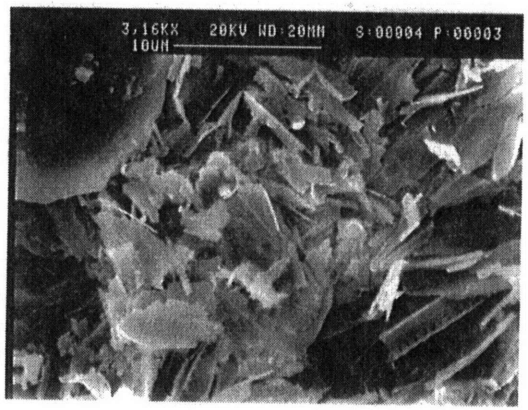

P3.

Figure 3.18 SEM Pictures of the Surface of Specimen SCS4

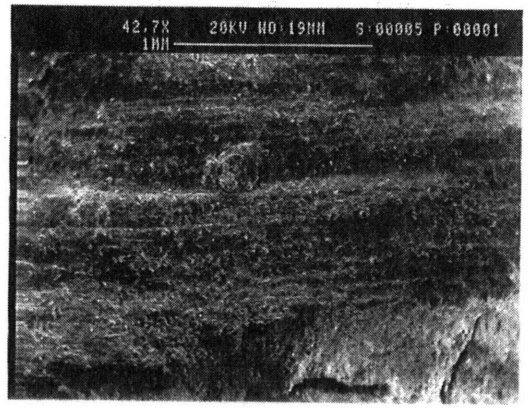

P1.

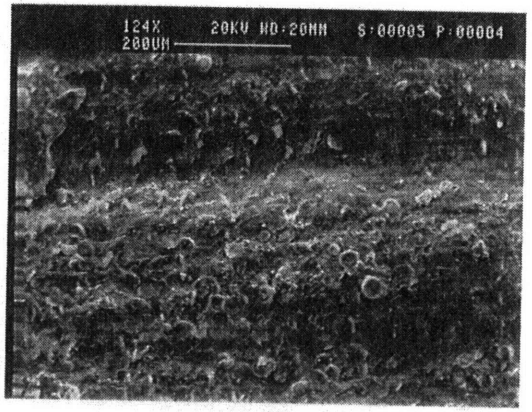

P2.

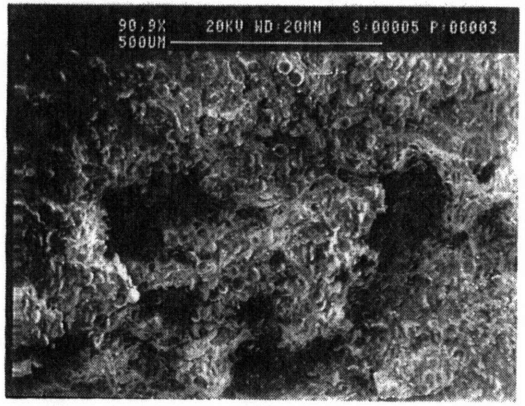

P3.

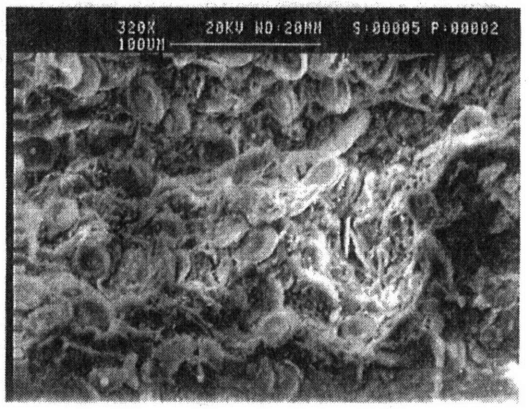

P4.

Figure 3.19 SEM Pictures of the Surface of Specimen SCS5

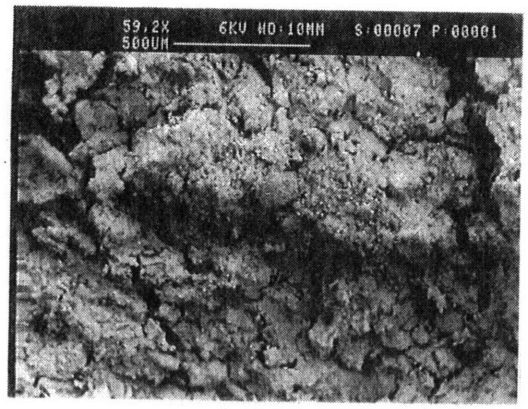

P1.

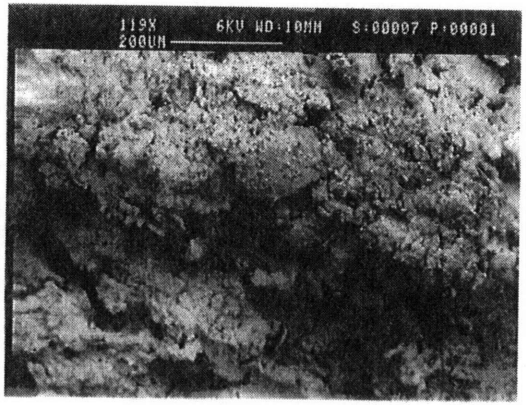

P2.

P3.

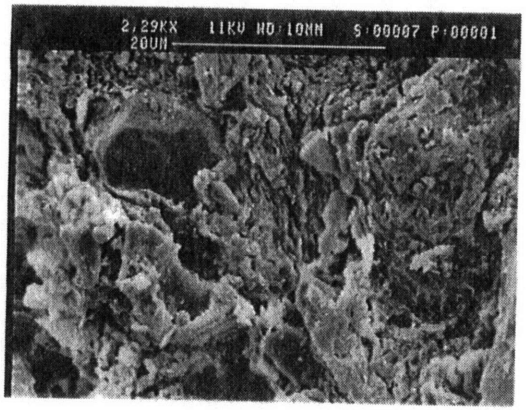

P4.

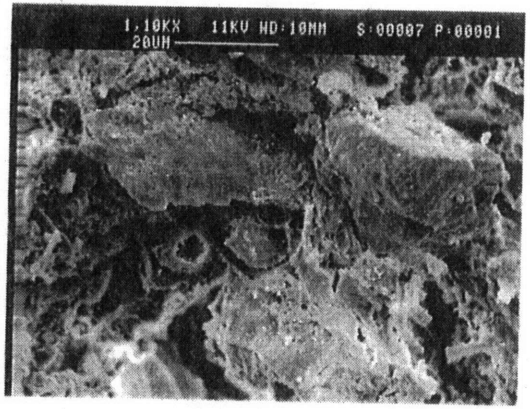

P5.

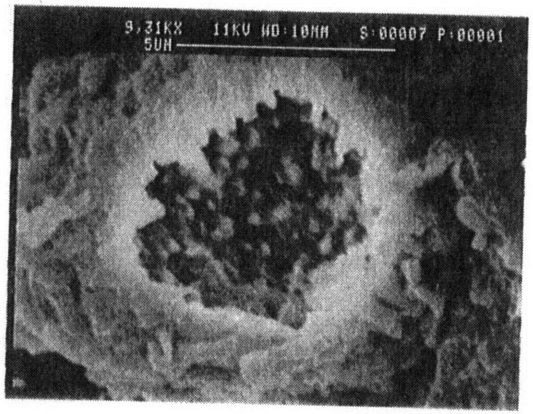

P6.

Figure 3.20 SEM Pictures of the Surface of Specimen S6

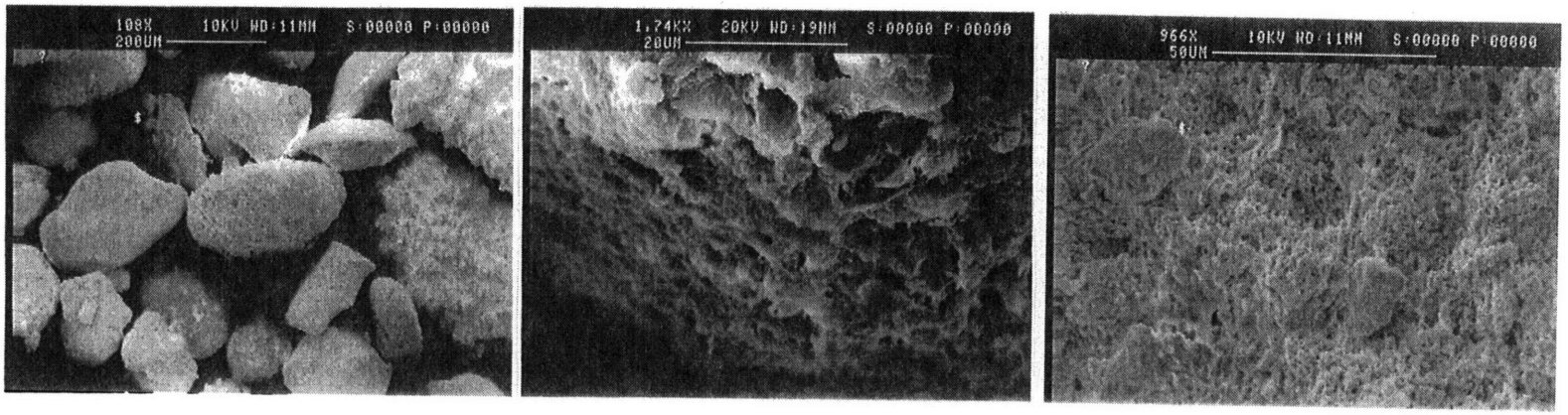

P1. P2. P3.

P4. P5.

Figure 3.21 SEM Pictures of the Surface of Specimen SJ-K

P1.

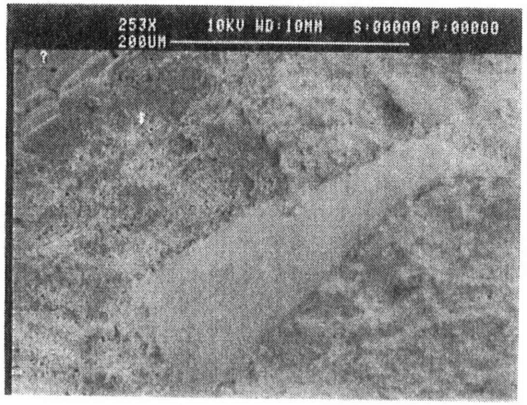

P2.

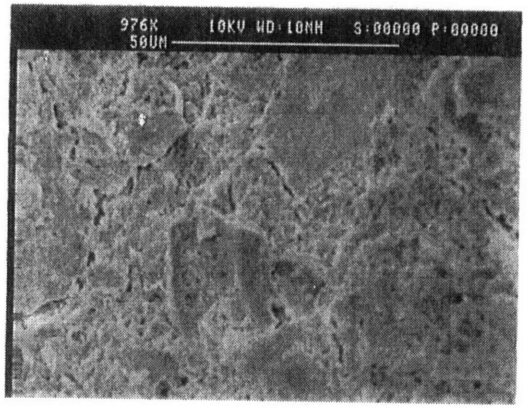

P3.

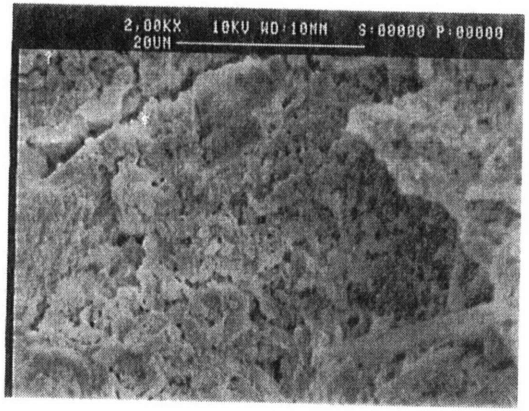

P4.

Figure 3.22 SEM Pictures of the Surface of Specimen SH (p.1/2)

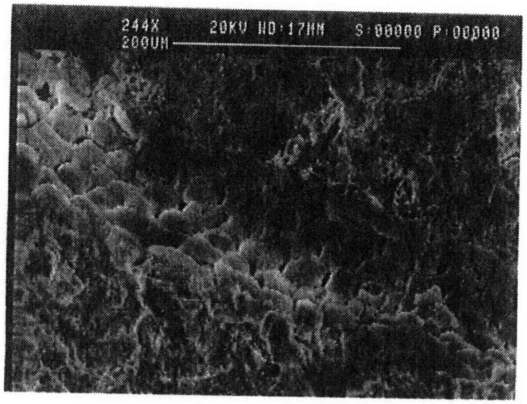

P5.

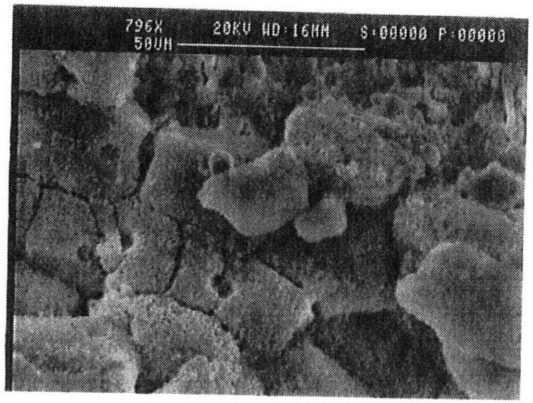

P6.

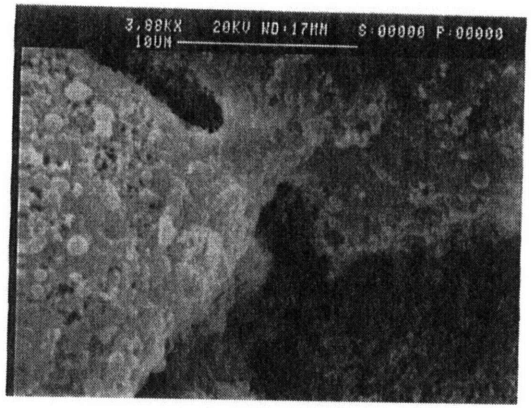

P7.

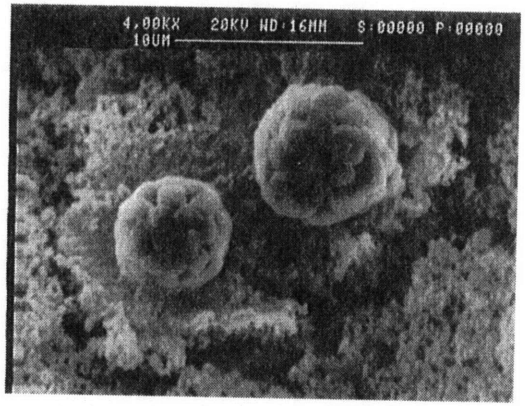

P8.

Figure 3.22 SEM Pictures of the Surface of Specimen SH (p.2/2)

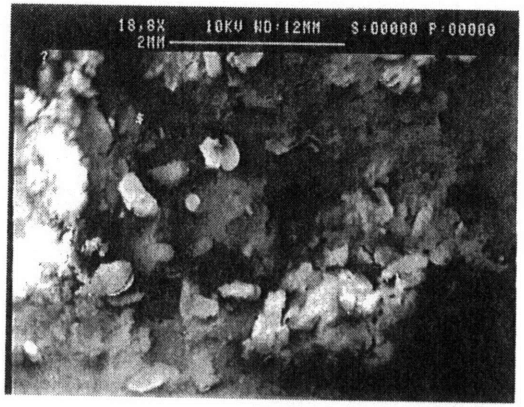

P1.

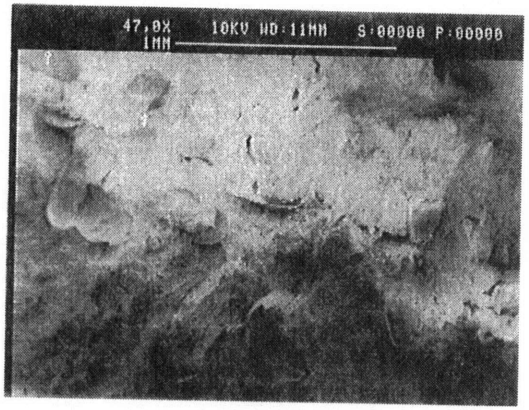

P2.

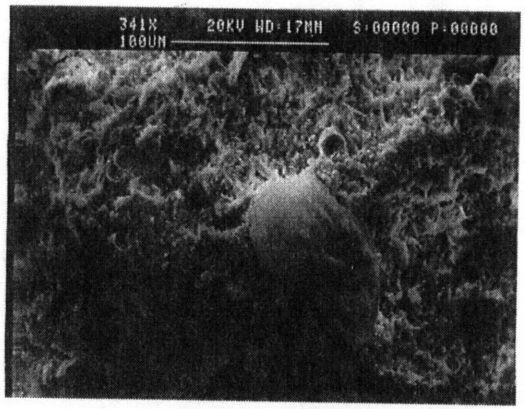

P3.

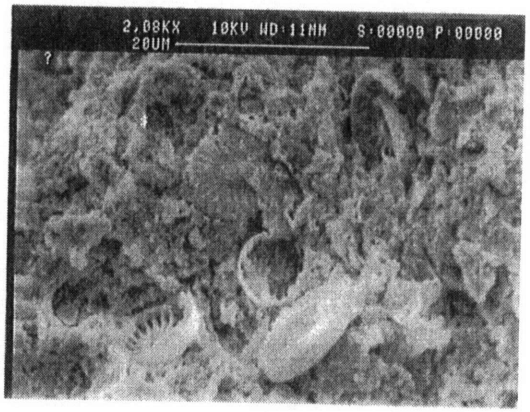

P4.

Figure 3.23 SEM Pictures of the Surface of Specimen SK

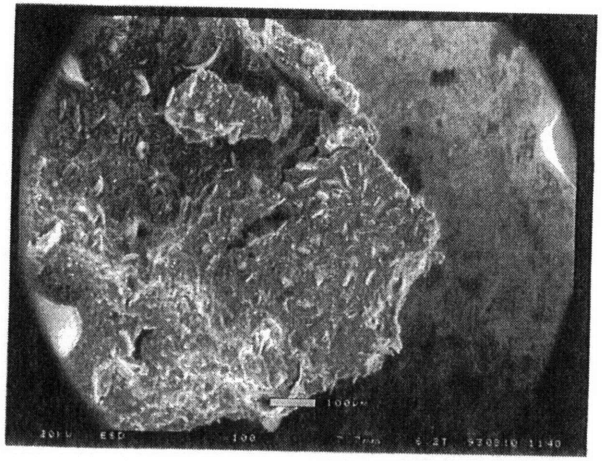

P1.

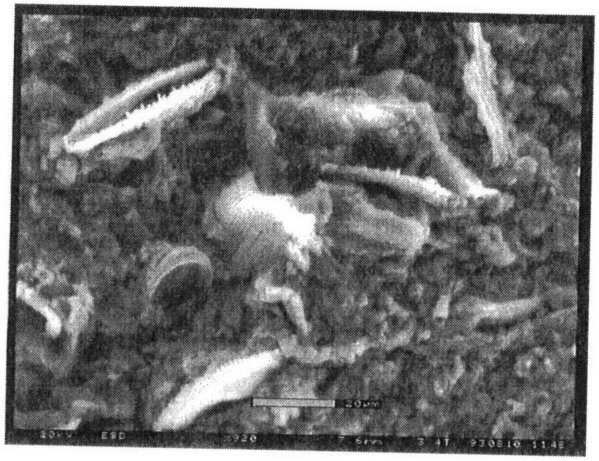

P2.

P3.

Figure 3.24 ESEM Pictures of the Surface of Specimen S7 (p.1/2)

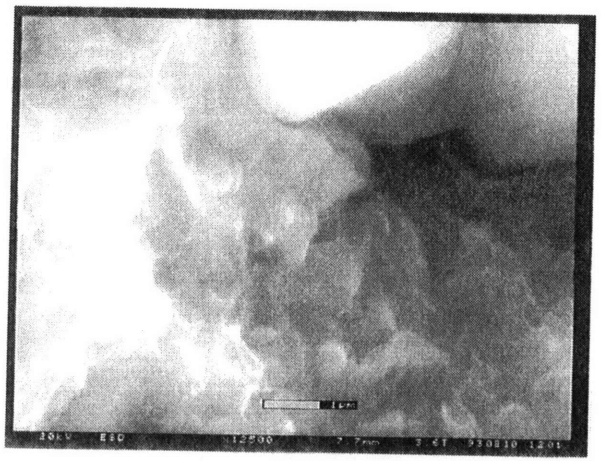

P4.

P5.

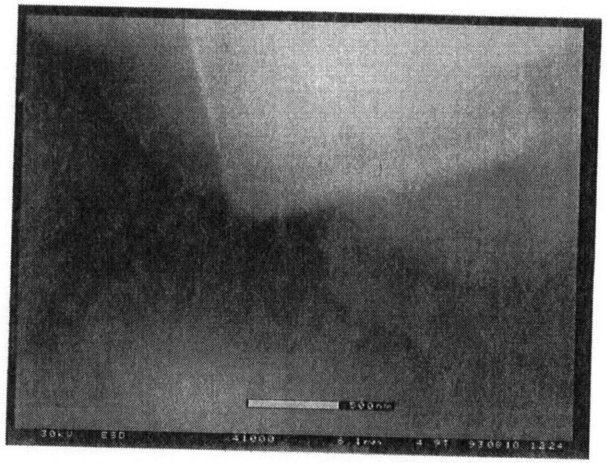

P6.

Figure 3.24 ESEM Pictures of the Surface of Specimen S7 (p.2/2)

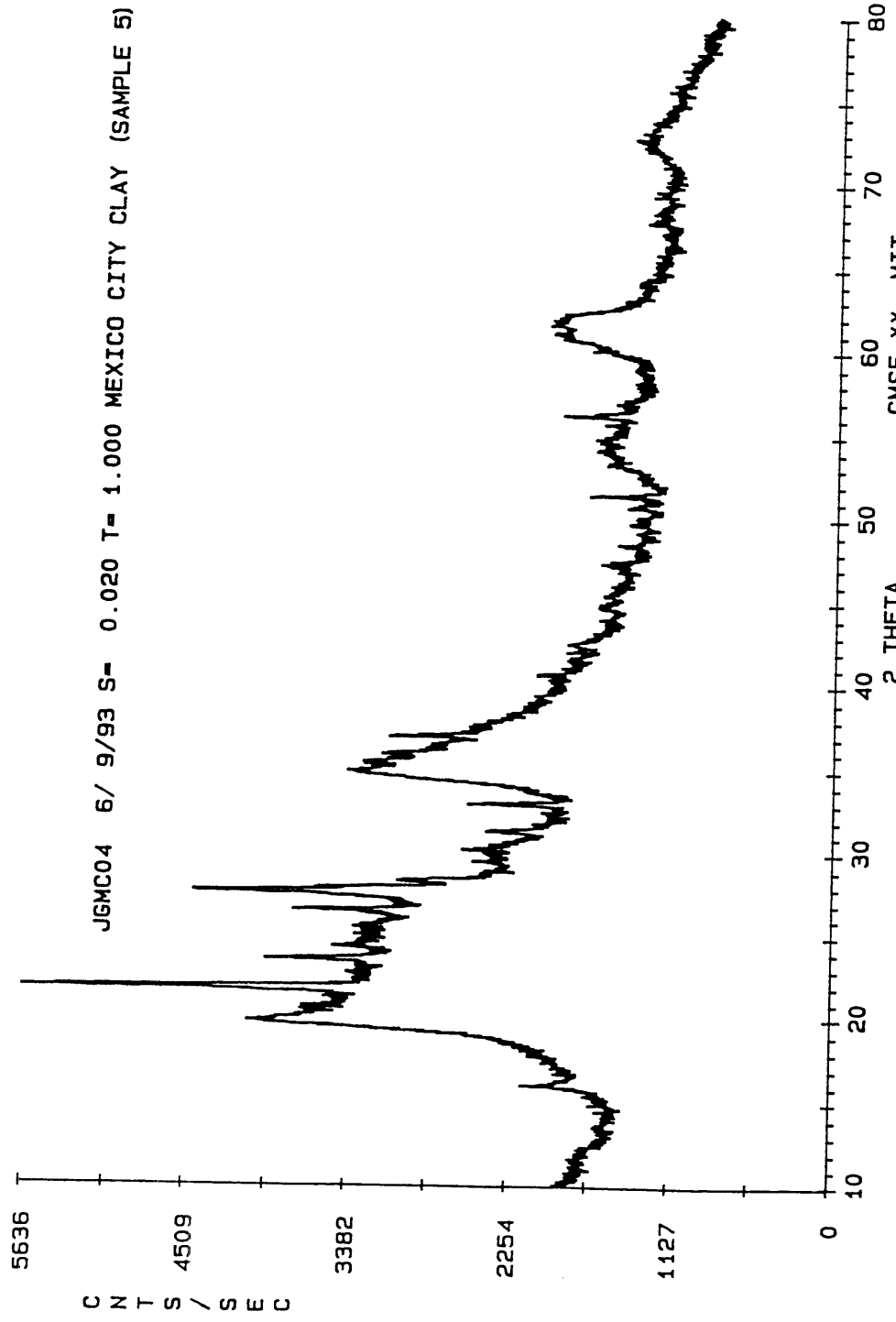

Figure 3.25 X-Ray Diffraction Pattern of Specimen S5X

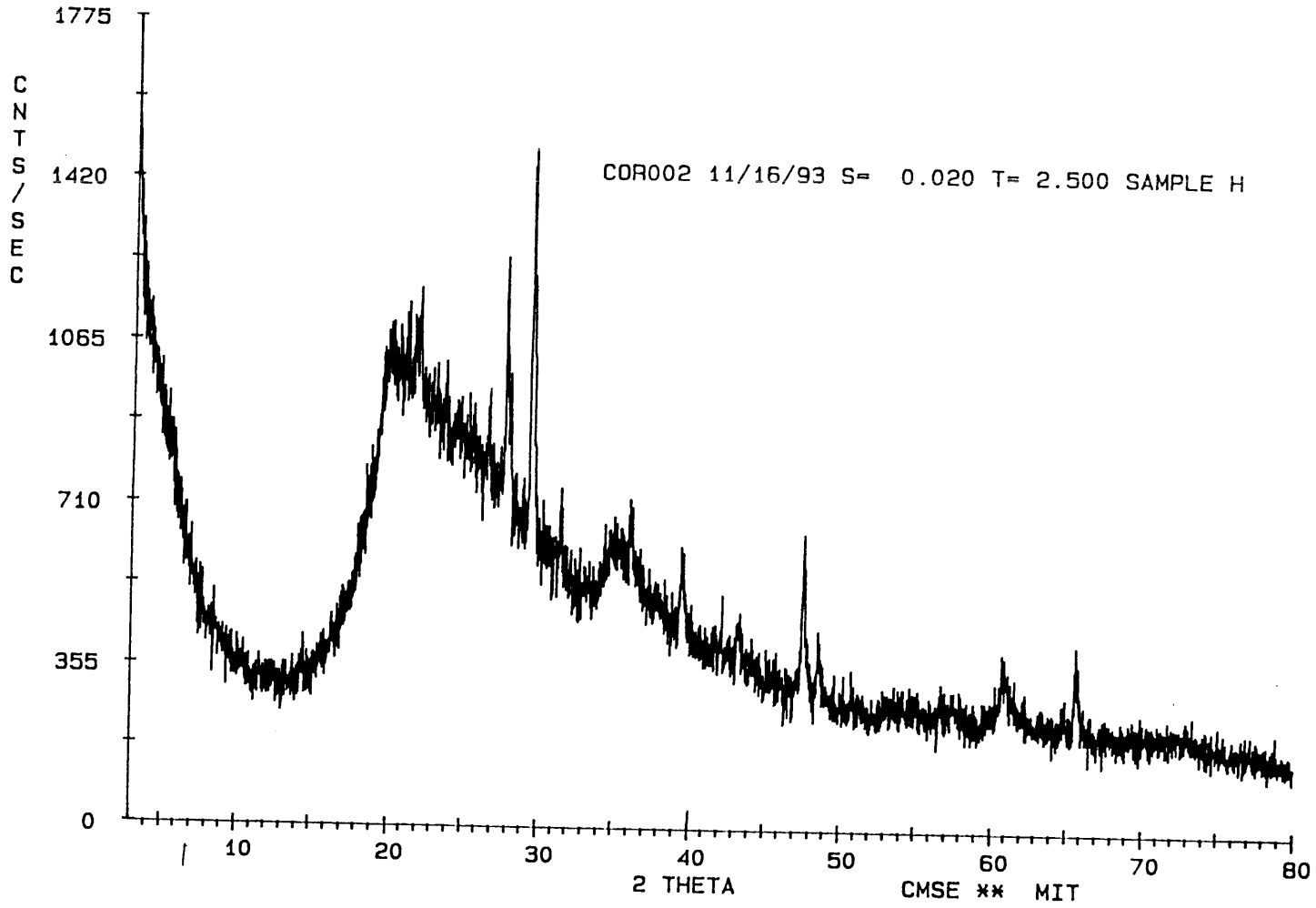

Figure 3.26 X-Ray Diffraction Pattern of Specimen SHX

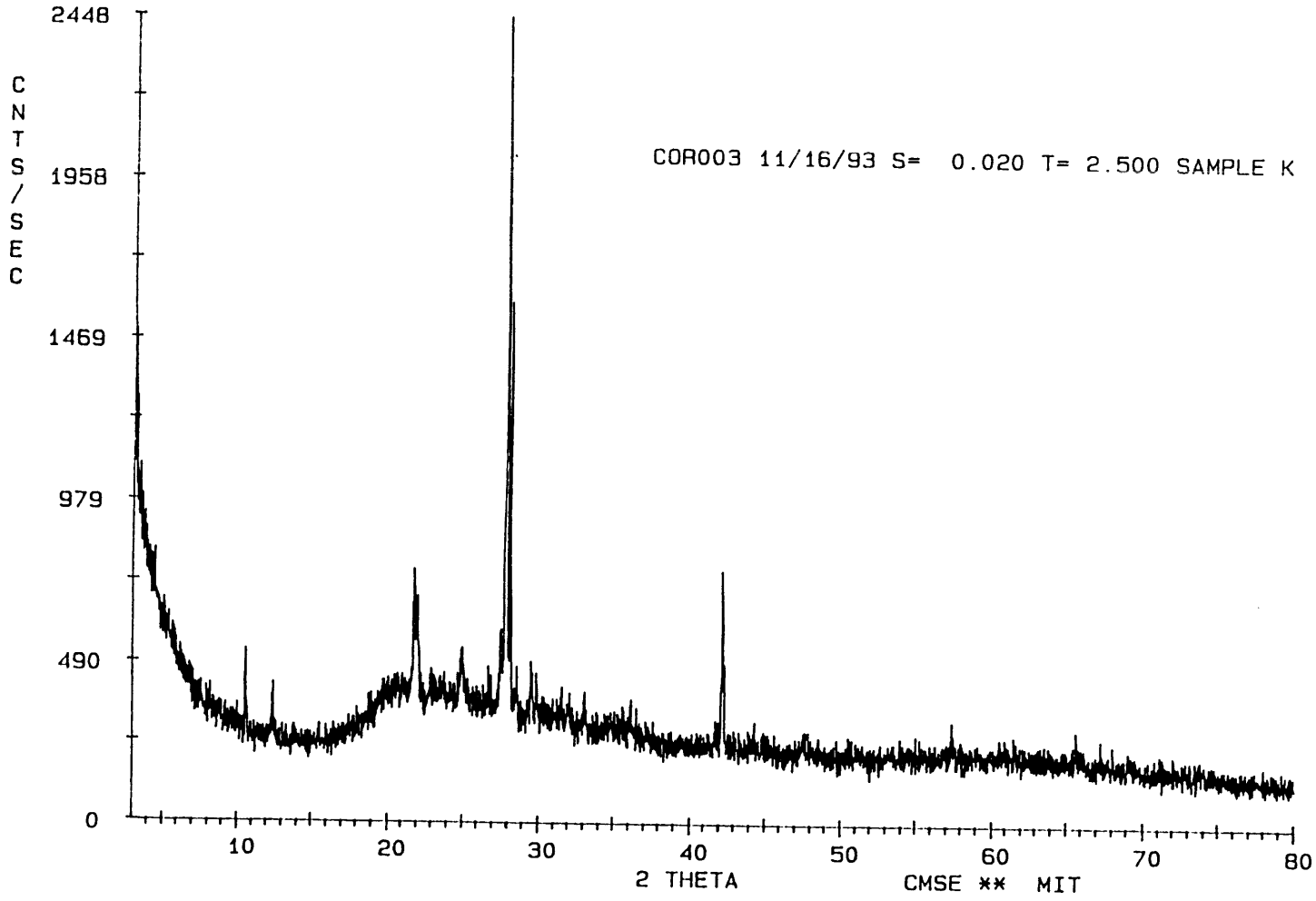

Figure 3.27 X-Ray Diffraction Pattern of Specimen SKX

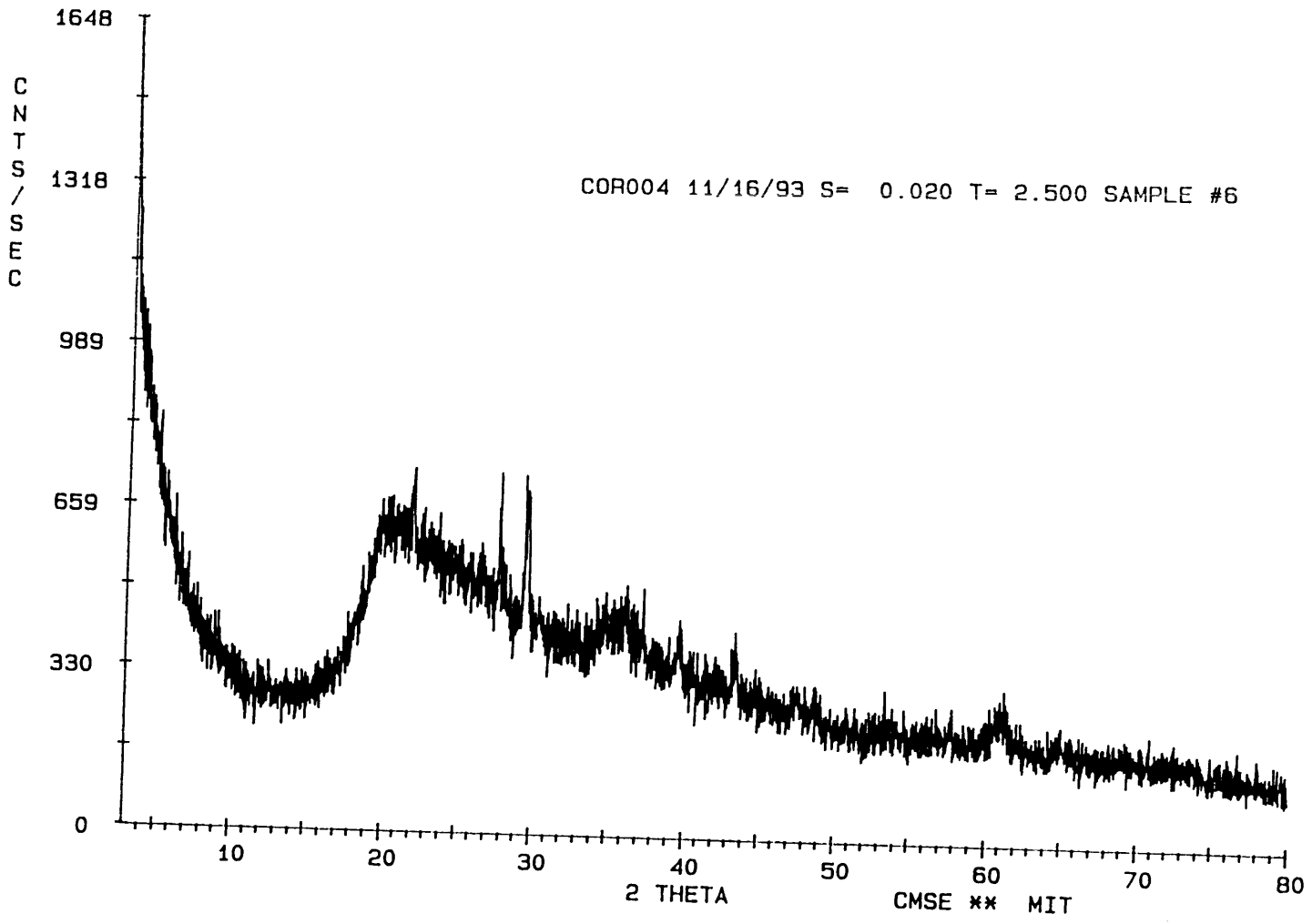

Figure 3.28 X-Ray Diffraction Pattern of Specimen S6X

CHAPTER 4
EVALUATION OF SAMPLE DISTURBANCE, STRESS HISTORY, AND CONSOLIDATION PROPERTIES

4.1 INTRODUCTION

This chapter presents a detailed evaluation of results from consolidation tests performed on undisturbed samples of México City Clay. The evaluation includes a discussion of methods for estimating preconsolidation pressure (σ'_p), development of the resulting stress history profile, determination of compressibility and flow properties, estimation of the lateral stress ratio (K_o), a discussion on sampling procedures, and determination of sampling disturbance. The stress history and consolidation properties are first developed for soil from the cathedral site and are then compared to data presented in the literature. The effects of sample disturbance will be discussed in conjunction with the consolidation properties, as it is well known that disturbance primarily affects some consolidation properties.

Consolidation data for this thesis were obtained from Constant Rate of Strain Consolidation (CRSC) tests and the consolidation phase of SHANSEP CK_oU direct simple shear (DSS) and SHANSEP CK_oU triaxial tests. Consolidation curves from all tests were used to determine the stress history profile and the compressibility characteristics of the deposit. In addition, the K_o consolidated triaxial tests provided lateral stress ratio data, and the CRSC tests provided information about the coefficient of consolidation and the permeability of the deposit. A summary of the consolidation data from the CRSC tests, the SHANSEP direct simple shear tests and the SHANSEP triaxial tests are shown in Tables 4.1, 4.2, and 4.3, respectively. The following summarizes the information contained in Tables 4.1 to 4.3. For all tests, the tables give the test location, the insitu phase relation data, the overburden stress, and the best estimate of the preconsolidation pressure (σ'_p), and the compressibility characteristics. Additional

information provided in the tables includes the (NC) K_o determined from the SHANSEP triaxial tests and the coefficient of consolidation and coefficient of permeability determined form the CRSC tests.

MIT Department of Civil and Environmental Engineering Research Report Number R94-01 contains the numerical and graphical data of all the constant rate of strain consolidation (CRSC) tests, K_o consolidated undrained direct simple shear (CK_oUDSS) tests, and K_o consolidated undrained triaxial compression and extension (CK_oUC/E) tests.

4.2 SAMPLING

4.2.1 Disturbance Overview

Geotechnical engineers routinely conduct site exploration and testing programs to determine the stratigraphy and engineering properties of a soil deposit. The information obtained is necessary for foundation analysis and design. A common component of soil exploration consists of drilling borings from which tube samples are recovered for purposes of soil identification and laboratory engineering testing. Laboratory tests generally provide well defined, controllable boundary and drainage conditions, in addition to uniform stresses (or strains) within soil specimens, thereby enabling easy interpretation of test results. Some disadvantages of laboratory testing include: (1) sampling disturbance effects that generally cause significant differences between properties measured in the laboratory and the in situ soil properties; and (2) uncertainties associated with the very small volume of soil normally tested.

In situ tests have attracted the interest among of geotechnical profession as a means of complementing laboratory tests in soil exploration. Although in situ tests can provide a more detailed description of the vertical variation of soil properties, they generally have complicated boundary conditions, significant stress (and strain) variations within the soil, and uncontrollable drainage conditions, which makes interpretation of in situ test results very difficult. Empirical relationships are required to estimate soil

parameters for design purposes. As a result, tube sampling and laboratory testing are still the principal methods used for determining the engineering properties of soils.

It has long been recognized that the influence of sampling disturbance makes it difficult to duplicate the in situ behavior of foundation soils in the laboratory. In fact, sample disturbance has such an impact on practices and procedures adopted by the geotechnical profession that, without its overwhelming effects, geotechnical engineering design practices would be very different from what they are today. For example, heavy reliance on empirical design procedures would probably be eliminated and replaced by more exact and reliable methods. These methods could then be easily adapted to suit new and different field conditions (Baligh et. al. 1987).

Research on the effects of sampling on the behavior of clayey soils was especially active in the 1940's, and culminated in the work of Hvorslev (1949), whose concepts, recommendations, and methods for sampling still constitute the basis of current practice. In more recent years, many investigators have attempted to establish the extent and nature of disturbance associated with sampling and laboratory testing. The results from some of these investigations are inconsistent. Therefore, no definite conclusion can be drawn as to which sampling techniques and laboratory testing procedures will best minimize disturbance. The papers consulted for this investigation will be discussed in the following paragraphs.

Table 4.4 from Jamiolkowski et al. (1985) summarizes sources of sample disturbance which can occur during sampling of cohesive soils from a drill hole. Baligh et al. (1987) classifies sources of disturbance in two categories: operator dependent disturbances and minimum sampling disturbances. Operator dependent disturbances refer to disturbances that are mainly dependent on the performance of operators in charge of field work, transportation, extrusion, trimming, and laboratory testing and hence can be reduced by close adherence to good practices of sampling and testing operations. On the other hand, minimum sampling disturbances refer to disturbances that, for a given set of

sampling tools and equipment, cannot be reduced by improving sampling operations. Minimum sampling disturbances are principally due to: (1) penetration of the sampling tube and sample retrieval to ground surface, (2) water content redistribution in the tube, and (3) extrusion of the sample from the tube. This means that, given the best available sampling equipment and exercising the most careful sampling methods, minimum (yet possibly significant) disturbances will occur (Baligh et al. 1987).

Two methods of obtaining undisturbed soil (clay) samples are generally used in practice: (1) a procedure in which a block sample is hand-cut from soil exposed in an excavation; and (2) sampling with a thin-walled tube sampler. It is generally acknowledged that hand cut blocks are the highest quality undisturbed samples due to their geometry and the fact that no boundary stresses or displacements are applied to the soil during the sampling process. However, excavation down to the level of sample recovery is required. This may cause two problems; (1) dewatering is necessary if the sampling depth is below the water table, and (2) it imposes a depth limit due to the stress change caused by the excavation. Additionally, the cost of extruding block samples makes them prohibitive for most site investigations (Gilbert 1992). For these reasons thin walled tube samplers are generally used in current practice.

Table 4.5 presents the principal types of thin-walled tube samplers (from Marcuson and Franklin 1979). The term "specific recovery ratio" used in the table is defined by Hvorslev (1949) as the ratio of the increment of length of sample entering the tube to the increment of tube advance. Figure 4.1 presents schematic drawings of Fixed Piston and Shelby Tube Open-Drive Samplers.

For most site investigations thin walled tube samplers yield good quality undisturbed soil samples. As mentioned earlier, operator dependent disturbances can be controlled or at least minimized by using the best available sampling technique for particular soil conditions. For example, in an effort to minimize sampling disturbance, La Rochelle et al. (1981) conceptualized a large diameter sampler based on observations and

studies of their previous work in sampling sensitive Canadian clays. Their design was based on the following principles:

a) the inside clearance of the tube should be eliminated;

b) the internal diameter of the tube should be precisely machined to meet strict tolerance with respect to roundness;

c) the cutting edge should be very sharp and shaped so as to force the change in volume towards the outside of the tube;

d) the piston should be eliminated;

e) suction or negative stress is very damaging to a sample and should be avoided at all stages of sampling. (This is done by eliminating the use of a piston in the initial stage of sampling and by overcoring around the sampling tube in the final stage);

f) the sample diameter should be large enough to reduce the relative amount of disturbed material around the intact core.

Figure 4.2 shows a schematic diagram of the sampler and its use (from La Rochelle et al. 1981). La Rochelle et al. compared the undrained strength and strain level at the maximum stress obtained for block samples to those obtained for 200 mm tube samples (in unconfined compression as well as unconsolidated undrained compression tests) and found that the results were nearly identical. Based on these results it was concluded that the Laval sampler is a cost effective alternative to block samples in investigations for projects requiring laboratory testing. However, it was also acknowledged that the use of this sampler is not economically feasible for routine investigations.

There is strong disagreement as to which geometric design and mechanical configuration produces the best samples in cohesive soils. All investigators reviewed for this thesis agree that the area ratio as defined by Hvorslev (1949) should be kept as small as possible, typically between 10 to 15%. There was also agreement on the need to keep the tube as strong and round (perfectly cylindrical) as possible, but this is difficult if the

wall section of the tube becomes too small. There is disagreement among investigators concerning the value of the inside clearance ratio and cutter geometry. La Rochelle et al. (1981) contend that inside tube relief allows and aggravates soil disturbance during sampling. Additionally, there is disagreement regarding the value of the piston sampler. Terzaghi and Peck (1968) and Hvorslev (1949) present arguments to show that the use of a thin-walled sampler with a fixed piston minimizes internal movement of soil inside the tube during sampling and therefore minimizes sampling disturbance. However, La Rochelle et al. (1981) present an argument that a fixed piston produces vacuum within the sampling tube which causes substantial sampling disturbance. The opinion of the Laval research team that vacuum/suction is very damaging to a soil sample is shared by researchers at NGI (Andersen and Kolstad 1979).

Finally, most sampling programs must employ procedures that may yield samples of less than ideal quality. Hence, practicing engineers need techniques for assessing sample quality, and they need to be aware of testing techniques that might be employed to minimize the adverse effects of sample disturbance (Jamiolkowski et al. 1985).

4.2.2 Description of Sampling Process Used for this Investigation

There are any number of procedures and equipment that can be used to drill a borehole. Usually the drilling equipment and procedure used is determined by the desired sample quality, the type of soil or soils to be sampled, and the site stratigraphy. One of the most commonly used drilling techniques to obtain undisturbed samples from cohesive deposits is wash drilling.

Wash drilling can be described as follows. The borehole is advanced using a fish tail or tricone bit, and circulating drilling mud (bentonite slurry) is used to clean out the cuttings and seal more permeable strata. If the soil conditions are good, the pressure exerted by the drilling mud on the wall of the borehole will be sufficient to stabilize the borehole. If drilling mud is not sufficient, then casing must be installed to stabilize the

borehole. Drilling mud is also used to reduce the amount of unloading experienced by the soil at the bottom of the borehole. To obtain undisturbed samples the following steps are taken; (1) the borehole is advanced to the required depth, (2) mud is circulated to clean the borehole, (3) the advancement tool is retrieved, (4) the sampler is lowered to the bottom of the borehole and then pushed into the soil to obtain the sample, (5) expansion of the soil in the sampler is allowed (approximately 5min), (6) the sample is sheared off by rotating the drilling rods 90°, and (7) the sample is brought to the surface.

As mentioned in Chapter 2, three boreholes were drilled for this investigation. Borehole S1 was drilled using hollow stem continuous flight augers and heavy weight drilling mud (γ_t=1.2t/m^3). Sampling was performed with 1 m long 3" diameter thin walled Shelby tube samplers. Figure 4.1 presents a schematic drawing of a Shelby tube open drive sampler, and Figure 4.3 shows a schematic drawing of a hollow stem continuous flight auger. Nine samples were obtained from this borehole, and the sampling depths can be found in Table 2.1. The sampling procedure was the following; (1) the auger is advanced to 2 meters above the first initial sampling depth, (2) the borehole is advanced to the required sampling depth with the wash method described above, (3) the sampler is continuously pushed into the soil to obtain a 80 cm long sample, and (4) the sample is retrieved. If the next sample immediately follows the previous sample the borehole is cleaned and the next sample is taken (step 3). Otherwise the drilling process is repeated (step 1).

During the drilling of this borehole a number of problems were encountered, the most important being the loss of drilling mud. At one point 12 gpm of drilling mud were added to the top of the boring in order to maintain a constant level inside the auger. The on-site explanation was that the pressure exerted by the drilling mud was such that hydraulic fracturing was occurring. This was later confirmed by the radiographs of tube samples from this boring and by the results of the K_o consolidated triaxial testing program. Figure 4.4 presents a radiograph of sample S1-3 which clearly shows the effects

of hydraulic fracturing. The occurrence of hydraulic fracturing can be explained as follows. México City Clay has a very low effective overburden stress (σ'_{vo}) due to a low total unit weight ($\gamma_t \approx 1.2 t/m^3$) a high water table, and an estimated average in situ K_o of 0.46 (explained in Section 4.6). A low σ'_{vo} and a low K_o result in a low horizontal effective stress ($\sigma'_{ho}=K_o \times \sigma'_{vo}$). When the pressure exerted by the drilling fluid exceeded the horizontal effective stress plus the undrained shear strength ($\sigma'_{ho}+s_u$), hydraulic fracturing occurred. Due to the lack of drilling mud circulation, it was impossible to clean the borehole before sampling. This resulted in recoveries of 1m instead of 80cm. The samples generally contained 80cm of undisturbed soil and 20cm of remolded material. All samples were obtained in 2.5, 12 hr work days.

Due to the difficulties encountered during the drilling of Borehole S1, Geotecnologia, S.A. suggested using their method to drill Borehole S2. Their method is identical to that used to drill borehole S1, except that all advancement is performed with the hollow stem auger, and no drilling fluid is used (i.e. the borehole is dry). Nine thin walled Shelby tube samples were obtained from this borehole, and the sampling depths can be found in Table 2.1. The sampling procedure can be described as follows; (1) advance the borehole by rotating the auger to approximately 20cm above the required sampling depth, (2) lower a 4" diameter Shelby tube and sample 20cm to clean the borehole and reach the required sampling depth, and (3) lower the 3" sampler and recover the sample. If sampling was continuous the next sample is taken without cleaning the borehole, otherwise the drilling process is repeated. Although this method allows fast borehole advancement and sample recovery and has a lower sample cost and site cleanliness, bottom heave of the borehole might occur due to the lack of drilling mud. Additionally, the 4" sampler cannot be lowered to clean out the borehole when continuous sampling is required. A 50% reduction of time was noted using Geotecnologia's method compared to the method used for borehole S1. All samples were obtained in 1.25, 12 hr work days.

Borehole S3 was drilled using a very light weight drilling mud ($\gamma_t < 1.1$ tons/m^3) and hollow stem augers. Samples were obtained using an Acker 3" fixed piston sampler (shown in Figure 4.1). Six samples were retrieved from this borehole, and the sampling depths can be found in Table 2.1. The sampling process was very similar to that used for borehole S1 with some adjustments; (1) the sampler was pushed 70cm (sampler limitation), (2) light weight drilling mud was used to stabilize the uncased section of the borehole and to restrain bottom heave (note: light weight rather than heavy weight mud was used since the possibility of hydraulic fracturing existed), and (3) a 4" sampler was used to clean out the borehole before sampling. Even with light weight drilling mud hydraulic fracturing occurred. This method had the slowest sampling rate due to the cumbersome operation of the sampler and inexperience with its use. The sampling rate was one sample per day. Because of time limitations only six samples were obtained.

Figure 4.5 shows a modified fixed piston sampler conceived by the author. It should be much easier to operate, and should produce a sampling rate which is just as fast as that of the thin walled Shelby tube sampler. The sampler is modified by adding a latching mechanism to the piston rods and by using NQ wireline drilling rods. The sampler is used in the following way (refer to Figure 4.5):

(a) the borehole is advanced to the sampling depth;

(b) the sampler is lowered to the bottom of the borehole and is held is place. Next, the overshot is lowered until it latches to the latching mechanism;

(c) the wireline cable is pulled until it becomes taught and then the sampler is pushed into the soil;

(d) the overshot is unlatched from the latching mechanism and retrieved to the surface;

(e) the sample is sheared by rotating the drilling rods and is then brought up to the surface.

After evaluating the samples, it was decided that all samples taken from boreholes S2 and S3 would be shipped to MIT. Since the quality of the samples from borehole S1 were questionable, only three samples were shipped. The samples were shipped by air in two wooden boxes (nine per box), each whit nine individual sections. After a tube was placed in its section, all open spaces were filled with sawdust to minimize movement of the tube during transportation.

4.2.3 Sample Disturbance Evaluation and Effects

The primary purpose in acquiring undisturbed samples from a soil mass is to perform laboratory tests to determine specific mechanical properties which are characteristic of the deposit. Properties of interest include stress-strain, strength, preconsolidation pressure, compressibility, and permeability characteristics. In most cases disturbance causes unconservative deviations in the measured behavior.

There are three basic techniques for assessing sample quality (i.e., amount of sample disturbance); radiography, measurement of effective stress after sampling, and evaluation of compression curves. The following discussion will primarily focus on the evaluation of compression curves, since radiography results were discussed in Chapter 2, and the effective stress was not measured after sampling.

Sample disturbance usually affects compression curves on "ordinary" sedimentary clays (soft to stiff consistency, low to moderate sensitivity) in the following manner (Jamiolkowski et al. 1985):

(1) decreases the void ratio (or increases the strain) at any given consolidation stress;

(2) makes it more difficult to define the point of minimum radius, thus obscuring and often lowering the value of the preconsolidation pressure;

(3) increases the compressibility during recompression (always true) and may decrease the compressibility in the virgin compression region.

No simple criteria exists to evaluate sample quality from compression curves. Whether or not sample disturbance is significant depends on the properties being assessed, (i.e., overconsolidated versus virgin behavior, preconsolidation pressure, etc.). Nevertheless, a comparative evaluation of compression curves within a given deposit can often indicate different degrees of disturbance from relative changes in compressibility and shapes of the curves. The only technique for reconstructing the in situ compression curve from a consolidation test compression curve was proposed by Schmertmann (1955). Unfortunately, this technique is not applicable for clays exhibiting variable and extremely high compressibility just beyond the preconsolidation pressure. One simple, but not precise, criteria that can be used to evaluate sample disturbance is the measured vertical strain at the effective overburden stress for deposits believed to have a relatively uniform stress history (Jamiolkowski et al. 1985).

Sample disturbance also affects the stress-strain measurements of samples of "undisturbed" cohesive soil. Varying amounts of disturbance yield strain levels at maximum stress which can be several times greater than those of the highest quality sample and Young's Modulus of Elasticity can be up to five times smaller (Gilbert 1992). The undrained shear strength decreases with increasing sample disturbance. Depending upon the sensitivity of the specimen and the amount of disturbance, the measured undrained strength of disturbed samples can be 50% less than the undrained strength of undisturbed samples. Nakase et al. (1978) suggests that the effect of disturbance on the undrained strength of a sample is greater for soils with low plasticity indices. The Recompression and SHANSEP reconsolidation techniques are used in many laboratories to minimize the adverse effects of sample disturbance when measuring the undrained strength. These techniques will be discussed further in Chapter 5.

4.3 ONE-DIMENSIONAL COMPRESSION CURVES AND DETERMINATION OF THE PRECONSOLIDATION PRESSURE

4.3.1 Typical Compression Curves

Preconsolidation pressures were determined from one-dimensional compression data obtained from CRSC tests, direct simple shear tests, and triaxial tests. Typical compression curves for each type of test are presented in Figures 4.6 through 4.8. For each curve, the effective overburden stress (σ'_{vo}), the preconsolidation pressure (σ'_p), the initial virgin compression ratio (CR), the strain at the overburden ($\varepsilon@\sigma'_{vo}$) and at the preconsolidation pressure ($\varepsilon@\sigma'_p$), and the depth of the specimen are shown. The curves presented in Figures 4.6 through 4.8 are representative of all types of curves encountered throughout this investigation.

The curves obtained during this study varied from being somewhat rounded to exhibiting a well defined "break" at the preconsolidation pressure (S-shaped curves). Figure 4.6 shows compression curves for CRSC tests CRS82, CRS83 and CRS84. As shown on the figure, the curves from tests CRS83 and CRS84 have a well defined break at the preconsolidation pressure, and a decreasing virgin compression slope at strains greater than 20 to 25% (S-shaped). The curve from test CRS82 was the most rounded curve encountered, and also yields the highest preconsolidation pressure of all tests.

Figures 4.7 and 4.8 show typical compression curves of CK_oUDSS and CK_oUTX tests. The curves encountered for each type of test were mostly consistent, and most curves had a well defined break at the preconsolidation pressure. The only CK_oUDSS tests that yielded S-shaped curves were those that reached axial strains higher than 25% during consolidation. No CK_oUTX test yielded S-shaped curves.

There were some differences in the shapes of the compression curves obtained from each type of test. After analyzing the compression curves it was evident that a decrease in the virgin compression slope starts at approximately 25% of axial strain. Compression curves obtained from CRSC and CK_oTX tests showed a lesser amount of

initial strain than the curves obtained from CK_0UDSS tests. The large initial strain is most probably due to a seating problem associated with the DSS device. Since the loading platen of the DSS device is fixed against rotation, initially it may not be completely flush with the top cap. This can cause small errors in the initial strain measurements during consolidation. Finally, the virgin compression slopes of CK_0UTX tests are steeper than the slopes of CRSC and CK_0UDSS tests from the same location. This might suggest that there is a relationship between sample geometry and the measured compressibility characteristics (explained in Section 4.3.2.).

Figure 4.9 plots axial strain at the overburden stress (ε_a (%) @ σ'_{vo}) versus the effective overburden stress for each type of test. As shown in the figure, CRSC and CK_0UTX tests yield a lesser amount of strain than the CK_0UDSS tests. As mentioned in section 4.2.3, plotting these values is useful for assessing sample disturbance. For most clays deposits which have a constant OCR with depth there should be a trend of increasing strain at the effective overburden stress with increasing effective stress. For México City Clay, the trend for CRS and CK_0UTX is constant or slightly decreasing not increasing. This suggests that the soil fabric is stiffer at higher consolidation stresses. Any test plotting below the trend (at higher strains) is probably more disturbed, and the farther away from the trend it plots the more disturbed it is. As shown in the figure, CRS77 yielded a much higher axial strain at the overburden than any other test, which indicates the presence of a substantial amount of disturbance. Additionally, tests CRS84 and TX228 yielded a slightly higher strain at the overburden, which indicates some degree of disturbance.

The figure shows that DSS tests generally plot below CRSC and CK_0UTX tests with a trend of increasing strain at the overburden. The discrepancies in the DSS data are most likely due to the seating problem discussed above. Therefore, since the $\varepsilon_a@\sigma'_{vo}$ data is unreliable, it cannot be used as a criteria for assessing disturbance in CK_0UDSS tests.

4.3.2 Comparison of Consolidation Testing Methods

Traditionally, consolidation data were obtained from incrementally loaded tests. It is often difficult to obtain a reliable estimate of σ'_p from incrementally loaded compression curves, as the curve is generally not well defined in the neighborhood of σ'_p. It is also difficult to apply the strain energy technique to estimate the preconsolidation pressure, as will be discussed in Section 4.3.3. Constant rate of strain (CRS) loading is now the preferred method of consolidation. The primary disadvantages of CRS loading are: 1) no rate of secondary (C_α) data, and 2) possible errors associated with high strain rates. If standard oedometer tests are going to be used, it is important that compression curves corresponding to the end of primary (EOP) consolidation be used to determine the preconsolidation pressure. The value of σ'_p may be significantly underestimated if the soil undergoes one or more cycles of secondary compression. For a detailed discussion of the CRS test the author refers the reader to Wissa et. al. (1971).

CRSC tests, and the consolidation portion of SHANSEP CK_oU direct simple shear and triaxial tests, all produce continuous compression curves. The CRSC test has the added advantage of obtaining continuous measurements of permeability (k) and hence coefficient of consolidation (c_v), while the consolidation portion of the SHANSEP CK_oU triaxial test has the added advantage of obtaining information on the lateral stress ratio of the specimen.

Results from all of the testing methods were used in the final stress history analysis, although there is some concern as to the reliability of the compression data resulting from the consolidation phase of direct simple shear and triaxial tests. As mentioned earlier, there is a seating problem associated with the CK_oUDSS test which most likely causes initial strains which are too large. In addition, since the wire reinforced membrane of the DSS sample is not entirely rigid, the soil may not be undergoing truly 1-D consolidation. There is a possibility that the triaxial test slightly overestimates the virgin compression ratio. Once the specimen was consolidated to the preconsolidation

pressure, the specimen tended to bend and bulge at certain locations. This behavior was evident at even slow strain rates (0.1% per hour). The distortion of the specimen , which is probably caused by local instability and lack of rigid confinement, might lead to an overestimation of the slope of the virgin compression line. Lo, (1962) reports the same behavior discussed above for incrementally K_o consolidated triaxial specimens.

4.3.3 Methods for Estimating Preconsolidation Pressure

Although several other methods have been proposed for estimating the preconsolidation pressure (e.g., Schmertmann 1955 and Butterfield 1979), the most widely used method is the construction developed by Casagrande (1936). According to the Casagrande method, the preconsolidation pressure (σ'_p) is defined by the intersection of two lines: 1) the bisector of the angle defined by a horizontal line through the minimum radius of curvature on the compression curve and a line tangent to the curve at that point, and 2) the extension of the virgin compression line (VCL). An example of this type of construction is shown in Figure 4.10a.

Recent work by Becker et. al. (1987) makes use of strain energy considerations to estimate the preconsolidation pressure. To use the "strain energy" (SE) technique, one plots the strain energy (work per unit volume) of each increment versus the final consolidation stress (σ'_{vc}) for that increment. The strain energy of each increment is calculated as:

$$W = \int \sigma'_{vc} d\varepsilon_n = \Sigma(\sigma'_{vcave} \times \Delta\varepsilon_n) \quad (4.1)$$

where σ'_{vcave} is the average vertical effective stress on the specimen during the given increment, and $\Delta\varepsilon_n$ is the change in natural strain (i.e., $\Delta H/H$) over the increment. The resulting curve resembles an inverted compression curve. The preconsolidation pressure (σ'_p) is defined by the intersection of two lines: 1) a line extending through the initial "linear" portion of the curve, approximately up to the overburden stress, and 2) a line extending through the maximum slope of the virgin compression line (VCL). Each slope

can be defined by a linear regression on the appropriate data. In order to use the strain energy technique, continuous loading tests must be used to produce a well defined compression curve which allows a reliable estimate to be made for both the initial slope and the maximum slope. The procedure used to determine the preconsolidation pressure using the strain energy technique is illustrated in Figure 4.10b.

For some SE curves, judgment is required to choose the initial slope of the curve if the initial region is not linear. In addition, when rounded initial curves were encountered, the overburden stress usually occurred after the initial "most linear" portion of the curve. Nonlinear initial regions were only encountered in triaxial tests. It is possible to define three initial linear regions: (1) a very small initial linear region, (2) a region defined by a line which passes through the origin of the curve and the point corresponding to the effective overburden stress, and (3) a region defined by a line which is drawn tangent to the point corresponding to the effective overburden stress. These three definitions of the initial linear portion of the curve correspond to the lowest, median and highest estimates of the preconsolidation pressure, respectively. The difference between the three estimates is generally less than 5%. A typical example can be seen in Figure 4.11b. The σ'_p reported in this thesis corresponds to the median value defined above. Using the SE technique on curves obtained from CRS and DSS tests presented no problems.

Preconsolidation pressures were calculated using both the Casagrande method and the strain energy technique for all tests. Figure 4.12 illustrates that there is good agreement between the σ'_p values estimated from the Casagrande method and those estimated from the strain energy technique. The figure also shows that the Casagrande method usually results in higher preconsolidation pressures than the strain energy technique by 10 to 15%.

The strain energy method has a sounder "theoretical" basis, can be easily computerized, and requires less judgment when applied to rounded compression curves.

The Casagrande construction, although it is more widely used and has a strong "empirical" basis, requires considerable judgment on the part of the engineer, and different interpretations of the same curve are common. Therefore, the values estimated from the strain energy technique were used in the final analysis of the stress history.

4.3.4 Normalization of Compression Curves

It is often desirable to compare compression curves from different tests on the same plot to better evaluate the behavior of the deposit and to assess disturbance. This is usually accomplished by plotting the curves in e - log σ'_v space. On this plot it is feasible to obtain the soil's unique virgin compression line and its change with stress level. Usually samples with higher in situ vertical stresses will have lower void ratios (i.e., decreasing void ratio with increasing vertical stress), and their compression curves will plot below and to the right of compression curves from samples with higher in situ void ratios.

It was shown in Chapter 3 that there is no relationship between void ratio and stress level at the site. Due to this peculiarity, nothing is accomplished by plotting the compression curves in e - log σ'_v space (see figures 4.6b, 4.7b, and 4.8). No systematic technique or method exists to normalize compression curves. Burland (1990) presents a method to compare compression curves by normalizing the void ratio by a parameter called "void index". He claims that changes in normalized curves obtained from the same soil are due to on depositional and post-depositional characteristics.

The author normalized the compression curves to different functions of the Atterberg limits. In order to diminish possible scatter induced by using the incorrect specific gravity, the compression curves were normalized in terms of water content and not void ratio (i.e., $W_n/f(Al)$ vs. σ'_v). In Chapter 3 the existence of strong correlations between natural water content and the liquid limit, and water content and the plasticity index were shown. Therefore, using any function of the Atterberg limits to normalize the compression curves, inherently normalizes the curves to some function of the water

content. The best results were obtained by normalizing the compression curve by the corrected liquid limit of the specimen at the initial water content (i.e., W_n/W_{lc}). The equation used for the corrected liquid limit is:

$$W_{lc} = -27.21 + (W_n \times 1.002) \quad \text{.....(4.2)}$$

Figures 4.13a, 4.14a and 4.15a show the compression curves plotted as normalized water content versus vertical effective stress (log-log space) for CRSC, and CK_oU direct simple shear and triaxial tests, respectively. As shown on the figures, normalization minimizes the initial water content scatter by adjusting the curves to a common initial state. In these figures the general trend of the virgin compression slope becomes more apparent. Lambe and Whitman (1969) suggest that changes in the virgin compression slope correspond to different mineralogies or different micro-structures.

Since there is no relationship between water content and effective overburden stress (σ'_{vo}) or water content and preconsolidation pressure (σ'_p), another "normalization parameter" is required to adjust each curve to the in situ initial stress level. One solution is to normalize the vertical effective stress of each curve by its estimated preconsolidation pressure. Figures 4.13b, 4.14b and 4.15b show all of the compression curves plotted as normalized water content versus the normalized vertical stress (W_n/W_{lc} vs. $\sigma'_{vc}/\sigma'p$ in log-log space) for CRSC, and CK_oU direct simple shear and triaxial tests, respectively. As shown in the figures, normalizing the effective stress results in a better defined virgin compression slope, and changes in microstructure are better appreciated. The same effect produced by normalizing by the preconsolidation pressure can be obtained by normalizing by the effective overburden stress (σ'_{vo}). In this particular case both techniques work because the overconsolidation ratio is constant with depth (Section 4.4.2). Unfortunately, it is not possible to determine if normalizing by σ'_{vo} would work in a site with changing OCR.

The author believes that the key to normalizing the compression curves lies in the three way relationship between water content, liquid limit, and initial stress level. This

investigation has shown that there is a correlation between water content and the liquid limit. It has also shown that no correlation exists between water content and initial stress level. Marsal and Mazari (1959) show very limited data that suggest that the liquid limit decreases with increasing consolidation stress. These three statements might imply that the water content and the initial stress level must be related by the liquid limit; and thus as the stress level increases, the microstructure of the soil changes, and hence the liquid limit and the capacity of the structure to retain water changes. The author acknowledges that this behavior has never been observed and does not conform to defined soil mechanics principles.

4.4 STRESS HISTORY

4.4.1 Background

Establishing a reliable stress history profile is essential for any soil investigation. Some of the most useful aspects of developing a stress history profile are as follows:

(a) For construction involving application of loads on thick strata of compressible clay, the amount of precompression (σ'_p-σ'_{vo}) has a very significant impact on long term consolidation settlements.

(b) The undrained strength of the clay at any depth is directly related to its in situ vertical effective stress (σ'_{vo}) and OCR (σ'_p/σ'_{vo}) via the SHANSEP equation (Ladd et al. 1977):

$$s_u/\sigma'_{vo} = S\,(OCR)^m \quad \text{.....(4.3)}$$

(c) The in situ OCR is needed to perform and evaluate any type of reconsolidated undrained shear strength test.

(d) The stress history profile is needed to correlate data from insitu test devices to other laboratory data. Correlations such as log of the net tip resistance versus log OCR can be developed.

4.4.2 Stress History at México City's Cathedral

As mentioned in Chapter 2, the effective stress profile used in the preparation of this thesis is that presented in SEDUE (1990). Figure 4.16 presents the stress history at the site of México City's Cathedral. Preconsolidation pressure, overburden stress, and OCR are tabulated for all tests in Tables 4.1, 4.2, and 4.3.

Elevation versus preconsolidation pressure is plotted in Figure 4.16a. This figure shows data obtained during this investigation and the data reported in SEDUE (1990) for Borehole SMC-1. As can be seen in the figure, there are no major differences in the preconsolidation pressures reported for Boreholes S2 and S3. Additionally, the figure shows that the preconsolidation pressures reported for borehole SMC-1 (from incremental oedometer) tend to be lower than those reported for boreholes S2 and S3, especially below a depth of -25m. This could be due to one or more of the following reasons:

(1) Samples from borehole SMC-1 experienced more sample disturbance than those from boreholes S2 and S3.

(2) An underestimation of the preconsolidation pressure by SEDUE (1990). The method to calculate the preconsolidation pressures in SEDUE was not reported, and the author calculated higher preconsolidation pressures using the Casagrande method of construction on the compression curves given in SEDUE.

(3) Loading method. As mentioned earlier, it is often difficult to obtain a reliable estimate of the preconsolidation pressure from incrementally loaded compression curves, as the curve is generally not well defined in the neighborhood of the preconsolidation pressure.

The author believes the main reason for the discrepancy between the values of σ'_p is a combination of sample disturbance and incorrect estimation of σ'_p. The main cause of sample disturbance is probably extrusion technique. MIT has produced a significant amount of data that show that extrusion technique is the critical factor in obtaining a

reliable measurement of σ'_p. Additionally, the data show that the best extrusion technique available is that used in this investigation (outlined in Chapter 2).

Figure 4.16a shows linear regressions with standard deviation lines for the cumulative data from boreholes S2 and S3 above and below a depth of -26m. Additionally, another linear regression with standard deviation lines is shown for the data from borehole SMC-1, above and below -26m. The equations resulting from the regression analysis are as follows:

This investigation (Boreholes S2 and S3);

Above depth -26m:

$\sigma'_p = (-0.041 \times \text{depth}) + 1.212$ S.D. = ± 0.284.....(4.4)

Below depth -26m:

$\sigma'_p = (-0.180 \times \text{depth}) - 2.471$ S.D. = ± 0.234.....(4.5)

Borehole SMC-1;

Above depth -26m:

$\sigma'_p = (-0.026 \times \text{depth}) + 1.098$ S.D. = ± 0.202.....(4.6)

Below depth -26m:

$\sigma'_p = (-0.124 \times \text{depth}) - 1.421$ S.D. = ± 0.221.....(4.7)

The preconsolidation pressures from tests CRS82 and CRS88 were not used in the linear regression analysis, since it is believed that the results from these tests are not entirely representative of the behavior of the soil mass. The depth of these two CRSC tests correspond to a peak of cone penetration net tip resistance, as shown in Figure 2.12. It was mentioned in Chapter 2 that the peaks correspond to isolated changes in the geological formation of the deposit.

The possibility that the scatter in the preconsolidation pressure values is due to changes in sample disturbance over small distances was investigated. Although the radiographs did not give any indication of sample disturbance, they did indicate sample heterogeneity in the form of significant changes in density, both vertically and horizontally,

within centimeters. Generally, low values of preconsolidation pressure and high values of axial strain at the overburden stress are good indications of sample disturbance. Such is the case for CRS77, which has a low preconsolidation pressure (OCR=1) and a high axial strain at the overburden stress. Figure 4.17a presents depth versus axial strain at the overburden, and Figure 4.17b presents depth versus axial strain at the preconsolidation pressure. Based on the amount of axial strain at the overburden stress, the results from the tests enclosed by dashed line boxes in Figure 4.16a have been influenced by some degree of sample disturbance. Most of the data points enclosed in the boxes are from CK_0UDSS tests. The large axial strains at the overburden stress observed for the CK_0UDSS tests can probably be attributed to seating problems associated with the device rather than an indication of sample disturbance. With the exception of tests CRS77, CRS84, and TX228, there are no tests that can clearly be labeled as disturbed. Generally, there should be a trend of increasing strain with depth due to larger stress relief during sampling. Both Figures, 4.17a and 4.17b, show a trend of constant or slightly decreasing strain with depth, which suggests that the soil's microstructure stiffens with increasing stress.

After comparing the preconsolidation pressures and the shapes of the compression curves obtained from samples from boreholes S2 and S3, it is impossible to determine which samples experienced the greatest amount of disturbance. Throughout the testing program, very large differences were observed in consistency, color, general appearance (structure), odor, etc. This is further evidence that the scatter in the preconsolidation pressure is due to true soil variability rather than sample disturbance.

Figure 4.16b plots depth versus OCR. The figure shows the average OCR for boreholes S2 and S3 and the average OCR for borehole SMC-1. Based on its geologic and stress history, the top portion of the clay was expected to be normally consolidated to somewhat overconsolidated, and the bottom portion normally consolidated. As the figure shows, this was not the case. The site presents a fairly constant OCR of 1.54 ± 0.22SD

with depth. This value is in accordance with values reported by Zeevaert (1949) and Mesri et. al. (1975). Zeevaert reports an average OCR of 1.5 for a vast number of samples within the lake zone, and Mesri et al. (1975) reports an OCR of 1.5 for the samples they studied.

The most significant aspect of the stress history occurs below a depth of -26m. It is well documented in the literature that the acquifer underlying México City has been exploited since the 1930's. The exploitation of the acquifer has resulted in a decrease of the pore pressure, an increase of the effective overburden stress, and hence consolidation of the clay deposit. As shown in Chapter 2, pore pressure dissipation starts approximately at a depth of -26m. Therefore, the clay stratum below -26m is in a continuous process of consolidation. This implies that the soil below a depth of -26m should be normally consolidated, based on the widely accepted formation process of the deposit presented in Chapter 2.

The fact that the bottom portion of the deposit does not seem to be normally consolidated (from the results of the consolidation tests) raises some interesting questions. In particular, how can the clay deposit be overconsolidated if it is undergoing a continuous consolidation process? Table 4.6 describes common preconsolidation pressure mechanisms which may be responsible for the overconsolidation of a soil deposit. The OCR profile may be explained in three different ways, each with its own implications.

(1) The clay deposit was formed under higher stresses than previously believed. This would imply that the regional settlement of México City corresponds to the recompression of the clay deposit, rather than the virgin compression. Once the clay deposit would become normally consolidated, regional settlement would increase. This scenario is highly unlikely since the breaks in the effective stress and preconsolidation pressure curves both occur at approximately -26 m.

(2) The apparent OCR was caused by drained creep (secondary compression), as defined by Jamiolkowski et al. (1985). This would imply that the rate at which the

effective overburden stress is increased by pore pressure dissipation is slower than the rate of secondary consolidation. This scenario would only be possible under if "Theory B" of secondary consolidation is valid.

(3) The apparent OCR is caused by physio-chemical mechanisms, as defined by Jamiolkowski et al. (1985). Although the mechanisms are not completely understood, some probable mechanisms contributing to the overconsolidation of the deposit are natural cementation due to silica, or thixotropy.

At this time no definite conclusion can be drawn as to the reasons why the OCR is constant with depth (OCR≈1.5).

4.5 CONSOLIDATION PROPERTIES

4.5.1 Compressibility

4.5.1.1 *Compression Index and Compression Ratio*

The virgin compression index (Cc) and virgin compression ratio ($CR=Cc/1+e_0$) were calculated for each CRSC, CK_0UDSS, and CK_0U triaxial test. Figure 4.18 plots depth versus Cc, and Figure 4.19 plots depth versus CR, and both values are listed in Tables 4.1, 4.2, and 4.3. Most of the compression curves encountered in this investigation were "S-shaped", characterized by a decreasing slope of the virgin compression line after an axial strain greater than 25%. The values of Cc and CR reported are those corresponding to the maximum (steepest) slope of the virgin compression line. In most cases, this portion of the curve was in the interval between 1.1 to 1.35 times the preconsolidation pressure.

As Figures 4.18 and 4.19 show, there is significant scatter in both Cc and CR with depth. The scatter is probably caused by the clay's heterogeneity. In some cases, at the same depth, the values of Cc and CR from triaxial tests are slightly higher than those from CRSC and DSS tests. As mentioned earlier, this is probably due to lack of rigid confinement and local instability of the sample during triaxial testing.

The values of Cc range from 2 to 12 and the approximate average is 6. The values of CR range from 0.5 to 1.5 and the approximate average is 0.9. There is so much scatter in the data that it is not practical to report a precise average value for the deposit, since it would not be representative. Section 4.5.1.4 will present an equation to estimate Cc based on the initial water content of the sample.

Comparison of the values of Cc and CR determined for each borehole, S2 and S3, did not give any indication as to which borehole experienced a greater amount of disturbance.

4.5.1.2 *Recompression Index and Recompression Ratio*

The recompression index (Cr) and recompression ratio ($RR=Cr/1+e_o$) were calculated for each CRSC, CK_oU direct simple shear and triaxial test, and the values are listed in Tables 4.1, 4.2, and 4.3. The recompression index and recompression ratio are important for construction considerations with respect to loading up to the preconsolidation pressure. Usually Cr and RR are defined by the slope of the line which passes through the point at which the reload curve intersects the unload curve and through the minimum vertical consolidation stress to which the sample was unloaded. No unload-reload cycles were performed during CK_oUDSS and CK_oUTX tests, and only two CRSC tests were unloaded and reloaded. The values of Cr and RR reported were calculated from the initial reload portion of the curve in the interval between 0.5 and 0.75 times the overburden stress. Figure 4.18 plots depth versus Cr, and Figure 4.19 plots depth versus RR.

There is a significant amount of scatter in the data. The values of Cr range from 0.15 to 0.6 and the approximate average value is 0.3. The values of RR range from 0.02 to 0.07 and the approximate average value is 0.04. Figure 4.19 shows a possible trend of decreasing RR with depth. As seen in the figure, CRS77 has a much higher recompression slope than any other test due to sample disturbance associated with the specimen as

discussed in Section 4.3.1. Tests CRS84 and TX228 also have slightly higher recompression slopes than the tests performed on specimens from the same depth. Section 4.5.1.4 will present an equation to estimate Cr based on the natural water content of the specimen.

The comparison of Cr and RR reported for each borehole, S2 and S3, did not provide enough information to determine which borehole experienced the larger amount of disturbance.

4.5.1.3 *Swell Index and Swell Ratio*

The swell index (Cs) and swell ratio ($SR=Cs/1+e_o$) were calculated for most of the CRSC tests, and the values are listed in Table 4.1. Usually, the swell ratio and swell index are defined by the slope of the line which passes through the maximum vertical consolidation stress and the unloading curve at an OCR of 10. In order to obtain good swelling data, CRSC tests must be allowed to dissipate excess pore pressures and to undergo a cycle of secondary compression at the maximum consolidation stress (usually 24 hrs). If pore pressures are not allowed to dissipate before unloading, the specimen will continue to deform in compression during the early stages of unloading. This alters the slope and shape of the swelling curve. The higher the excess pore pressure at the beginning of unloading, the more the specimen will deform in compression before swelling. In only two tests, CRS87 and CRS89, were the excess pore pressures allowed to completely dissipate before the initial unloading took place. These tests were then reloaded beyond the maximum vertical stress and unloaded without pore pressure dissipation. Figure 4.20a and 4.20b show both unloading curves for tests CRS87 and CRS89, respectively. It was found for both tests that the tangent slope at OCR=10 for the two unloading curves (with and without pore pressure dissipation) was the same (Figure 4.20). Based on this observation, Cs and SR were calculated as the tangent slope at OCR=10 for the rest of the tests.

Figures 4.18 and 4.19 plot depth versus Cs and depth versus SR, respectively. As with the other compressibility characteristics, there is a significant amount of scatter in the data. Also, there seems to be a trend of decreasing Cs and SR with depth. The values of Cs range from 0.1 to 0.8, with an approximate average of 0.4. The values of SR range from 0.02 to 0.10, with an approximate average of 0.05. Section 4.5.1.4 will present a method to estimate Cs based on recompression information.

4.1.5.4 *Compressibility Correlations*

Many researchers have shown that empirical correlations between liquid limit and compression index and between void ratio and compression index are significant. As mentioned in Chapter 3, there is a strong relationship between natural water content and liquid limit. In addition, void ratio is directly proportional to water content (Gw=Se). Therefore, for México City Clay, it is possible to establish a correlation between water content and compression index. Figure 4.21a shows the compression index versus natural water content of the specimen (W_n) and Figure 4.21b shows the recompression index versus natural water content. Figure 4.21a shows that there is a strong correlation between W_n and Cc for CRSC data.

Mesri et al. (1975) showed that for his samples of México City Clay, $Cc = 0.0259 \times W_n(\%)$. Figure 4.21a shows that this equation generally results in higher values of Cc than those obtained for this investigation. The probable cause for this discrepancy is that the Mesri et al. data was obtained from incremental oedometer tests loaded under a load increment of one. With these testing conditions, there are few data points in the vicinity of σ'_p and therefore, significant judgment is required by the engineer to construct the compression curve. This might lead to an overestimate of the preconsolidation pressure and the virgin compression slope.

Based on a second order regression performed on all data from this investigation, the following equation is suggested to calculate the maximum compression index from the natural water content of the soil:

$$Cc = \frac{-48.9 + [2386 - (-10 * (62.6 - W_n\%))]^{0.5}}{-5.1} \quad \text{.....(4.8)}$$

The r value of the 2nd order regression is 0.794. Since the regression was performed on a limited data set, Equation 4.8 will yield incorrect values of Cc for natural water contents above 290%. Marsal and Mazari (1956) present statistical data between water content and a_v, the coefficient of compressibility, that suggest that the relationship between water content and compressibility is exponential, especially beyond water contents of 300%.

Figure 4.21b shows that there is a strong relationship between the recompression slope and natural water content. Additionally, this plot substantiates the fact that CRSC tests CRS77 and CRS84 experienced sample disturbance, since both tests plot a significantly higher than the trend. The fact that test CRS73 plots below the trend suggests that the structure of the sample may have some degree of cementation. The following equation, obtained from a second order regression, is suggested to calculate the initial recompression index (between 0.5 and 0.75 σ'_{vo}) based on the natural water content.

$$Cr = \frac{-719 + [517433 - (-2429 * (83.9 - W_n\%))]^{0.5}}{-1214} \quad \text{.....(4.9)}$$

The r value of the 2nd order regression is 0.859. Since the regression was performed on a limited data set, Equation 4.9 will yield incorrect values of Cr for natural water contents above 290%.

Figure 4.22 shows depth versus Compressibility Ratios. As shown in the figure the ratio between recompression and compression (RR/CR or Cr/Cc) remains fairly constant with depth with an average of 6.19% ± 2.455SD (CRS77 was not used to calculate the average). The ratio of Cr/Cc using values of Cr and Cc estimated with

Equations 4.8 and 4.9 increases with water content. Mesri and Castro (1987) report a value of Cr/Cc = 6% for brown México City Clay (Mesri and Castro definitions of Cr and Cc are defined in Figure 4.23). Figure 4.23 also shows the preconsolidation pressure resulting from secondary compression for brown México City Clay. The following facts suggest that secondary compression is the cause of the constant overconsolidation profile of the cathedral site: (1) The average value of the Cr/Cc ratio obtained during this investigation is consistent with the value reported by Mesri and Castro, and (2) according to Mesri and Rokhsar (1974) low values of Cr/Cc are generally associated with clays that have developed overconsolidation as a result of secondary compression.

As shown in Figure 4.22, the ratio of the recompression to the swell slope (Cr/Cs or RR/SR) remains fairly constant with depth with the exception of tests CRS77 and CRS84 which have been determined to be disturbed. The average value excluding tests CRS77 and CRS84 is 62% ± 22SD. Figure 4.22 also shows the ratio of the swell to the virgin compression slope (Cs/Cc or SR/CR). There is a significant amount of scatter in the data and the average is 8.88% ± 2.99SD. The literature suggests that the value of Cr/Cs ≈ 100%, and the Cs/Cc lies between 10 to 20%. The probable cause for the difference between the values obtained in this investigation and those suggested in the literature is different definitions of the compressibility indices. Generally, the Cr and Cs slopes are obtained from the unload-reload cycle of a consolidation test. As discussed in Section 4.5.1.2 and 4.5.1.3, the values of Cr and Cs presented in this thesis were obtained in a different fashion.

4.5.1.5 *Secondary Compression Index*

There is no established method to evaluate the secondary compression index, $C_{\alpha e}$ ($C_{\alpha e} = \Delta e/\Delta \log t$), for CRS consolidated tests in which the specimen is loaded to a particular consolidation stress, and then that stress is maintained for a specified amount of time. Since the time scale in such tests is the elapsed time and not the time for a single

stress increment (as in an incrementally loaded test), the time to the end of primary consolidation (t_p) cannot be determined using conventional graphical construction methods (i.e., log of time or square root of time method). Since C_α is based on log t, the value is dependent on where the time scale begins. No analytical technique presently exists to adjust the time scale to determine t_p for a given loading sequence.

Three CRSC tests and all CK_oU direct simple shear and triaxial tests were loaded to some maximum stress state, and that stress was maintained for an extended period of time (≈24 hrs). Sheahan (1991) developed a method to evaluate $C_{\alpha e}$ for these types of tests. It is based on two concepts: (1) the transition from primary to secondary consolidation can be identified as the point when excess pore pressures (Δu_e) are zero; and (2) the e-log t relationship during secondary compression is linear for a determined compression index (Cc) based on Mesri's $C_{\alpha e}$/Cc concept (e.g., Mesri and Godlewski 1977).

Figure 4.24 shows typical void ratio versus elapsed time behavior for test TX227 (OCR=2). The inset plot shows the complete loading time history while the outer plot is a close-up view of the end of loading (while final consolidation stresses are being held constant). As for all tests, the specimen was loaded at an axial strain rate which was slow enough to prevent any significant excess pore pressure. Thus, at the end of the constant rate of strain loading, the end of primary consolidation (EOP) occurs almost immediately. Secondary compression (see Figure 4.24) begins at almost the same point and appears as a rapid strain rate decay over time. The goal of Sheahan's method is to linearize the e-log t data in the secondary compression range so $C_{\alpha e}$ can be evaluated. This is accomplished by adjusting the elapsed time scale until the e-log t curve is linear, (i.e., until the r^2 (goodness of fit) value is maximized). Figure 4.25a shows typical triaxial data at the maximum vertical consolidation stress, and Figure 4.25b shows triaxial data after unloading to an OCR of 2. The rate of secondary consolidation was determined at the

maximum consolidation stress for all CK_oU DSS and TX tests, and for 3 CRSC tests. The results can be found in Tables 4.1 through 4.3.

Mesri and Godlewski (1977) developed the $C_{\alpha e}/Cc$ concept, which is based on the observation that the magnitude and behavior of C_α with time is directly related to the magnitude and behavior of Cc with consolidation pressure. According to Mesri and Godlewski, the value of $C_{\alpha e}/Cc$, together with the end of primary e-logσ'_v curve, completely define the secondary compression behavior of any soil. Figure 4.26 plots $C_{\alpha e}$ versus Cc for all tests. The values of Cc reported in the figure were calculated at the stress level at which secondary compression began, (i.e., as defined by Mesri and Castro 1987). As shown in the figure, there appears to be a consistent difference between triaxial data with respect to DSS and CRS data. This might be due to the lateral deformation experienced by the triaxial specimens during hold stress. Once again, this deformation is due to a lack of rigid confinement of the specimen. According to Mesri and Castro, the main reason for the scatter in $C_{\alpha e}$ versus Cc plots is the use of $C_{\alpha e}$ and Cc pairs that do not exactly correspond to each other. This might explain some of the scatter in the data shown in Figure 4.26. Additionally, the values of $C_{\alpha e}$ calculated by Sheahan's method might have some degree of error, and the estimated values of Cc from DSS and triaxial tests might also have some error associated with them (see Section 4.5.1.1). The average value of $C_{\alpha e}/Cc$ for this investigation is 0.050 ± 0.009SD. Mesri has published 3 values of $C_{\alpha e}/Cc$ for México City Clay as follows:

(a) Mesri and Choi (1984) reported a value of $C_{\alpha e}/Cc = 0.046$.

(b) Mesri and Godlewski (1977) reported a value of $C_{\alpha e}/Cc = 0.03$ to 0.035.

(c) Mesri et al. (1975) reported a value of $C_{\alpha e}/Cc = 0.3$.

The author believes that the most accurate value of $C_{\alpha e}/Cc$ is that reported by Mesri and Choi, since Mesri and Godlewski used data from Mesri et al. which is probably biased by a loading schedule based on a load increment ratio of one.

4.5.2 Flow Properties

4.5.2.1 *Coefficient of Consolidation*

Typical consolidation data resulting from a CRSC tests are shown in Figure 4.27 for test CRS89. Figure 4.27a presents the compression curve, and Figure 4.27b plots the coefficient of consolidation (c_v) versus the vertical consolidation stress for both loading and unloading portions of the test. The values of c_v from CRSC tests are calculated from the permeability and compressibility using the following equation:

$$c_v=(k_v/m_v)\ x\ \gamma_w \quad (4.10)$$

were k_v=the permeability for vertical flow; $m_v=\Delta\varepsilon/\Delta\sigma'_v$; and γ_w=unit weight of water. The data show that during loading c_v decreases during initial recompression and then remains constant in the normally consolidated region. All CRSC tests were characterized by a fairly constant value of c_v(NC). At the start of unloading, c_v increases substantially and then decreases steadily. During the second reloading and unloading, c_v decreases much faster than during the first loading and unloading. As expected the c_v-logσ'_{vc} curves for the first loading and unloading intersect near the preconsolidation pressure.

Figure 4.28 plots depth versus c_v (NC). The normally consolidated values of c_v were calculated by averaging the values of c_v in the region between 1.4 and 1.8 times the preconsolidation pressure. The average ± SD of c_v (NC) is reported for each test in Table 4.1. Figure 4.29 plots an apparent relation betwee c_v (NC) and the natural water content. The figure shows that, tests CRS82 and CRS85 plot above of the trend. As defined by Equation 4.10, c_v is directly proportional to the measured permeability. In section 4.5.2.2. it will be shown that the permeability results from tests CRS82 and CRS85 are not reliable due to low excess pore pressures. Therefore, the c_v values for the two tests are inaccurate. Ideally, 5 to 15% of excess pore pressure should be induced duirng constant rate of straining to obtain good quality c_v and permeability (k_v) data. The relationship presented in Figure 4.29 explains the scatter of c_v with depth. The coefficient

of consolidation is a function of the W_n, and it was shown in Chapter 3 that the water content changes significantly with depth. Therefore c_v should significantly with depth.

Based on a linear regression on the data from this investigation (excluding CRS82 and CRS85) the author suggests the use of the following equation to estimate values of c_v (NC) from the natural water content:

$$\log c_v \text{ (NC)} = 7.383 + (-4.65 \times \log W_n \text{ (\%)}) \quad SD\pm 0.316 \quad \text{.....(4.11)}$$

The only value of c_v found in the literature is from Marsal and Mazari (1956). They report an average value of 0.001 cm^2/sec, but this value is questionable due to discrepancies between their measured consolidation curves and Terzaghi's theoretical consolidation curve.

4.5.2.2 *Coefficient of Permeability*

The results presented for the permeability coefficient (k_v) are based on all CRSC tests. Typical e - log k_v data resulting from a CRSC test is shown in Figure 4.30 for test CRS76. Figure 4.30a presents a typical e-log k_v curve during loading, and Figure 4.30b presents the same curve during unloading. The values of k_v from CRSC tests are calculated using the following equation:

$$k_v = 1/2\ [(\varepsilon^{\circ} \gamma_w H^2)/U_b] \quad \text{.....(4.12)}$$

were γ_w= unit weight of water; H= drainage height; U_b= base excess pore pressure; and ε°= strain rate. The data show that there is a nearly linear relationship between the void ratio and the log of the permeability. Permeability decreases as the void ratio decreases during loading, and permeability increases as the void ratio increases during unloading. The slope of the of e - log k_v line is denoted by C_k. As shown in Figure 4.30a there is an initial phase were the data is no good since steady state conditions have not yet developed. Additionally, as the test progresses the slope of C_k increases until it reaches a constant value (i.e., linear relationship). The slope possibly changes due the closure of possible voids, fractures, and channels. The values of C_k presented in this investigation were

obtained from the portion of the e-log k_v curve where the slope remains constant. For some tests some degree of judgment was required to define the C_k line, as there was some scatter in the permeability data due to low excess pore pressures and noise associated with the equipment. Since k_v is inversely proportional to the excess pore pressure, 5 to 15% of excess pore pressure should be induced during constant rate of straining to obtain good quality data.

Figure 4.30b shows that the unloading portion of the e-log k_v curve has a different slope than the loading curve. There is some uncertainty in the measured permeability during unloading. Therefore no values of C_k are presented for unloading. To estimate the permeability at the in situ void ratio (k_o), it was assumed that C_k was constant through the entire loading range. The k_o values were backfigured by simply extending the C_k line back to the insitu void ratio, as shown in Figure 4.30a. The values of C_k and k_o for each test are reported in Table 4.1.

Figure 4.31 plots depth versus k_o. Although for most deposits k_o decreases with depth, for México City Clay it remains somewhat constant (except at a depth of -26m where large scatter and high values are present). Figure 4.32 plots the initial void ratio e_i versus k_o. The figure shows that there is no significant relation between e_i and k_o. This suggests that the value of k_o is not dependent on e_i, but rather is dependent on the initial micro-structure of the soil. As mentioned in Chapter 3, the initial micro-structure of the soil is probably controlled by the amount and geometry of the microfossils present.

Figure 4.32 also shows the change in k_v during the loading portion of each test. The change was calculated using C_k and e_i. As shown in the figure, the tests have almost parallel loading curves, with the exception of tests CRS82 and CRS85. The discrepancy in the slopes measured for these two tests, is attributed to the fact that very low excess pore pressures were induced during loading. The low excess pore pressures were probably the result of fractures in the specimen or voids between the sample and the ring that caused a hydraulic short.

Researchers have found that for most soils $C_k = 0.5e_i$. Figure 4.33 plots C_k versus e_i. The figure shows that this relationship slightly overestimates C_k for México City Clay. The average ratio of C_k to e_i for the data of this investigation is 0.45. The figure also shows that the results of tests CRS82 and CRS85 are anomalous. Based on the data from this investigation, the author suggests using the following equation to estimate C_k based on the initial void ratio:

$$C_k = 0.45 \times e_i \quad \text{.....(4.13)}$$

Figure 4.34 plots natural water content versus k_o. As shown in the figure there is a significant relationship between the values plotted. Based on a linear regression of the data from this investigation the following equation is suggested to calculate k_o based on the initial water content:

$$\log k_o = (-2.58 \times \log W_n(\%)) - 1 \quad SD \pm 0.317 \quad \text{.....(4.14)}$$

CRSC tests CRS82 and 85 were not used in the regression analysis.

Mesri et al. (1975) reported that there is a unique relationship between k_v and the void ratio for the samples of México City Clay they studied. Mesri et al. computed coefficients of permeability from incremental oedometer tests by fitting Terzaghi's theory of consolidation to plots of measured deformation against the square root of time. The results of this investigation have shown that k_v is a function of the initial microstructure of the specimen. Since Mesri's samples were all obtained at an approximate depth of -15m, it is very likely that all of the samples had the same microstructure. Therefore, it is not surprising that they found this unique relationship between k_v and e. It is important to acknowledge that this relationship is not valid for México City Clay as a whole, as there will be a unique relationship for each microstructure encountered in a specific deposit as shown in Figure 4.32.

4.6 LATERAL STRESS RATIO K_o

The lateral stress ratio (or coefficient of earth pressure) at rest (K_o) is an important soil parameter used in many geotechnical applications. The determination of K_o is necessary to estimate the in situ horizontal stress for soil deposits having a one-dimensional stress (strain) history ($\sigma'_{ho} = K_o\sigma'_{vo}$). A K_o profile was developed for the cathedral site using data from the consolidation phase of SHANSEP CK_oU triaxial tests.

An empirical equation developed by Schmidt (1966) and Alpan (1967) was used to relate the increase in K_o with OCR. The same equation was then used to estimate K_o as a function of OCR for the clay deposit beneath México City's cathedral. The equation is as follows:

$$K_o(OC) = K_c(NC) \times (OCR)^n \quad \text{.....(4.15)}$$

where $K_o(OC)$ equals the overconsolidated or in situ K_o; $K_o(NC)$ equals the normally consolidated value of K_o, as described below; and n is a parameter used to relate the change in K_o with OCR.

During the consolidation phase of a SHANSEP CK_oU triaxial test, K_o conditions are maintained by controlling the horizontal consolidation stress (σ'_{hc}) on the specimen so that volumetric strain (ε_v) always remains equal to the axial strain (ε_a), thus maintaining a constant cross sectional area. This process is controlled by the MIT automated triaxial testing system. Throughout the K_o consolidation phase, the lateral to vertical stress ratio is monitored. A typical one-dimensional compression curve and a plot of lateral stress ratio (K_c) versus log vertical effective stress are presented for triaxial test TX233, which was unloaded to an OCR of 2, in Figure 4.35. K_c decreases through the overconsolidated region until approximately the preconsolidation pressure, and then it increases. Once the soil is consolidated into the virgin compression region, K_c either becomes approximately constant or continues to increase. In some cases, K_c increased significantly. The value of K_c in the virgin compression region is referred to as the normally consolidated value of K_o ($K_o(NC)$).

Once the specimen is consolidated to the maximum desired consolidation stress (σ'_{vm}), this stress is maintained for 24 hrs to allow for the dissipation of excess pore pressures and one cycle of secondary consolidation. For this study, K_o(NC) was calculated as the average value of K_c during the hold stress portion of the test (i.e., at $\sigma'_{vc} = \sigma'_{vm}$).

The results of the consolidation phase of 10 SHANSEP CK_oU triaxial tests were used to evaluate the normally consolidated value of K_o at the cathedral site. The mean values of K_o(NC) obtained during virgin compression are listed in Table 4.3, and Figure 4.36 plots depth versus K_o(NC). As shown in the figure, K_o(NC) remains fairly constant with depth and the average value is 0.36 ± 0.04SD. Lo (1962) reports an average value for K_o(NC) of 0.33, and a ϕ'(NC) of 47°, for K_o consolidated México City Clay triaxial samples. Diaz-Rodriguez et al. (1992) report a value for K_o(NC) of 0.3, and a ϕ'(NC) of 43°, for one K_o consolidated México City Clay triaxial sample.

The lateral to vertical stress ratio during unloading, K_o(OC), is used to develop an estimate of the n parameter, which represents the overconsolidated behavior of K_o. Four of the ten SHANSEP triaxial tests were used to determine the behavior of K_o during unloading. The tests represent OCRs of 1.25, 1.66 and 2. It should be noted that the K_o unloading data may not be very reliable as it was measured at very low OCRs. Figure 4.37 presents the results from the four overconsolidated tests. The lateral stress ratio during unloading (K_o(OC)) is normalized to the normally consolidated lateral stress ratio K_o(NC) and plotted versus OCR on a log-log plot. At OCRs below 1.25 there is a lot of scatter in the data since computer control requires some time before steady conditions develop. Initial scatter does not affect the results so long as the slope of the unloading path is not affected. The important information from this figure is the slope of the lines, not the intercept. An n value of 0.58 was chosen to relate the increase in K_o with OCR at the cathedral site.

A constant value of in situ K_o=0.45 was estimated for the clay deposit at the cathedral site. This value was calculated using the final estimate of OCR with depth presented in Figure 4.15b, Equation 4.15, K_o(NC) = 0.36, and an "n" value of 0.58. This estimate assumes that the soil was unloaded to the current OCR, which is highly unlikely. Since the nature of the overconsolidation of the deposit cannot be precisely determined at this time, the actual K_o may be somewhat different than predicted. Nevertheless the value should fall between 0.36 and 0.45.

Jaky (1944) proposed the following equation to estimate K_o for NC soils:

$$K_o = 1\text{-}\sin\phi' \quad (4.16)$$

Figure 4.38 plots the measured K_o(NC) values versus 1-sinϕ_{mo} and 1-sinϕ'_p for SHANSEP CK_oUC/E OCR=1 tests, where ϕ'_{mo} is the friction angle at maximum obliquity and ϕ'_p is the friction angle at peak strength. One of the four values at maximum obliquity from the compression tests fall within the 1-sinϕ' + 0.05 line, whereas none of the extension tests fell within this line. The rest of the data plotted above the 1-sinϕ' + 0.05 line. Although all the values are well within the range of scatter reported in the extensive summary by Mayne and Kulhwany (1982), the data show that the extension ϕ'_{mo} is very often too high. The figure also shows the data reported by Lo (1962) and Diaz-Rodriguez et al. (1992) that plot in the vicinity of the data from this investigation.

4.7. CONCLUSIONS

4.7.1 Sample Quality

After analyzing and comparing consolidation data from all tests, it is not possible to determine which of the boreholes yielded the best quality samples. There does not seem to be any difference in sample quality between samples obtained from Shelby tubes and those obtained with the Acker fixed piston sampler. Unless the fixed piston sampler is redesigned to reduce sampling time, the author suggests the use of Shelby tubes to sample México City Clay. This suggestion is based on sampling time and cost. Additionally, the author suggests; (1) not using drilling fluid (bentonite slurry) due to the possibility of hydraulic fracturing, and (2) the use of casing or hollow stem augers to stabilize the borehole. Data from this investigation suggest that disturbance due to the unloading of soil is significantly less than the disturbance caused by hydraulic fracturing. Also, the author suggests the use of the extrusion technique detailed in Chapter 2, based on extensive data produced by MIT and the results of this investigation.

Probably the best techniques presently available for determining sampling disturbance are; (1) plotting the axial strain at the overburden versus the vertical in situ stress and (2) comparison of compression curves. Unfortunately, these techniques only allow for a relative comparison of results. The analysis of the results showed that CRSC tests CRS77 and CRS84, and triaxial test TX228 were affected by sample disturbance. This conclusion was drawn based on the following rationale:

CRS77- highest axial strain at the effective overburden stress; low preconsolidation pressure (OCR=1); and high recompression index.

CRS84- high axial strain at the effective overburden stress; somewhat low preconsolidation pressure; high recompression index; and low compression index.

TX228- high axial strain at the effective overburden stress; somewhat low preconsolidation pressure; and slightly high recompression index.

Additionally, the analysis of the results showed that the measured values of the coefficient of consolidation and the coefficient of permeability for CRSC tests CRS82 and CRS85 are anomalous, due to low excess pore pressures induced during consolidation.

4.7.2 The Soil

It was found that México City Clay has a constant OCR profile of 1.5 with depth. The author believes that secondary compression is the principle cause of the preconsolidation pressure. Unfortunately, at this point in time there is not enough information to confirm this hypothesis.

The following section summarizes the compressibility results from this investigation.

(1) The maximum Compression Index (Cc) of the soil tested ranges between 2 and 12, and the approximate average is 6. The maximum Compression Ratio (CR) ranges between 0.5 and 1.5, and the approximate average is 0.9. A correlation between Cc and the initial water content of the specimen was found. It is possible to estimate Cc based on the initial water content using the following equation (only valid for water contents below 290%):

$$Cc = \frac{-48.9 + [2386 - (-10 * (62.6 - W_n\%))]^{0.5}}{-5.1} \quad \text{.....(4.8)}$$

(2) The Recompression Index (Cr) and the Recompression Ratio (RR) were calculated from the initial reload portion of the curve in the interval between 0.5 and 0.75 times the overburden pressure. The values of Cr range from 0.15 to 0.6, and the approximate average is 0.3. The values of RR range from 0.02 to 0.07, and the approximate average is 0.04. The data might suggest a possible trend of decreasing RR with depth. It is possible to estimate Cr from the initial water content using the following equation (only valid for water contents below 290%):

$$Cr = \frac{-719 + [517433 - (-2429 * (83.9 - W_n\%))]^{0.5}}{-1214} \quad \text{.....(4.9)}$$

(3) The Swell Index (Cs) and the Swell Ratio (SR) were calculated as the tangent slope of the unloading curve at OCR=10. The data suggest a possible trend of decreasing Cs and SR with depth. The values for Cs range from 0.1 to 0.8, with an approximate average value of 0.4. The values for SR range from 0.02 to 0.10, with an approximate average value of 0.05.

(4) The following Compressibility Ratios were calculated: Cr/Cc ≈ 6.2%; Cr/Cs ≈ 62%; Cs/Cc ≈ 9%. The ratio of Cr/Cc using values of Cr and Cc estimated with Equations 4.8 and 4.9 increases with water content.

(5) The ratio of the Secondary Compression Index to the Compression Index ($C_{\alpha e}$/Cc) equals 0.05.

The following section summarizes the flow properties results presented in this investigation.

(1) The average normally consolidated value of the coefficient of consolidation varies significantly with depth. The following equation explains the scatter of c_v with depth since c_v is a function of the natural water content and significant changes of water content with depth have already been shown.

$$\log c_v\,(NC) = 7.383 + (-4.65 \times \log W_n\,(\%)) \quad SD\pm 0.316 \text{.....(4.11)}$$

(2) The coefficient of permeability remains somewhat constant with depth (except at a a depth of -26m where large scatter and high values are present).

(3) C_k (slope of e vs. log k_v plot) equals 0.45 times the in-situ void ratio. The permeability at the insitu void ratio (k_o) can be estimated from the natural water content using the following equation:

$$\log k_o = (-2.58 \times \log W_n(\%)) - 1 \quad SD\pm 0.317 \text{.....(4.14)}$$

A Lateral Stress ratio (K_o) profile was developed for the cathedral site using data from the consolidation phase of SHANSEP CK_oU triaxial tests. The normally

consolidated K_O remains mostly constant with depth (average = 0.36). Additionally, a constant value of K_O = 0.45 with depth was calculated using an empirical equation developed by Schmidt (1966) and Alpan (1967). Since the nature of the OCR profile cannot be determined at this time, the actual K_O may be somewhat lower than predicted. The value should be between 0.36 and 0.45.

The most interesting aspect of this chapter of the thesis is the apparent relationship between water content and most compressibility and flow properties of the soil. This fact strongly suggests that the initial water content is dependent on the initial micro-structure of the soil. Using the equations presented throughout this chapter it is possible to estimate the compressibility and flow properties of a specimen based only on the specimens natural water content.

During the 1960's, Dr. Lambe at MIT expressed that he believed the behavior of cohesive soils could be understood through studying their microstructure. Data from this investigation strongly suggests that, for México City Clay, Dr. Lambe's hypothesis was correct. In order to fully understand the behavior of México City Clay, a thorough investigation of the clay's microstructure and the relationship between microstructure and compressibility and flow characteristics is necessary.

Table 4.1 Summary of Consolidation Results from CRSC Tests

Test Depth (m) Sample	W_n (%) e_i S_i (%)	W_{lc} G_s W_n (S=100%)	σ'_{vo} σ'_p (C) σ'_p (SE)	$\varepsilon_a@\sigma'_{vo}$ $\varepsilon_a@\sigma'_p$ SE ε^o_a (%/hr)	CR_{max} RR SR ΔOCR=10	Cc_{max} Cr Cs ΔOCR=10	$C_{\alpha e}$ Cc	c_v ±SD	Ck k_o	γ_t (t/m^3)
CRS73	277.11	307.09	1.09	1.89	1.196	9.106				
-12.71	6.62	2.37	2.27	6.56	0.024	0.185		6.32E-05	3.707	1.17
S2-1	99.3	279.32	2.24	0.60	0.098	0.747		1.86E-05	2.55E-08	
CRS75	211.17	242.70	1.11	2.03	0.647	3.967				
-14.36	5.14	2.39	2.15	6.38	0.033	0.205		9.53E-05	2.309	1.21
S2-3	98.3	215.06	2.02	0.59	0.087	0.534		2.72E-05	2.31E-08	
CRS76	309.02	339.62	1.09	3.03	0.722	6.267				
-12.37	7.67	2.46	1.55	7.54	0.062	0.536		7.02E-05	3.431	1.16
S3-1	99.1	311.79	1.55	0.58	0.084	0.728		3.46E-05	4.01E-08	
CRS77	300.23	331.34	1.10	10.02	0.688	6.038				
-13.56	7.77	2.56	1.04	10.11	0.123	1.080		1.01E-04	3.983	1.17
S3-1	98.9	303.52	1.11	0.58	0.053	0.465		2.02E-04	7.88E-08	
CRS79	196.98	225.54	1.44	2.48	0.894	5.165				
-24.12	4.77	2.41	2.40	5.95	0.031	0.177		2.18E-04	2.454	1.24
S2-4	99.4	197.93	2.43	0.58	–	–		6.77E-05	6.18E-08	
CRS80	236.11	265.99	1.52	2.96	0.816	5.381				
-25.63	5.60	2.35	2.54	7.01	0.047	0.311		7.21E-04	2.420	1.20
S3-6	99.2	238.30	2.44	0.58	–	–		2.57E-04	2.37E-07	
CRS82	152.50	197.32	1.47	2.09	0.414	2.228				
-24.76	4.38	2.58	4.94	9.68	0.024	0.129		4.65E-02	0.064	1.21
S2-5	89.8	169.77	5.10	1.32	0.042	0.226		1.11E-02	3.14E-05	
CRS83	265.60	304.65	1.87	2.75	1.507	12.135				
-28.71	6.95	2.51	3.16	7.11	0.044	0.351		1.58E-04	3.161	1.15
S2-7	95.9	276.89	3.06	0.76	–	–		3.47E-05	7.11E-08	
CRS84	169.63	198.81	1.52	4.84	0.498	2.668				
-25.66	4.35	2.54	1.94	7.06	0.063	0.334		1.63E-03	1.899	1.28
S2-6	99.0	171.26	1.96	0.57	0.026	0.139		3.95E-04	4.54E-07	
CRS85	273.50	328.21	1.45	3.61	0.657	5.633				
-24.36	7.57	2.52	2.51	8.78	0.046	0.396		4.00E-03	1.371	1.10
S3-4	91.0	300.40	2.66	0.70	0.053	0.454		3.86E-03	5.21E-06	
CRS87	205.21	234.82	2.79	2.50	0.805	4.740				
-35.45	4.89	2.36	4.33	5.41	0.037	0.221	0.102	4.18E-04	1.661	1.22
S2-9	99.0	207.20	4.06	0.57	0.028	0.165	2.566	8.20E-05	5.50E-08	
CRS88	114.74	153.82	1.47	2.34	0.336	1.434				
-24.73	3.26	2.58	4.29	6.76	0.028	0.120	0.057	8.45E-03	1.750	1.30
S2-5	90.7	126.36	4.26	0.55	0.038	0.162	1.434	8.91E-04	5.07E-07	
CRS89	262.76	294.41	1.08	2.88	0.742	5.611				
-12.27	6.56	2.46	2.12	7.52	0.043	0.324	0.256	1.49E-04	2.298	1.18
S3-1	98.5	266.67	2.06	0.57	0.047	0.355	5.610	–	6.44E-08	
CRS90	262.53	296.45	1.08	3.20	0.780	5.931				
-12.24	6.61	2.46	2.17	8.39	0.048	0.361		1.27E-04	3.401	1.17
S3-1	97.8	268.70	2.09	1.40	0.095	0.723		3.94E-05	4.61E-08	
CRS92	184.06	213.76	1.08	2.37	0.788	4.394				
-12.21	4.58	2.46	1.80	7.61	0.042	0.237		3.01E-04	2.306	1.25
S3-1	98.9	186.18	1.83	0.16	–	–		1.33E-04	1.32E-07	

Table 4.2 Summary of Consolidation Results from SHANSEP CK_oUDSS Tests

Test Depth (m) Sample	W_n (%) e_i S_i (%)	Wlc G_s Wn (S=100%)	σ'_{vo} σ'_p (C) σ'_p (SE)	$\varepsilon_a@\sigma'_{vo}$ $\varepsilon_a@\sigma'_p$ SE ε°_a (%/hr)	CR max RR	Cc max Cr	$C_{\alpha e}$ Cc	Test OCR σ'_{vm} σ'_{vc}	γ_t (t/m^3)	Remarks
DSS311	272.89	322.22	1.10	4.55				1		
-13.56	7.39	2.51	1.78	8.14	0.931	7.809	0.349	2.809	1.12	
S2-2	92.7	294.42	1.69	0.75	0.070	0.590	6.791	2.809		
DSS315	298.19	328.21	1.10	4.05				1		
-13.51	7.54	2.51	1.83	7.72	0.880	7.513	0.371	2.215	1.17	
S2-2	99.3	300.40	1.71	0.75	0.061	0.525	7.512	2.215		
DSS317	294.49	326.45	1.10	4.39				1		Cc not reliable. Secondary
-13.46	7.50	2.51	1.67	6.44	—	—	—	1.792	1.17	Compression data no good
S2-2	98.6	298.65	1.40	0.75	0.062	0.524	—	1.792		due to Equip. Problems
DSS318	314.83	343.74	1.08	3.31				1		
-12.34	7.77	2.46	1.87	7.11	0.793	6.948	0.337	2.228	1.16	
S3-1	99.7	315.89	1.74	0.75	0.053	0.472	6.948	2.228		
DSS320	228.84	261.58	1.08	3.17				1		To close to preconsolidation
-12.31	5.75	2.46	1.87	6.48	–	—	—	2.219	1.2	pressure to obatin reliable
S3-1	97.8	233.90	1.83	0.75	0.050	0.330	—	2.219		estimate of Cc
DSS322	245.24	276.55	1.43	3.54				1		
-24.06	6.00	2.41	2.28	7.18	0.788	5.521	0.203	4.025	1.19	
S2-4	98.6	248.84	2.24	0.75	0.051	0.354	4.198	4.025		
DSS324	274.04	303.49	1.52	4.35				1		
-25.61	6.65	2.35	2.54	8.53	0.835	6.380	0.230	3.588	1.15	
S3-6	96.9	275.73	2.52	1.00	0.061	0.472	5.949	3.588		
DSS327	283.53	314.28	1.87	5.39				1		
-28.79	7.19	2.51	2.61	8.43	1.136	9.301	0.311	3.831	1.18	
S2-7	99.0	286.49	2.57	0.50	0.073	0.594	7.645	3.831		
DSS330	294.13	328.32	1.11	3.77				1.250		
-14.28	7.15	2.38	1.73	7.33	0.621	5.506	0.258	3.028	1.15	
S3-3	97.9	300.50	1.74	0.50	0.056	0.453	5.057	2.420		
DSS337	287.77	320.71	1.52	5.58				1.601		Secondary Compression
-25.58	6.86	2.35	1.88	6.70	0.611	4.800	—	3.754	1.16	Data no good due to
S3-6	98.6	291.92	1.78	0.50	0.085	0.669	—	2.345		Equipment Prob.
DSS340	281.52	310.33	1.86	4.16				2.000		
-28.68	7.09	2.51	2.80	7.58	1.418	11.463	0.356	4.009	1.18	
S2-7	99.6	282.55	2.72	0.49	0.062	0.502	8.128	2.004		
DSS342	259.54	294.14	2.77	4.01				1		
-35.31	6.29	2.36	4.15	6.44	0.790	5.750	0.269	6.011	1.16	
S2-9	97.4	266.40	3.94	0.50	0.035	0.255	5.755	6.011		

Table 4.3 Summary of Consolidation Results from SHANSEP CK_oUC/E Triaxial Tests

Test Depth (m) Sample	W_n (%) e_i S_i (%)	Wlc G_s W_n*	σ'_{vo} σ'_p (C) σ'_p (SE)	$\varepsilon_a@\sigma'_{vo}$ $\varepsilon_a@\sigma'_p$ SE ε^e_a (%/hr)	CR_{max} RR	Cc_{max} Cr	$C_{\alpha e}$ Cc	Test OCR σ'_{vm} σ'_{vc}	NC K_o / OC K_o ε_a σ'_{vm} (%) ε_v σ'_{vm} (%)	B U_b	γ_t (t/m^3)	Remarks
TRIAXIAL COMPRESSSION												
TX201	278.00	276.12	1.11	2.747				1	0.388			
-14.30	6.41	2.58	1.98	6.720	0.559	4.144	0.259	2.540	14.031	0.98	1.32	
S2-3	112.0	248.41	1.95	0.09	0.053	0.395	4.414	2.540	13.965	2.06		
TX221	232.40	267.73	1.98	2.522				1	0.362			
-29.51	5.79	2.41	2.81	5.857	0.951	6.453	0.373	3.412	16.307	0.98	1.18	
S2-8	97.0	240.04	2.79	0.51	0.042	0.285	6.453	3.412	15.893	3.14		
TX222	296.20	266.29	1.10	3.000				1	0.398			
-13.46	7.70	2.56	1.51	6.615	0.949	8.251	0.545	1.830	16.360	0.99	1.16	
S3-2	99.0	238.60	1.49	0.30	0.056	0.504	8.251	1.830	16.250	3.37		
TX223	234.90	350.98	2.78	1.742				1	0.335			Rate of Strain to Slow to Impede Secondary Compression
-35.37	5.63	2.36	3.75	4.790	0.958	6.351		4.468	12.020	0.98	1.19	
S2-9	98.0	323.12	3.67	0.09	0.042	0.277		4.468	11.920	3.04		
TX225	277.20	212.48	1.48	2.910				1.240	.332/.352			
-24.96	6.99	2.55	2.32	5.810	0.913	7.295	0.338	2.676	13.878	0.98	1.20	
S3-5	101.0	184.90	2.25	.09, .3	0.056	0.449	7.295	2.150	13.774	3.34		
TX226	321.10	298.50	1.09	2.140				1.650	.294/.375			Final Rate of Strain to Slow to Impede Secondary Compression
-12.57	7.66	2.37	1.79	5.470	1.239	10.727		1.982	12.659	1.00	1.15	
S2-1	99.0	270.75	1.77	.44..09..27..11	0.039	0.337		1.201	12.504	3.20		
TX227	184.90	276.59	1.43	2.380				2	.366/.427			
-23.98	4.46	2.41	2.26	5.300	1.096	6.093	0.413	2.515	13.390	0.98	1.26	
S2-4	100.0	248.88	2.20	0.40	0.040	0.220	6.093	1.256	13.167	3.29		
TRIAXIAL EXTENSION												
TX228	266.50	328.40	1.97	4.100				1	0.373			
-29.41	6.53	2.41	2.67	7.300	1.229	9.249	0.496	2.940	16.596	1.00	1.17	
S2-8	98.0	270.95	2.51	0.28	0.064	0.482	9.249	2.940	16.488	3.31		
TX230	246.60	301.80	1.10	2.759				1	0.398			
-13.37	6.25	2.51	1.56	5.617	0.727	5.271	0.356	1.914	15.477	1.00	1.20	
S2-2	99.0	274.04	1.56	0.29	0.046	0.330	5.271	1.914	15.517	3.30		
TX233	211.70	232.09	1.51	2.190				1.960	.317/.464			
-25.47	4.81	2.35	2.34	4.910	0.795	4.616	0.218	2.761	12.670	1.00	1.26	
S3-6	104.0	204.47	2.25	0.51	0.041	0.240	4.616	1.403	12.600	3.27		

* Calculated assuming S=100%

Table 4.4 Sources of Sample Disturbance in Cohesive Soils (from Jamiolkowski et al. 1985)

Heading	Item	Remarks
1. Stress Relief	1.1. Change in stresses due to drilling hole	. Excessive reduction in σ_v due to light drilling mud causes excessive deformations in extension
		. Overpressure causes excessive deformations in compression
	1.2. Eventual removal of in situ shear stress	. Resultant shear strain should usually be small
	1.3. Eventual reduction (removal) of confining stress	. Loss of negative u (soil suction) due to presence of coarser grained materials
		. Expansion of gas (bubbles and/or dissolved gas)
2. Sampling Technique	2.1. Sampler geometry: Diameter/Length Area ratio Clearance ratio Accessories -- piston, coring tube, inner foil, etc.	These variables affect:
		. Recovery ratio
		. Adhesion along sample walls
		. Thickness of remolded zone along interior wall
	2.2. Method of advancing sampler	. Continuous pushing better than hammering
	2.3. Method of extraction	. To reduce suction effect at bottom of sample, use vacuum breaker
3. Handing procedures	3.1. Transportation	. Avoid shocks, changes in temperature, etc.
	3.2. Storage	. Best to store at in situ temperature to minimize bacteria growth, etc.
		. Avoid chemical reactions with sampling tube
		. Opportunity for water migration increases with storage time
	3.3. Extrusion, trimming, etc.	. Minimize further straining

Table 4.5 Major Types of Thin–Walled Tube Samplers (from Gilbert 1992; after Marcuson and Franklin 1979)

Sampler	Procedure	Applicability	Limitations and Pitfalls
a. Fixed-Piston Sampler	Thin-walled tube is pushed into soil, with fixed piston in contact with top of sample during push. (US Army 1972, Ch. 3; Hvorslev 1949, pp 128-130; USBR 1960, pp 349-379.)	Undisturbed samples in cohesive soils, silts, and sands, above or below the water table.	Some types do not have positive prevention of piston movement.
b. Hydraulic Piston Sampler (Osterberg)	Thin-walled tube is pushed into soil by hydraulic pressure. Fixed piston in contact with top of sample during push. (Osterberg 1952 and 1973; US Army 1972, Ch. 3).	Undisturbed samples in cohesive soils, silts, and sands, above or below the water table.	Not possible to limit the length of push or determine amount of partial sampler penetration during push. Earlier version does not have vacuum breaker in piston.
c. Stationary Piston Sampler	Thin-walled tube is pushed into soil. Piston at top of sample is free to move upward but is restrained from downward movement by a friction lock.	Undisturbed samples in stiff cohesive soils; representative samples in soft to medium cohesive soils, silts, and some sands.	Piston does not provide positive control of specific recovery ratio.
d. Free-Piston Sampler	Thin-walled tube is pushed into soil. Piston rests on top of soil sample during push (US Army 1972 Ch. 3; Hvorslev 1949, p 131).	Undisturbed samples in stiff cohesive soils; representative samples in soft to medium cohesive soils, and silts.	Not suitable for sampling in cohesionless soils. Free piston provides no control of specific recovery ratio.
e. Open-Drive Sampler	Thin-walled, open tube is pushed into soil (US Army 1972, p 133; USBR 1960, pp 361-367).	Undisturbed samples in stiff cohesive soils. Representative samples in soft to medium cohesive soils and silts.	Not suitable for sampling in cohesionless soils. No control of specific recovery ratio.
f. Pitcher Sampler	Thin-walled tube is pushed into soil by spring above sampler while outer core bit reams hole. Cuttings removed by circulating drilling fluid (Terzaghi and Peck 1968, pp 310-312).	Undisturbed samples in hard, brittle, cohesive soils and sands with cementation. Representative samples in soft to medium cohesive soils and silts. Disturbed samples may be obtained in cohesionless materials with variable success.	Frequently ineffective in cohesionless soils.
g. Denison Sampler	Hole is advanced and reamed by core drill while sample is retained in nonrotating inner core barrel with core-catcher. Cuttings removed by circulating drilling fluid. (US Army 1972, pp 312-313; USBR 1960, pp 355-361).	Undisturbed samples in stiff to hard cohesive soil, sands with cementation, and soft rocks. Disturbed samples may be obtained in cohesionless materials with variable success.	Not suitable for undisturbed sampling in loose cohesionless soils or soft cohesive soils.
h. Submersible Vibratory (Vibracore) Sampler	Core tube is driven into soil by vibrator. (Tirey 1972)	Continuous representative samples in unconsolidated marine sediments.	Because of high area ratio and effects of vibration, samples are disturbed.
i. Underwater Piston Corer	Core tube attached to drop weight is driven into soil by gravity after a controlled height of free fall. Cable-supported piston remains in contact with soil surface during drive (Noorany 1972).	Representative samples in unconsolidated marine sediments.	Samples may be seriously disturbed (McCoy 1972).
j. Gravity Corer	Open-core tube attached to drop weight is driven into soil by gravity after free fall (Noorany 1972).	Representative samples at shallow depth in unconsolidated marine sediments.	No control of specific recovery ratio. Samples are disturbed.

Table 4.6 Preconsolidation Pressure Mechanisms (For Horizontal Deposits with Geostatic Stresses) (from Jamiolkowski et al. 1985)

Category	Description	Stress History Profile	In situ Stress Condition	Remarks / References
A) Mechanical One Dimensional	1) Changes in total vertical stress (overburden, glaciers, etc.) 2) Changes in pore pressure (water table, seepage conditions, etc.)	Uniform with constant $\sigma'_p - \sigma'_{vo}$ (except with seepage)	K_o, but value at given OCR varies for reload vs. unload	Most obvious and easiest to identify
B) Desiccation	1) Drying due to evaporation vegetation, etc. 2) Drying due to freezing	Often highly erratic	Can deviate from K_o, e.g. isotropic capillary stresses	Drying crusts found at surface of most and deposits; can be at depth within deltaic deposits
C) Drained Creep (Aging)	1) Long term secondary compression	Uniform with constant σ'_p / σ'_{vo}	K_o, but not necessarily normally consolidated value	Leonards and Altschaeffl (1964); Bjerrum (1967)
D) Physico-Chemical	1) Natural cementation due to carbonates, silica, etc. 2) Other causes of bonding due to ion exchange, thixotropy, "weathering" etc.	Not Uniform	No Information	Poorly understood and often difficult to prove. Very pronounced in eastern Canadian clays, e.g. Sangrey (1972), Bjerrum (1973), Quigley (1980)

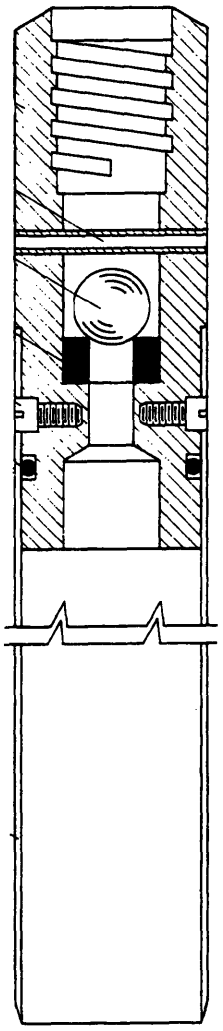

Shelby Open–Drive Sampler

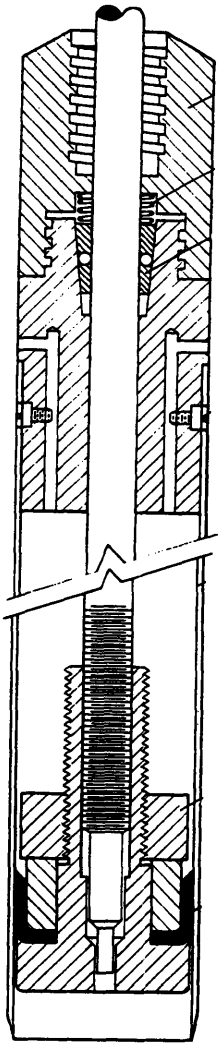

Fixed Piston Sampler

Figure 4.1 Schematic Drawings of an Acker 3" Fixed Piston Sampler and Shelby Open–Drive Sampler

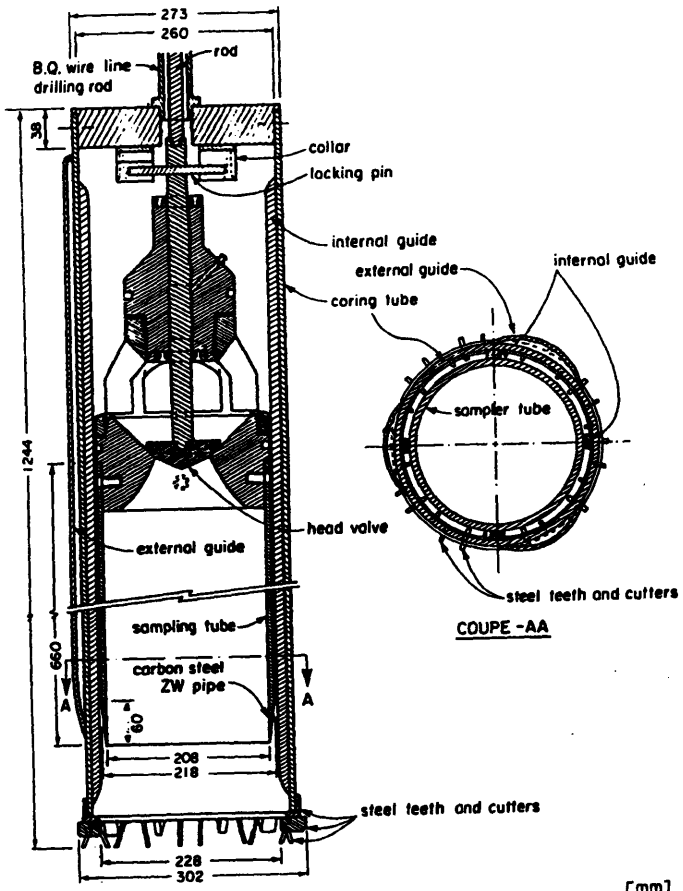

Drawing of the sampling and coring tubes.

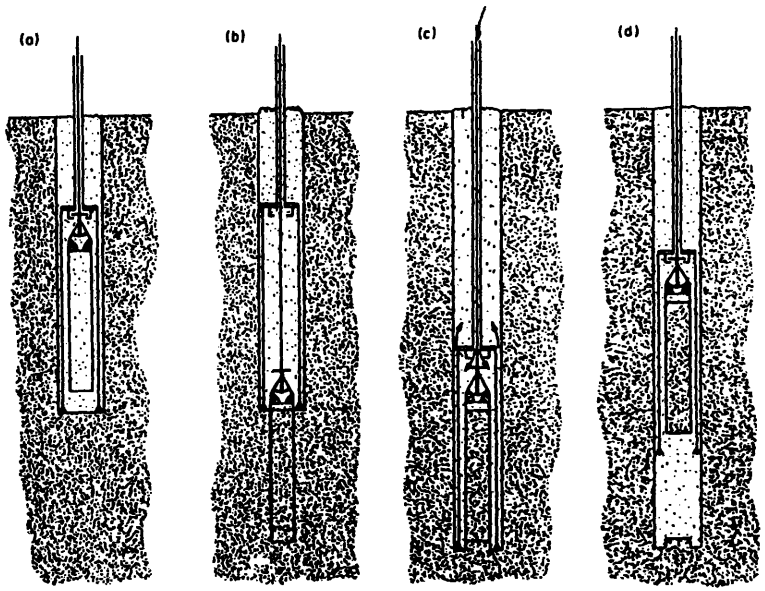

General operation of the sampler.

Figure 4.2 Schematic Drawing of La Rochelle et al. (1981) Sampler Design and Use

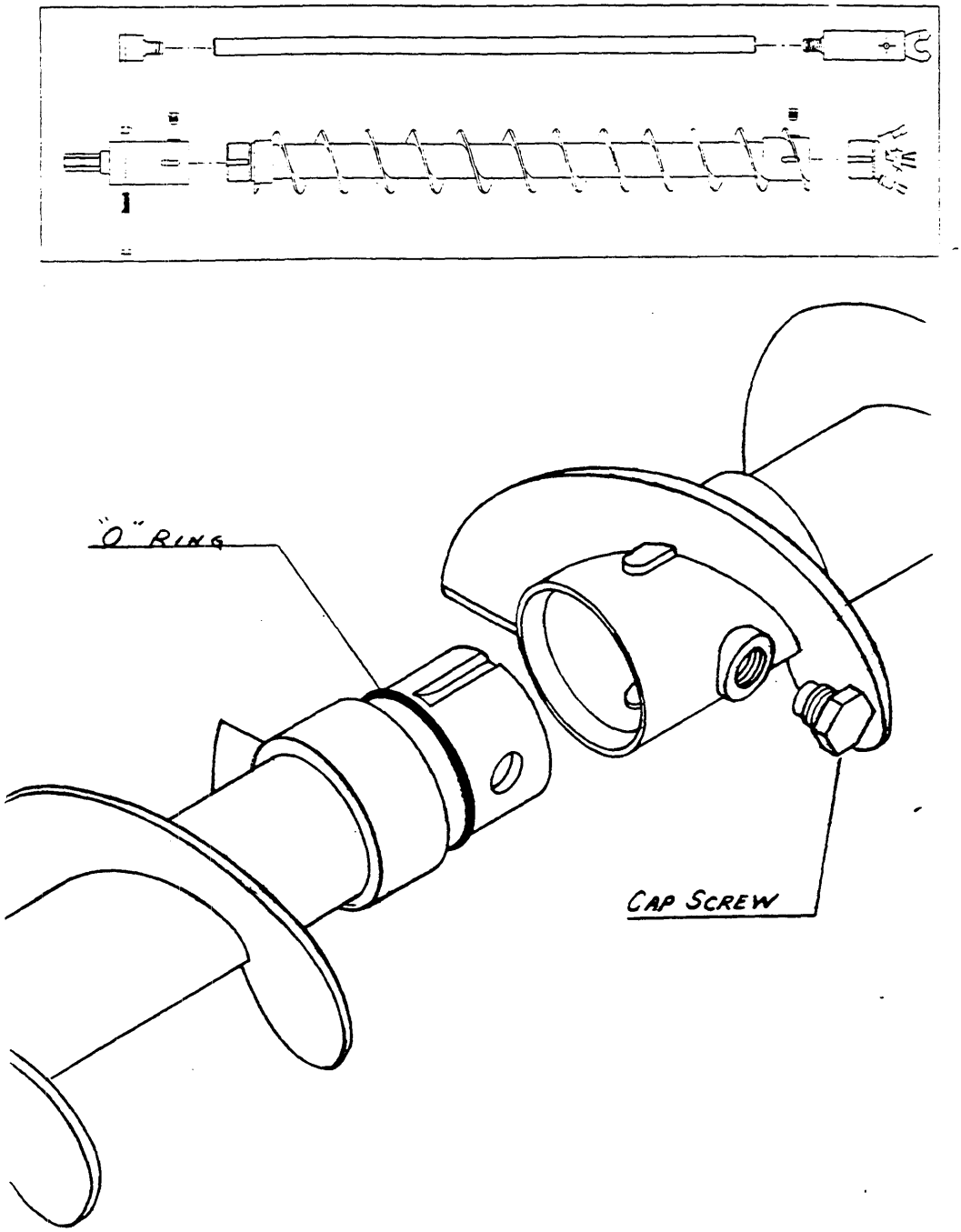

Figure 4.3 Schematic Drawing of a Hollow Stem Continuous Flight Auger

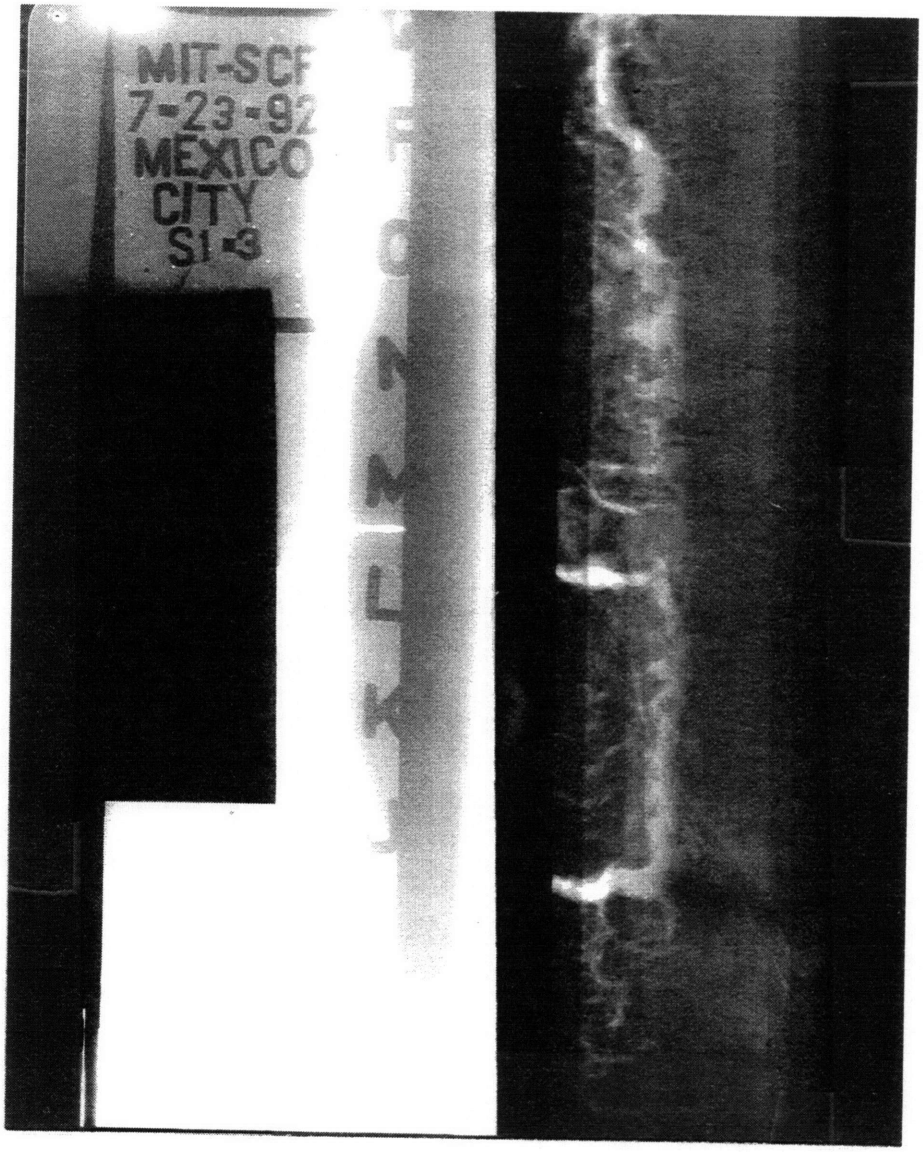

Figure 4.4 Radiograph Results of Sample Tube S1-3

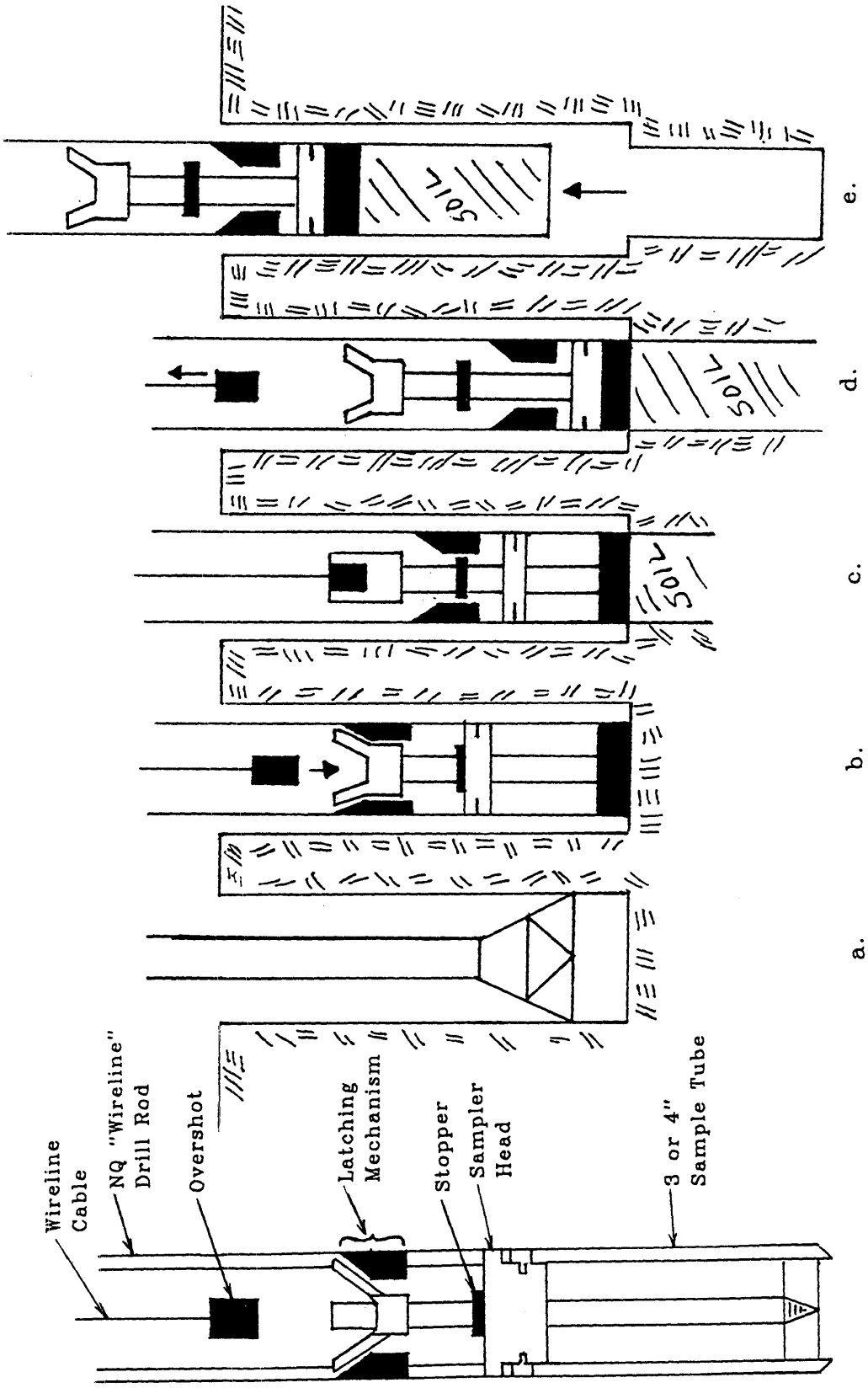

Figure 4.5 Schematic Drawing of a Modified Fixed Piston Sampler Proposed by Author

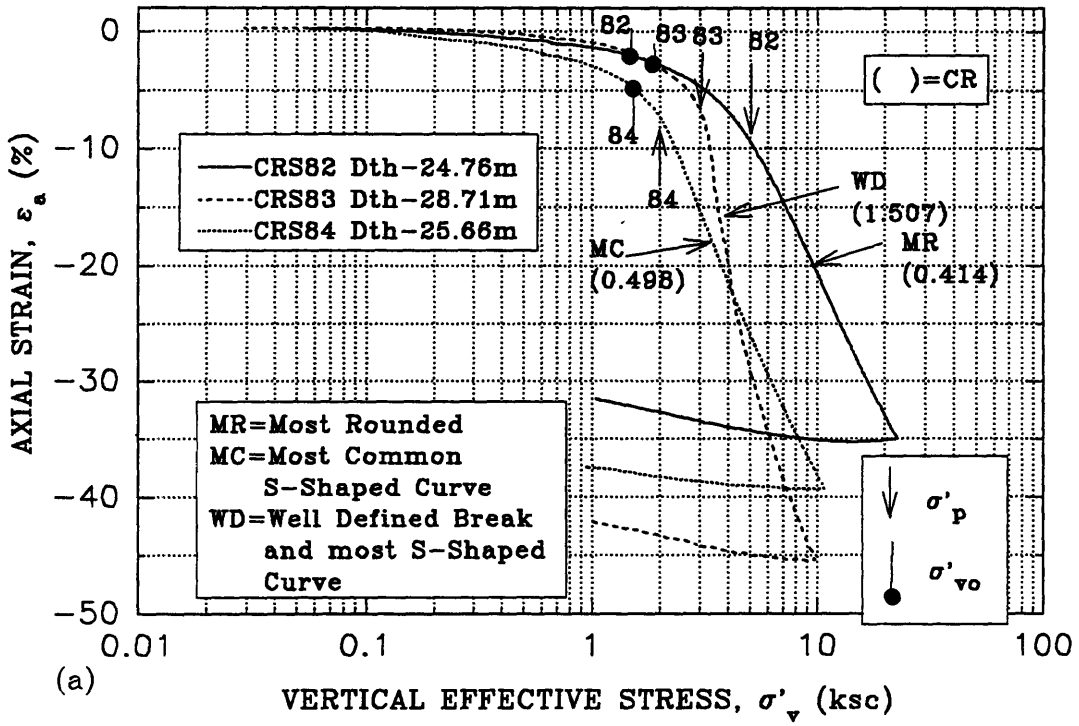

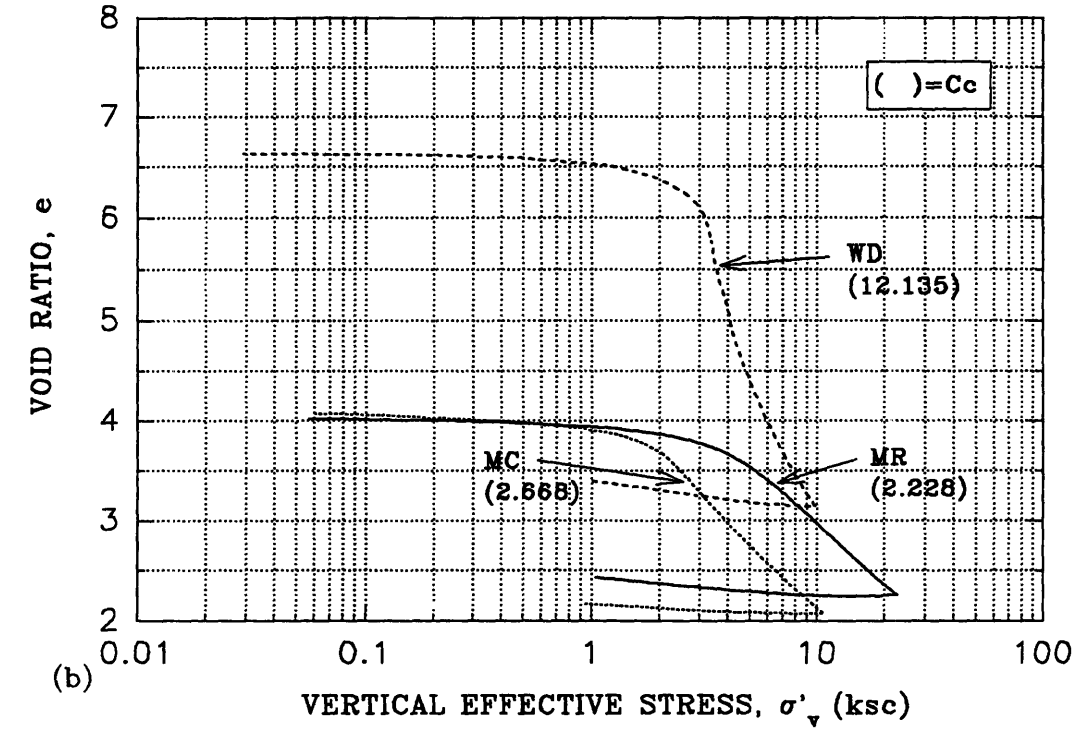

Figure 4.6 Typical Compression Curves from CRSC Tests
(a) Axial Strain vs. σ'_v (b) Void Ratio vs. σ'_v

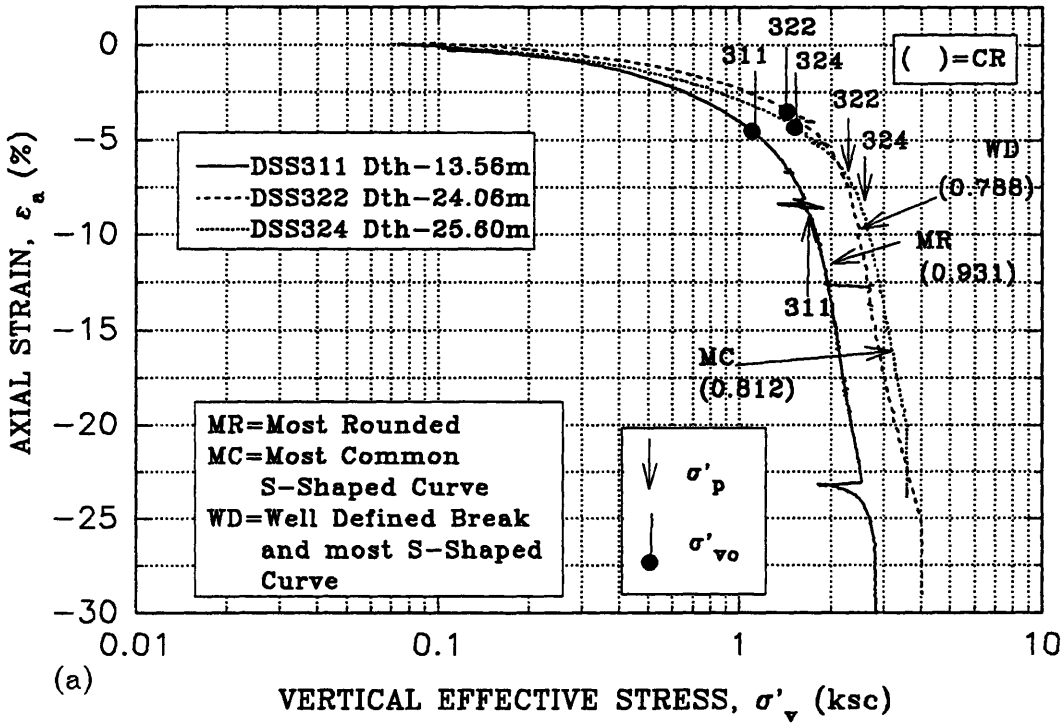

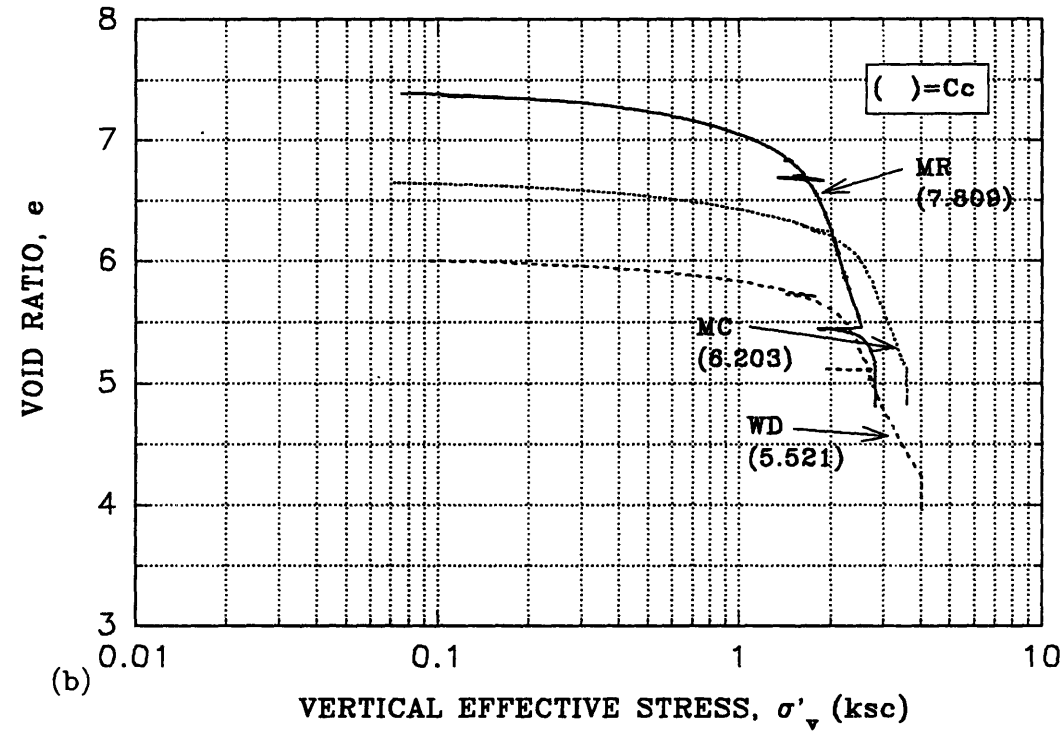

Figure 4.7 Typical Compression Curves from CK_oUDSS Tests

(a) Axial Strain vs. σ'_v (b) Void Ratio vs. σ'_v

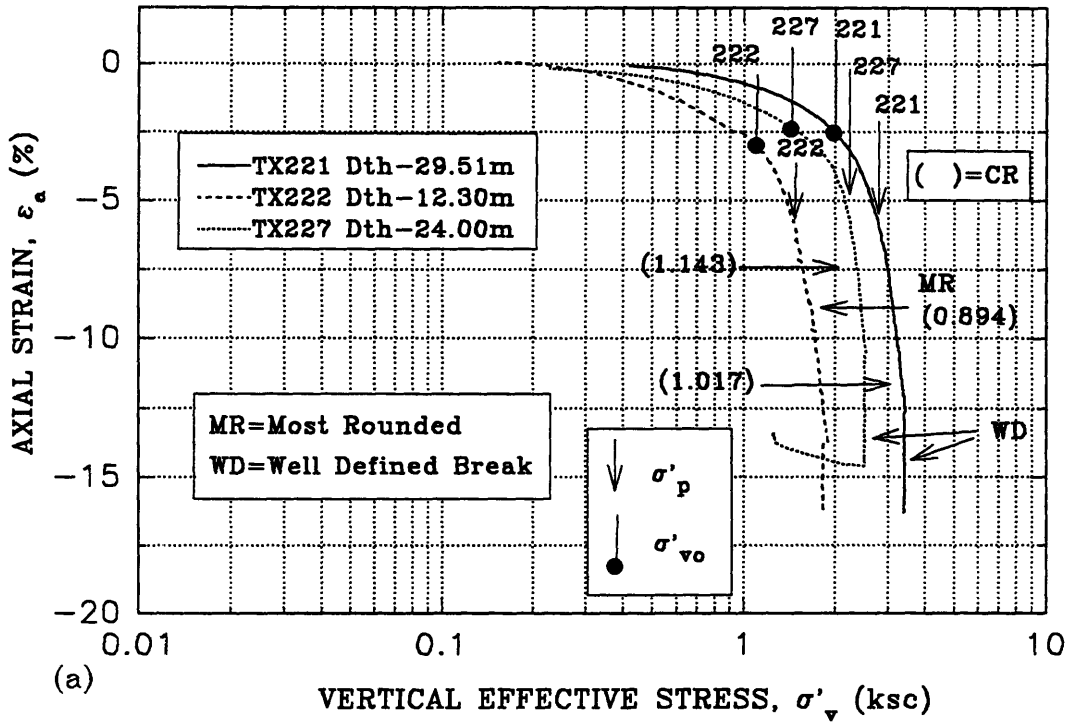

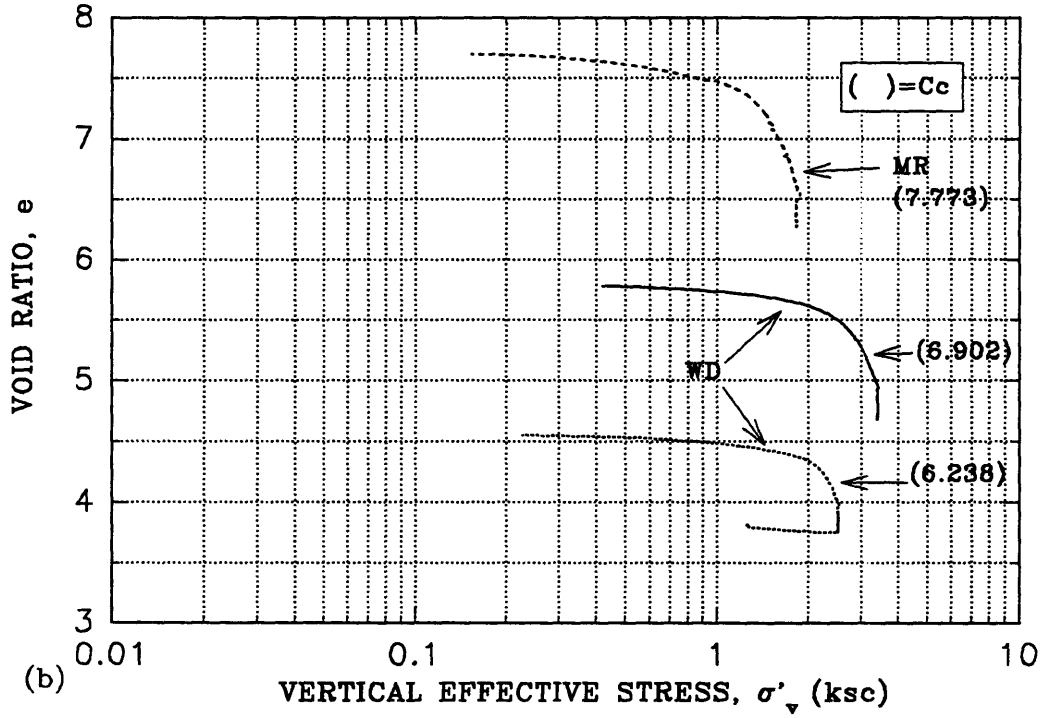

Figure 4.8 Typical Compression Curves from SHANSEP CK_oU Triaxial Tests
(a) Axial Strain vs. σ'_v (b) Void Ratio vs. σ'_v

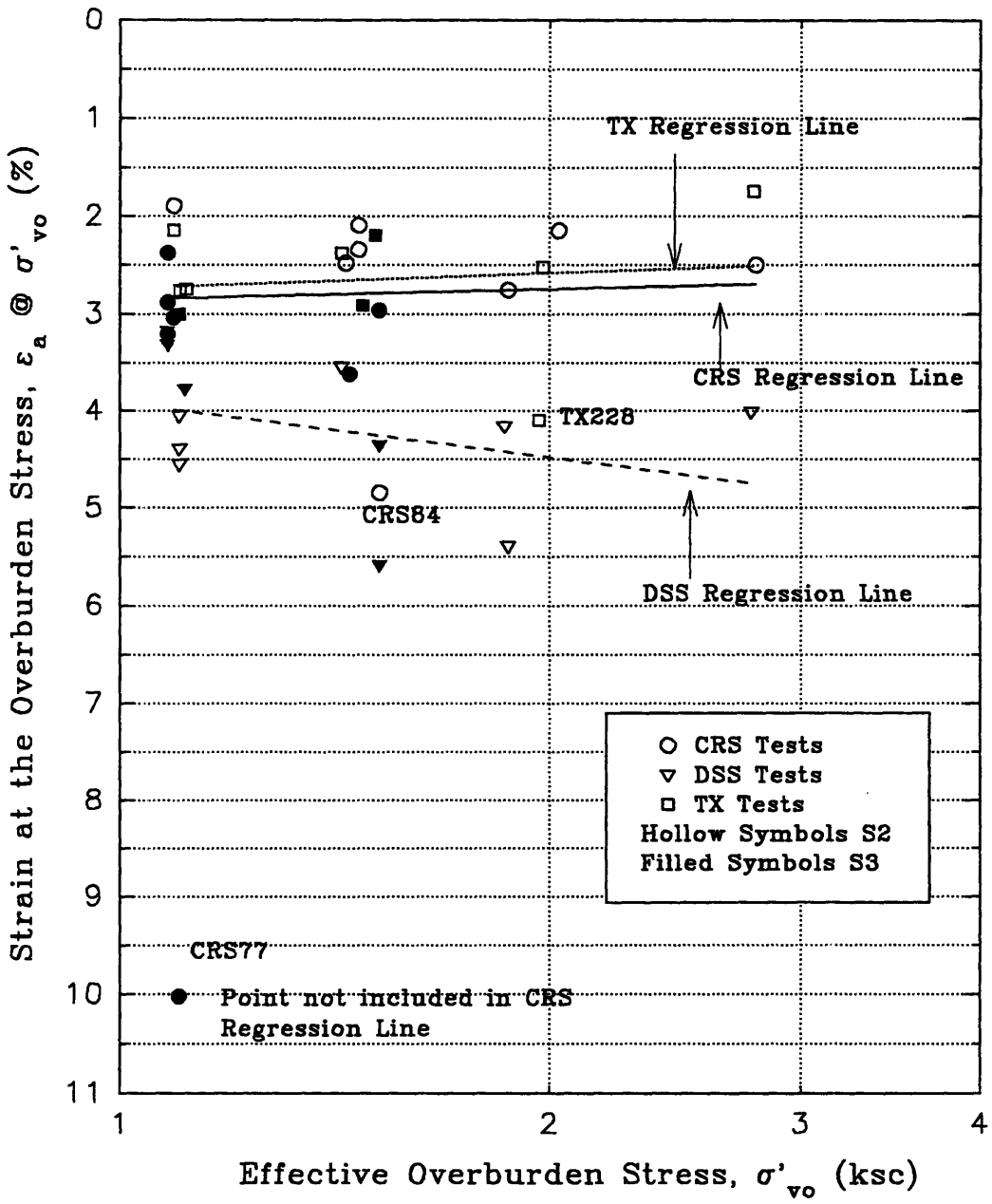

Figure 4.9 Strain at the Overburden Stress vs. Effective Overburden Stress

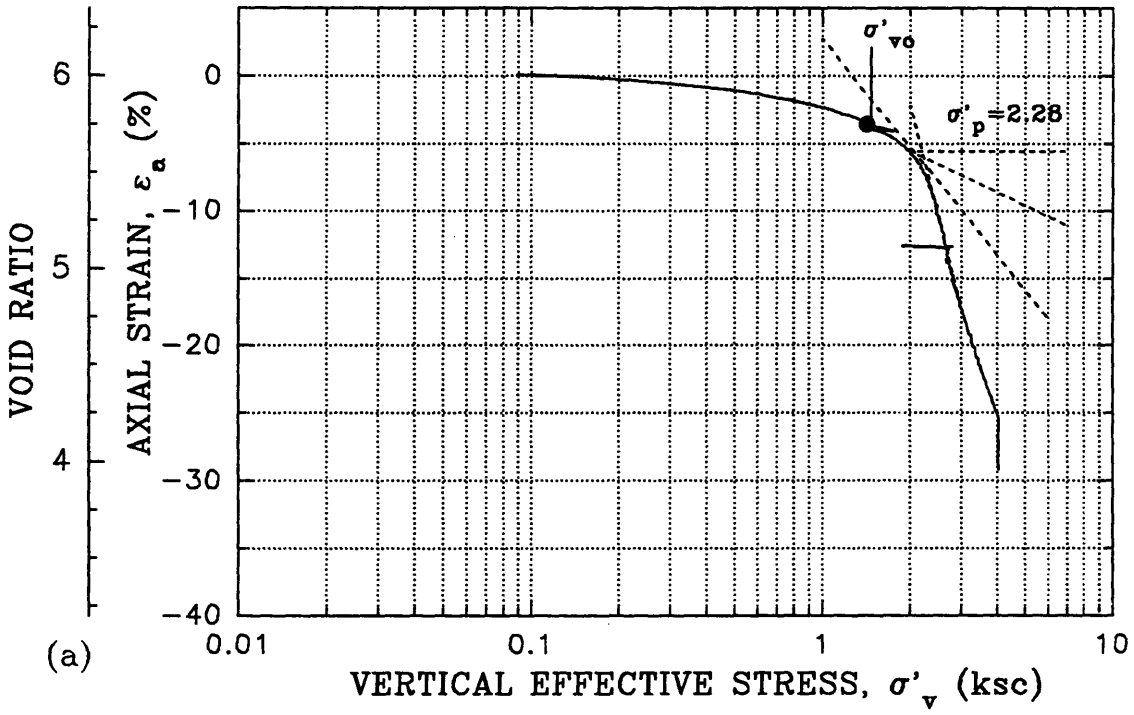

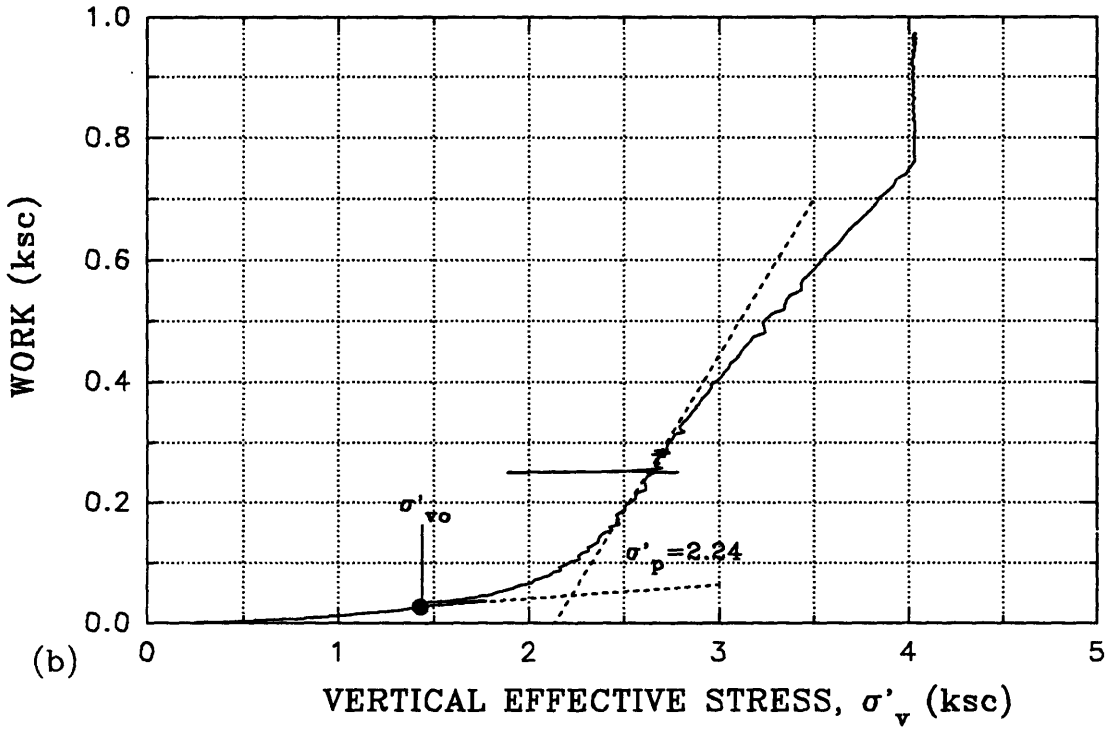

Figure 4.10 Consolidation Results – DSS322
(a)Casagrande Construction (b) Strain Energy

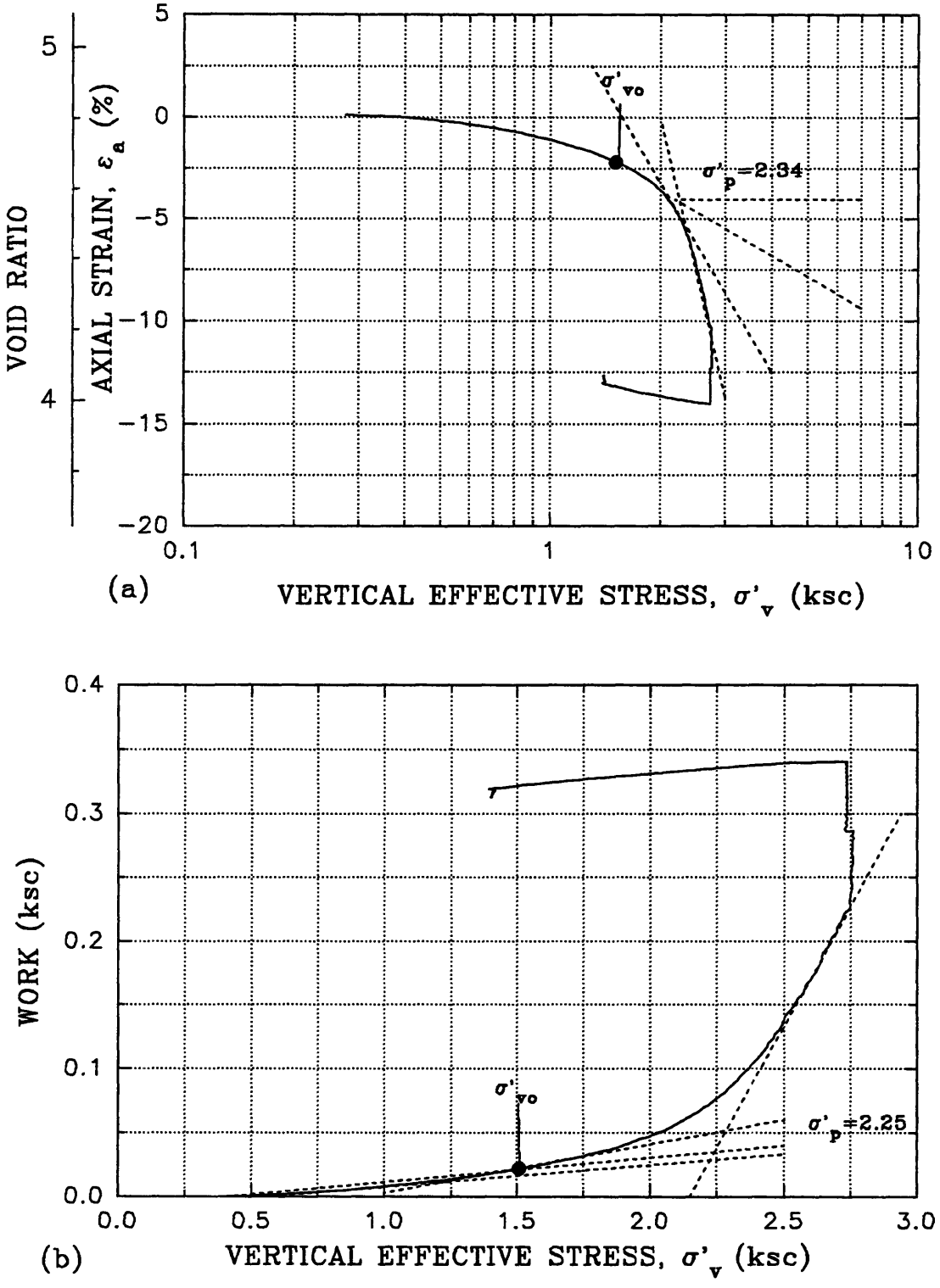

Figure 4.11 Consolidation Results – TX233
(a) Casagrande Construction (b) Strain Energy

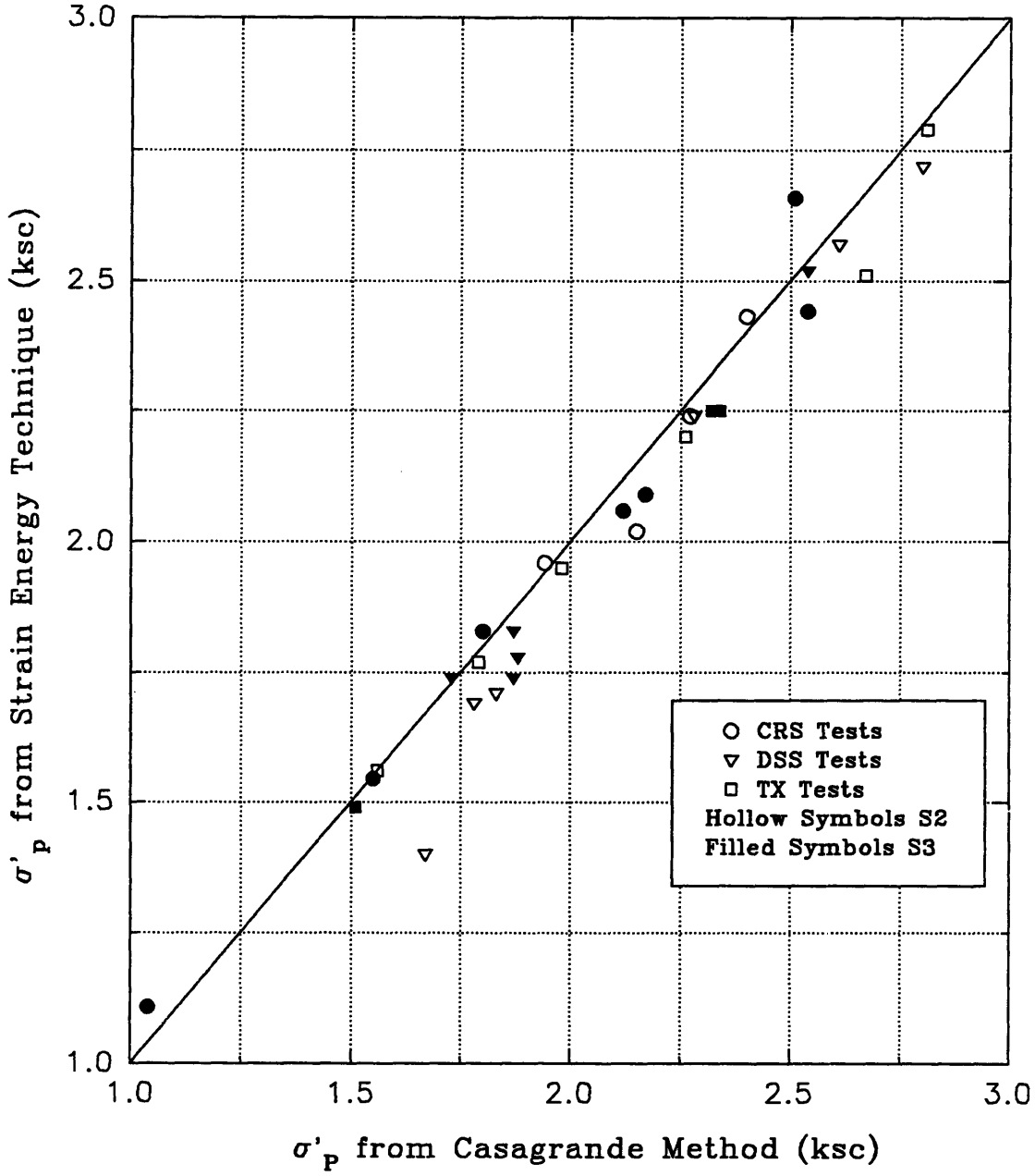

Figure 4.12 Casagrande Method vs. Strain Energy Technique from CRSC Tests, CK_oUDSS and CK_oU TX Tests

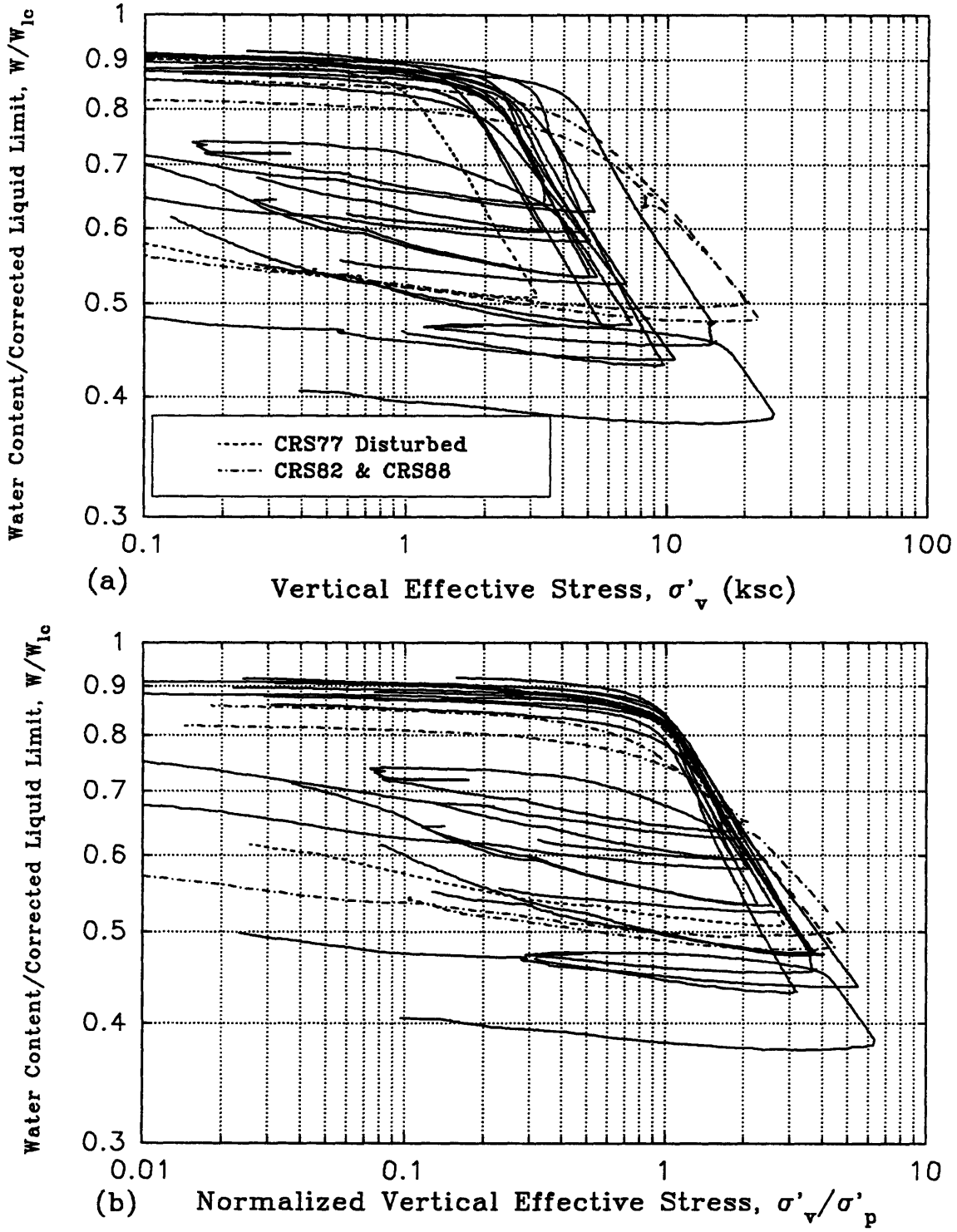

Figure 4.13 Compression Curves from all CRSC Tests
(a) Normalized Water Content vs. σ'_v
(b) Normalized Water Content vs. Normalized σ'_v

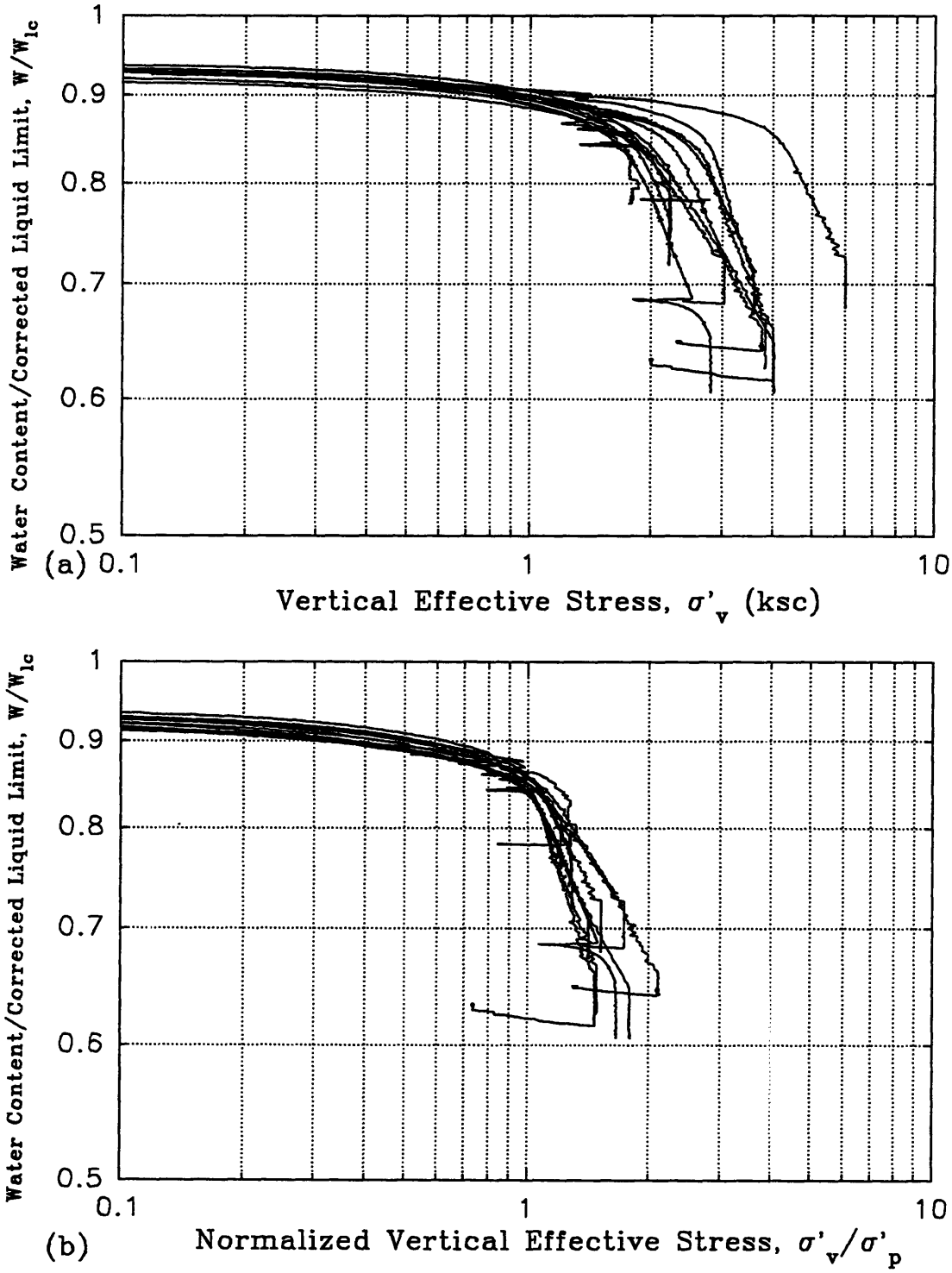

Figure 4.14 Compression Curves from all SHANSEP CK_oUDSS Tests

(a) Normalized Water Content vs. σ'_v

(b) Normalized Water Content vs. Normalized σ'_v

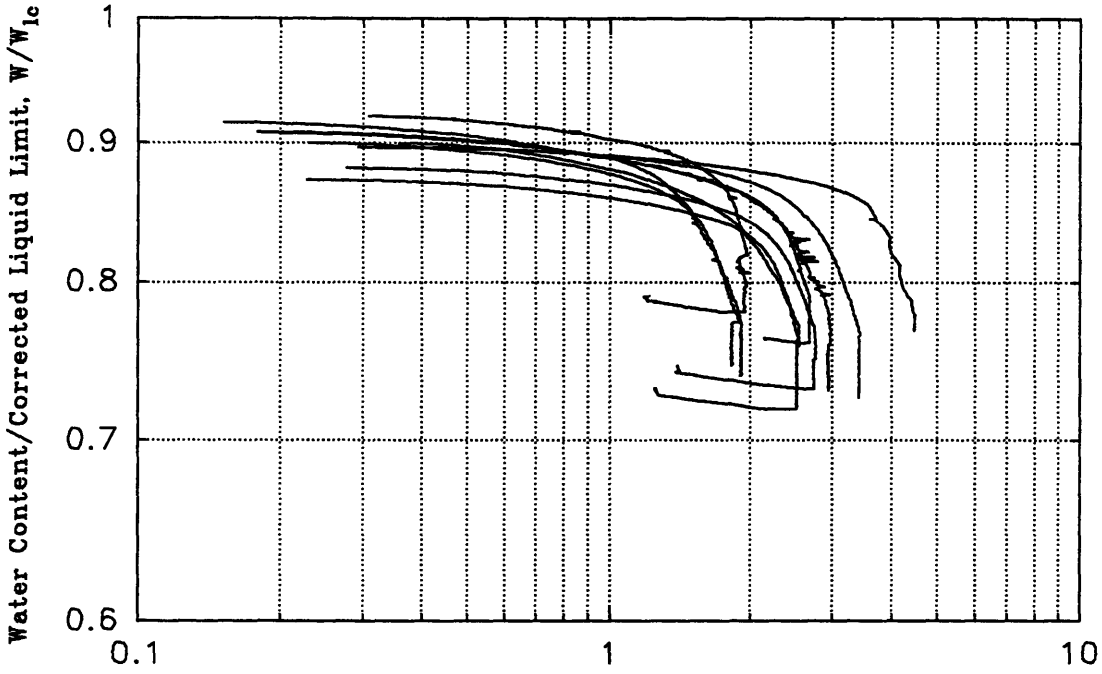

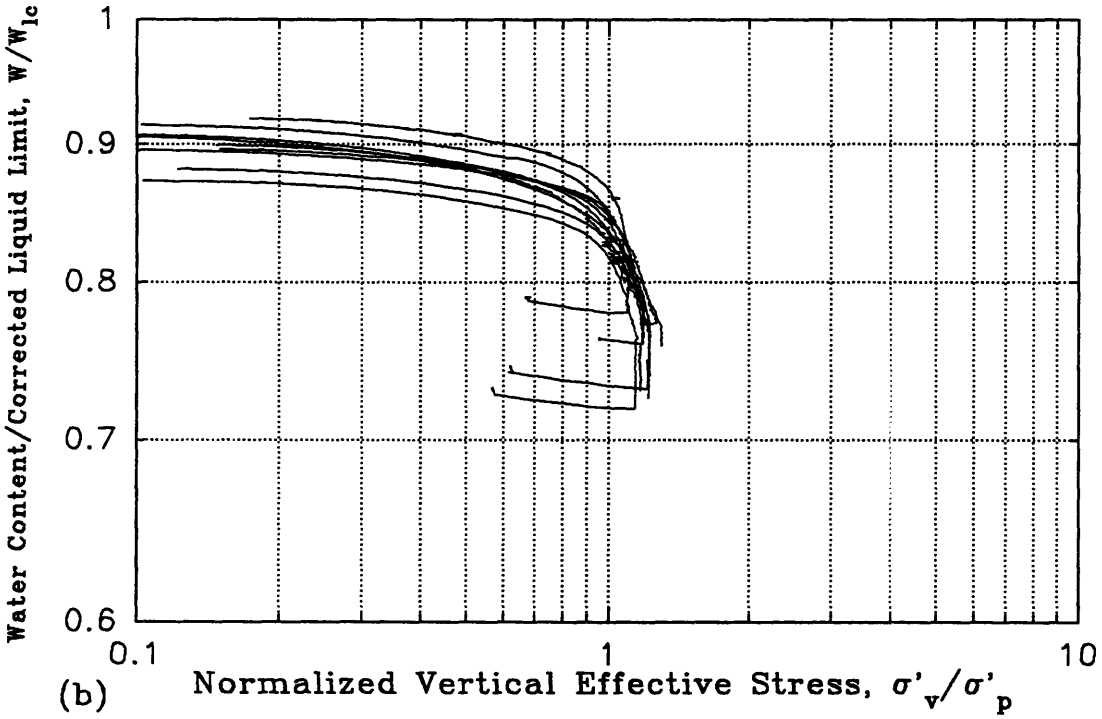

Figure 4.15 Compression Curves from all SHANSEP CK_oU Triaxial Tests
(a) Normalized Water Content vs. σ'_v
(b) Normalized Water Content vs. Normalized σ'_v

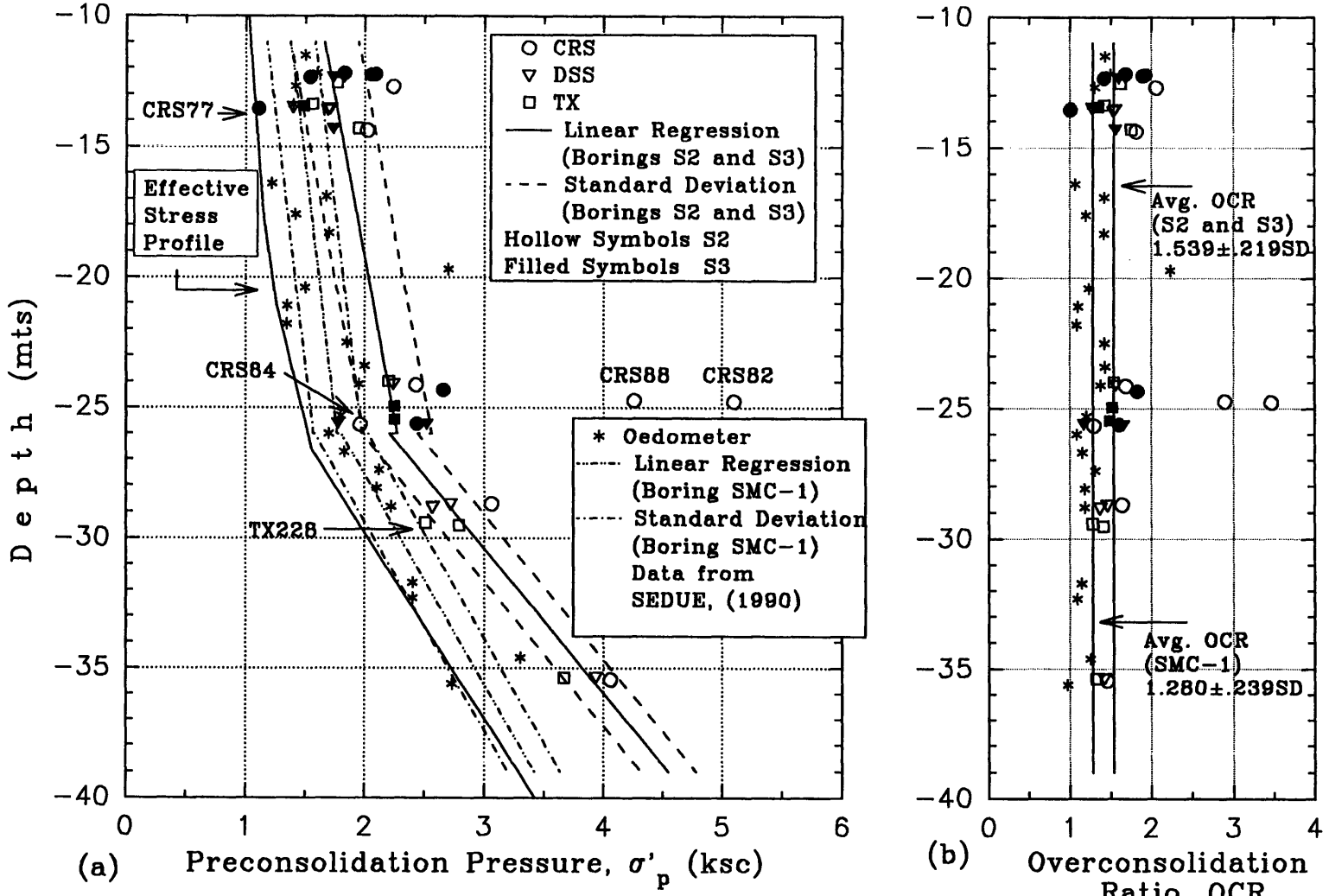

Figure 4.16 Stress History at México City's Cathedral
(a) Depth vs. σ'_p (b) Depth vs. OCR

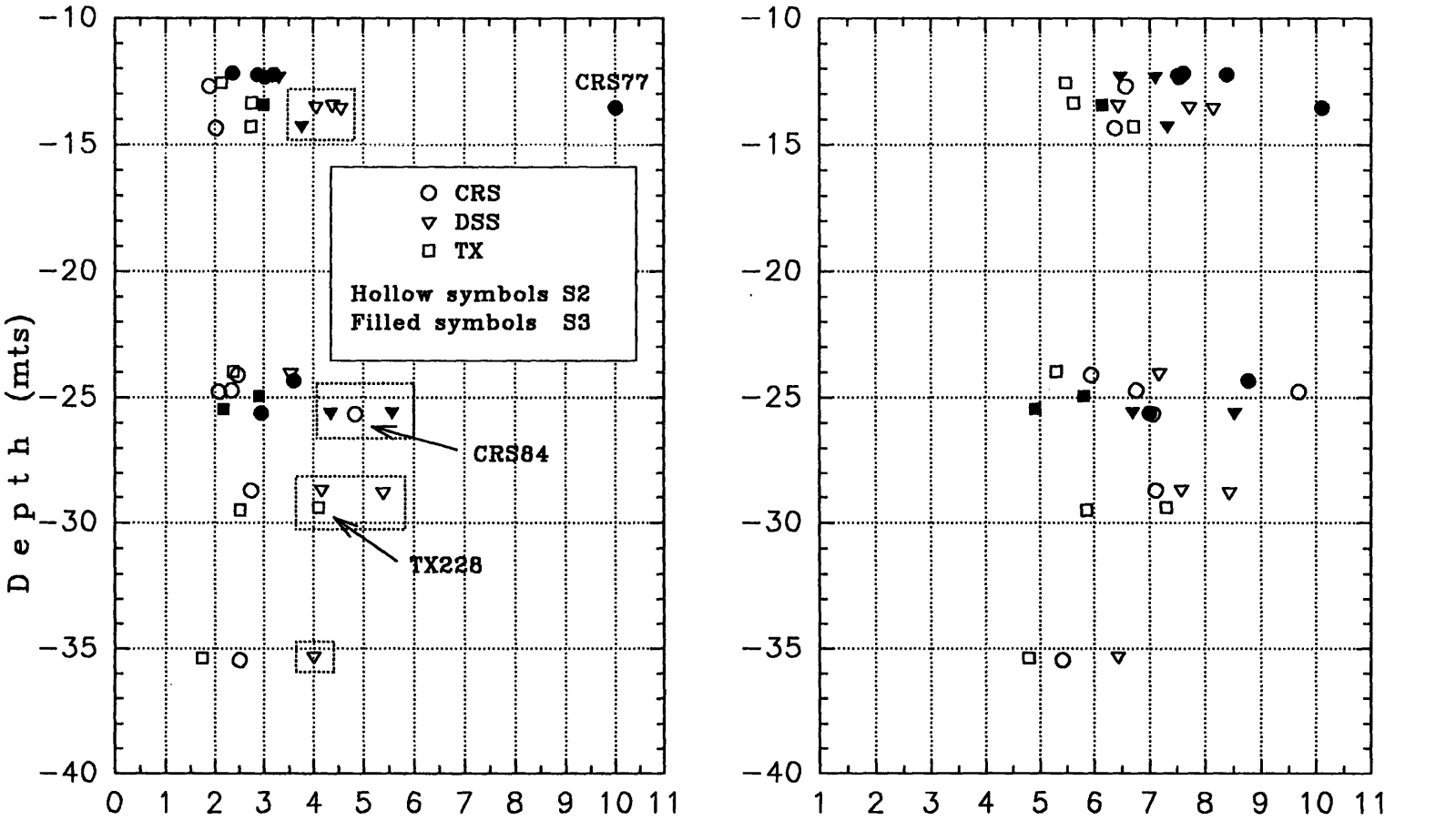

a) Strain at the Overburden, $\varepsilon_a @ \sigma'_{vo}$ (%)

b) Strain at the Preconsolidation Pressure, $\varepsilon_a @ \sigma'_p$ (%)

Figure 4.17 a) Depth vs. Strain at the Overburden Stress
b) Depth vs. Strain at the Preconsolidation Pressure

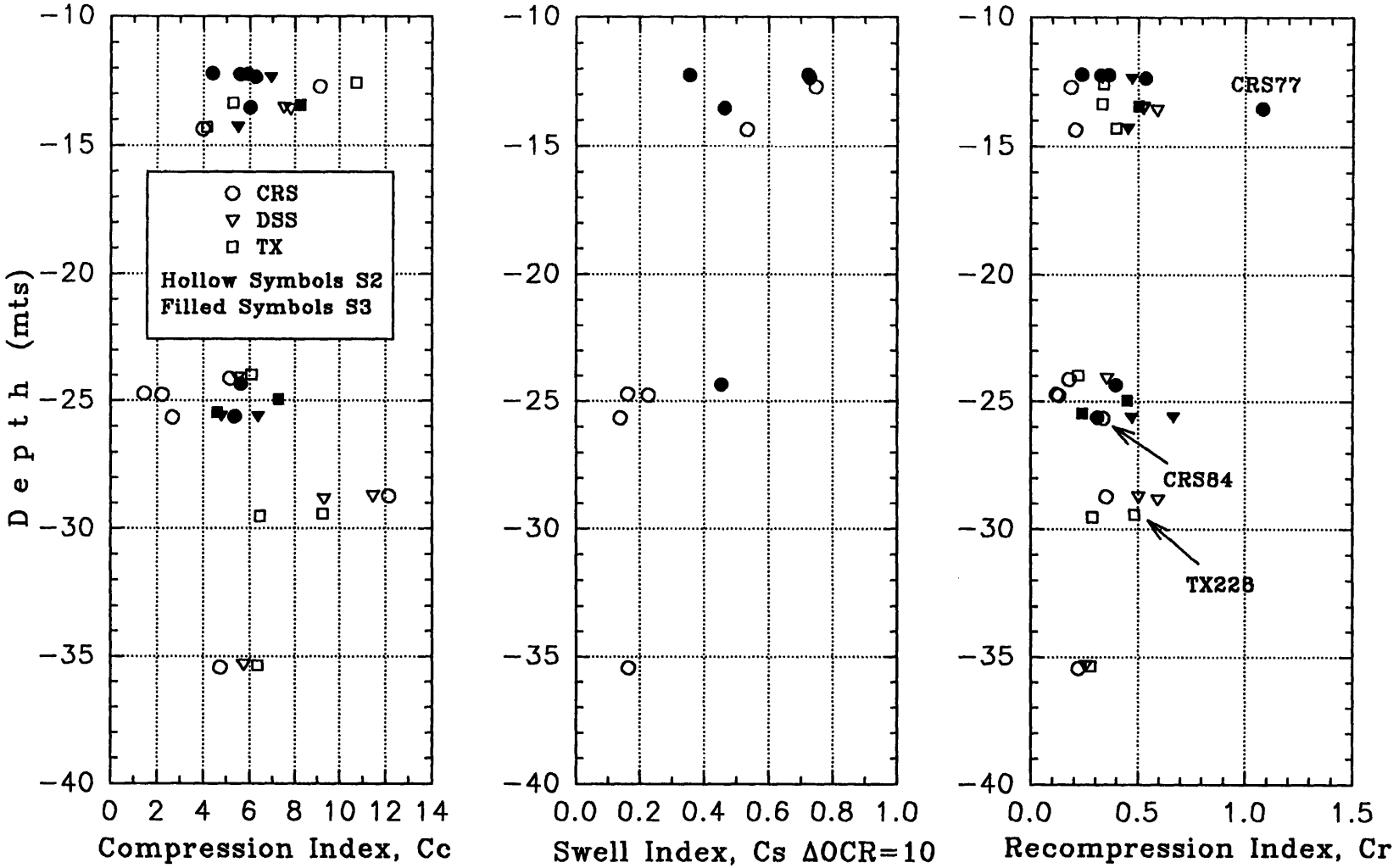

Figure 4.18 Depth vs. Virgin Compression Index, Swell Index, and Recompression Index for CRSC, and SHANSEP CK_oU Direct Simple Shear and Triaxial Tests

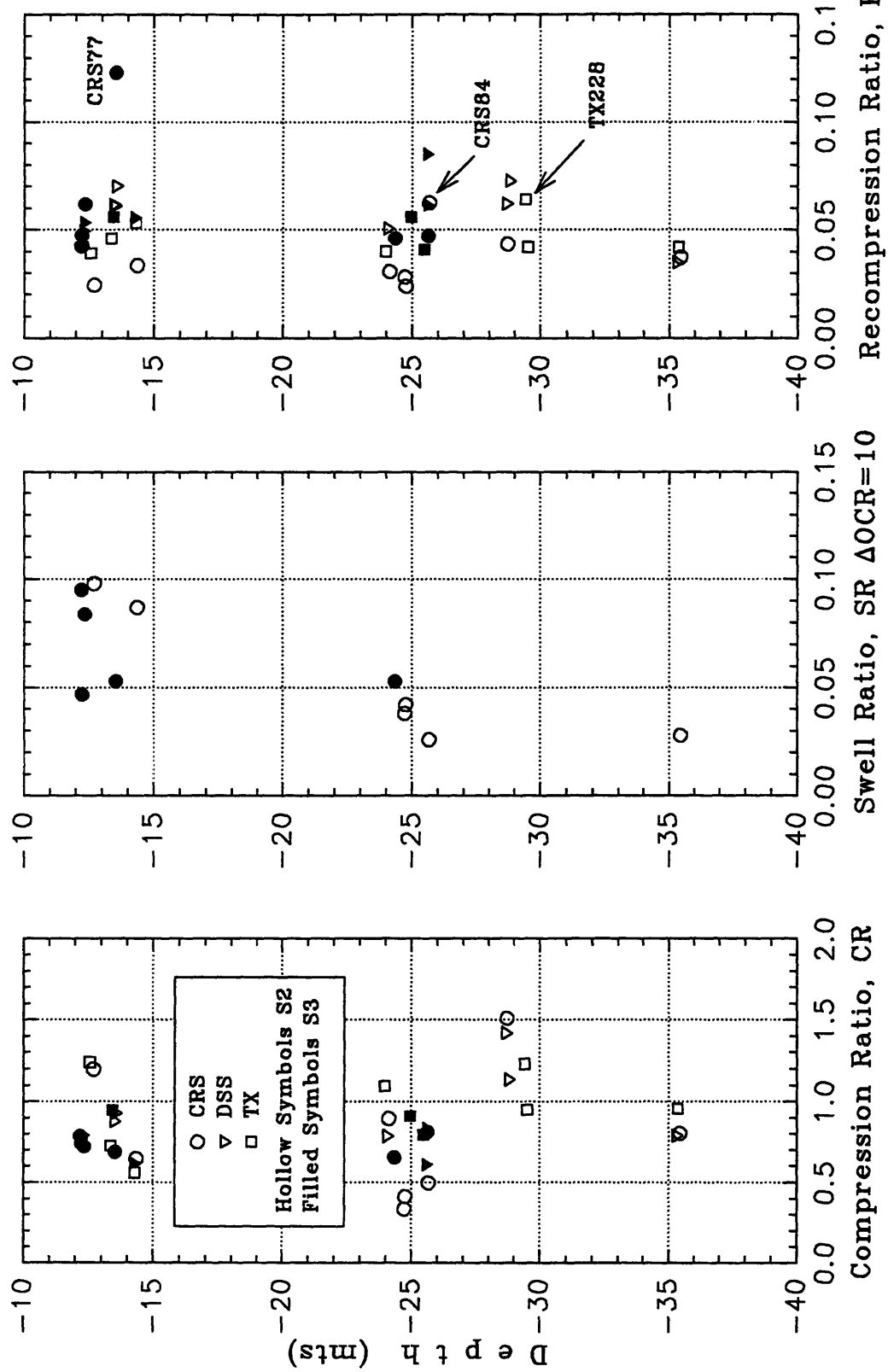

Figure 4.19 Depth vs. Virgin Compression Ratio, Swell Ratio, and Recompression Ratio for CRSC, and SHANSEP CK_oU Direct Simple Shear and Triaxial Tests

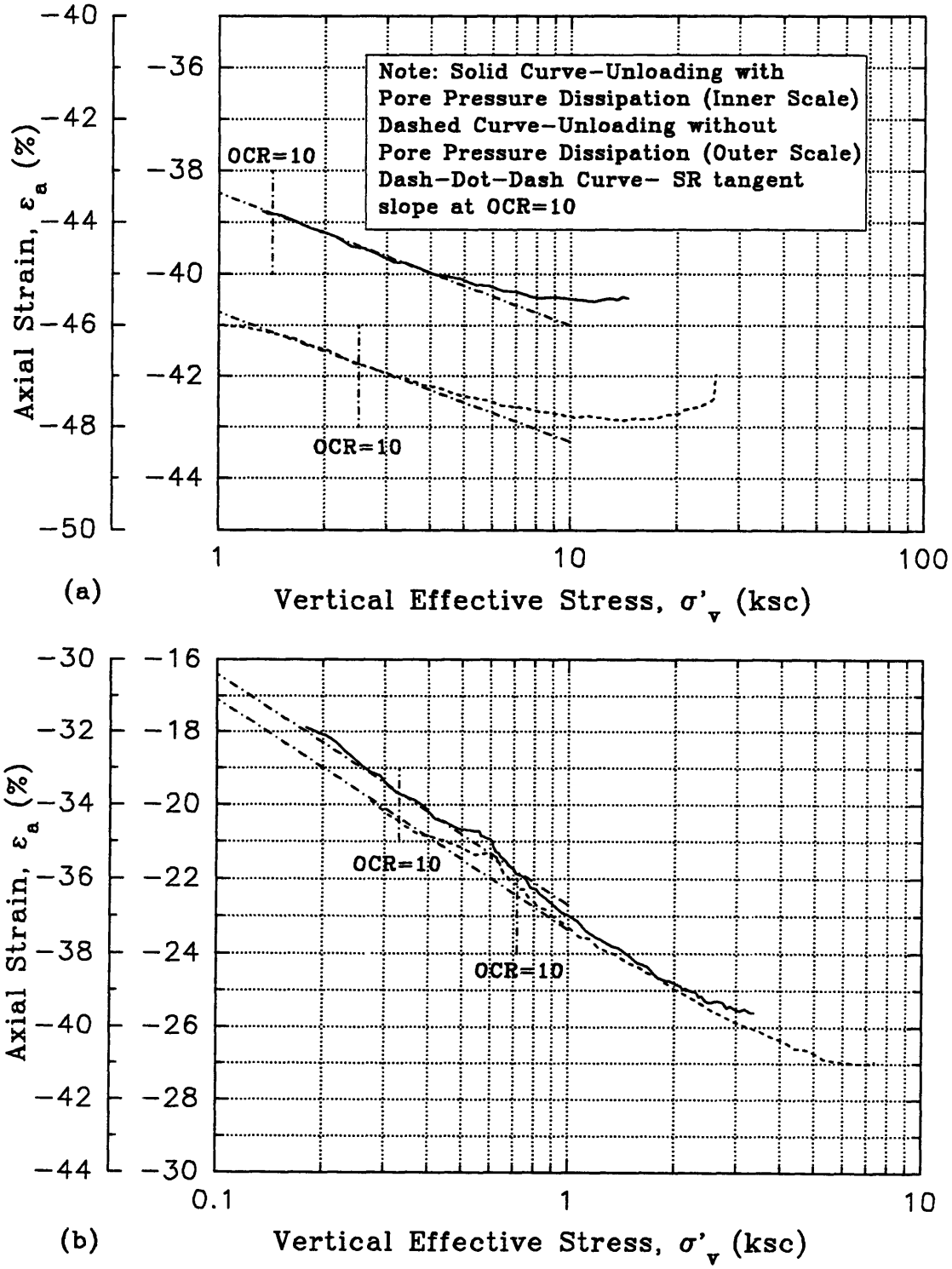

Figure 4.20 Unloading Compression Curves
(a) CRS87 (b) CRS89

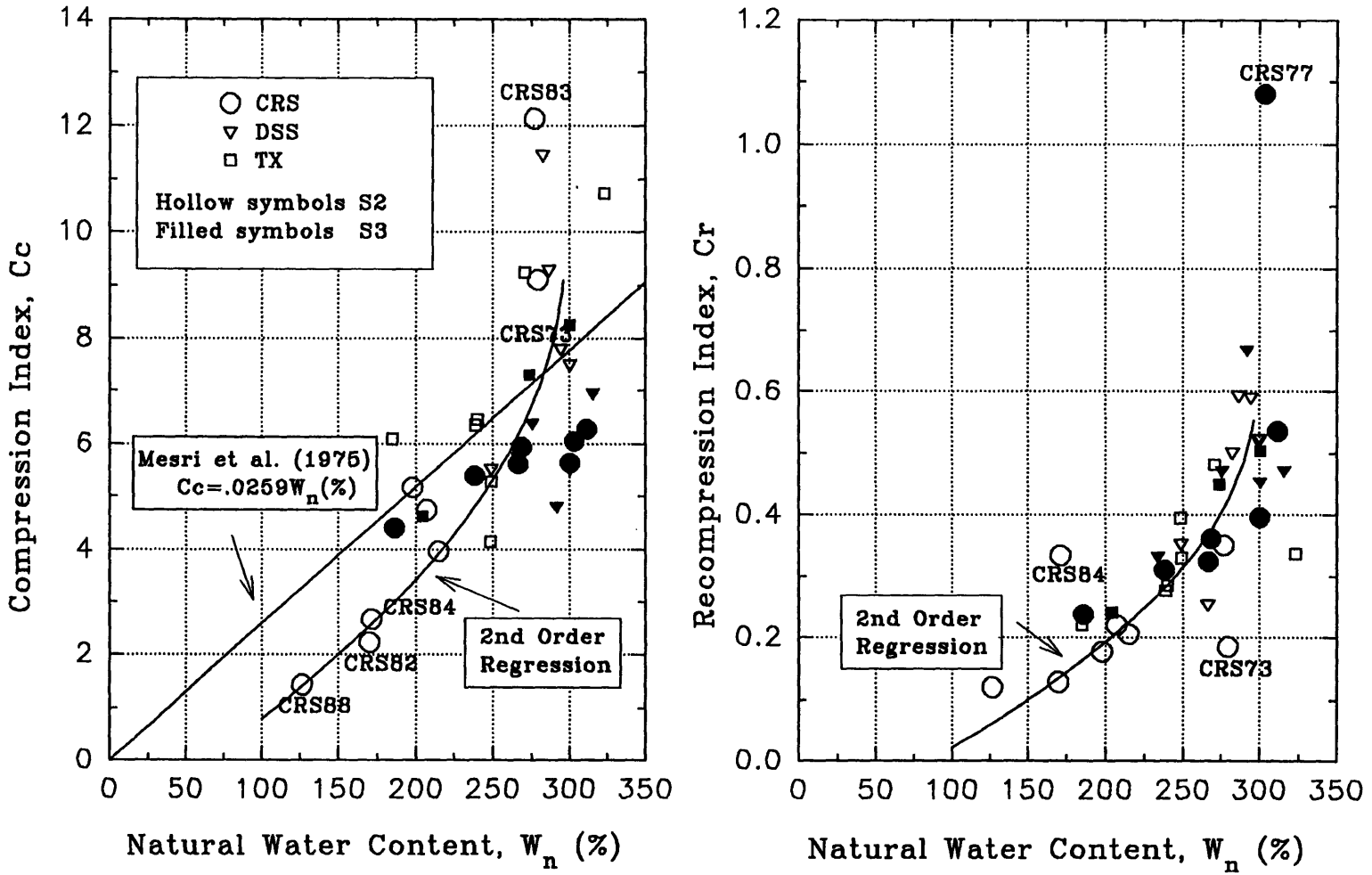

Figure 4.21 Compressibility Index Relationships
a) Compression Index vs. Natural Water Content
b) Recompression Index vs. Natural Water Content

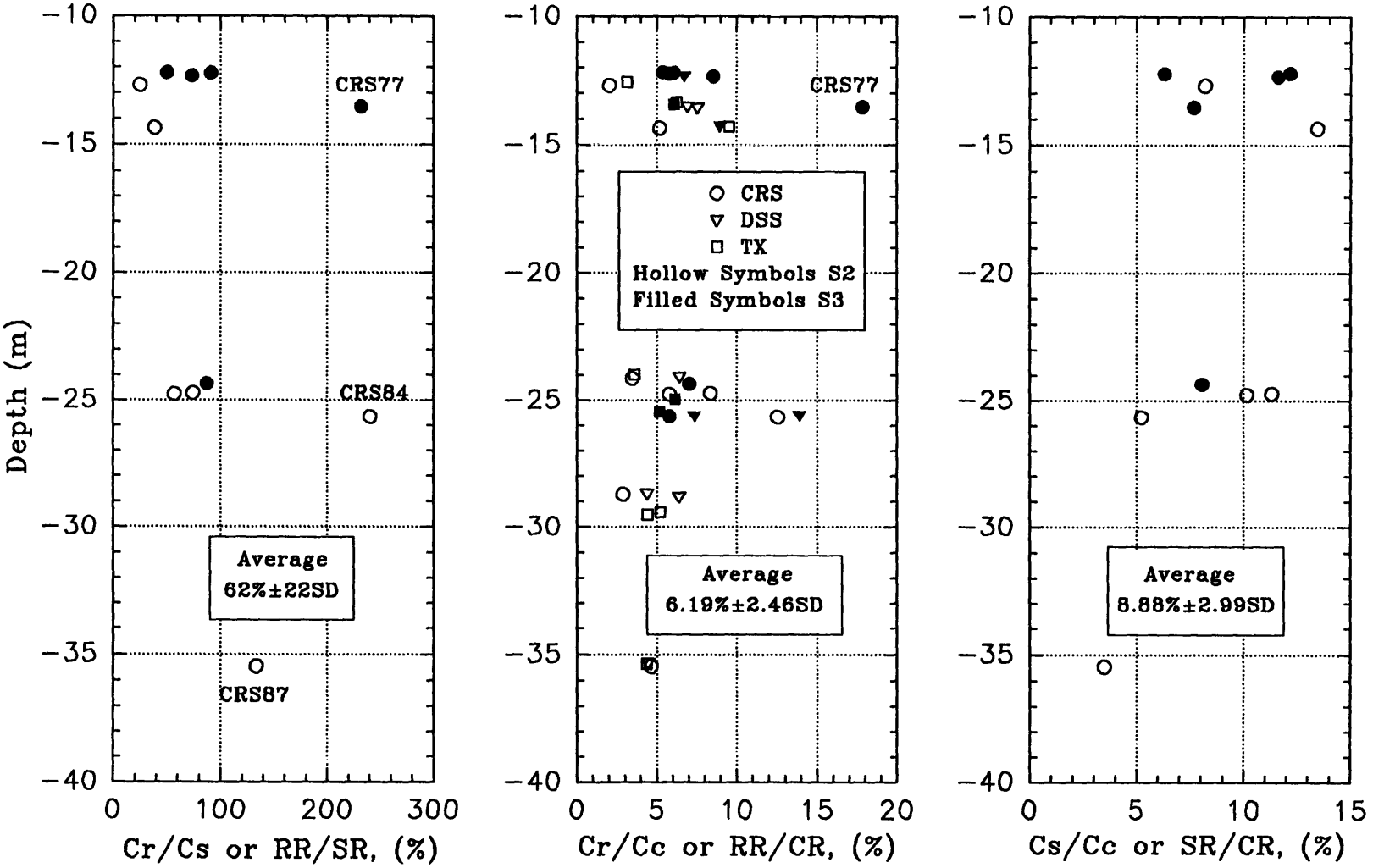

Figure 4.22 Depth vs. Compressibility Ratios

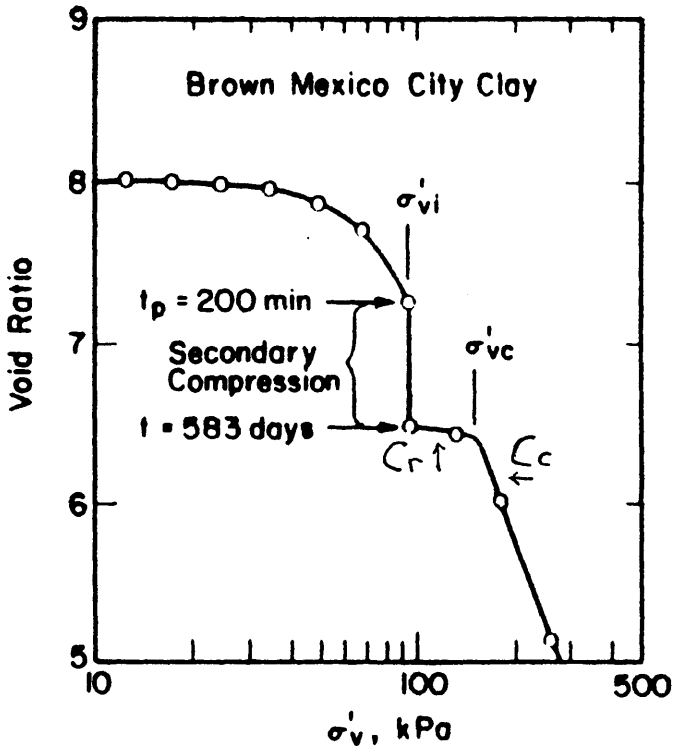

Figure 4.23 Preconsolidation Pressure due to Secondary Compression (from Mesri and Castro 1987)

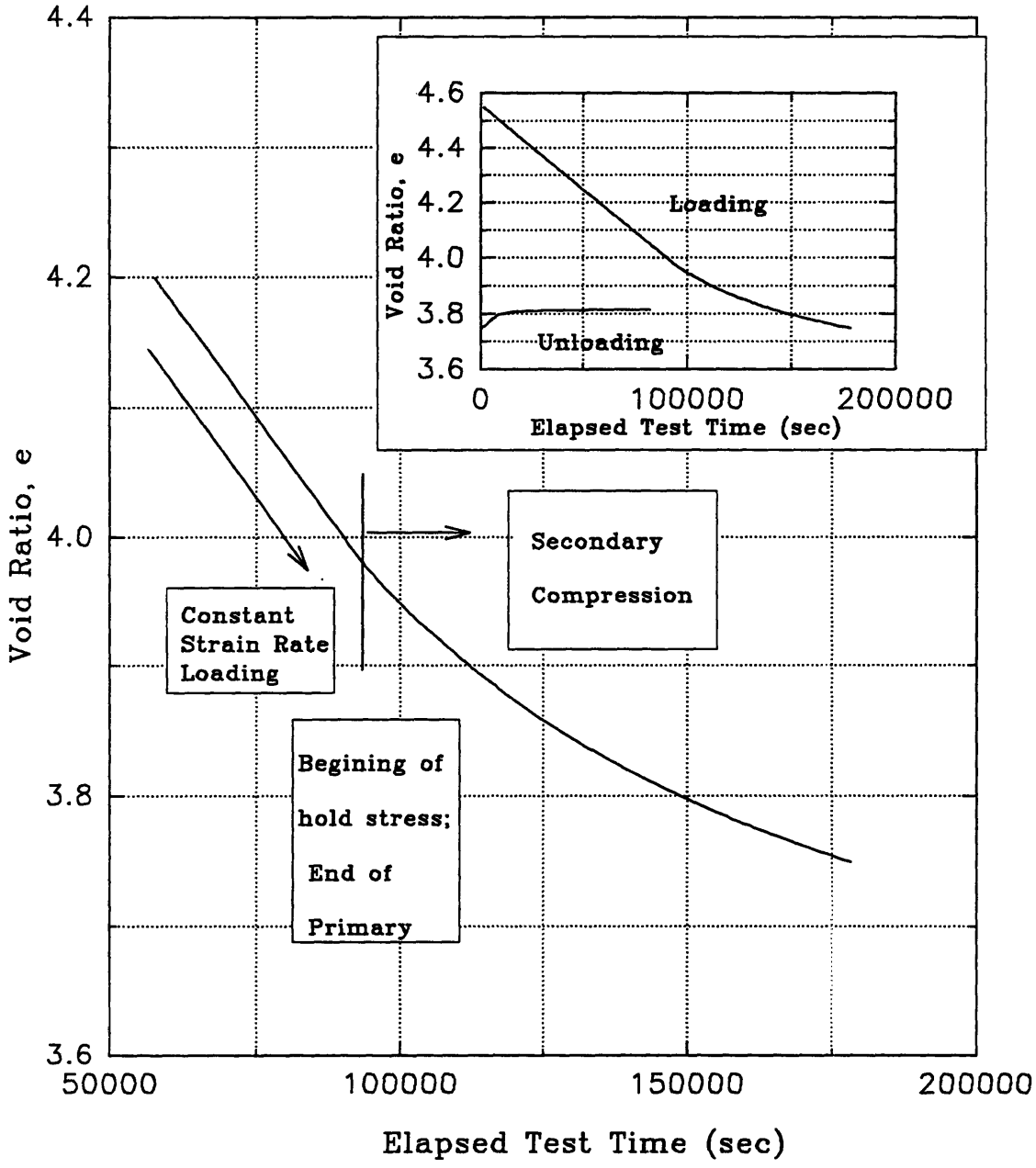

Figure 4.24 CK_oUC Consolidation Results – TX227
Void Ratio vs. Elapsed Test Time

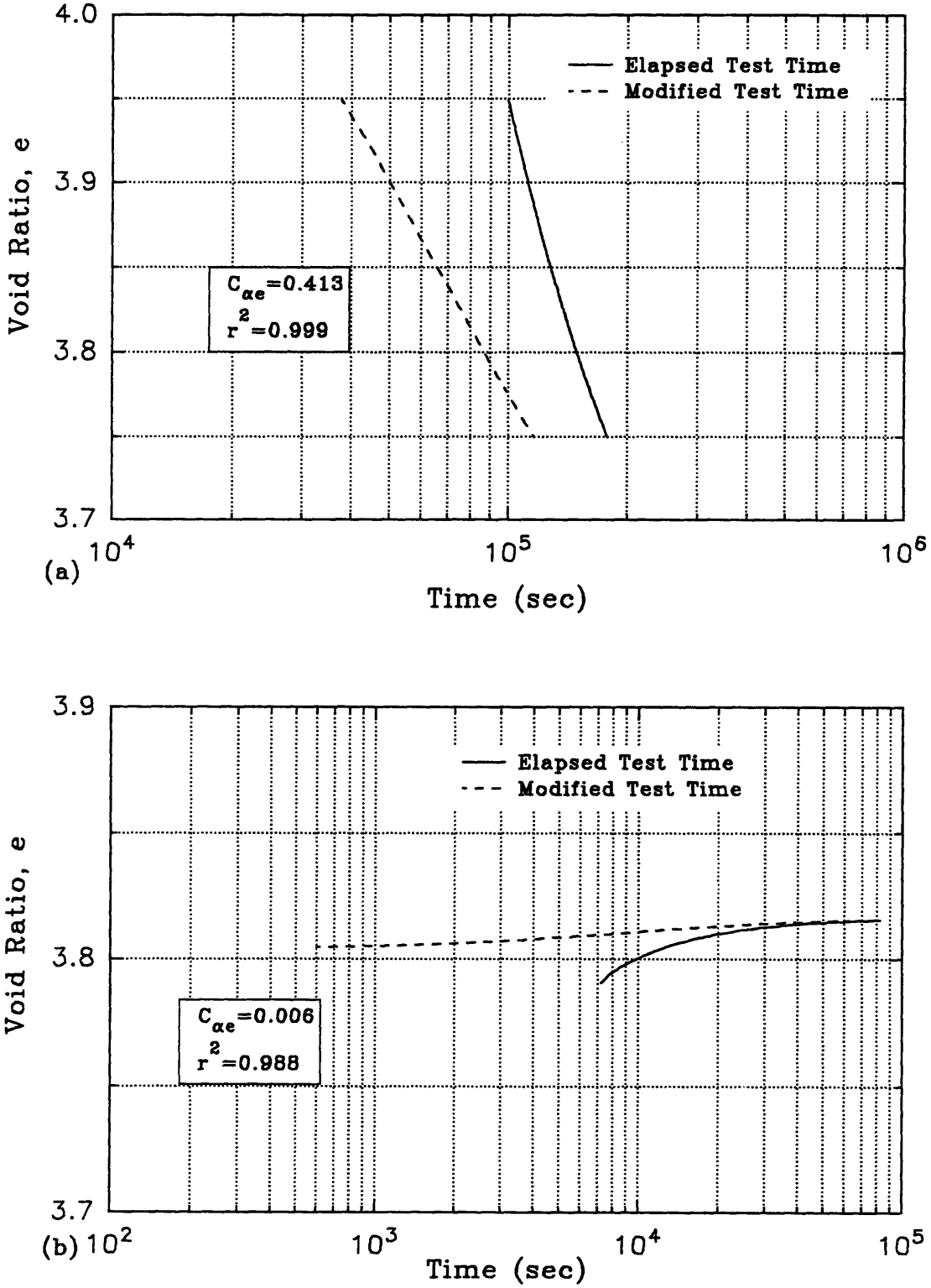

Figure 4.25 Consolidation Results – TX227
(a) Hold Stress at σ'_{vm} (b) Hold Stress at σ'_{vc}

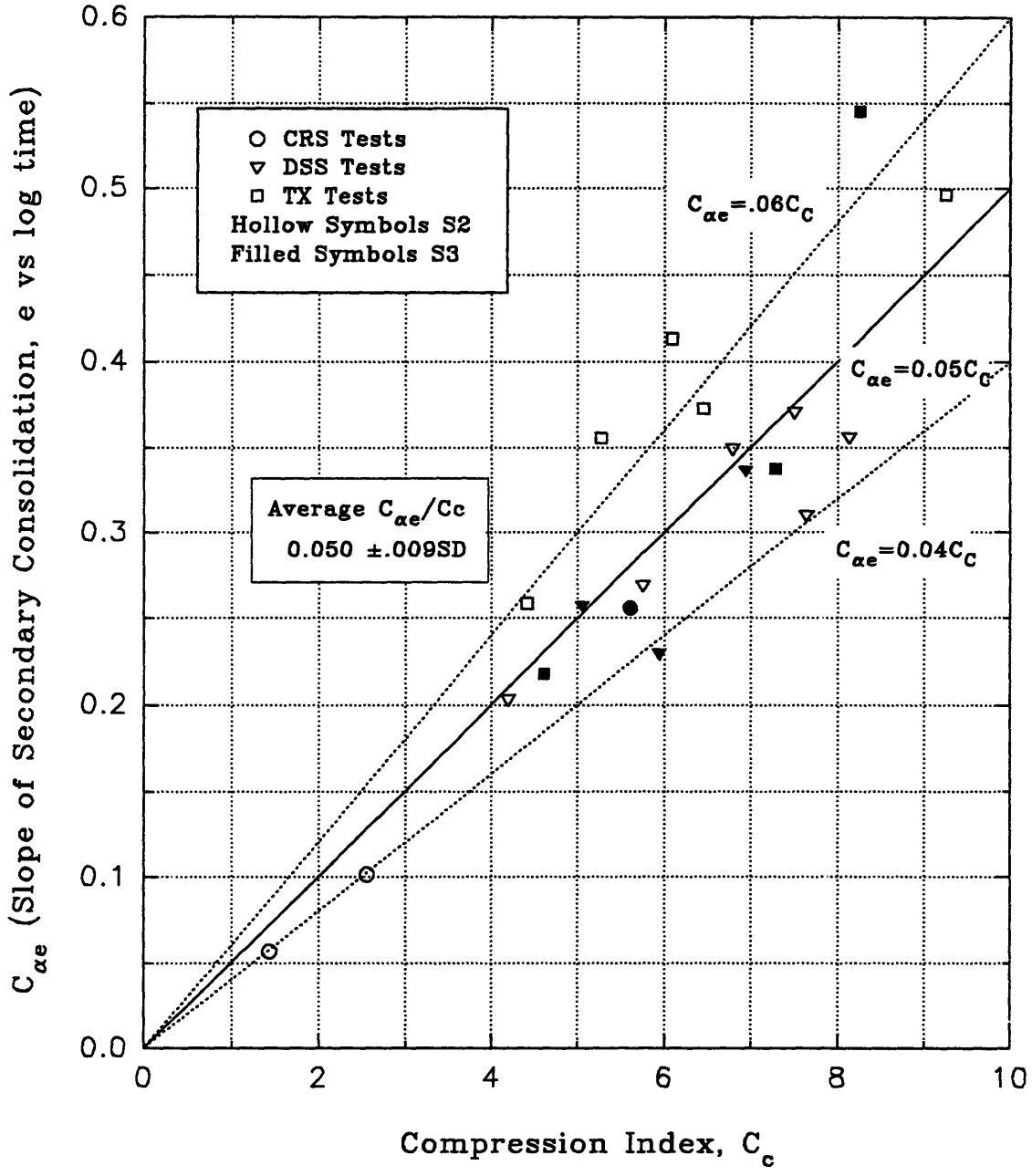

Figure 4.26 Relationship between Secondary Compression Index (NC) and Compression Index

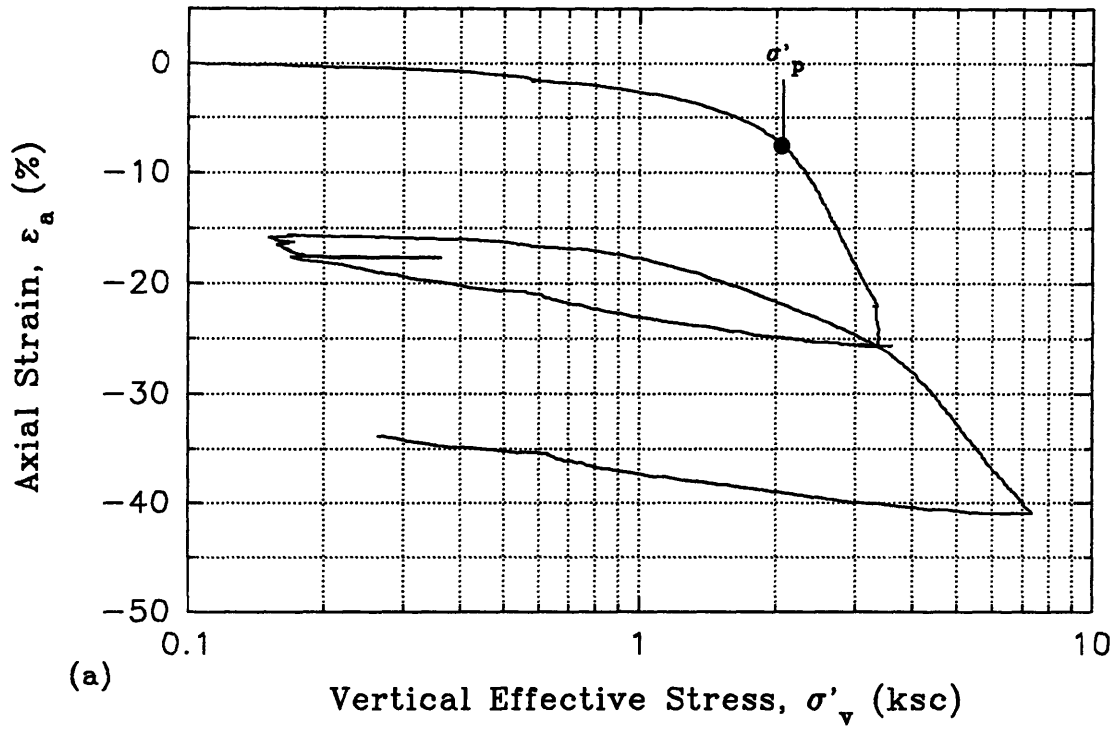

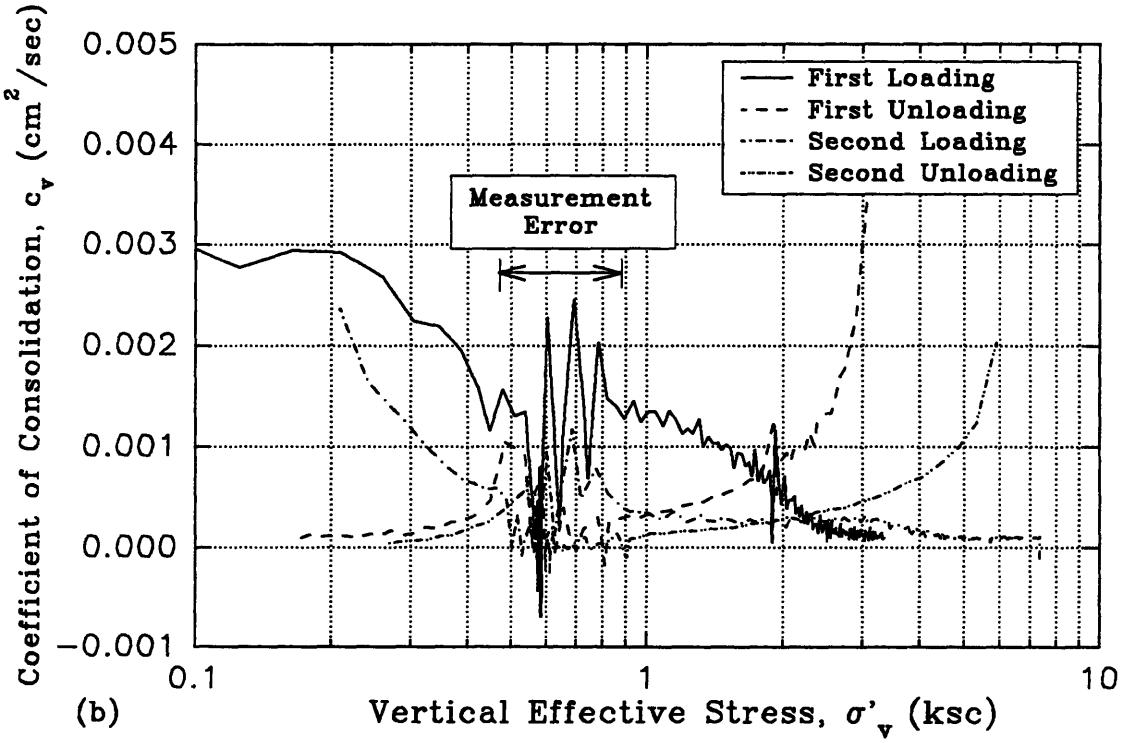

Figure 4.27 CRSC Consolidation Results–CRS89
(a) Compression Curve
(b) Coefficient of Consolidation (c_v) vs σ'_v

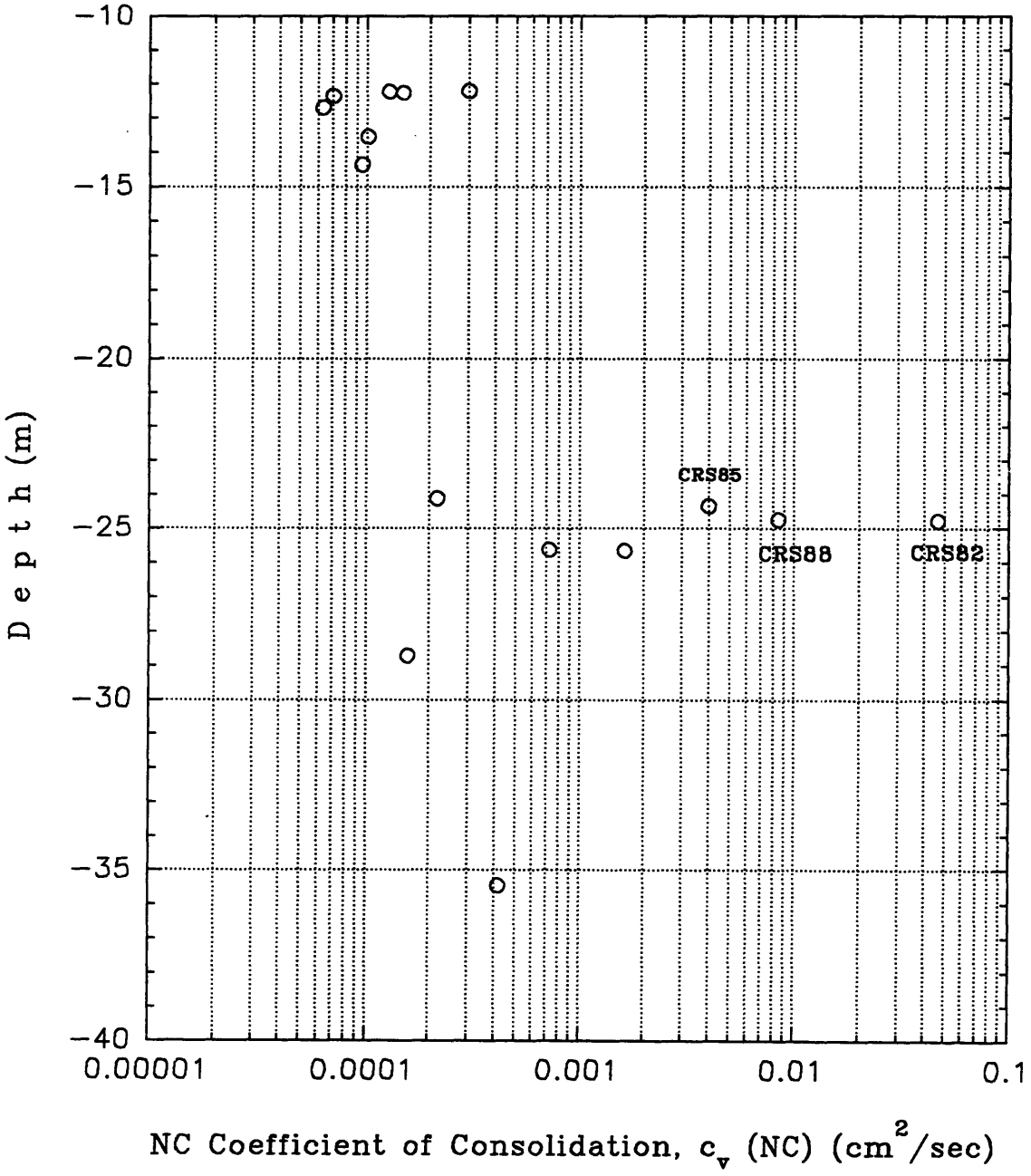

Figure 4.28 Depth vs. NC Coefficient of Consolidation

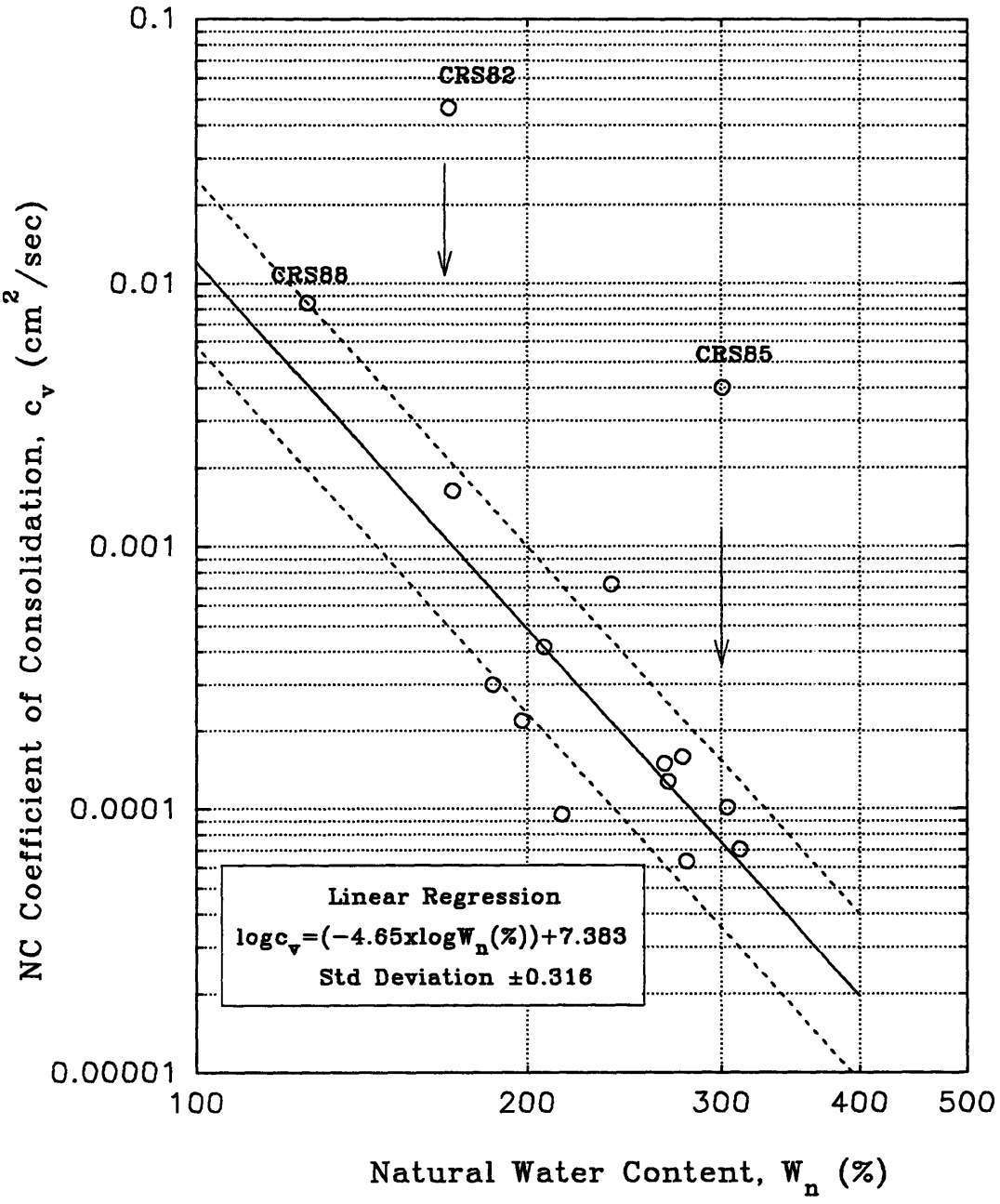

Figure 4.29 NC Coefficient of Consolidation (NC) vs. Natural Water Content; CRSC Data

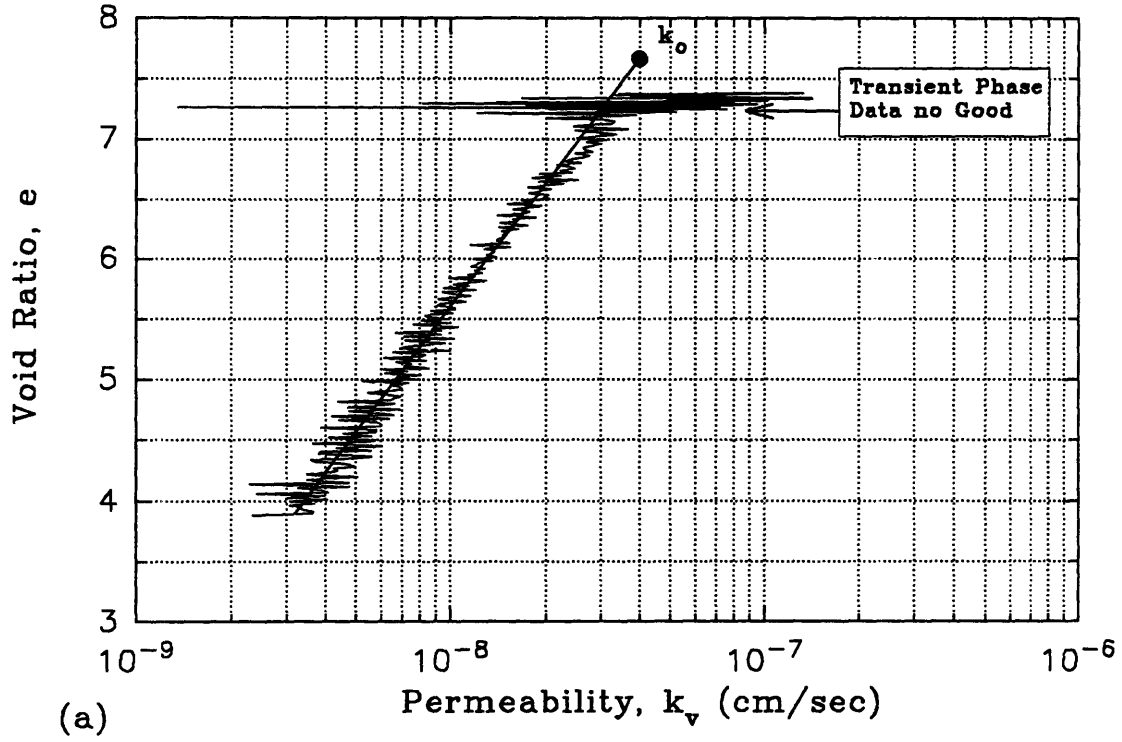

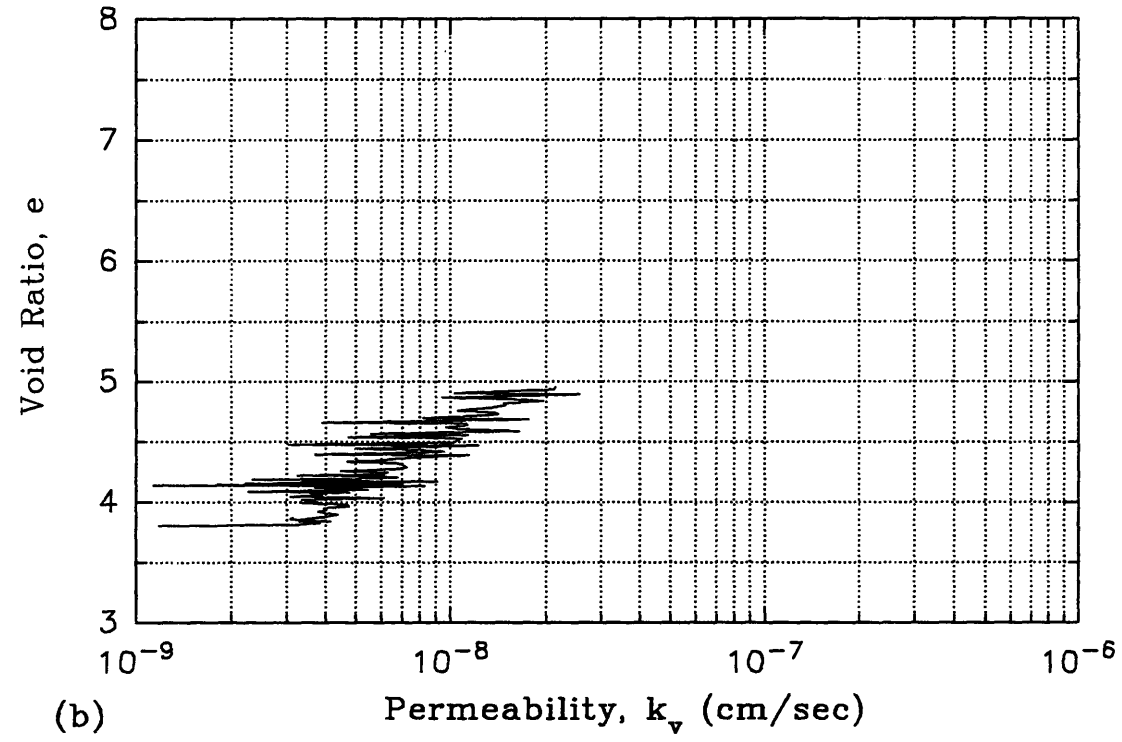

Figure 4.30 CRSC Consolidation Results – CRS76
(a) Void Ratio vs. Permeability; Loading Data
(b) Void Ratio vs. Permeability; Unloading Data

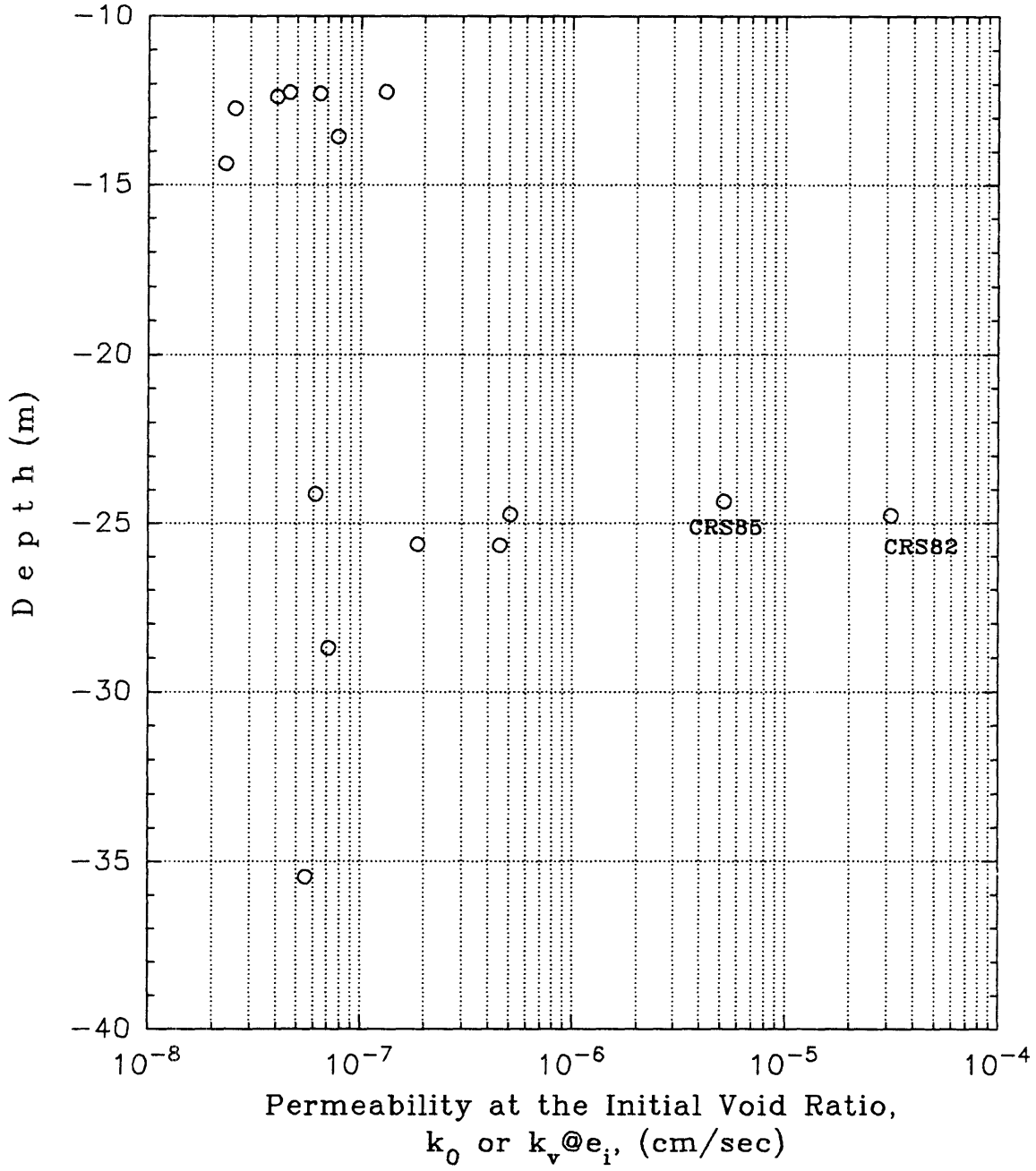

Figure 4.31 Depth vs. Permeability at the Initial Void Ratio

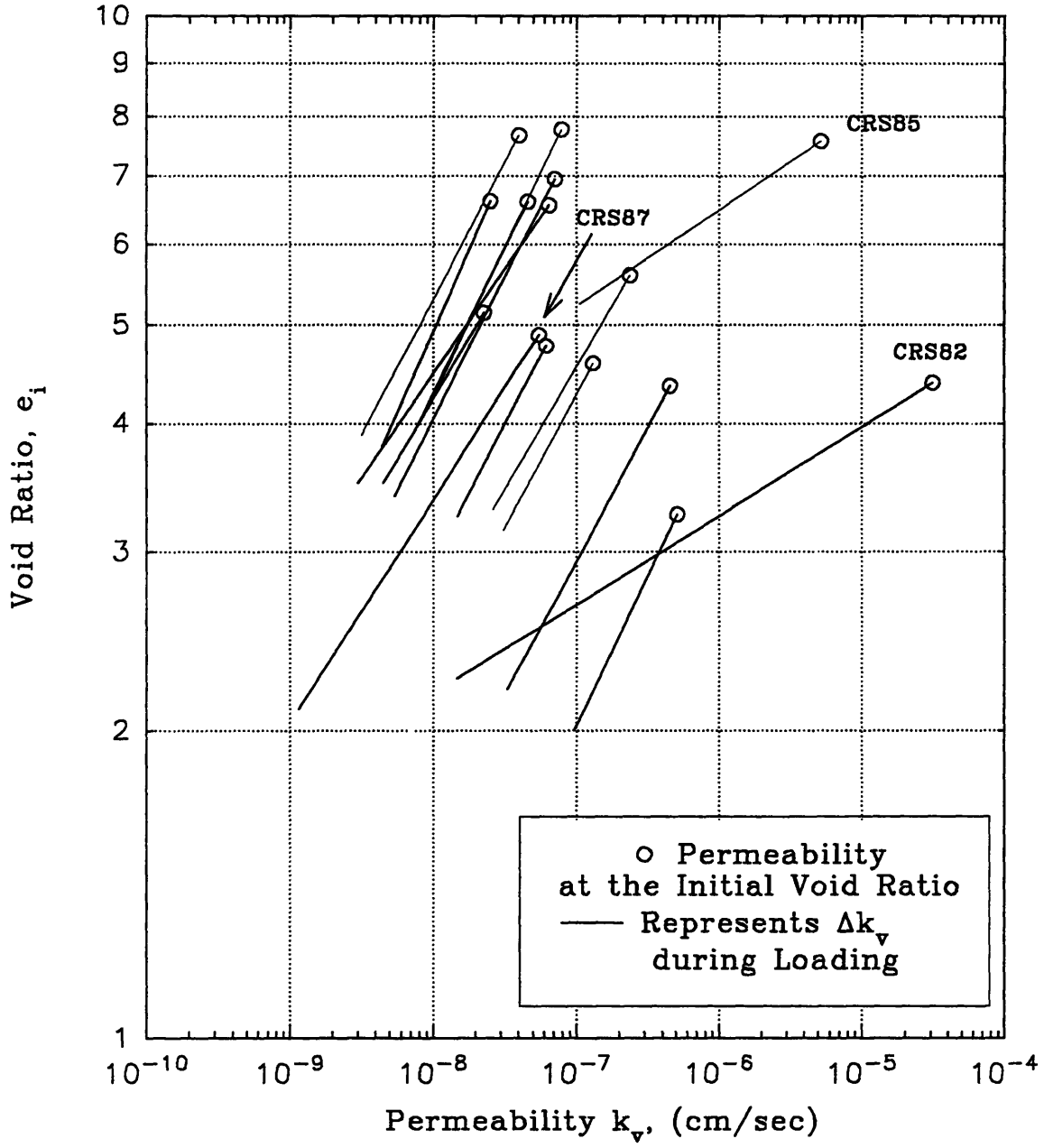

Figure 4.32 Void Ratio vs. Permeability

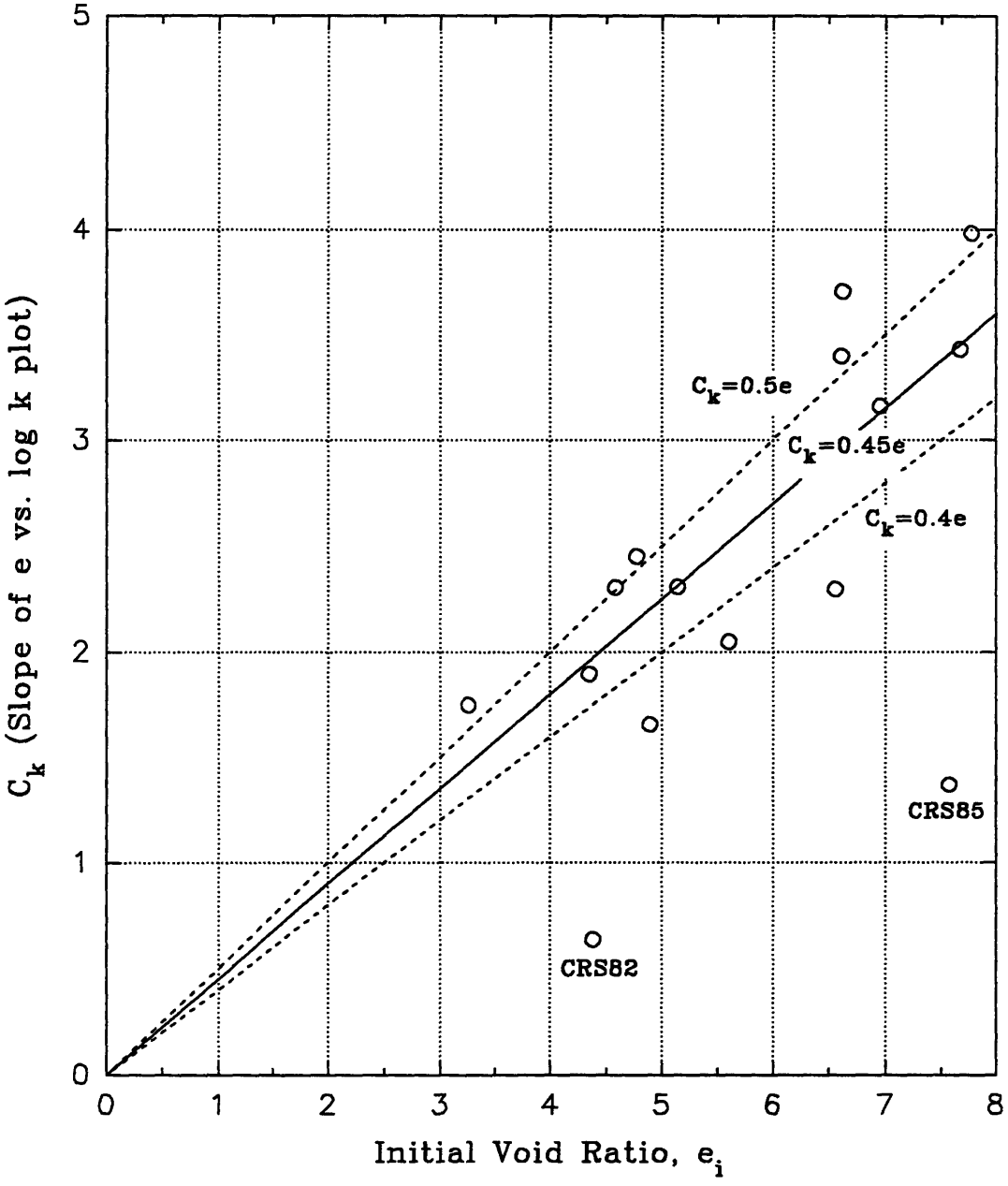

Figure 4.33 C_k vs. Initial Void Ratio

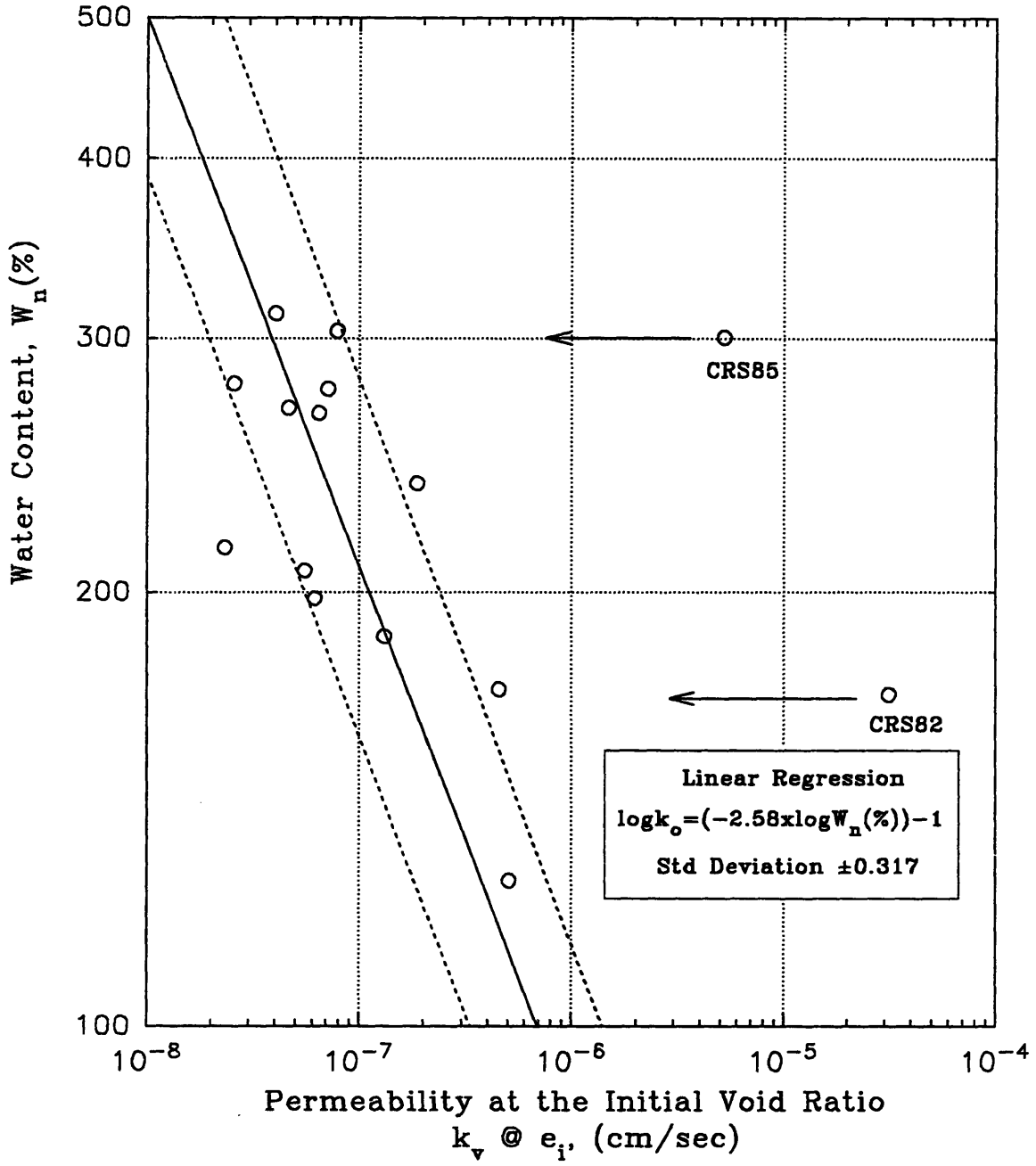

Figure 4.34 Water Content vs. Permeability at the Initlal Void Ratio

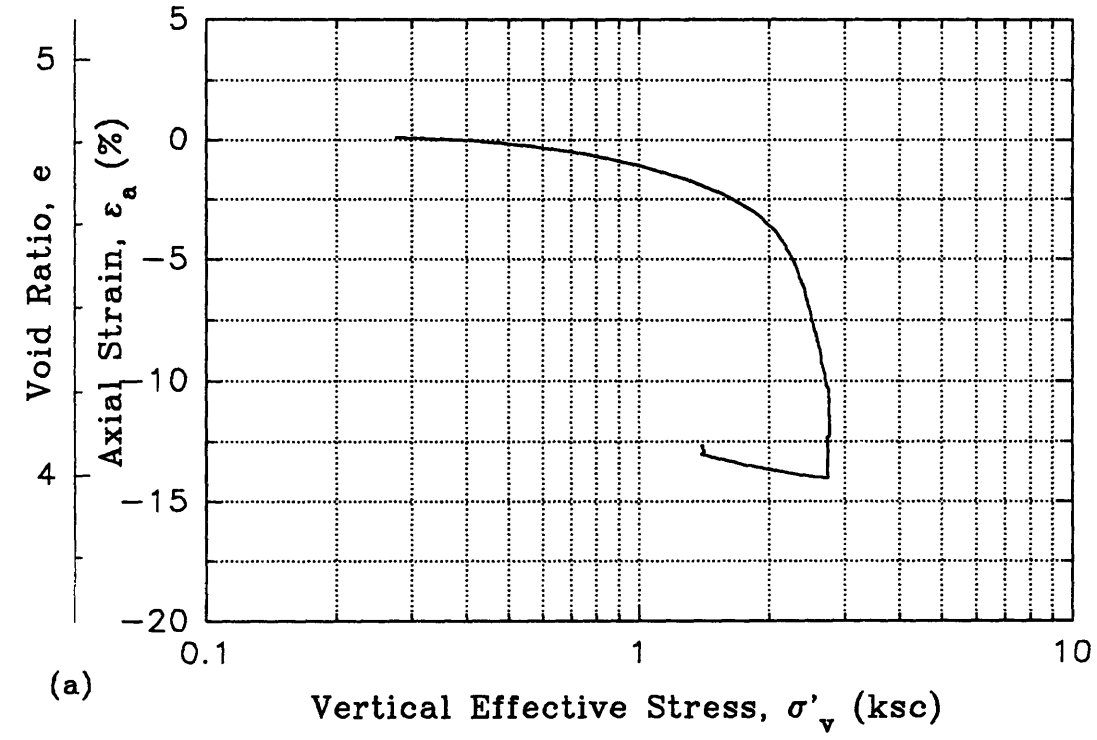

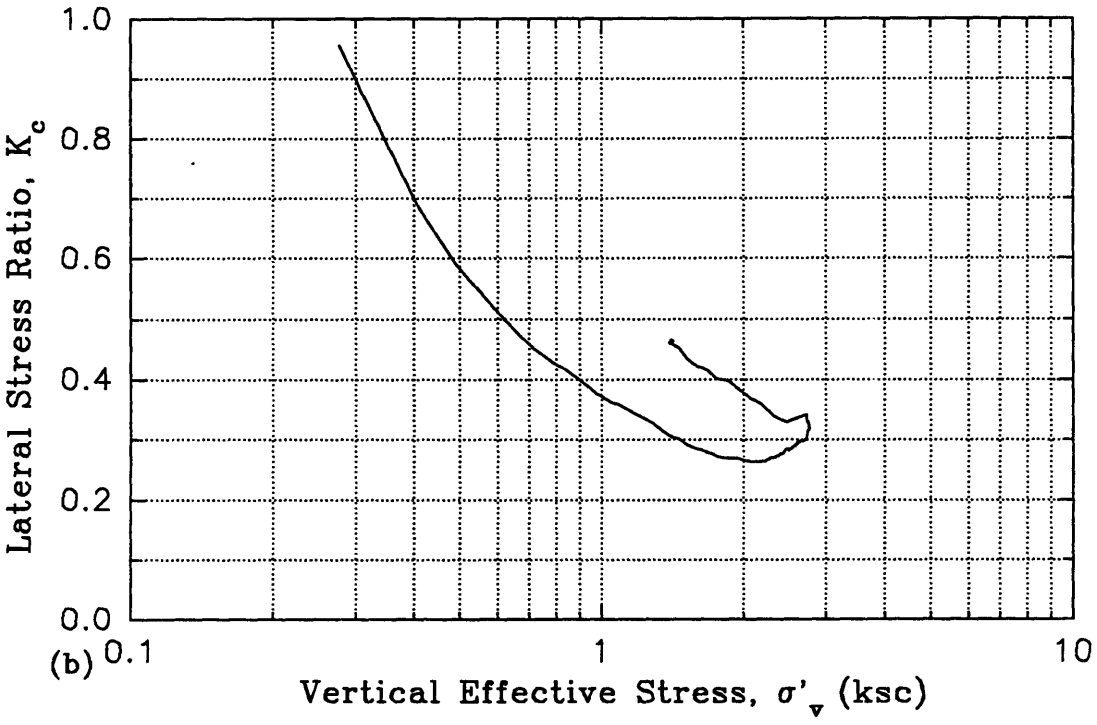

Figure 4.35 Consolidation Results – TX233
OCR=2, σ'_{vo}=1.51ksc, σ'_p=2.25ksc, Depth−25.47m
(a)Compression Curve (b) K_c vs. σ'_{vc}

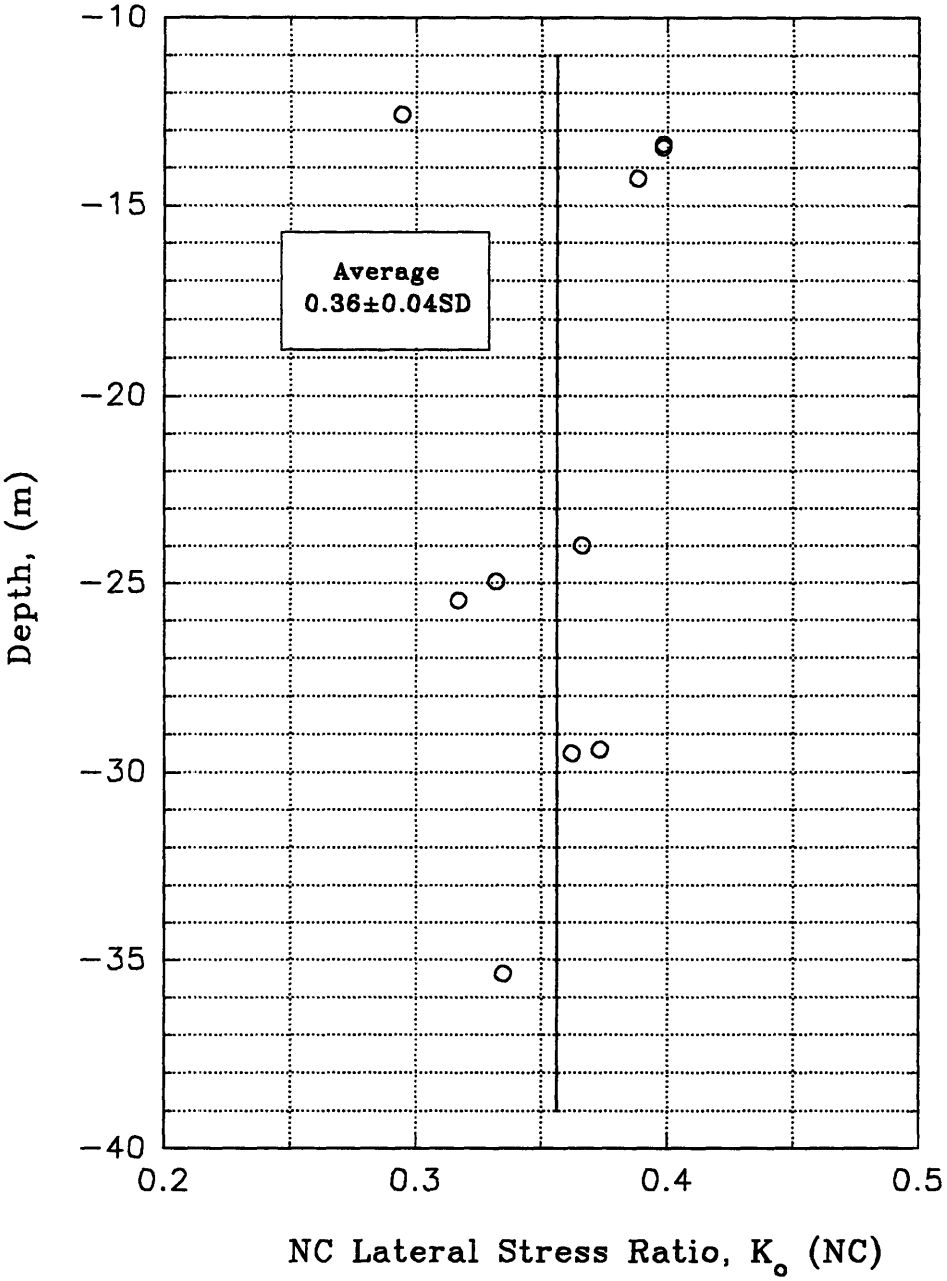

Figure 4.36 Depth vs. NC Lateral Stress Ratio

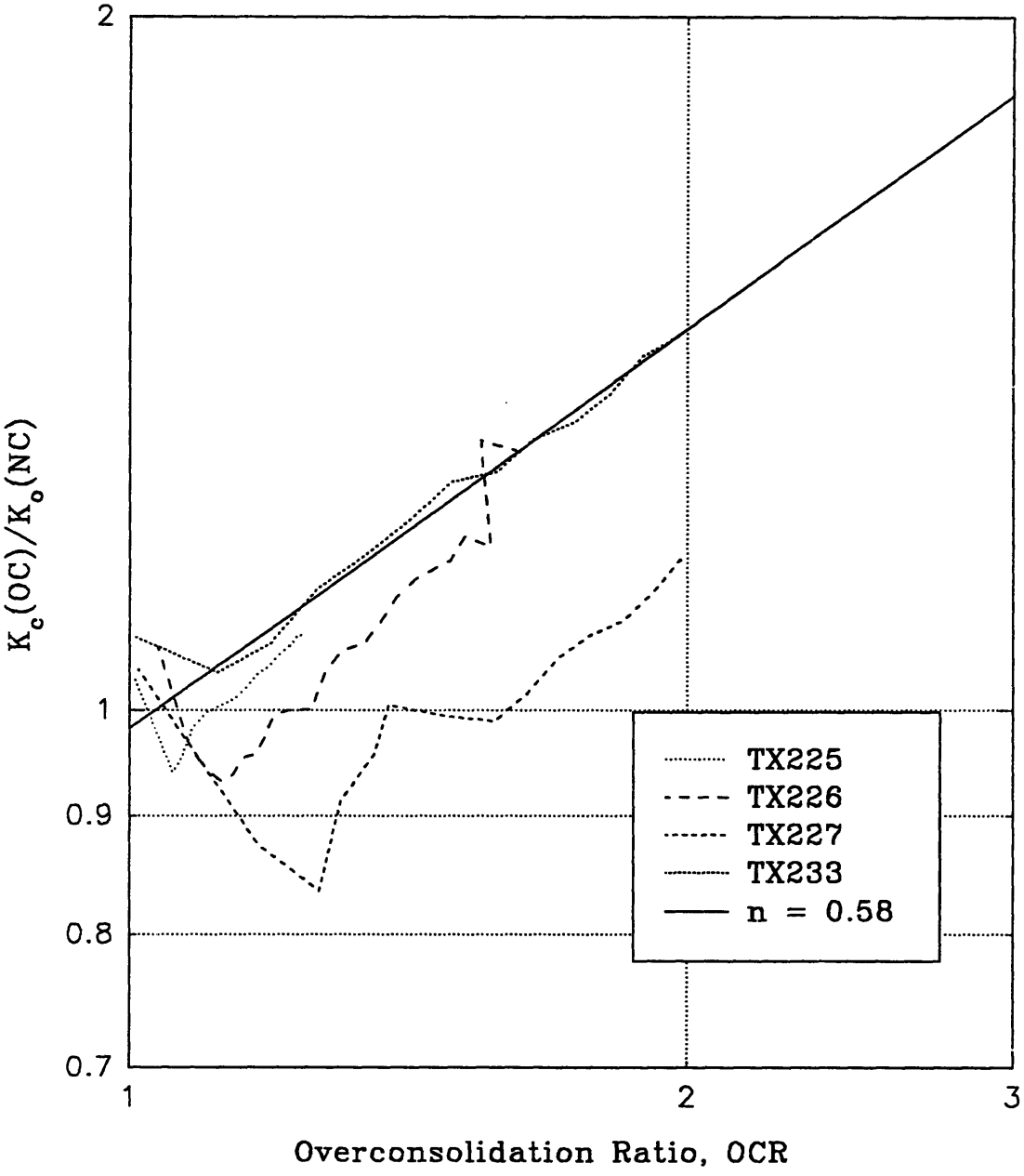

Figure 4.37 $K_c(OC)/K_o(NC)$ vs. Overconsolidation Ratio

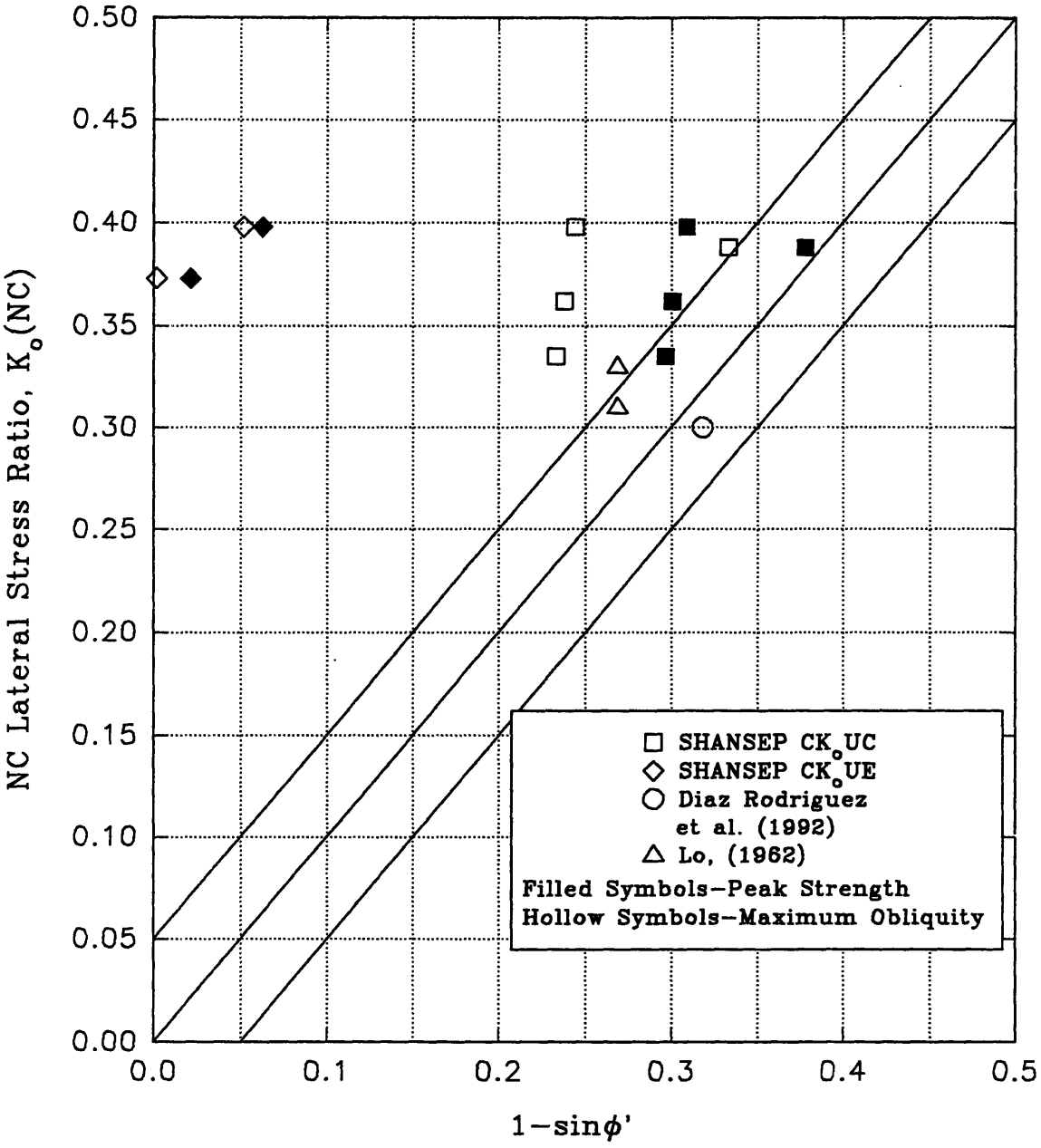

Figure 4.38 NC Lateral Stress Ratio vs. 1−sinϕ' for Triaxial Tests; OCR=1

CHAPTER 5
RESULTS OF SHANSEP STRENGTH TESTING PROGRAM

5.1 INTRODUCTION

The primary goal of the SHANSEP K_o consolidated-undrained (CK_oU) strength testing program was to obtain reliable measurements of the normalized undrained shear behavior of the clay deposit underlying México City's cathedral. CK_oU tests were sheared in triaxial compression, triaxial extension, and direct simple shear in order to assess the stress-strain-strength anisotropy of México City Clay. One-dimensional compression data from the SHANSEP testing program were also used to help evaluate the stress history, consolidation properties, and the in situ lateral stress ratio (K_o) for the clay beneath the cathedral, as discussed in Chapter 4. The following is a summary of the SHANSEP testing program that was implemented for this study:

		Number of Tests for nominal OCR =			
Mode of Shearing	Total	1	1.25	1.6	2
Direct Simple Shear	13	10	1	1	1
Triaxial Compression	7	4	1	1	1
Triaxial Extension	3	2	-	-	1

This chapter first discusses reconsolidation techniques, then presents the results of the direct simple shear tests, triaxial compression, and triaxial extension tests. For each mode of shearing, the general undrained shear behavior of the clay beneath the cathedral will be summarized, followed by a discussion of parameters including undrained strength ratio, effective stress failure envelope, undrained Young's modulus, and strain at failure. Where possible, the parameters obtained for México City Clay beneath the cathedral will

be compared to parameters reported in the literature for other samples of México City Clay.

5.2 SAMPLE DISTURBANCE AND RECONSOLIDATION TECHNIQUES

Most of the discussion presented in this section has been summarized from Jamiolkowski et al. (1985).

In Chapter 4, the effects of sample disturbance on the consolidation and compressibility properties of cohesive soils were explained. This section will discuss the effects of sample disturbance on the measured undrained shear strength of cohesive samples, as well as procedures that can be used to minimize these effects.

The in situ soil structure will always be altered by the sampling process and hence can never be exactly duplicated in the laboratory. It is now recognized that unconsolidated-undrained (UU) type testing produces highly unreliable and variable results for at least two reasons: (1) variable degrees of disturbance often cause a substantial reduction in the preshear effective stress, σ'_s; and (2) even "perfect sampling" significantly alters stress-strain characteristics, since shearing starts from isotropic rather than the in situ K_o stress conditions (Ladd and Lambe 1963). Hence, consolidated undrained (CU) tests must be employed in order to minimize the adverse effects of sampling disturbance. The two principle variables associated with CU tests are the vertical consolidation stress, σ'_{vc}, and the consolidation stress ratio, $K_c=\sigma'_{hc}/\sigma'_{vc}$. The latter should approximate the in situ K_o, both to help restore the in situ soil structure and to give more meaningful stress-strain data. Thus, CIU tests have little merit, unless K_o is near unity. K_o consolidated undrained (CK_oU) tests which use a consolidation stress ratio, K_c, approximately equal to the in situ K_o are necessary to obtain a reliable estimate of the undrained strength.

Variables to be considered when conducting the consolidation portion of a CK_oU test include the preshear values of: (1) the vertical consolidation stress, σ'_{vc}; (2) the

consolidation stress ratio, K_c; and (3) the stress path used to reach the preshear conditions. The following discussion will focus on the merits of the Recompression and SHANSEP reconsolidation techniques. Both methods are often used to reconsolidate specimens to minimize the adverse effects of sample disturbance.

The two techniques are illustrated in Figure 5.1, which shows hypothetical in situ and laboratory K_o compression curves for a slightly overconsolidated soft clay. Points 1 and 2 designate the in situ condition and the preshear effective stress for a UU test, respectively (the latter assuming no change in water content during sampling). Test specimens following the Recompression technique are reconsolidated to $\sigma'_{vc}=\sigma'_{vo}$ (Point 3). Points A through D correspond to typical reconsolidation stresses for a test specimen following the SHANSEP technique.

SHANSEP is an acronym for Stress History and Normalized Soil Engineering Properties. As described by Ladd and Foott (1974) and Ladd et al. (1977), the SHANSEP technique involves the following basic steps (for a given layer of soil and a given mode of failure):

(1) establish the initial stress history, i.e. the profiles of σ'_{vo} and σ'_p, which determines the range of OCR values for which data are required;

(2) perform a series of CK_oU shear tests on specimens consolidated beyond the in situ preconsolidation pressures (to σ'_{vc} greater than 1.5-2 times σ'_p) to measure the behavior of normally consolidated clay and also on specimens rebounded to varying OCRs to measure overconsolidated behavior;

(3) express the results in terms of log undrained strength ratio versus log OCR (to obtain the normalized soil parameters (NSP), S and m);

(4) use these NSP relationships and the stress history information to compute profiles of undrained shear strength.

Although SHANSEP was originally developed based on empirical observation that it yielded reasonable results, the rationale for the SHANSEP reconsolidation technique to

minimize disturbance effects was predicted on the assumption that natural clays exhibit normalized behavior. Referring to Figure 5.1, for most soils laboratory compression curves typically approach the in situ virgin compression curve when σ'_{vc} exceeds about 1.5 to 2 times σ'_p. Thus test specimens A and B should have a structure similar to the in situ normally consolidated clay and hence yield reasonably NSP. Likewise, tests C and D give data on samples having a well defined overconsolidation ratio. SHANSEP assumes mechanically overconsolidated behavior to represent all preconsolidation pressure mechanisms, and hence involves obvious errors with highly structured, sensitive clays and naturally cemented deposits.

Although additional research is necesarry to quantify the likely errors associated with using the Recompression and SHANSEP techniques for the wide range of sample qualities and soil types encountered in practice, Ladd (1991) offers the following guidelines and comments for CK_oU test programs.

The Recompression technique:

(1) Is clearly preferred when block quality samples are available.

(2) Is more accurate for highly structured, brittle clays such as those found in eastern Canada. SHANSEP may significantly underpredict peak triaxial strengths and probably gives somewhat conservative design strengths after considering anisotropy and strain compatibility.

(3) Is preferred for strongly cemented soils and for testing highly weathered and heavily overconsolidated crusts where SHANSEP is often difficult to apply.

(4) Should not be used for truly normally consolidated soils (OCR=1), such as those encountered in tailings slimes, dredged materials, and recent deltaic deposits, since reconsolidation to $\sigma'_{vo} = \sigma'_p$ will clearly overestimate the in situ strength.

(5) Should always be accompanied by measurements of the in situ stress history in order to: estimate K_o; check that the measured undrained strength ratio values are reasonable; and extrapolate and interpolate the "point" data versus OCR.

The SHANSEP technique:

(1) Requires a more accurate estimate of the in situ stress history and is strictly applicable only to mechanically overconsolidated and truly normally consolidated deposits having ideal normalized behavior.

(2) Is probably preferred for testing conventional tube samples from low OCR deposits of "ordinary" clays (relatively low sensitivity), where the preconsolidation pressure is caused mainly by the mechanical-desiccation-aging mechanisms. SHANSEP may tend to underestimate undrained strengths in some deposits

(3) Has the distinct advantage of developing normalized stress-strain-strength parameters that can be used for subsequent projects involving the same deposit (especially if they have yielded acceptable results based on evaluated field experience).

The Recompression and SHANSEP techniques both involve a controlled stress path consolidation. Both techniques require an accurate control of σ'_{hc} and σ'_{vc}. Additionally, the SHANSEP technique requires that σ'_{hc} and σ'_{vc} be controlled in a such a way as to produce one dimensional consolidation of the sample. Maintainng stress path consolidation is difficult and costly during triaxial testing without using automation. Therefore, many laboratories use a simplified technique via isotropic consolidation to $\sigma'_{hc}=K_o\sigma'_{vc}$, followed by drained loading to reach σ'_{vc}. This is reasonable, provided that the first step does not cross the "yield envelope" for isotropic consolidation.

Both the SHANSEP and Recompresion approaches require that specimens be sheared in different failure modes in order to assess stress-strain-strength anisotropy of the soil. Also, it should be recognized when dealing with overconsolidated deposits that the Recompression technique reloads the soil and the SHANSEP technique unloads the soil to the relevant OCR. Hence, the resulting undrained strength ratios may be different because of the hysteresis loop exhibited by one-dimensional unload reload cycles.

5.3 SHANSEP TECHNIQUE PROOF TESTS

As mentioned in the previous section, the SHANSEP technique requires that the specimen be consolidated to 1.5 to 2 times the σ'_p. For México City Clay, this results in 30 to 40% axial deformation of the specimen, whereas for most other soils, consolidation to 1.5 to 2 times the σ'_p results in axial deformations of 10 to 15%. Generally, laboratory strength testing devices are not capable of consolidating specimens to axial strain as high as those required for México City Clay. Therefore, specimens for this investigation were consolidated to a minimum axial strain of 10%.

Figure 5.2 presents consolidation and shear results for Normally Consolidated SHANSEP CK_oU DSS tests, DSS311, DSS315, and DSS317. The objective of these tests was to determine if changes in consolidation stress, e.g. different amounts of axial deformation, would cause a change in either the normalized undrained strength or the stress-strain relationships of the specimens. The three "proof" tests specimens were obtained from a four inch section of sample S2-2. The following table presents a summary of the testing conditions for each test:

Test	Depth (m)	e_i	e_f	ε_a	σ'_{vc}	τ_h/σ'_{vc}
DSS311	-13.56	7.39	5.68	-30.76	2.81	0.342
DSS315	-13.51	7.54	6.71	-20.21	2.22	0.334
DSS317	-13.46	7.50	7.26	-14.40	1.79	0.362

Figure 5.2 shows that increasing axial deformation of the soil does not significantly change the normalized undrained strength or the stress-strain relationships of the specimens. Hence, the soil exhibits normalized behavior. As shown in the figure, DSS317 yielded a slightly higher undrained strength ratio. Since this test was consolidated to just beyond the preconsolidation pressure, σ'_p, and therefore was not truly normally consolidated, it was expected to yield a higher normalized undrained strength.

Additionally, DSS311 yielded a larger shear strain to failure, but the initial stress-strain relationship was not affected.

Since the results of the three CK_0UDSS tests discussed above established that the soil exihibits normalized behavior when normally consolidated, it was decided to reconsolidate all undrained strength test specimens using the SHANSEP technique.

5.4 SHANSEP CK_0 UNDRAINED SHEAR STRENGTH TEST PROGRAM

5.4.1 Overview

As mentioned above 12 SHANSEP CK_0U direct simple shear (DSS) tests, 7 SHANSEP CK_0U triaxial compression tests (TC), and 3 CK_0U triaxial extension (TE) tests were performed for this study. Ten of the SHANSEP CK_0UDSS tests were sheared normally consolidated, and three tests were sheared at OCRs of 1.25, 1.60, and 2.0. Four of the SHANSEP TC tests were sheared normally consolidated, and three tests were sheared at OCRs of 1.24, 1.65, and 2.0. Two of the SHANSEP TE tests were sheared normally consolidated, and one test was sheared at an OCR of 2. Based on the estimated stress history of the site, it was not deemed necessary to perform overconsolidated tests with OCRs higher than 2. The data from SHANSEP CK_0UDSS tests is summarized in Table 5.1, and the data from both CK_0UC and CK_0UE tests are summarized in Table 5.2. The shear results from all tests are presented in numerical and graphical form in MIT Department of Civil and Environmental Engineering Research Report Number R94-01.

5.4.2 General Undrained Shear Behavior

5.4.2.1 *SHANSEP CK_0UDSS Tests*

Figures 5.3 through 5.5 present the CK_0U direct simple shear behavior of the clay underlying México City's cathedral. Figure 5.3 presents the effective stress paths normalized to the maximum vertical consolidation stress (σ'_{vm}) for all DSS tests. The figure illustrates how the curves from tests performed at various OCRs merge towards a

common failure envelope at large strains. It should be noted that the near vertical shape of the overconsolidated effective stress path is very uncommon compared to the effective stress path found for other soils at the same OCR. Generally, the overconsolidated stress path for a DSS tests travels up and to the right intially until it reaches the NC effective stress path. It then follows the normally consolidated stress path to the left.

Figure 5.4a presents horizontal normalized shear stress-shear strain curves (τ_h/σ'_{vc} vs. γ) and Figure 5.4b plots the normalized pore pressure ($\Delta u/\sigma'_{vc}$) versus shear strain (γ). The curves generally follow a well defined trend as summarized below.

As the OCR increases:

a) the normalized shear strength (τ_h/σ'_{vc}) increases;

b) the peak shear stress generally occurs at the same shear strains;

c) more strain softening occurs;

d) the amount of negative normalized pore pressure that is generated increases.

The plots in Figure 5.4b also show that for normally consolidated soil, the normalized pore pressure increases steadily as the specimen shears. As the OCR increases the normalized pore pressure decreases initially, approximately until failure, and then increases at about the same rate. The oscillation in the pore pressure is caused by difficulty in maintaining height control during shear.

Figure 5.5 plots the undrained secant Young's modulus normalized to the vertical consolidation stress (E_u/σ'_{vc}) versus shear strain on a log-log plot. The figure illustrates that for a given shear strain, the normalized undrained modulus increases with OCR. Additionally, one should note the very small band in which the normalized undrained modulus plots (especially for shear strains greater than 1%) for a variety of stress levels and initial water contents.

5.4.2.2 *SHANSEP CK_oU Triaxial Compression and Extension Tests*

Figures 5.6 through 5.10 illustrate typical undrained triaxial compression and extension shear behavior. Figure 5.6 presents the effective stress paths normalized to the maximum vertical consolidation stress (σ'_{vm}) for all triaxial compression and extension tests. As the figure shows, the effective stress paths approach a common failure envelope at large strains. It should be noted that the NC effective stress paths do not begin from the same relative position due to changes in the effective stress of the specimens prior to shear. The effective stress change is caused by a slight change in the pore pressure that occurs during the leak test with the drainage lines closed (as described in Chapter 2), and by a decrease in the pore pressure which occurs while changing the computer algorithm from consolidation to shear. Additionally, the effective stress path from triaxial test TX201 (OCR=1) plots below the other stress paths, which suggests that this test underestimates the NC undrained shear strength. As shown in the figure, the OC triaxial compression effective stress paths clearly climb above the NC failure envelope.

Figures 5.7a and 5.8a present the shear stress - axial strain curves (q/σ'_{vc} vs. ε_a) for triaxial compression and triaxial extension tests respectively. The following observations were made from these curves:

NC Behavior:

- The normalized undrained strength ratio for both triaxial compression and extension is very high compared to the values reported for most other soils. Additionally, there is some scatter in the triaxial compression results.
- The strain at failure in triaxial compression is extremely large, approximately one order of magnitude higher than it is for most soils.
- The soil presents very significant strain softening over a large region of strain in triaxial compression and extension, although not as much in triaxial extension.

Increasing OCR causes:

- an increase in the peak value of the strength normalized to the vertical consolidation stress (q/σ'_{vc}) in both triaxial compression and extension;
- an increase in strain softening in both compression and extension;
- an increase in the axial strain at failure (ε_{af}) in compression;
- a decrease in the axial strain at failure (ε_{af}) in extension.

Figure 5.7b and 5.8b present the normalized shear induced pore pressure [$u_s/\sigma'_{vc}= (\Delta u-\sigma_{oct})/\sigma'_{vc}$] versus axial strain for triaxial compression and triaxial extension tests, respectively. In both triaxial compression and extension, for normally consolidated samples, u_s/σ'_{vc} increases with increasing axial strain. In triaxial compression, as expected at small strains, an increase in the OCR causes a reduction in the amount of u_s/σ'_{vc} generated, and at OCR=2 negative pore pressures are measured. However, the trend of u_s/σ'_{vc} with strain is similar for all OCRs after the initial OC effect is developed (ε_a>2%).

Figure 5.7c and 5.8c present friction angle (ϕ') versus axial strain for triaxial compression and triaxial extension tests respectively. In triaxial compression, increasing the OCR increases ϕ' at failure, and in extension increasing the OCR decreases ϕ' at failure. Additionally, it should be observed that for triaxial extension tests (all OCRs) and triaxial compression tests (OCRs>1), the peak and maximum obliquity conditions occur more or less simultaneously, which is probably due to brittle failure of the sample.

Figures 5.9 and 5.10 present the secant undrained Young's modulus normalized to the vertical consolidation stress (E_u/σ'_{vc}) versus axial strain on a log-log plot for triaxial compression and triaxial extension, respectively. The figures illustrate that for any given axial strain the normalized undrained modulus increases with increasing OCR. It should be noted that the results for the NC normalized undrained modulus from triaxial compression tests are very consistent, i.e., they plot in a very narrow band, even at axial

strains as low as 0.01%. Additionally, the decrease of the normalized undrained modulus with increasing axial strain is not as marked as it is for other soils.

5.4.3 Undrained Strength Ratio

5.4.3.1 *SHANSEP CK_oUDSS Tests*

Figure 5.11 plots the variation in the normally consolidated peak undrained strength ratio for direct simple shear ($S_d=\tau_h/\sigma'_{vc}$) with depth. The NC undrained strength ratio (USR) is essentially constant with depth with an average of $S_d=0.346\pm0.010SD$.

The undrained strength normalized to the consolidation stress (c_u/σ'_{vc}) for a particular mode of failure can be related to the stress history at a site via the SHANSEP equation:

$$c_u / \sigma'_{vo} = S\,(OCR)^m \quad \text{.....(5.1)}$$

where c_u=undrained shear strength for a particular mode of failure; σ'_{vo}=the vertical effective stress; S=the normally consolidated value of c_u / σ'_{vc}; OCR=overconsolidation ratio (σ'_p/σ'_{vo}); and m=the strength increase exponent.

Figure 5.12 presents the peak USR in direct simple shear ($S_d=\tau_h/\sigma'_{vc}$) versus the test OCR on a log-log plot. A linear regression on the data yielded the following SHANSEP undrained shear strength parameters:

$$S_d = 0.344$$

$$m = 1.018$$

$$r^2 = 0.985$$

5.4.3.2 *SHANSEP CK_oU Triaxial Compression and Extension Tests*

Figure 5.11 plots the variation in the peak normally consolidated (NC) undrained strength ratio for triaxial compression ($S_c=q_f/\sigma'_{vc}$), and triaxial extension ($S_e=q_f/\sigma'_{vc}$) with depth. The data might suggest a trend of increasing S_c and S_e with depth, as indicated by dashed lines on the figure. Not enough data was obtained to verify this trend. For the purposes of this study, both S_c and S_e are assumed to be constant with depth.

The following average values were computed; S_c=0.404±0.015SD, and S_e=0.329± 0.018SD.

Figure 5.13 plots the peak NC undrained strength ratio versus preshear lateral stress ratio (K_o(NC)). The data illustrate a very well defined relationship between S_c and K_o(NC), i.e., as the normally consolidated value of K_o increases, there is a linear decrease in the normally consolidated value of the peak USR. A linear regression was performed on the data and yielded the following equation:

$$S_c = -0.494 \times K_o(NC) + 0.587, \quad r^2=0.913 \qquad (5.2)$$

This relationship has been established for various soils studied at MIT. Figure 5.14 plots some data that was obtained at MIT and the data obtained for this investigation. As shown in the figure, there is a unique relation between the NC USR and K_o(NC) for all of the data.

Berman (1993) presents an analysis to understand why a change in S_c is associated with a change in K_o(NC). The undrained strength ratio can be related to K_o(NC) through the following equation which is derived from the geometry of the effective stress failure envelope and the effective stress path of the specimen during undrained shear:

$$q_f / \sigma'_{vc} = S_c = \frac{[K_o + (1-K_o) A_f] \sin \phi'_f}{1 + (2A_f - 1) \sin \phi'_f} \qquad (5.3)$$

Berman made the following observations:

(1) There is an increase in ε_{af} with increasing K_o(NC). This trend is expected since a larger K_o generally requires a larger stress increment to reach failure.

(2) There is an increase in A_f with increasing K_o(NC). This trend is consistent with the increasing strain at failure (i.e., for OCR=1, A_f always increases with increasing ε_a).

(3) There is a decrease in ϕ'_f with increasing K_o(NC). This trend would not necessarily be predicted since an increasing strain at failure will cause an increase

in the mobilized friction angle, whereas the smaller initial shear stress corresponding to a higher K_o will tend to reduce ϕ'_f at the peak strength. Berman's data showed the latter effect to predominate.

(4) Thus, the decrease in S_c with increasing K_o results both from an increase in A_f and a decrease in ϕ'_f, with the latter trend being predominant.

Figure 5.15 plots the pore pressure parameter, A_f, the axial strain at failure, ε_{af}, and the peak friction angle, ϕ'_p, in triaxial compression versus K_o(NC) for the data of this investigation. The figure shows the same general trends as reported by Berman, although the trends are not as well defined.

As the following table shows, there is good agreement between the measured S_c and the predicted values (S_{cp}). Equation 5.3 and the measured values for A_f, ε_{af}, ϕ'_p, and K_o(NC) were used to compute S_{cp}.

Test	S_c	S_{cp}
TX201	.389	.393
TX221	.410	.422
TX222	.394	.420
TX223	.421	.427

Figure 5.16 presents $q_f(C)/\sigma'_{vc}$ and $q_f(E)/\sigma'_{vc}$ versus the test OCR on a log-log plot. A linear regression on both sets of data yield the SHANSEP parameters, S and m, used to calculate the undrained strength from a knowledge of the stress history at the site. The SHANSEP parameters for each mode of failure are the following:

Mode of Failure	S	m	r^2
Compression	0.407	0.991	0.964
Extension	0.329	0.681	0.978

5.4.4 Failure Envelope

5.4.4.1 *SHANSEP CK_oUDSS Tests*

Since it is well known that the DSS is not a reliable test for obtaining Mohr-Coulomb failure envelopes (Ladd and Edgers 1972), a failure "type" envelope, which plots values at 30% shear strain for each test, is evaluated for the SHANSEP CK_oUDSS testing program. Figure 5.17 plots the normalized shear stress (τ_h/σ'_{vm}) versus the normalized vertical stress ($\sigma'_{vc}/\sigma'_{vm}$) for normally consolidated and overconsolidated tests. The "failure" envelope at large strain can be defined by the following equation:

$$\tau_h/\sigma'_{vm}=c'/\sigma'_{vm} + \tan\psi'(\sigma'_{vc}/\sigma'_{vm}) \quad (5.4)$$

and a linear regression on the cathedral's data (from Figure 5.17) gives:

$$\tau_h/\sigma'_{vm}=0.684(\sigma'_{vc}/\sigma'_{vm}) \quad (5.5)$$

where the "friction angle" at large strain (ψ' @ γ=30%) is 34.4°.

5.4.4.2 *SHANSEP CK_oU Triaxial Compression and Extension Tests*

The normalized shear stress (q/σ'_{vm}) versus the normalized effective stress (p'/σ'_{vm}) at maximum obliquity is presented in Figure 5.18 for normally consolidated and overconsolidated triaxial compression and extension tests. The following equation defines the q-p' effective stress failure envelope at maximum obliquity:

$$q/\sigma'_{vm} = a'/\sigma'_{vm} + \sin\phi' \, (p'/\sigma'_{vm}) \quad (5.6)$$

The corresponding Mohr-Coulomb relationship commonly used to describe the stresses on the failure plane (τ_f and ϕ'_f) is:

$$\tau_f/\sigma'_{vm} = c'/\sigma'_{vm} + \tan\phi' \, (\sigma'_f/\sigma'_{vm}) \quad (5.7)$$

where the Mohr-Coulomb cohesion intercept, $c' = a' / \cos\phi'$.

Two linear regressions were performed on the data. One on the NC (OCRs≤1.25) compression data, and the second one on OC (OCRs>1.25) compression data and all extension data. The regression analysis yielded the following equations:

For NC samples failed in triaxial compression (OCRs≤1.25):

$$q/\sigma'_{vm} = 0.757\ (p'/\sigma'_{vm})\ \ r^2=0.986 \quad \text{.....(5.8)}$$

For OC samples failed in triaxial compression (OCRs>1.25) and all samples failed in triaxial extension:

$$q/\sigma'_{vm} = 0.917(p'/\sigma'_{vm})\ \ r^2=0.913 \quad \text{.....(5.9)}$$

Both maximum obliquity failure envelopes are plotted in Figure 5.18. Both failure envelopes are characterized by a cohesion intercept equal to zero. The friction angles of the maximum obliquity failure envelopes are; 49.2° for NC (OCRs≤1.25) samples sheared in triaxial compression, and 66.4° for OC (OCRs>1.25) samples failed in triaxial compression and all samples failed in triaxial extension.

A linear regression analysis similar to that performed for the maximum obliquity data was performed for the peak data (from Figure 5.19). The analysis yielded the following equations:

For NC samples failed in triaxial compression (OCRs<1.25):

$$q/\sigma'_{vm} = 0.705\ (p'/\sigma'_{vm})\ \ r^2=0.189 \quad \text{.....(5.10)}$$

For OC samples failed in triaxial compression (OCRs>1.25) and all samples failed in triaxial extension:

$$q/\sigma'_{vm} = 0.896(p'/\sigma'_{vm})\ \ r^2=0.903 \quad \text{.....(5.11)}$$

Both peak failure envelopes are plotted in Figure 5.19. The peak failure envelopes, are also characterized by a cohesion intercept equal to zero. The friction angles of the peak failure envelopes are; 44.9° for NC (OCRs≤1.25) samples sheared in triaxial compression, and 63.6° for OC (OCRs>1,25) samples failed in triaxial compression and all samples failed in triaxial extension.

It should be noted that the failure envelope for OCRs greater than those tested may have a cohesion intercept. Therefore, the above equations should be used with caution for OCRs greater than 2.

Lo (1962) reports maximum obliquity and peak friction angles of 47° for CK_oUC normally consolidated and overconsolidated samples of México City Clay. Leon et al. (1974) report a peak friction angle of 41.8° for CIUC normally consolidated samples, and Diaz Rodriguez et. al. (1992) report a peak friction angle of 43° for CIUC normally consolidated samples. The consistency in the reported friction angles is impressive, especially considering that the physical properties of the clay studied for each investigation varied widely (W_n of 240 to 460%, PI of 180 to 490%).

5.4.5 Other Parameters

Strain at Failure

Figure 5.20 presents depth versus the shear strain at the peak shear stress for NC CK_oUDSS tests, and the axial strain at the peak shear stress for NC CK_oUC/E triaxial tests. The average value for the shear strain at failure (from DSS tests) is 13.18%± 1.73SD. As shown in the figure, all tests failed at a shear strain of approximately 12.5%, with the exception of two tests. The triaxial compression tests failed at a constant axial strain of 1.34%±0.09SD and the triaxial extension tests failed at an average axial strain of 16.15%±0.60SD. It should be noted that SHANSEP triaxial extension tests have a tendency to overestimate the strain at failure. The data in the figure suggest that the strain at failure remains constant with depth for each mode of shearing.

Strain at failure for CK_oUDSS tests and CK_oUC/E triaxial tests are plotted versus OCR on a log-log plot in Figure 5.21. The plot indicates that for direct simple shear and triaxial extension, the strain at failure decreases with increasing OCR. For triaxial compression the strain at failure increases with increasing OCR. For most other soils, the strain at failure will increase with increasing OCR for all modes of shearing.

Normalized Young's Modulus

Figure 5.22 presents depth versus E_{u50}/σ'_{vc} for normally consolidated CK_oUDSS tests and CK_oUC/E triaxial tests. There is scatter in the data, and there might be a trend

of increasing E_{u50}/σ'_{vc} with depth for CK_oUDSS and CK_oUC tests. At this time there is not enough data to verify this trend.

Figure 5.23 presents the normalized undrained modulus versus log OCR for CK_oUDSS tests and CK_oUC/E triaxial tests. As the figure shows, E_{u50}/σ'_{vc} increases with OCR for CK_oUC/E triaxial tests. For CK_oUDSS tests, E_{u50}/σ'_{vc} increases initially and then remains fairly constant.

5.5 SUMMARY OF SHANSEP RESULTS AND EFFECTS OF ANISOTROPY

5.5.1 Normally Consolidated México City Clay

For Direct Simple Shear:

1) The data in Figure 5.11 indicate that the value of $S_d=\tau_h/\sigma'_{vc}$ remains constant with depth at 0.346±0.010SD.

2) The friction angle at γ=30% is 34.4° for NC and OC samples.

3) The shear strain at failure for NC samples remains constant with depth at 13.18 ±0.731SD.

4) The value of E_{u50}/σ'_{vc} might increase with depth, but at this time it is not possible to verify this. A E_{u50}/σ'_{vc} value of 40 is recommended, but additional research is necessary to better understand and determine a more reliable estimate of this parameter.

For Triaxial Compression:

1) The data in Figure 5.11 might suggest that the value of $S_c=q_f(C)/\sigma'_{vc}$ increases with depth. A constant value of S_c with depth of 0.404±0.015SD is suggested.

2) There is a very well defined trend between S_c and $K_o(NC)$, as illustrated in Figure 5.13, e.i., an increase in $K_o(NC)$ is associated with a decrease in S_c.

3) The friction angle at maximum obliquity is 49.2° and the peak friction angle is 44.9°, for OCRs≤1.25.

4) The strain at failure remains constant with depth at ε_{af}=1.338±0.091SD.

5) The value of E_{u50}/σ'_{vc} might increase with depth, but at this time it is not possible to verify this. An E_{u50}/σ'_{vc} value of 45 is recommended, but additional research is necessary to better understand and determine a more reliable estimate of this parameter.

For Triaxial Extension:

1) The data in Figure 5.11 might suggest that the value of $S_c=q_f(C)/\sigma'_{vc}$ increases with depth. A constant value of S_c with depth of 0.329±.018SD is suggested.

2) The friction angle at maximum obliquity is 66.4° and the peak friction angle is 63.6°.

3) The strain at failure remains constant with depth at ε_{af}=16.15±0.6SD.

5) The recommended value of E_{u50}/σ'_{vc} which is based on two tests is 40.

It is important to point out that the values recommended above are extremely unique, and that no other known soil has normalized soil parameters similar to those obtained for México City Clay. Figure 5.24 (from Ladd 1986) presents undrained strength ratio versus plasticity index for various normally consolidated clays and silts. The data show: (1) $S_c = 0.32 \pm 0.03$ and there is no trend with the plasticity index; (2) generally much lower DSS strengths that tend to decrease with decreasing plasticity; and (3) even smaller ratios for samples sheared in triaxial extension, especially at low plasticity. The data and the literature clearly demonstrate that most OCR = 1 soils exhibit significant undrained strength anisotropy that generally becomes most important in lean clays, especially if they are also sensitive. The data from this investigation suggests that the plasticity index does not affect the undrained strength ratio for México City Clay. Additionally, México City Clay exhibits very little undrained strength anisotropy, and it has the highest undrained strength ratios of any soil ever published for triaxial compression, triaxial extension, and direct simple shear. Accompanying these high undrained strength ratios are some of the highest friction angles ever recorded.

Another unique aspect of México City Clay is its high strain to failure. Most normally consolidated clays tested under CK_oU conditions and sheared in triaxial compression fail at axial strains between between 0.1 and 0.3%. Normally consolidated México City Clay tested under the same conditions fails at an average axial strain of 1.34%. Diaz-Rodriguez et al. (1992) report that the typical strain to failure for México City Clay is 2% for specimens tested under CIU conditions and sheared in triaxial compression. México City Clay exhibits a relatively low E_{u50}/σ'_{vc} compared to most clays. Additionally, the value of E_{u50}/σ'_{vc} for direct simple shear, triaxial compression, and triaxial extension are very similar compared to most clays. This finding is not surprising since México City Clay has a relatively low shear strength anisotropy.

5.5.2 Overconsolidated México City Clay

This section summarizes the results of the SHANSEP OC CK_oU testing programs and gives recommendations for normalized stress-strain-strength parameters.

For USR versus OCR:

The estimates of S and m for México City Clay underlying the cathedral are:

DSS	S_d=0.344	m_d=1.018
TC	S_c=0.407	m_c=0.991
TE	S_e=0.329	m_e=0.681

It was stated in the previous section that the undrained strength ratios for México City Clay are exceptionally high. Additionally, the m values for triaxial compression and direct simple shear are also exceptionally high. Ladd (1989) recommends an average m value of 0.8±0.1SD for a typical clay. The parameters listed above should only be used to estimate undrained strengths for OCRs between 1 and 2. Based on data reported in the literature it is likely that the m value of México City Clay will decrease as the OCR increases. It should also be

noted that there is a significant amount of uncertainty associated with the m value for triaxial extension, since it is based on only one data point.

The SHANSEP parameters listed above were used to calculate the best estimate of the undrained shear strength profile for different modes of shearing at the cathedral site. The undrained shear strength profile is based on an OCR which remains constant with depth (OCR=1.5) as shown in Figure 4.16. Figure 5.25 plots the undrained shear strength profiles. The figure also plots the UU data from Boring SMC-1 presented in SEDUE (1990). As shown in the figure, UU tests significantly underestimate the undrained shear strength.

For Effective Stress Failure Envelope at Maximum Obliquity and Peak Shear Stress:

The estimates of parameters for the Mohr-Coulomb effective stress failure envelope (ESFE) are as follows:

For Triaxial Compression OCRs≤1.25:

Maximum Obliquity	Peak Shear Stress
c'/σ_{vm} =0 and ϕ'_{mo}=49.2°	c'/σ_{vm} =0 and ϕ'_{p}=44.9°

For Triaxial Compression OCRs>1.25 and Triaxial Extension all OCRs

Maximum Obliquity	Peak Shear Stress
c'/σ_{vm} =0 and ϕ'_{mo}=66.4°	c'/σ_{vm} =0 and ϕ'_{p}=63.6°

It should be noted that the failure envelope for OCRs greater than those tested may have a cohesion intercept. Therefore, the above equations should be used with caution for OCRs greater than 2.

The DSS test is not reliable for obtaining a Mohr-Coulomb type failure envelope. The "failure" envelope at a shear strain of 30% is as follows:

DSS All OCRs c/σ'_{vm}=0 and ψ'=34.4°

For Strain At Failure versus OCR:

The shear strain at failure (γ_f) is plotted versus OCR on a log-log plot for direct simple shear tests in Figure 5.21. Figure 5.21 also plots the axial strain at failure (ε_{af}) for triaxial compression and extension tests. For triaxial compression the strain increases as the OCR increases. For direct simple shear and triaxial extension the strain decreases as the OCR increases. For most soils in any mode of shearing, the strain af failure will increase with increasing OCR.

For Normalized Undrained Modulus versus OCR:

The normalized undrained Young's modulus (E_{u50}/σ'_{vc}) is plotted versus OCR on a log-log plot for direct simple shear, triaxial compression, and triaxial extension in Figure 5.23. Based on the data, one observes the following trends in mean values:

DSS $E_{u50}/\sigma'_{vc} \approx 40$, increases slightly and then remains constant at a value of ≈ 85.

TC $E_{u50}/\sigma'_{vc} \approx 45$, increases significantly with OCR.

TE $E_{u50}/\sigma'_{vc} \approx 40$, increases slightly with OCR.

Table 5.1 Summary of Shear Results from SHANSEP CK_oUDSS Tests

Test Sample Depth (m)	IN SITU		PRE SHEAR			AT PEAK		AT LARGE STRAIN			E_{50}/σ'_{vc} E_u/σ'_{vc} @γ=1.0%	Remarks
	W_n e_i	σ'_{vo} S_i (%)	W_c e_c	σ'_{vm} σ'_{vc}	OCR ε_a (%)	τ_h/σ'_{vc} σ'_v/σ'_{vc}	γ (%) ψ'	τ_h/σ'_{vc} σ'_v/σ'_{vc}	τ_h/σ'_{vm} σ'_v/σ'_{vm}	γ (%) ψ'		
DSS311 S2-2	272.88	1.10	170.08	2.809	1	0.342	13.43	0.272	0.272	29.95	39	
-13.56	0.00	93.0	5.68	2.809	30.76	0.668	27.1	0.405	0.405	33.9	41	
DSS315 S2-2	298.19	1.10	229.43	2.215	1	0.334	11.67	0.250	0.250	29.92	38	
-13.51	7.54	98.0	6.71	2.215	20.21	0.685	26.0	0.392	0.392	32.5	40	
DSS317 S2-2	294.49	1.10	245.73	1.792	1	0.362	11.21	0.259	0.259	29.95	43	
-13.46	7.50	96.0	7.26	1.792	14.40	0.714	27.9	0.378	0.378	34.4	45	
DSS318 S3-1	314.83	1.08	249.47	2.228	1	0.391	13.78	0.327	0.327	29.87	–	Shear Str. Rate too Fast
-12.34	7.77	99.0	7.38	2.228	18.33	0.686	29.7	0.486	0.486	33.9	–	Test not used in Results
DSS320 S3-1	228.84	1.08	188.96	2.219	1	0.340	16.22	0.308	0.308	29.90	32	
-12.31	5.75	98.0	5.64	2.219	14.52	0.653	27.6	0.475	0.475	33.0	37	
DSS322 S2-4	245.24	1.43	160.51	4.025	1	0.357	12.60	0.267	0.267	29.84	53	
-24.06	6.00	99.0	4.73	4.025	29.18	0.682	27.6	0.366	0.366	36.1	52	
DSS324 S3-6	274.04	1.52	196.45	3.588	1	0.344	15.71	0.254	0.254	29.95	41	
-25.61	6.65	96.0	5.75	3.588	23.85	0.656	27.7	0.373	0.373	34.3	46	
DSS327 S2-7	283.53	1.87	186.08	3.831	1	0.333	12.78	0.236	0.236	29.85	40	
-28.79	7.19	99.0	5.74	3.831	28.66	0.659	26.8	0.335	0.335	34.0	44	
DSS330 S3-3	294.13	1.11	212.27	3.028	1.251	0.413	7.81	0.296	0.237	29.42	52	
-14.28	7.15	98.0	6.27	2.420	23.25	0.834	26.3	0.437	0.349	34.2	69	
DSS337 S3-6	287.77	1.52	199.59	3.754	1.601	0.550	11.35	0.434	0.271	29.91	82	
-25.58	6.86	99.0	5.28	2.345	26.37	0.994	29.0	0.589	0.368	36.4	87	
DSS340 S2-7	281.52	1.86	191.56	4.009	2.002	0.711	9.41	0.488	0.244	30.14	88	
-28.68	7.09	100.0	5.69	2.004	27.91	1.133	32.1	0.587	0.293	39.8	91	
DSS342 S2-9	259.54	2.77	191.01	6.011	1	0.352	11.83	0.263	0.263	29.90	52	
-35.31	6.29	97.0	5.34	6.011	22.92	0.680	27.4	0.376	0.376	35.0	52	

Table 5.2 Summary of Shear Results from SHANSEP CK_oUC/E Triaxial Tests

Test Sample Depth (m)	IN SITU		PRE SHEAR			AT PEAK			AT MAXIMUM OBLIQUITY				E_{50}/σ'_{vc} E_u/σ'_{vc} @ε_a=0.1%
	W_n e_i	σ'_{vo} S_i (%)	W_c K_c	σ'_{vm} σ'_{vc}	OCR ε_v (%)	q'/σ'_{vc} p'/σ'_{vc}	ε_a (%) ϕ'	A_f	q'/σ'_{vc} p'/σ'_{vc}	q'/σ'_{vm} p'/σ'_{vm}	ε_a (%) ϕ'	A_f	
TRIAXIAL COMPRESSION													
TX201 S2-3	278.00	1.11	205.12	2.540	1.00	0.389	1.415	0.86	0.360	0.360	3.87	1.89	44
-14.3	6.41	112.0	0.388	2.540	13.97	0.625	38.5		0.540	0.540	41.8		86
TX221 S2-8	232.40	1.98	194.73	3.412	1.00	0.410	1.201	0.88	0.363	0.363	3.39	2.50	49
-29.51	5.79	97.0	0.362	3.412	15.89	0.587	44.4		0.476	0.476	49.7		90
TX222 S3-2	296.20	1.10	245.26	1.827	1.00	0.394	1.426	0.88	0.302	0.302	8.00	–	46
-13.46	7.70	99.0	0.398	1.827	16.25	0.571	43.7		0.399	0.399	49.1		74
TX223 S2-9	234.90	2.78	205.31	4.468	1.00	0.421	1.309	0.81	0.340	0.340	6.74	26.08	64
-35.37	5.63	98.0	0.335	4.468	11.92	0.599	44.7		0.443	0.443	50.1		98
TX225 S3-5	277.20	1.48	231.51	2.676	1.24	0.512	1.291	0.40	0.492	0.395	2.10	0.55	70
-24.96	6.99	101.0	0.352	2.150	13.77	0.700	47.0		0.660	0.530	48.3		98
TX226 S2-1	321.10	1.09	271.93	1.945	1.65	0.734	2.077	0.37	0.734	0.453	2.077	0.37	103
-12.57	7.66	99.0	0.375	1.201	12.50	0.807	65.5		0.807	0.498	65.5		338
TX227 S2-4	184.90	1.43	151.05	2.515	2.00	0.754	1.879	0.32	0.754	0.376	1.879	0.32	122
-23.98	4.46	100.0	0.427	1.256	13.17	0.881	58.9		0.881	0.440	58.7		245
TRIAXIAL EXTENSION													
TX228 S2-8	266.50	1.97	216.61	2.940	1.00	-0.342	-16.750	0.74	-0.340	-0.340	-17.84	0.75	36
-29.41	6.53	98.0	0.373	2.940	16.49	0.349	78.1		0.341	0.341	85.6		150
TX230 S2-2	246.60	1.10	206.14	1.914	1.00	-0.316	-15.550	0.79	-0.313	-0.313	-16.34	0.80	42
-13.37	6.25	99.0	0.398	1.914	15.52	0.377	57.0		0.330	0.330	71.5		195
TX233 S3-6	211.70	1.51	172.48	2.754	1.96	-0.520	-13.000	0.61	-0.520	-0.265	-13.00	0.61	52
-25.47	4.81	104.0	0.464	1.403	12.59	0.562	67.5		0.562	0.286	67.5		–

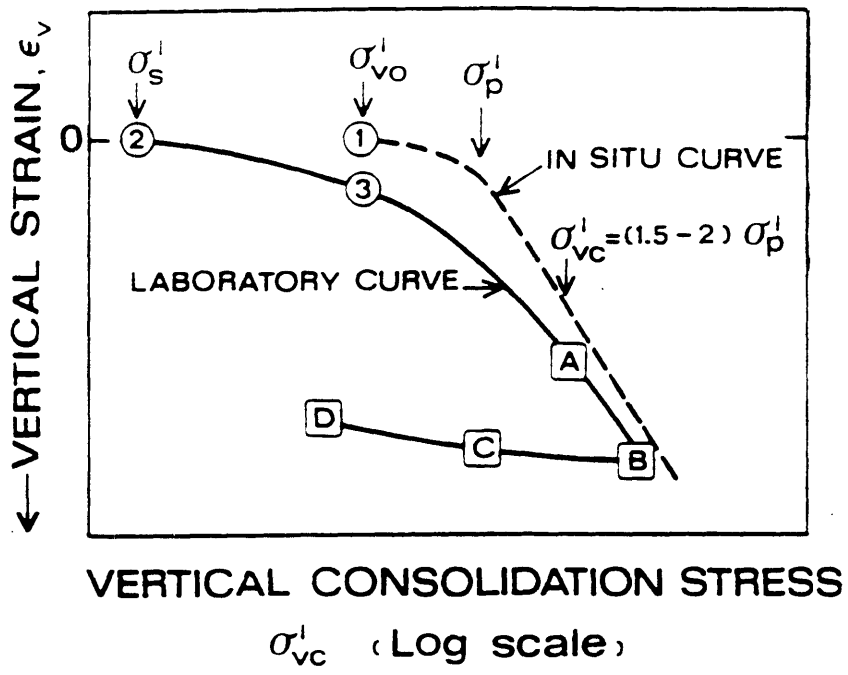

Figure 5.1 Consolidation Procedure for Laboratory CK_oU Testing (from Ladd et al. 1977)

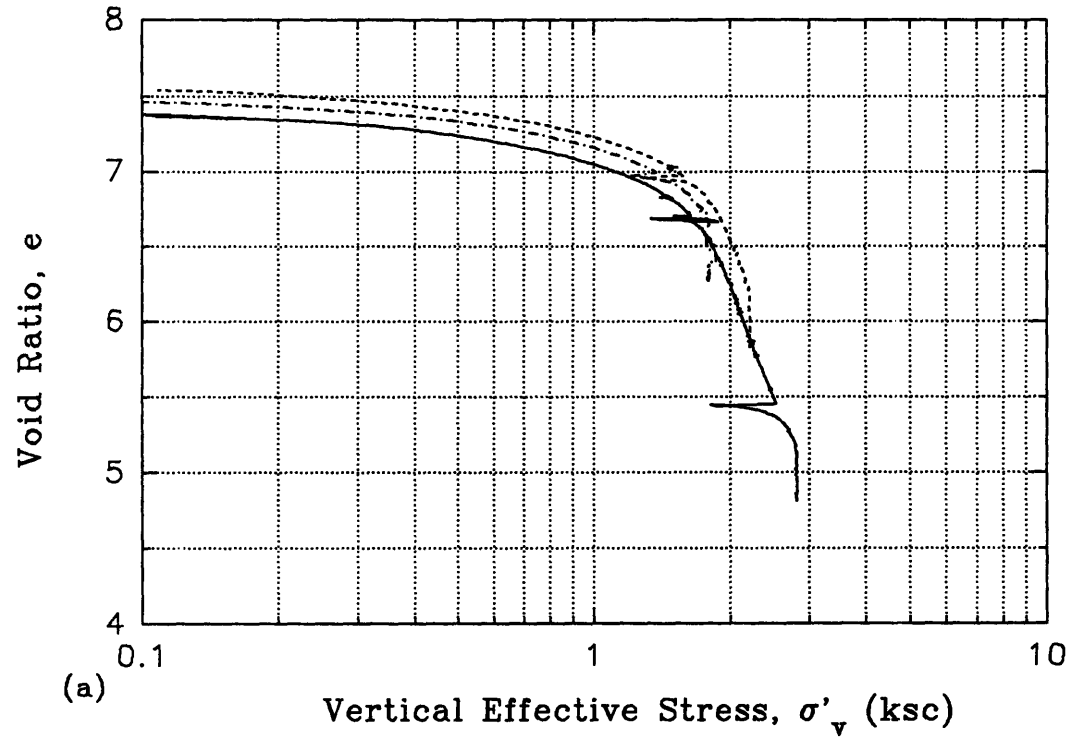

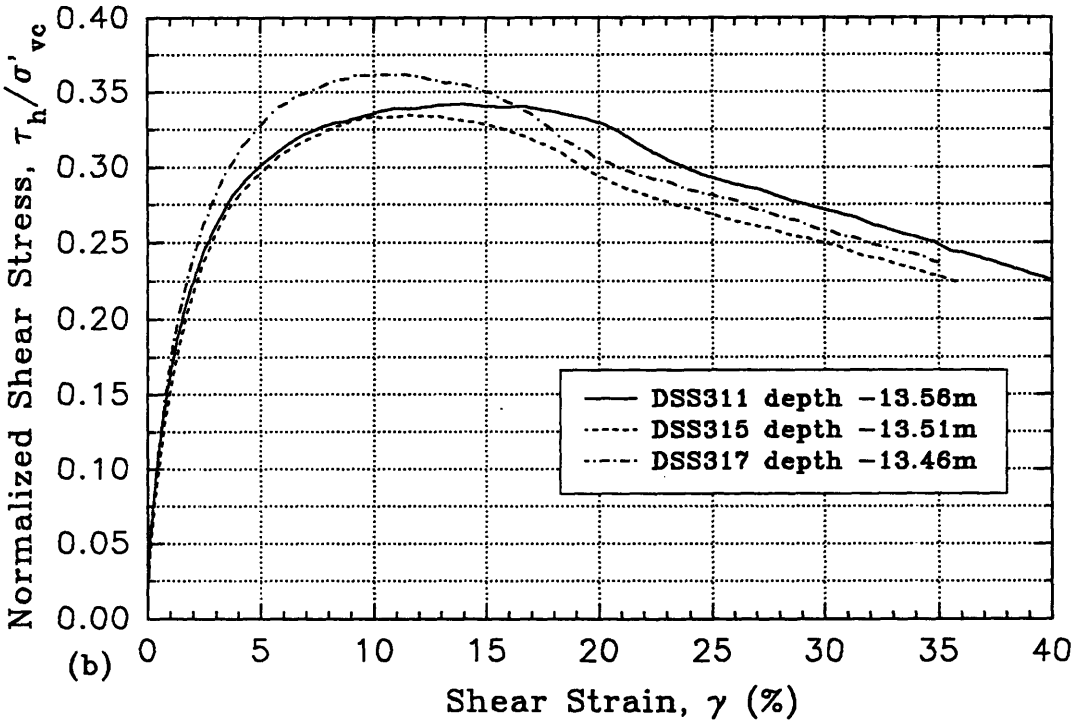

Figure 5.2 Consolidation and Shear Results:
DSS311, DSS315, DSS317
(a)Compression Curve
(b)Normalized Shear Stress vs. Shear Strain

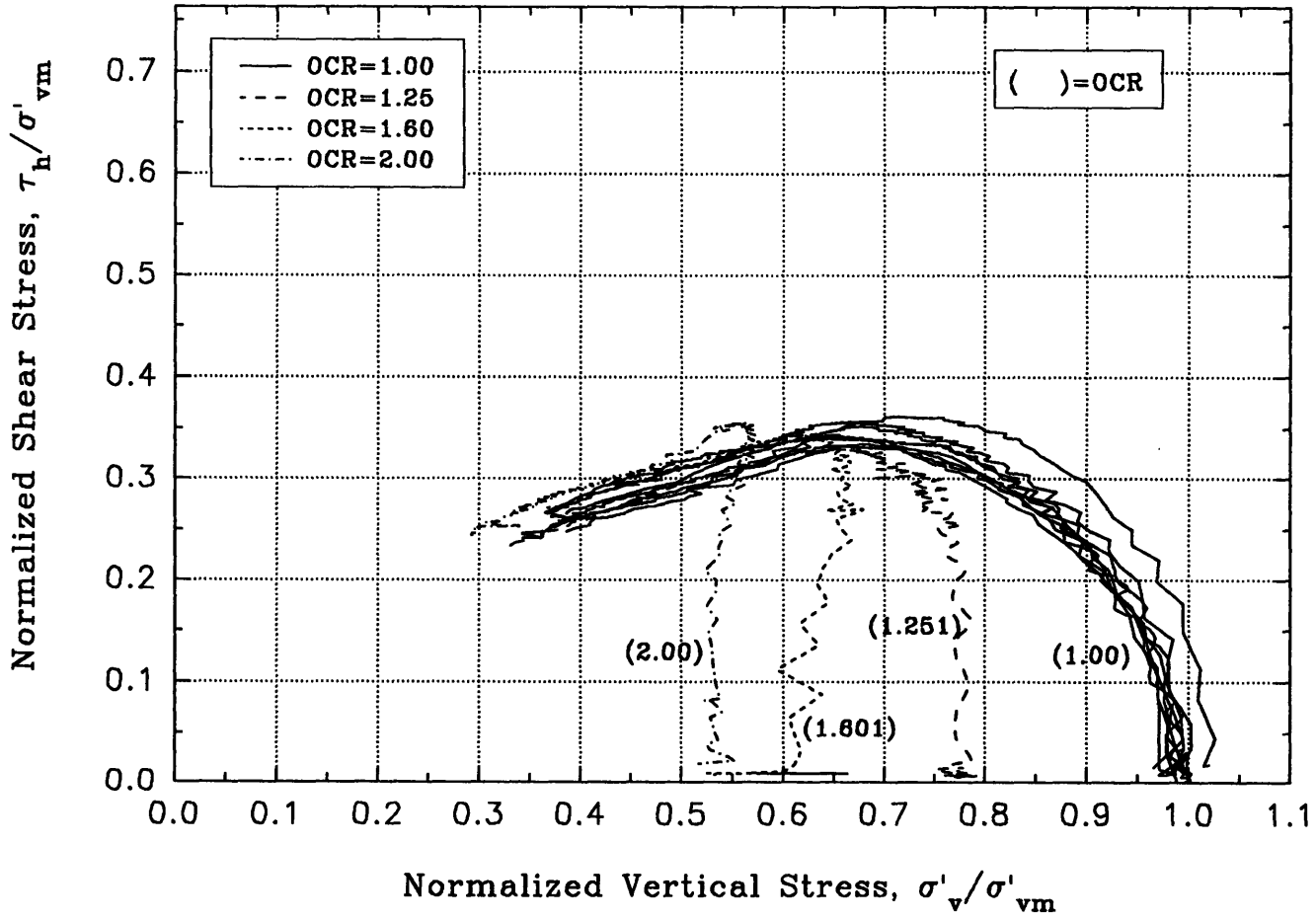

Figure 5.3 Normalized Stress Paths for SHANSEP CK_oUDSS Tests at Varying OCR

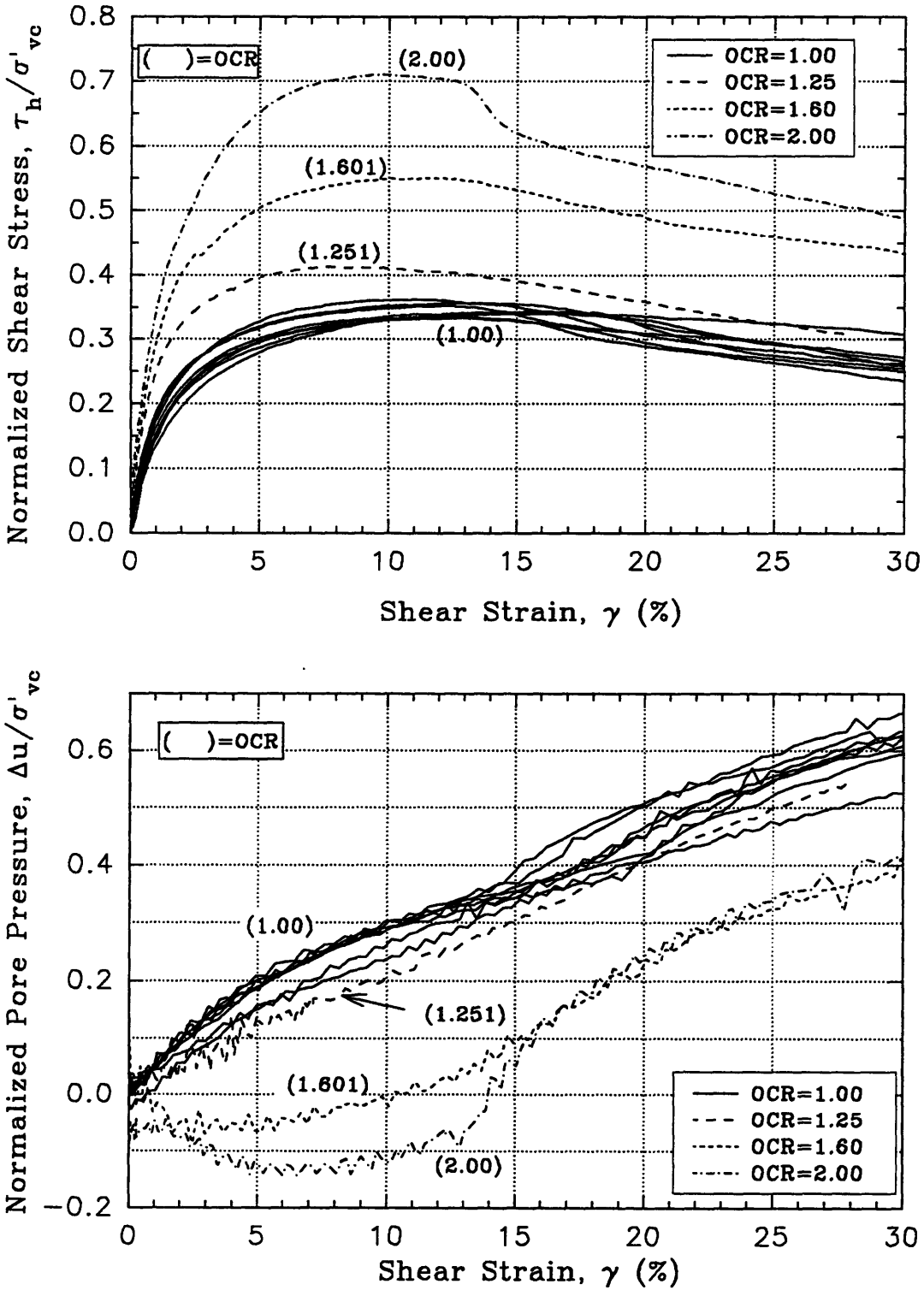

Figure 5.4 SHANSEP CK_oUDSS Tests at Varying OCR
(a) Normalized Shear Stress vs. Shear Strain
(b) Normalized Pore Pressure vs. Shear Strain

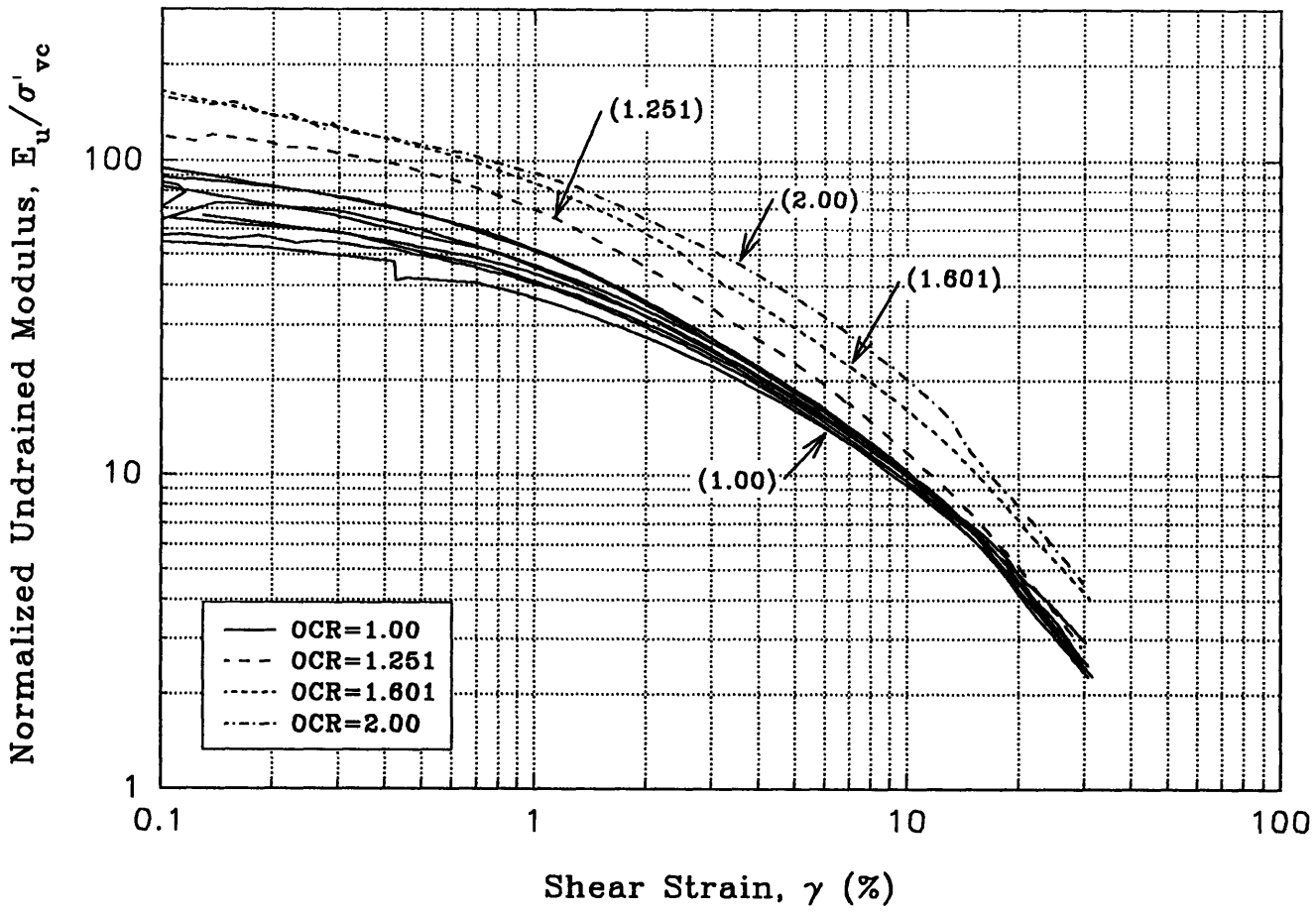

Figure 5.5 Normalized Undrained Modulus vs. Shear Strain for SHANSEP CK_oUDSS Tests at Varying OCR

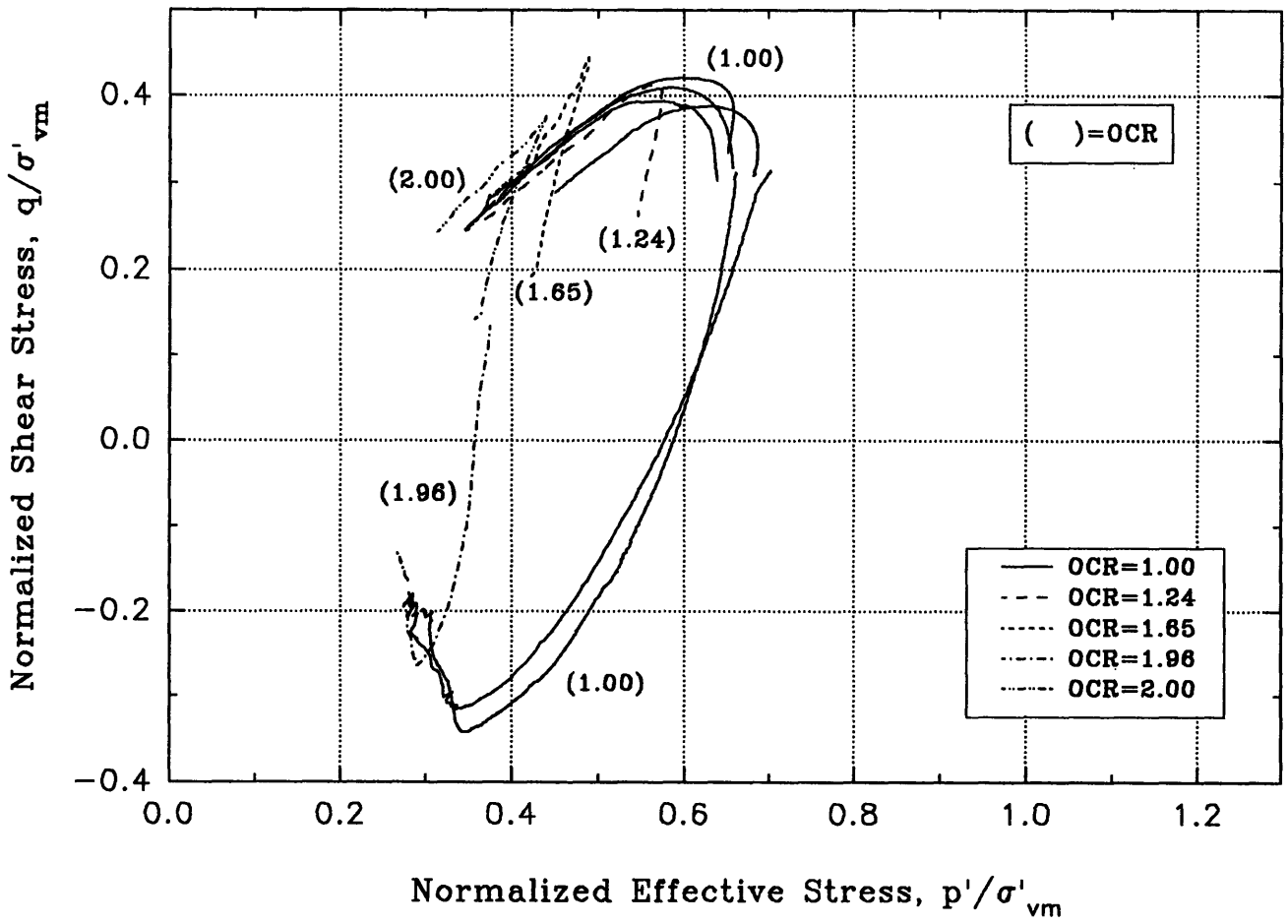

Figure 5.6 Normalized Effective Stress Paths for SHANSEP CK_0UC/E Triaxial Tests at Varying OCR

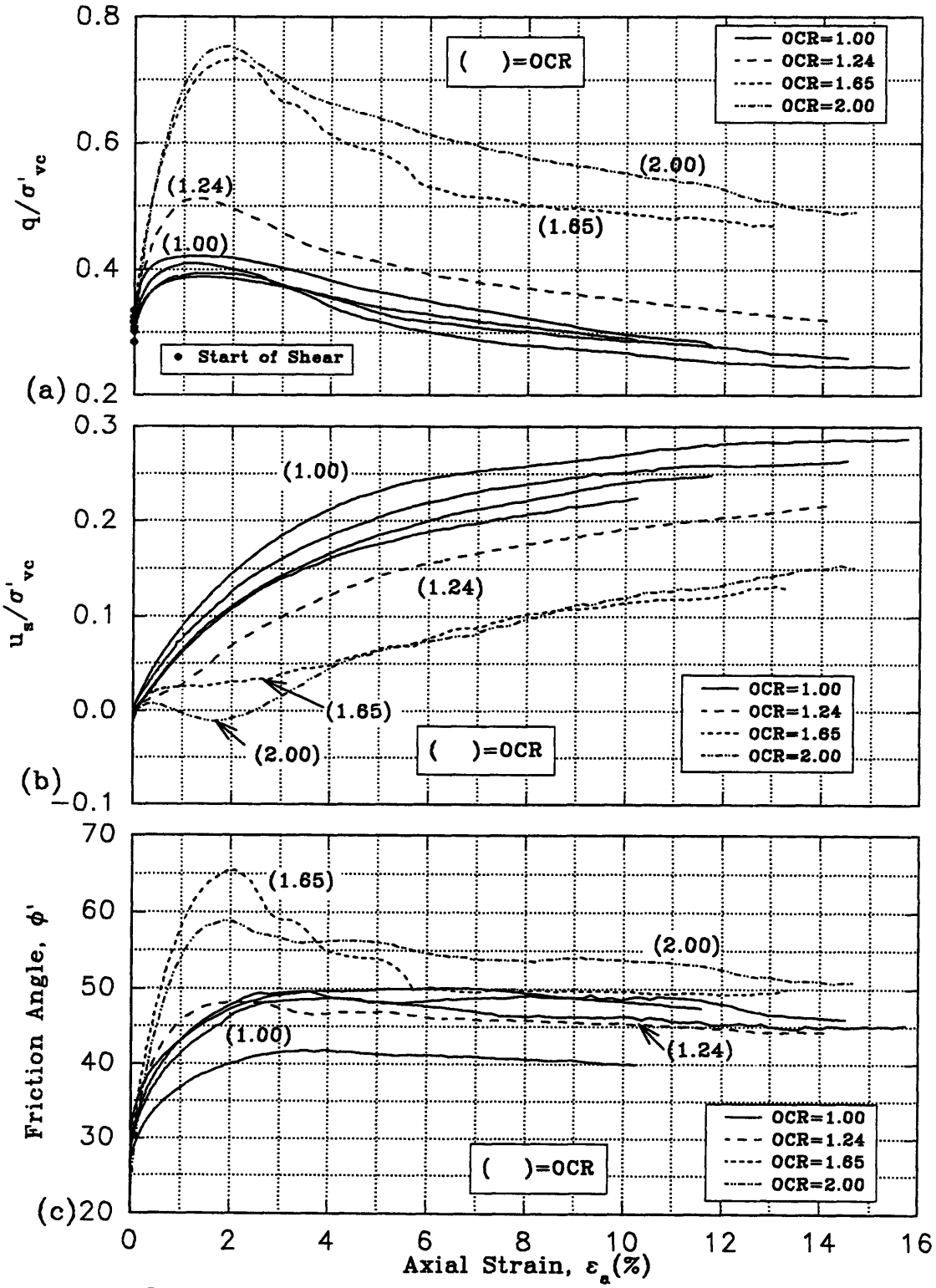

Figure 5.7 SHANSEP CK_oUC Triaxial Tests at Varying OCR
(a) Normalized Shear Stress vs. Axial Strain
(b) Normalized Pore Pressure vs. Axial Strain
(c) Friction Angle vs. Axial Strain

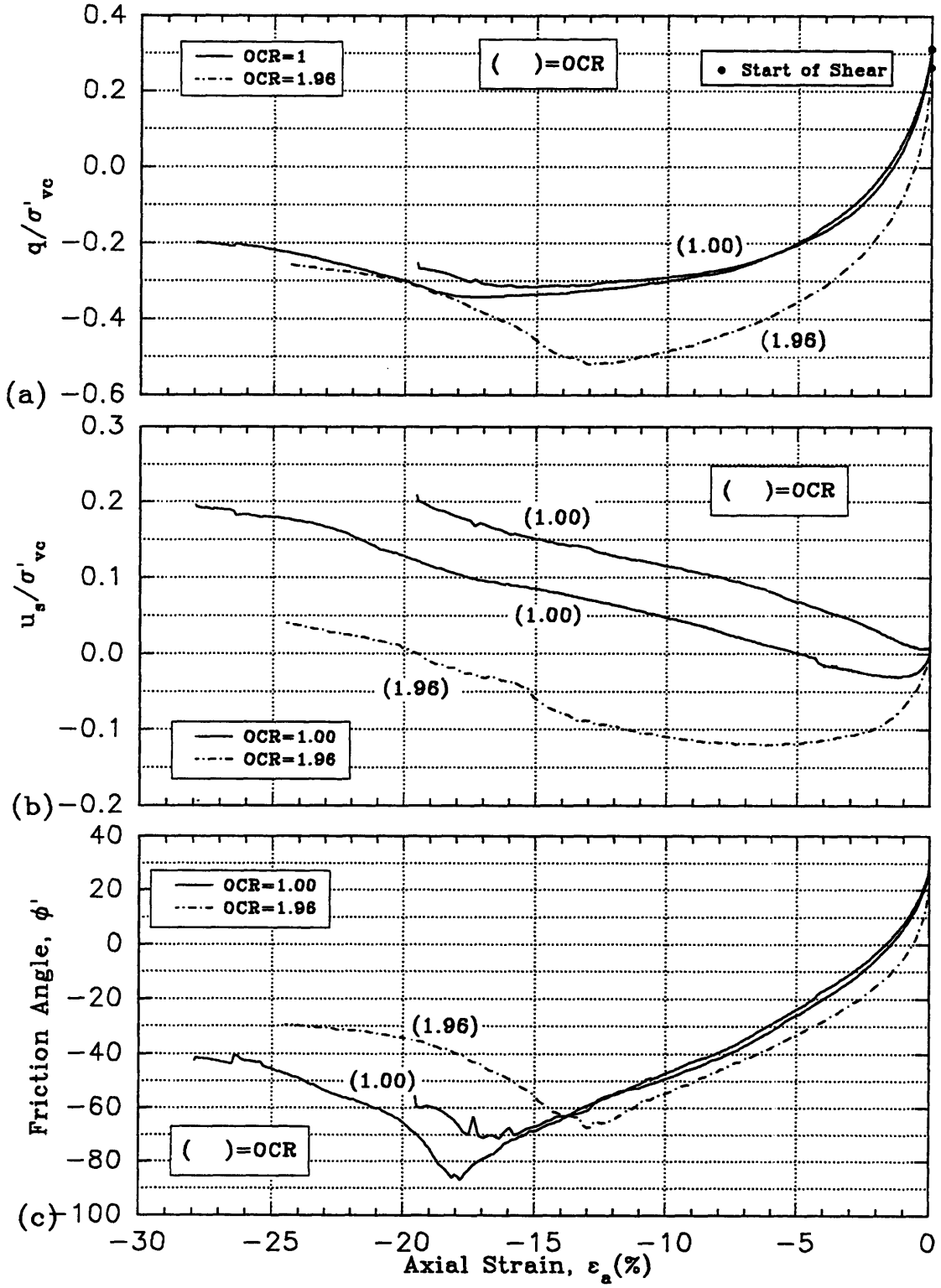

Figure 5.8 SHANSEP CK_oUE Triaxial Tests at Varying OCR
(a) Normalized Shear Stress vs. Axial Strain
(b) Normalized Pore Pressure vs. Axial Strain
(c) Friction Angle vs. Axial Strain

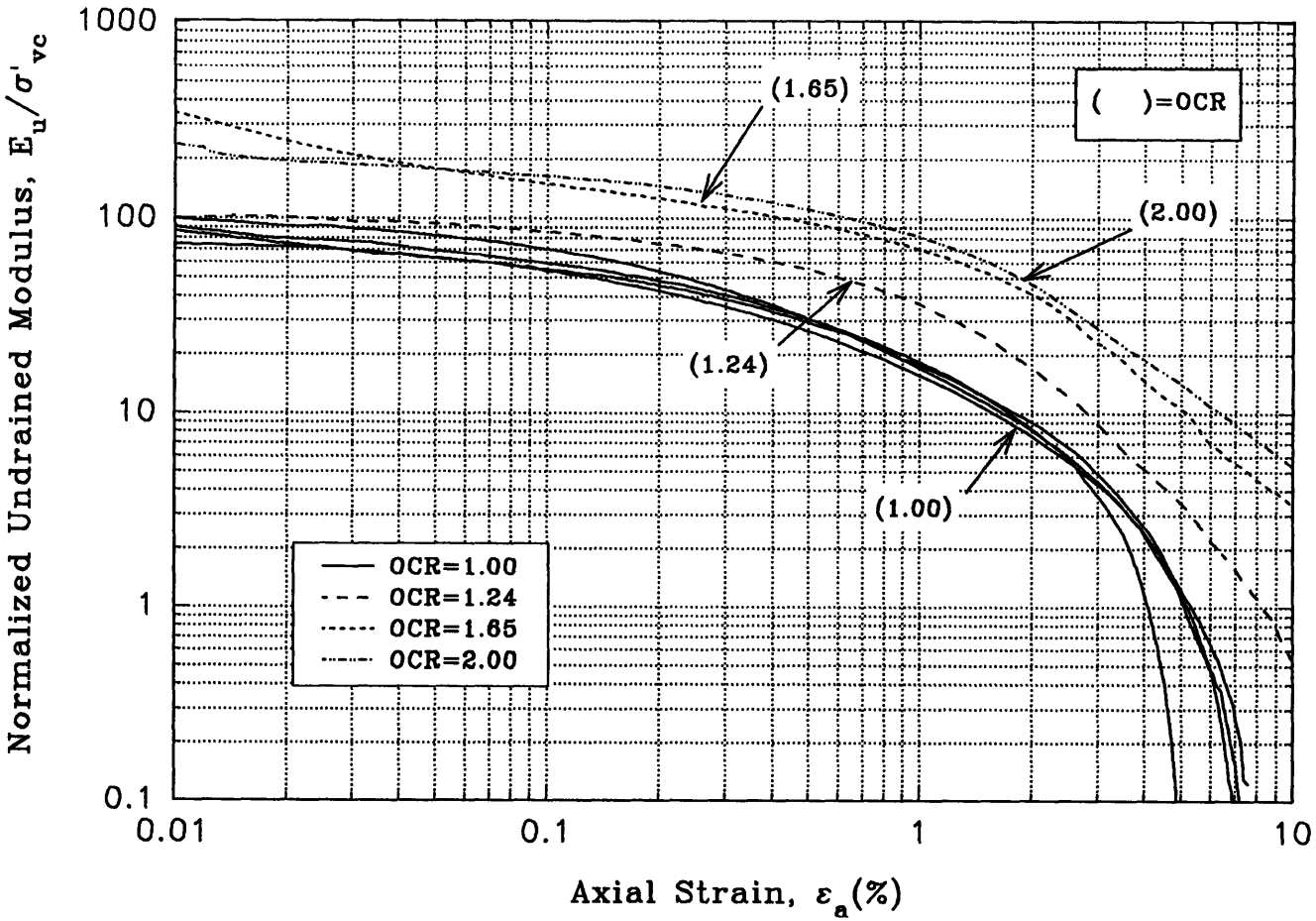

Figure 5.9 Normalized Undrained Modulus vs. Axial Strain for SHANSEP CK_oUC Triaxial Tests at Varying OCR

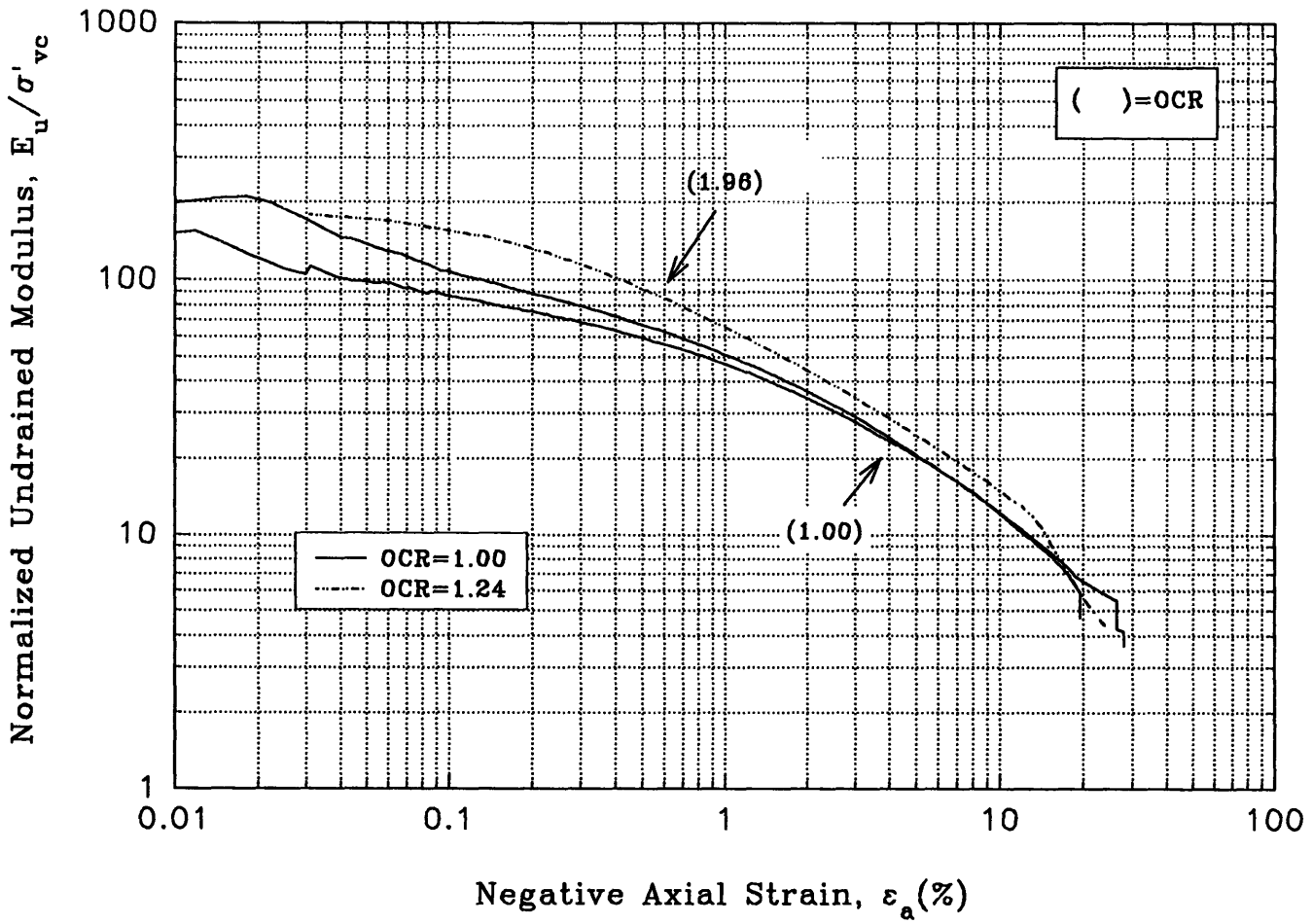

Figure 5.10 Normalized Undrained Modulus vs. Axial Strain for SHANSEP CK_oUE Triaxial Tests at Varying OCR

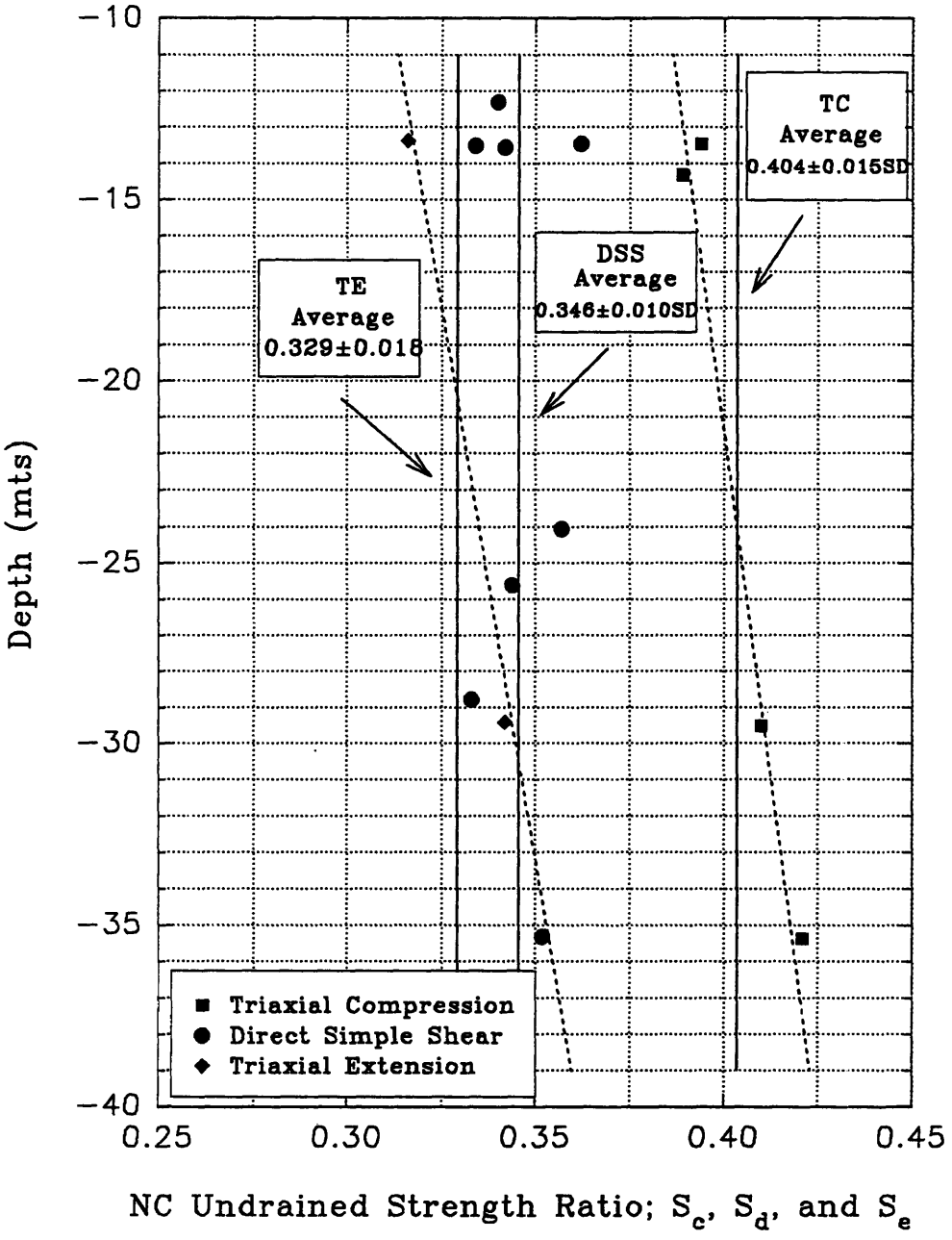

Figure 5.11 Depth vs. NC Undrained Strength Ratio for SHANSEP CK_oUC/E Triaxial Tests and CK_oUDSS Tests

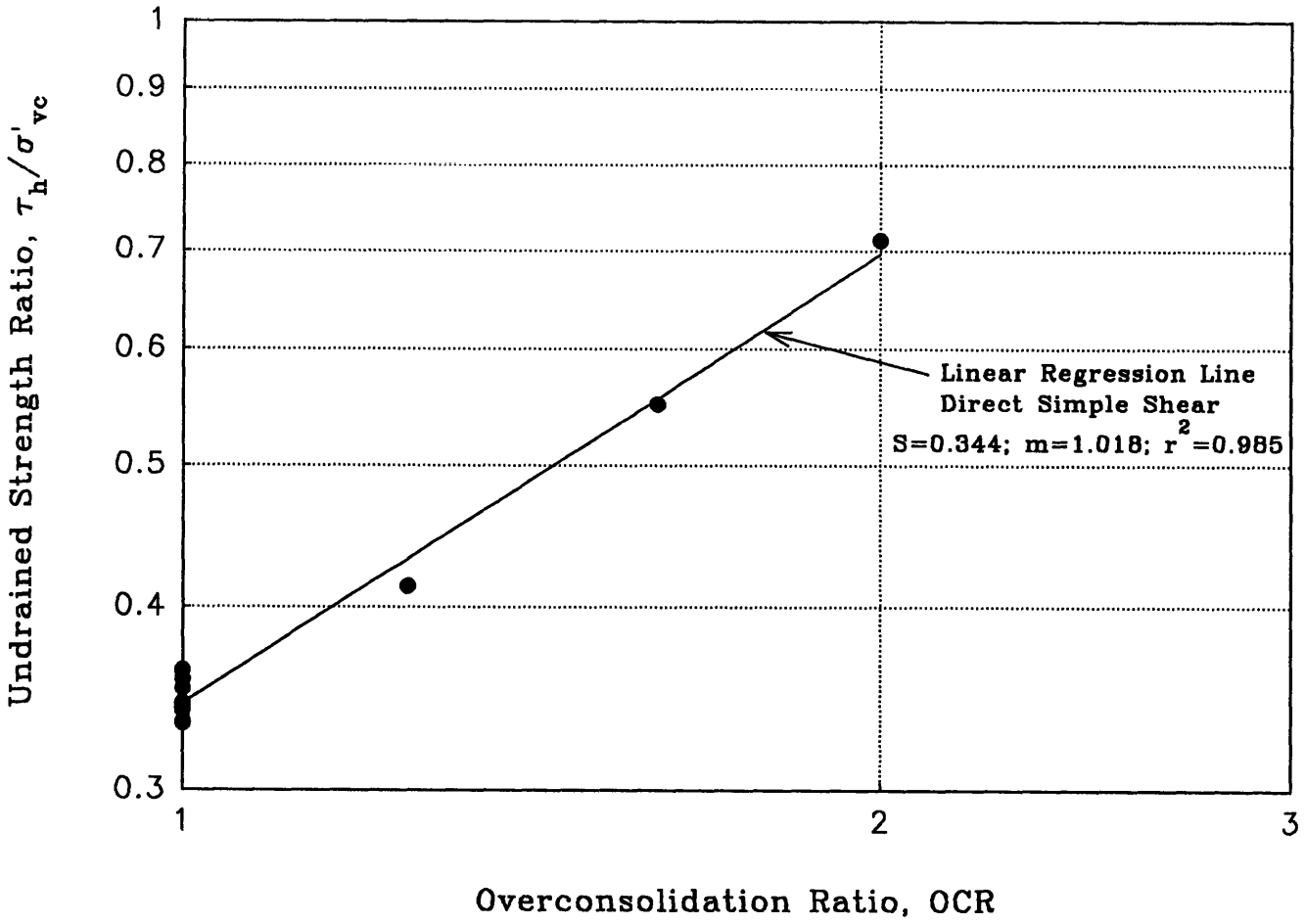

Figure 5.12 Undrained Strength Ratio vs. Overconsolidation Ratio for SHANSEP CK_oUDSS Tests

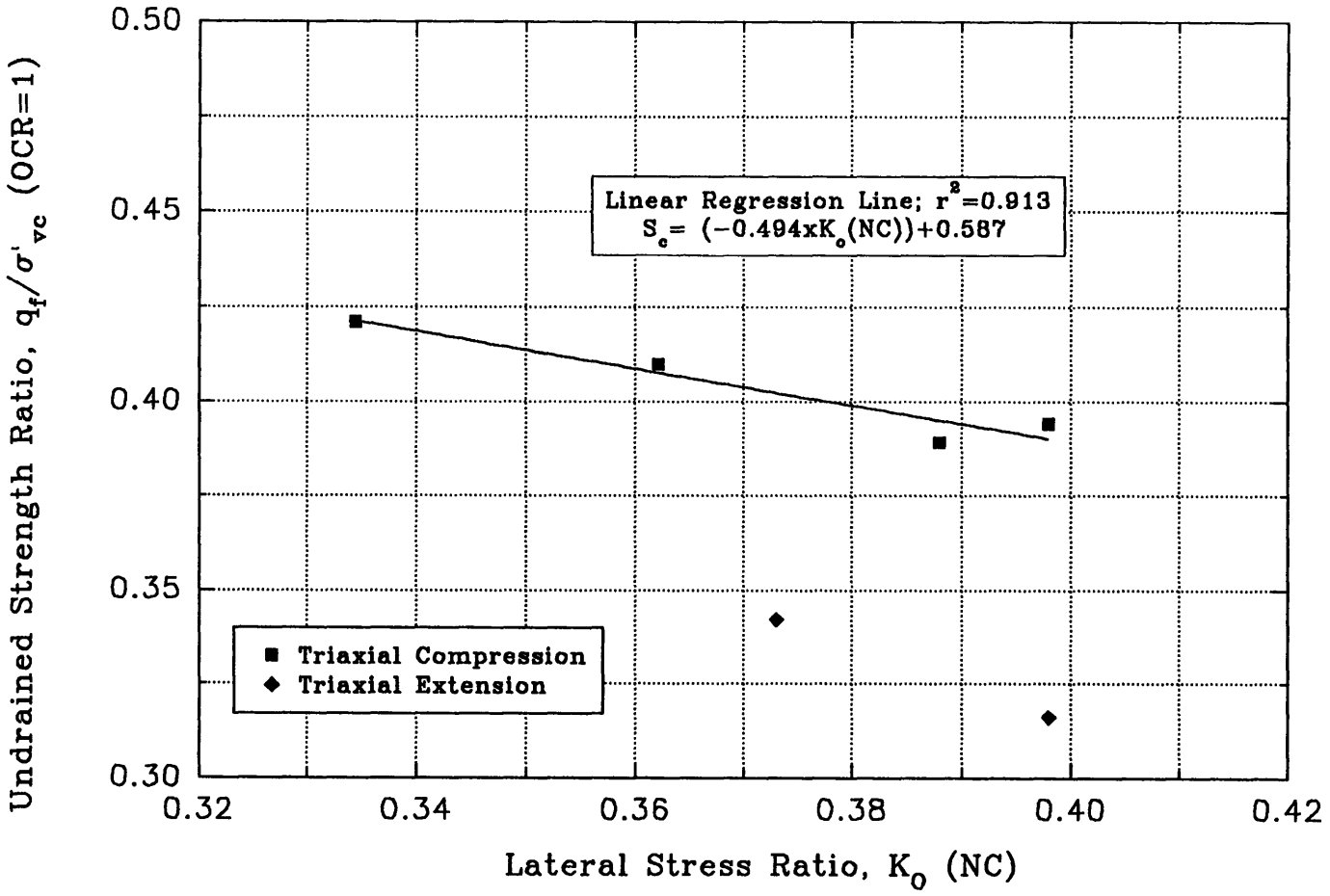

Figure 5.13 NC Undrained Strength Ratio vs. Lateral Stress Ratio for SHANSEP CK_oUC/E Triaxial Tests

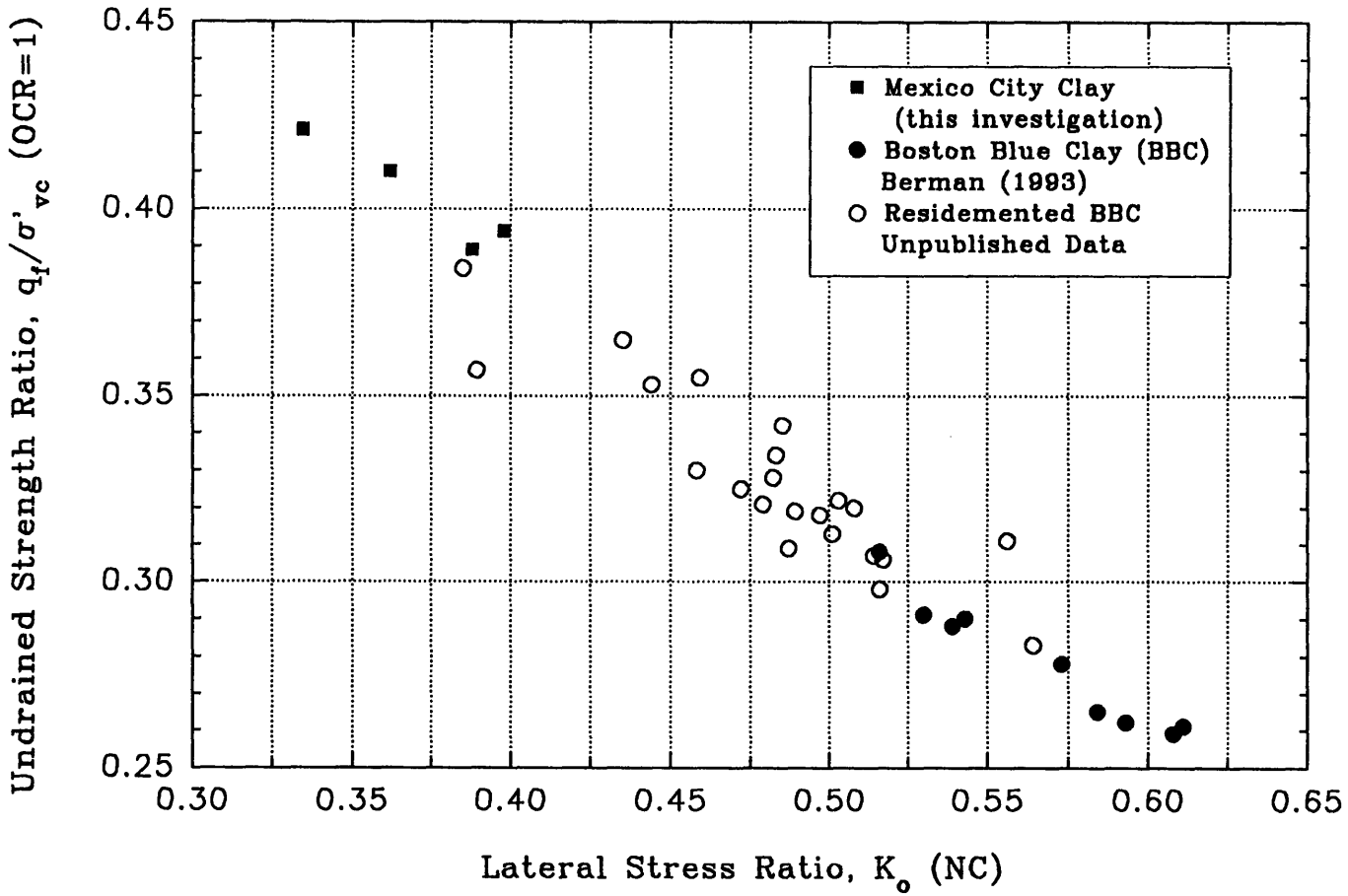

Figure 5.14 NC Undrained Strength Ratio vs. Lateral Stress Ratio for SHANSEP CK_oUC Triaxial Tests; for Various Soils.

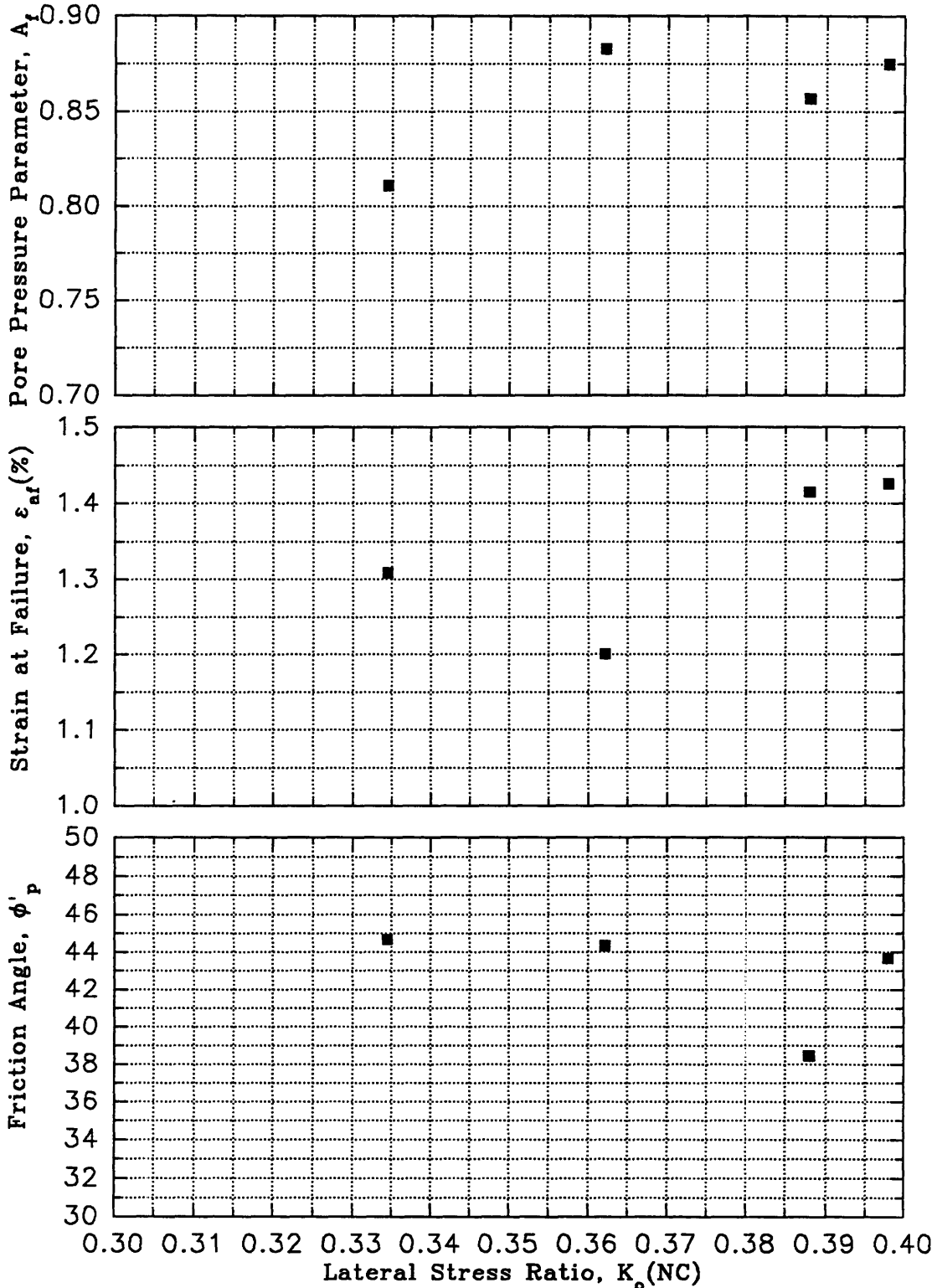

Figure 5.15 Lateral Stress Ratio vs. Pore Pressure Parameter Strain at Failure, and Peak Friction Angle

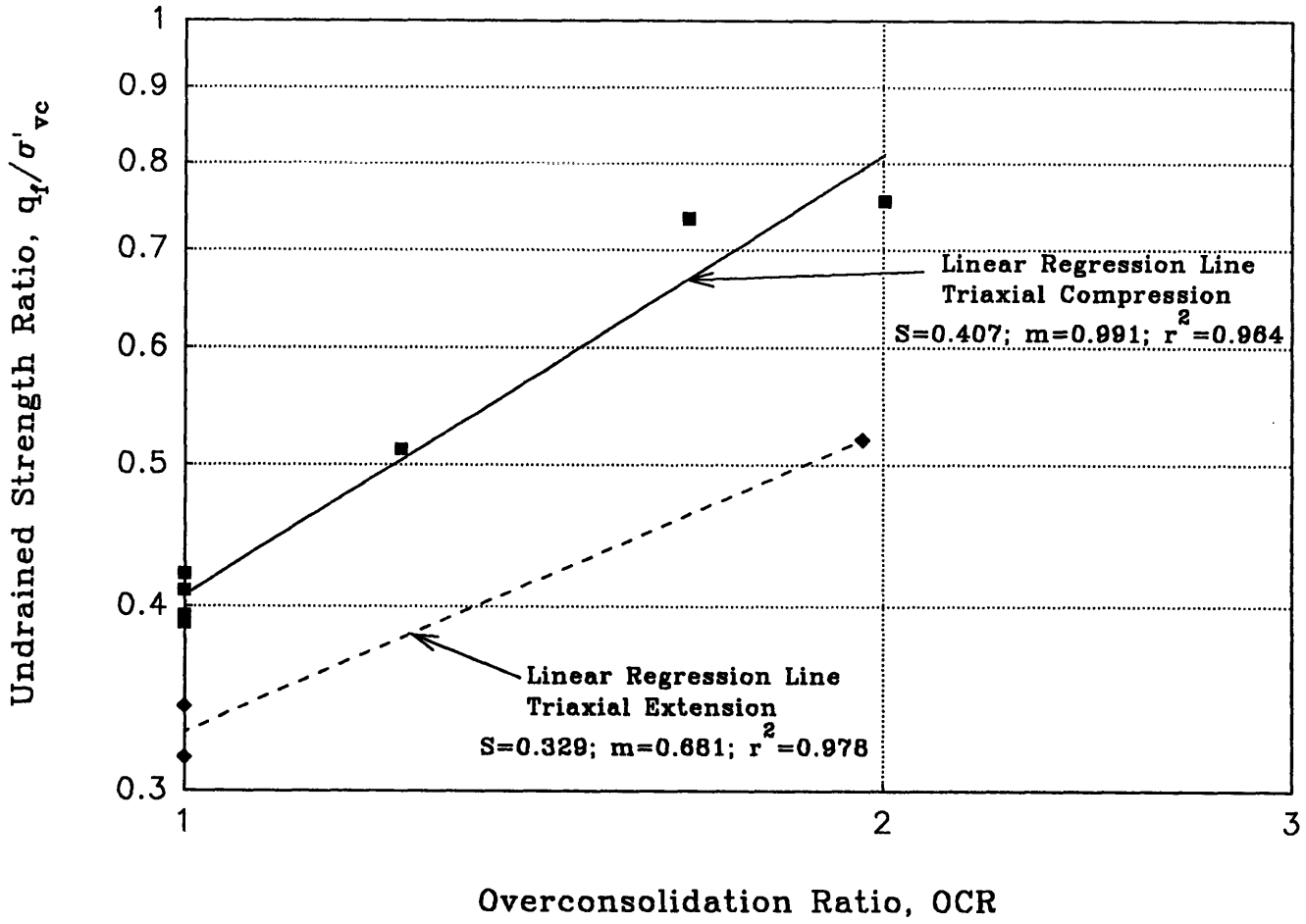

Figure 5.16 Undrained Strength Ratio vs. Overconsolidation Ratio for SHANSEP CK_oUC/E Triaxial Tests

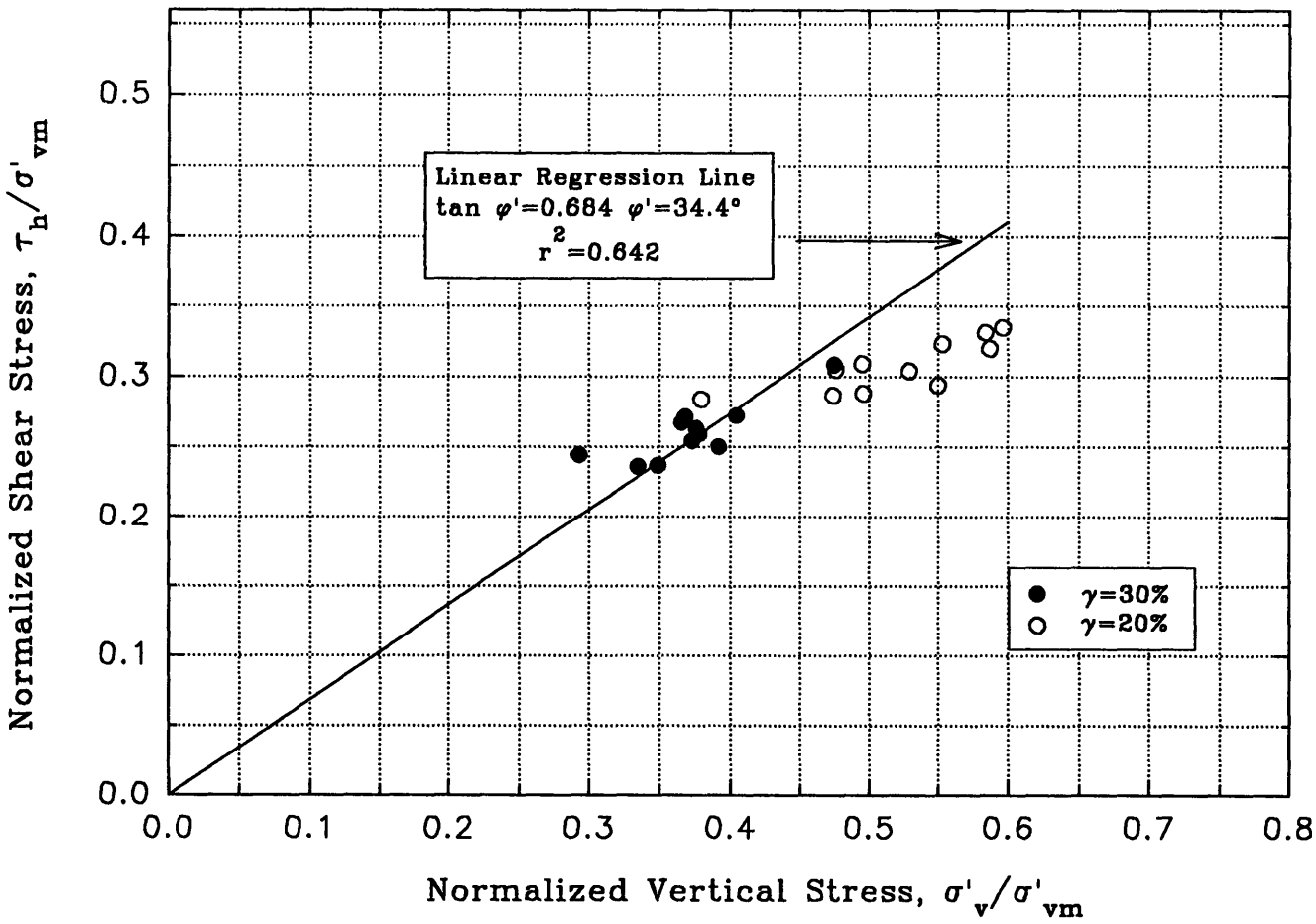

Figure 5.17 "Failure" Envelope at Large Strain
for SHANSEP CK_oUDSS Tests

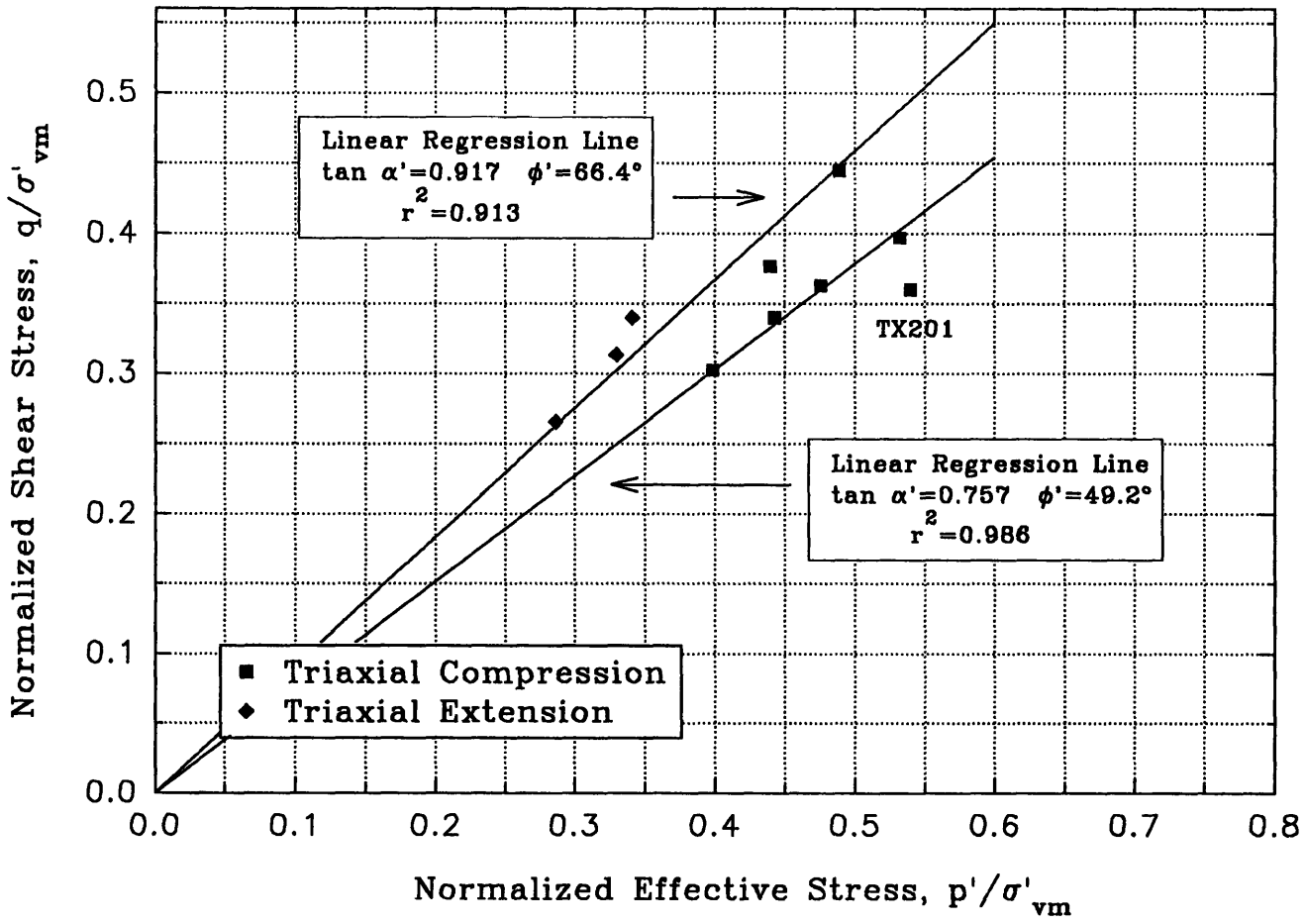

Figure 5.18 Effective Stress Failure Envelope at Maximum Obliquity for SHANSEP CK_oUC/E Triaxial Tests

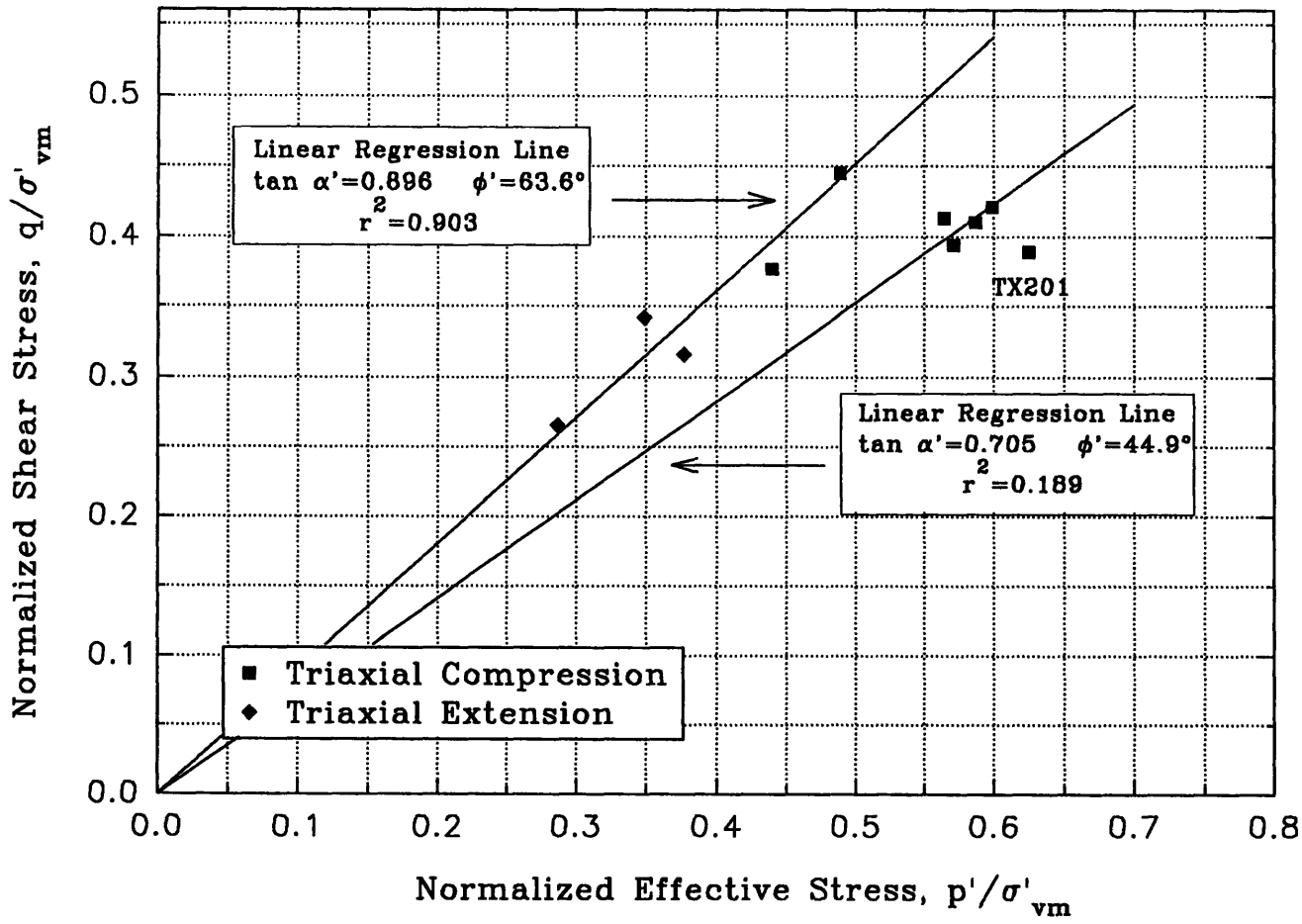

Figure 5.19 Effective Stress Failure Envelope at the Peak Shear Stress for SHANSEP CK_oUC/E Triaxial Tests

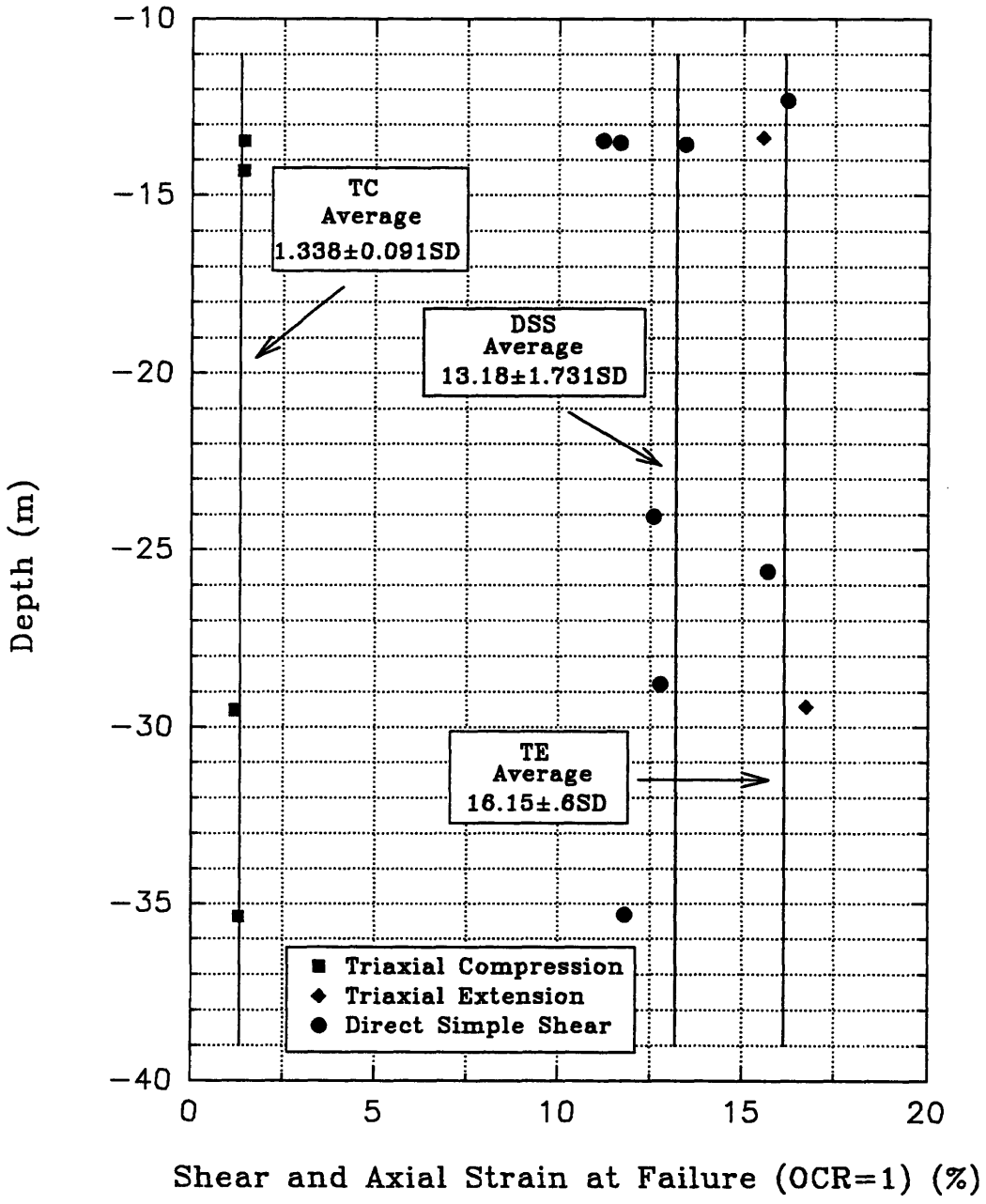

Figure 5.20 Depth vs. Strain at Failure for SHANSEP CK_oUC/E Triaxial Tests and CK_oUDSS Tests at OCR=1

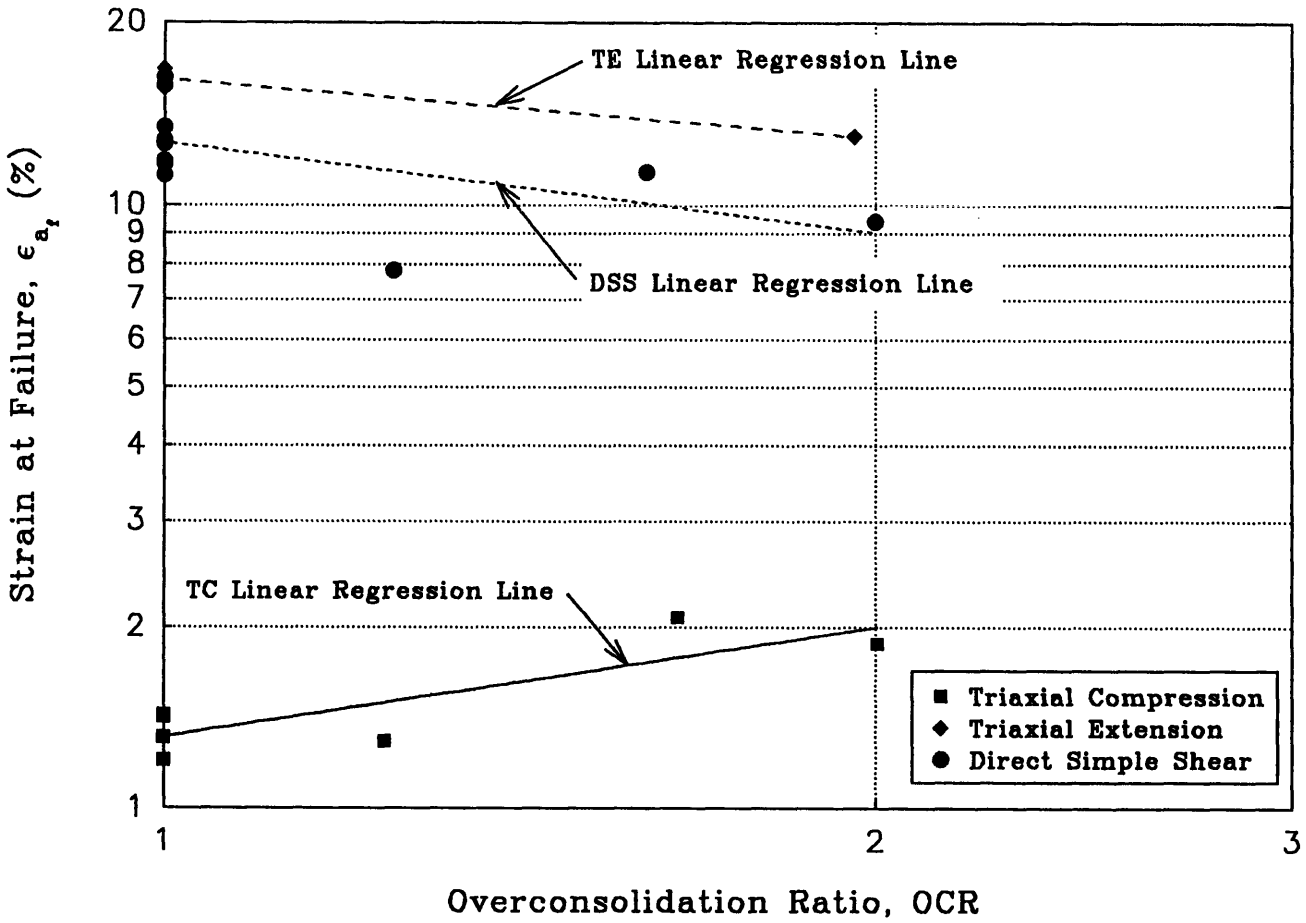

Figure 5.21 Strain at Failure vs. Overconsolidation Ratio for SHANSEP CK_oUC/E Triaxial and CK_oUDSS Tests

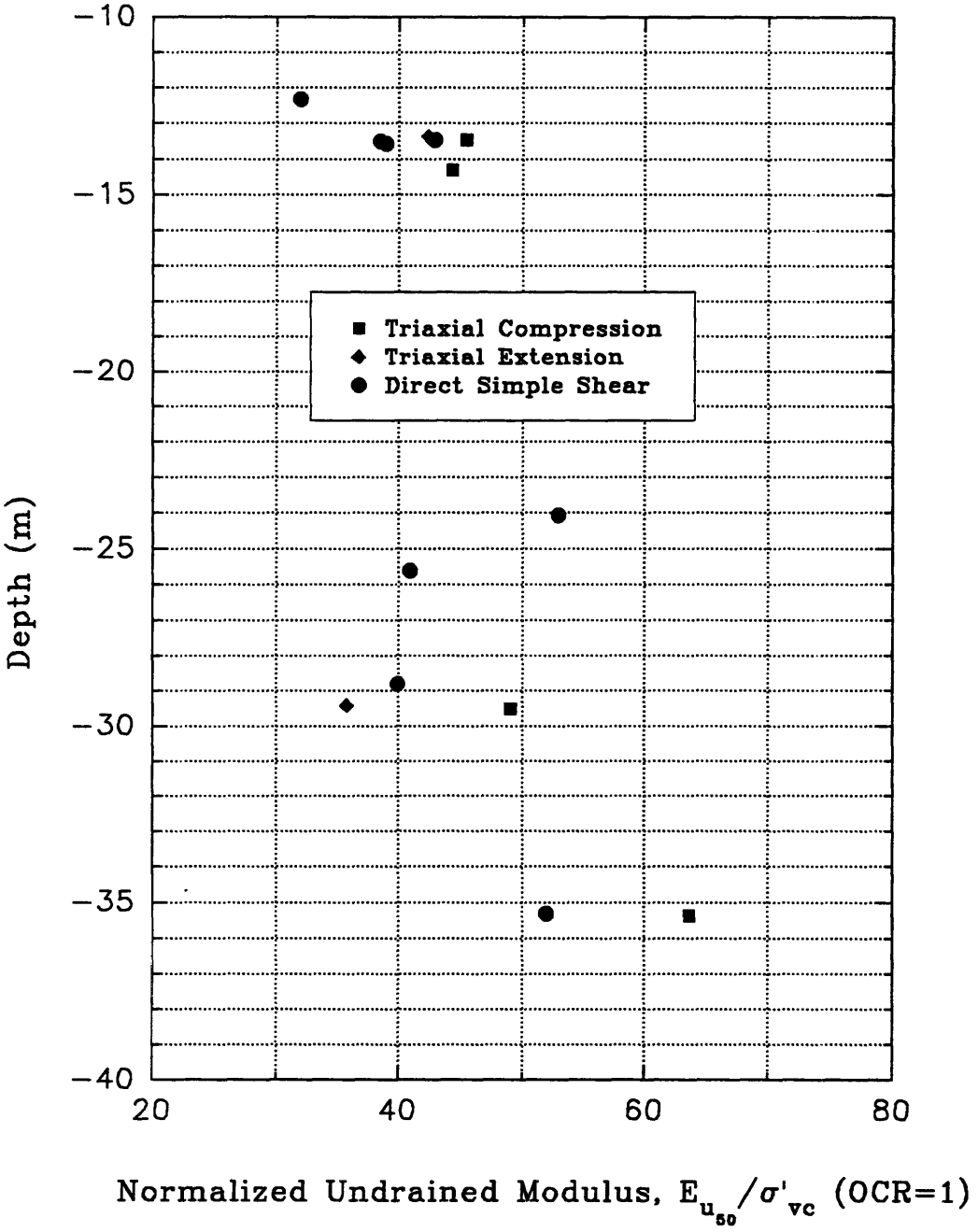

Figure 5.22 Depth vs. Normalized Undrained Modulus for SHANSEP CK_oUC/E Triaxial Tests and CK_oUDSS Tests at OCR=1

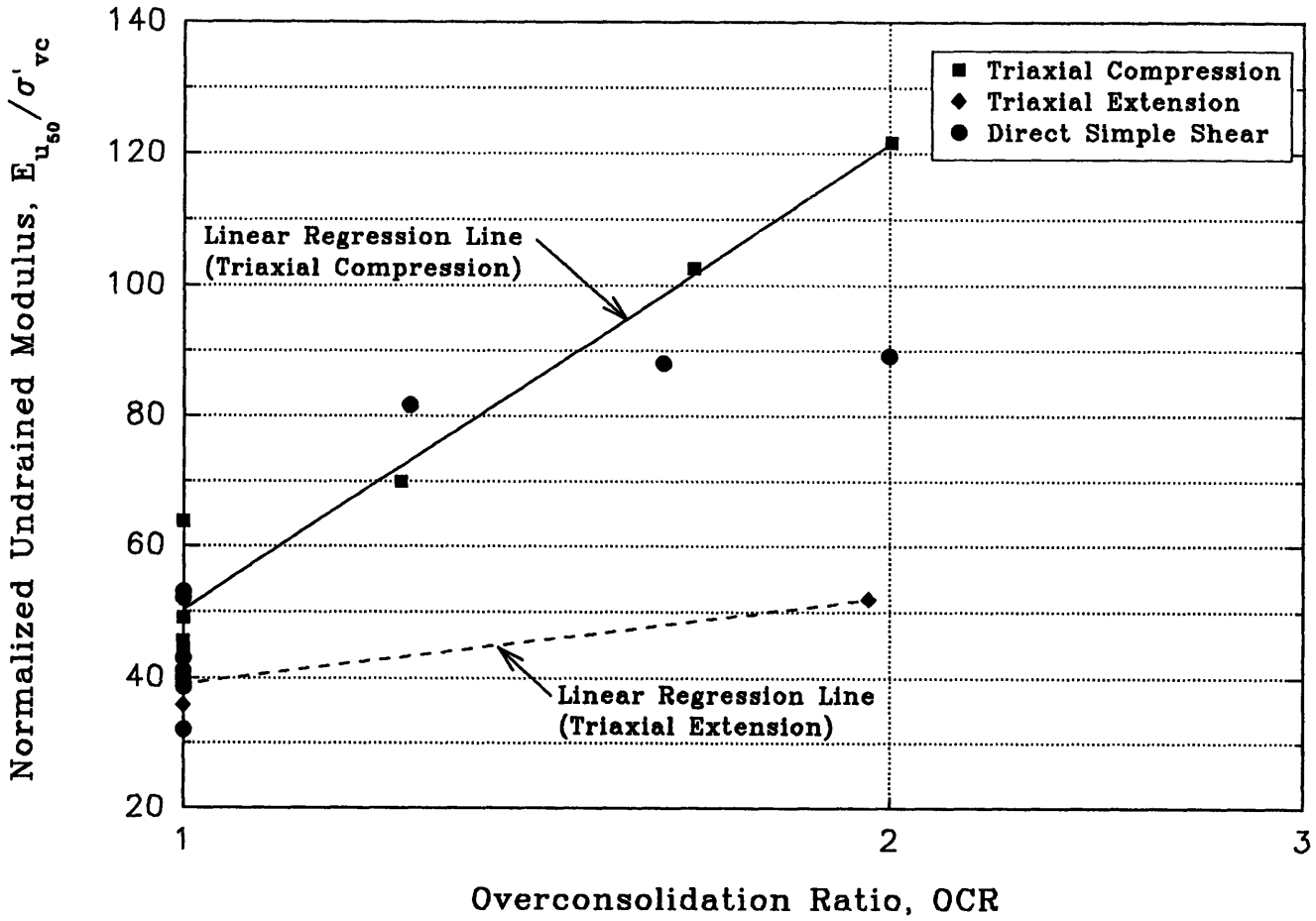

Figure 5.23 Normalized Undrained Modulus vs. Overconsolidation Ratio for SHANSEP CK_oUC/E Triaxial Tests and CK_oUDSS Tests

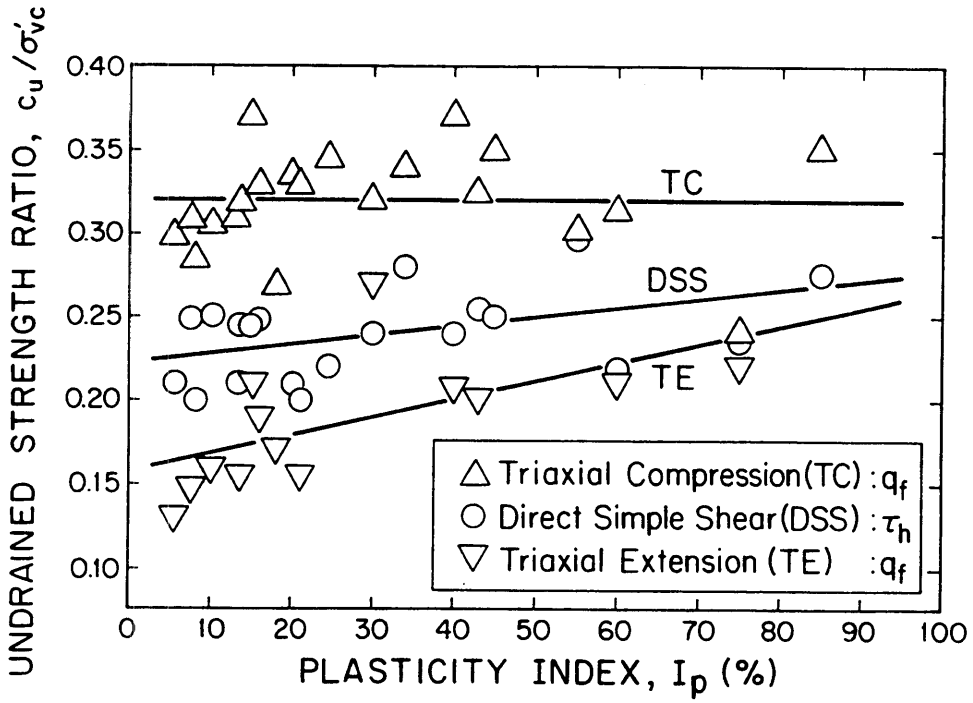

Figure 5.24 Undrained Strength Ratio versus Plasticity Index for Various Soils (from Ladd 1991)

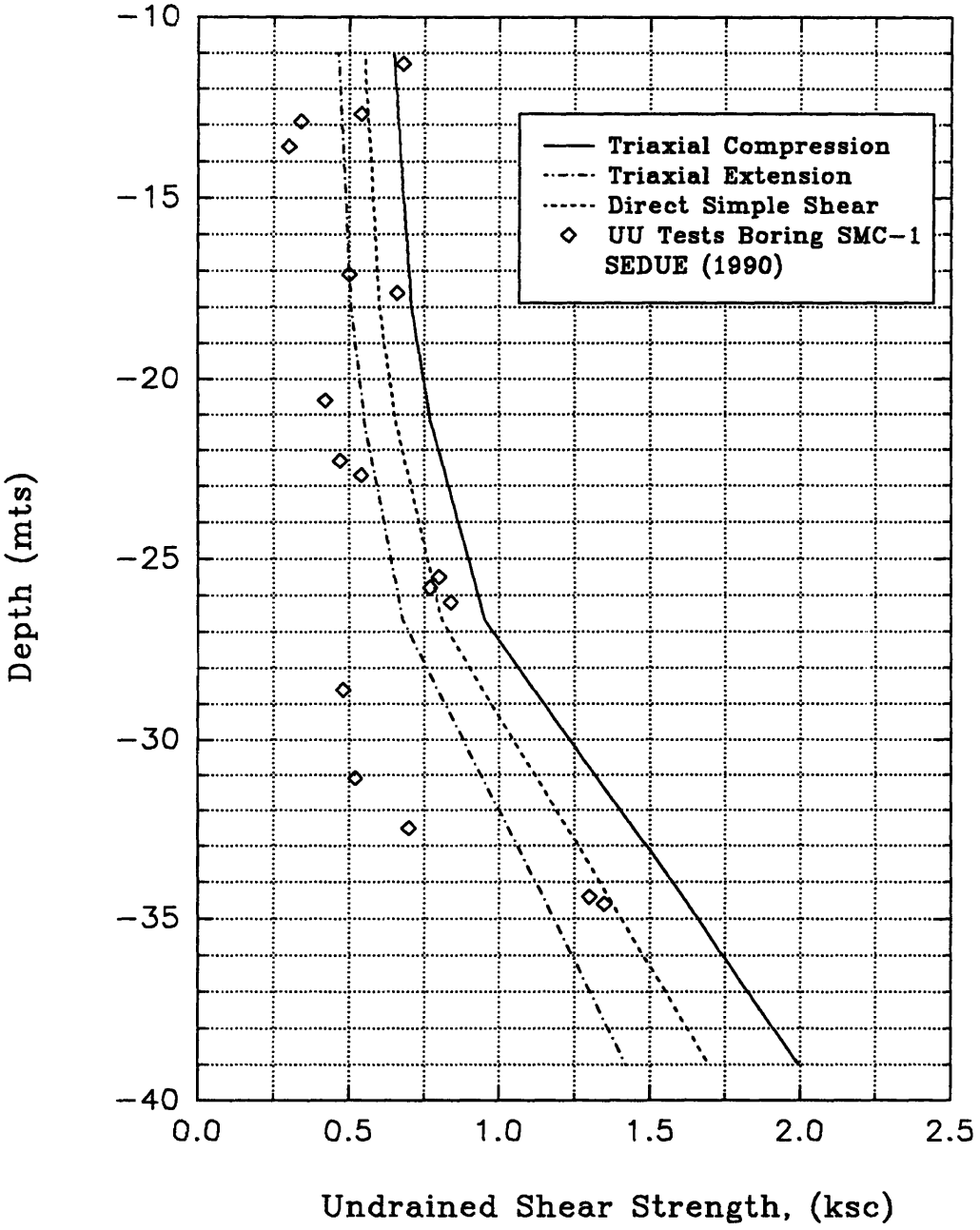

Figure 5.25 Depth vs. SHANSEP Undrained Shear Strength for Different Modes of Shear

CHAPTER 6
SUMMARY, CONCLUSIONS AND RECOMMENDATIONS

6.1 INTRODUCTION

For all practical purposes the Valley of México can be considered a closed basin. The valley has an area of 7160 km^2. The valley's maximum length in the north-south direction is approximately 135 km, and the width at the center of the valley is approximately 76 km. The Valley of México is surrounded by a large number of volcanoes and volcanic deposits from the Middle Tertiary, Pliocene and Pleistocene eras. The latest filling of the valley occurred during the Pleistocene. The upper section of the fill was deposited in the lakes formed during the late Pleistocene, and consists of a fine grained soil mass with a large quantity of microfossils, layers of fine grained clastic material, sand, and gravel. This portion of the fill has traditionally been called México City Clay. The thickness of the clay deposit varies throughout the valley, and in the center of the city has an approximate thickness of 50 m.

México City Clay has rather unusual index and engineering properties. Some of its index properties are:

(a) natural water contents ranging from 100 to 600%.

(b) void ratios ranging from 2 to 10.

(c) specific gravity of approximately 2.5.

(c) liquid limits ranging from 100 to 500%, and plastic limits ranging from 20 to 150%.

México City Clay has a high initial stiffness and an almost elastic behavior during recompression. Once the preconsolidation pressure is exceeded, the soil is highly compressible, and compression ratios greater than one are common. Additionally, the soil has a low undrained strength (due to the low consolidation effective stress of the soil) and

an unusually high undrained strength ratio. These unusual properties give rise to intricate foundation problems when tall and heavy buildings are designed and erected. In addition to the unusual soil characteristics, pumping from the aquifer underlying México City has increased the effective stress on the soil, which has led to increased rates of regional settlement.

The research for this thesis was prompted by the author's belief that there was a need for an encompassing study of México City Clay using state of the art equipment and techniques. The last study of this type was performed by Marsal and Mazari in 1959.

The objectives and corresponding scope of the research can be divided into the three following components:

1) *Characterize the engineering properties of México City Clay at México City's Cathedral.*

This objective was accomplished with sophisticated laboratory tests run on high quality undisturbed samples using automated equipment and SHANSEP K_o consolidated-undrained shear tests.

2) *Understand the general natural characteristics of México City Clay in the context of its depositional history and mineralogy.*

This objective was accomplished by studying the microstructure of the soil with Scanning Electron Microscopy and identifying the mineralogy with compositional analysis and X-ray diffraction tests.

3) *Evaluate the influence of various sampling methods relative to sample disturbance.*

This objective was accomplished by evaluating the results of sophisticated laboratory tests run on undisturbed samples obtained from three different boreholes. The boreholes were drilled using two different samplers and three drilling techniques.

6.2 SUMMARY OF SAMPLING AND TESTING PROGRAM

A total of three boreholes were drilled to obtain undisturbed samples for this investigation. The drilling and sampling techniques used in each of the boreholes are summarized as follows:

(1) Borehole 1 (S1) employed thin walled Shelby tube sampling, a heavy weight drilling mud ($\gamma_t \approx 1.2$ t/m^3), and hollow stem augers;

(2) Borehole 2 (S2) employed thin walled Shelby tube sampling and hollow stem augers. No drilling fluid was used, and hence, the borehole was dry;

(3) Borehole 3 (S3) employed fixed piston sampling, a light weight drilling mud, ($\gamma_t < 1.1$ t/m^3), and hollow stem augers.

Figure 2.16 shows the location of these boreholes. A total of 24 tube samples were obtained, nine from Borehole S1, nine from Borehole S2, and six from Borehole S3. After assessing the quality of the samples, it was decided to air ship the 18 highest quality samples to MIT. The samples shipped were: samples 1, 8, and 9 from Borehole S1; samples 1 through 9 from Borehole S2; and samples 1 through 6 from Borehole S3. Table 2.1 presents the sampling depths for all boreholes. Appendix A contains the boring logs and sample logs of boreholes S2 and S3.

All tubes were radiographed at MIT's X-ray facility in order to assess sample quality, general material type, presence of inclusions and variation in macro-fabric. The radiographs indicated that the overall quality of the sampling in Boreholes S2 and S3 was excellent. The radiographs also indicated that the quality of the sampling in Borehole S1 was poor. Hydraulic fracturing is the cause for the poor sample quality of the samples from Borehole S1. Hydraulic fracturing of the soil was caused by the pressure exerted by the drilling fluid. Radiography proved to be a great tool for assessing the macro-fabric of the soil. Radiographs clearly showed the heterogeneity of the soil. Significant changes in relative density of the soil are common and generally occur within centimeters. The changes in relative density are attributable to changes in mineralogy and changes in

material type (i.e., sand, pyroclastic material, etc.). Appendix A contains sample logs for all the samples sent to MIT. The logs give detailed descriptions of the macro-fabric of each tube, which was determined primarily from the radiographs.

The experimental portion of this research consisted of the following laboratory testing:

1) tests for index properties including; natural water content, torvane strength, Atterberg limits, total unit weight, grain size distribution, specific gravity, salt concentration, and pH;

2) tests to evaluate the microstructure and mineralogy of the soil which included scanning electron microscopy, environmental scanning electron microscopy, and X-ray diffraction;

3) tests to evaluate the stress history and consolidation properties of the soil including; 15 constant rate of strain consolidation (CRSC) tests, 12 SHANSEP K_O-consolidated undrained direct simple shear (CK_OUDSS) tests, and 10 SHANSEP K_O-consolidated undrained triaxial compression and extension (CK_OUC/E) tests.

A distribution of the laboratory tests performed is presented in Table 2.1.

6.3 SUBSURFACE CONDITIONS, INDEX PROPERTIES, MICROSTRUCTURE AND MINERALOGY

6.3.1 Subsurface Conditions

Figure 2.14 shows the inferred stratigraphy from the three CPTs in front of the main entrance of the cathedral (from Tamez et al. 1992) and Figure 2.15 shows the perimetrical stratigraphy of the cathedral (from Tamez et al. 1992). The stratigraphy of the site, as presented in SEDUE (1990) consists of six main substrata; rellenos (fill), costra superficial (superficial crust), serie arcillosa superior (upper clay series), primera capa dura

(first hard layer), serie arcillosa inferior (lower clay series), and depositos profundos (deep deposits). The stratigraphy at the site is typical for the Lake Zone.

In the preparation of this thesis, it was assumed that the ground water conditions and effective stress profile presented in SEDUE (1990) prevailed at the time samples were obtained for this study. Some simple calculations were performed to verify the effective stress profile in SEDUE (1990) . The effective stress profile used for this investigation is described by Equations 2.1 through 2.4

6.3.2 Index Properties

Natural water contents were measured each time a sample tube was cut to perform an engineering test, from the trimmings of each engineering test, and at the end of each engineering test from the initial wet weight of the test specimen and the final weight of solids. Figure 3.1 plots depth versus all of the natural water contents calculated for this investigation. The data show significant scatter and no relationship exists between water content and effective consolidation stress (i.e., depth).

Figure 3.2 plots depth versus Atterberg limits, plasticity index, and liquidity index. Figures 3.3 and 3.5 present the correlations found between natural water content and liquid limit, and natural water content and plasticity index, respectively. It is possible to estimate the liquid limit and the plasticity index from the natural water content of the sample using Equations 2.1 and 2.2. These equations should only be used for natural water contents below 300% since data in the literature suggest that these equations are not valid at higher water contents. These correlations imply that the natural water content is a function of the initial microstructure of the soil. Also, these correlations are of significant importance and should be researched more thoroughly, since they have never been reported for any other soil.

Tests were performed on each tube to determine the specific gravity of the soil grains, and the salt concentration and pH of the pore fluid. The average specific gravity is

2.46±0.08SD. Figure 3.12 plots depth versus salt concentration and pH. Above an approximate depth of -25m salt concentrations and pH vary significantly, but below -25m they remain fairly constant. The range of values measured for salt concentration are 1 to 6 g/liter of pore fluid or 2.5 to 17 g/kg of soil. The values of pH measured range from 7 to 9. The average salt concentration below -25m is 1.87±0.4SD g/liter or 4.52±0.96SD g/kg of soil. The average pH below -25m is 7.68±0.35SD. At a depth of -25m, pore pressures are less than hydrostatic values. The decrease in pore pressure is due to the pumping of the aquifer underlying México City. Constant salt concentration and pH, and hydrostatic pore pressures above -25m together suggest the presence of a permeable layer at approximately -25m. This layer allows sufficient flow and head to stop the decrease in pore pressure above -25m, and to dilute the pore fluid below -25m.

Two hydrometer tests were performed, but no results are presented as the tests yielded unreliable results due to flocculation of the soil slurry. The tests were performed in accordance with ASTM guidelines using sodium hexametaphosphate as a dispersing agent. The author refers the reader to ASTM STP 1095. This article presents a procedure to prevent flocculation in hydrometer tests by previously treating the soil sample.

Figure 3.13 plots depth versus total unit weight and void ratio. The average total unit weight is 1.19±0.05SD g/c^3, and the average void ratio is 6.15±1.52SD.

6.3.3 Microstructure and Mineralogy

An overview of work by Zeevaert (1949), Marsal and Mazari (1959), Leonards and Girault (1961), Lo (1962), Girault (1964), Mesri et al. (1975), and Peralta (1989) is presented. The SEM and ESEM pictures show that the samples of México City Clay studied are largely composed of amorphous siliceous material. This amorphous material is composed of microfossils; mainly diatoms and siliceous skeletons. The production of diatoms is proportional to the silica content of the water (Mesri et al. 1975). Apparently,

the great quantities of silica produced by the weathering of volcanic glass initiated a great bloom of diatoms in the lakes that occupied the valley of México.

Compositional analysis performed inside the SEM revealed that silica and iron are the most predominant elements of all the specimens studied. Silica and iron wher generally found in a ratio of 2:1. The fact iron was the second most predominant element together with the low amount of aluminum measure might suggest that the specimens studied for this investigation are neither montmorillonite or illite.

X-ray diffraction tests revealed the presence of a crystal structure which is typical of clay minerals (i.e., units of silica tetrahedrons and octahedral sheets). The results also revealed that the arrangement of these units is not very consistent (i.e., no basal reflection).

The compositional analysis of the specimens and the X-ray diffraction results together suggest unusual and poorly developed particles.

This investigation describes México City Clay as a soil composed of (1) basic crystalline units that do not have a consistent enough arrangement to conform to a well defined clay mineral, and (2) a considerable amount of amorphous siliceous material (i.e., microfossils).

6.4 EVALUATION OF SAMPLE DISTURBANCE, STRESS HISTORY, AND CONSOLIDATION PROPERTIES

6.4.1 General Overview

The compression curves from all of the consolidation tests (i.e., constant rate of strain consolidation tests and the K_o consolidated portion of the SHANSEP direct simple shear and triaxial tests) were used to evaluate sample disturbance, stress history, and the compressibility characteristics of the clay deposit. In addition, the K_o consolidated triaxial tests provided lateral stress ratio data, and the CRSC tests provided information about the coefficient of consolidation and the permeability of the deposit. Tables 4.1 through 4.3

present a summary of the consolidation results from all tests. The consolidation results from all tests are presented in numerical and graphical form in MIT Department of Civil and Environmental Engineering Research Report Number R94-01.

6.4.2 Sample Quality

After analyzing and comparing consolidation data from all tests it was not possible to determine which of the boreholes (i.e., sampling techniques) S2 or S3 yielded the highest quality samples. No difference can be discerned in sample quality between thin walled Shelby tube samples and fixed piston samples. Until the fixed piston sampler is redesigned to reduce sampling time, the author suggests the use of Shelby tubes to sample México City Clay. This suggestion is based on sampling time and cost.

Data from this investigation suggests that the disturbance caused by unloading of the soil is significantly less than the disturbance caused by hydraulic fracturing. Therefore, the author suggests drilling without drilling fluid (bentonite slurry) to avoid hydraulic fracturing of the soil. Casing or hollow stem augers should be used to stabilize the borehole. Also, the author suggests using the extrusion technique detailed in Chapter 2 to minimize disturbance, based on extensive data produced by MIT and by this investigation.

6.4.3 Stress History and Compressibility Characteristics

It was found that México City Clay has a constant OCR profile of 1.5 with depth (Figure 4.16b). The author believes that secondary compression and physiochemical effects are the principal cause for the constant OCR profile. Additional research is necessary to verify this.

The following section summarizes the compressibility results obtained during this investigation.

(1) The maximum Compression Index (Cc) of the soil tested ranges between 2 and 12, and the approximate average is 6. The maximum Compression Ratio (CR) ranges between 0.5 and 1.5, and the approximate average is 0.9.

(2) A correlation was found between Cc and the initial water content of the specimen was found. It is possible to estimate Cc from the natural water content with the following equation:

$$Cc = \frac{-48.9 + [2386 - (-10.0 * (62.6 - W_n\%))]^{0.5}}{-5.1}$$

This equation should only be used for natural water contents below 290%.

(3) The Recompression Index (Cr) and the Recompression Ratio (RR) were calculated from the initial reload portion of the curve in the interval between 0.5 and 0.75 times the overburden pressure. The values of Cr range from 0.15 to 0.6, and the approximate value is 0.3. The values of RR range from 0.02 to 0.07 and the approximate average is 0.04. The data might suggest a trend of decreasing value of RR with depth.

(4) A correlation was found between Cr and the natural water content of the specimen was found. It is possible to estimate Cr from on the natural water content with the following equation:

$$Cr = \frac{-719 + [517433 - (-2429 * (83.9 - W_n\%))]^{0.5}}{-1214}$$

This equation should only be used for natural water contents below 290%.

(5) The Swell Index (Cs) and the Swell Ratio (SR) were calculated as the tangent slope of the unloading curve at OCR=10. The data suggest a possible trend of decreasing Cs and SR with depth. The values of Cs range from 0.1 to 0.8 with an approximate average of 0.4. The values of SR range from 0.02 to 0.10 with an approximate average of 0.05.

(6) Additionally, the following Compressibility Ratios were calculated from the data, Cr/Cc ≈ 6.2%, Cr/Cs ≈ 62%, Cs/Cc ≈ 9%. The Cr/Cc ratio, calculated using values of Cr and Cc estimated from the equations listed above increases with increasing water content.

(7) The ratio of the Secondary Compression Index to the Compression Index ($C_{\alpha e}/Cc$) equals 0.05.

6.4.4 Coefficient of Consolidation and Permeability

The following section summarizes the flow properties results obtained during this investigation.

(1) The average normally consolidated value of the coefficient of consolidation varies significantly with depth. A correlation was found between c_v(NC) and the specimen's natural water content. The NC value of c_v can be estimated from the natural water content with the following equation:

$$\log c_v\,(NC) = 7.383 + (-4.65 \times \log W_n\,(\%)) \quad SD\pm 0.316$$

This equation should be used with caution for natural water contents above 300%.

(2) The coefficient of permeability remains somewhat constant with depth, except at a depth of -26m where large scatter and high values are present.

(3) C_k (slope of e vs. log k_v plot) equals 0.45 of the in situ void ratio, and the permeability at the in situ void ratio ($k_{o)}$ can be estimated from the natural water content and the following equation:

$$\log k_o = (-2.58 \times \log W_n(\%)) - 1 \quad SD\pm 0.317$$

This equation should be used with caution for natural water contents above 300%.

6.4.5 Lateral Stress Ratio K_o

A K_o profile was developed for the cathedral site using data from the consolidation phase of SHANSEP CK_oU triaxial tests. The normally consolidated K_o

remains fairly constant with depth at an average value of 0.36. Additionally, a constant value of K_o = 0.45 with depth was calculated using an empirical equation developed by Schmidt (1966) and Alpan (1967). Since the nature of the overconsolidation of the deposit cannot be precisely determined at this time, the actual K_o may be somewhat different than predicted. Nevertheless the value should fall between 0.36 and 0.45.

6.5 SHANSEP UNDRAINED STRENGTH TESTING PROGRAM

6.5.1 General Overview

The undrained strength-deformation properties of the soil at the cathedral site were determined from a combination of SHANSEP K_o consolidated undrained direct simple shear (CK_oUDSS) tests and SHANSEP K_o consolidated undrained triaxial compression and extension (CK_oUC/E) tests. Tables 5.1 through 5.3 summarize the results of the SHANSEP testing program. The shear results from all tests are presented in numerical and graphical form in MIT Department of Civil and Environmental Engineering Research Report Number R94-01.

6.5.2 NC Strength-Deformation Properties

For Direct Simple Shear:

1) The data in Figure 5.11 indicate that the value of $S_d=\tau_h/\sigma'_{vc}$ remains constant with depth at 0.346±0.010SD.

2) The friction angle at γ=30% is 34.4° for NC and OC samples.

3) The shear strain at failure for NC samples remains constant with depth at 13.18 ±0.73SD.

4) The value of E_{u50}/σ'_{vc} might increase with depth, but at this time it is not possible to verify this. A E_{u50}/σ'_{vc} value of 40 is recommended based on the available data, but more research is needed to better understand and estimate this parameter.

For Triaxial Compression:

1) The data in Figure 5.11 might suggest that the value of $S_c=q_f(C)/\sigma'_{vc}$ increases with depth, but this trend cannot be confirmed. This thesis suggests a constant value of S_c with depth of 0.404±0.015SD.

2) There is a very well defined trend between S_c and $K_o(NC)$, as illustrated in Figure 5.13, e.g., an increase in $K_o(NC)$ leads to a decrease in S_c.

3) The friction angle at maximum obliquity is 49.2° and the peak strength friction angle is 44.9°, for OCRs≤1.25.

4) The strain at failure remains constant with depth at ε_{af}=1.34±0.09SD.

5) The value of E_{u50}/σ'_{vc} might increase with depth, but at this time it is not possible to verify this. A E_{u50}/σ'_{vc} value of 45 is recommended based on the available data, but more research is needed to better understand and estimate this parameter.

For Triaxial Extension:

1) The data in Figure 5.11 might suggest that the value of $S_e=q_f(C)/\sigma'_{vc}$ increases with depth, but this trend is not confirmed. This thesis suggests a constant value of S_e with depth of 0.329±0.018SD.

2) The friction angle at maximum obliquity is 66.4° and the peak strength friction angle is 63.6°.

3) The strain at failure remains constant with depth at ε_{af}=16.15±0.60SD. It is likely that this number is too high since SHANSEP extension tests have a tendency to overestimate the strain at failure.

5) The recommended value of E_{u50}/σ'_{vc} =40 is based on two tests.

It is important to point out that the average soil parameters listed above are extremely unique, to México City Clay, and that no other known soil has comparable

normalized soil parameters. Figure 5.24 from Ladd (1986), presents undrained strength ratio versus plasticity index for various normally consolidated clays and silts. The data show $q_f/\sigma'_{vc} = 0.32 \pm 0.03$ for triaxial compression and no trend with plasticity index; generally much lower DSS strengths that tend to decrease with lower plasticity; and even smaller ratios for shear in triaxial extension, especially at low plasticity indices. The data in Figure 5.24, along with other data presented in the literature, clearly demonstrate that most OCR = 1 soils exhibit significant undrained strength anisotropy that generally becomes most important in lean clays, especially if they are also sensitive. The data from this investigation suggests that the plasticity index does not affect the undrained strength ratio of México City Clay. Additionally, México City clay exhibits very low undrained strength anisotropy, and has the highest undrained strength ratios ever published for triaxial compression and extension, and direct simple shear. Accompanying these high undrained strength ratios are some of the highest friction angles ever recorded.

Another unique aspect of México City Clay is its high strain to failure. Most normally consolidated clays tested under CK_oU conditions in triaxial compression fail at 0.1 to 0.3% of axial strain, while NC México City Clay tested under the same conditions failed at an average axial strain of 1.34%. Diaz-Rodriguez et al. (1992) report that the typical strain at failure for México City Clay tested under CIU conditions in triaxial compression is 2%. México City clay exhibits a relatively low E_{u50}/σ'_{vc} compared to most soils. Most soils have very different values of E_{u50}/σ'_{vc} for different modes of shearing, whereas México City Clay has very similar values. This should not be surprising since México City Clay has relatively low shear strength anisotropy.

6.5.3 OC Strength-Deformation Properties

For USR versus OCR:

The estimates of S and m for México City Clay underlying the cathedral are:

DSS	S_d=0.344	m_d=1.000
TC	S_c=0.407	m_c=0.991
TE	S_e=0.329	m_e=0.681

It was stated in the previous section that the undrained strength ratios for México City Clay are exceptionally high. Additionally, the m values for triaxial compression and direct simple shear are exceptionally high. Ladd (1991) recommends an average m value of 0.8±0.1SD for direct simple shear tests. The parameters listed above should only be used to estimate the undrained strengths of soils with OCRs between 1 and 2. Based on data reported in the literature, it is likely that the m value of the soil will decrease as OCR increases. There is a significant amount of uncertainty associated with the m value for triaxial extension, since it is based on only one overconsolidated data point.

The SHANSEP parameters listed above were used to calculate the best estimate of the undrained shear strength profile for different modes of shearing at the cathedral site. These estimates were compared to UU data from Boring SMC-1 presented in SEDUE (1990). The comparison showed that UU tests significantly underestimate the undrained shear strength of the soil.

For Effective Stress Failure Envelope at Maximum Obliquity and Peak Strength:

The estimates of parameters for the Mohr-Coulomb effective stress failure envelope (ESFE) are as follows:

For Triaxial Compression OCRs≤1.25:

Maximum Obliquity	Peak Shear Stress
$c'/\sigma = 0$ and $\phi'_{mo} = 49.2°$	$c'/\sigma = 0$ and $\phi'_{mo} = 44.9°$

For Triaxial Compression OCRs>1.25 and Triaxial Extension all OCRs

Maximum Obliquity	Peak Shear Stress
$c'/\sigma = 0$ and $\phi'_{mo} = 66.4°$	$c'/\sigma = 0$ and $\phi'_{mo} = 63.6°$

It should be noted that the failure envelope for OCRs greater than those tested may have a cohesion intercept. Therefore, the above equations should be used with caution for OCRs greater than 2.

The DSS test is not reliable for obtaining a Mohr-Coulomb type failure envelope. The "failure envelope" at a shear strain of 30% is as follows:

DSS All OCRs $c/\sigma'_{vm} = 0$ and $\psi' = 34.4°$

For Strain At Failure versus OCR:

The shear strain at failure (γ_f) is plotted versus OCR on a log-log plot for direct simple shear tests in Figure 5.21. Figure 5.21 also plots the axial strain at failure (ε_{af}) for triaxial compression and extension tests. For triaxial compression the strain increases as the OCR increases. For direct simple shear and triaxial extension, the strain decreases as the OCR increases. For most soils in any mode of shearing, the strain at failure will increase with increasing OCR.

For Normalized Undrained Modulus versus OCR:

The normalized undrained Young's modulus (E_{u50}/σ'_{vc}) is plotted versus OCR on a log-log plot for, direct simple shear, triaxial compression, and triaxial extension in Figure 5.23. Based on the data, one observes the following trends in mean values:

DSS $E_{u50}/\sigma'_{vc} \approx 40$, slightly increases and then remains constant at ≈ 85.

TC $E_{u50}/\sigma'_{vc} \approx 45$, then significantly increases with OCR.

TE $E_{u50}/\sigma'_{vc} \approx 40$, then slightly increases with OCR.

CHAPTER 7
REFERENCES

1. American Society for Testing Materials (1992), 1992 Annual Book of ASTM Standards, Section 4 (Construction), Vol. 4.08, ASTM, Philadelphia, PA.

2. Andresen, A. AA., & Kolstad, P. (1979), "The NGI 54-mm sampler for undisturbed sampling of clays and representative sampling of coarser materials," Proceedings of the International Symposium of Soil Sampling, Singapore, pp. 13-21.

3. ASTM STP 1095 (1990), "Effects of Small Concentrations of Soluble Salts on Hydrometer Analysis," by Miguel Picornell, Quasi S. El-Jurf, and Mohd A. ABD Rahim, pp. 185-195.

4. Baligh, M. M., Azzouz, A. S. & Chin, C. T. (1987), "Disturbance due to 'ideal' tube sampling," ASCE, Journal of Geotechnical Engineering, Vol. 113, No. 7, pp. 739-757.

5. Becker, D. E., Crooks, J. H. A., Been, K. & Jefferies, M. G. (1987), "Work as a criterion for determining in situ and yield stresses in clays," Canadian Geotechnical Journal, Vol. 24, No. 4, pp. 549-564.

6. Berman, Debra R. (1993), "Characterization of the Engineering Properties of Boston Blue Clay at the MIT Campus," Master's of Science Thesis, Department of Civil and Environmental Engineering, MIT, Cambridge, MA.

7. Bjerrum, L. & Landva, A. (1966), "Direct simple shear tests on a Norwegian quick clay," Geotechnique, Vol. 16, pp. 1-20.

8. Burland, J. B. (1990), "On the compressibility and shear strength of natural clays," Geotechnique, Vol. 40, No. 3, pp. 329-378.

9. Butterfield, R. (1979), "A natural compression law for soils (an advance on e-log p'),"Geotechnique, Vol. 29, No. 4.

10. Carrillo, N. (1969), "Influence of Artesian Wells in the Sinking of México City," Nabor Carrillo; The Subsidence of México City and Texcoco Project, 7th International Conference on Soil Mechanics and Foundation Engineering, Secretaria de Hacienda y Credito Publico Fiduciaria: Nacional Financiera, S. A., México, pp. 7-45.

11. Casagrande, A. (1936), "The determination of the pre-consolidation load and its practical significance," Proceedings of the 1st International Conference on

Soil Mechanics and Foundation Engineering, Cambridge, MA, Vol. 3, pp. 60-64.

12. Casagrande, A. & Wilson, S. D. (1951), "Effect of rate of loading on the strength of clays and shales at constant water content," Geotechnique, Vol. 2, No. 3, pp. 251-263.

13. Diaz-Rodriguez, J. A., Leroueil, S. & Aleman, J. D. (1992), "Yielding of México City Clay and other natural clays," ASCE, Journal of Geotechnical Engineering, Vol. 118, No. 7, pp. 981-995.

14. de La Beaumelle, A. C. (1991), "Evaluation of SHANSEP Strength-Deformation Properties of Undisturbed Boston Blue Clay for Automated Triaxial Testing," Master's of Science Thesis, Department of Civil Engineering, MIT, Cambridge, MA.

15. Estabrook, A. H. (1991), "Comparison of Recompression and SHANSEP Strength-Deformation Properties of Undisturbed Boston Blue Clay from Automated Triaxial Testing," Master's of Science Thesis, Department of Civil Engineering, MIT, Cambridge, MA.

16. Gilbert, P. A. (1992), "Effect of Sampling Disturbance on Laboratory-Measured Soil Properties," Miscellaneous Paper Gl-92-35, Prepared for Department of the Army Waterways Experiment Station, Vicksburg, Miss., Under CWIS Work Unit No. 32676, 49 pp.

17. Girault, P. (1964), "Mineralogia de las Arcillas del Valle de México," Revista Ingeniera, October, UNAM, México, pp. 511-518.

18. Gomez Looh, B. (1987), "Analisis por Difraccion de Rayos X de las Arcillas del Subsuelo de la Ciudad de México," Undergraduate Thesis, UNAM, Department of Chemistry, México.

19. Grim, R. E. (1962), Applied Clay Mineralogy, 2nd Edition, McGraw-Hill, New York.

20. Hadge, W. E. (1979), "A Relationship Between the Drained and Undrained Cyclic Behavior of Sand," Master's of Science Thesis, Department of Civil Engineering, MIT, Cambridge, MA.

21. Hiriart, F. & Marsal, R. J. (1969), "The subsidence of México City," Nabor Carrillo; The Subsidence of México City and Texcoco Project, 7th International Conference on Soil Mechanics and Foundation Engineering, Secretaria de Hacienda y Credito Publico Fiduciaria: Nacional Financiera, S. A., México, pp. 109-147.

22. Hvorslev, J. M. (1949), "Subsurface Exploration and Sampling of Soils for Civil Engineering Purposes," Waterways Experiment Station, Vicksburg, Miss., 521 pp.

23. Jaky, J. (1944), "The coefficient of earth pressure at rest," Journal Society of Hungarian Architects and Engineers, Budapest, Hungary, October, pp. 355-358.

24. Jamiolkowski, M., Ladd, C. C., Germaine, J. T. & Lancellotta, R. (1985), "New developments in field and laboratory testing of soils: Theme lecture 2," Proceedings of the 11th International Conference on Soil Mechanics and Foundation Engineering, San Francisco, Vol. 1, pp. 57-153.

25. Ladd, C. C. (1986), "Stability evaluation during staged construction," The 22nd Terzaghi Lecture, Presented at the ASCE 1986 Annual Convention. Same as:

26. Ladd, C. C. (1991), "Stability evaluation during staged construction," ASCE, Journal of Geotechnical Engineering, Vol. 117, No. 4, pp. 542-615.

27. Ladd, C. C. & Edgers, L. (1972), "Consolidated-undrained direct simple shear tests on saturated clays," MIT Research Report R72-82, No. 284, Department of Civil Engineering, MIT, Cambridge, MA, 354 pp.

28. Ladd, C. C. & Foott, R. (1974), "New design procedure for stability of soft clays," Journal of Geotechnical Engineering Division, Vol. 100, No. GT7, pp. 763-786.

29. Ladd, C. C., Foott, R., Ishihara, K., Schlosser, F. & Poulos, H. G. (1977), "Stress-deformation and strength characteristics, state-of-the-art-report," Proceedings of the 9th International Conference on Soil Mechanics and Foundation Engineering, Tokyo, Vol. 2, pp. 421-494.

30. Ladd, C. C. & Lambe, T. W. (1963), "The Strength of 'Undisturbed' Clay Determined from Undrained Tests," American Society for Testing and Materials, STP 361, pp. 342-371.

31. Lambe, T. W. & Whitman, R. V. (1969), Soil Mechanics, 1st edition, John Wiley & Sons, Inc., New York, NY.

32. La Rochelle, P., Sarrailh, J., Tavenas, F. & Leroueil, S. (1981) "Causes of sampling disturbances and design of a new sampler for sensitive soils," Canadian Geotechnical Journal, Vol. 18, No. 1, pp. 52-66.

33. Leon, J. L., Alberro, J. & Hiriart, G. (1974), "Estudio de Relaciones Esfuerzo-Deformacion y Resistencia de las Arcillas del Lago de Texcoco," Tech. Report, Instituto de Ingenieria, UNAM to Comision del Lago de Texcoco.

34. Leonards, G. A., & Girault, P. (1961), "A study of the one-dimensional consolidation test," Proceedings 5th International Conference of Soil Mechanics and Foundation Engineering, No. 1, pp. 213-218.

35. Lo, K. Y. (1962), "Shear strength properties of a sample of volcanic material of the valley of México," Geotechnique, Vol. 12, No. 4, pp. 303-318.

36. Marcuson, W. F., III, & Franklin, A. G. (1979), "State of the art of undisturbed sampling of cohesionless soils," Proceedings of the International Symposium of Soil Sampling, Singapore, pp. 57-71.

37. Marsal, R. J. & Mazari, Y. M. (1959), "The Subsoil of México City," 1st Panamerican Conference on Soil Mechanics and Foundation Engineering, México, September.

38. Martin, R. T. (1970), "Suggested Method of Test for Determination of Soluble Salts in Soil," ASTM STP 479, pp. 288-290.

39. Mayne, P. W. & Kulhawy, F. H. (1982), "K_O-OCR relationships in soil," ASCE, Journal of Geotechnical Engineering Division, Vol. 108, No. 6, pp. 851-872.

40. Mesri, G. & Castro, A. (1987), "C_α/C_c concept and K_O during secondary compression, "Journal of Geotechnical Engineering, Vol. 113, No. 3, pp. 230-247.

41. Mesri, G. & Choi, Y. K. (1984), "Time effects on the stress-strain behavior of natural soft clays," Discussion, Geotechnique, Vol. 34, No. 3, pp. 439-442.

42. Mesri, G. & Godlewski, P. M. (1977), "Time- and stress-compressibility interrelationship," ASCE, Journal of the Geotechnical Engineering Division, Vol. 103, No. GT5, pp. 417-430.

43. Mesri, G. & Rokhsar, A. (1974), "Theory of consolidation for clays," Journal of the Geotechnical Engineering Division, ASCE, Vol. 100, No. 8, pp. 889-904.

44. Mesri, G., Rokhsar, A. & Bohor, B. F. (1975), "Composition and compressibility of Typical Samples of México City Clay," Geotechnique, Vol. 25, No. 3, pp. 527-554.

45. Mitchell, J. K. (1976), Fundamentals of Soil Behavior, John Wiley & Sons, Inc., New York.

46. Mooser, F. (1956), "Los ciclos del Vulcanismo que formaron la Cuenca de México", 20th International Geological Conference, México.

47. Mooser, F. (1992) Personal Correspondence.

48. Moum, J. & Rosenqvist, I. T. (1961), "The mechanical properties of montmorillonite and illite clays related to the electrolytes of the pore water," Proceedings of the 5th International Conference on Soil Mechanics and Foundation Engineering, Vol. 1, pp. 263-267.

49. Nakase, A., Kusakabe, O. & Nomura, H. (1978), "On the correlation between disturbance of cohesive soil and the grading," Proceedings; 1978 Sampling Symposium, Japanese Society of Soil Mechanics and Foundation Engineering (in Japanese).

50. Ortega, O. J. (1992), "Computer Automation of the Consolidated-Undrained Direct Simple Shear Test," Master's of Science Thesis, Department of Civil Engineering, MIT, Cambridge, MA.

51. Peralta, R. (1989), "Sobre el Origen de Algunas Propiedades Mecanicas de la Formacion Arcillosa Superior del Valle de México," Symposium of Geologic Topics of the Valley of México City, Méxican Society of Soil Mechanics, pp. 43-53.

52. Secretaria de Desarrollo Urbano y Ecologia (SEDUE) (1990), Estudio de las Cimentaciones de la Catedral y el Sagrario Metropolitanos de la Ciudad del México, Report prepared by TGC Geotecnia.

53. Sheahan, T. C. (1988), "Modification and Implementation of a Computer Controlled Triaxial Apparatus," Master's of Science Thesis, Department of Civil Engineering, MIT, Cambridge, MA.

54. Sheahan, T. C. (1991), "An Experimental Study of the Time-Dependent Undrained Shear Behavior of Resedimented Boston Blue Clay Using Automated Stress Path Triaxial Equipment," Doctor of Science Thesis, Department of Civil Engineering, MIT, Cambridge, MA.

55. Sheahan, T. C., Germaine, J. T. & Ladd, C. C. (1990), "Automated testing of soft clays: and upgraded commercial system," ASTM, Geotechnical Testing Journal, Vol. 13, No. 13, pp. 153-163.

56. Schmertmann, J. H. (1955), "The undisturbed consolidation of clay," Transactions, ASCE, Vol. 120, pp. 1201-1233.

57. Schmidt, B. (1966), "Earth pressures at rest related to stress history," Canadian Geotechnical Journal, Vol. 3, No. 4, pp. 239-242.

58. Skempton, A. W. (1953), "The colloidal activity of clays," Proceedings of the 3rd International Conference on Soil Mechanics and Foundation Engineering, Vol. 1, pp. 57-61.

59. Skempton, A. W. & Northey, R. D. (1952), "The sensitivity of clays," Geotechnique, Vol. 3, No. 1, pp. 30-53.

60. Tamez, E., Santoyo, E. & Cuevas, A. (1992), "La Catedral y el Sagrario de la Ciudad de México Corrección del Comportamiento de sus Cimentaciones," Raul J. Marsal Volume, Sociedad Mexicana de Mecánica de Suelos, A.C., México, pp. 61-130.

61. Terzaghi, K. & Peck, R. R. (1968), Soil Mechanics in Engineering Practice, 2nd Edition, John Wiley and Sons, Inc., New York, NY.

62. Wissa, A. E. Z., Christian, J. T., Davis, E. H. & Heiberg, S. (1971), "Consolidation at Constant Rate of Strain," ASCE, Journal of Soil Mechanics and Foundation Engineering, Vol. 97, No. SM10, pp. 1343-1413.

63. Zeevaert, L. (1949), "An Investigation of the Engineering Characteristics of the Volcanic Lacustrine Clay Deposits Beneath México City," Doctor of Science Thesis, University of Illinois.

Appendix A

Boring and Sample Logs

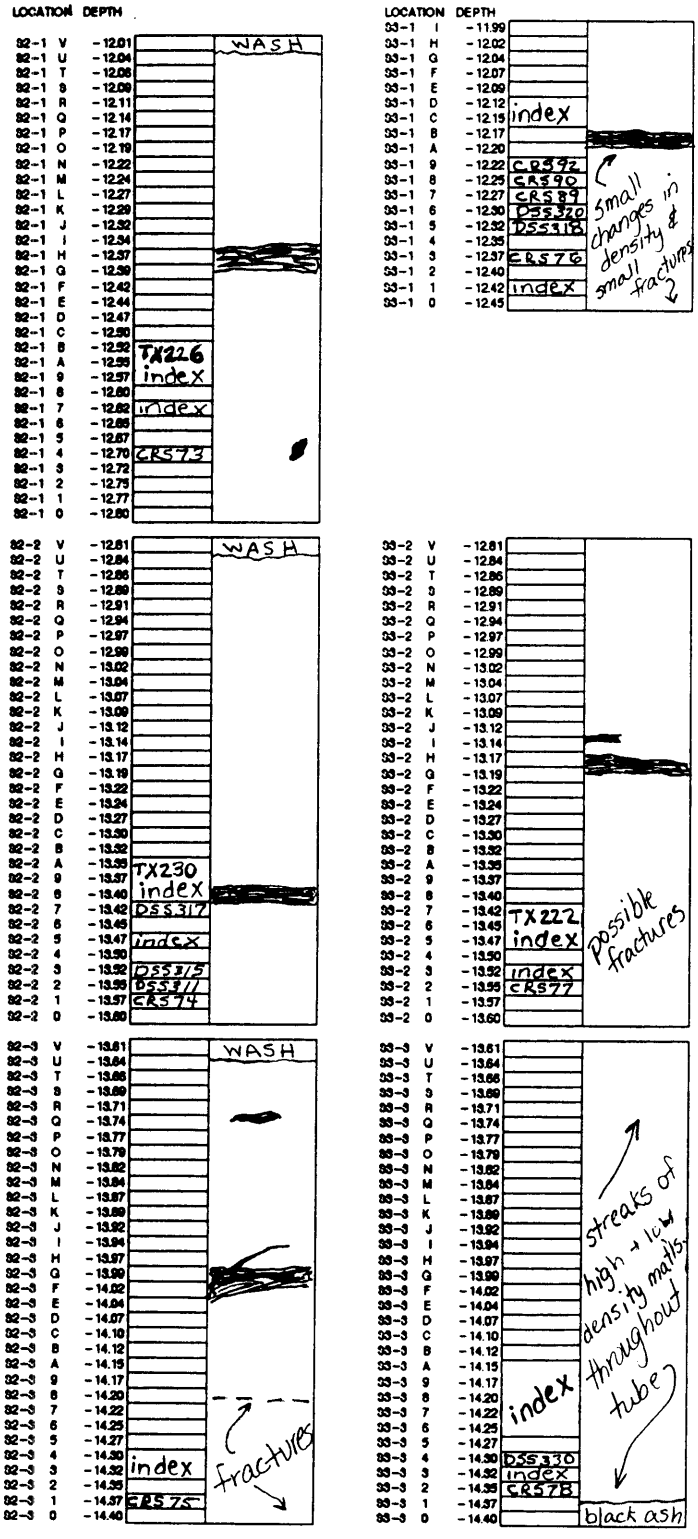
LOCATION DEPTH
S2-1 V -12.81
S2-1 U -12.84
S2-1 T -12.86
S2-1 S -12.89
S2-1 R -12.91
S2-1 Q -12.94
S2-1 P -12.97
S2-1 O -12.99
S2-1 N -13.02
S2-1 M -13.04
S2-1 L -13.07
S2-1 K -13.09
S2-1 J -13.12
S2-1 I -13.14
S2-1 H -13.17
S2-1 G -13.19
S2-1 F -13.22
S2-1 E -13.24
S2-1 D -13.27
S2-1 C -13.30
S2-1 B -13.32
S2-1 A -13.35
S2-1 9 -13.37
S2-1 8 -13.40
S2-1 7 -13.42
S2-1 6 -13.45
S2-1 5 -13.47
S2-1 4 -13.50
S2-1 3 -13.52
S2-1 2 -13.55
S2-1 1 -13.57
S2-1 0 -13.60
WASH
TX226
index
index
CR573
LOCATION DEPTH
S3-1 I -11.99
S3-1 H -12.02
S3-1 G -12.04
S3-1 F -12.07
S3-1 E -12.09
S3-1 D -12.12
S3-1 C -12.15
S3-1 B -12.17
S3-1 A -12.20
S3-1 9 -12.22
S3-1 8 -12.25
S3-1 7 -12.27
S3-1 6 -12.30
S3-1 5 -12.32
S3-1 4 -12.35
S3-1 3 -12.37
S3-1 2 -12.40
S3-1 1 -12.42
S3-1 0 -12.45
index
CR592
CR590
CR589
DSS320
DSS318
CR576
index
small changes in density & small fractures
S2-2 V -12.81
S2-2 U -12.84
S2-2 T -12.86
S2-2 S -12.89
S2-2 R -12.91
S2-2 Q -12.94
S2-2 P -12.97
S2-2 O -12.99
S2-2 N -13.02
S2-2 M -13.04
S2-2 L -13.07
S2-2 K -13.09
S2-2 J -13.12
S2-2 I -13.14
S2-2 H -13.17
S2-2 G -13.19
S2-2 F -13.22
S2-2 E -13.24
S2-2 D -13.27
S2-2 C -13.30
S2-2 B -13.32
S2-2 A -13.35
S2-2 9 -13.37
S2-2 8 -13.40
S2-2 7 -13.42
S2-2 6 -13.45
S2-2 5 -13.47
S2-2 4 -13.50
S2-2 3 -13.52
S2-2 2 -13.55
S2-2 1 -13.57
S2-2 0 -13.60
WASH
TX230
index
DSS317
index
DSS315
DSS311
CR574
S3-2 V -12.81
S3-2 U -12.84
S3-2 T -12.86
S3-2 S -12.89
S3-2 R -12.91
S3-2 Q -12.94
S3-2 P -12.97
S3-2 O -12.99
S3-2 N -13.02
S3-2 M -13.04
S3-2 L -13.07
S3-2 K -13.09
S3-2 J -13.12
S3-2 I -13.14
S3-2 H -13.17
S3-2 G -13.19
S3-2 F -13.22
S3-2 E -13.24
S3-2 D -13.27
S3-2 C -13.30
S3-2 B -13.32
S3-2 A -13.35
S3-2 9 -13.37
S3-2 8 -13.40
S3-2 7 -13.42
S3-2 6 -13.45
S3-2 5 -13.47
S3-2 4 -13.50
S3-2 3 -13.52
S3-2 2 -13.55
S3-2 1 -13.57
S3-2 0 -13.60
TX222
index
index
CR577
possible fractures
S2-3 V -13.61
S2-3 U -13.64
S2-3 T -13.66
S2-3 S -13.69
S2-3 R -13.71
S2-3 Q -13.74
S2-3 P -13.77
S2-3 O -13.79
S2-3 N -13.82
S2-3 M -13.84
S2-3 L -13.87
S2-3 K -13.89
S2-3 J -13.92
S2-3 I -13.94
S2-3 H -13.97
S2-3 G -13.99
S2-3 F -14.02
S2-3 E -14.04
S2-3 D -14.07
S2-3 C -14.10
S2-3 B -14.12
S2-3 A -14.15
S2-3 9 -14.17
S2-3 8 -14.20
S2-3 7 -14.22
S2-3 6 -14.25
S2-3 5 -14.27
S2-3 4 -14.30
S2-3 3 -14.32
S2-3 2 -14.35
S2-3 1 -14.37
S2-3 0 -14.40
WASH
index
CR575
fractures
S3-3 V -13.61
S3-3 U -13.64
S3-3 T -13.66
S3-3 S -13.69
S3-3 R -13.71
S3-3 Q -13.74
S3-3 P -13.77
S3-3 O -13.79
S3-3 N -13.82
S3-3 M -13.84
S3-3 L -13.87
S3-3 K -13.89
S3-3 J -13.92
S3-3 I -13.94
S3-3 H -13.97
S3-3 G -13.99
S3-3 F -14.02
S3-3 E -14.04
S3-3 D -14.07
S3-3 C -14.10
S3-3 B -14.12
S3-3 A -14.15
S3-3 9 -14.17
S3-3 8 -14.20
S3-3 7 -14.22
S3-3 6 -14.25
S3-3 5 -14.27
S3-3 4 -14.30
S3-3 3 -14.32
S3-3 2 -14.35
S3-3 1 -14.37
S3-3 0 -14.40
index
DSS330
index
CR578
streaks of high → low density matls throughout tube
black ash

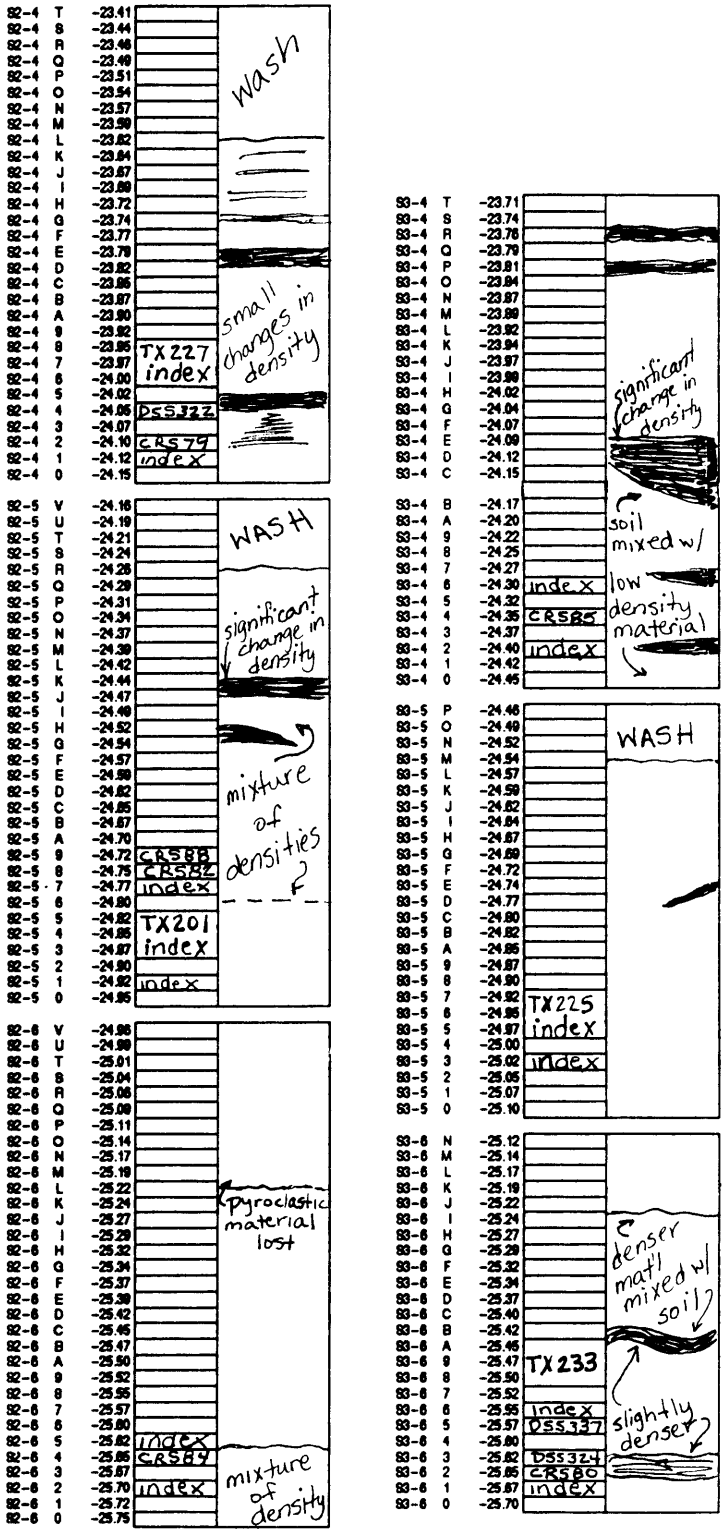
82-4 T -23.41
82-4 S -23.44
82-4 R -23.46
82-4 Q -23.49
82-4 P -23.51
82-4 O -23.54
82-4 N -23.57
82-4 M -23.59
82-4 L -23.62
82-4 K -23.64
82-4 J -23.67
82-4 I -23.69
82-4 H -23.72
82-4 G -23.74
82-4 F -23.77
82-4 E -23.79
82-4 D -23.82
82-4 C -23.85
82-4 B -23.87
82-4 A -23.90
82-4 9 -23.92
82-4 8 -23.95
82-4 7 -23.97
82-4 6 -24.00
82-4 5 -24.02
82-4 4 -24.05
82-4 3 -24.07
82-4 2 -24.10
82-4 1 -24.12
82-4 0 -24.15
TX227 index
DSS322
CRS579
index
wash
small changes in density
82-5 V -24.16
82-5 U -24.19
82-5 T -24.21
82-5 S -24.24
82-5 R -24.26
82-5 Q -24.29
82-5 P -24.31
82-5 O -24.34
82-5 N -24.37
82-5 M -24.39
82-5 L -24.42
82-5 K -24.44
82-5 J -24.47
82-5 I -24.49
82-5 H -24.52
82-5 G -24.54
82-5 F -24.57
82-5 E -24.59
82-5 D -24.62
82-5 C -24.65
82-5 B -24.67
82-5 A -24.70
82-5 9 -24.72
82-5 8 -24.75
82-5 7 -24.77
82-5 6 -24.80
82-5 5 -24.82
82-5 4 -24.85
82-5 3 -24.87
82-5 2 -24.90
82-5 1 -24.92
82-5 0 -24.95
CRS588
CRS582
index
TX201 index
index
WASH
significant change in density
mixture of densities
82-6 V -24.98
82-6 U -24.99
82-6 T -25.01
82-6 S -25.04
82-6 R -25.06
82-6 Q -25.09
82-6 P -25.11
82-6 O -25.14
82-6 N -25.17
82-6 M -25.19
82-6 L -25.22
82-6 K -25.24
82-6 J -25.27
82-6 I -25.29
82-6 H -25.32
82-6 G -25.34
82-6 F -25.37
82-6 E -25.39
82-6 D -25.42
82-6 C -25.45
82-6 B -25.47
82-6 A -25.50
82-6 9 -25.52
82-6 8 -25.55
82-6 7 -25.57
82-6 6 -25.60
82-6 5 -25.62
82-6 4 -25.65
82-6 3 -25.67
82-6 2 -25.70
82-6 1 -25.72
82-6 0 -25.75
index
CRS589
index
Pyroclastic material lost
mixture of density
93-4 T -23.71
93-4 S -23.74
93-4 R -23.76
93-4 Q -23.79
93-4 P -23.81
93-4 O -23.84
93-4 N -23.87
93-4 M -23.89
93-4 L -23.92
93-4 K -23.94
93-4 J -23.97
93-4 I -23.99
93-4 H -24.02
93-4 G -24.04
93-4 F -24.07
93-4 E -24.09
93-4 D -24.12
93-4 C -24.15
93-4 B -24.17
93-4 A -24.20
93-4 9 -24.22
93-4 8 -24.25
93-4 7 -24.27
93-4 6 -24.30
93-4 5 -24.32
93-4 4 -24.35
93-4 3 -24.37
93-4 2 -24.40
93-4 1 -24.42
93-4 0 -24.45
index
CRS585
index
significant change in density
soil mixed w/ low density material
93-5 P -24.46
93-5 O -24.49
93-5 N -24.52
93-5 M -24.54
93-5 L -24.57
93-5 K -24.59
93-5 J -24.62
93-5 I -24.64
93-5 H -24.67
93-5 G -24.69
93-5 F -24.72
93-5 E -24.74
93-5 D -24.77
93-5 C -24.80
93-5 B -24.82
93-5 A -24.85
93-5 9 -24.87
93-5 8 -24.90
93-5 7 -24.92
93-5 6 -24.95
93-5 5 -24.97
93-5 4 -25.00
93-5 3 -25.02
93-5 2 -25.05
93-5 1 -25.07
93-5 0 -25.10
TX225 index
index
WASH
93-6 N -25.12
93-6 M -25.14
93-6 L -25.17
93-6 K -25.19
93-6 J -25.22
93-6 I -25.24
93-6 H -25.27
93-6 G -25.29
93-6 F -25.32
93-6 E -25.34
93-6 D -25.37
93-6 C -25.40
93-6 B -25.42
93-6 A -25.45
93-6 9 -25.47
93-6 8 -25.50
93-6 7 -25.52
93-6 6 -25.55
93-6 5 -25.57
93-6 4 -25.60
93-6 3 -25.62
93-6 2 -25.65
93-6 1 -25.67
93-6 0 -25.70
TX233
index
DSS337
DSS324
CRS580
index
denser matl mixed w/ soil?
slightly denser

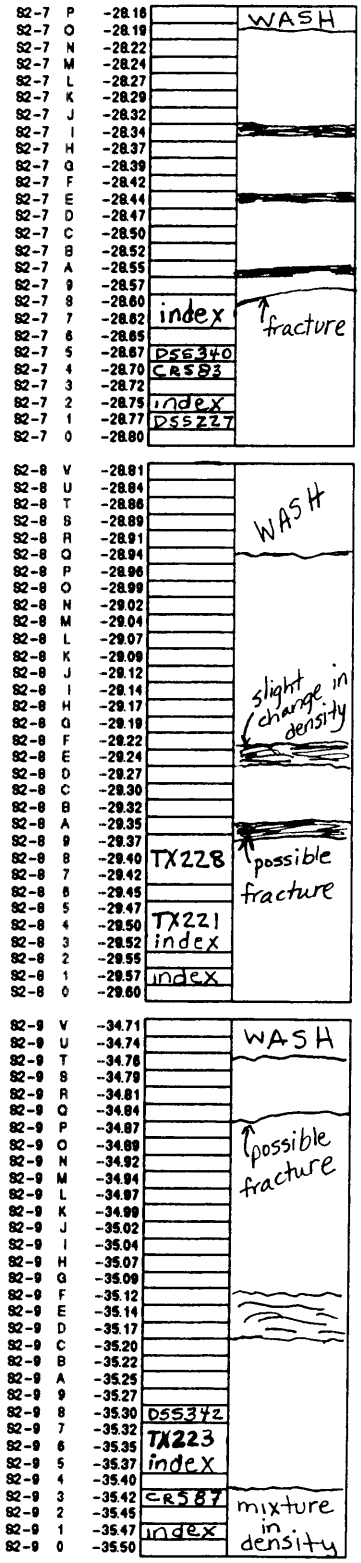
82-7 P -28.16
82-7 O -28.19
82-7 N -28.22
82-7 M -28.24
82-7 L -28.27
82-7 K -28.29
82-7 J -28.32
82-7 I -28.34
82-7 H -28.37
82-7 G -28.39
82-7 F -28.42
82-7 E -28.44
82-7 D -28.47
82-7 C -28.50
82-7 B -28.52
82-7 A -28.55
82-7 9 -28.57
82-7 8 -28.60
82-7 7 -28.62
82-7 6 -28.65
82-7 5 -28.67
82-7 4 -28.70
82-7 3 -28.72
82-7 2 -28.75
82-7 1 -28.77
82-7 0 -28.80
WASH
index
fracture
DS5340
CR583
index
DS5227
82-8 V -28.81
82-8 U -28.84
82-8 T -28.86
82-8 S -28.89
82-8 R -28.91
82-8 Q -28.94
82-8 P -28.96
82-8 O -28.99
82-8 N -29.02
82-8 M -29.04
82-8 L -29.07
82-8 K -29.09
82-8 J -29.12
82-8 I -29.14
82-8 H -29.17
82-8 G -29.19
82-8 F -29.22
82-8 E -29.24
82-8 D -29.27
82-8 C -29.30
82-8 B -29.32
82-8 A -29.35
82-8 9 -29.37
82-8 8 -29.40
82-8 7 -29.42
82-8 6 -29.45
82-8 5 -29.47
82-8 4 -29.50
82-8 3 -29.52
82-8 2 -29.55
82-8 1 -29.57
82-8 0 -29.60
WASH
slight change in density
TX228
possible fracture
TX221
index
index
82-9 V -34.71
82-9 U -34.74
82-9 T -34.76
82-9 S -34.79
82-9 R -34.81
82-9 Q -34.84
82-9 P -34.87
82-9 O -34.89
82-9 N -34.92
82-9 M -34.94
82-9 L -34.97
82-9 K -34.99
82-9 J -35.02
82-9 I -35.04
82-9 H -35.07
82-9 G -35.09
82-9 F -35.12
82-9 E -35.14
82-9 D -35.17
82-9 C -35.20
82-9 B -35.22
82-9 A -35.25
82-9 9 -35.27
82-9 8 -35.30
82-9 7 -35.32
82-9 6 -35.35
82-9 5 -35.37
82-9 4 -35.40
82-9 3 -35.42
82-9 2 -35.45
82-9 1 -35.47
82-9 0 -35.50
WASH
possible fracture
DS5342
TX223
index
CR587
index
mixture in density

RADIOGRAPHY LOG
MASSACHUSETTS INSTITUTE OF TECHNOLOGY

Project Eng. Properties of the Soil Beneath Mexico City's Cathedral
Sample No. 1 Boring No. S2
Depth 12.00 - 12.80 Depth @ 0" 12.80
Sample Type Shelby Tube Date June 1992

Note: Shaded areas indicate material of greater density.

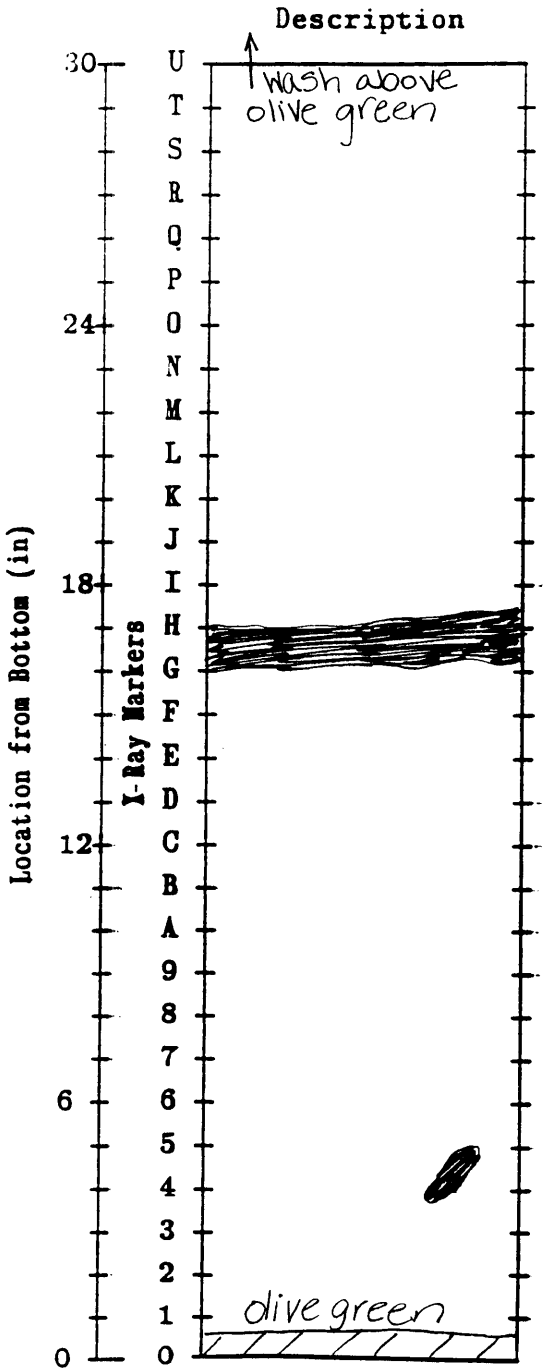

Engineering Test	Index Test	Wn (%)	Avg. TV (ksc)
TX226	specific gravity	312.9	0.58
		320.3	0.48
	A.L.		
	salt conc + pH	281.9	0.48
CR573		274.2	0.48
		268.7	0.48

RADIOGRAPHY LOG
MASSACHUSETTS INSTITUTE OF TECHNOLOGY

Project: Eng. Properties of the Soil Beneath Mexico City's Cathedral
Sample No.: 2
Depth: 12.8-13.6 m
Sample Type: Shelby Tube
Boring No.: S2
Depth @ 0": 13.6
Date: June 1992

Note: Shaded areas indicate material of greater density.

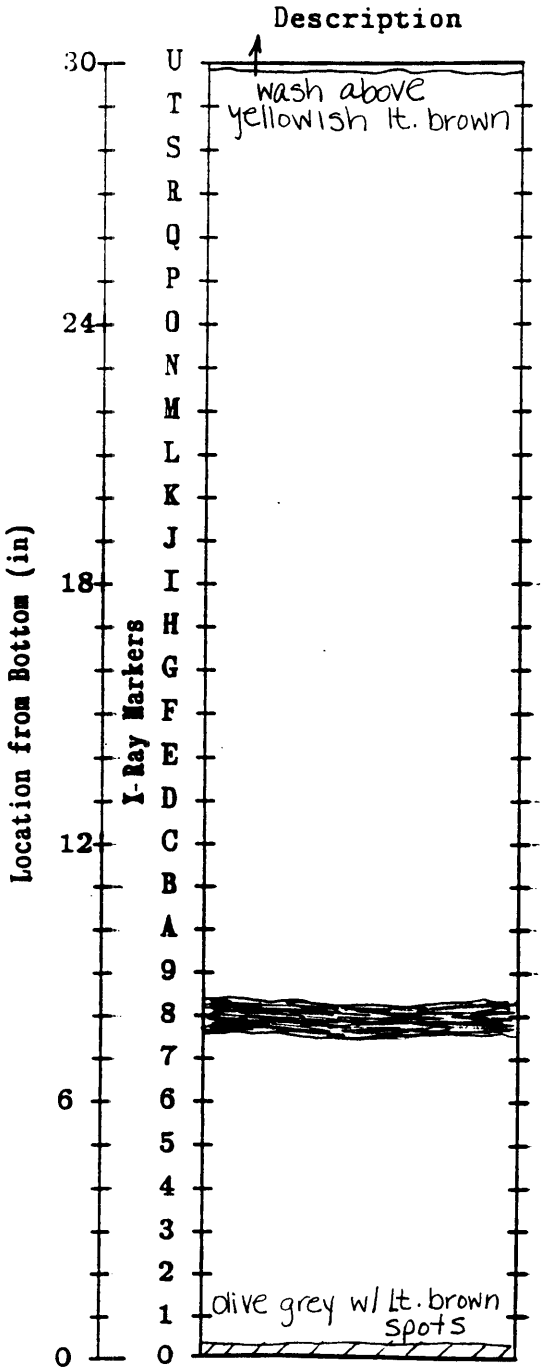

Engineering Test	Index Test	Wn (%)	Avg. TV (KSC)
TX 230	specific gravity	274.4	
DSS317		285.1	0.48
	A.L.		
	salt conc + PH	280.1	0.47
DSS315		285.8	0.41
DSS 311			
CRS 74		286.0	0.43

RADIOGRAPHY LOG
MASSACHUSETTS INSTITUTE OF TECHNOLOGY

Project Eng. Properties of the Soil Beneath Mexico City's Cathedral
Sample No. 3
Boring No. S2
Depth 13.60-14.4 m
Depth @ 0" 14.40
Sample Type Shelby Tube
Date June 1992

Note: shaded areas indicate material of greater density.

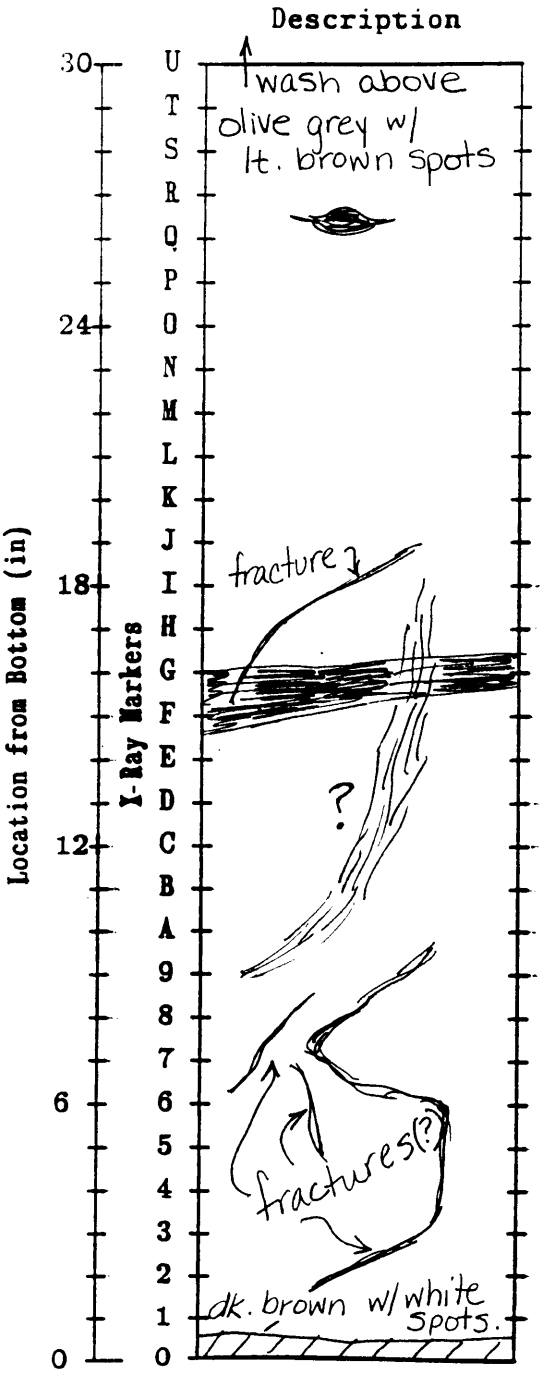

Engineering Test	Index Test	Wn (%)	Avg. TV (ksc)
	specific gravity; A.L.;	217.8	0.57
CRS75	salt conc & pH	204.6	0.49

RADIOGRAPHY LOG
MASSACHUSETTS INSTITUTE OF TECHNOLOGY

Project	Eng. Properties of the Soil Beneath Mexico City's Cathedral		
Sample No.	4	Boring No.	52
Depth	23.40-24.15	Depth @ 0"	24.15
Sample Type	Shelby Tube	Date	June 1992

Note: Shaded areas indicate material of greater density.

Description

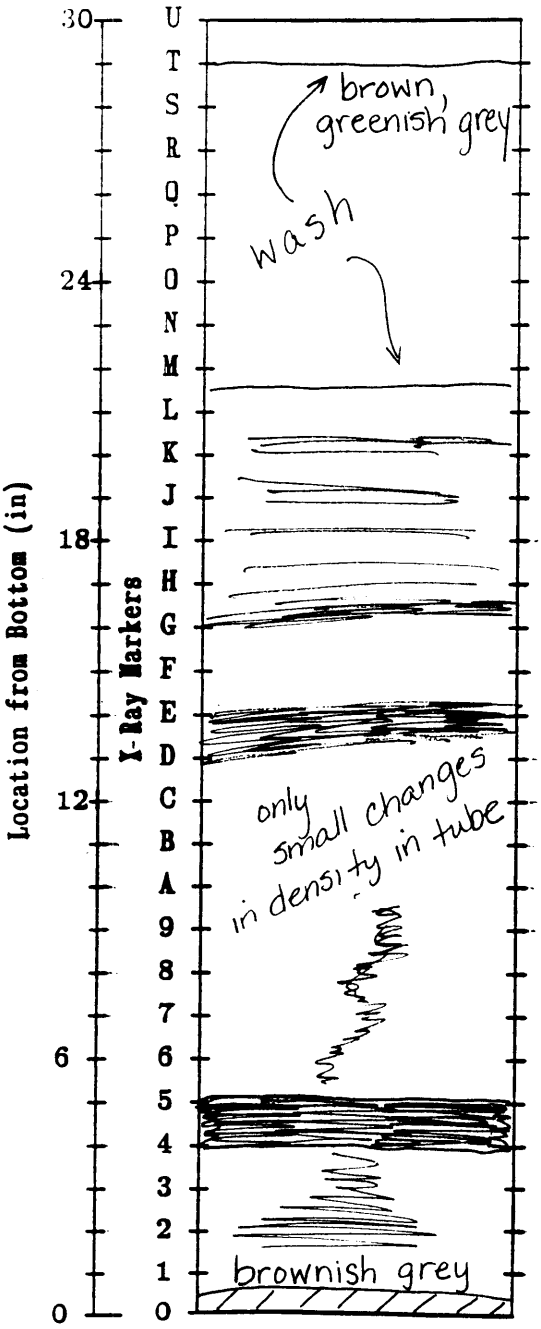

Engineering Test	Index Test	Wn (%)	Avg. TV (ksc)
TX227	specific gravity	164.0	0.59
DSS322		148.0	
CRS 79		227.3	0.58
	A.L. Salt conc +pH	190.3	0.57

RADIOGRAPHY LOG
MASSACHUSETTS INSTITUTE OF TECHNOLOGY

Project: Eng. Properties of the Soil Beneath Mexico City's Cathedral
Sample No.: S
Depth: 24.15 - 24.95 m
Sample Type: Shelby Tube
Boring No.: S2
Depth @ 0": 24.95
Date: June 1992

Note: Shaded areas indicate material of greater density.

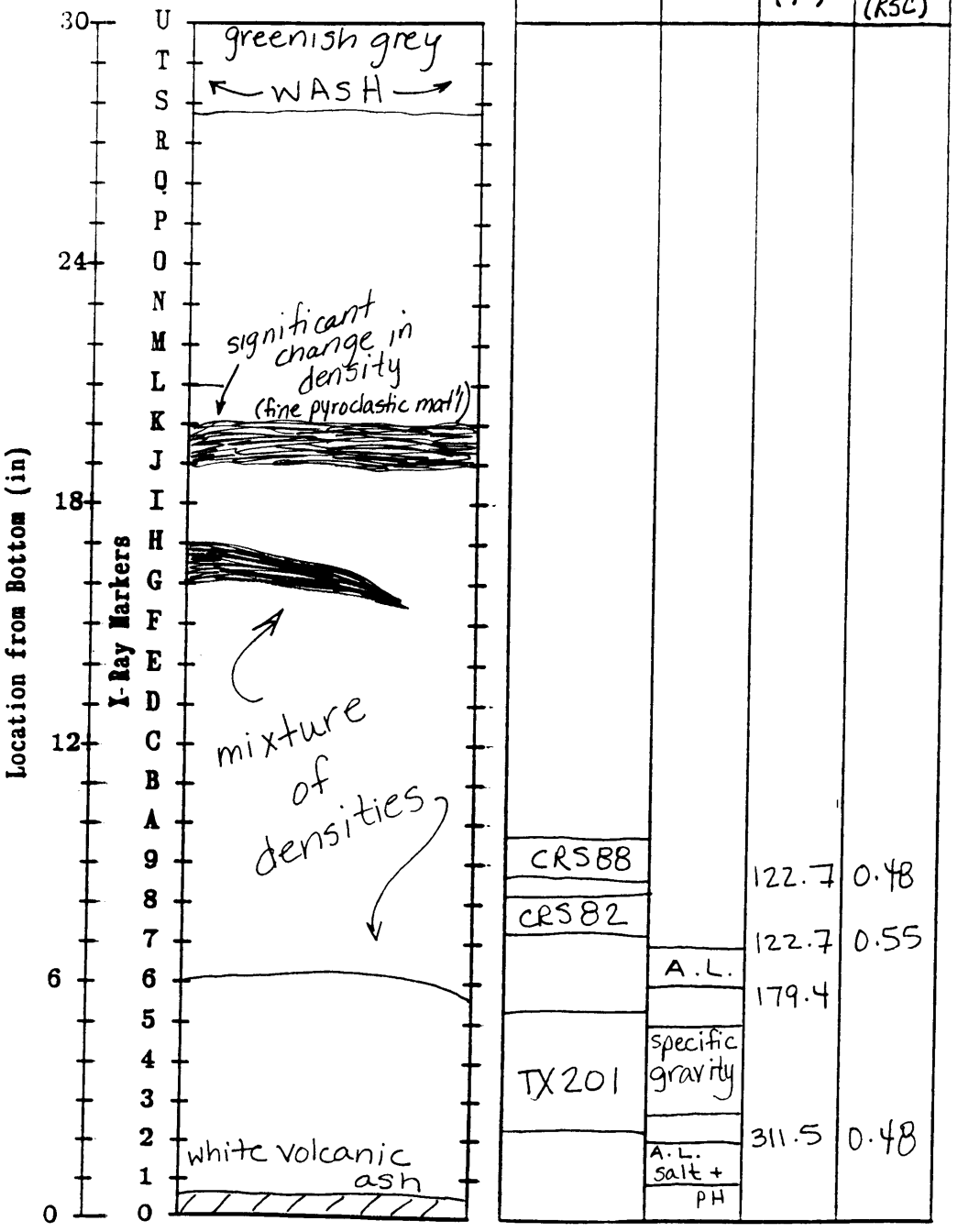

RADIOGRAPHY LOG
MASSACHUSETTS INSTITUTE OF TECHNOLOGY

Project: Eng. Properties of the Soil Beneath Mexico City's Cathedral
Sample No.: 6 — Boring No.: S2
Depth: 24.95 - 25.75m — Depth @ 0": 25.75
Sample Type: Shelby Tube — Date: June 1992
Note: Shaded areas indicate material of greater density.

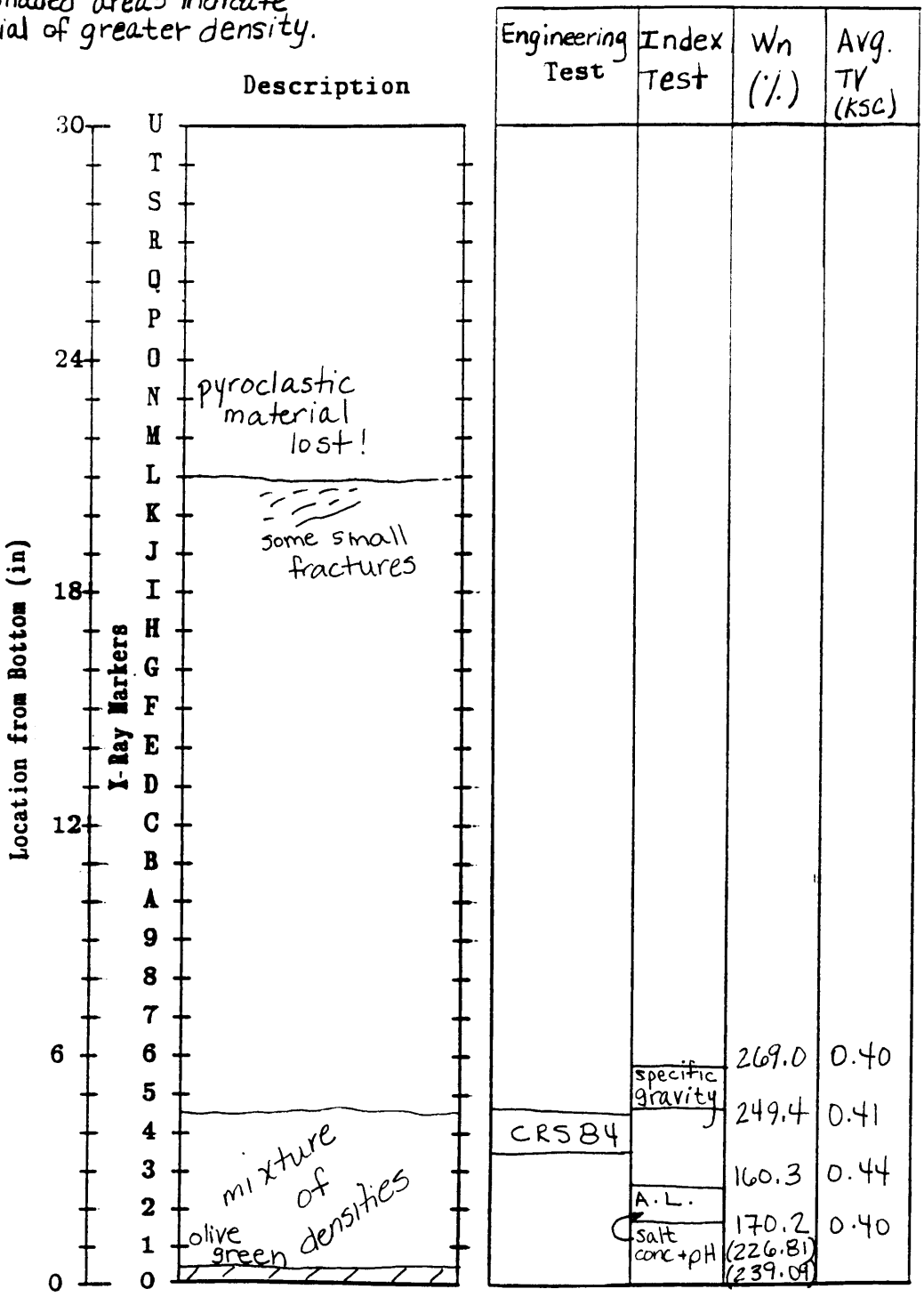

Engineering Test	Index Test	Wn (%)	Avg. TV (KSC)
	specific gravity	269.0	0.40
CRS84		249.4	0.41
		160.3	0.44
	A.L.	170.2	0.40
	salt conc + pH	(226.81) (239.09)	

RADIOGRAPHY LOG
MASSACHUSETTS INSTITUTE OF TECHNOLOGY

Project: Eng. Properties of the Soil Beneath Mexico City's Cathedral
Sample No.: 7
Depth: 28.15 - 28.80m
Sample Type: Shelby Tube
Boring No.: S2
Depth @ 0": 28.80
Date: June 1992

Note: Shaded areas indicate material of greater density.

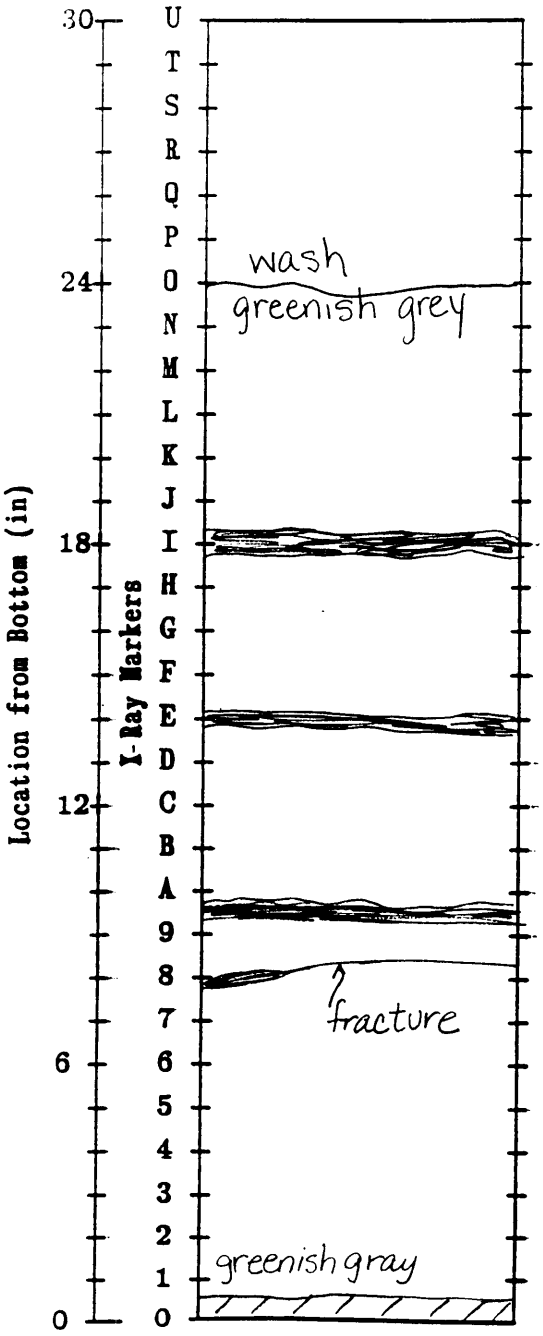

Engineering Test	Index Test	Wn (%)	Avg. TV (KSC)
	specific gravity	279.6	0.60
		273.5	0.47
DSS340			
		260.7	
CRS83			
		226.7	0.48
	A.L. ↗	257.5	0.40
DSS227	salt conc + pH		

RADIOGRAPHY LOG
MASSACHUSETTS INSTITUTE OF TECHNOLOGY

Project	Eng. Properties of the Soil Beneath Mexico City's Cathedral		
Sample No.	8	Boring No.	S2
Depth	28.80-29.60m	Depth @ 0"	29.60
Sample Type	Shelby Tube	Date	June 1992

Note: Shaded areas indicate material of greater density.

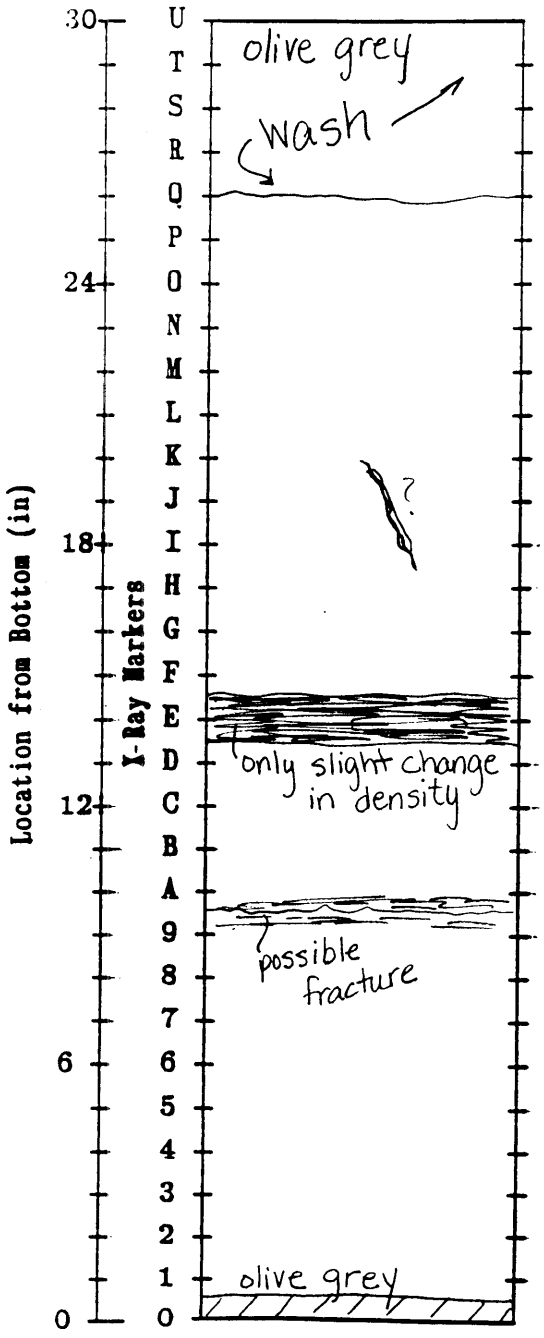

Engineering Test	Index Test	Wn (%)	Avg. TV (ksc)
		291.8	0.75
TX228			
		286.9	0.68
TX221	Specific gravity		
		267.8	0.52
	A.L.		
	Salt+pH		

RADIOGRAPHY LOG
MASSACHUSETTS INSTITUTE OF TECHNOLOGY

Project Eng. Properties of the Soil Beneath Mexico City's Cathedral
Sample No. 9 Boring No. S2
Depth 34.70 - 35.50m Depth @ 0" 35.50
Sample Type Shelby Tube Date June 1992

Note: Shaded areas indicate material of greater density.

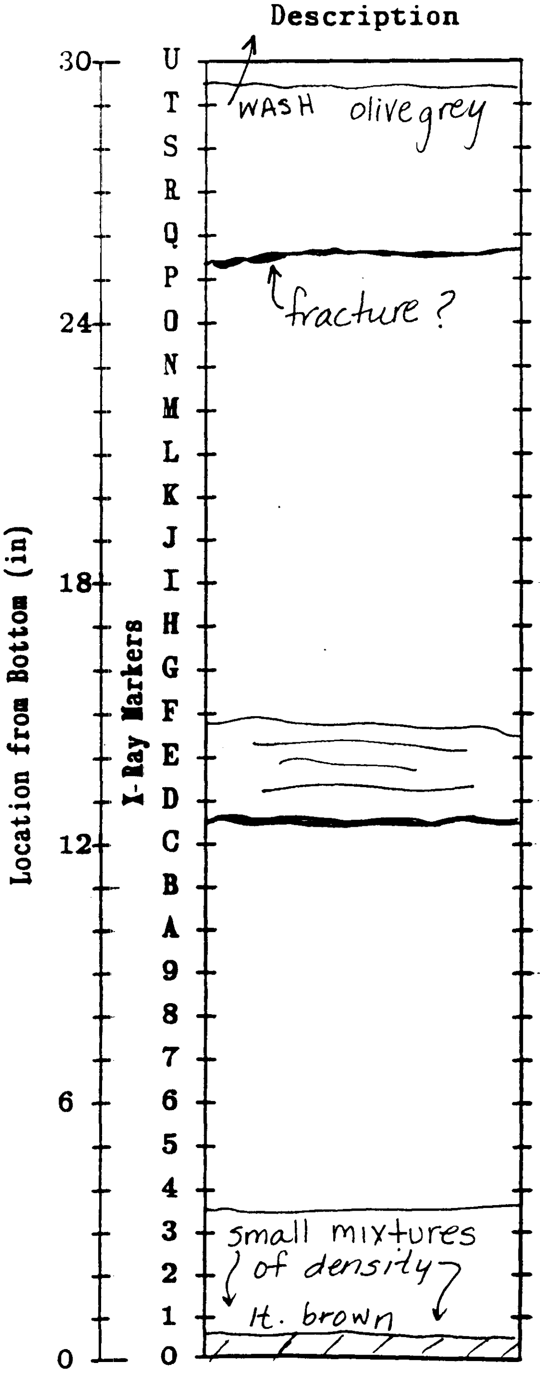

Engineering Test	Index Test	Wn (%)	Avg. TV (ksc)
DSS342		244.7	0.91
TX223	specific gravity		
CRS87	salt + pH	185.4	0.63
	A.L.	206.2	0.65

RADIOGRAPHY LOG
MASSACHUSETTS INSTITUTE OF TECHNOLOGY

Project: Eng. Properties of the Soil Beneath Mexico City's Cathedral
Sample No.: 1
Depth: 12.00-12.45m
Sample Type: Fixed Piston
Boring No.: S3
Depth @ 0": 12.45
Date: June 1992

Note: Shaded areas indicate material of greater density.

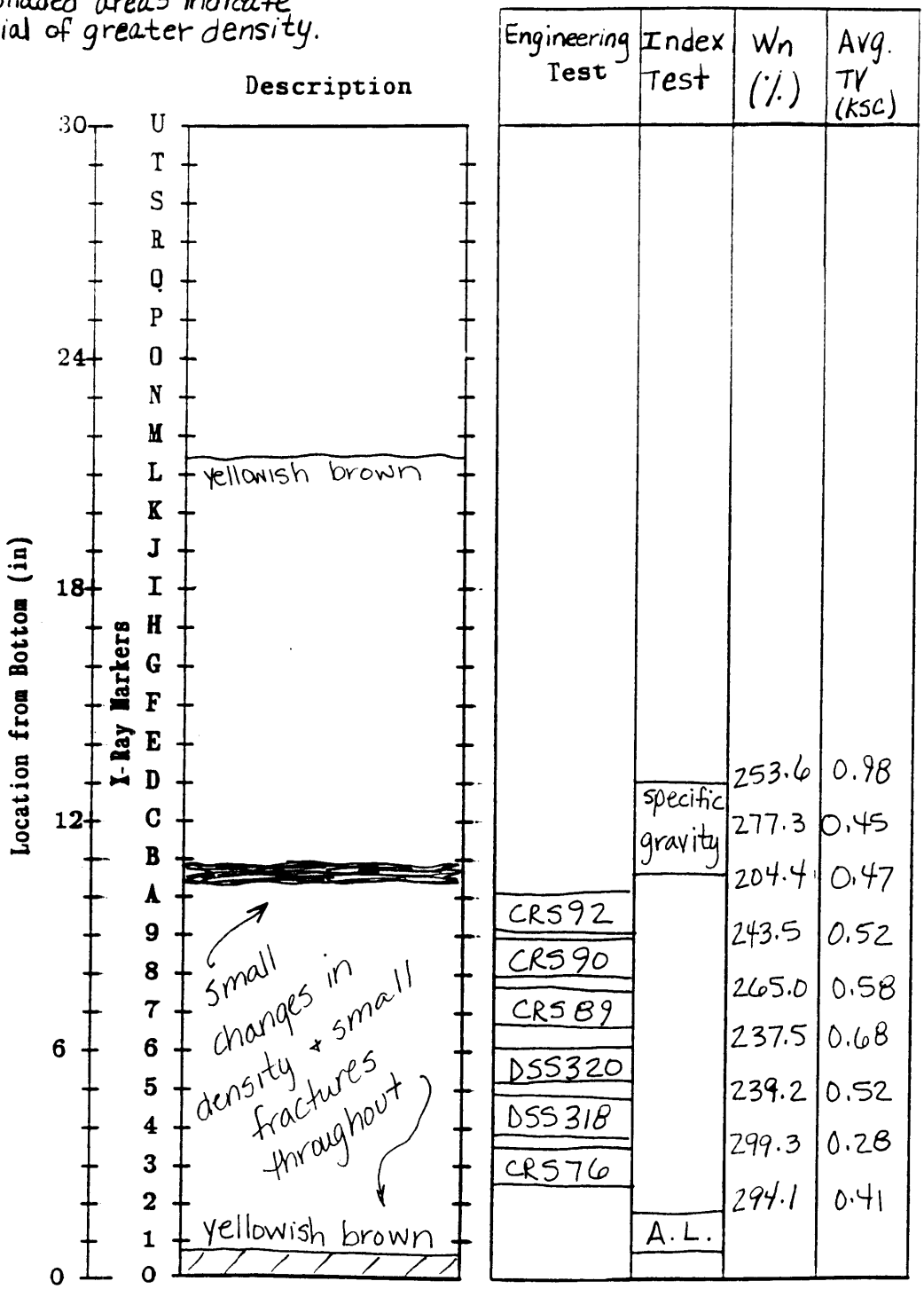

RADIOGRAPHY LOG
MASSACHUSETTS INSTITUTE OF TECHNOLOGY

Project Eng. Properties of the Soil Beneath Mexico City's Cathedral

Sample No. 2 **Boring No.** S3

Depth 12.80-13.60 m **Depth @ 0"** 13.60

Sample Type Fixed Piston **Date** June 1992

Note: shaded areas indicate material of greater density.

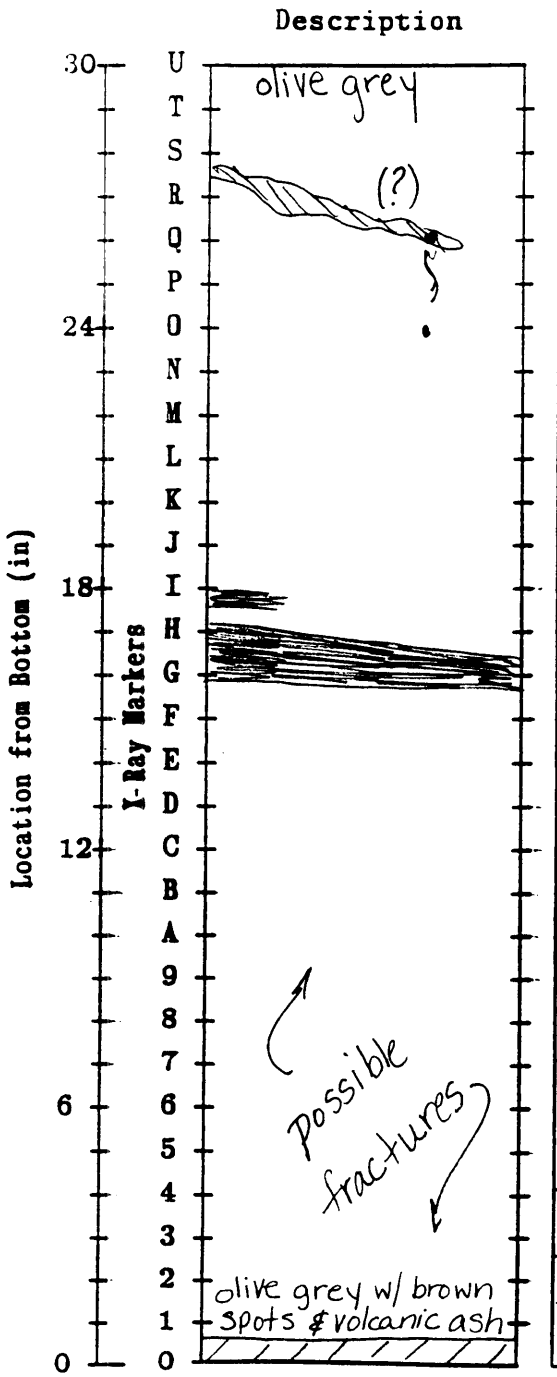

Engineering Test	Index Test	Wn (%)	Avg. TV (ksc)
TX222	Specific gravity	296.1	0.45
	A.L.	253.9	0.47
CRS 77	salt + pH	251.3	0.38

RADIOGRAPHY LOG
MASSACHUSETTS INSTITUTE OF TECHNOLOGY

Project: Eng. Properties of the Soil Beneath Mexico City's Cathedral
Sample No.: 3
Depth: 13.60m - 14.40m
Sample Type: Fixed Piston
Boring No.: S3
Depth @ 0": 14.40 m
Date: June 1992

Note: Shaded areas indicate material of greater density.

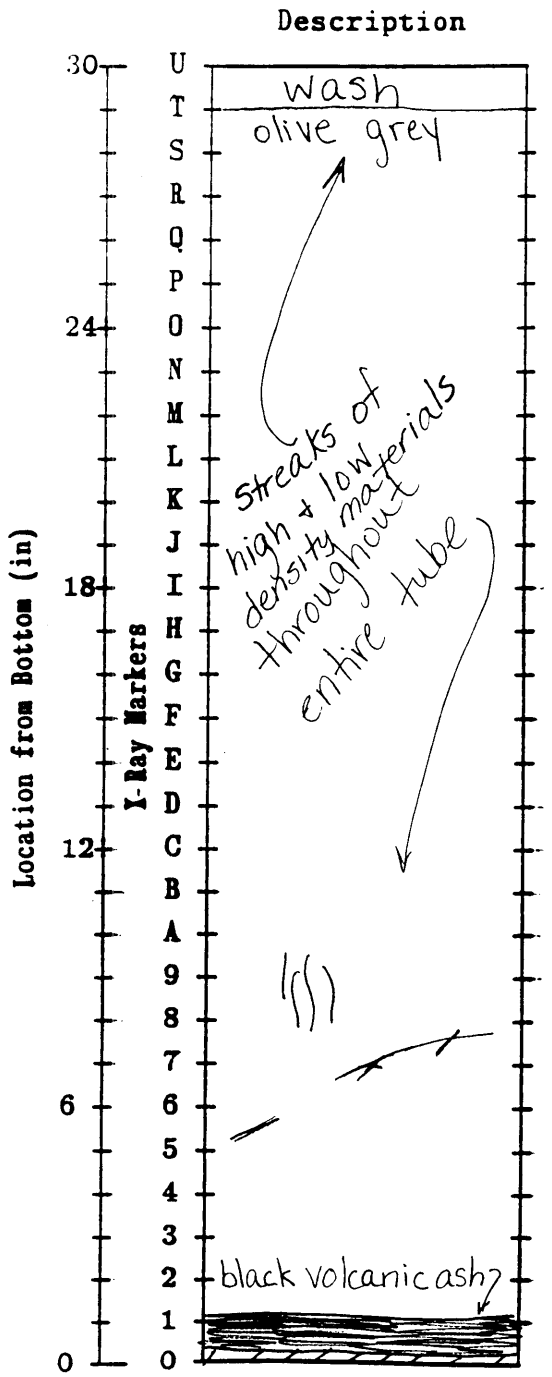

Engineering Test	Index Test	Wn (%)	Avg. TV (KSC)
		260.48	
		263.54	0.52
			0.56
	grain size analysis		
		240.50	0.59
	specific gravity		0.57
		288.57	0.48
DSS 330			
		292.02	0.48
	A.L.	277.35	0.45
CRS 78		251.96	0.37

RADIOGRAPHY LOG
MASSACHUSETTS INSTITUTE OF TECHNOLOGY

Project: Eng. Properties of the Soil Beneath Mexico City's Cathedral
Sample No.: 4
Depth: 23.70-24.75 m
Sample Type: Fixed Piston
Boring No.: S3
Depth @ 0": 24.75 m
Date: June 1992

Note: Shaded areas indicate material of greater density.

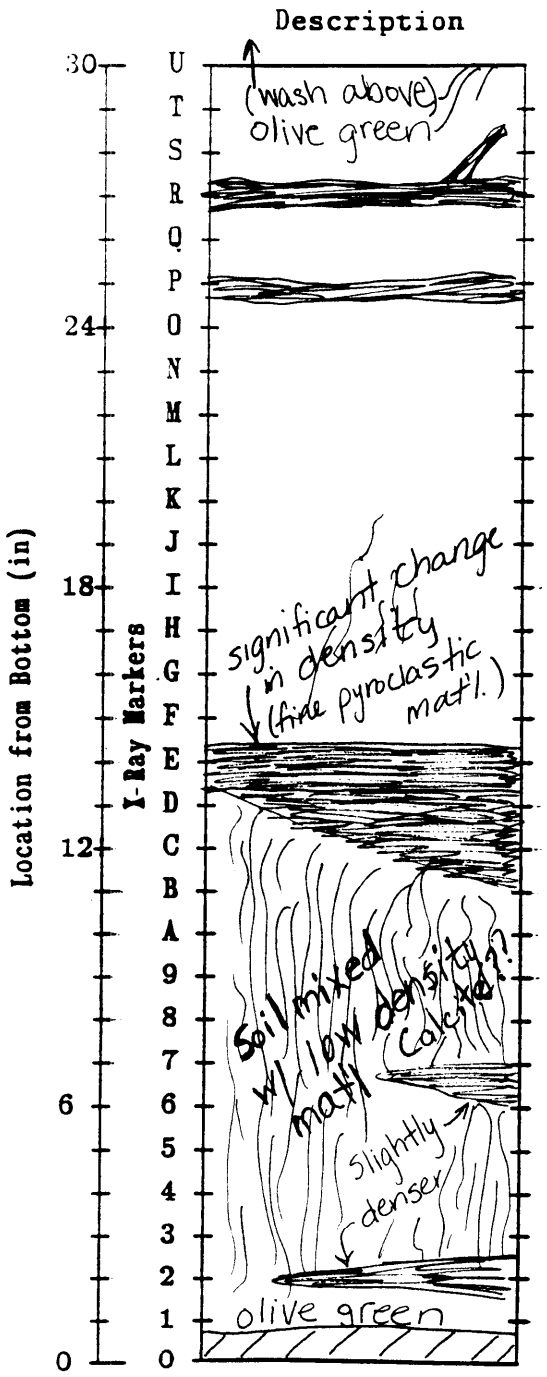

Engineering Test	Index Test	Wn (%)	Avg. TV (KSC)
	specific gravity	270.8	0.54
		273.5	0.46
CRS85		272.6	0.47
	A.L.		
	salt conc. + pH	384.3	0.35

RADIOGRAPHY LOG
MASSACHUSETTS INSTITUTE OF TECHNOLOGY

Project: Eng. Properties of the Soil Beneath Mexico City's Cathedral
Sample No.: 5
Depth: 24.35 - 25.10m
Sample Type: Fixed Piston
Boring No.: S3
Depth @ 0": 25.10m
Date: June 1992

Note: Shaded areas indicate material of greater density.

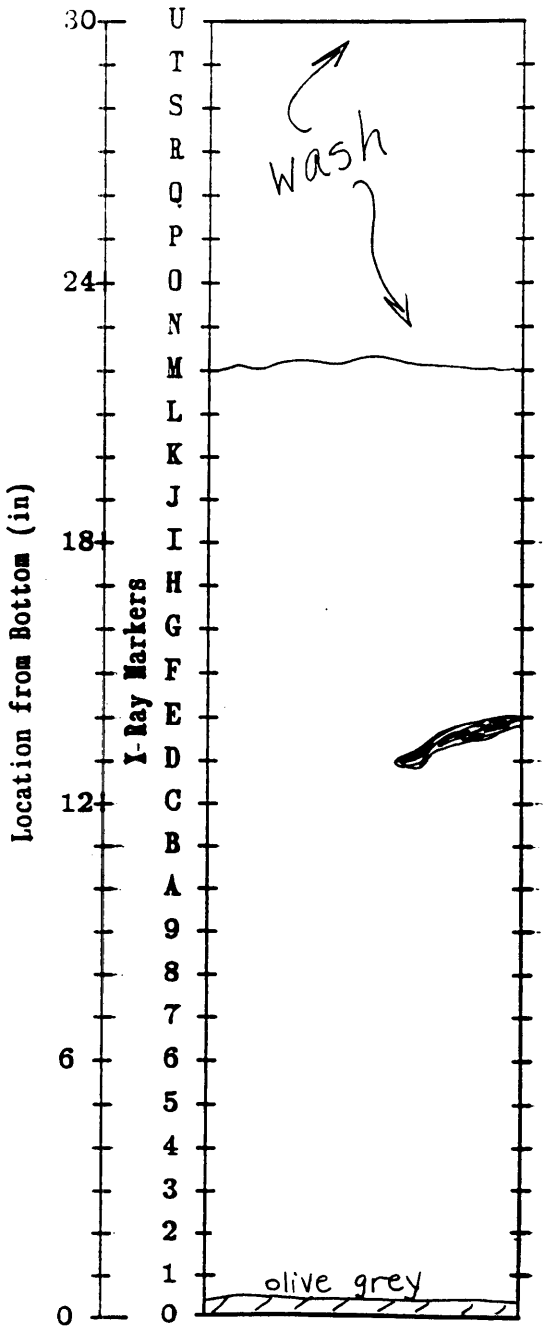

Engineering Test	Index Test	Wn (%)	Avg. TV (KSC)
		264.8	0.53
TX225	Specific gravity		
	salt conc + pH	263.5	
	A.L.		
	salt conc + pH	201.2	0.48

RADIOGRAPHY LOG
MASSACHUSETTS INSTITUTE OF TECHNOLOGY

Project: Eng. Properties of the Soil Beneath Mexico City's Cathedral
Sample No.: C0
Depth: 24.95 - 25.7 m
Sample Type: Fixed Piston
Boring No.: S3
Depth @ 0": 25.7 m
Date: June 1992

Note: Shaded areas indicate material of greater density.

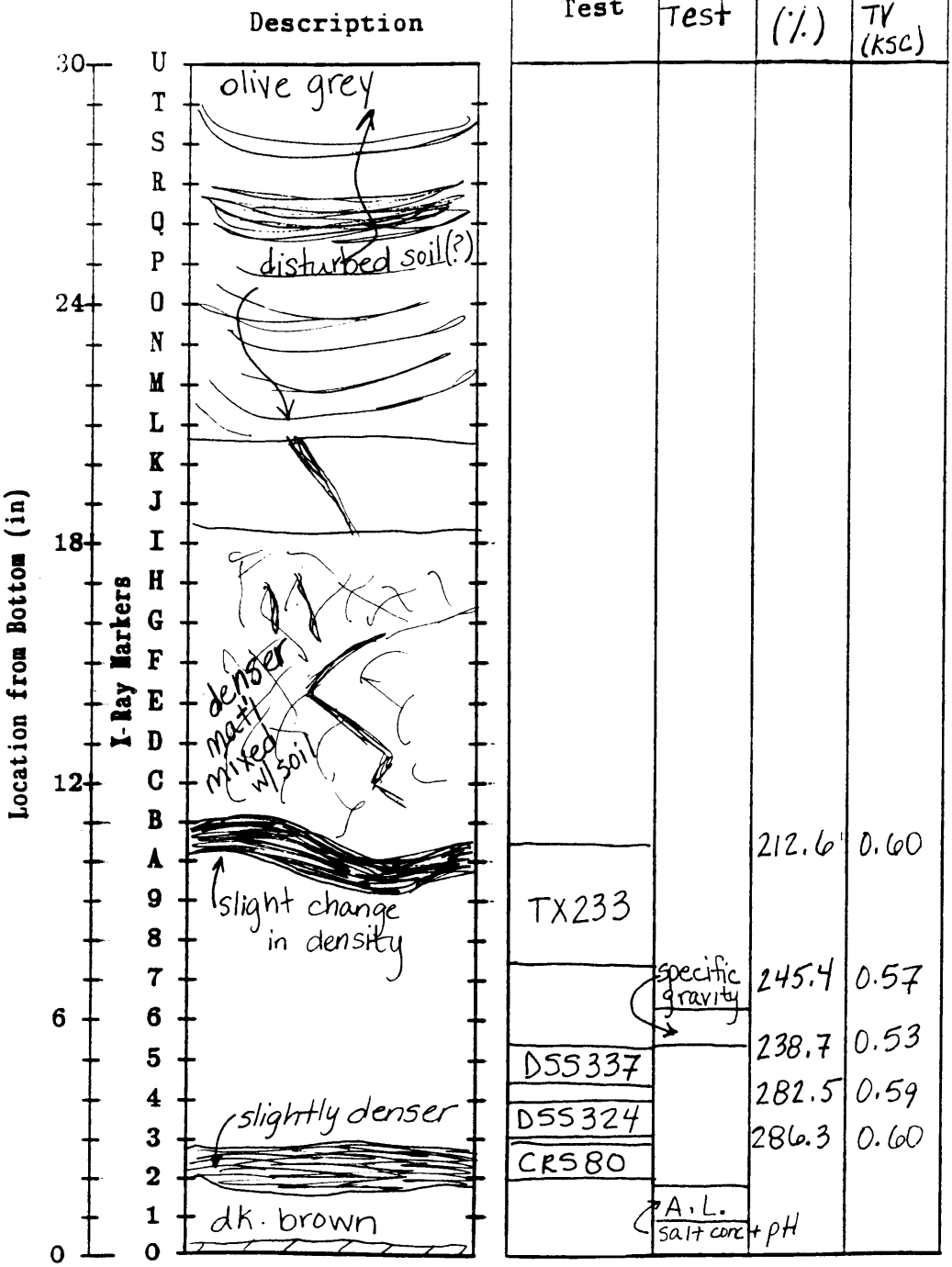

RADIOGRAPHY LOG
MASSACHUSETTS INSTITUTE OF TECHNOLOGY

Project Eng. Properties of the Soil Beneath Mexico City's Cathedral
Sample No. 3
Boring No. S1
Depth 23.50 - 24.30m
Depth @ 0" 24.30 m
Sample Type Shelby Tube
Date June 1992

Note: Shaded areas indicate material of greater density.

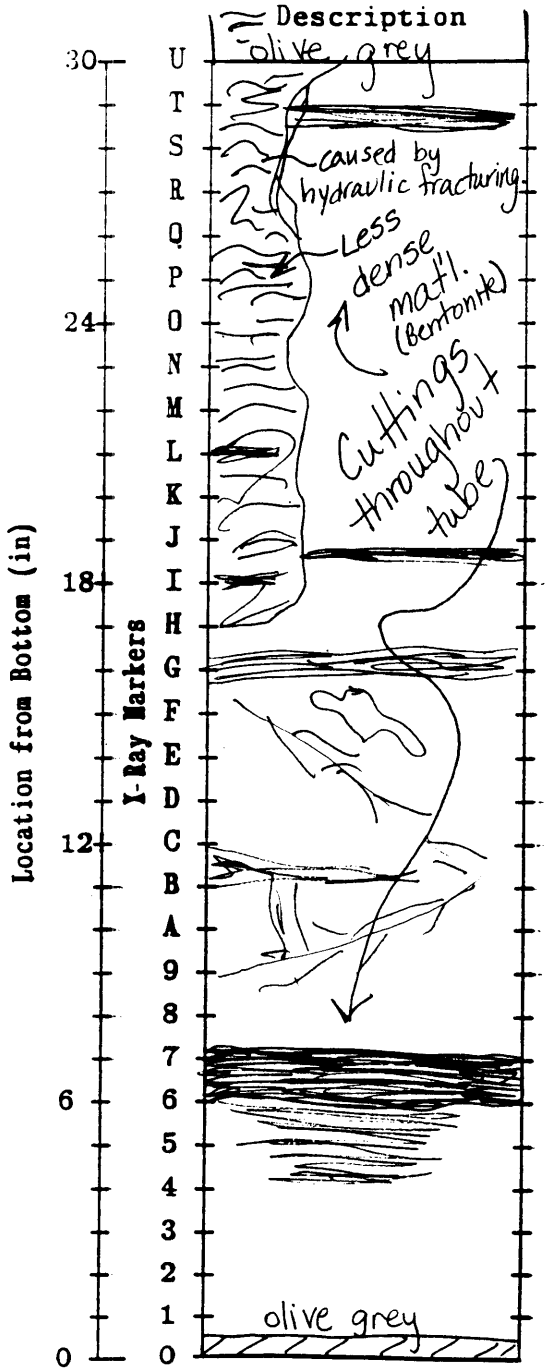

Engineering Test	Index Test	Wn (%)	Avg. TV (ksc)
	A.L.	211.1	

RADIOGRAPHY LOG
MASSACHUSETTS INSTITUTE OF TECHNOLOGY

Project: Eng. Properties of the Soil Beneath Mexico City's Cathedral
Sample No.: 8
Depth: 28.40 - 29.20m
Sample Type: Shelby Tube
~~Note: Shaded areas indicate material of greater density~~

Boring No.: 51
Depth @ 0": 29.20m
Date: June 1992

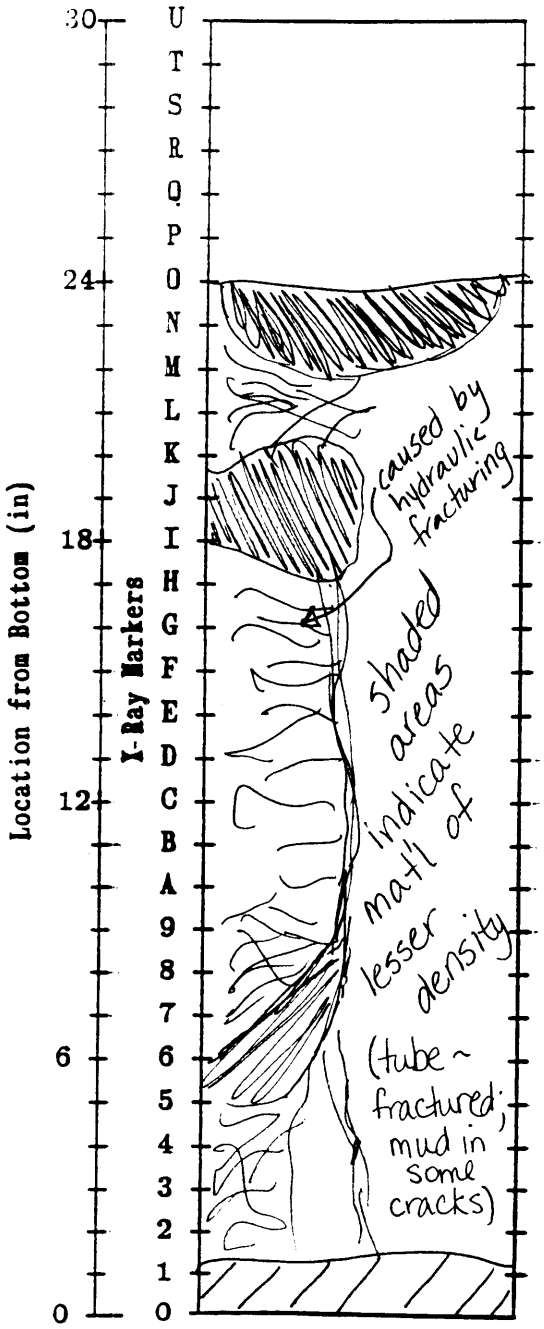

Engineering Test	Index Test	Wn (%)	Avg. TV (KSC)
	A.L.	303.7	0.48

RADIOGRAPHY LOG
MASSACHUSETTS INSTITUTE OF TECHNOLOGY

Project: Eng. Properties of the Soil Beneath Mexico City's Cathedral
Sample No.: 9
Depth: 29.20-29.85 m
Sample Type: Shelby Tube
Boring No.: S1
Depth @ 0": 29.85 m
Date: June 1992

Note: Shaded areas indicate material of greater density.

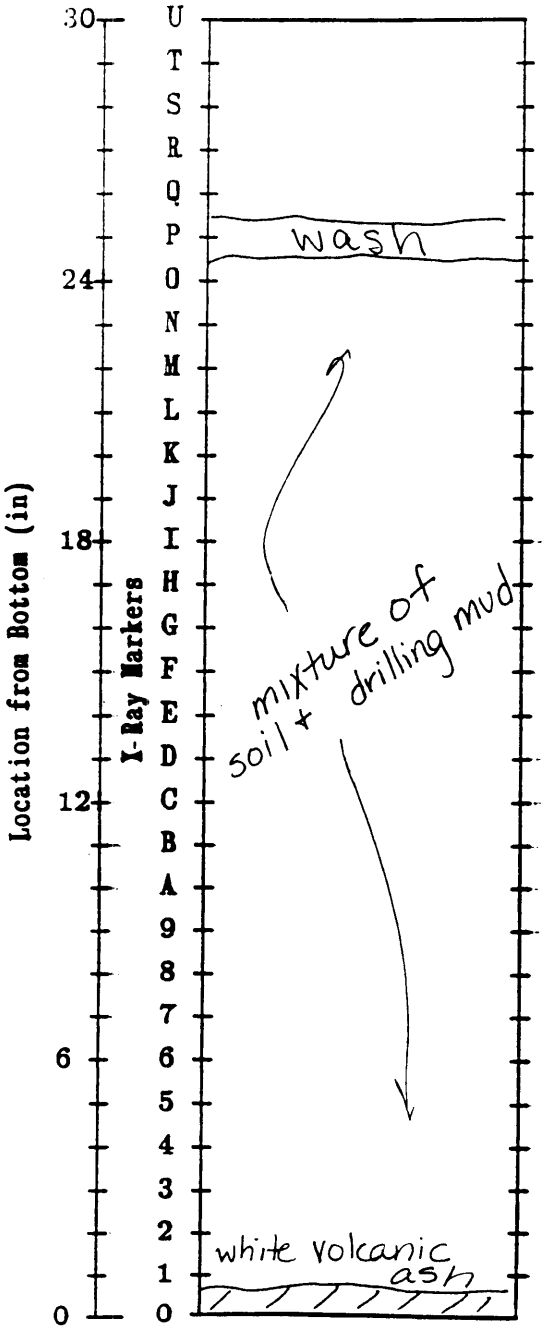

Engineering Test	Index Test	Wn (%)	Avg. TV (KSC)
	A.L.	252.3	0.42

Appendix B

Summary of Laboratory Results from SEDUE 1990

LIST OF SYMBOLS FOR TABLES B.1 THROUGH B.6

Subestrato – Substrata
Arcilla – Clay
Convencionales – Conventional 24 hr data
Primarias – End of Primary tests (< 24 hr data)
Muestra (MTA) – Sample
Prof – Depth
SUCS – USCS soil classification symbol
Ss – Specific Gravity
Wi – Natural Water Content (%)
ei – Void Ratio
Gi – Saturation (%)
σc – Preconsolidation Stress (ksc)
σo – In situ Effective Stress (ksc)
qc – Net Tip Resistance (ksc)
TX – Triaxial Test Number
γn – Volumetric Weight (kg/m^3)
Cuu – Cohesion from UU Triaxial Tests (ksc)
E50 – Modulus of Elasticity (ksc)
Nk – Cone Correlation Factor
Mv – Coefficient of Volume Change
Mvr – Coefficient of Volume Change in Unloading

Table B.1 Summary of Consolidation Results; boring SMC-1 (from SEDUE 1990)

SUBESTRATO	MTA	PROF	SUCS	Ss	CONVENCIONALES				PRIMARIAS					
					Wi	ei	Gi	$\bar{\sigma}c$	Wi	ei	Gi	$\bar{\sigma}c$	$\bar{\sigma}o$	qc
Arcilla 1	14-4	11.50	CH	2.42	321.3	7.84	99.1	1.23	320.3	7.87	98.4	1.50	1.05	4.6
	15-4	12.20	CH	2.38	276.3	6.76	97.4	1.19	331.6	8.04	98.4	1.60	1.07	4.9
	16-3	12.70	CH	2.32	*	*	*	*	307.7	7.23	98.8	1.42	1.09	4.9
	17-3	13.40	CH	2.38	*	*	*	*	306.8	7.43	98.3	1.40	1.10	6.8
Arcilla 2	20-3	15.70	CH	2.30	278.9	6.51	98.6	0.54	*	*	*	*	1.12	5.3
	21-4	16.40	CH	2.18	*	*	*	*	267.7	6.00	97.3	1.22	1.15	5.4
	22-3	16.90	CH	2.18	*	*	*	*	281.0	6.18	99.0	1.68	1.18	5.5
	23-3	17.60	CH	2.35	*	*	*	*	263.4	6.25	99.3	1.42	1.19	5.7
	24-3	18.30	CH	2.36	*	*	*	*	228.8	5.23	103.3	1.70	1.20	5.8
Arcilla 3	26-3	19.70	CH	2.52	*	*	*	*	223.3	5.91	95.0	2.70	1.21	5.9
	27-3	20.40	CH	2.35	*	*	*	*	249.9	5.98	98.2	1.50	1.22	6.0
	28-3	21.10	CH	2.28	*	*	*	*	309.3	7.23	97.3	1.35	1.23	6.2
	29-3	21.80	CH	2.45	319.8	7.96	98.4	1.33	372.5	9.22	99.0	1.35	1.25	6.2
	30-3	22.50	CH	2.34	*	*	*	*	202.2	4.69	100.6	1.85	1.30	6.5
	31-4	23.40	CH	2.33	*	*	*	*	184.6	4.33	99.5	2.00	1.40	6.7
	32-4	24.10	CH	2.05	*	*	*	*	187.9	3.75	102.7	1.95	1.42	6.9
	33-3	24.60	CH	2.23	268.9	6.18	97.0	2.42	*	*	*	*	1.46	7.0
	34-3	25.30	CH	2.26	*	*	*	*	207.9	4.75	99.1	1.80	1.50	7.0
Arcilla 4	35-3	26.00	CH	2.29	*	*	*	*	273.1	6.63	94.4	1.70	1.57	7.2
	36-3	26.70	CH	2.15	*	*	*	*	273.8	6.02	97.8	1.83	1.59	7.6
	37-3	27.40	CH	2.48	*	*	*	*	235.4	6.10	95.7	2.12	1.62	7.6
Arcilla 5	38-3	28.10	CH	2.49	*	*	*	*	262.3	6.65	98.2	2.10	1.78	8.0
	39-3	28.80	CH	2.38	274.7	6.56	99.4	1.65	288.0	6.93	98.7	2.22	1.88	8.0
Arcilla 6	43-4	31.7	CH	2.33	*	*	*	*	284.0	6.77	97.7	2.40	2.10	10.0
	44-3	32.3	CH	2.34	*	*	*	*	265.7	6.36	97.7	2.40	2.20	10.0
Arcilla 7	47-4	34.60	CH	2.31	225.6	5.23	99.7	3.00	241.5	5.58	100.1	3.30	2.64	13.0
	49-2	35.60	CH	2.21	*	*	*	*	224.6	4.99	99.5	2.73	2.82	13.0
Arcilla 8	58-3	41.20	CH	2.46	*	*	*	*	158.0	3.97	97.6	3.50	3.50	20.3
	58-4	41.30	CH	2.40	*	*	*	*	159.0	3.89	98.0	2.65	3.50	20.3
Arcilla 9	60-4	42.40	CH	2.37	159.8	3.80	99.7	2.95	187.5	4.44	100.1	3.15	3.40	17.5
	61-3	43.70	CH	2.34	*	*	*	*	163.9	3.90	98.6	2.65	3.60	17.5
Arcilla 10	62-3	44.40	CH	2.40	*	*	*	*	104.3	2.64	95.0	2.95	3.70	17.9
	66-4	48.10	CH	2.38	*	*	*	*	140.2	2.38	100.4	2.80	3.90	17.8
	67-4	49.00	CH	2.32	135.5	3.12	100.8	3.60	164.7	3.81	100.1	2.95	4.00	19.8
Arcilla 11	105-4	72.5	CH	2.18	*	*	*	*	235.2	5.17	99.1	4.10	-	-

Table B.2 Summary of Triaxial Test Results; boring SMC-1 (from SEDUE 1990)

SUBESTRATO	MUESTRA	PROF	TX	Wi	ei	Ss	Gi	γ_n	Cuu	E50	qc	Nk
Arcilla 1	14-3	11.30	UU-1	317.3	8.12	2.61	101.7	1192	0.68	45.0	4.6	6.8
	16-3	12.70	UU-2	308.1	7.63	2.45	98.9	1158	0.54	45.0	4.9	9.1
	16-4	12.90	UU-3	296.8	6.68	2.27	100.9	1173	0.34	48.0	5.0	14.7
	17-4	13.60	UU-4	293.3	6.68	2.27	99.6	1161	0.30	35.0	6.8	22.3
Arcilla 2	22-4	17.10	UU-5	279.8	6.12	2.15	98.5	1149	0.50	70.0	6.0	12.0
	23-3	17.60	UU-6	183.0	4.49	2.44	100.0	1259	0.66	50.0	6.6	10.0
Arcilla 3	27-4	20.60	UU-7	373.1	8.35	2.22	99.1	1122	0.42	33.0	6.0	14.3
	30-2	22.30	UU-8	309.8	7.62	2.44	99.2	1168	0.47	35.0	6.5	13.8
	30-4	22.70	UU-9	222.3	4.87	2.22	101.5	1220	0.54	50.0	6.7	12.4
Arcilla 4	34-4	25.50	UU-10	157.6	3.78	2.39	99.8	1291	0.80	84.0	7.0	8.8
	35-2	25.80	UU-11	205.9	4.75	2.31	100.1	1229	0.77	87.0	7.2	9.4
	35-4	26.20	UU-12	308.4	7.08	2.26	98.5	1142	0.84	61.0	7.6	9.0
Arcilla 5	39-2	28.60	UU-13	248.4	5.96	2.38	98.5	1183	0.48	34.0	8.0	16.7
Arcilla 6	42-4	31.10	UU-14	247.2	6.01	2.39	98.4	1185	0.52	*	9.8	18.8
	44-4	32.50	UU-15	171.8	3.74	2.19	100.7	1257	0.70	103.0	10.5	15.0
Arcilla 7	47-3	34.40	UU-16	203.4	4.67	2.29	99.6	1224	1.30	177.0	12.8	9.8
	47-4	34.60	UU-17	240.1	5.95	2.48	100.0	1213	1.35	159.0	13.0	9.6
Capa dura	51-4	36.70	UU-18	36.9	1.08	2.54	87.0	1671	5.6	387.0	357.7	63.9
	54-2	38.1	UU-19	56.3	1.34	2.48	103.9	1654	3.7	260.0	382.6	103.4
Arcilla 8	57-3	40.50	UU-20	175.6	4.31	2.43	99.2	1265	2.46	266.0	19.5	7.9
Arcilla 9	61-2	43.50	UU-21	169.0	3.79	2.27	101.2	1274	1.25	98.7	17.5	14.0
Arcilla 10	62-2	44.20	UU-22	174.6	4.22	2.44	100.7	1280	1.50	137.0	17.9	11.9
	62-4	44.60	UU-23	156.7	3.65	2.31	99.1	1274	1.15	178.0	18.0	15.7
	65-3	47.10	UU-24	110.2	2.67	2.38	98.3	1364	1.30	135.0	19.8	15.2
Arcilla 11	98-4	68.40	UU-25	124.3	3.09	2.46	98.8	1348	2.00	177.0	-	-

Table B.3 Summary of Consolidation Results; boring SMC-2 (from SEDUE 1990)

SUBESTRATO	MTA	PROF	SUCS	Ss	CONVENCIONALES				PRIMARIAS					
					Wi	ei	Gi	σc	Wi	ei	Gi	σc	σo	qc
Arcilla 1	13-4	12.00	CH	2.46	270.2	6.77	98.1	1.75	272.0	6.73	99.2	2.05	1.20	7.7
	14-4	12.70	CH	2.51	270.9	6.92	98.2	1.60	286.2	7.34	97.8	1.98	1.23	8.2
	15-3	13.20	CH	2.47	280.8	7.07	98.2	1.87	276.8	6.95	98.5	1.95	1.25	7.7
	16-2	13.70	CH	2.80	282.7	8.11	97.5	1.42	271.3	7.86	96.6	1.90	1.25	10.1
Arcilla 2	17-4	14.80	CH	2.29	*	*	*	*	274.4	6.41	98.3	2.20	1.30	10.2
	18-2	15.10	CH	2.48	283.4	7.17	97.8	1.40	259.7	6.58	97.7	1.70	1.30	10.7
	19-3	16.00	CH	2.32	276.7	6.52	98.5	1.60	274.4	6.44	98.9	1.90	1.30	10.7
	20-3	16.70	CH	2.39	296.0	7.26	97.5	1.60	262.0	6.41	97.7	1.90	1.35	10.3
	21-4	17.70	CH	2.63	209.5	5.75	95.6	1.80	217.8	5.88	97.2	1.45	1.38	10.5
	22-2	18.00	CH	2.52	*	*	*	*	226.5	5.89	96.9	2.60	1.38	10.5
	22-4	18.40	CH	2.45	193.4	4.87	97.2	1.78	*	*	*	*	*	*
Arcilla 3	24-3	19.50	CH	2.39	229.0	5.60	97.9	2.18	205.4	5.06	97.1	2.60	1.41	11.0
	25-3	20.90	CH	2.51	300.2	7.60	98.9	1.92	175.4	4.43	99.3	1.80	1.46	9.1
	26-4	22.50	CH	2.40	226.1	5.48	99.2	2.20	210.0	5.12	98.5	2.40	1.50	10.0
Arcilla 4	27-4	24.60	CH	2.58	275.8	7.43	95.9	2.28	236.5	6.31	96.8	2.10	1.70	10.8
	28-4	25.30	CH	2.61	207.8	5.70	95.2	2.00	223.5	5.74	96.7	2.10	1.70	9.8
	29-4	25.50	CH	2.13	249.0	5.41	98.0	1.80	266.8	5.70	99.7	2.40	1.70	11.7
Arcilla 5	30-4	26.70	CH	2.50	211.8	5.58	94.9	3.50	215.0	5.89	91.4	3.80	1.80	12.0
	32-4	28.10	CH	2.49	248.2	6.27	98.7	2.30	264.4	6.68	98.7	2.60	2.00	10.0
	33-3	28.80	CH	2.42	279.2	6.80	99.4	2.50	254.1	6.23	98.6	2.70	2.20	12.8
	34-3	29.30	CH	2.36	233.2	5.52	99.7	3.00	228.8	5.48	98.6	3.05	2.20	13.0
Arcilla 6	35-2	29.80	CH	2.38	*	*	*	*	212.4	5.16	98.0	2.20	2.40	14.5
	35-3	30.00	CH	2.14	233.2	4.99	100.1	2.60	230.9	4.94	100.0	2.80	2.40	14.7
	36-3	30.70	CH	2.35	*	*	*	*	196.5	4.75	97.4	2.50	2.60	14.7
Arcilla 7	36-4	30.90	CH	2.33	190.7	4.50	98.6	2.55	220.1	5.13	99.8	3.00	2.50	13.8
	37-4	31.60	CH	2.29	179.7	4.14	99.5	1.80	172.9	4.05	98.0	2.60	2.60	14.0
	38-3	32.10	CH	2.40	202.4	4.84	100.2	3.00	203.5	4.90	99.5	3.90	2.70	14.1
	39-3	32.80	CH	2.37	211.6	5.06	99.3	3.50	197.7	4.71	99.6	3.60	2.80	14.7
	40-3	33.50	CH	2.39	232.5	5.53	100.4	2.90	206.5	4.98	99.1	3.95	3.00	15.0
	41-3	34.20	CH	2.35	243.8	5.74	99.9	4.20	259.6	6.11	100.0	4.15	3.10	16.0
	42-3	34.90	CH	2.26	242.0	5.53	98.9	3.80	237.4	5.45	98.5	3.40	3.25	17.7
Arcilla 8	49-2	39.60	CH	2.50	*	*	*	*	153.5	3.97	96.7	2.75	4.10	18.7
	49-4	40.00	CH	2.44	*	*	*	*	191.1	4.76	98.0	3.91	4.20	18.9
Arcilla 9	54-2	42.80	CH	2.30	148.7	3.39	100.9	3.60	172.9	3.93	101.2	4.35	4.10	25.0
Arcilla 10	55-3	43.80	CH	2.51	171.1	4.31	99.4	3.90	176.2	4.45	99.2	4.95	4.20	26.0
	60-2	47.10	CH	2.44	140.9	3.45	99.7	3.50	166.2	4.10	99.0	4.40	4.48	44.5
	61-3	48.00	CH	2.41	165.1	4.17	95.3	4.20	132.0	3.22	98.6	4.60	4.60	44.5

Table B.4 Summary of Triaxial Test Results; boring SMC-2 (from SEDUE 1990)

SUBESTRATO	MUESTRA	PROF	TX	Wi	ei	Ss	Gi	γ_n	Cuu	E50	qc	Nk	
	12-3	11.10	UU-1	144.3	3.56	2.38	96.5	1276	0.34	148.2	9.6	28.2	
	13-3	11.80	UU-2	135.2	3.13	2.31	99.8	1316	0.59	99.2	9.8	16.1	
	14-2	12.30	UU-3	195.4	4.61	2.40	101.5	1260	0.60	72.6	7.7	12.8	
Arcilla 1	14-3	12.50	UU-4	319.5	7.65	2.40	100.1	1162	0.65	84.1	8.2	12.2	
	15-4	13.40	UU-5	275.3	6.76	2.45	99.6	1184	0.45	74.0	7.7	18.3	
	16-3	13.90	UU-6	295.7	7.35	2.49	100.0	1178	0.32	72.4	10.1	31.6	
	17-2	14.20	UU-7	293.0	6.62	2.28	100.7	1173	0.37	29.8	10.2	27.6	
	18-4	15.50	UU-8	220.9	5.35	2.41	99.6	1219	0.48	41.9	10.7	22.3	
	19-4	16.20	UU-9	248.3	6.39	2.53	98.5	1195	0.43	67.9	10.7	24.9	
Arcilla 2	20-2	16.50	UU-10	257.4	5.74	2.25	100.9	1194	0.71	72.8	10.3	14.5	
	21-2	17.30	UU-11	155.6	3.99	2.54	99.0	1301	0.68	52.6	10.5	15.4	
	22-3	18.20	UU-12	169.0	4.20	2.45	98.4	1273	0.65	83.3	10.5	16.2	
	24-2	19.30	UU-13	157.6	4.04	2.50	96.7	1279	0.75	110.8	11.0	14.7	
	24-2	19.30	QU-1	157.5	4.04	2.50	97.5	1278	0.82	120.3	11.0	13.4	
Arcilla 3	25-4	21.10	UU-14	312.4	7.59	2.43	100.0	1168	0.60	64.2	9.1	19.8	
	26-3	22.30	UU-15	205.7	5.24	2.53	99.2	1238	0.70	91.3	10.0	14.3	
	26-3	22.30	QU-2	203.0	5.18	2.53	99.1	1239	0.95	92.9	10.9	11.5	
	27-3	24.40	UU-16	247.9	6.95	2.52	89.8	1101	0.43	77.8	10.8	25.1	
Arcilla 4	28-3	25.10	UU-17	192.8	4.71	2.45	100.2	1255	0.60	75.7	9.8	16.3	
	29-2	25.60	UU-18	272.4	5.93	2.19	100.4	1175	1.20	141.7	11.7	9.8	
	30-3	26.70	UU-19	206.8	5.19	2.39	95.4	1186	0.70	58.5	12.0	17.1	
	31-4	27.40	UU-20	235.8	5.57	2.37	100.4	1212	0.68	113.4	9.1	13.4	
Arcilla 5	32-2	27.70	UU-21	257.1	6.06	2.37	100.4	1197	0.80	96.9	11.0	13.8	
	33-2	28.40	UU-22	261.8	6.33	2.43	100.3	1197	1.10	120.1	10.0	9.09	
	34-2	29.10	UU-23	246.1	5.96	2.41	99.4	1198	0.75	87.40	12.8	17.1	
	35-4	30.20	UU-24	225.2	5.33	2.36	99.6	1211	0.95	129.9	14.7	15.5	
Arcilla 6	36-2	30.50	UU-25	192.7	4.67	2.41	99.4	1244	1.10	67.0	12.8	11.6	
	37-2	31.20	UU-26	195.8	4.42	2.21	100.5	1238	1.20	142.5	13.8	11.5	
	38-2	31.90	UU-27	207.1	5.13	2.49	100.4	1246	1.25	163.6	12.6	10.1	
Arcilla 7	40-2	33.30	UU-28	197.3	4.48	2.30	101.2	1247	1.48	165.4	14.7	9.9	
	41-4	34.40	UU-39	230.4	5.65	2.44	99.4	1211	1.35	142.8	13.5	10.0	
	42-4	35.10	UU-30	202.0	4.59	2.30	101.5	1246	1.60	140.6	17.7	11.1	
	44-4	36.50	UU-31	35.7	1.13	2.63	82.2	1682	1.75	230.0	233.4	133.4	
Capa dura	45-3	37.00	UU-32	79.3	2.16	2.48	91.0	1406	2.60	223.0	41.3	15.9	
	47-4	38.60	UU-33	47.7	1.39	2.63	90.7	1629	0.90	260.0	302.5	336.1	
Arcilla 8	48-2	38.90	UU-34	174.0	4.29	2.47	100.0	1276	1.75	141.0	23.2	13.3	
Arcilla 9	52-4	41.10	UU-35	139.7	3.35	2.37	98.8	1306	1.00	152.0	24.2	24.2	
	54-4	43.20	UU-36	164.1	4.05	2.43	98.3	1269	1.60	153.6	25.0	15.6	
Arcilla 10	55-2	43.60	UU-37	172.6	4.34	2.50	99.4	1275	1.60	170.6	25.6	16.0	
	55-4	44.00	UU-38	153.4	3.73	2.42	99.2	1292	2.50	331.0	26.0	10.4	
	60-3	47.30	UU-49	164.2	4.07	2.50	101.0	1305	1.50	188.2	44.5	29.7	
DEPOSITOS	70-4	53.80	CU-1	41.8	1.32	2.59	82.3	1585	1.00	858.6	41.5	41.5	ϕ=29°
PROFUNDOS	79-3	57.70	CU-2	42.9	1.22	2.55	89.5	1640	2.60	1324.4	111.6	42.9	ϕ=32°

Table B.5 Average Properties from boring SMC-1
(from SEDUE 1990)

			Triaxiales UU			Consolidaciones convencionales					
Arcilla	Wi(*) %	qc kg/cm2	Wi(**) %	Cuu kg/cm2	E50 kg/cm2	Wi(**) %	e	$\bar{\sigma}c$ kg/cm2	$\bar{\sigma}o$ kg/cm2	Mv cm2/kg	Mvr cm2/kg
1	277.7	5.3	303.9	0.47	43.3	316.6	7.64	1.48	1.08	0.139	0.054
2	215.7	5.5	231.4	0.58	60.0	260.2	5.92	1.51	1.17	0.086	0.054
3	241.0	6.5	304.8	0.41	34.5	242.2	5.73	1.81	1.33	0.076	0.049
4	227.1	7.5	224.0	0.80	77.3	260.8	6.25	1.88	1.59	0.072	0.043
5	258.8	8.0	248.4	0.48	34.0	275.2	6.79	2.16	1.83	0.072	0.044
6	211.1	10.0	209.5	0.61	103.0	--	--	--	--	--	--
7	238.6	13.0	221.8	1.33	168.0	233.1	5.29	3.02	2.73	0.099	0.091
Capa dura	48.1		46.6	4.65	323.5	--	--	--	--	--	--
8	177.9	20.3	175.6	2.46	266.0	--	--	--	--	--	--
9	164.6	17.5	169.0	1.25	98.7	175.7	4.17	2.90	3.50	--	--
10	148.9	18.5	147.2	1.32	150.0	136.4	2.94	2.90	3.86	--	--
11	158.4	--	124.3	2.00	177.0	235.2	5.17	2.60	4.10	--	--

Table B.6 Average Properties from boring SMC-2
(from SEDUE 1990)

			Triaxiales UU			Consolidaciones convencionales					
Arcilla	Wi(*) %	qc kg/cm2	Wi(**) %	Cuu kg/cm2	E50 kg/cm2	Wi(**) %	e	$\bar{\sigma}c$ kg/cm2	$\bar{\sigma}o$ kg/cm2	Mv cm2/kg	Mvr cm2/kg
1	228.0	8.4	237.0	0.47	82.9	276.6	7.22	1.97	1.23	0.168	0.064
2	228.2	9.0	210.2	0.59	63.7	252.5	6.27	1.96	1.34	0.147	0.052
3	237.7	10.4	207.4	0.76	95.9	196.9	4.87	2.27	1.46	0.101	0.050
4	227.0	10.8	237.7	0.74	98.4	242.3	5.92	2.20	1.70	0.064	0.054
5	237.9	11.0	241.5	0.81	95.3	240.6	6.07	3.04	2.05	0.078	0.043
6	211.8	13.4	209.0	1.03	98.5	230.9	4.94	2.80	2.40	0.102	0.020
7	239.0	14.5	206.5	1.38	151.0	214.0	5.05	3.51	2.85	0.065	0.047
Capa dura	51.9	268.0	54.2	1.47	237.7	--	--	--	--	--	--
8	165.9	23.2	174.0	1.75	141.0	--	--	--	--	--	--
9	143.6	24.2	139.7	1.00	152.0	172.9	3.93	4.35	4.10	0.042	0.030
10	152.0	30.3	163.6	1.80	210.9	158.4	3.92	4.65	4.23	0.012	0.020
Dep Prof	38.0	111.6	42.4	1.80	1091.5	--	--	--	--	--	--

Notes:
(*) Average values obtained with all of the values shown in Figures 2.12 and 2.13
(**) Average values obtained from the triaxial and consolidation tests

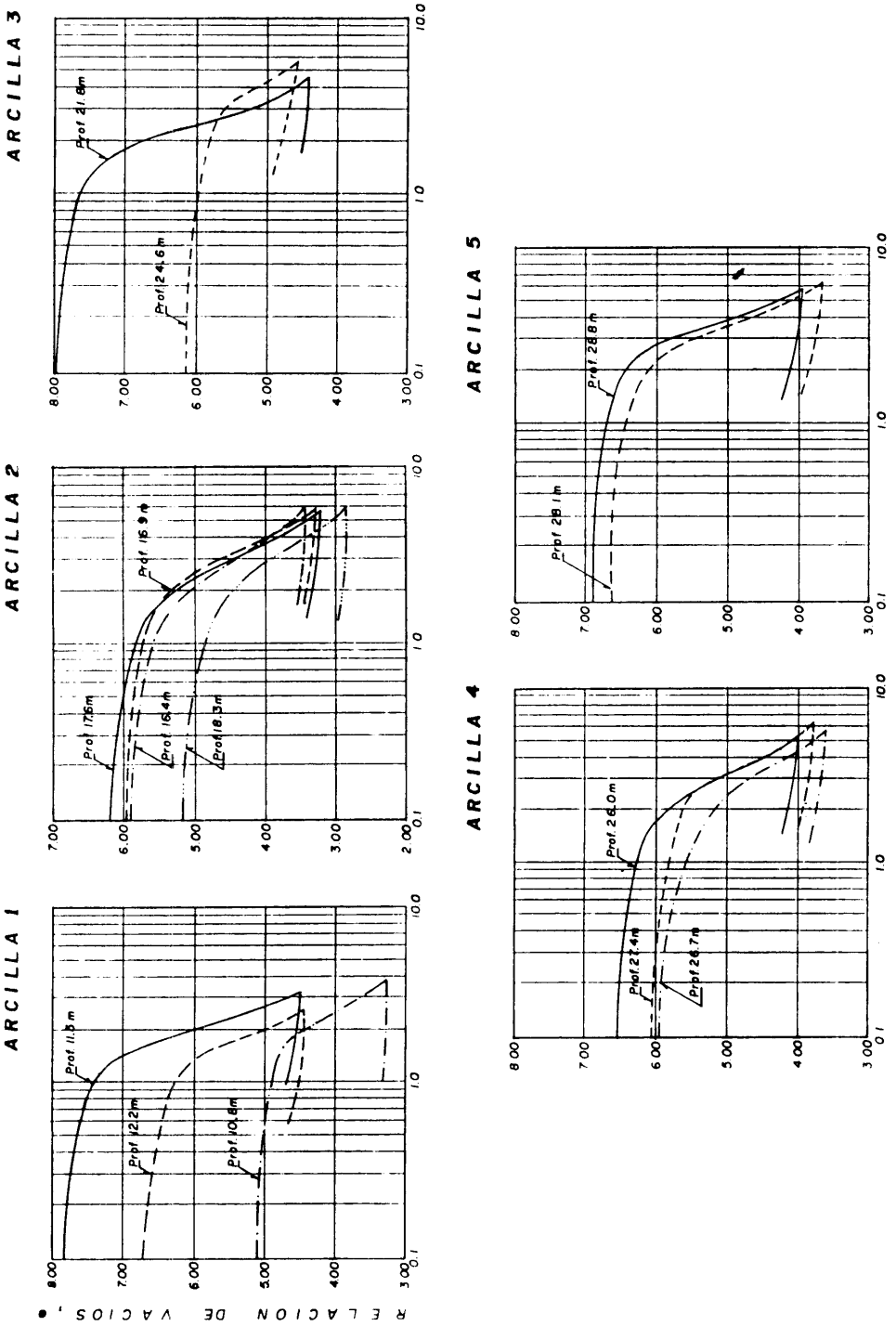

Figure B.1 Consolidation Curves from Clay Substratas 1 through 5; boring SMC-1 (from SEDUE 1990)

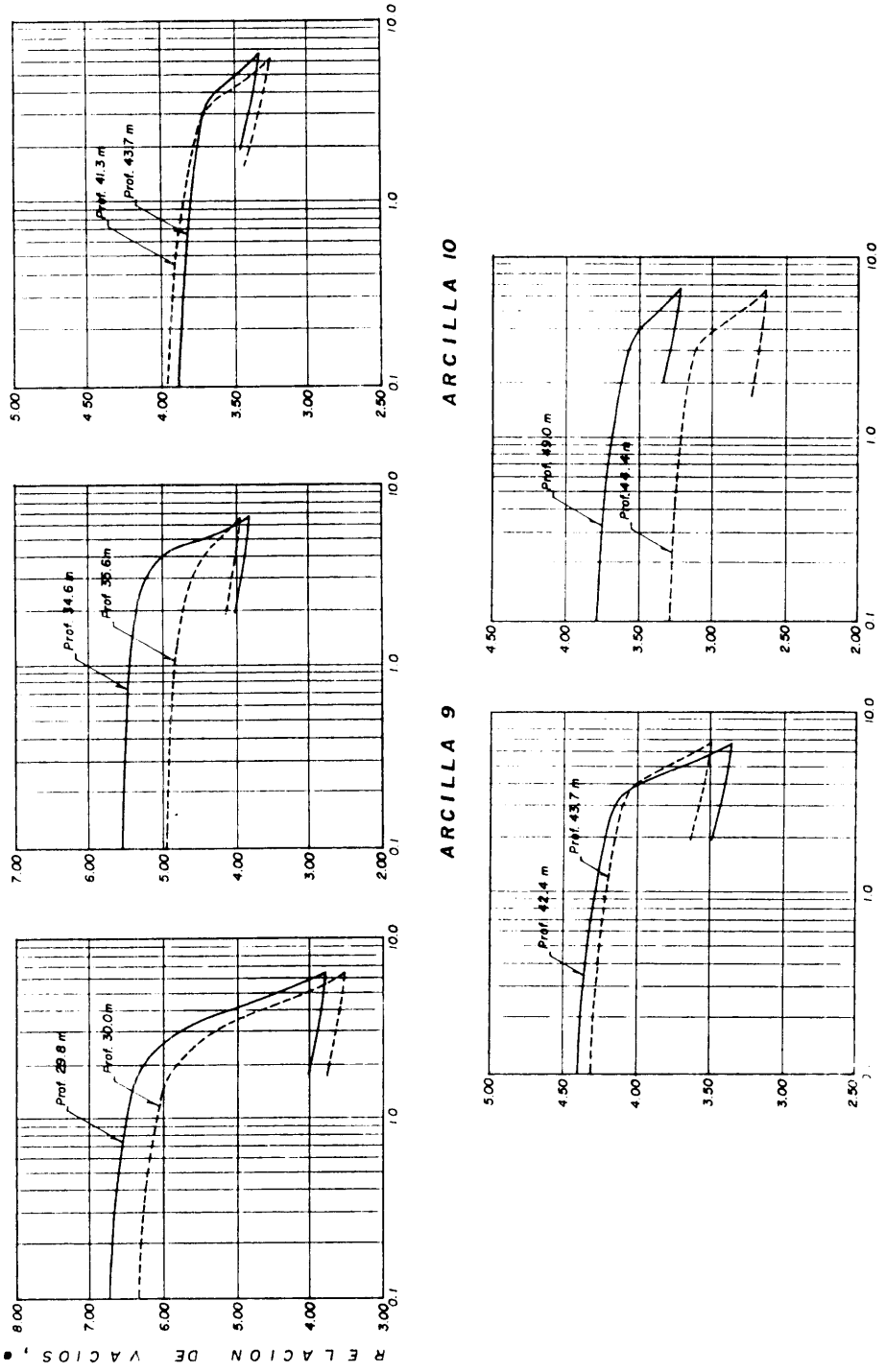

Figure B.2 Consolidation Curves from Clay Substratas 6 through 10; boring SMC-1 (from SEDUE 1990)

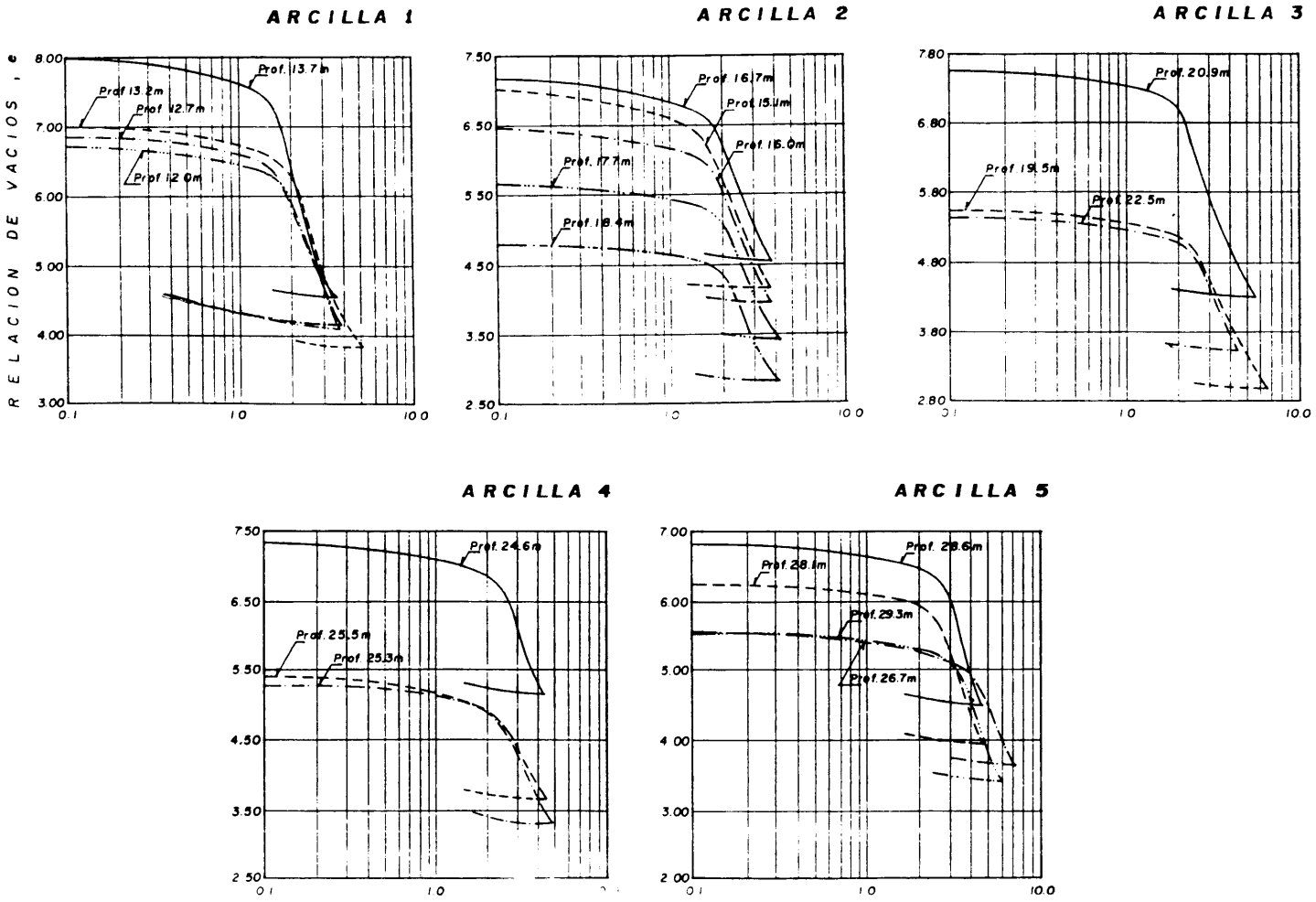

Figure B.3 Consolidation Curves from Clay Substratas 1 through 5; boring SMC-2 (from SEDUE 1990)

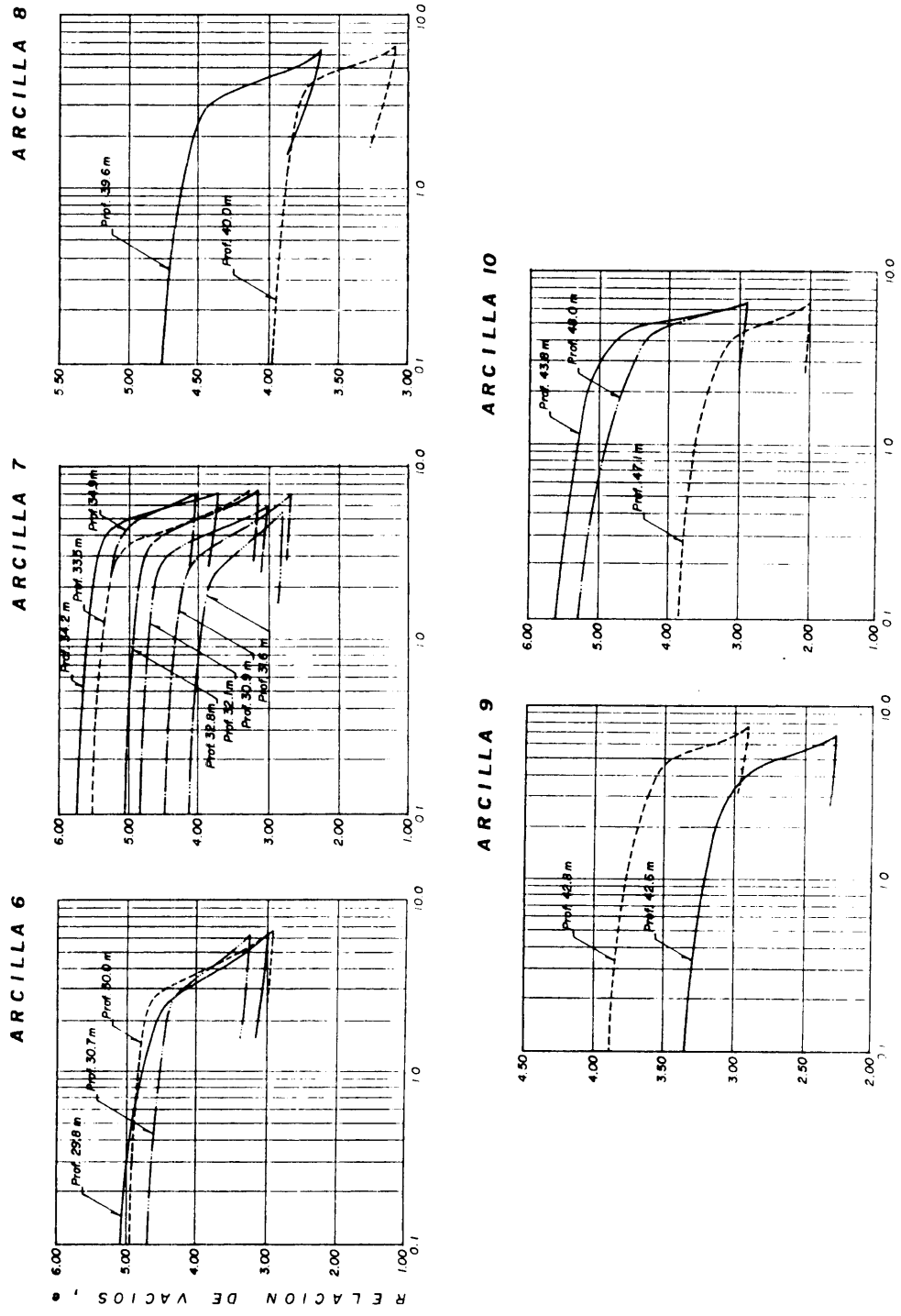

Figure B.4 Consolidation Curves from Clay Substratas 6 through 10; boring SMC-2 (from SEDUE 1990)

Appendix C

Micro-Structure and Mineralogy Results

SEM Compositional Analysis

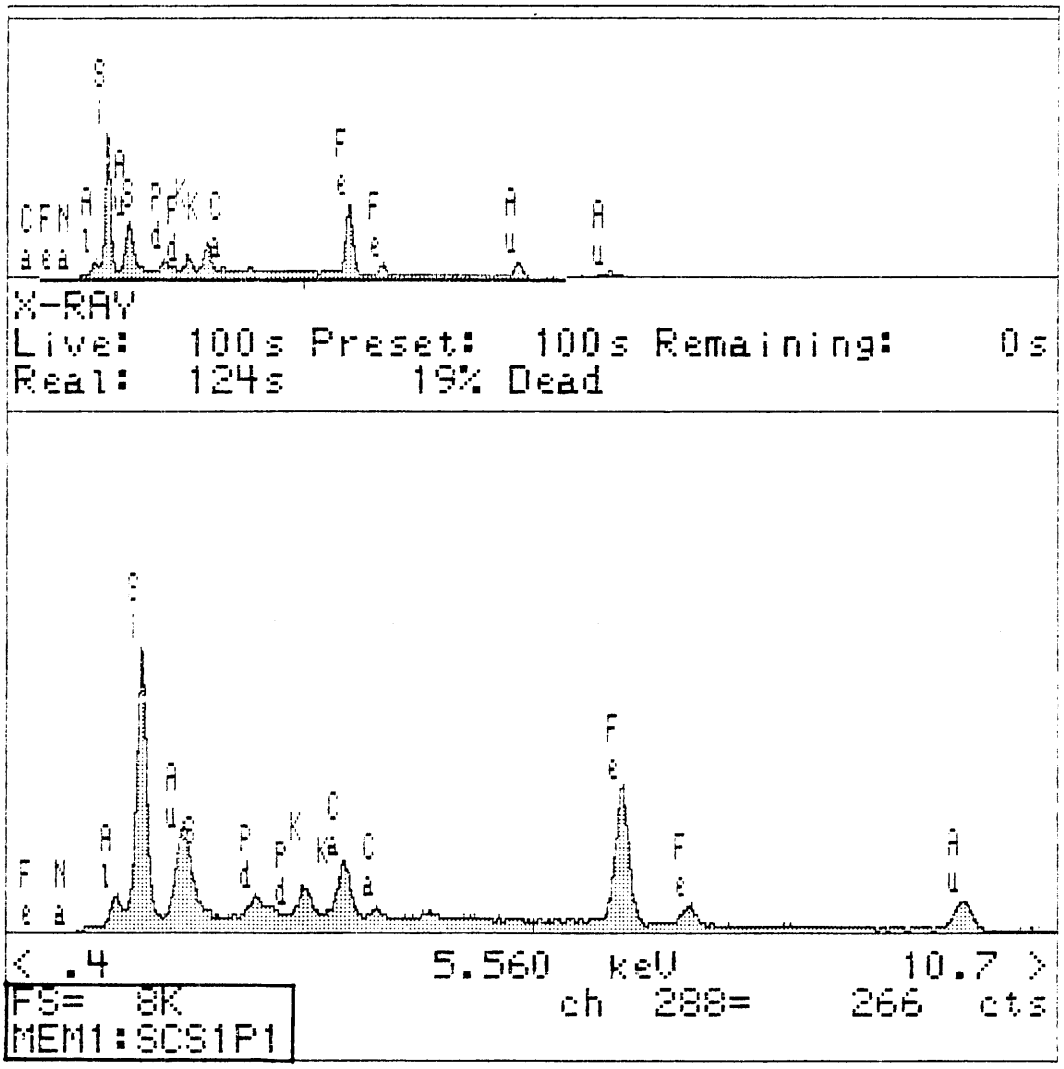
X-RAY
Live: 100s Preset: 100s Remaining: 0s
Real: 124s 19% Dead
< .4
5.560 keV
10.7 >
FS= 8K
MEM1:SCS1P1
ch 288= 266 cts

```
Specimen spectrum,                          FILENAME:SWR:SCS1P1
SCS1P1                                        LIVETIME(spec.)=    1ØØ
  ENERGY     RES      AREA
    13.2    95.57     62941
TOTAL AREA=    22Ø997
......
Peak at    4.52 keV omitted?
Peak at    4.92 keV omitted?
Peak at    9.72 keV omitted?
Peak at   11.48 keV omitted?
Peak at   13.4Ø keV omitted?
FIT INDEX=12.87

ELMT        APP.CONC    ERROR(WT%)
AuM : Ø      9.932        .283
PdL : Ø      2.163        .2Ø1
AlK : Ø      1.115        .Ø67
SiK : Ø     1Ø.Ø58        .1Ø1
S K : Ø       .468        .Ø94
K K : Ø      1.587        .Ø8Ø
CaK : Ø      3.Ø94        .Ø92
FeK : Ø     17.231        .279
...[ 3 ZAF'S]

2Ø.ØØ kV  TILT=   .ØØ ELEV=35.ØØ AZIM=   .ØØ COSINE=1.ØØØ

Spectrum: SCS1P1

All elmts analysed,NORMALISED

ELMT        ZAF    %ELMT    ATOM.%
AuM : Ø   .643    26.927     7.Ø94
PdL : Ø   .672     5.612     2.737
AlK : Ø   .683     2.848     5.478
SiK : Ø   .792    22.151    4Ø.921
S K : Ø   .673     1.213     1.963
K K : Ø   .893     3.1Ø1     4.116
CaK : Ø   .88Ø     6.13Ø     7.937
FeK : Ø   .938    32.Ø24    29.755
TOTAL            1ØØ.ØØ5  1ØØ.ØØØ
```

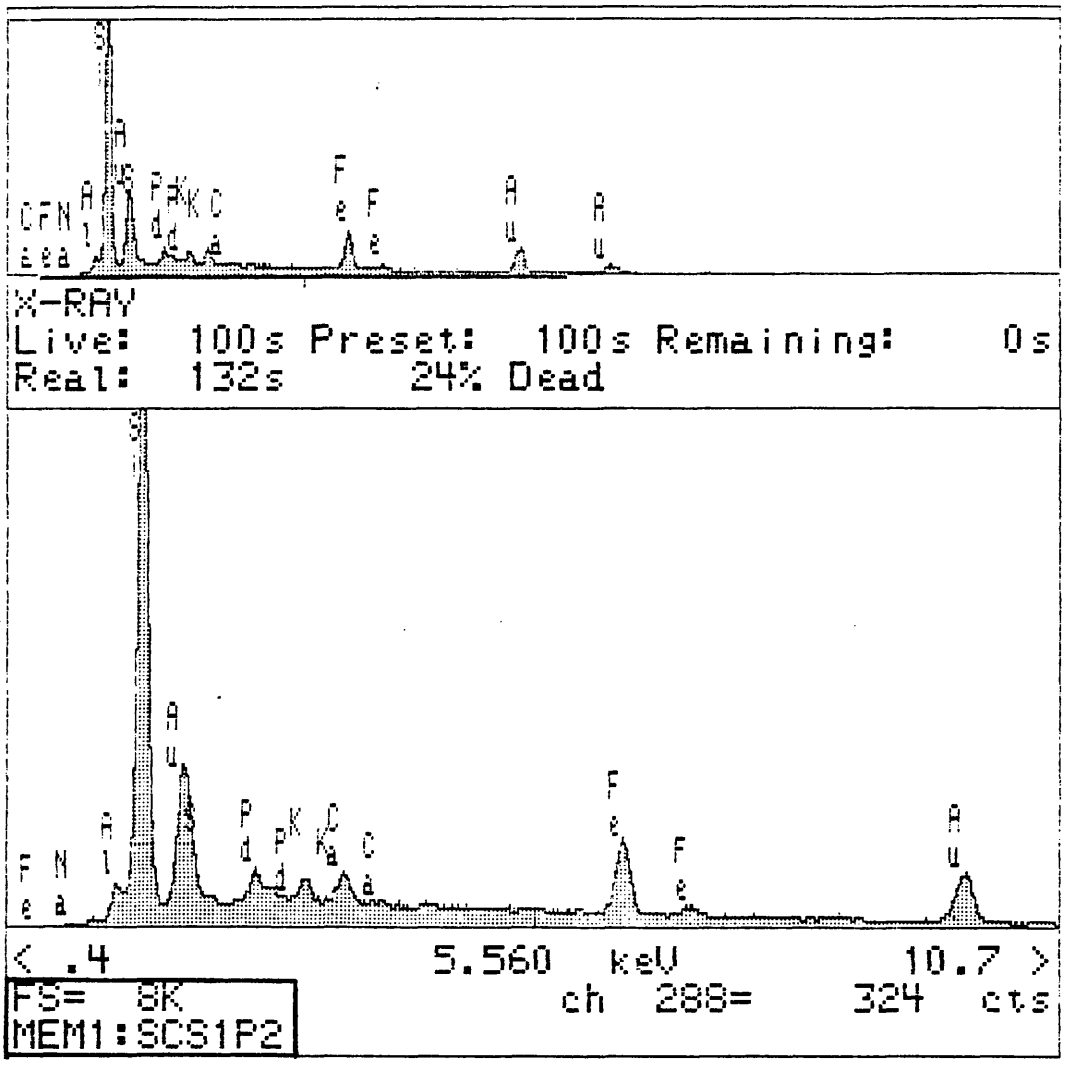
X-RAY
Live: 100s Preset: 100s Remaining: 0s
Real: 132s 24% Dead
< .4
5.560 keV
10.7 >
FS= 8K
MEM1:SCS1P2
ch 288= 324 cts

```
Specimen spectrum,                          FILENAME:SWR:SCS1P2
SCS1P2                                        LIVETIME(spec.)=    100
  ENERGY     RES      AREA
    13.4    95.06     62506
TOTAL AREA=    303710
......
Peak at    4.50 keV omitted?
Peak at    8.50 keV omitted?
Peak at    9.72 keV omitted?
Peak at   11.48 keV omitted?
Peak at   13.38 keV omitted?
FIT INDEX=22.54

ELMT        APP.CONC    ERROR(WT%)
AuM : Ø     15.441        .342
PdL : Ø      3.393        .242
AlK : Ø       .885        .Ø76
SiK : Ø     24.999        .151
S K : Ø       .1Ø7        .11Ø* < 2 Sigma*
K K : Ø      1.223        .Ø87
CaK : Ø      1.6Ø9        .Ø9Ø
FeK : Ø      9.262        .238
...[ 3 ZAF'S]

2Ø.ØØ kV  TILT=   .ØØ ELEV=35.ØØ AZIM=   .ØØ COSINE=1.ØØØ

Spectrum: SCS1P2

All elmts analysed,NORMALISED

ELMT        ZAF     %ELMT    ATOM.%
AuM : Ø   .6Ø3    34.618     8.69Ø
PdL : Ø   .619     7.4ØØ     3.439
AlK : Ø   .785     1.522     2.789
SiK : Ø   .888    38.Ø15    66.911
S K : Ø   .6Ø7      .239      .368
K K : Ø   .825     2.ØØ3     2.533
CaK : Ø   .821     2.645     3.263
FeK : Ø   .922    13.564    12.ØØ8
TOTAL            1ØØ.ØØ6   1ØØ.ØØØ
```

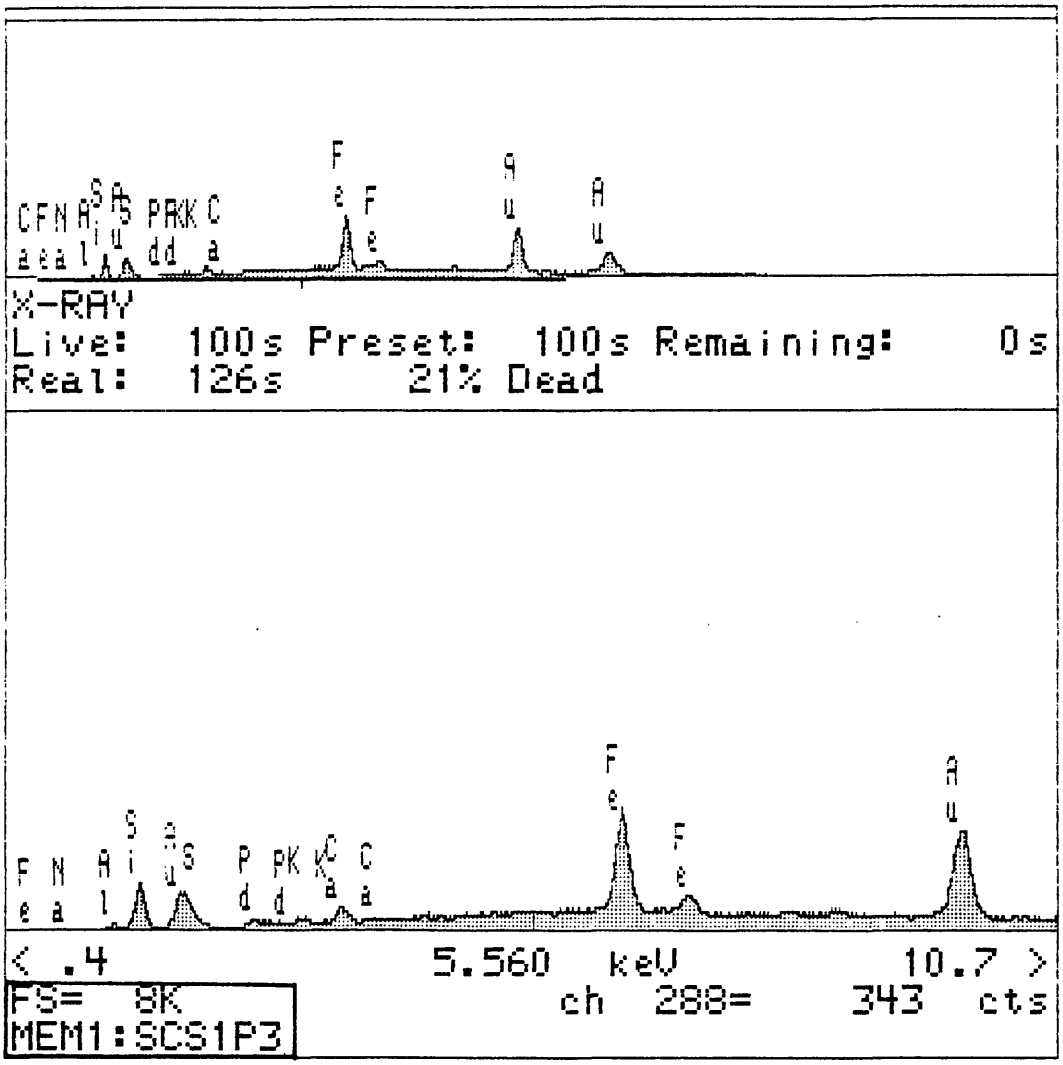
X-RAY
Live: 100s Preset: 100s Remaining: 0s
Real: 126s 21% Dead
< .4
5.560 keV
10.7 >
ch 288= 343 cts
FS= 8K
MEM1:SCS1P3

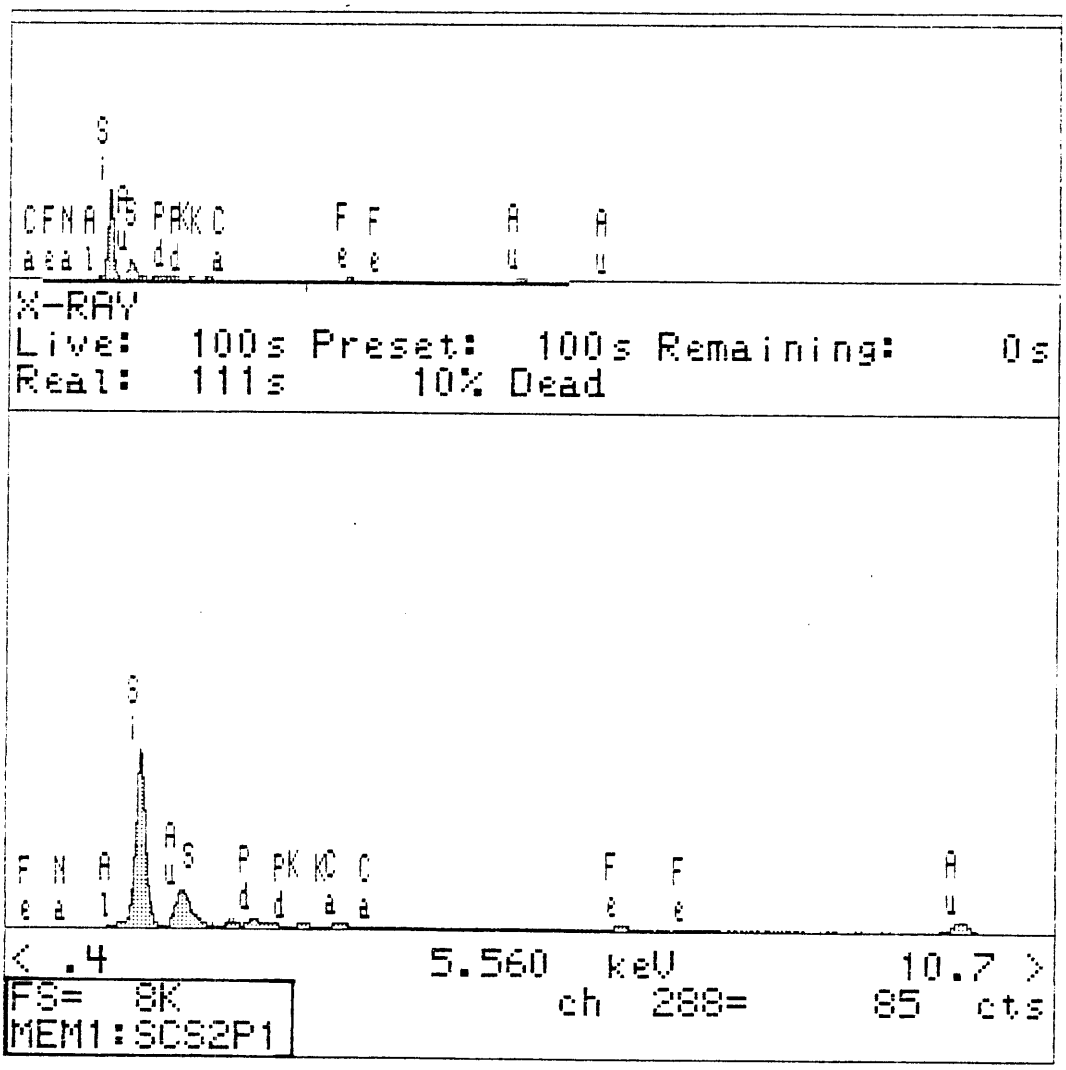
X-RAY
Live: 100s Preset: 100s Remaining: 0s
Real: 111s 10% Dead
< .4
5.560 keV
10.7 >
FS= 8K
MEM1:SCS2P1
ch 288= 85 cts

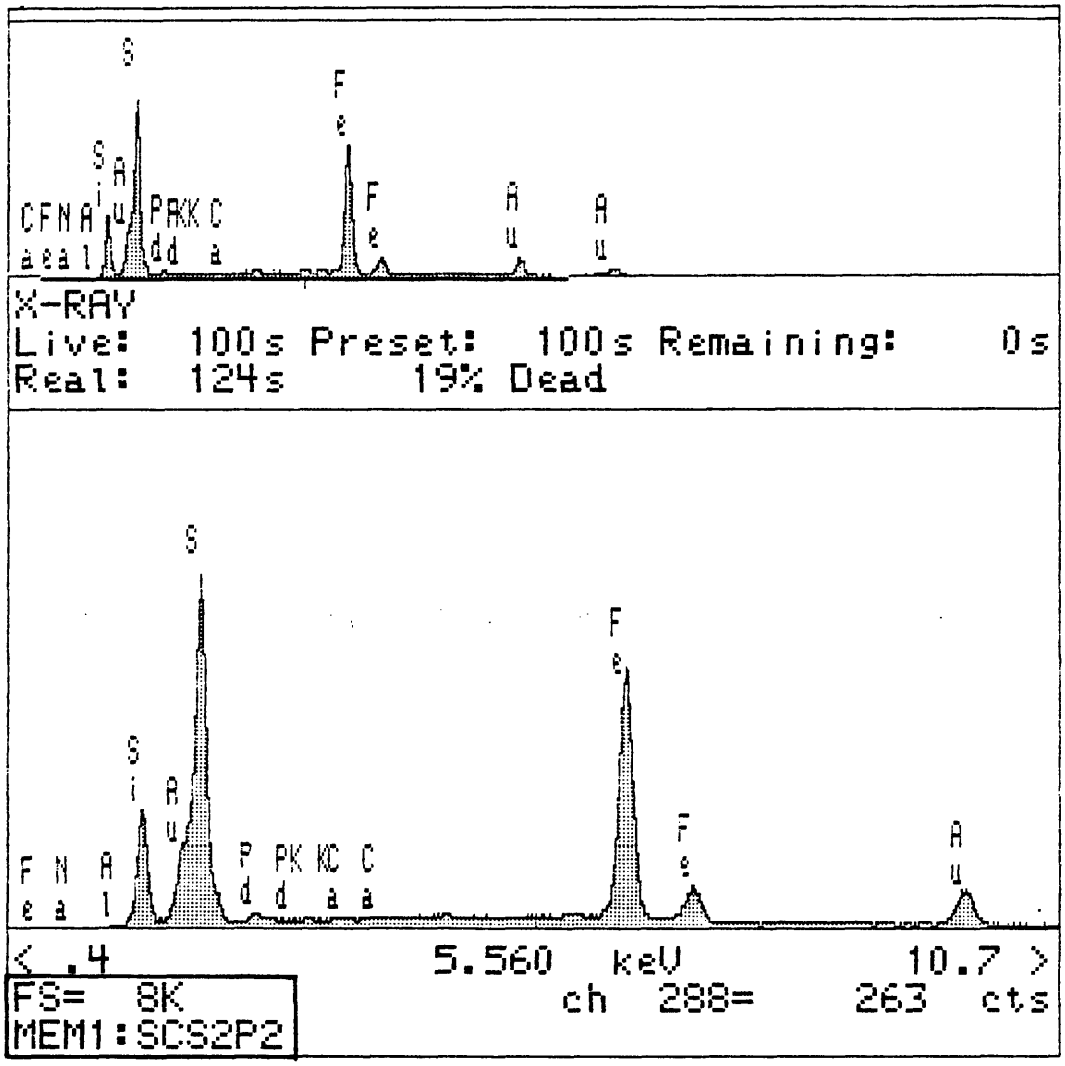
X-RAY
Live: 100s Preset: 100s Remaining: 0s
Real: 124s 19% Dead
< .4
5.560 keV
10.7 >
FS= 8K
MEM1:SCS2P2
ch 288= 263 cts

```
Specimen spectrum,                          FILENAME:SWR:SCS2P2
SCS2P2                                        LIVETIME(spec.)=    100
  ENERGY      RES       AREA
    13.0    96.26      62964
TOTAL AREA=    223366
......
Peak at    8.48 keV omitted?
Peak at    9.72 keV omitted?
Peak at   11.50 keV omitted?
FIT INDEX=11.77

ELMT        APP.CONC    ERROR(WT%)
AuM : 0      8.110        .314
PdL : 0       .935        .141
AlK : 0       .025        .031* < 2 Sigma*
SiK : 0      4.441        .067
S K : 0     14.551        .164
K K : 0       .071        .048* < 2 Sigma*
CaK : 0       .132        .052
FeK : 0     31.595        .351
...[ 3 ZAF'S]

20.00 kV  TILT=   .00 ELEV=35.00 AZIM=   .00 COSINE=1.000

Spectrum: SCS2P2

All elmts analysed,NORMALISED

ELMT        ZAF     %ELMT     ATOM.%
AuM : 0   .703     16.068      3.954
PdL : 0   .648      2.011       .916
AlK : 0   .627       .056       .101
SiK : 0   .764      8.105     13.986
S K : 0   .772     26.269     39.716
K K : 0   .890       .112       .139
CaK : 0   .908       .202       .244
FeK : 0   .933     47.178     40.945
TOTAL             100.000    100.000
```

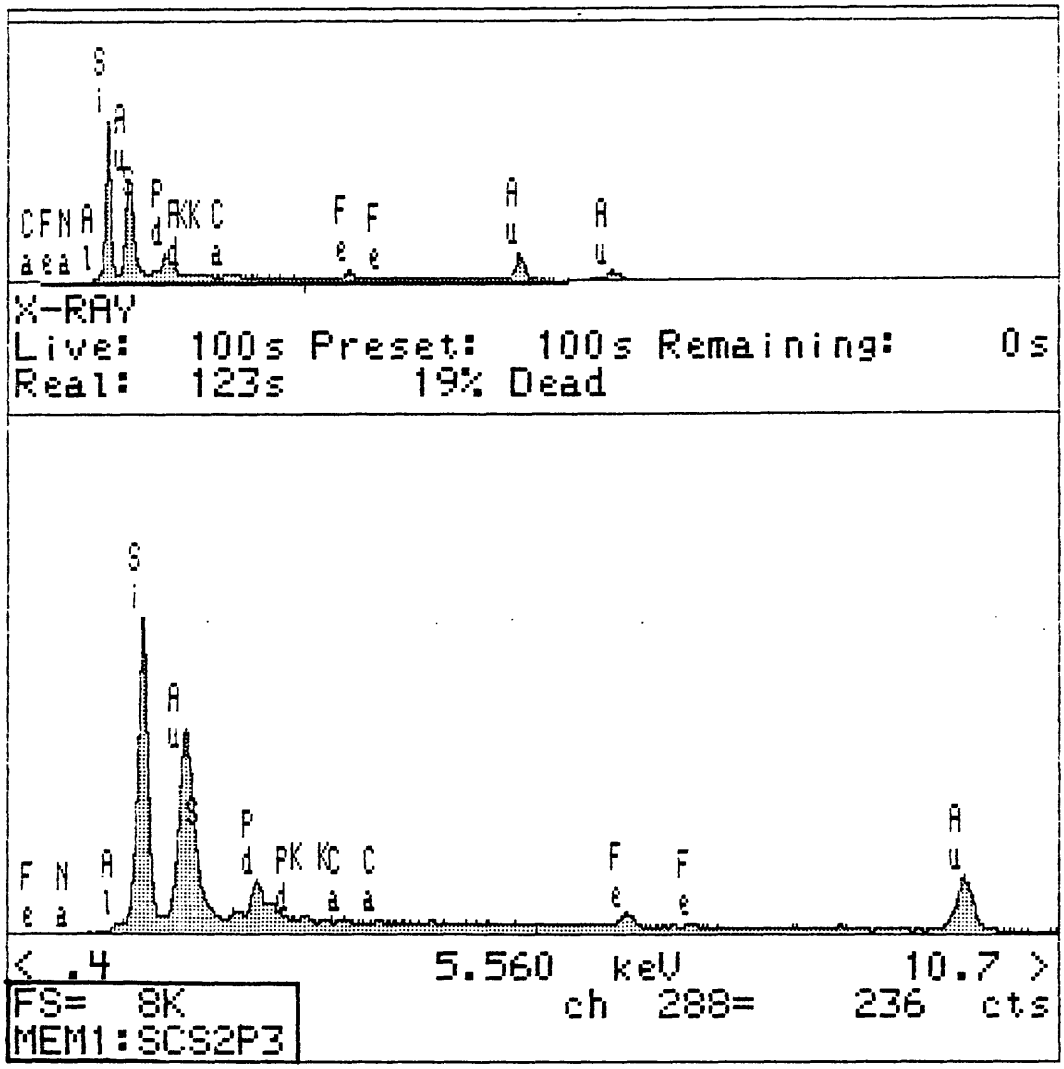
X-RAY
Live: 100s Preset: 100s Remaining: 0s
Real: 123s 19% Dead
< .4
5.560 keV
10.7 >
FS= 8K
MEM1:SCS2P3
ch 288= 236 cts

```
Specimen spectrum,                          FILENAME:SWR:SCS2P3
 SCS2P3                                       LIVETIME(spec.)=    100
  ENERGY     RES      AREA
    13.0    95.92     63147
TOTAL AREA=    208913
......
Peak at    8.50 keV omitted?
Peak at    9.72 keV omitted?
Peak at   11.48 keV omitted?
Peak at   13.36 keV omitted?
FIT INDEX=10.02

ELMT       APP.CONC    ERROR(WT%)
AuM : 0    20.778        .350
PdL : 0     3.829        .225
AlK : 0     -.025        .048* < 2 Sigma*
SiK : 0    11.246        .105
S K : 0      .930        .110
K K : 0      .222        .061
CaK : 0      .193        .059
FeK : 0     1.460        .145
...[ 3 ZAF'S]

20.00 kV  TILT=   .00 ELEV=35.00 AZIM=   .00 COSINE=1.000

Spectrum: SCS2P3

All elmts analysed,NORMALISED

ELMT       ZAF     %ELMT     ATOM.%
AuM : 0   .730    57.421    20.764
PdL : 0   .618    12.483     8.356
AlK : 0   .839      .000      .000
SiK : 0   .981    23.104    58.593
S K : 0   .627     2.990     6.642
K K : 0   .810      .552     1.006
CaK : 0   .809      .482      .856
FeK : 0   .989     2.974     3.793
TOTAL            100.006   100.000
-------------------------------------------------------------------------
```

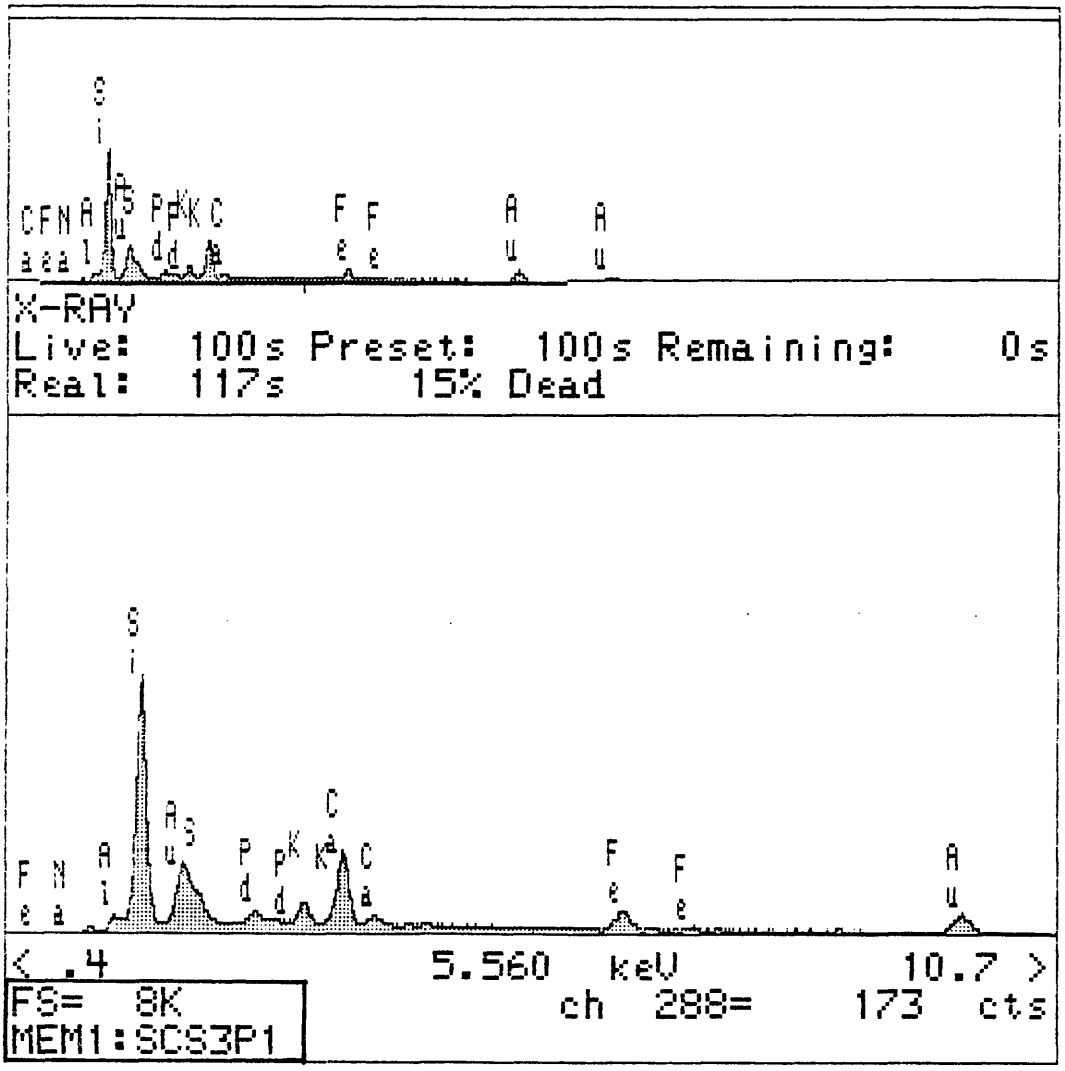
X-RAY
Live: 100s Preset: 100s Remaining: 0s
Real: 117s 15% Dead
< .4
5.560 keV
10.7 >
FS= 8K
MEM1:SCS3P1
ch 288= 173 cts

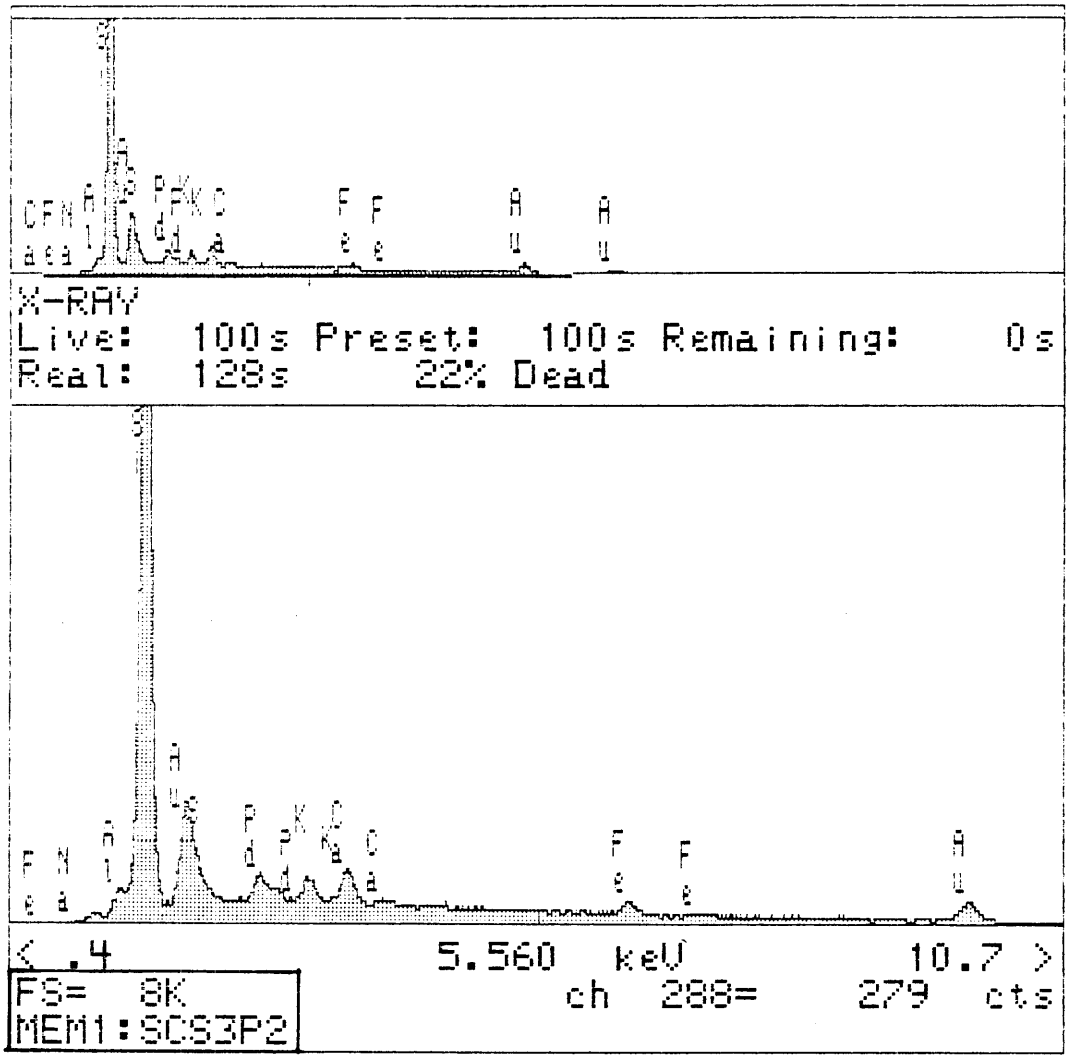
X-RAY
Live: 100s Preset: 100s Remaining: 0s
Real: 128s 22% Dead
< .4
5.560 keV
10.7 >
FS= 8K
MEM1:SCS3P2
ch 288= 279 cts

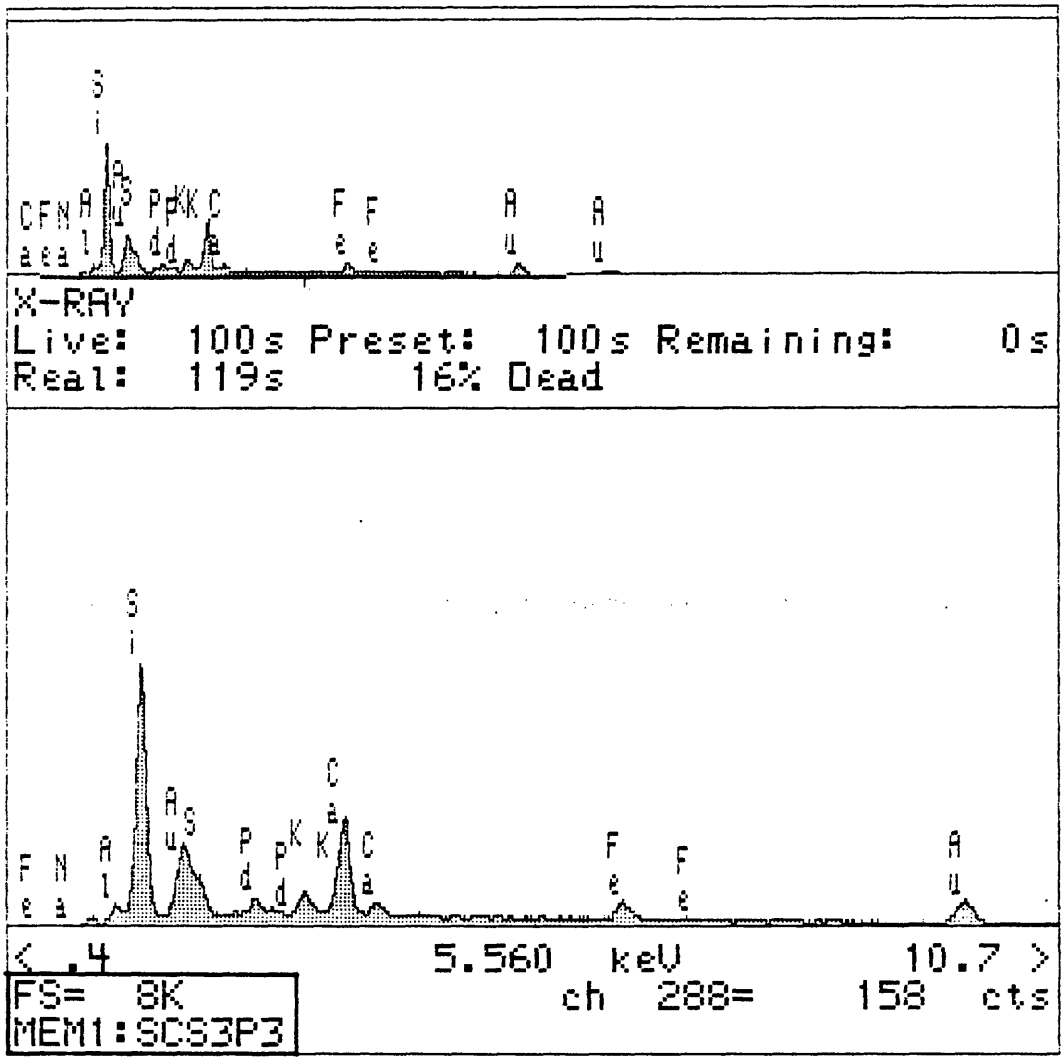
X-RAY
Live: 100s Preset: 100s Remaining: 0s
Real: 119s 16% Dead
< .4
5.560 keV
10.7 >
FS= 8K
MEM1:SCS3P3
ch 288= 158 cts

```
Specimen spectrum,                          FILENAME:SWR:SCS3P3
SCS3P3                                        LIVETIME(spec.)=    1ØØ
  ENERGY     RES      AREA
    12.8    95.16     634Ø4
TOTAL AREA=    168950
......
Peak at    9.72 keV omitted?
Peak at   11.48 keV omitted?
FIT INDEX=1Ø.12

ELMT        APP.CONC    ERROR(WT%)
AuM : Ø      7.75Ø        .255
PdL : Ø      1.561        .174
AlK : Ø       .6Ø7        .Ø55
SiK : Ø      9.518        .Ø95
S K : Ø      1.472        .Ø91
K K : Ø      1.227        .Ø7Ø
CaK : Ø      5.629        .1Ø2
FeK : Ø      2.14Ø        .146
...[ 3 ZAF'S]

2Ø.ØØ kV  TILT=   .ØØ ELEV=35.ØØ AZIM=   .ØØ COSINE=1.ØØØ

Spectrum: SCS3P3

All elmts analysed,NORMALISED

ELMT        ZAF     %ELMT    ATOM.%
AuM : Ø   .654    3Ø.815     7.469
PdL : Ø   .637     6.362     2.Ø55
AlK : Ø   .8Ø5     1.958     3.465
SiK : Ø   .9Ø1    27.443    46.64Ø
S K : Ø   .658     5.814     8.657
K K : Ø   .848     3.757     4.587
CaK : Ø   .828    17.65Ø    21.Ø24
FeK : Ø   .896     6.2Ø5     5.3Ø4
TOTAL            1ØØ.ØØ4   1ØØ.ØØØ
```

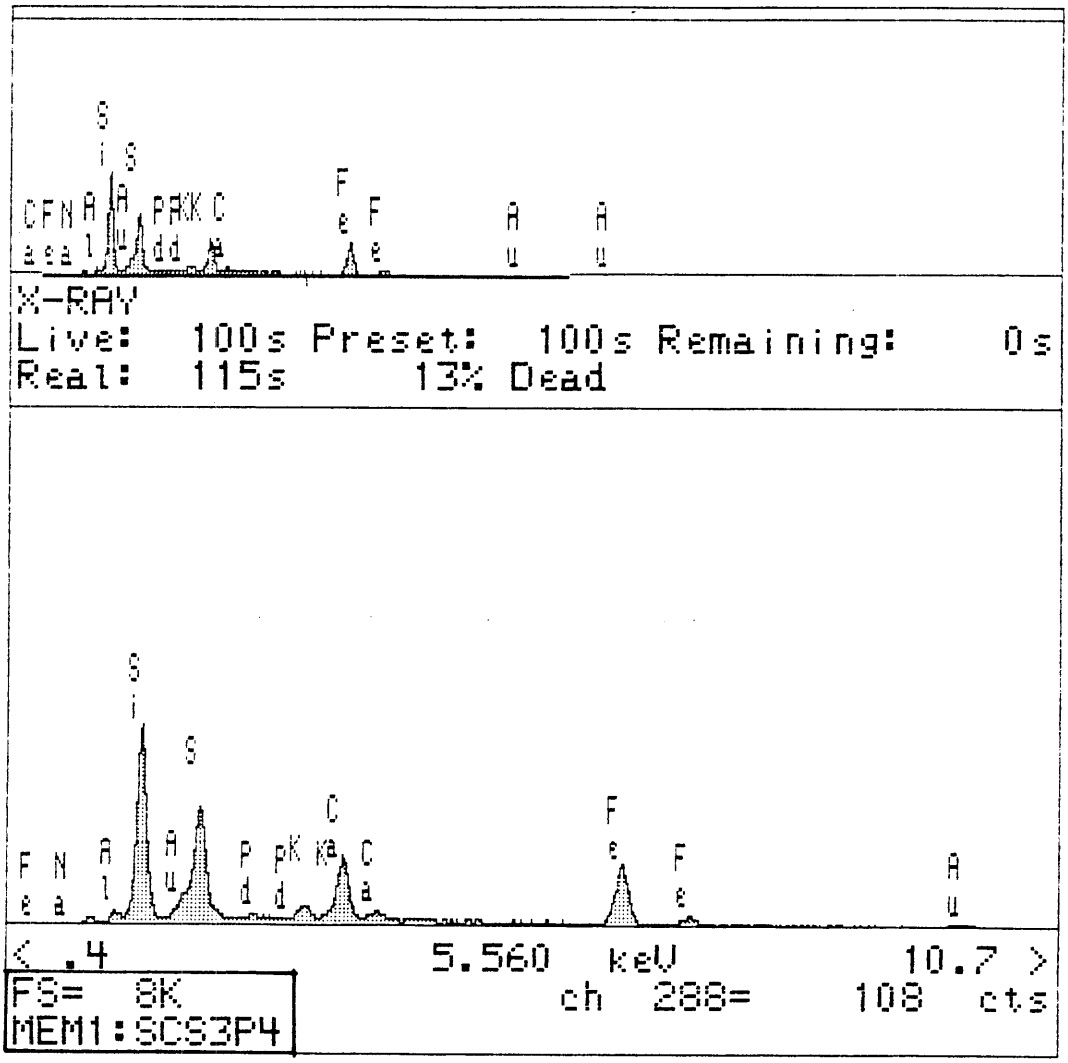
X-RAY
Live: 100s Preset: 100s Remaining: 0s
Real: 115s 13% Dead
< .4
5.560 keV
10.7 >
FS= 8K
MEM1:SCS3P4
ch 288= 108 cts

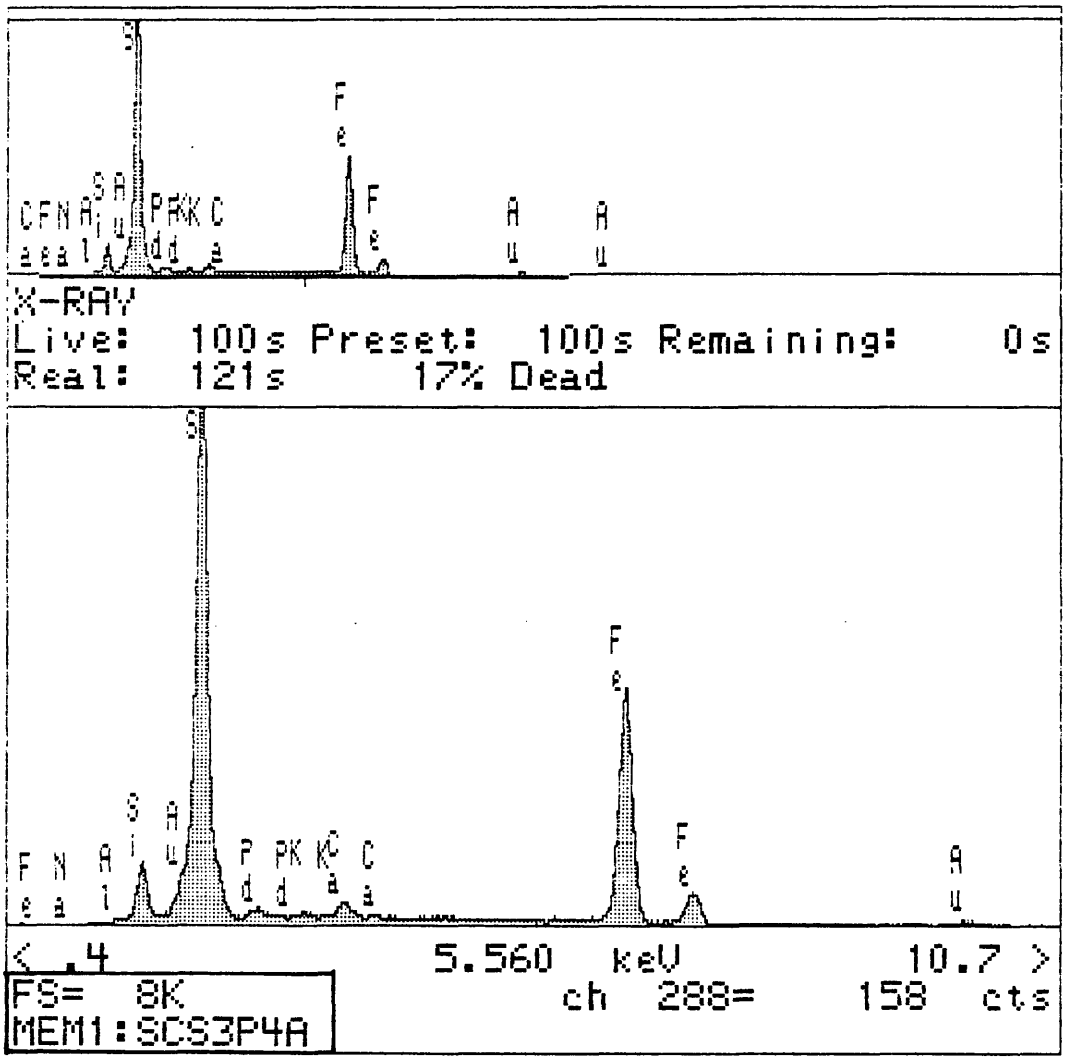
X-RAY
Live: 100s Preset: 100s Remaining: 0s
Real: 121s 17% Dead
< .4
5.560 keV
10.7 >
FS= 8K
MEM1:SCS3P4A
ch 288= 158 cts

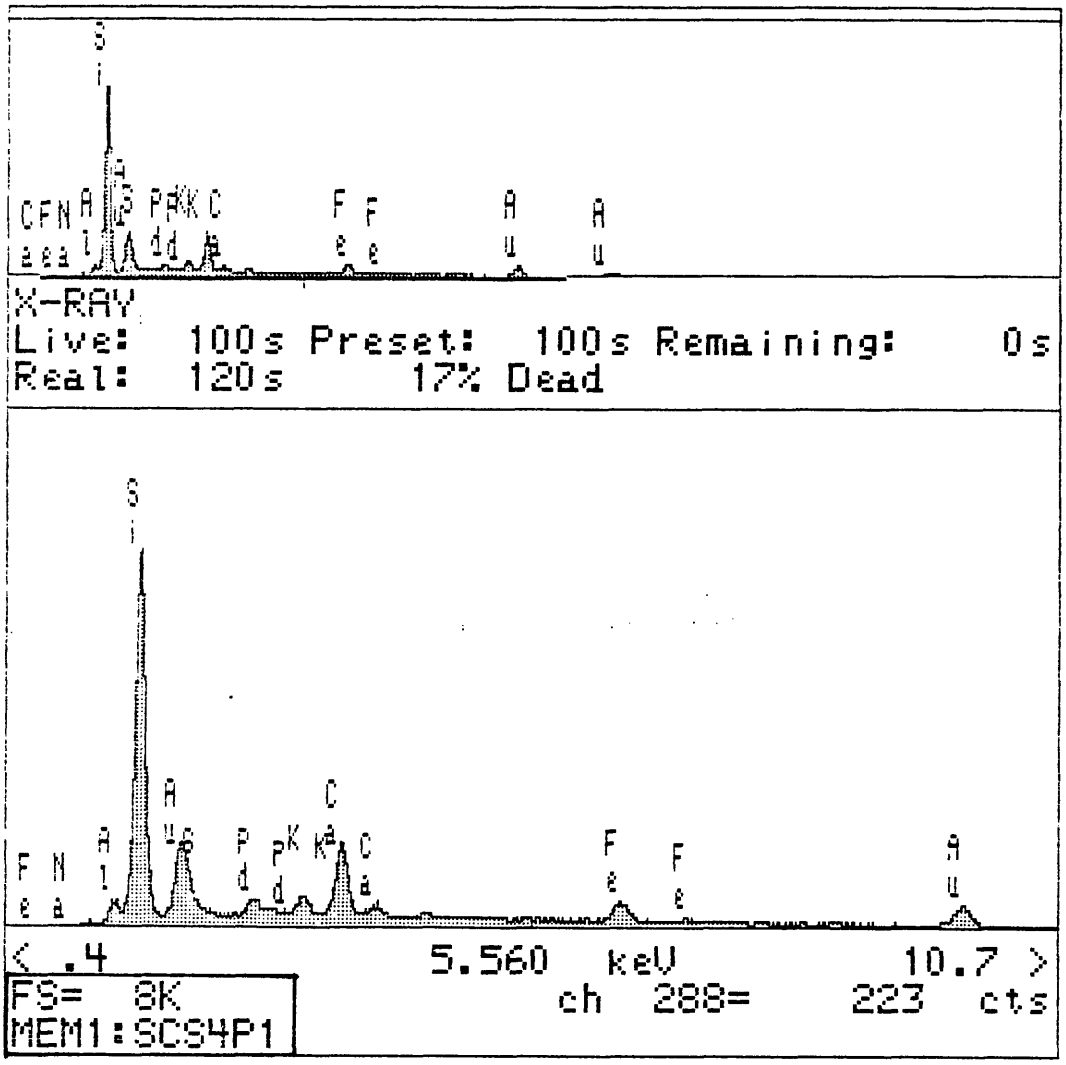
X-RAY
Live: 100s Preset: 100s Remaining: 0s
Real: 120s 17% Dead
< .4
5.560 keV
10.7 >
FS= 8K
MEM1:SCS4P1
ch 288= 223 cts

```
Specimen spectrum,                          FILENAME:SWR:SCS4P1
SCS4P1                                        LIVETIME(spec.)=    100
  ENERGY     RES      AREA
    12.4    95.Ø4     62960
TOTAL AREA=    176971
......
Peak at    4.5Ø keV omitted?
Peak at    9.72 keV omitted?
Peak at   11.48 keV omitted?
FIT INDEX=12.65

ELMT        APP.CONC    ERROR(WT%)
AuM : Ø      7.922        .253
PdL : Ø      1.844        .177
AlK : Ø       .69Ø        .Ø59
SiK : Ø     13.677        .112
S K : Ø       .23Ø        .Ø84
K K : Ø       .928        .Ø7Ø
CaK : Ø      4.Ø47        .Ø94
FeK : Ø      2.324        .151
...[ 3 ZAF'S]

2Ø.ØØ kV  TILT=   .ØØ ELEV=35.ØØ AZIM=   .ØØ COSINE=1.ØØØ

Spectrum: SCS4P1

All elmts analysed,NORMALISED

ELMT        ZAF     %ELMT    ATOM.%
AuM : Ø   .6Ø9    31.787     7.566
PdL : Ø   .627     7.186     3.166
AlK : Ø   .817     2.Ø63     3.585
SiK : Ø   .9Ø5    36.899    61.584
S K : Ø   .62Ø      .983     1.438
K K : Ø   .833     2.721     3.262
CaK : Ø   .82Ø    12.Ø54    14.1ØØ
FeK : Ø   .899     6.312     5.299
TOTAL            1ØØ.ØØ5   1ØØ.ØØØ
-------------------------------------------------------------------------
```

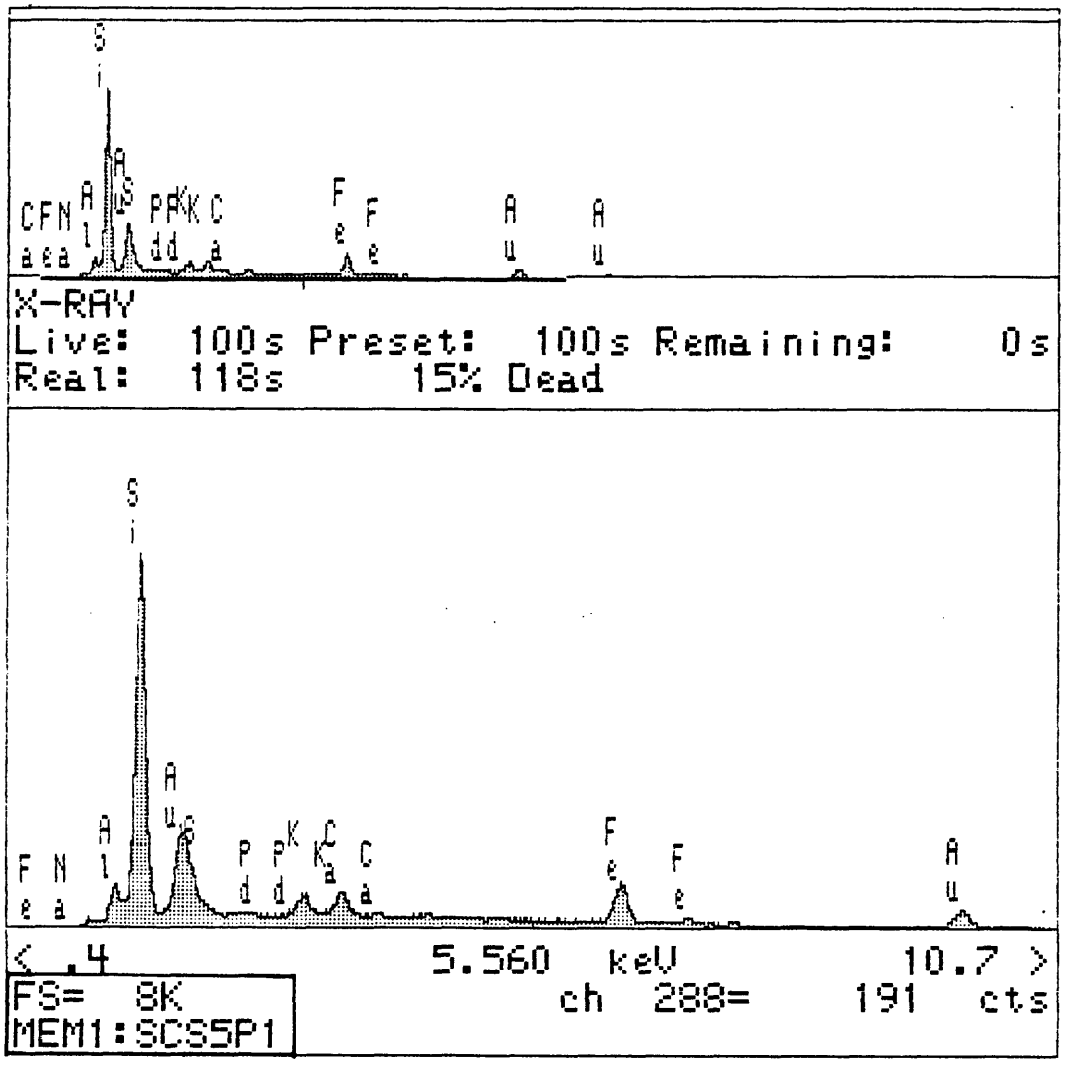
X-RAY
Live: 100s Preset: 100s Remaining: 0s
Real: 118s 15% Dead
< .4
5.560 keV
10.7 >
FS= 8K
MEM1:SCS5P1
ch 288= 191 cts

```
Specimen spectrum,                          FILENAME:SWR:SCS5P1
SCS5P1                                        LIVETIME(spec.)=    100
  ENERGY     RES      AREA
    11.9    96.94     63734
TOTAL AREA=    165321
......
Peak at    4.52 keV omitted?
Peak at    9.72 keV omitted?
Peak at   11.46 keV omitted?
FIT INDEX=12.30

ELMT        APP.CONC    ERROR(WT%)
AuM : Ø      9.427        .274
PdL : Ø      -.044        .155* < 2 Sigma*
AlK : Ø      1.382        .070
SiK : Ø     13.553        .114
S K : Ø       .511        .090
K K : Ø      1.055        .069
CaK : Ø      1.276        .072
FeK : Ø      4.957        .173
...[ 3 ZAF'S]

20.00 kV   TILT=   .00 ELEV=35.00 AZIM=   .00 COSINE=1.000

Spectrum: SCS5P1

All elmts analysed,NORMALISED

ELMT        ZAF     %ELMT    ATOM.%
AuM : Ø   .600    37.470     8.994
PdL : Ø   .599      .000      .000
AlK : Ø   .808     4.079     7.148
SiK : Ø   .879    36.745    61.849
S K : Ø   .592     2.061     3.039
K K : Ø   .823     3.056     3.695
CaK : Ø   .828     3.677     4.337
FeK : Ø   .915    12.919    10.937
TOTAL            100.005   100.000
```

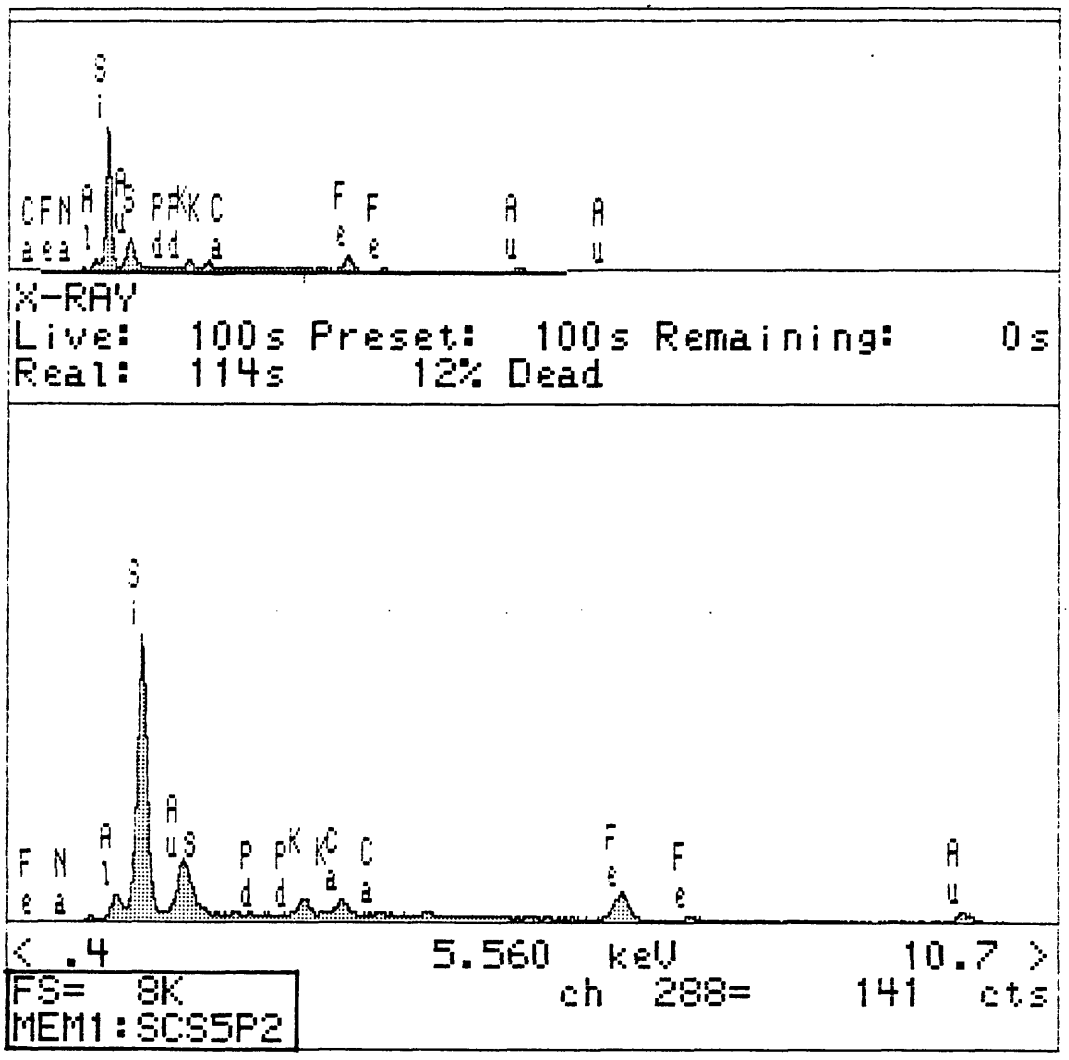
X-RAY
Live: 100s Preset: 100s Remaining: 0s
Real: 114s 12% Dead
< .4
5.560 keV
10.7 >
FS= 8K
MEM1:SCS5P2
ch 288= 141 cts

X-Ray Diffraction Results

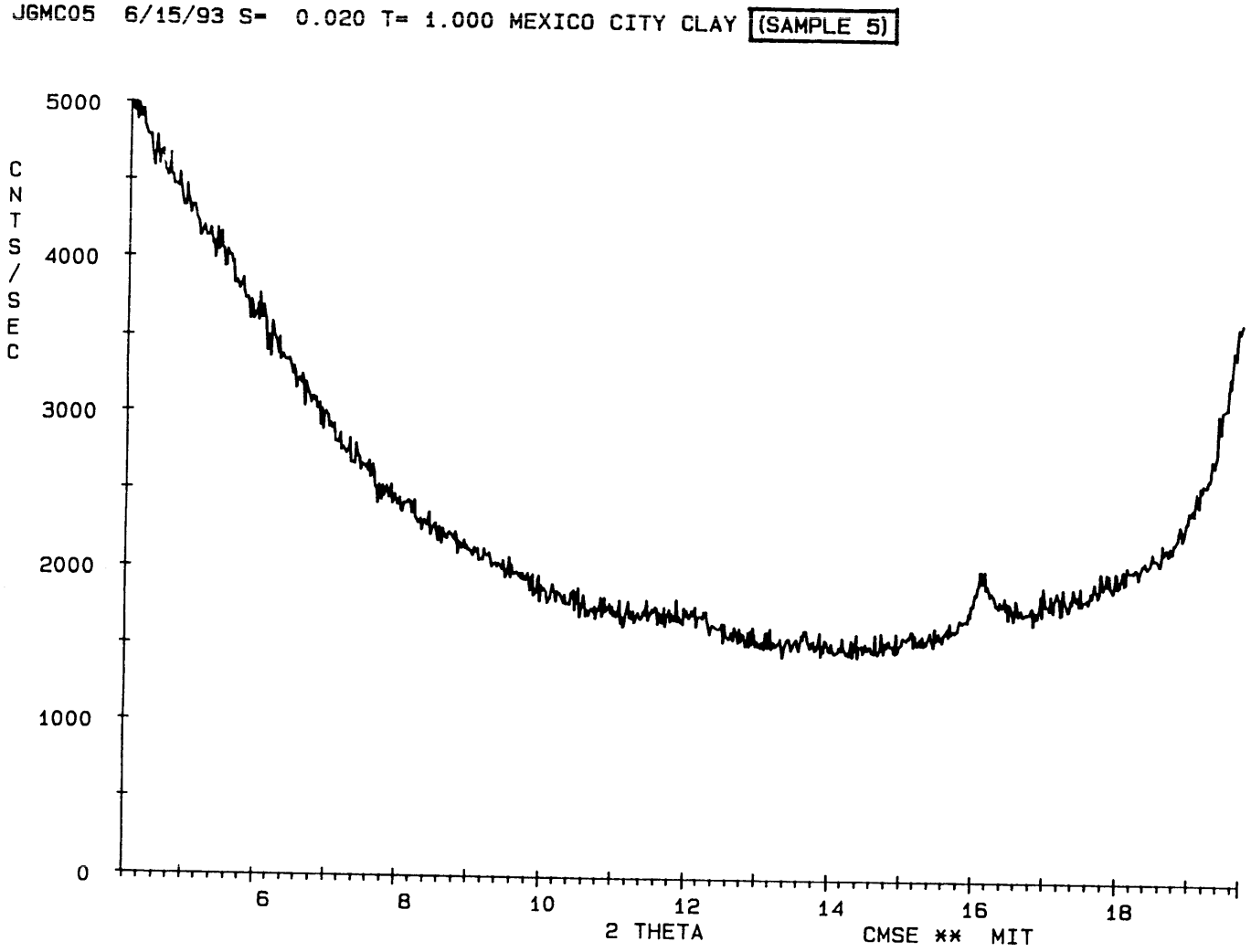
JGMC05 6/15/93 S= 0.020 T= 1.000 MEXICO CITY CLAY (SAMPLE 5)
5000
4000
3000
2000
1000
0
CNTS/SEC
6
8
10
12
14
16
18
2 THETA
CMSE ** MIT

JGMC05 6/15/93 S= 0.020 T= 1.000 MEXICO CITY CLAY (SAMPLE 5)

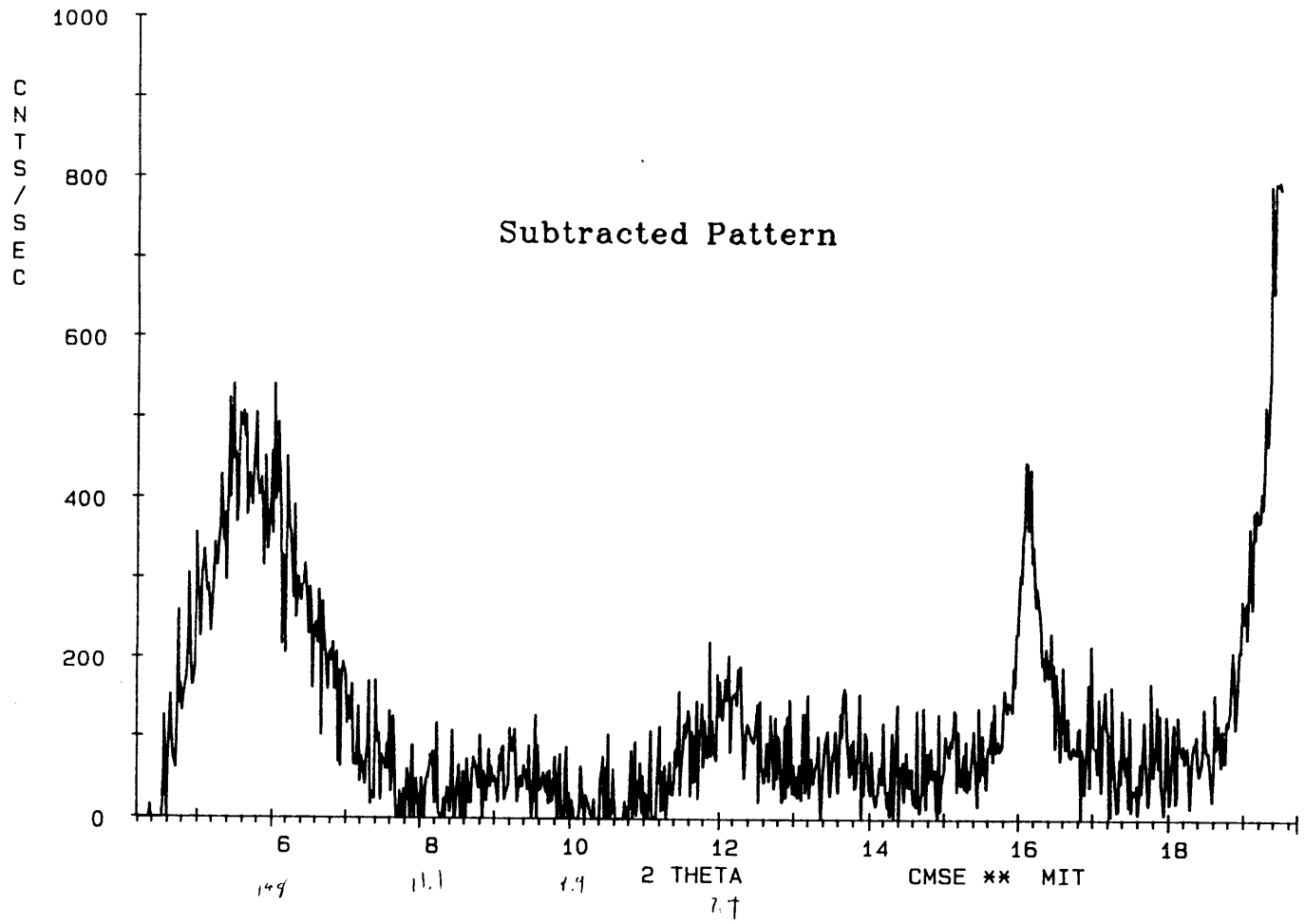

PEAKS FILE LISTING

ATA FILE: JGMC04.PKS
AMPLE IDENTIFICATION:
TART 2THETA: 10.000
TEP SIZE: 0.020
OUNTING TIME: 1.000
EAKS FOUND ON:

COLLECTED ON 9-JUN-93 AT 13:53:15
MEXICO CITY CLAY (SAMPLE 5)
STOP 2THETA: 80.000
SCAN SPEED: 1.000

9-JUN-93 AT 16:39:01

PEAK FINDING PARAMETERS

THRESHOLD VALUES: 5.0,10.0
RELATIVE CUTOFF INTENSITY: 1.0
YPICAL FULL WIDTH-HALF MAXIMUM: 0.20
INIMUM FULL WIDTH-HALF MAXIMUM: 0.10
ALPHA 2 REMOVAL USING CODE: 1

	PEAK	2-THETA	D-SPACE	I(REL)	I(CPS)	FWHM	
U	1	13.603	6.5042	1.94	42.0	0.000	U
	2	16.120	5.4939	22.40	483.6	0.245	
U	3	16.703	5.3035	5.97	129.0	0.000	U
	4	19.840	4.4714	50.92	1099.4	0.659	
	5	20.000	4.4360	38.89	839.8	0.339	
	6	20.320	4.3668	21.23	458.4	0.120	
	7	20.600	4.3081	18.51	399.7	0.163	
	8	20.780	4.2712	15.81	341.3	0.171	
	9	21.900	4.0552	100.00	2159.1	0.180	
	10	23.600	3.7668	34.83	752.1	0.167	
U	11	24.364	3.6505	16.61	358.6	0.000	U
U	12	24.496	3.6310	11.76	253.9	0.000	U
	13	25.640	3.4716	5.24	113.1	0.100	
	14	26.600	3.3484	31.72	684.8	0.155	
	15	27.720	3.2156	74.95	1618.2	0.284	
	16	27.980	3.1863	38.79	837.6	0.103	
	17	28.400	3.1401	18.81	406.1	0.209	
	18	29.560	3.0195	10.21	220.4	0.122	
U	19	29.656	3.0100	6.54	141.1	0.000	U
U	20	29.882	2.9877	9.01	194.5	0.000	U
	21	30.000	2.9762	11.52	248.8	0.158	
	22	30.220	2.9550	18.22	393.4	0.116	
U	23	30.341	2.9436	17.07	368.5	0.000	U
	24	30.580	2.9211	14.75	318.5	0.143	
	25	30.740	2.9062	11.07	239.0	0.156	
U	26	30.877	2.8937	7.78	167.9	0.000	U
	27	31.360	2.8502	14.85	320.7	0.184	
B	28	32.983	2.7135	11.09	239.5	0.000	B
	29	34.480	2.5991	20.05	432.9	0.128	
	30	34.720	2.5817	33.25	718.0	0.200	
	31	35.500	2.5267	24.88	537.2	0.360	
	32	35.980	2.4941	15.28	329.9	0.117	
	33	37.000	2.4276	19.04	411.0	0.128	
U	34	39.345	2.2882	1.22	26.4	0.000	U
U	35	40.222	2.2403	5.73	123.7	0.000	U
U	36	40.604	2.2201	7.51	162.2	0.000	U
B	37	41.632	2.1676	7.92	171.1	0.000	B
	38	42.100	2.1446	9.04	195.1	0.102	
	39	42.560	2.1225	13.02	281.0	0.246	
U	40	44.075	2.0530	3.92	84.7	0.000	U

	41	44.680	2.0266	7.36	158.8	0.104	
	42	44.900	2.0171	7.63	164.8	0.180	
	43	45.460	1.9936	7.46	161.1	0.168	
	44	45.600	1.9876	5.78	124.7	0.120	
U	45	46.923	1.9348	5.59	120.6	0.000	U
	46	47.320	1.9195	12.45	268.9	0.158	
	47	48.480	1.8762	10.17	219.7	0.185	
	48	49.220	1.8497	5.95	128.5	0.138	
	49	49.740	1.8316	8.89	192.0	0.138	
	50	50.080	1.8200	6.23	134.5	0.114	
U	51	50.801	1.7958	9.68	209.0	0.000	U
U	52	51.393	1.7765	12.71	274.4	0.000	U
	53	53.300	1.7174	10.11	218.3	0.180	
	54	53.400	1.7144	9.23	199.3	0.105	
U	55	54.238	1.6898	6.67	144.1	0.000	U
	56	54.820	1.6733	9.11	196.8	0.173	
U	57	55.671	1.6497	3.68	79.5	0.000	U
	58	56.180	1.6359	18.19	392.6	0.192	
U	59	56.915	1.6165	4.05	87.4	0.000	U
U	60	59.883	1.5433	7.96	171.8	0.000	U
U	61	59.981	1.5410	8.62	186.1	0.000	U
	62	60.100	1.5383	14.18	306.2	0.140	
	63	60.220	1.5355	10.50	226.7	0.100	
	64	60.720	1.5240	19.30	416.8	0.240	
	65	61.080	1.5159	23.94	516.9	0.320	
	66	61.580	1.5048	24.04	519.0	0.340	
	67	61.880	1.4982	22.84	493.1	0.100	
	68	62.180	1.4917	18.70	403.7	0.211	
	69	63.960	1.4544	4.25	91.7	0.127	
	70	64.180	1.4500	7.27	157.0	0.185	
	71	65.180	1.4301	6.36	137.3	0.140	
	72	65.440	1.4251	7.36	158.8	0.104	
	73	65.600	1.4220	5.59	120.8	0.140	
	74	65.840	1.4174	7.52	162.3	0.180	
	75	67.020	1.3953	4.60	99.3	0.129	
	76	67.720	1.3825	9.95	214.8	0.177	
	77	67.940	1.3786	8.07	174.2	0.140	
	78	68.260	1.3729	8.37	180.7	0.155	
	79	69.060	1.3589	3.88	83.7	0.178	
	80	69.360	1.3538	6.01	129.8	0.100	
	81	69.560	1.3504	7.86	169.7	0.173	
	82	71.480	1.3188	4.09	88.2	0.101	
	83	72.200	1.3074	10.26	221.5	0.149	
	84	72.440	1.3036	9.87	213.2	0.176	
	85	72.720	1.2993	12.88	278.0	0.225	
	86	73.460	1.2880	7.52	162.3	0.240	
	87	79.420	1.2057	5.04	108.7	0.126	

PEAKS FILE LISTING

DATA FILE: COR003.PKS COLLECTED ON 16-NOV-93 AT 14:02:07
SAMPLE IDENTIFICATION: SAMPLE K
START 2THETA: 3.000 STOP 2THETA: 80.000
STEP SIZE: 0.020 SCAN SPEED: 2.500
COUNTING TIME: 2.000
PEAKS FOUND ON: 16-NOV-93 AT 15:28:25

PEAK FINDING PARAMETERS

THRESHOLD VALUES:	5.0,10.0
RELATIVE CUTOFF INTENSITY:	0.5
TYPICAL FULL WIDTH-HALF MAXIMUM:	0.20
MINIMUM FULL WIDTH-HALF MAXIMUM:	0.10
ALPHA 2 REMOVAL USING CODE:	1

	PEAK	2-THETA	D-SPACE	I(REL)	I(CPS)	FWHM	
	1	10.580	8.3549	13.88	296.9	0.127	
U	2	12.246	7.2220	4.51	96.4	0.000	U
	3	19.800	4.4803	7.04	150.4	0.149	
	4	21.740	4.0847	18.85	403.0	0.264	
	5	22.020	4.0334	16.93	361.9	0.183	
	6	24.900	3.5730	9.63	205.9	0.216	
	7	27.480	3.2431	13.13	280.8	0.206	
	8	27.800	3.2065	100.00	2138.1	0.119	
	9	28.060	3.1774	59.67	1275.9	0.113	
U	10	28.521	3.1271	8.36	178.7	0.000	U
U	11	28.928	3.0840	2.71	58.0	0.000	U
	12	29.480	3.0275	9.54	204.1	0.183	
	13	29.840	2.9918	8.06	172.4	0.103	
	14	33.080	2.7058	7.26	155.3	0.106	
U	15	36.189	2.4802	5.59	119.4	0.000	U
	16	42.220	2.1388	27.03	577.9	0.148	
U	17	47.623	1.9080	5.01	107.1	0.000	U
U	18	48.498	1.8756	4.27	91.2	0.000	U
	19	57.360	1.6051	6.79	145.2	0.132	
U	20	65.795	1.4182	4.04	86.4	0.000	U
U	21	69.279	1.3552	2.36	50.5	0.000	U
U	22	73.905	1.2814	2.90	62.0	0.000	U

PEAKS FILE LISTING

DATA FILE: COR002.PKS
COLLECTED ON 16-NOV-93 AT 13:28:00
SAMPLE IDENTIFICATION: SAMPLE H
START 2THETA: 3.000
STOP 2THETA: 80.000
STEP SIZE: 0.020
SCAN SPEED: 2.500
COUNTING TIME: 2.000
PEAKS FOUND ON: 16-NOV-93 AT 14:39:21

PEAK FINDING PARAMETERS

THRESHOLD VALUES:	5.0,10.0
RELATIVE CUTOFF INTENSITY:	0.5
TYPICAL FULL WIDTH-HALF MAXIMUM:	0.20
MINIMUM FULL WIDTH-HALF MAXIMUM:	0.10
ALPHA 2 REMOVAL USING CODE:	1

	PEAK	2-THETA	D-SPACE	I(REL)	I(CPS)	FWHM	
	1	20.060	4.4228	38.11	314.5	0.126	
	2	20.660	4.2957	34.45	284.3	0.164	
	3	21.980	4.0406	39.04	322.2	0.166	
U	4	23.705	3.7503	17.29	149.5	0.000	U
U	5	24.715	3.5994	21.10	182.4	0.000	U
U	6	26.579	3.3510	22.60	195.4	0.000	U
	7	27.760	3.2111	68.20	562.7	0.178	
	8	29.420	3.0335	100.00	825.1	0.242	
	9	31.440	2.8431	26.00	214.5	0.172	
U	10	36.043	2.4899	24.27	209.9	0.000	U
	11	39.440	2.2829	29.00	239.3	0.104	
	12	39.740	2.2663	17.26	142.4	0.107	
U	13	43.241	2.0906	14.97	129.4	0.000	U
	14	47.560	1.9103	46.15	380.8	0.157	
	15	48.560	1.8733	21.31	175.8	0.137	
	16	60.800	1.5222	20.68	170.6	0.153	
	17	61.100	1.5155	14.47	119.4	0.114	
U	18	64.798	1.4376	9.69	83.8	0.000	U
	19	65.760	1.4189	23.32	192.4	0.140	